Semiconductor Photonics:
Nano-Structured Materials and Devices

Edited by

S.J. Chua, J.H. Teng, O. Wada,
R. de la Rue and X.H. Tang

TRANS TECH PUBLICATIONS

UTSA Library
C10797175

WITHDRAWN
UTSA LIBRARIES

Semiconductor Photonics: Nano-Structured Materials and Devices

RENEWALS 458-4574
DATE DUE

GAYLORD PRINTED IN U.S.A.

Digitized by the Internet Archive
in 2022 with funding from
Kahle/Austin Foundation

https://archive.org/details/semiconductorpho0000unse

Semiconductor Photonics: Nano-Structured Materials and Devices

Edited by

S. J. CHUA, J. H. TENG, O. WADA,
R. DE LA RUE and X. H. TANG

TRANS TECH PUBLICATIONS LTD
Switzerland • UK • USA

Copyright © 2008 Trans Tech Publications Ltd, Switzerland

All rights reserved. No part of the contents of this book may be reproduced or transmitted in any form or by any means without the written permission of the publisher.

Trans Tech Publications Ltd
Laubisrutistr. 24
CH-8712 Stafa-Zurich
Switzerland
http://www.ttp.net

Volume 31 of
Advanced Materials Research
ISSN 1022-6680

Full text available online at *http://www.scientific.net*

***Distributed** worldwide by*

Trans Tech Publications Ltd
Laubisrutistr. 24
CH-8712 Stafa-Zurich
Switzerland

Fax: +41 (44) 922 10 33
e-mail: sales@ttp.net

and in the Americas by

Trans Tech Publications Inc.
PO Box 699, May Street
Enfield, NH 03748
USA

Phone: +1 (603) 632-7377
Fax: +1 (603) 632-5611
e-mail: sales-usa@ttp.net

Printed in the Netherlands

Library
University of Texas

Introduction

This special issue is a collection of papers presented in Symposium D, Semiconductor Photonics: Nano-structured Materials and Devices, in the International Conference on Materials for Advanced Technologies (ICMAT) 2007. The conference was organized by the Singapore Materials Research Society and held in Singapore on July 1-6, 2007. It was co-sponsored by the National University of Singapore, the Institute of Materials Research and Engineering and the Nanyang Technological University. The symposium attracted 157 registered participants from Asia Pacific, Europe and USA. The papers and presentations cover a wide range of topics in nano-structure related semiconductor photonics, such as quantum dot, quantum wire, nano-wire, nano-rod, nano-crystals, photonic crystals, ZnO material, III-V compound semiconductors, Si photonics, and organic optoelectronic devices. Only original research papers, which have been peer reviewed, are collected in this special issue. We hope this issue will be a useful reference for some of the recent progress in the active and wide-ranging area of semiconductor photonics in both materials and devices. We would like to thank all the authors and the reviewers of the papers published in this issue for their invaluable contributions.

S. J. CHUA	National University of Singapore, Singapore
J. H. TENG	Institute of Materials Research and Engineering, Singapore
O. WADA	Kobe University, Japan
R. DE LA RUE	University of Glasgow, UK
X. H. TANG	Nanyang Technological University, Singapore

Table of Contents

Introduction v

Quantum Dots by QED
T. Prevenslik 1

Charge Effect in Organic Field-Effect Transistors - Analyzing Hall Measurements in the Accumulation Layer
H.L. Kwok 4

Surface Optical Waves in Semi-Infinite One-Dimensional Photonic Crystals Containing Alternating Layers of Positive and Negative Media
A. Soltani Vala, J. Barvestani and M. Kalafi 7

Titania/Ormosils Organic-Inorganic Hybrid Thin Films Doped with Azobenzene Small Molecules for Optical Switch Applications
W.X. Que, M. Sun, C.Y. Jia, L. Cheng, Z. Sun, L.L. Wang and X. Hu 11

Sol-Gel Fabrication of Low Temperature Organic-Inorganic Hybrid Film Patterns for Photonic Applications
W.X. Que, X.M. Ren, W. Zhang, W.J. Jiang, Y. Gao and X. Hu 14

Morphology and Crystal Quality of InAs QDs Grown by MOVPE Using Different Growth Modes
Z.Y. Yin, X.H. Tang, J.X. Zhang, D. Sentosa, J.H. Teng, A.Y. Du and M.K. Chin 17

Modulation of Three Dimensional Photonic Band Gap in Visible Region
Y.P. Liu, Y.P. Guo, Z.J. Yan, C.M. Huang and Y.Y. Wang 20

Raman Scattering from GaAs Nanowires Grown by Molecular Beam Epitaxy
N. Begum, A.S. Bhatti, M. Piccin, G. Bais, F. Jabeen, S. Rubini, F. Martelli and A. Franciosi 23

Design and Analysis of 2D Photonic Crystal Waveguides for High Coupling Efficiency
M. Wu, H.R. Liu, W.J. Tong and D.X. Huang 27

Novel Passivation Method in the Fabrication of Submicron InGaAsP/InP Ridge Waveguide Lasers
E.L. Lim, J.H. Teng, S.J. Chua, J.R. Dong, N. Ang and L.F. Chong 30

Cu-Doped SiO_2 Induced Atomic Interdiffusion in Semiconductor Nano Heterostructures
V. Hongpinyo, Y.H. Ding, J. Anderson, H.S. Djie, B.S. Ooi, R.R. Du, A. Ganjoo and H. Jain 33

DFB Lasers with Tilted Waveguide for Multi-Wavelength Generation
L.F. Chong, J.H. Teng, E.L. Lim, N.S.S. Ang, J.R. Dong and S.J. Chua 36

Enhanced UV Photodetector Responsivity in Porous GaN/Si(111) by Metal-Assisted Electroless Etching
L.S. Chuah, Z. Hassan and H. Abu Hassan 39

Growth, Surface Morphology and Optical Properties of Gallium Nitride Nanowires
V. Suresh Kumar and J. Kumar 42

Optical Reflection from a Monolayer of Embedded Nano-Objects Covered by a Thick Capping Layer
C.M.J. Wijers and O. Voskoboynikov 52

Visible Light Emission from Ordered Nanopatterned InP Surface
S.K. Mohanta, R.K. Soni, S. Tripathy and S.J. Chua 56

Dependence of the Absorption Spectra of III-V Semiconductor Quantum Dots on the Size Distribution
S. Kumar, D. Biswas and T. Das 59

Conspicuous Presence of Higher Order Transitions in the Photoluminescence of $In_xGa_{1-x}N$/GaN Quantum Wells
D. Biswas, T. Das, S. Kabi and S. Kumar 62

The Study of Femto-Second Laser Induced Damage Threshold on Semi-Insulating GaAs Wafer
C.Y. Li and Y.G. Wang 65

Temperature-Controlled Catalytic Growth and Photoluminescence Properties of ZnO Nanostructures
P.T. Huy, T.T. An, N.D. Chien and D.J. Kim 68

Fabrication and Optical Properties of ZnO Quantum Dots
X.H. Zhang, S.J. Chua, A.M. Yong, S.Y. Chow, H.Y. Yang, S.P. Lau, S.F. Yu and X.W. Sun 71

Intense Photoluminescence and Photoluminescence Enhancement of Silicon Nanocrystals by Ultraviolet Irradiation
P.T. Huy and P.H. Duong 74

Nitrogen Interstitial Defects in GaNAs Films Grown by MOCVD
D. Sentosa, X.H. Tang, S.J. Chua and Z.Y. Yin 77

Influence of Hydrogen Dilution of Silane on the Properties of nc-Si:H Films Grown by Layer-by-Layer Deposition Technique
G.B. Tong, S.M. Ab. Gani and S. Abdul Rahman 80

Defect Mediated Photonic Behavior of ZnO Nanocrystals
Y.Y. Tay, S. Li and M.L. Liang 83

Surface Structure Dependent Growth of InAs/InAlAs Quantum Wires on InP(100).
M.F. Casco, J.V. Misa, M. Defensor, A. Garcia and A. Salvador 86

Characteristics of Ge Nanocrystals Grown by RF Magnetron Sputtering
R.K. Singha, K. Das, S. Das, A. Dhar and S.K. Ray 89

Photoluminescence and Fractal Properties of Diverse Carbothermal Zinc Oxide Nanostructures
E.R. Magdaluyo, I.H.J. Arellano, A.K.G. Tapia, R.V. Samargo and L.M. Payawan 92

Band Structure and Optical Gain of 1.3 um GaAsSbN/GaAs Compressively Strained Quantum Well Laser
B. Dong, W.J. Fan and Y.X. Dang 95

Fabrication of Photonic Crystals by Holographic Lithography Method
J.B. Yeo and H.Y. Lee 98

Optical and Structural Properties of Multi Deposition Film Derived SiO_2-TiO_2 Systems by Sol-Gel Process
M.Z.A. Malek, M.T. Zainuddin, A.M. Abdullah and A. Isnin 101

Investigation of Intersubband Transition in GaAs/AlGaAs Quantum Well Infrared Photodetectors
D.S. Li, W.J. Fan, Y.X. Dang, B.S. Ma, D.H. Zhang and S.F. Yoon 105

Growth of GaN Nano-Column on Si (111) Substrate Using Au+Ga Alloy Seeding by Pulsed Flow Method Using MOCVD
J.C. Song, D.H. Kang, S.H. Lee, E.S. Jang, D.W. Kim, K. Santhakumar and C.R. Lee 108

Raman study of Epitaxial lateral Overgrowth of GaN on Patterned Sapphire Substrate
D.H. Kang, J.C. Song, H. Song, D.W. Kim, I.H. Lee, K. Santhakumar and C.R. Lee 111

Mn, Cu Doping and Optical Properties of Highly Crystalline Ultralong ZnS Nanowires
N.D. Chien, H.V. Chung, P.T. Huy, D.J. Kim and M. Ferrari 114

***In Situ* Visualization of Layer Transitions during Convective Self-Assembly in a Sessile Drop**
L. Gao, Q.F. Yan, C.C. Wong and Y.M. Chiang 117

Optical and Surface Morphological Study of GaN Nanocolumn Grown on Gallium Coated Si by Molecular Beam Epitaxy
K. Santhakumar, D.H. Kang, J.C. Song, D.W. Kim, J.S. Kim, M.D. Kim and C.R. Lee 120

Nanometer-Scale $In_{0.5}Ga_{0.5}As$ Ring-Like Structure Grown by Droplet Epitaxy
N. Pankaow, S. Panyakeow and S. Ratanathammaphan 123

The Gas Sensitvity Character of WO_3 Nanosized Material
S.Z. Huang, W. Lin and W.Z. Chen 126

Effect of Oxygen Flow Rate and Temperature on the Structure of DC Sputtered Nanocrystalline Copper Oxide Films
M.J. Chiang, C.W. Wu and H.E. Cheng 129

In-Mole-Fraction and Thickness of Ultra-Thin InGaAs Insertion Layers Effects on the Structural and Optical Properties of InAs Quantum Dots
P. Boonpeng, S. Panyakeow and S. Ratanathammaphan 132

Investigation of Electrical Properties in Chalcogenide Thin Film According to Wave Length
H. Choi, H.K. Kim, Y.W. Koo, K.H. Nam, S.M. Koo, W.J. Cho and H.B. Chung 135

Luminescence Properties of ZnS:Er Quantum Dots with NIR Excitation
X.S. Zhang, X.Y. Dong, G.Y. Kai, D.Q. Dong, Y.F. Zhang and Z. Wang 138

The Synthesis and Crystallography of Some Novel ZnO Nano- and Micro-Crystals and Structures
Z.M. Li, F.Q. Xu and W.H. Zhang 141

Degradation of Photoluminescence in CdTe Nanoparticles Due to Cl_2 Contamination
H.C. Gardner, B. Patel, C. Bertoni, D.E. Gallardo and S. Dunn 150

Preparation and Characterization of Zn-Se Bilayer Structure
M. Singh, J.S. Arora, K. Awasthi, R. Nathawat and Y.K. Vijay 153

The Formation of InP Ring-Shape Nanostructures on $In_{0.49}Ga_{0.51}P$ Grown by Droplet Epitaxy
W. Jewasuwan, S. Panyakeow and S. Ratanathammaphan 158

Development of Low Size Dispersion, High Volume Fraction and Strong Quantum Confined CdS_xSe_{1-x} Quantum Dots Embedded in Borosilicate Glass Matrix and Study of their Optical Properties
A. Verma, P.K. Bhatnagar, P.C. Mathur, S. Nagpal, P.K. Pandey and J. Kumar 161

Tuning of Energy Band Gaps in Ternary Semiconductors
R. Jain 164

Luminescence Properties of ZnS:Mn Quantum Dots
X.S. Zhang, L. Li, D.Q. Dong, Z. Wang and X.Y. Dong 167

Surface and Structure of Porous Silicon Layers
J.M. Lu and X. Cheng 170

Broadband Emission in InAs/InGaAlAs Quantum-Dash-in-Well Laser
B.S. Ooi, H.S. Djie, A.S. Helmy and J.C.M. Hwang 173

Improved Carbon Counter Electrodes for Dye Sensitized Solar Cells
H.S. Lee, H.Y. Lee, S.Y. Ahn, K.H. Kim and J.Y. Kwon 176

Development of Fabrication Process and Electrostatic Microactuator for a Mechanically Tunable 2-D Photonic Crystal
B.P. Chaudhuri, B. Thubthimthong and F.A. Chollet 179

Nano-Scale Bandgap Engineering Using Nitrogen Implantation: Quantum-Well, Quantum-Dash and Quantum-Dot Nanostructures
Y.H. Ding, V. Hongpinyo, H.S. Djie and B.S. Ooi 182

Higher Crystalline Volume Yields from Excimer Laser Crystallization of Amorphous Silicon with an Asymmetrical Peak Pulse Profile
A.A.D.T. Adikaari, N.K. Mudugamuwa and S.R.P. Silva 185

Distributed Feedback Laser Using Buried Dielectric Grating
J.H. Teng, L.F. Chong, J.R. Dong, S.J. Chua, N.S.S. Ang, Y.J. Wang and E.L. Lim 189

Electrical Properties and UV Response of Single ZnO Nanorod
H.Q. Le and S.J. Chua 192

Population Dynamics of Excitons in Silicon Nanocrystals Structures under Strong Optical Excitation
O.A. Shalygina, D.M. Zhigunov, D.A. Palenov, V.Y. Timoshenko, P.K. Kashkarov, M. Zacharias and P.M. Koenraad 196

Investigation of Morphology and Photoluminescence of Hydrothermally-Grown ZnO Nanorods Grown on Substrates Pre-Coated with ZnO Nanoparticles
C.B. Tay and S.J. Chua 199

Dicing Laminated Wafer for QFN 3D Stacked Die Packaging
S. Abdullah, Z. Endut, I. Ahmad, A. Jalar and S.M. Yusof 202

DFB Waveguide All-Optical Switching Devices Employing Pump-Induced Refractive Index Change in GaInAsP
T. Mizumoto, Y. Akano, K. Tamura and M. Yoshimura 206

Study of Thermal-Anneal-Induced Rearrangement of N-Bonding Configurations in GaInNAs/GaAs Quantum Well
V. Dixit, H.F. Liu and N. Xiang 209

Nano Size Lanthanum Doped Semiconductors: Synthesis, Characterization and their Photocatalytic Activity
S. Anandan, Y. Ikuma, T. Kudoh, Y. Ogita and V. Murugesan 212

Structural Investigation of Cubic-Phase InN on GaAs (001) Grown by MBE under In- and N-Rich Growth Conditions
S. Kuntharin, S. Sanorpim, T. Nakamura, R. Katayama and K. Onabe 215

MOVPE Growth Window for High-Nitrogen GaAsN Alloy Films for Long Wavelength Emission
S. Sanorpim, F. Nakajima, R. Katayama and K. Onabe 218

A Comparison of the Structural Quality of High-In Content InGaAsN Films Grown on InGaAs Pseudosubstrate and on GaAs Substrate
S. Sanorpim, P. Kongjaeng, R. Katayama and K. Onabe 221

Optical Transitions in InGaPN/GaP Single Quantum Wells on GaP(100) Substrates by MOVPE
S. Sanorpim, D. Kaewket, S. Tungasmita, R. Katayama and K. Onabe 224

Annihilation of Threading Dislocations in Regrown GaN on Electrochemically Etched Nanoporous GaN Template with Optimization of Buffer Layer Growth
C.B. Soh, H. Hartono, S.Y. Chow and S.J. Chua 227

Optical Nanowires for Microwave Applications
D. Decoster, M. Carette, M. Lesecq, D. Lauvernier, M. Zegaoui, D. Bernard, J.P. Vilcot and J. Chazelas 230

Quantum Information Processing in Photonic Crystals
M.R. Singh 236

Phase Transition in Photonic Crystals Doped with Nanoparticles
M.R. Singh 242

InGaAsP/InP Electroabsorption Modulator with Single-Sided Large Optical Cavity by Low-Pressure MOCVD
H. Yang, M.K. Chin, D.C.S. Lim, S.Y. Lee, C.W. Lee and H.L. Zhu 246

Demonstration of the Formation of Porous Silicon Films with Superior Properties Formed on Polished (100) Si with Screen-Printed Back Contacts
P. Singh, S.N. Sharma, G. Bhagavannarayana, M. Husain and M. Lal 249

Author Index 255

Keyword Index 259

Advanced Materials Research Vol. 31 (2008) pp 1-3
online at http://www scientific net
© 2008 Trans Tech Publications, Switzerland

Quantum Dots by QED

Thomas Prevenslik
4H Greenmont, Discovery Bay, Hong Kong
Email: waiguoren0@163.com

Keywords: quantum dots, QED

Abstract. High quantum dot (QD) efficiency may be explained by excitons generated in the quantum electrodynamics (QED) confinement of electromagnetic (EM) radiation during the absorption of the laser radiation. There is general agreement that by the Mie theory laser photons are fully absorbed by QDs smaller than the laser wavelength. But how the absorbed laser photons are conserved by a QD is another matter. Classically, absorbed laser radiation is treated as heat that in a body having specific heat is conserved by an increase in temperature. However, the specific heats of QDs vanish at frequencies in the near infrared (NIR) and higher, and therefore an increase in temperature cannot conserve the absorbed laser photons. Instead by QED, the laser photon energy is first suppressed because the photon frequency is lower than the EM confinement frequency imposed by the QD geometry. To conserve the loss of suppressed EM energy, an equivalent gain must occur. But the only EM energy allowed in a QED confinement has a frequency equal to or greater than its EM resonance, and therefore the laser photons are then up-converted to the QD confinement frequency - the process called cavity QED induced EM radiation. High QD efficiency is the consequence of multiple excitons generated in proportion to very high QED induced Planck energy because at the nanoscale the EM confinement frequencies range from the vacuum ultraviolet (VUV) to soft x-rays (SXRs). Extensions of QED induced EM radiation are made to surface enhanced Raman spectroscopy (SERS) and light emission from porous silicon (PS).

Introduction

The efficiency of QDs is the electrical power produced as a percentage of the absorbed radiation. Efficiency in the conversion of photons to excitons in bulk semiconductors is usually based on the 1 photon – 1 exciton rule for photons having Planck energy greater than the band gap, the upper limit determined [1] to be about 31 %. The highest QD conversion efficiency [2] sometimes called carrier multiplication (CM) is typically about 66 %. Currently, high QD efficiency is explained by impact ionization [3] that allows more than 1 exciton to be successively generated in the absorption of 1 photon with Planck energy greater than the band gap of the semiconductor. But impact ionization by successive absorption takes time while experiments [4] show the excitons are formed instantaneously. Further, impact ionization fails to explain [5] almost the same QD efficiencies found for the widely different CdSe and PbSe semiconductors.

Subsequently, the "coherent–CM" mechanism was proposed [6,7], but required very large Coulomb coupling that could not be experimentally [5] verified, thereby prompting the similar QD efficiencies found for the quite different CdSe and PbSe to be explained by *virtual* exciton states.

In this paper, QDs upon the absorption of laser photons generate multiple excitons in proportion to the Planck energy induced by QED induced EM radiation, the proportionality known since the 1950's for excitons [8] generated in bulk Ge under x-rays (XRs). *Virtual* exciton states are not necessary. Prior applications of QED induced EM radiation [9] were directed to frequency up-conversion of photons in evacuated nanocavities, say by bubbles in the electrification of flowing liquids or by the Casimir effect for gaps between solids. The only difference between QED confinement of photons in solid NPs and evacuated cavities is the refractive index, but even this difference is inconsequential because the refractive index may be treated as unity for QDs small in relation to the photon wavelength, and therefore QED induced EM radiation in QDs is the same as that in nanocavities.

Theoretical Background

QED induced EM radiation for a laser photon absorbed in the QD is shown in Fig. 1. The QD is taken to be spherical of radius R having an EM confinement frequency beyond the VUV. By the Mie theory, a laser photon is absorbed in the QD. Absent specific heat at VUV frequencies, the EM energy of the absorbed laser photon cannot be conserved by an increase in QD temperature. Instead, the laser photon absorbed in the QD momentarily has a frequency lower than the VUV confinement frequency, and therefore is suppressed by QED. To conserve the loss of suppressed photon energy under QED constraints, an equivalent amount of EM energy is gained at the EM confinement frequency. Depending on the QD diameters, the suppressed laser photon is up-converted to frequencies from the VUV to SXRs. Multiple excitons are then generated in proportion to the Planck energy of the QED induced EM radiation.

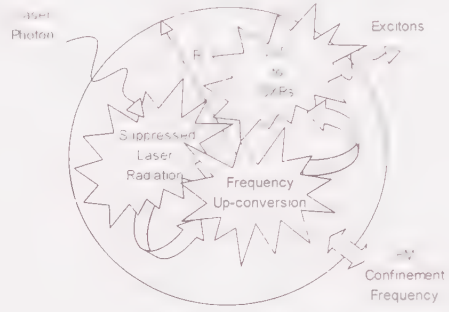

Figure 1 Spontaneous Multiple Excitons in QDs by QED

Thermal Conservation. In the alternative to conserving the absorbed laser photon by QED, the absorbed laser photon may be conserved by an increase in QD temperature. Treating the QD as a collection of atoms having 3 DOF with each DOF as a Planck oscillator given by the Einstein-Hopf relation, the dimensionless specific heat C* is given by,

$$U = 3N_A \frac{\frac{hc}{\lambda}}{\left[\exp\left(\frac{hc}{\lambda kT}\right)-1\right]} \quad \rightarrow \quad C = \frac{\partial U}{\partial T} \quad \rightarrow \quad C^* = \frac{C}{3N_A k} = \frac{\left(\frac{hc}{\lambda kT}\right)^2 \exp\left[\frac{hc}{\lambda kT}\right]}{\left[\exp\left(\frac{hc}{\lambda kT}\right)-1\right]^2} \qquad (1)$$

where, U is the total QD energy, h and k are Planck's and Boltzmann's constants, λ is wavelength, T is absolute temperature, and N_A is the number of atoms. For EM confinement frequencies higher than the IR, $C^* \rightarrow 0$ and the EM energy of the absorbed laser photon cannot be conserved by an increase in temperature.

QED Conservation. By QED, the EM energy of the absorbed laser photon is conserved by an increasing its frequency to the EM confinement frequency, thereby inducing Planck energy far in excess of the typical semiconductor band-gaps. Excitons are formed in proportion to the Planck energy, thereby exceeding the 1 photon – 1 exciton rule for the bulk. The EM confinement wavelength λ_{EM} imposed by the QD geometry upon the absorption of the laser photon and the Planck energy E induced in the QD is,

$$\lambda_{EM} = 4n_r R = 2n_r D \quad \text{and} \quad E = \frac{hc}{4Rn_r} = \frac{hc}{2Dn_r} \qquad (2)$$

where, D is the QD diameter, D = 2R, and n_r is the refractive index of the NP. For QDs having D smaller than the photon wavelength, $n_r = 1$.

Discussion

QDs avoid the limitation of the 1 photon – 1 exciton rule in the bulk because QED induces the absorbed laser photon to increase its frequency to VUV SXR levels, thereby providing Planck energies far beyond the band-gap necessary for generating multiple excitons. For bulk Ge, every 2.5 eV of XR energy [8] generated 1 exciton. Recently, 3 – NIR laser photons at 800 nm were found [6] to generate 7 excitons in QDs of PbSe. Fig. 2(a) shows Planck energy E and the number of excitons for Ge, and (b) gives the number of excitons v Planck energy E for PbSe and Ge.

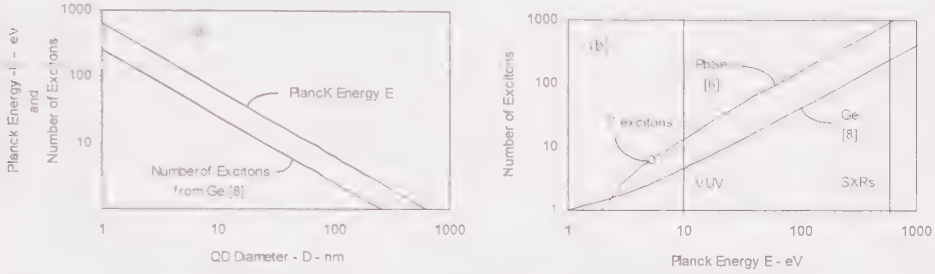

Figure 2 – (a) Planck Energy and Number of Excitons v QD Diameter
(b) Number of Excitons v. Planck Energy for Ge and PbSe.

Conclusions

QDs generate multiple excitons in proportion to the Planck energy induced by QED. However, the number of excitons depends on the laser energy available. At the upper limit, the 1 nm PbSe QD inducing SXR Planck energies of 621 eV requires a pulsed NIR femtosecond laser [6] supplying about 400 NIR photons at 800 nm to generate 870 excitons.

Extensions

Since the 1970's, SERS is not well understood although numerous electric field and chemical enhancement mechanisms have been proposed. QED induced EM radiation offers yet another explanation in that similar to QDs high Planck energy is produced in nanoscale roughened metal surfaces. Similarly, QED induced radiation explains the enhanced emission from PS.

References

[1] W. Shockley and H. Quiesser, J. Appl. Phys. Vol. 32, pp. 510-9 (1966)

[2] A. Zunger, MRS Bulletin, February, pp. 35-52 (1998)

[3] R. D. Schaller, et al., Nano Letters, Vol. 5, pp. 424-9 (2005)

[4] R. Ellingson, et al., Nano Lett. 5, pp. 865, (2005)

[5] R. D. Schaller, et al., Appl. Phys. Lett., 87, pp. 253102 (2005)

[6] V. I. Klimov, J. Phys. Chem. B, 110, pp. 16827-45 (2006)

[7] J. Nozik, Physica E, Vol. 14, pp. 115-9 (2002)

[8] S. Koc, Czech. J. Phys. 7, pp. 91-5 (1957)

[9] T. Prevenslik, See information on http://www.geocities.com/thomas_prevenslik

Advanced Materials Research Vol. 31 (2008) pp 4-6
online at http://www.scientific.net
© 2008 Trans Tech Publications, Switzerland

Charge Effect in Organic Field-effect Transistors - Analyzing Hall Measurements in the Accumulation Layer

H.L. Kwok

Centre of Advanced Materials & Related Technology and Dept. of ECE, University of Victoria, Victoria, Canada
Harry.kwok@ece.uvic.ca

Keywords Hall and conductivity measurements, trap states, hopping, mean free distance

Abstract. Hall measurement is an effective means to measure carrier density and mobility in metals and semiconductors. This work examined the carrier mobility determined in the accumulation layer of organic field-effect transistors (OFETS) and proposed a method to explain data taken from rubrene single-crystal devices. The model was used to extract information on the trap states and the properties of the transport layer at different temperature.

1. Introduction

The study of charge transport in organic field-effect transistors (OFET) is important in understanding the operation of these devices. There is however some significant difficulties in determining accurately the carrier density in the accumulation layer formed by induced charges in the presence of a gate bias. Interface charges for instance often obscure the channel properties by changing the turn-on voltage. Recently, Podzorov et al[1] reported interesting measurements of OFETs formed on rubrene single crystals and observed different mobility values when the data were extracted separately from Hall measurements and capacitance-voltage (*C-V*) measurements. This work attempts to analyze the data in greater details and put forward a model that explains the difference. The main distinction between this work and the proposed model in [1] lies in the fact that we have chosen to explain the observed mobility difference in terms of a broadening in the interface charge layer at low temperature. We are able to deduce the activation energy of the trapped carriers and the energy level linked to the trap states. Our observations suggest that charge transport in the accumulation layer is similar to that of metals at room temperature (and higher), while at low temperature current flow extend into the rubrene substrate and charge transport is due to hopping. We also discuss potentially how the performance of the rubrene single-crystal OFETs is optimized.

2. Theory

Hall measurement was originally developed for measuring carrier densities in metals and semiconductors[2]. Assuming "free" carriers move longitudinally in a rectangular sample, the application of a transverse magnetic field will produce carrier flow sideway resulting in charge accumulation in the orthogonal direction. This generates a Hall voltage V_H, which is inversely proportional to the carrier density. Similarly, Hall measurement is applicable to the accumulation layer of an OFET, even though the situation maybe complicated by the presence of trap states and interface scattering. As suggested in [1], the baseline voltage of V_H tends to change over time and V_H ought to be measured differentially by reversing the polarity of the magnetic field. An additional pair of electrodes placed along the channel should be used to determine the channel conductivity. Ideally, trapped charges do not possess a well-defined drift velocity and their effect will not show up during Hall measurements. The Hall mobility is:

$$\mu_H = V_H \sigma / BI \qquad (1)$$

where σ is conductivity, B is the magnetic flux density, and I is the terminal current. Alternatively, mobility can be determined if the carrier density is measured from the capacitance-voltage (*C-V*) curves of the OFET. This will be called conductivity mobility μ_C, which involves both the "free" carriers as well as the trapped charges. It is given by:

$$\mu_C = (\mu_f p_f + \mu_t p_t)/(p_f + p_t) \quad (2)$$

where μ_f (= μ_H) is the "free" carrier mobility, p_f is the "free" carrier density, μ_t is the trapped carrier mobility, and p_t is the trapped charge density.

Assuming $p_t/p_f = \alpha$, it can be shown that:

$$\mu_C = \mu_H/(1 + \alpha) + \mu_t/(1/\alpha + 1) \quad (3)$$

The observed conductivity mobility is therefore a weighted sum of μ_H and μ_t. In the limits, one can identify two transport regimes: one when "free" carriers dominate and another when trapped charges have the greater effect.

3. Results

In the previous section, our analysis identifies the two regimes depending on the relative importance of μ_H and μ_t. Fig.1a shows the hole mobilities from Hall and the *C-V* measurements reported in [1]. As mentioned earlier, μ_H arises from the "free" carriers and has 1/T dependence. This appears to be the case at all temperature. The effect of the trap states (as reflected in μ_t) on the other hand only shows up more at low temperature when the trap states are filled. Assuming $\mu_t = \mu_0 \exp(-\Delta/kT)$, the slope gives an activation energy[3] Δ = 39 meV and $\mu_0 = 1.05 \times 10^2$ $cm^2V^{-1}s^{-1}$.

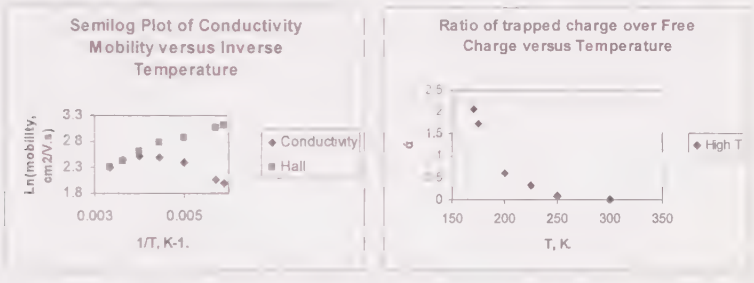

Fig.1: a) Hall and conductivity mobility data as a function of inverse temperature; and b) a plot of ά versus T.

Log of ratio of trapped charge over free charge versus Inverse Temperature
1/kT, eV-1.
Mean Free Distance versus Temperature
Mean free distance, nm.
T K.

Fig.2: a) A plot of log(ά) versus 1/kT; and b) a plot of the mean free distance versus temperature.

Assuming the contribution from μ_t to be small at high temperature, we computed α (= p_t/p_f) using Eqn (3) and plotted it as a function of temperature in Fig.1b. As observed, only a very small fraction of the trap states is occupied at high temperature. Since the trap states are at equilibrium with the HOMO (in the case of a p-type organic semiconductor), it is possible to estimate the energy location of the trap states measured from the HOMO using a plot of log(α) versus 1/kT as shown in Fig.2a. The slope of the curve suggests a trap level ~ 0.4 eV above the HOMO (note that the energy gap of rubrene is ~ 2.3 eV). It is also of interest to estimate the mean free distance l of the trapped charges. This could be done assuming a thermal velocity given by $v = \sqrt{3kT/m}$, where k is the Boltzmann constant, and m is the electron mass. The mean free distance is given by: l =

$(3mkT)^{1/2}\mu_C/q$. Fig.2b shows a plot of l versus T. As observed, l varies from ~ 0.7 nm at 300K to ~ 1.1 nm at 150K.

4. Discussion

Our model put forward to represent the OFET assumes a 2-dimensional charge sheet in the accumulation layer and current flow both in the charge sheet and in the crystalline substrate. "Free" holes reside in the accumulation layer is responsible for current flow at room temperature which may be associated with polaron states (charge states associated with lattice vibrations[4]). At room temperature, traps are primarily empty due to thermal excitation and the Hall voltage is inversely linked to the hole density (Eqn.(1)). As temperature decreases, the trap states begin to fill but their presence will not be felt in the Hall measurements which are unaffected by the trapped charges. Measurements of the conductivity mobility however are reduced as the trapped charges contribute differently to current flow in comparison with the "free" carriers. As more "free" carriers move into the crystalline substrate at low temperature, hopping mobility becomes important. The computed mean free distance of the trapped charges also increases from about 0.7 nm at 300K to more than 1 nm at 150K. Since the intermolecular distance of rubrene is ~ 1nm, one can expect increasing importance in intermolecular charge transport at low temperature. There remains the important question of what is the limiting factor for the "low" carrier mobility observed in the rubrene single-crystal OFETs (bearing in mind that the measured value is high compared to most organic semiconductors). We believe this is linked to the small mean free distance of the holes/polarons in the accumulation layer (with a value even lower than found in metals). Assuming charge hopping mobility to be primarily thermally activated[5], the intrinsic carrier mobility in rubrene single-crystal OFET at room temperature can be higher than ~ 20 $cm^2V^{-1}s^{-1}$.

5. Conclusions

Hall measurement remains a useful tool in determining carrier mobility in the 2-dimensional accumulation layer of the OFETs. While rubrene single-crystal OFETs have high carrier mobility amongst similar devices, their ability to conduct a sizable current is hampered by the short mean free distance of the carriers. Based on our observations, there is evidence to suggest that current conduction in the accumulation layer may be akin to metallic charge transport (with 1/T dependence). In the crystalline bulk, charge mobility is dominated by hopping which in principle can be further improved if the thermal activation energy of the trap states is lowered.

Acknowledgements: This work is supported in part by NSERC, Canada.

References

[1] V. Podzorov, E. Menard, J.A. Rogers, and M.E. Gershenson, Phys Rev Lett, **95** (2005) pp.226601-1-4.
[2] H.L. Kwok, *Electronic Materials*, PWB Publishing, Boston USA (1997).
[3] S. Nakasuji, D. Dobrosavljevic, D. Tanaskovic, M.Minakata, H. Fukazawa, and Y. Maeno, Phys. Rev Lett, **93**, (2004) pp.146401-1-4.
[4] K.Hannewald, V.M. Strojanovic, J.M.T. Schellekens, and P.A. Bobbert, Phys Rev **B69**, (2004) pp.075211-1-7.
[5] A. Troisi, and G. Orlandi, Phys Rev Lett, **96** (2006) pp.086601-1-4.

Advanced Materials Research Vol. 31 (2008) pp 7-10
online at http://www.scientific.net
© 2008 Trans Tech Publications, Switzerland

Surface optical waves in semi-infinite one-dimensional photonic crystals containing alternating layers of positive and negative media

A Soltani-Vala[1, 2], J Barvestani[1, 2, a], M Kalafi[1, 2]

[1]Research Institute for Applied Physics and Astronomy, Tabriz University, Tabriz 51665-163, Iran

[2]Physics Faculty, University of Tabriz

[a]barvestani@tabrizu.ac.ir

Keywords: photonic crystals, surface states, left handed material

Abstract. An analytical direct matching procedure within the Kronig-Penney model applied to analyze the dispersion behavior of the localized surface states supported in the surface of a semi-infinite one-dimensional photonic crystals truncated with air. The photonic crystal containing alternating layers of positive and negative media. In the case of the conventional indices, as the incident light changes from normal to oblique incidence, the surface modes shifts into higher frequencies. For this reason, the phenomenon of photonic band gap has been used only under a narrow range of frequencies of light incident at a particular angle or in a particular angular range. We have showed that by choosing some proper value for the PC parameters, zero and negative dispersion of surface modes emerge in a large range of $k_{\parallel}$, and, due to the different nature of the band structure the surface modes are more localized compared to those appeared in the conventional PC.

PACS: 42.65.-k, 42.70.Mp, 42.70.Qs, 73.20.At, 78.20.Nv, 63.20.Pw, 68.65.Cd

1. Introduction

Aside from their intrinsic interest, surface electromagnetic waves have recently been proposed as a way to efficiently inject light into a photonic crystal waveguide, or to extract a focused beam from a channel [1-4]. It is well known that when an ideal infinite PC is truncated, localized surface waves can appear on the truncation surface of semi-infinite PC. These modes are electromagnetic fields that decay exponentially along the normal direction away from the surface into both the bulk crystals and the homogeneous background [5-8]. Surface modes have become a familiar physical concept in the optics and physics community thanks to the long-history investigation on surface plasmons, a kind of localized surface wave that is typically excited in metal films. Surface plasmons have already found use in a wide variety of areas such as nonlinear optics, optical modulators and sensors [9, 10]. In the case of the conventional indices, as the incident light changes from normal to oblique incidence, the surface modes shifts into higher frequencies. For this reason, the phenomenon of photonic band gap has been used only under a narrow range of frequencies of light incident at a particular angle or in a particular angular range.

In this paper, we have theoretically investigated localized surface states supported at the surface of a semi-infinite 1D PC containing alternating layers of positive and negative media. Negative media in which the dielectric permittivity ε and magnetic permeability μ are simultaneously negative, have received a great deal of attention during the last few years [11]. In our calculations, the dielectric permittivity and magnetic permeability are, in general, assumed to take constant values. Although these parameters in left hand materials are in general frequency dependent, our results can be used to design specific metamaterials that would lead to a typical behavior around a given frequency. We have demonstrated that stacking alternating layers of positive and negative leads to a type of surface modes which possesses such properties as independence on the incident angels. This kind of dispersion has been reported in one-dimensional PC containing a defect layer with a negative refraction index. The zero and negative dispersion phenomena may be useful in the design of large incident angle filters and narrow frequency and sharp angular filters, respectively [12]. This paper is arranged as follows. In section 2, we theoretically applied the direct matching

procedure for solution of localized surface optical modes in 1D PCs. We have followed similar procedure used by Steslica *et al* [13] in study of the localized electronic states in semiconductors superlattices. In section 3, the dispersion of surface modes has been investigated. Finally, section 4 concludes with brief comments.

2. The basic equations

In order to obtain the surface states in 1D PCs, the direct matching procedure within the Kronig-Penney model have been used [13]. Suppose each unit cell is composed of two layers, which are stacked along the z-axis direction with d_i and ε_i the thickness and the dielectric constant of the i th layer, respectively. Due to translational invariance in the XOY plane, the parallel wave vector $k_{||}$ is a conservative quantity in all domains of the crystal. For the TE polarization, electric field is parallel to interfaces (we choose **y** direction). The dispersion relation of the PC has the well–known form

$$\cos(kd) - \cos(k_{1z}d_1)\cos(k_{2z}d_2) - \frac{1}{2}\left(\frac{F_1}{F_2} + \frac{F_2}{F_1}\right)\sin(k_{1z}d_1)\sin(k_{2z}d_2) = B(\omega) \tag{1}$$

where the perpendicular wave vector component in each medium is given by $k_{iz} = [\varepsilon_i\mu_i(\omega/c)^2 - k_{||}^2]^{1/2}$, $F_i = k_{iz}/\mu_i$, (i= 1, 2), $k_{||}^2 = k_x^2 + k_y^2$, ω is the angular frequency, $d = d_1 + d_2$ is the lattice constant, and c is the light speed in vacuum [11]. It is well known that when any periodic system is limited, k should be complex

$$k = i\eta + \frac{n\pi}{d},\ \eta > 0, n = 0, \pm 1, \pm 2, \ldots \tag{2}$$

An explicit form of the Electric field in layer 1, $0 < z < d_1$, can be written as [13]

$$E_y^{PC}(z) = C_1(\sin(k_{1z}z) + \gamma\cos(k_{1z}z)) \tag{3}$$

Here γ is given by

$$\gamma = \frac{\sin(k_{1z}d_1) + \frac{F_1}{F_2}\cdot e^{ikd}\sin(k_{2z}d_2)}{e^{ikd}\cos(k_{2z}d_2) - \cos(k_{1z}d_1)}. \tag{4}$$

In order to preserve the finite nature of the electric field at $z \to -\infty$, it has to be taken as

$$E_y^s(z) = A_s e^{k_s z} \qquad k_s = [\varepsilon_s\mu_s(\omega/c)^2 - k_{||}^2]^{1/2} \tag{5}$$

the s indices related to the homogeneous semi-infinite media. To obtain the surface modes, by applying the boundary conditions at the interface of vacuum and PC we get the dispersion relation of the surface states $\frac{F_1}{\gamma} - F_s = 0,\ F_s = k_s/\mu_s$ (6)

which decay exponentially along the normal direction away from the surface into both the bulk crystals and the homogeneous background (see ref [14] for details). By eliminating η between (1) and (6) and use of (2), we get the following relation

$$S(\omega) = B(\omega) \mp [B^2(\omega) - 1]^{1/2} \qquad S(\omega) = (-1)^n e^{-\eta d} \tag{7}$$

Where – and + correspond to n even and n odd, respectively [15]. By doing this procedure, some spurious solutions are introduced. This can be identified and should be rejected by applying existence condition, $e^{-\eta d} < 1$ [16].

3. Results and Discussion

In this section, we discuss the numerical results obtained for the surface modes of a semi-infinite 1D PC containing alternating layers of positive and negative media. In contrary to the conventional PC, our calculations show that by choosing some proper value for the PC parameters, zero and negative dispersion of surface modes emerge in a large range of $k_{||}$. Figure 1a, b display the projected band structure for two choices of different appropriate parameters. The system under consideration has a configuration air$|\ \varepsilon_1\ \mu_1\ |\ \varepsilon_2\ \mu_2\ |\ \varepsilon_1\ \mu_1\ |\ \varepsilon_2\ \mu_2\ |\ldots$.

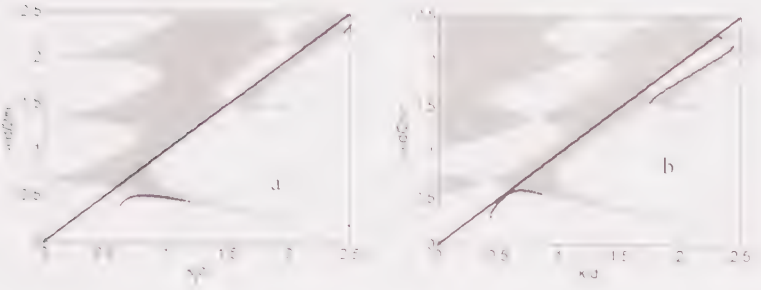

Figure 1. Calculated bulk and surface modes for TE polarization in a semi-infinite 1D PC containing alternating layers of positive and negative media when the terminating layer is left handed. The curves give $\omega d/c$ as a function of $k_{\parallel}d$. The gray and white regions are pass and forbidden bands, respectively. The dotted curves in the gaps are surface modes. The layer thicknesses are $d_1=2d/3$ and $d_2=d/3$, where $d=d_1+d_2$ is the lattice constant. The PC parameters choose as **a)** $\varepsilon_2=5$, $\mu_2=1$ and $\mu_1=-1$ and average index of refraction in the superlattice $n\rangle=(n_1d_1+n_2d_2)/d$ is zero. **b)** $\varepsilon_1=-1.5$, $\mu_1=-1$, $\varepsilon_2=5$ and $\mu_2=1$.

Now we change the stack sequence of the composite layers in the semi- infinite PC with respect to the air background so that the whole system has a configuration $|\text{air}|\varepsilon_2\ \mu_2|\ \varepsilon_1\ \mu_1|\ \varepsilon_2\ \mu_2|\varepsilon_1\ \mu_1\ |\ldots$. The calculated dispersion curves of the surface modes in these structures are displayed in figure 2. We can see from figure 2 that the surface modes are substantially different from the configuration in which the termination layer is left handed one. The dispersion of the surface modes is positive and similar to the dispersion of the surface modes in the conventional right handed PC. However, due to the different nature of the band structure in sample 2, e.g. wide band gap, the surface modes are more localized compared to those appeared in the conventional PC [17].

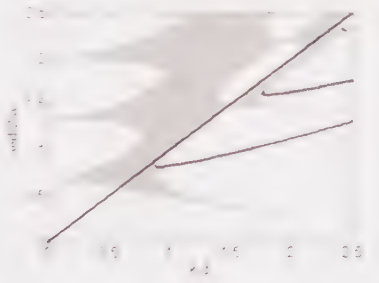

Figure 2. Calculated bulk and surface modes in a semi-infinite 1D PC containing alternating layers of positive and negative media when the terminating layer is right handed. Figure parameters are similar to the figure 1 a.

4. Conclusion

The direct matching procedure have been applied to obtain the localized surface optical modes in a semi-infinite 1D PC containing alternating layers of positive and negative media. We demonstrated that stacking alternating layers of positive and negative leads to a type of surface modes which posses zero and negative dispersion and also we show that if the terminating layer be right handed, we obtained the better localization.

References

[1] Moreno E, Martin Moreno L and Garcia-Vidal F J, *Phys. Rev. B* **69** 121402R (2004)

[2] Moreno E, Martin Moreno L and Garcia-Vidal F J, *Phot. And Nanostr.* **2** 97 (2004)

[3] Kramper P, Agio M, Soukoulis C M, Bimer A, Muller F, Wehrspohn, Gosele U and Sandoghdar V, *Phys. Rev. Lett.* **92** 113903(2003)

[4] Rahachou A I and Zozoulenko, "Wave guiding properties of surface states in photonic crystals", arxiv: physics/0510273

[5] Meade R D, Brommer K D, Rappe A M and Joannopoulos J D, *Phys. Rev. B* **44** 10961 (1991)

[6] Robertson W M and May M S, *Appl. Phys. Lett.* **74** 1800 (1999)

[7] Ramos-Mendieta F and Halvei P, *Phys. Rev. B* **59** 15112 (1999)

[8] Qiu M and He S, Phys. *Lett. A* **282** 85 (2001)

[9] Lin L L and Li Z Y, *Phys. Rev. B* **63** 033310 (2001)

[10] Solgaard O, Ho F, Thackara J I and Bloom D M, *Appl. Phys. Lett.* **61** 2500 (1992)

[11] Bria D, Djafari-Rouhani B, Akjouj A, Dobrzynski L, Vigneron J P, El Boudouti E H and Nougaui A, *Phys. Rev. E* **69** 066613 (2004)

[12] Liang G, Han P and Wang H, *Opt. Lett.* **29** 192 (2004)

[13] Steslicka M, Kucharczyk R, Akjouj A, Djafari-Rouhani B, Dobrzynski L and Davison S G *S. S. Reports* **47** 93 (2002)

[14] M. Kalafi, A. Soltani-Vala, J. Barvestani, *Optics Communications*, **272**, 403 (2007).

[15] Steslicka M, Kucharczyk R and Glasser M L *Phys. Rev. B* **42** 1458 (1990)

[16] Steslicka M, Kucharczyk R, Dobrzynski L, Djafari-Rouhani B, El Boudouti E H and Jaskolski W, Prog. *Surf. Sci* **46** 219 (1994)

[17] Sang H Y, Li Z Y, Gu B Y, *Physics Letters A.* **331** 414 (2004)

Advanced Materials Research Vol. 31 (2008) pp 11-13
online at http://www.scientific.net
© 2008 Trans Tech Publications, Switzerland

Titania/Ormosils Organic-Inorganic Hybrid Thin Films Doped with Azobenzene Small Molecules for Optical Switch Applications

Wenxiu Que[1,2,a], M. Sun[1], C. Y. Jia[1], L. Cheng[1], Z. Sun[2,b],
L. L. Wang[2] and X. Hu[3,c]

[1] Electronic Materials Research Laboratory, School of Electronic & Information Engineering, Xi'an Jiaotong University, Xi'an 710049, P. R. China

[2] Nanotech Center, Department of Physics, East China Normal University, Shanghai 200062, P. R. China

[3] School of Materials Science and Engineering, Nanyang Technological University, Nanyang Avenue, Singapore 639798, Singapore

[a] wxque@mail.xjtu.edu.cn, [b] zsun@phy.ecnu.edu.cn, [c] asxhu@ntu.edu.sg

Keywords: Sol-gel technique, Organic-inorganic hybrid, Thin films, Azobenzene, Optical switch.

Abstract. Titania organically modified silanes (ormosils) organic-inorganic hybrid thin films doped with azobenzene small molecules are prepared by a low temperature sol-gel spin-coating process for optical switch applications. Acid-catalyzed solutions of γ-glycidoxypropyltrimethoxysilane and methyltrimethoxysilane mixed with tetrapropyl orthotitanate are used as matrix precursors. Atomic force microscopy is used to study the morphological properties of the hybrid thin films. Results indicate that crack-free thin films with a thickness of about 1.3μm can be obtained by a single spin-coating process after a low heat treatment temperature. The propagation mode properties of the hybrid thin films are also studied by employing a prism coupling technique. The photo-responsive properties of the hybrid films baked at different temperatures are induced by an irradiation with UV light and subsequent visible light.

Introduction

Polymers incorporating azodyes or containing azo units chemically or physically have attracted a great deal of attention and become promising photonic-based materials. The desirable properties of these materials are attributed to the photoisomerization of the azodye groups accompanied by reorientation of azobenzene groups through photochemical *trans-cis-trans* isomerization circles under photoirradiation [1-3]. Hence extensively studies have been made of azobenzene-doped photochromic materials, where small molecular weight azobenzene compounds are dispersed in polymer binders [4-5], by many research groups due to their promising photonic applications. Organic-inorganic hybrid materials have also been extensively investigated and convinced that the optical properties of them can be largely enhanced as compared with organic polymer materials. This is because the introduction of organic groups into an inorganic network improves mechanical properties and the modification of an inorganic network structure with organic groups gives larger space for the isomerization of organic photoactive molecules as compared to inorganic glasses [6]. Therefore, organic-inorganic hybrids are thus anticipated as desirable materials for photonic applications, which can trap organic molecules. In this work, we report on the photoresponsive and optical properties of the TiO$_2$–γ-glycidoxypropyltrimethoxysilane (GLYMO) and methyltrimethoxy –silane (MTES) organic-inorganic hybrid materials doped with azobenzene small molecules for optical switching applications.

Experimental

Organic-inorganic hybrid material of molar composition 20TiO$_2$-40GLYMO-40MTES were prepared by a sol-gel technique. Details of preparation processing were described elsewhere [7]

The 4-(4-hydroxybutyloxy) azobenzene compound as azodye was added to the sol-gel hybrid solution in the weight ratio of 0.5%. The final mixture was stirred for about 25-30 hrs at room temperature. We used quartz glass as substrates and they were ultrasonically cleaned in acetone and ethanol, respectively, rinsed with the de-ionized water and dried in pure N_2 gas. Two layers and three layers of the sol-gel film were spun onto the substrate at 3000 rpm for 35 seconds. The film-coated samples were then dried in vacuum oven for 10 hrs at a temperature of 100°C. The propagation modes, the refractive index and the thickness of the hybrid films were measured by an m-line apparatus based on prism coupling technique. The UV-VIS absorption spectra were obtained from the hybrid films in the range of 300-600nm with a Shimadzu UV-2501 PC UV-Vis spectrophotometer. The UV irradiation light was produced by a Driel Instrument 66901 500 Watts mercury lamp through a filter centered at 370 nm with a circular cooling water system to maintain the lamp temperature at about 5°C. The UV irradiation light intensity was 2.0mW/cm^2. The morphology and the roughness of the as-prepared hybrid films were observed by a Digital Instruments Nanoscope IIIa AFM using the tapping mode.

Results and discussion

The waveguide properties of the hybrid film were measured, and the thickness and the refractive index of the two-layer hybrid film are about 2.4 μm and 1.51 at the wavelength of 1539 nm, respectively. The results indicate that when organic groups are integrated in the glass, the bulky organic components fill the pores between the inorganic oxide chains and the materials can reach its final density at a low temperature. Figure 1 shows the propagation modes of the three-layer hybrid planar waveguide film baked at 100°C based on the prism coupling technique at the wavelength of 1539 nm. It can be see from the Figure 1 that the hybrid films can support several TE modes. However, only the two highest indices for each polarization are higher than this value of the refractive index of the substrate, that is to say, only two modes of TE_0 and TE_1 can be guided modes of the waveguide. The other dips observed in the intensity spectra are substrate modes due to their refractive indices smaller than the value of the substrate refractive index. Especially, a dense thick film can be obtained at the baking temperature of 100°C, which means this material system may enable direct integration with semiconductor sources and waveguide devices.

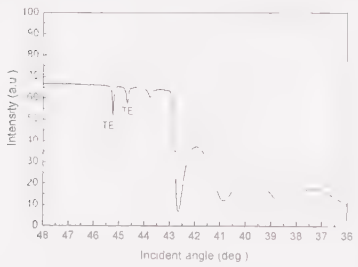

Fig.1 TE Modes of the hybrid planar waveguide at the wavelength of 1539 nm

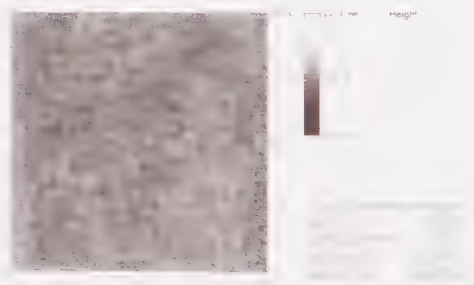

Fig.2 AFM image of the hybrid planar waveguide film heated at the temperature of 100°C

The morphologies and the roughness of the hybrid waveguide film were observed by AFM. The results as shown in Figure 2 indicate that a dense and porous-free hybrid film can be easily obtained at a heat treatment temperature of 100°C. The value of the root mean square (RMS) surface roughness of the hybrid film was examined over a 10 μm^2 area and the surface roughness of hybrid film obtained under present processing condition is 0.57 nm. It seems from Figure 2 that a blurry surface relief pattern can be observed, which is probably related to material displacement caused by trans-cis cycling of the azobenzene chromophore or reorientation of the azobenzene groups leading to birefringence in the hybrid film due to heating induction.

Figures 3 show the UV-visible absorption spectral changes of the hybrid film with an irradiation time by irradiation with non-polarized UV (370 nm) light, and subsequent irradiation with visible (410 nm) light. At room temperature, azobenzene chromospheres are expected to be in the more stable *trans* state in the dark. It can be seen from the absorption spectra of the Fig.3(a) in the range of 300-600 nm that there have been a major absorption peak at 352 nm and a weak one at 437 nm. When the hybrid film is irradiated by the non-polarized UV light of 370 nm, azobenzene chromospheres undergoes a *trans-cis* photoisomerization process. The intensity of the absorption peak at 352 nm gradually decreases with an increase of irradiation time until an equilibrium state is reached. At the same time, the weak peak at 437 nm becomes more pronounced. The photostationary state is reached in about 105 seconds under the present irradiation conditions. Figure 3(b) shows that when the hybrid film is irradiated by the visible light of 410 nm, azobenzene chromospheres undergoes a *cis-trans* photoisomerization process.

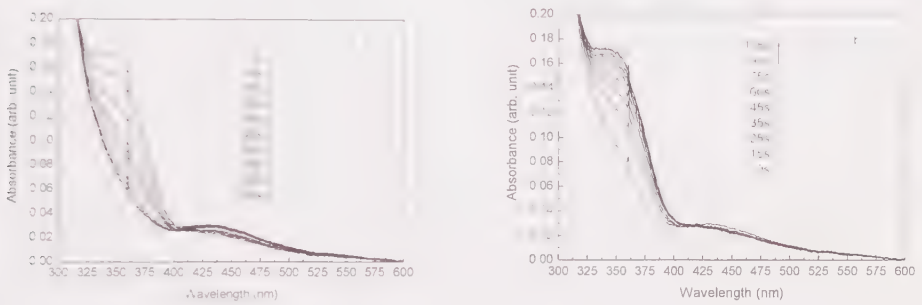

Fig.3 UV absorbance change of the hybrid film on irradiation (a) at 370 nm UV light (b) at 410nm Vis light

Summary

TiO_2/GLYMO/MTES organic-inorganic hybrid films doped with azobenzene small molecules for optical switch applications have been prepared by the low-temperature sol-gel technique. Single layer optical waveguide thin film with a thickness of about 1.30 μm has been obtained by the spin-coating technique and at a heat treatment temperature of 100°C. The optical waveguide and microstructural properties of the hybrid films have been studied by the prism coupling technique and AFM. Photoresponsive properties of the hybrid films have been studied.

Acknowledgment

This work was supported by the National Natural Science Foundation of China under Grant No. 60477003.

References

[1] A. A. Blevins and G. J. Blanchard: J. Phys. Chem. B 108 (2004) 4962.

[2] S. W. Magennis, F. S. Mackay, A. C. Jones, K. M. Tait, and P. J. Sadler: Chem. Mater. 17 (2005) 2059.

[3] A. Sharma, M. Dokhanian, A. Kassu, and A> N. Parekh: Opt. Lett. 30 (2005) 501.

[4] H. Nakano, T. Takahashi, T. Kadota, and Y. Shirota: Adv. Mater. 14(2002) 1157.

[5] F. X. Huang, Y. Q. Wu, D. H. Guo, and F. X. Gan: Thin Solid Films 483 (2005) 251.

[6] D. Levy, S. Einhorn, and D. Avnir: J. Non-cryst. Solids 113 (1989) 137.

[7] W. X. Que and X. Hu: J. Phys. D: Appl. Phys. 36 (2003) 908.

Advanced Materials Research Vol. 31 (2008) pp 14-16
online at http://www.scientific.net
© 2008 Trans Tech Publications, Switzerland

Sol-Gel Fabrication of Low Temperature Organic-Inorganic Hybrid Film Patterns for Photonic Applications

Wenxiu Que[1 a], X. M. Ren[2 b], W. Zhang[1], W. J. Jiang[1], Y. Gao[2], and X. Hu[3 c]

[1] Electronic Materials Research Laboratory, School of Electronic & Information Engineering, Xi'an Jiaotong University, Xi'an 710049, P. R. China

[2] Department of Electronic Engineering, Xi'an University of Technology, Xi'an 710048, P. R. China

[3] School of Materials Science and Engineering, Nanyang Technological University, Nanyang Avenue, Singapore 639798, Singapore

[a] wxque@mail.xjtu.edu.cn, [b] renxm@mail.xait.edu.cn, [c] asxhu@ntu.edu.sg

Keywords: Sol-gel technique, Organic-inorganic hybrid, Thin films, Patterns, Photonic applications.

Abstract. Titania/organically modified silane hybrid thin films for photonic applications were prepared by combining a low temperature sol-gel technique and a spin-coating process from an organic-inorganic hybrid system. Effects of the titanium content and heat treatment temperature on the structural and optical properties of the hybrid thin films were characterized by atomic force microscopy and UV-visible spectroscopy. It is found that the optical and microstructural properties of the hybrid thin films depend on the heat-treatment temperature and titanium molar contents. The thickness and the refractive index of the hybrid thin films were also measured and found to be related to the heat treatment temperature and titanium molar content. These results indicate that a dense and high transparent hybrid thin film can be obtained at a low heat treatment temperature. Potential photonic device structural patterns can easily fabricated from the as-prepared hybrid thin films by using etching process.

Introduction

The fabrication of photonics integrated circuits generally requires control of the refractive index, the dimension of the waveguide structure and other optical properties of the materials. Among the various techniques under development, the use of sol-gel process for the fabrication of optical waveguides has attracted considerable attention, much of which has been focused on planar waveguides for use at visible wavelengths, where the requirements on performance and geometry are generally modest. Especially, sol-gel integrated optics is beginning to show potential photonics applications and it stimulates studies on optical waveguide materials. Many researchers have spent a great deal of effort to realize useful materials for optical waveguide applications and such sol-gel materials as silica, titania or zirconia have been investigated for optical applications [1-3]. However, the required heat-treatment temperature is generally quite high, and it is very difficult to produce a thick single layer of pure inorganic sol-gel film. The use of organically modified silane precursors may help solve these problems to allow obtaining thicker films [4-6]. This is because when organic groups are incorporated in the glass, the bulky organic components fill the pores between the inorganic oxide chains. Thus, the material can reach its final density at a low temperature. In this work, we present our recent study on the effects of the titanium content and the heat treatment temperature on the structural and optical properties of the hybrid organic-inorganic hybrid thin films and pattern fabrication from the as-prepared hybrid thin films by using wet etching process.

Experimental study

The hybrid thin films sols with different titanium contents were synthesized from γ-glycidoxypropyl -trimethoxysilane (GLYMO) and tetrabutyl titanate (TPOT). Hydrochloric acid (HCl, 37wt % in water) was used as catalyst, acetylacetone (AcacH) as chelating agent of titanium alkoxide, ethanol as solvent and de-ionized water (H_2O) for hydrolysis. Water and hydrochloric acid were added as

last components drop by drop. The molar ratio of H_2O/GLYMO was 4 and the molar ratio of AcacH/TPOT was also kept constant at 4. The molar ratio of HCl/GLYMO was 0.01. The studied molar ratios of GLYMO:TiO_2 including 0.8:0.2, 0.7:0.3, 0.6:0.4, and 0.5:0.5. The final sols were left to react under stirring for about 30 hours at room temperature. Spin coating was performed to deposit the hybrid thin films with the agitated sols. One layer of the sol-gel film was spun onto the substrate at 3500 rpm for 35 s. Then, the coated film was directly put in the furnace and baked for 10 minutes at different temperatures of 100, 200, 300, 400, and 500°C. The refractive index and the thickness of the hybrid films were measured by an M-2000UI ellipsometer. The UV-VIS transmission spectra were obtained from the hybrid films deposited on microscope glass slides in the range of 200-800nm with a V-570 spectrometer.

Results and discussion

Figure 1 shows the dependence of the refractive index and the thickness of the films spun on silicon substrates and baked at 100°C on the titanium content. Evidently, with an increase of the titanium content, the thickness of the film drops and the refractive index of the film increases. It can be observed that a film with thickness more than 1.30 μm can be obtained by a single spin-coating process, and the refractive index of the film can be varied from 1.55 to 1.61 at the wavelength of 633 nm. These results indicate that when organic groups are integrated in the glass, the bulky organic components fill the pores between the inorganic oxide chains and the materials can reach its final density at a low temperature. With increase the baking temperature, the thermal decomposition of the organic solvents and the combustion of the organic compounds occur, leading to the film becomes thinner. For those films with 0.5 M titanium content and baked at different temperatures, results indicates that as baking temperature rises, the refractive index increases obviously. This is expected as the hybrid film would be more condensed when it is baked at a higher temperature. It should be mentioned that the hybrid thin film may become inorganic SiO_2-TiO_2 coating if the baking temperature is further increased. For example, an inorganic film with a thickness of more than 0.3 μm can be reached by single spin coating process with the baking temperature increase up to 500°C. These results indicate that the refractive index of the hybrid films can be easily tuned by changing the titanium content and the baking temperature. Especially, a dense thick film can be obtained at the baking temperature of 100°C, which means this material system may enable direct integration with semiconductor sources and detectors.

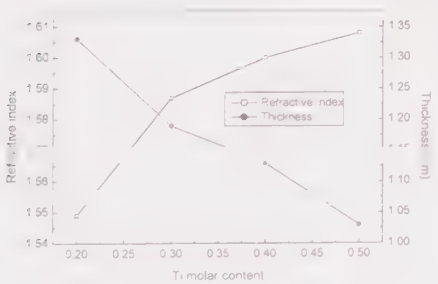

Fig.1 Dependence of the thickness and refractive index of the thin films on Ti molar content

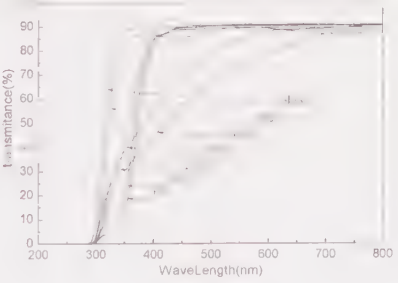

Fig.2 Optical transmittance spectra of the thin films baked at different temperatures

Figure 2 shows the optical transmittance spectra of the films with 0.5 M titanium content and baked at different temperatures. Note that these are single layer films with a thickness from 0.30μm to 1.03μm. It can be seen that the films obtained at room temperature and 100°C both have high transmittance, except for the absorption from the organic solvents or the acetylacetonate complex in the range between 300 nm and 440 nm. Evidently, the absorption of the organic solvents or the

acetylacetonate complex disappears gradually with the increase to 500°C of the baking temperature, which agrees well with that obtained in Ref. [3]. This behavior of an obvious absorption from 300 nm to 700 nm can be explained as follows. The films baked between 200 and 400°C are porous due to the incomplete decomposition of the organic compounds. As a result, a relatively large degree of scattering of light from the pores is expected. When the baking temperature is increased to 500°C, the organic compounds have been completely decomposed and a purely inorganic dense film may be obtained. Consequently, the scattering and absorption caused by the relatively large pores is thus substantially suppressed. Fig. 3 shows optical microscopy photography of the electrode patterns fabricated from the as-prepared hybrid film with 0.2 M titanium content by wet etching of HF solution (volume ratio of HF to H_2O is 3:10). It can be seen that the etching time in the Fig.3(a) is not enough. These results indicate that a low cost fabrication of the potential photonic devices is probably achieved from the as-prepared low-temperature hybrid thin films.

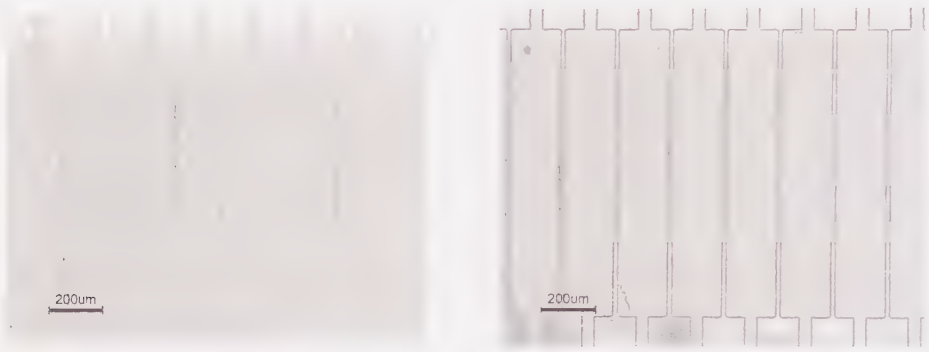

(a) 240 second (b) 255 second

Fig.3 Optical microscopy photography of the patterns fabricated by wet etching at different etching time

Summary

Sol-gel-derived TiO_2/GLYMO hybrid films have been studied in the optical slab-waveguide configuration. Single layer optical waveguide thin film with a thickness of more than 1.30 μm has been prepared by the sol-gel spin-coating technique and low temperature heat treatment. The effects of the titanium content and the heat treatment temperature on the structural and optical properties of the hybrid films have been studied by the prism coupling technique and UV-VIS spectroscopy. Patterns have been fabricated from the as-prepared hybrid thin films by using wet etching process.

Acknowledgment

This work was supported by the National Natural Science Foundation of China under Grant No. 60477003.

References

[1] M. Zevin and R. Reisfeld: Opt. Mater. 8 (1997) 37.

[2] R. M. Almeida: J. Non-Cryst. Solids 259 (1999) 176.

[3] P. Innocenzi, A. Martucci, M. Guglielmi, L. Armelao, S. Pelli, G. C. Righini and G. C. Battaglin: J. Non-Cryst. Solids 259 (1999) 182.

[4] S. Motakef, J. M. Boulton and D. R. Uhlmann: Opt. Lett. 19 (1994) 1125.

[5] A. Jitianu, M. Gartner, M. Zaharescu, D. Cristea, E. Manea: Mater. Sci. Eng. C 23 (2003) 301.

[6] G. R. Atkins and R. B. Charters: J. Sol-Gel Sci. and Technol. 26 (2003) 919.

Advanced Materials Research Vol. 31 (2008) pp 17-19
online at http://www.scientific.net
© 2008 Trans Tech Publications, Switzerland

Morphology and Crystal Quality of InAs QDs Grown by MOVPE Using Different Growth Modes

Yin Zongyou[1], Tang Xiaohong[1,*], Zhang Jixuan[2], Deny Sentosa[1], Teng Jinghua[3], Du Anyan[4] and Chin Mee Koy[1]

[1] Nanyang Technological University, Singapore 639798
[2] National University of Singapore, Singapore 117574
[3] Institute of Material Engineering and Research, Singapore 117602
[4] Institute of Microelectronics, Singapore 117685

* Corresponding author: exhtang@ntu.edu.sg

Keywords: Quantum dots, morphology, crystal quality, MOVPE, growth modes

Abstract Morphology and crystal-quality of InAs $In_{0.53}Ga_{0.47}As$/InP quantum dots (QDs) grown by metal-organic vapor phase epitaxy (MOVPE) in N_2 ambient using different growth modes have been studied. It is found that the morphology and crystal-quality of InAs QDs are dependant on the growth modes. After optimizing the dots' growth modes, dots' size dispersion and crystal-quality are both improved greatly, resulting in the enhancement factor of ~ 2.9 in the photoluminescence (PL) peak-intensity from single QD. When the dots are buried, the dot size decrease compared with the free-standing dots due to the soon capping layer deposition during dots' being buried. The thermal activation energy measured is comparable to the valence-band offset in the QD system calculated by 8 kp theory model. This indicates the PL quenching induced by the interface defects is suppressed due to the defect density lowering in the QDs grown by such optimized growth mode.

Introduction: InAs/InP QDs systems have been investigated intensively because of their promising applications in ultra-low-loss optical fiber communications targeting at 1.55 μm emission wavelength [1]. On the other hand, InAs/InP QDs are expected to be able to emit in the mid-infrared (IR), 2-4 μm, wavelength region by inserting InGaAs layer between InAs QDs and InP matrix, so promising for a variety of military, biomedical and environmental applications [2, 3]. However, the InAs QDs grown on InGaAs/InP matrixes are generally with large morphology distribution due to the un-uniform strain relaxation of wetting layer and the anisotropic surface diffusion of In adatoms during the dots growth [4]. In this article, the InAs QDs grown on $In_{0.53}Ga_{0.47}As$/InP matrix with the different growth modes targeting at reducing the dot-size dispersion and improving dots' crystal-quality have been investigated.

Experiments: The InAs $In_{0.53}Ga_{0.47}As$/InP quantum dots (QDs) were grown by different growth modes using metal-organic vapor phase epitaxy (MOVPE) in N_2 ambient. The reactor pressure, temperature and the input InAs material was set at 20 mbar, 550 °C and 6.7 monolayers (ML), respectively, for growing the InAs QDs on the $In_{0.53}Ga_{0.47}As$/InP matrix. The morphology of uncapped and capped QDs was studied using atomic force microscope (AFM) and transmission electron microscope (TEM), respectively. Emissions of the uncapped and capped QDs have been investigated by (PL) measurement. The studied three QD growth modes are listed in Table 1,

Table 1 Growth modes comparison for growing InAs QDs on $In_{0.53}Ga_{0.47}As$/InP matrix for samples (a)-(c).

QDs' growth mode	Source flux & duration time during growths
(a) Ordinary SK	200 sccm & 8 s (TMIn)
(b) ALE × 8 cycles	50 sccm & 2 s (TMIn) → 1 s interruption → 40 sccm & 3 s (TBA) → 1 s interruption
(c) Two-step	200 sccm & 4 s (TMIn) → 1 s interruption → 4-cycle ALE growths

including Stranski-Krastanow (SK) growth, atomic layer epitaxy (ALE) and two-step with fast nucleation growth plus ALE. The SK mode for sample (a) is the conventional QDs self-assembly growth method. For the ALE growth mode, the group-III TMIn source and group-V TBA source were switched on and off alternatively, so to make the growth in atomic layers in each cycle. Between on and off the MO sources, a short interruption was introduced in. Multi-repeat of such growth procedures is used to realize multiple-cycle growth of InAs QDs layer for sample (b). Two-step growth modes for (c) are designed to grow QDs in two steps: fast nucleation growth in step 1 and QDs formation in step 2 ALE growth.

Results and Discussions: As shown in Fig. 1, the dots' size dispersion and PL performance were both improved greatly from sample (a) to (c). This indicates the optimized two-step growth mode is advantageous to suppress the large islands formation under the kinetically self-limiting growth [5] and to reduce the grown-in non-crystalline defects [6] in the dots. Based on the dot density and PL peak intensity, the average PL peak intensity per dot was calculated and plotted in Fig. 2 for the three QDs. It's found the PL peak intensity per dot of two-step grown QDs was increased by ~290% compared with that of SK grown dots. This explains why the PL peak intensity of (c) is

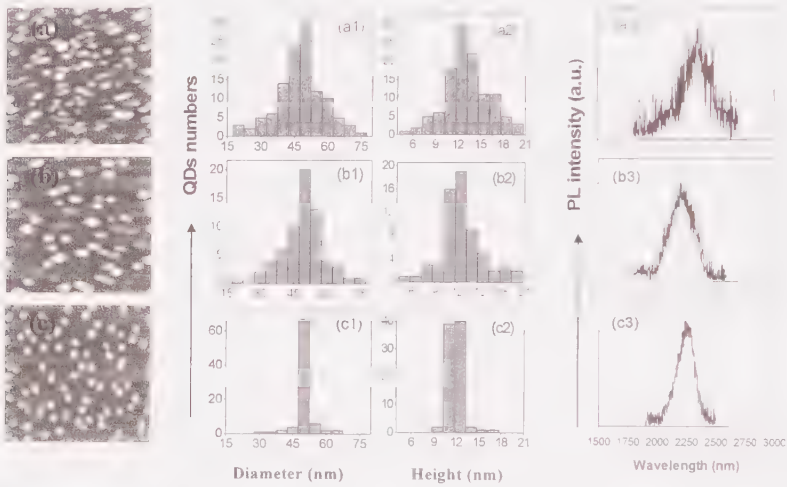

Fig.1. AFM images, diameter/height distribution and PL spectra of the QDs (a) - (c).

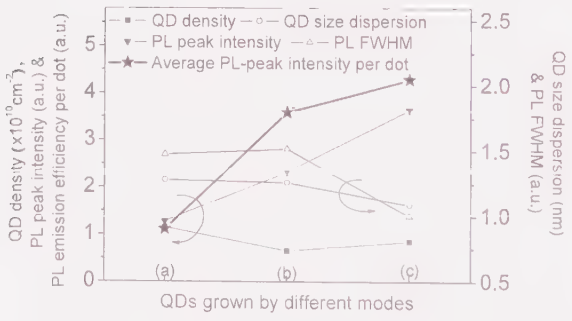
QD density
QD size dispersion
PL peak intensity
PL FWHM
Average PL-peak intensity per dot
QD density (x10^10 cm^-2), PL peak intensity (a.u.) & PL emission efficiency per dot (a.u.)
QD size dispersion (nm) & PL FWHM (a.u.)
(a)
(b)
(c)
QDs grown by different modes

Fig.2 Comparison of QD density, size dispersion, PL peak intensity, PL linewidth and PL peak emission intensity per dot for the uncapped QD samples (a) - (c).

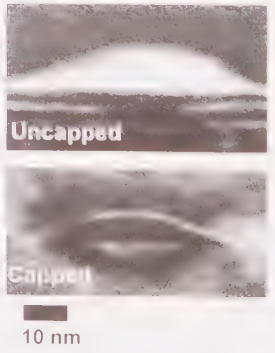

Fig.3 Typical single-QD's TEM images of sample-(c) based uncapped and capped QDs.

much higher than that of (a), although (c) has far lower dot density than (a).

When the dots of (c) were capped by $In_{0.53}Ga_{0.47}As$ layer, the dot's size decreased as observed from the TEM images in Fig. 3. This is because the dots are capped soon after the post-growth interruption. But, for the free-standing dots, after QDs post-growth interruption, reactor temperature was ramped down with TBA source protection. It takes around 40 mins for reactor temperature to lower from 550 °C to 300 °C. We think during this process, the dots are still on the growth due to the remained Indium atoms around the substrate, thus increasing the dot's size. The PL spectra for the capped dots are shown in Fig. 4-(i) and the corresponding temperature dependence of PL integrated intensity are shown in Fig. 4-(ii). It's observed no emission peak from the wetting layer and only one peak originates from the dots. The dots' emission curve becomes broadened with the barrier layer's emission appearance due to the thermal emission effect. For this capped QD structure, the calculated valence band offset by using the approximated 8 kp theory model [7] was comparable to the activation energy (~ 60meV) after theoretical fitting on the measured data. This shows the PL quenching channels in the QDs structures were not from the so-called grown-in interface defects. So, the QDs grown by such two-step growth mode has low density defects in the interface between the dots and barrier layers.

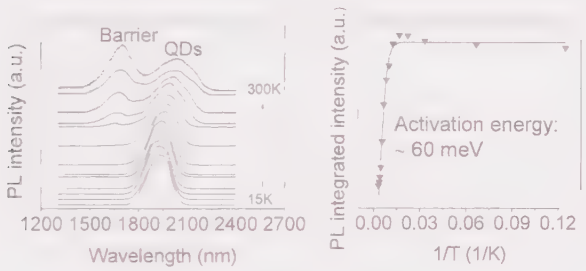

Fig.4 (i) Temperature PL spectra and (ii) temperature dependence of PL integrated intensity of the capped-QDs.

Summary: Size dispersion and crystal-quality of MOVPE grown InAs/$In_{0.53}Ga_{0.47}As$/InP QDs are both improved greatly after the growth modes optimization, achieving an enhancement factor of ~ 2.9 in PL peak-intensity from the single dot. The buried dots have smaller size than free-standing dots due to the continued dots' growth during the long-time reactor temperature ramping down process. The measured activation energy is similar to the calculated valence-band offset in the capped QDs, indicating the suppressing of PL quenching through the interface defects due to the reduced defect density in the dots grown by such optimized two step growth mode.

Acknowledgement: The authors would like to thank A*STAR and NTU for funding this research.

[1] Q. Gong, R. Notzel and J. H. Wolter: *InAs/InP quantum dots emitting in the 1.55 μm wavelength region by inserting submonolayer GaP interlayers*, Appl. Phys. Lett. Vol. 85 (2004), p. 1404.

[2] Y. M. Qiu and D. Uhl: *Self-assembled InAsSb quantum dots on (001) InP substrates*, Appl. Phys. Lett. Vol. 84 (2004), p. 1510.

[3] S. M. Landi, M. P. Pires, C. V. Tribuzy and P. S. S. Guimaraes: *InAs/InGaAs/InP structures for quantum dot infrared photodetectors*, Phys. Stat. Sol. Vol. 2 (2005), p. 3171.

[4] Z. H. Zhang, G. W. Pickrell, K. L. Chang and K. Y. Cheng: *Surface morphology control of InAs nanostructures grown on InGaAs/InP*, Appl. Phys. Lett. Vol. 82 (2003), p. 4555.

[5] M. Kastner and G. Voigtlander: *Kinetically self-limiting growth of Ge islands on Si(001)*, Phys. Rev. Lett. Vol. 82 (1999), p. 2745.

[6] A. A. El-Emawy, S. Birudavolu, P. S. Wong and D. L. Huffaker: *Formation trends in quantum dot growth using metalorganic chemical vapor deposition*, J. Appl. Phys. Vol. 93, (2003), p. 3529.

[7] Z. Y. Yin, X. H. Tang, D. H. Zhang and A. Y. Du: *Effects of InxGa1−xAs matrix layer on InAs quantum dot formation and their emission wavelength*, J. Appl. Phys. Vol. 100 (2006), p. 033109.

Advanced Materials Research Vol. 31 (2008) pp 20-22
online at http://www.scientific.net
© 2008 Trans Tech Publications, Switzerland

Modulation of three dimensional photonic band gap in visible region

Y.P.Liu[1, a], Y.P.Guo[1, b], Z.J.Yan[1,c], C.M.Huang[1,d], Y.Y.Wang[1,e]

School of Physics and Technology, Lanzhou University, Lanzhou, 730000, P.R.China.
[a]Liuyping05@lzu.cn, [b]Guoyp@lzu.edu.cn, [c]Yanzj03@lzu.cn, [d]Huangcm04@lzu.cn,
[e]wangyy@lzu.edu.cn

Keywords: Photonic crystals; Vertical deposition method; Photonic band gap

Abstract. Three dimensional (3D) SiO_2 photonic crystals films were fabricated on quartz substrate by vertical deposition method. The effects of various preparation parameters on optical properties were studied by optical transmission measurements. Bragg reflection on parallel sets of (111) planes were observed in all the samples. The center wavelength of [111] photonic band gap (PBG) varied from 450 nm to 680 nm with the increasing sphere size. For a given sphere size, the (111) Bragg reflection of as-deposited sample shifted towards lower wavelengths as the sintering temperature T increased. The role of evaporation temperature on the optical properties of the film was also investigated. The PBG can be correspondingly modulated in visible region by changing various preparation parameters.

Introduction

Photonic crystals (PhCs), as characterized by a spatial periodic modulation of dielectric constant, have attracted much attention in the last decade. In analogy to electrons in a semiconductor, electromagnetic wave propagation in a photonic crystal can be inhibited for a certain frequency range, that thus results in the formation of a photonic band gap [1, 2]. The concept and PhCs devices based on the band gap phenomena have been extended to the fields of optoelectronics [3], optical data storages [4], chemical and biochemical sensor [5] and tissue engineering [6], etc. To fabricate high quality PhCs, a number of preparation methods were developed in the past decade. A common way for fabricating PhCs is the gravity sedimentation of colloides from dispersions [7]. However, gravity sedimentation samples generally contain polycrystalline domains of varying sizes and the films thickness are difficult to control. Nagayama et al. [8] firstly exploited the vertical deposition method to assemble monolayer PhCs films. Single-crystal colloidal crystals with controlled thickness have been obtained through the vertical deposition [9]. In application of three dimensional (3D) PhCs, their optical properties should be controllable in the visible and infrared regimes. The PBG of SiO_2 PhCs can be controlled in a range of 110 nm by means of thermal treatment [7]. Studies have shown that the optical properties of polystyrene (PS) PhCs also can be tuned by changing the evaporation temperature [10, 11]. In this report, vertical deposition method was employed to fabricate 3D SiO_2 PhCs. The photonic band gap can be controlled in the visible region by the mean of both sphere size and thermal treatment.

Experimental

Photonic crystals were grown on quartz substrate by vertical deposition method. Three sphere diameters, 200nm, 235nm and 280nm were used in the experiment. The evaporation temperatures used in the experiment were 30 °C, 35 °C and 40 °C, respectively. Before the samples were annealed, the samples were dried at 100 °C in ambient atmosphere for 8-10 hours. The samples were annealed in a temperature range of 200-1000 °C for 2 hours.

Results and Discussion

Figure 1 is a typical SEM image of self-assembled 3D SiO_2 PhCs with an average sphere size of 235 nm. The sample was deposited by vertical deposition method at 35 °C. The SEM surface image shows that the sample exhibits ordered close-packed arrangement of SiO_2 spheres. The

triangular arrangement observed corresponds to a (111) surface either of a face center cubic (fcc) system or a (001) surface of a hexagonal close packed (hcp) one. Theoretical calculations have indicated that the fcc structure is more stabilized slightly [12].

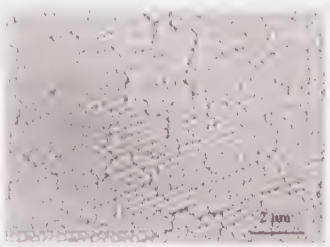

Fig.1 SEM image of self-assembled 3D SiO_2 PhCs prepared with sphere size of 235 nm.

Optical transmission measurements are obtained at normal incidence in the wavelength range of 250-800 nm. Three evaporation temperatures, 30 °C, 35 °C and 40 °C were used in the experiment respectively. Fig.2 shows the optical properties of SiO_2 (235 nm) colloidal crystals deposited at different evaporation temperatures. A pronounced attenuation band around 520 nm in transmission spectra can be observed in all three samples. The attenuation band corresponds to the coherent Bragg reflection on the parallel set to (111) planes of the SiO_2 PhCs. The transmission in the pass band is above 80% at 800 nm for three samples. Compared with those deposited at 30 °C and 40 °C, the sample deposited at 35 °C shows the narrowest gap width of 35 nm and the lowest transmission at the gap center of 8.5%. The increase of evaporation temperature apparently improves the relaxation and mobility of the colloidal spheres on crystal surface to explore possible lattice site, so the defects are reduced during the deposition process. Moreover, the higher evaporation temperature can lead to a preferential tendency towards stacking positions of fcc structures, which are well known as a thermodynamically stable crystalline phase [12]. On the other hand, a too high temperature can lead to a faster evaporation rate, resulting in some defects in the films. Defects in the films destroy the periodic array, and thus lead to the derogation of the PhCs optical properties. In this report, the temperature of evaporation was optimized at 35 °C, which was used in the following experiments.

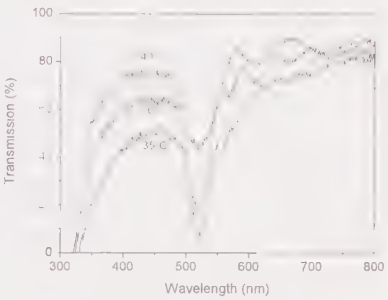

Fig.2 Transmission spectra for photonic crystals samples deposited at different temperatures.

Light transmission spectra of photonic crystals prepared with three different sizes (200 nm, 235 nm and 280 nm) of colloidal spheres are shown in Fig. 3. The optical band gap in [111] direction are observed around 450 nm, 520 nm and 680 nm for the three samples, respectively. As the size of colloidal sphere increases, the center wavelength of the photonic band gap moves towards longer wavelengths. Compared with the samples prepared with the sizes of colloidal spheres of 200 nm and 235 nm, the sample made with sphere size of 280nm shows a higher transmission at the center of the PBG. The higher light transmission at the center of the PBG might be related to the larger size of spheres and slower movement in colloidal suspension, resulting in unbalanced crystalline growth [11]. In our experiments, three different sizes of spheres were used to modulate the PBG in the visible region. In fact, PBG in ultraviolet band and infrared band also can be obtained using the spheres size below 200 nm and above 280 nm.

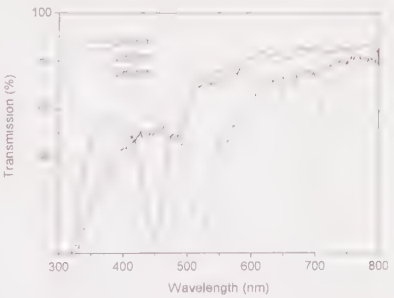

Fig.3 Light transmission spectra of photonic crystals prepared with three different colloidal spheres.

Figure 4 shows the transmission spectra of sample (235 nm) annealed in a temperature range of 200-1000 °C. It can be seen that the clear attenuation band in transmission is around 534 nm for the as-grown sample. The center wavelength of the PBG shifts towards lower wavelength as the annealing temperature increases. There is a change of 62 nm in the center wavelength between the as-grown sample and the sample annealed at 1000 °C. The center wavelength of PBG as a function of annealing temperature for the sample prepared with the sphere size of 235 nm was re-plotted, and three different stages can be clearly distinguished as that shown in Fig.5. A large shift (49 nm) of the PBG was obtained between T = 35 °C and T = 500 °C, due to the decomposition of organic composite and evaporation of hydrate in this anneal process. In the range of T = 500 °C to T=800 °C, there is only a small change of 11 nm. The condensation of the surface silanol groups occurs above 200 °C [13], and brings about shrinkage of the structure. The structure shrinkage is responsible for the shift of the PBG in this annealing temperature range. For the annealing temperature above 800 °C, the shift of the center wavelength of PBG was almost not observed, indicating that no further contraction occurs and a much higher mechanical stability was formed.

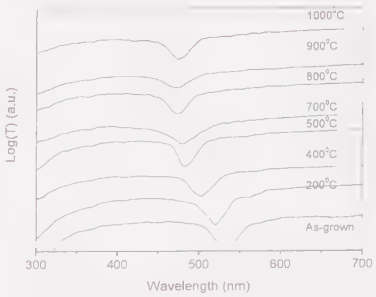

Fig.4 Transmission spectra of PhCs samples annealed in a temperature range of 200-1000 °C.

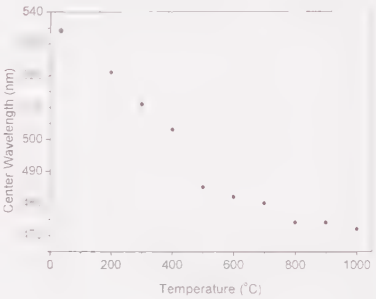

Fig.5 The center wavelength of PBG plotted against the annealing temperature for the sample.

Conclusions

The center wavelength of PBG in [111] direction can be modulated in whole visible region by choosing different spheres size. For a given size, the PBG shifts in a relatively narrower wavelength scale through changing anneal temperature. The results show that the PBG of 3D PhCs can be easily and accurately modified in visible region by the mean of both sphere sizes and annealing temperature, which provides a promising way for their potential applications of 3D PhCs in photonics and electronics.

References

[1] E. Yablonovitch: Phys. Rev. Lett Vol. 58 (1987), p. 2059.
[2] S. John: Phys. Rev. Lett Vol. 58 (1987), p. 2486.
[3] O. Painter, R.K.Lee, A. Scherer, P.D.Dapkus, and I. Kim: Science Vol. 284 (1999), p. 1819.
[4] J. Lim, M. Lee and E. Kim: Appl. Phys. Lett Vol. 86 (2005), p. 191105.
[5] K. Lee and S.A. Asher: J. Am. Chem. Soc Vol. 122 (2000), p. 9534.
[6] N.A. Kotov, Y. Liu, S. Wang, M. Motamedi and J. Cortiella: Langmuir Vol. 20 (2004), p. 7887.
[7] H. Miguez, F. Meseguer, C. Lopez, A. Blanco and V. Fornes: Adv. Mater Vol. 10 (1998), p. 480.
[8] N.D Denkov, O.D. Velev, P.A. Kralchevsky and K. Nagayama: Nature Vol. 361 (1993), p. 26.
[9] P. Jiang, J.F. Bertone, K.S. Hwang and V.L. Colvin: Chem. Mater Vol. 11 (1999), p. 2132.
[10] Y.H. Ye, F. LeBlanc, A. Hache and V.V. Truong: Appl. Phys. Lett Vol. 78 (2001), p. 52.
[11] S.L. Kuai, X.F. Hu, A. Hache and V.V. Truong: J. Cryst. Growth Vol. 267 (2004), p. 317.
[12] L. Woodcock: Nature (London) Vol. 385 (1997), p. 141.
[13] H.E. Bergna: *The Colloid Chemistry of Silica* (Washington DC, ACS 1994).

Advanced Materials Research Vol. 31 (2008) pp 23-26
online at http://www.scientific.net
© 2008 Trans Tech Publications, Switzerland

Raman scattering from GaAs nanowires grown by molecular beam epitaxy

N Begum[1,a], A S Bhatti[1,b], M Piccin[2], G Bais[2], F Jabeen[2], S Rubini[2], F Martelli[2,c] and A Franciosi[2]

[1] Department of Physics, COMSATS Institution of Information Technology, Jauhar Campus Islamabad, Pakistan

2 Laboratorio Nazionale TASC INFM-CNR, S.S. 14, km 163,5, 34012 Trieste, Italy.

[a]narjisgh@hotmail.com, [b]asbhatti@comsats.edu.pk, [c]martelli@infm.tasc.it,

Keywords: Raman Scattering, Phonon Modes, Nanowires

Abstract. Self-assembled nanowires have attracted much attention due to their potential applications in electronics and optoelectronics. A recent interest in Mn catalyzed GaAs nanowires are due to their potential use in spintronic devices at nanoscale. High densities of Au- and Mn-catalyzed self-assembled GaAs nanowires (NWs) with diameter in the range of 20 to 200 nm and length of few microns were synthesized by molecular beam epitaxy (MBE) on different substrates at varied substrate temperatures. These nanowires were investigated by means of μ-Raman spectroscopy at room temperature. The Raman spectra from NWs show an energy downshift and a broadening of the LO and TO phonon lines that differ from those of epitaxial GaAs. We suggest that those downshift and broadening are due to the relaxation of the q=0 selection rule in the presence of structural defects in the nanowires. The results indicate that the use of Mn instead of Au as growth catalyst does not affect the structural quality of the nanowires drastically.

Introduction

Semiconductor nanowires (NWs), future building blocks of several kinds of nano-sized devices, are presently among the most pursued topics in physics due to the flexibility in tailoring the chemistry of nanowires [1]. GaAs is one of the most likely candidates due to already existing technology platform. GaAs NWs have already been grown by several techniques, including laser ablation [2] metal-organic vapor phase epitaxy [3] and molecular beam epitaxy (MBE) [4]. Due to the self-assembled nature of the NWs, which are also obtained on non-crystalline substrates, the growth is often accompanied by defect formation. The structural characteristics of the NWs highlight several aspects related to crystalline quality, lattice structure and structural defects. For example, III – As NWs often have a Wurtzite lattice structure quite contrary to usual zincblende structure [5]. Au is commonly used as catalyst for the growth of semiconductor nanowires. However, Mn, magnetic in nature, has also been recently shown not only to act as a catalyst in the growth of GaAs NWs but it also diffuses into the nanowire body [6], a step towards the possible fabrication of dilute ferromagnetic semiconducting NWs based on GaAs.

Raman scattering is a useful, fast and non-destructive tool to characterize the purity of crystals and microstructures by studying the vibrational modes that provide information about lattice structure or the presence of structural defects. We employed μ-Raman spectroscopy to investigate the quality of Au and Mn catalyzed GaAs NWs grown on different substrates. We will show that the crystal quality of the NWs obtained with the two different catalysts is not much different.

Experimental

GaAs NWs have been grown on SiO_2 and GaAs substrates by catalyst-assisted solid-source MBE using either Au or Mn as growth catalysts. Catalyst metal (1 nm thick) was deposited on the substrate at room temperature and then wires were grown for 30 minutes at different growth temperatures using Ga and As elemental sources. Complete details on the wire growth can be found elsewhere [6, 7]. High density of NW has been obtained on SiO_2 using either Au (a) or Mn (b) as catalyst. NWs lengths are as high as 20 μm while the diameters range from few tens to about 200 nm. In order to measure the light scattered by single nanowires, the wires were mechanically transferred onto a Si substrate after the growth. μ-Raman scattering measurements were performed with a μ-Raman spectrometer (Renishaw 1000) exciting samples with 514.5 nm line of an Ar^+ laser with a spot diameter of about 0.4 μm at room temperature in a backscattering geometry with and/or without polarization selection. All of the Raman spectra have been recorded at excitation intensities that do not induce a measurable lattice heating in the wires thus minimizing the possibilities of artifacts due to excessive heat. In general we found that the TO mode of the NW is much sensitive to excessive heating as it shifted around 1.5 cm^{-1} while LO mode remained insensitive, a phenomenon already observed in Si NWs [8].

Results and Discussion

Fig. 1 shows representative Raman spectra taken on a single Au-catalyzed wire (top spectrum) and a single Mn-catalyzed wire (middle spectrum), both grown on SiO_2 substrate, together with a reference spectrum obtained from a GaAs epilayers grown on GaAs(001) by MBE (bottom-most spectrum). Raman spectra from the NWs grown with different catalysts look identical to each other but show varied difference with respect to the Raman from the reference spectrum. First, in the wires the Raman signal related to the TO phonon is much stronger than that related to the LO phonon. Second, both TO and LO signals in the wires are downshifted and asymmetrically broadened with respect to the epilayer. Additionally, the LO peak shows a partially resolved structure. Third, a further signal, at about 255 cm^{-1} is observed in the wires. The features shown in Fig. 1 are general and have been observed in all wires but the magnitude of the downshift of modes varied from wire to wire.

At low excitation intensities, with negligible heating effects, the downshift of the Raman lines observed in the wires is always larger for the LO phonon than for the TO phonon. The values of the downshift with respect to the epilayer vary from wire to wire and even within the same wire depending on the position of the laser spot. This is shown in Fig. 2 for wires grown with both metal catalysts on SiO_2. In the upper part of the figure a wire is schematically shown with the indication of the locations where the Raman spectra have been measured, i.e., at the ends and at the centre of each nanowire. The spectra clearly show that the Raman shift may be different at other locations of the same wire. In general there is no specific trend in the magnitude of the Raman downshift moving from one end towards the other. For example, the location corresponding to the largest shift may be found at any NW position, e.g., near one of the tips or at the NW centre, depending on the specific NW. As from the comparison between Fig. 2(a) and Fig. 2(b) we point out that the signal at 255 cm^{-1} is not found in all wires.

The lineshape analysis of over 100s of recorded spectra revealed the average range of downshift of Raman modes of NWs, LO mode varied from 2.5 to 12 cm^{-1} and TO mode varied from 0.2 to 8.5 cm^{-1}. The range, of course, depends strongly on the dimension of the wire. Within a single wire the variation is in general smaller except in few NWs where the measured variation is larger. In short, we have found no significant difference between the wires grown on SiO_2 using Au or Mn as growth catalyst. In the case of Au catalyzed wires grown on GaAs (111) the measured downshifts are on the average small and vary in the range between 3.2 – 5.8 cm^{-1} and 1.3 – 2.0 cm^{-1} for the LO – and TO – phonon modes, respectively. From the LO and TO modes Raman shifts, deformed GaAs lattice constants (5.375Å, 5.358Å) were determined for both (Au, Mn) catalyzed

nanowires, respectively and were found comparable. These calculations shows that there is not much change in the lattice constant calculated for the Mn catalyzed and Au-catalyzed NWs, thus proving that Au can be replaced by the Mn catalyst.

There is also a third peak observed around 255cm^{-1}, which arise due to the low frequency vibrations which may become Raman active at high defect densities [9]. At larger defect densities, the mean distance between these defect can be small enough to reduce the coherence length of phonons. This results in the relaxation of Raman selection rule (q=0) and letting the low energy phonons with $q\neq0$ become observable. So appearance and strength of this peak is a signature of high defect density at that point.

Conclusions

The energy downshift of the LO and TO Raman lines observed in (Au, Mn) may be ascribed to the presence of lattice defects within the wires. The downshift of the modes and hence the defect density vary from wire to wire, even with position within a single wires, hence affecting the high quality of the NW. An important conclusion drawn from the present study is that the structural quality of Mn-catalyzed NWs is comparable to that of Au-catalyzed wires, a feature that confirms Mn as an interesting alternative catalyst, especially in view of the possible fabrication of dilute ferromagnetic GaAs based nanowires. Present study points out that much effort will be necessary to control the growth process and obtain increased homogeneity in the nanowire structural properties.

Acknowledgments: Authors ASB and NB are thankful to ICTP – TRIL, Trieste, Italy, Higher Education Commission, Pakistan financial support.

References

[1] See *Nature* (news) **441** 265 (2006)
[2] T. Akiyama, K. Nakayama, T. Ito, *Phys. Rev. B* **73** 235308 (2006)
[3] W. S. Shi, Y. F. Zheng, N. Wang, C. S. Lee, and S. T. Lee, *Appl. Phys. Lett.* **78,** 3304 (2001)
[4] Reest Aarnoud L. Verheijen Marcel A. Wunnicke Olaf, Serafin Stacey, Wondergem Harry and Bakkers Erik P A M *Nanotechnology* **17** S271 (2006)
[5] J C Harmand, G. Patriarche, N. Péré-Laperne, M-N. Mérat-Combes, L. Travers and F. Glas *Appl. Phys. Lett.* **87,** 203101 (2005)
[6] F. Martelli, S. Rubini, M. Piccin, G. Bais, F. Jabeen, S. De Franceschi, V. Grillo, E. Carlino, F. D'Acapito, F. Boscherini, S. Cabrini, M. Lazzarino, L. Businaro, F. Romanato and A. Franciosi, *Nano Letters* **6,** 2130 (2006)
[7] M. Piccin, G. Bais, V. Grillo, F. Jabeen, S. De Franceschi, E. Carlino, M. Lazzarino, F. Romanato, L. Businaro, S. Rubini, F. Martelli and A. Franciosi, *Physica E*, in the press, doi: http://dx.doi.org/10.1016/j.physe.2006.07.002
[8] S. Piscanec, M. Cantoro, A. C. Ferrari, J. A. Zapien, Y. Lifshitz, S. T. Lee, S. Hofmann and J. Robertson, *Phys. Rev. B* **68,** 241312. (2003)
[9] S. W. da Silva, D. I. Lubyshev, and P. Basmaji, Yu. A. Pusep, P. S. Pizani, and J. C. Galzerani, R. S. Katiyar and G. Morell, J. Appl. Phys. **82,** 6247 (1997)

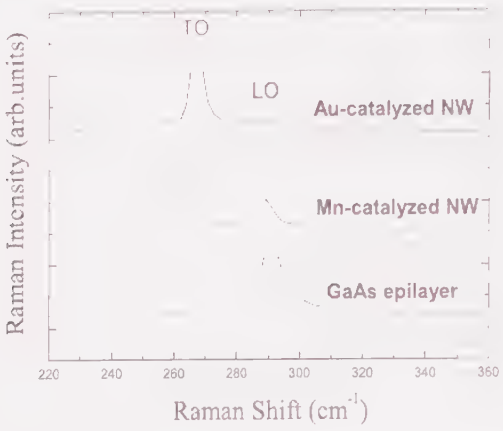

Figure 1: Comparison of micro-Raman spectra from Au and (b) Mn catalyzed nanowires and (c) GaAs epilayers. All the spectra were taken at excitation density of 0.318 mW/μm^2.

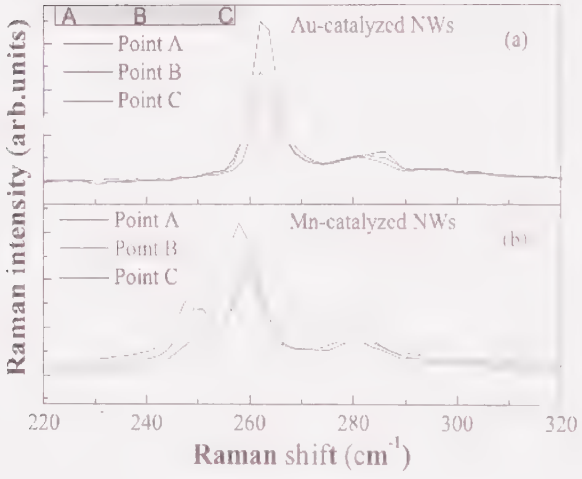

Figure 2: Raman at different points of a single nanowire of Au and Mn-catalyzed GaAs NWs. The inset schematically shows the single nanowire indicating the points where Raman spectra are taken.

Advanced Materials Research Vol. 31 (2008) pp 27-29
online at http://www.scientific.net
© 2008 Trans Tech Publications, Switzerland

Design and Analysis of 2D Photonic Crystal Waveguides for high Coupling Efficiency

Ming Wu[1, 2, a], Hairong Liu[2, b], WeiJun Tong[3] and Dexiu Huang[1]

[1] Wuhan National Laboratory for Optoelectronics, Wuhan, Hubei, P. R. China
[2] Huazhong University of Science and Technology, Wuhan, Hubei, P. R. China
[3] Yangze Optic Fiber and Cable Co. Ltd., Wuhan, Hubei, P. R. China
[a] vachelwu@126.com, [b] hrliu@mail.hust.edu.cn

Keywords: photonic crystal waveguide; coupling efficiency; tapered waveguide.

Abstract. In this paper we have proposed a photonic crystal structure to enhance the coupling efficiency between photonic crystal waveguide (PCW) and the conventional dielectric waveguide. The proposed waveguide characterized with employing the taper structure and varying the holes' radius in the taper. Two-dimensional (2D) finite-difference time-domain (FDTD) method has been used to analyze the structure. The simulation results show that the coupling efficiency can be achieved as high as 81.6% at the wavelength of 1.55*um*.

Introduction

Photonic crystals are artificial optical materials with a periodic modulation on the order of the wavelength of light. Photonic crystals provide a flexible platform for the realization of photonic integrated circuits (PIC) and optoelectronic integrated circuits (OEIC). High efficient coupling technique between the photonic crystal waveguides (PCW) and the conventional dielectric waveguides is needed. However, the coupling loss is high because of the different width and different propagation mechanism between PCW and conventional dielectric waveguides[1-3]. In this paper, we have proposed a new coupling structure to enhance the coupling efficiency between PCW and the conventional dielectric waveguides. In the following sections we will introduce and discuss the characteristics of the proposed structure. The analysis results and conclusion will also be presented.

Design of photonic crystal structure to enhance the coupling efficiency

The studied photonic crystal structure is two-dimensional (2D) triangular array of air holes surrounded by silicon material. Fig. 1 shows the structure named as W1 PCW by introducing a line defect in the photonic crystal along the Γ-K direction. The radius of air holes is R=0.3a, while the lattice constant is a=0.375*um*. The normalized frequencies (a/λ) are between 0.208 and 0.276. This lattice constant value is appropriate for transmission at the standard optical communication wavelength of 1.55*um*. The width of W1 PCW is 0.425*um*. However the width of the conventional dielectric waveguide is commonly 2-5*um*. The width difference of the above two kinds of waveguides is large. It will be arouse the strong reflection and scattering loss at the interface of the two kinds of waveguides, so the coupling efficiency will be very low.

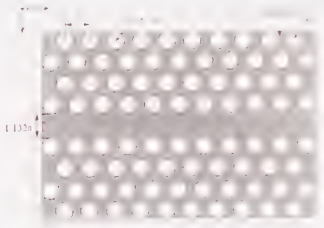

Fig. 1 Schematics of the W1 PCW.

There are two ways to realize the taper structure to increase the coupling efficiency between PCW and the conventional dielectric waveguide. The photonic crystal taper structure by removing holes is shown in Fig. 2(a). This aims to put the width of the photonic crystal match to the width of the conventional dielectric waveguide. On the other hand, it is already known that PCW have a significantly different mode profile and propagation mechanism compared to the conventional dielectric waveguides, and the mode mismatch between PCW and conventional dielectric waveguide is also the baffle to enhance the coupling efficiency. One of the ways to reduce the mode mismatch is by changing the holes radius. The photonic crystal taper structure by changing radius of holes is shown in Fig. 2(b) with the radius of the two steps taper are r_1=R/3 and r_2=R/2 respectively.

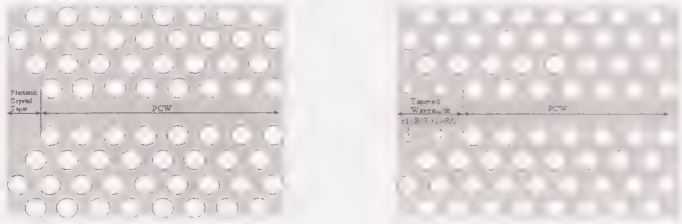

(a) (b)

Fig. 2 Photonic crystal taper structures: (a) photonic crystal taper structure by removing holes only; (b) Photonic crystal taper structure by changing radius of holes only.

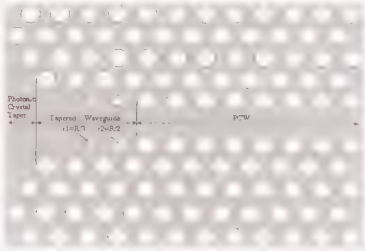

Fig. 3 Photonic crystal taper structure by removing holes and changing holes radius simultaneously.

In order to improve the coupling efficiency between PCW and conventional waveguide, we need solve these two issues that affect the coupling efficiency which are the width mismatch and mode mismatch between these two structures. Here we adopt the advantages of the taper structure with removing holes and the taper structure with varying the radius of holes to obtain high coupling efficiency. The proposed structure by removing holes and changing holes radius simultaneously is shown in Fig. 3, where the radius of the two holes in the rows adjacent to the defect region are r_1=R/3 and r_2=R/2 respectively.

Simulation results and analysis

We have used commercial software named as *Fullwave* provided by *Rsoft Company* to calculate the coupling efficiency. The simulation result of the butt coupled structure, directly coupling light from the conventional dielectric waveguide into the W1 PCW, is lower as 29.6%. In the photonic crystal taper structure by removing holes shown as Fig. 2(a), the transmission increases from 29.6% in butt coupled to 49.0%. And the taper waveguide by changing radius of holes shown as Fig. 2(b) is obtained 64.3% transmission. The coupling efficiency using the tapered waveguide by changing radius of holes is obviously enhanced from the result, and higher than the photonic crystal taper by removing holes.

The proposed taper structure shown in Fig. 3 by removing holes and changing holes radius simultaneously is achieved 81.6% transmission. From this simulated result, the effect enhancing the coupling efficiency is very notable in our designed structure. Fig. 4 shows the simulation transmission spectrum as a function of the wavelength for the three coupling structures. From the results presented in Fig. 4, it can be seen that the highest coupling efficiency value is 83.8% at the wavelength 1.59um for our designed coupling structure. And the coupling efficiency is higher than 80% at the wavelength from 1.54um to 1.64um. The 100nm bandwidth is very useful to design the DWDM device. The highest coupling efficiency values existent around the wavelength 1.55um in the two other coupling structures.

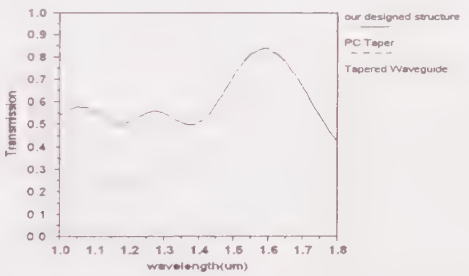

Fig. 4 Transmission spectrum of the coupling structure.

Conclusions

Photonic crystal taper by removing holes and changing holes radius simultaneously has been proposed to increase the coupling efficiency between PCW and the conventional dielectric waveguides. We have analyzed the coupling efficiency of the proposed structure by 2D FDTD. The simulation results show that the transmission can be achieved as high as 81.6% at the wavelength 1.55um. The 100nm bandwidth with high coupling efficiency is obtained in this coupling structure.

References

1. P. Sanchis, J. Marti, 'High efficiency coupling technique for plananar photonic crystal waveguides', Electron. Lett., **32**(17), pp.961-962, 15th Aug (2002).
2. G. Chietera, 'Numerical design for efficiently coupling conventional and photonic crystal waveguides', Micro. and Opt. Tech. Lett., **42**(3), pp.196-199, Aug (2004).
3. B.Z. Steinberg, A. Boag, 'Substructuring approach to optimization of matching for photonic crystal waveguides', Micro. and Opt. Tech. Lett., **48**(9), pp.1866-1870, Aug (2006).

Advanced Materials Research Vol. 31 (2008) pp 30-32
online at http://www.scientific.net
© 2008 Trans Tech Publications, Switzerland

Novel Passivation Method in the Fabrication of Submicron InGaAsP/InP Ridge Waveguide Lasers

E. L. Lim, J. H. Teng*, S. J. Chua, J. R. Dong, N. Ang, and L. F. Chong

Institute of Materials Research and Engineering, 3 Research Link, Singapore 117602

*jh-teng@imre.a-star,edu.sg

Keywords: passivation, metal contact, semiconductor laser, ridge waveguide, lift-off, nanophotonics.

Abstract. One challenge for the realization of electrically drive nano-photonic devices is the formation of metal contacts and passivation. In this paper, we report a novel self-aligned method suitable for the formation of the metal contact and passivation for submicron photonic devices. Two different dielectric materials with high selectivity in wet chemical etching and a wet etching of semiconductor to create an undercut are involved. The whole process is completely compatible with existing compound semiconductor process. As a demonstration of this method, the fabrication and characterization of an InGaAsP/InP submicron-ridge waveguide lasers is presented. The method is extendable to high aspect ratio-submicron ridge waveguide and other device fabrication.

Introduction

The convergence of photonics with electronics requires small foot-print optical component for on-chip integration. Various functionalities have been demonstrated using submicron waveguide structure such as micro-sized optical switch [1], directional waveguide [2], and nanoscale waveguide coupled micro-ring laser [3]. Current injection into such a submicron waveguide is an important step to realize more complex functionalities, such as electrically pumped laser diode, wavelength tuning or optical switching by carrier injection, etc. The metal contacts to the ridge or mesa structures in the active devices are typically formed by creating a via-hole through the passivation layer. The position of this via hole is defined by aligning a mask during a photolithography process. Because of the optical resolution and the tolerance of the photolithography process, the width of this via hole normally is significantly smaller than the width of the area of the semiconductor where the metal contact is to be created. Normal photolithography reaches its limitation at about 0.8-1 μm, depends on the photoresist used. Hence, it is a challenge to make metal contacts and passivation to submicron or even nano-meter sized semiconductor devices. Several methods that uses polymers, such as Benzocyclobutene(BCB), have been proposed to form passivation and metal contacts for submicron photonic devices [3,4]. However, the use of polymers renders the sample unsuitable for high temperature process, such as metal alloying process, after the passivation. In this paper, we propose a novel passivation method by using two dielectric materials, i.e., SiO_2 and Si_3N_4, to form self-aligned metal contact and passivation to submicron ridge or mesa structures. An InGaAsP/InP ridge waveguide laser with ridge width of 0.7 μm was demonstrated using the method proposed.

The Proposed Method

The key steps of the method are illustrated in Fig 1. (a) Deposit a silicon dioxide layer on top of the semiconductor substrate and pattern it to the required shape, e.g., ridge structure, using normal photolithography process. (b) Etch the semiconductor substrate to form the undercut underneath the SiO_2 mask, which typically created by using wet etch. (c) Deposit a passivation layer of silicon nitride (Si_3N_4) using either sputtering method or plasma enhanced chemical vapor deposition (PECVD) method. Due to the shadowing effect of the hanging SiO_2 mask, Si_3N_4 deposited in the

semiconductor undercut part and on the bottom of the exposed SiO_2 mask will be greatly reduced. (d) Lift off the SiO_2 mask by etching the sample in the BHF etchant by exploiting the high wet etching selectivity between SiO_2 and Si_3N_4, which is about 7 in BHF). The etching time required for the lift-off process to occur strongly depends on width of the SiO_2 hard mask that lies exactly on top of the ridge waveguide, which is indicated as "w" as indicated in Fig. 1(c). Furthermore, the thickness of the Si_3N_4, "t" as indicated in Fig. 1(c), should be chosen such that the remaining Si_3N_4 on the substrate is sufficient for passivation purpose. After this step, the top surface of the ridge structure, normally is the highly doped semiconductors for contact purpose, is completely exposed while the side wall and bottom of the ridge structure is still covered by the Si_3N_4 film. (e) Deposit the metal layer to form the metal contact. The metal line will be self-aligned to the ridge structure.

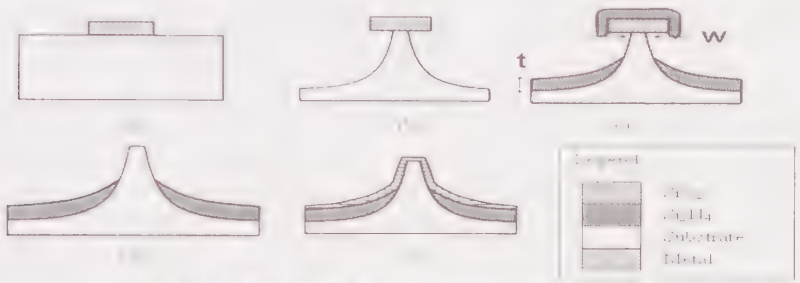

Figure 1. Process steps for the proposed method

Figure 2. The cross section of the structure before (a) and after (b) the lift-off of the dielectric hard mask.

Device Fabrication

We explored this method and successfully demonstrated a submicron InGaAsP/InP ridge waveguide lasers. The sample used was an InGaAsP/InP four quantum well separate confinement laser structure grown by metalorganic chemical vapor deposition (MOCVD). A 500-nm-thick SiO_2 was deposited by PECVD and followed by a photolithography process to create ridge structure with a ridge width of 0.8 μm. Reactive ion etching (RIE) using CHF_3 and Ar plasma was employed to dry etch the silicon dioxide to define the hard mask for the following semiconductor ridge etching.. The InP ridge waveguide was dry-etched by using $CH_4/Cl_2/H_2$-based inductively coupled plasma etching process and followed by wet etch (HBr:HNO_3:H_2O=1:1:10) to further shrink the ridge width and to create the undercut. The total etching depth was ~ 1.2 μm and the ridge width had decreased to ~0.7 μm. After this, 350-nm-thick Si_3N_4 layer was deposited onto the sample by PECVD. The sample was then soaked inside BHF to expose the top InP contact layer by lifting off through the SiO_2 hard mask. The cross sections of the structure before and after lift off are shown in Fig. 2 (a) and (b)

respectively. The p type metal contact of Ti/Pd/Au was then deposited on to the sample using e-beam evaporation. After thinning the wafer, n type metal AuGe/Ni/Au was evaporated and metal alloying was conducted by rapid thermal annealing at 420°C. Without using the method introduced above, it is almost impossible to align a metal contact to this narrow ridge structure by using the normal open contact window process. It is also not feasible to do the high temperature annealing by using the BCB passivation method.

Results and discussion

The laser chip with a cavity length of ~660 μm was cleaved and mounted p-side up on a heat sink and tested under pulse current injected at 15 °C. Pulse width was 0.5 μs and duty cycle was 2.5%. The threshold current of the laser was ~140 mA, which corresponded to current density of 30.3 $kAcm^{-2}$. Fig. 3 shows the current-light characteristics for the laser and Fig. 4 shows the spectrum of the laser that lased at multimode around 1558 nm when the injection current was 180 mA.

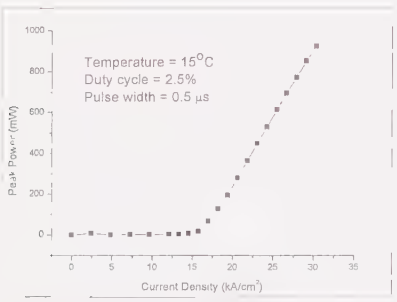

Figure 4 The current-light characteristics of the 0.7μm-wide ridge waveguide laser.

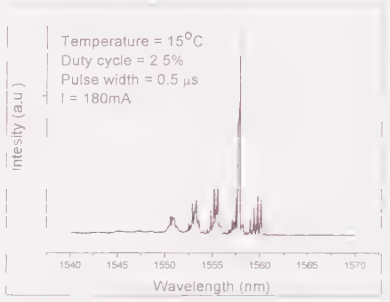

Figure 3 The lasing spectrum of the 0.7μm-wide ridge waveguide laser.

Conclusion

A novel self-aligned passivation method suitable for submicron photonic device fabrication is presented. The method uses two different dielectric materials with a different wet etching selectivity and a two-step wet etching procedure. An undercut is formed in the first wet etching step. Due to the difference in the wet etching rate of the passivation layer and the sacrificial layer, the desired part of the semiconductor is exposed in the second wet etching step for the formation of the metal contact. The method is compatible with existing processing technology and high temperature process. A submicron ridge waveguide laser was successfully demonstrated using this method.

References

[1] P. Miska, M. Beaugeois, C. Lethien, A. Beaurain, H.-W. Li, J.-P. Vilcot, D. Decoster, J. Chazelas, M. Bouazaoui, L. Dobrzynski, A. Akjouj, B. Djafari-Rouhani, and J.-O. Vasseur. Microwave and Optical Tech. Lett, 45, 315 (2005).

[2] M. K. Chin, C. W. Lee, S. Y. Lee, and S. Darmawan, Appl. Opt. 44, 3077 (2005).

[3] S. Park, S. S. Kim, L. Wang and S.T. Ho, IEEE J. Select. Topics Quantum Electro., 3, 351 (2005).

[4] J. F. Zheng, H. V. Demir, V. A. Sabnis, O. Fidaner, J. S. Harris, D. A. B. Miller, J. Vac. Sci. Technol. B, **24**, 3 (2006). [5] R J. F. Zheng, H. V. Demir, V. A. Sabnis, O. Fidaner, J. S. Harris, D. A. B. Miller, J. Vac. Sci. Technol. B, 24, 3 (2006).

Advanced Materials Research Vol. 31 (2008) pp 33-35
online at http://www.scientific.net
© 2008 Trans Tech Publications, Switzerland

Cu-doped SiO_2 Induced Atomic Interdiffusion in Semiconductor Nano heterostructures

V. Hongpinyo[1,a], Y.-H. Ding[1], J. Anderson[1], H. S. Djie[1], B. S. Ooi[1,b]
R. R. Du[2], A. Ganjoo[2] and H. Jain[2]

[1]Center for Optical Technologies and Electrical and Computer Engineering Department
Lehigh University, Bethlehem, PA 18015, USA
[2]International Materials Institution and Materials Science Engineering Department, Lehigh University, Bethlehem, PA 18015, USA
[a]vih205@lehigh.edu, [b]bsooi@lehigh.edu

Keywords: photonic integrated circuits, quantum well, quantum well intermixing, impurity free vacancy induced disordering, impurity diffusion.

Abstract. We investigate the influence of Cu impurity incorporation into the silica cap during the sputtering process on the enhancement of intermixing rate of semiconductor quantum nanostructures. Using the Cu:SiO_2 process, we observed bandgap shift of over 200 meV from various GaAs-based quantum well (QW) heterostructures such as GaAs/AlGaAs, InAlGaP/GaAs, and GaAs/AlGaAs systems at significantly lower activation energy than the conventional impurity free vacancy disordering process (IFVD) using undoped SiO_2 cap. The results suggest that the Cu:SiO_2 process is a promising intermixing technique for the monolithic integration of multiple active passive photonic components on GaAs-based material systems.

Introduction

Engineering of optical and material properties of semiconductor quantum confined nano heterostructures using interdiffusion or intermixing technology has gained significant interest. This technique provides a simple and cost effective route to the realization of monolithic semiconductor photonic integrated circuits (PICs). In addition, this technique produces excellent alignment, negligible reflection losses, and intrinsic mode matching between integrated devices, hence providing a very enticing vision for the future of high-density PICs. The process takes an advantage of the inherent metastable III-V compound semiconductor to spatially modify the material bandgap via the introduction of beneficial impurities or point defects followed by a thermal annealing stage. Among the well-established quantum-well intermixing (QWI) techniques such as impurity free vacancy disordering (IFVD), impurity induced disordering (IID), laser irradiation and plasma irradiation induced intermixing, IFVD based sputtered silica cap induced QWI technique has been widely known as a promising and reliable approach to universally tune the bandgap of various InP and GaAs-based quantum-well and quantum-dot nanostructures [1,2]. However, the intermixing mechanism of the sputtered silica process is not well established. Also, the present knowledge is insufficient to explain why the intermixing effect occurs at relatively low activation energy as compared to other processes.

Besides the sputtered silica process, most processes are material and QW structure dependent. For example, IFVD technique using SiO_2 to promote group-III interdiffusion is an effective QWI process for GaAs-based QWs [3]. However, this process gives a relatively low reproducibility in InP-based systems. Although IID-based processes have demonstrated to induce large degree of QWI in both InP and GaAs structures, the intermixing rate of this process is dependent on specific type of impurity and QW system. Our long term goal of this study is to develop a highly reliable universal QWI process by adopting the combination intermixing effects from IID and IFVD in a single process step. This approach is achieved by means of incorporating Cu as IID source into SiO_2 dielectric that also acts as the IFVD source. Copper impurity is introduced into the SiO_2 film via the co-sputtering method. In this paper, we investigate the effectiveness of this process in various GaAs-based QW structures.

Experiments

Three GaAs-based QW wafers grown using metal-organic vapor phase epitaxy (MOVPE) technique were used in this experiment. The first wafer was a GaAs/AlGaAs double quantum well (DQW) structure. The DQW region was undoped and consisted of two 10 nm-wide GaAs QWs, separated by a 10 nm $Al_{0.2}Ga_{0.8}As$ barrier. The structure was completed by $Al_{0.4}Ga_{0.6}As$ lower cladding of 1.5 μm (with n-doping) and upper cladding of 1.5 μm (with p-doping). The top contact layer consists of a 100 nm p^+ GaAs. The active layer of the second wafer consisted of a single 10 nm AlGaAs QW, sandwiched between two 10 nm $Al_{0.3}Ga_{0.7}As$ barriers. The third wafer was a lattice matched InGaP/InAlGaP red laser structure that consists of a single InAlGaP, sandwiched between two 50 nm $GaIn_xP_{1-x}$ barriers. The as-grown materials for the first, second and third wafers exhibit a photoluminescence (PL) peak at around 802 nm, 740 nm and 608 nm at 77K, respectively.

Samples from these three wafers were deposited with 200 nm thick $Cu:SiO_2$ using a diode sputtering system. The deposition process was performed at 100 W RF power, 2 mTorr using Ar plasma. Co-sputtering of copper was achieved by covering ~5% of the 2" quartz substrate with high purity copper foils. The intermixing stage was performed using a rapid thermal processor (RTP). Samples were annealed under various temperatures for 2 minutes. The samples were placed face down, sandwiched by two fresh pieces of GaAs proximity caps to provide an As overpressure environment during annealing process and further to prevent the sample surface from outdiffusion. The PL measurement was performed at 77 K using a 62.5-μm-diameter optical fiber as a signal probe. A 532 nm diode pumped solid state laser was used as excitation source for GaAs/AlGaAs double quantum well and AlGaAs/GaAs QW laser structure, and a 488 nm blue laser was used as an excitation source for the InGaP/InAlGaP laser.

Results and Discussion

Figure 1 shows the 77K PL spectra from the annealed $Cu:SiO_2$ GaAs/AlGaAs DQW samples at temperature ranging between 875 °C - 950 °C. A significant bandgap shift of 153 meV (72nm) has been observed from sample annealed at a relatively low temperature of 875°C for 2 minutes. The degree of intermixing progressively increases with increasing annealing temperature with a blue shift as large as 270meV (119nm) observed from sample annealed at 950°C. Compared to the conventional IFVD using undoped SiO_2 on similar material system, the $Cu:SiO_2$ process gives over 100°C lower annealing temperature for similar degree of intermixing.

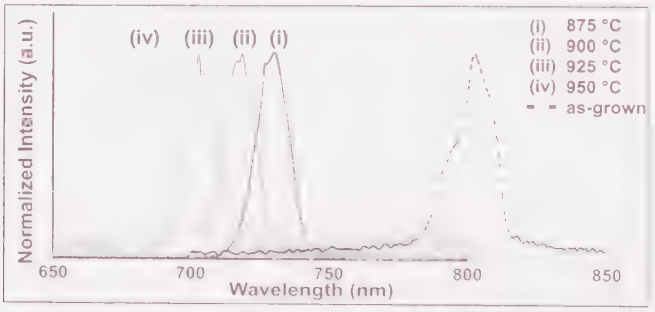

FIG. 1 PL spectra at 77K from the GaAs/AlGaAs DQW samples after annealed at various temperatures from 875 °C to 950 °C. The spectrum from the as-grown sample is represented in dotted line.

Similar to the GaAs/AlGaAs DQW structure, large degrees of QWI have been measured at relatively low activation energy in InGaP/InAlGaAs and AlGaAs/GaAs QW structures intermixed by the $Cu:SiO_2$ process. Figure 2 gives the summary of the bandgap shift from the InGaP/InAlGaAs and AlGaAs/GaAs samples annealed at various temperatures. It can be seen that blue bandgap shift of over 150 meV has been observed from both material systems.

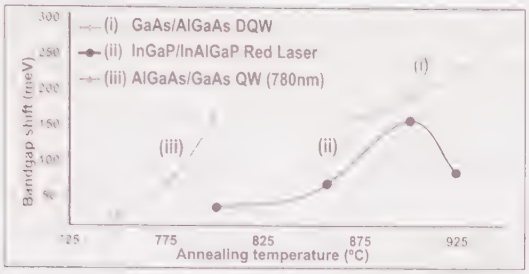

FIG.2 The bandgap shift as a function of annealing temperature for the InGaP/InAlGaP and AlGaAs/GaAs QW structures

From these results, it is obvious that the activation energy of the Cu:SiO_2 process is significantly lower than other QWI technologies [3,4]. There are two QWI mechanisms involved in this process, i.e., Cu-impurity induced disordering and IFVD from the SiO_2 cap. Cu is known as a highly diffusive impurity in III-V semiconductors. The generation of group-III vacancies usually required a high annealing temperature to activate. Therefore, it can be concluded that the moderate intermixing rate observed in all samples is attributed to Cu induced disordering. As Cu concentration is limited in the SiO_2 film, further enhancement of QWI observed at high temperature might be primarily attributed to the group-III vacancies induced by the SiO_2 film. From the results, it is interesting to note that no significant broadening of PL is observed. This suggests that a good optical quality is preserved and not affected by the intermixing process. This result indicates that the sputtered silica can be utilized as an effective intermixing technique for GaAs-based QW structures.

Conclusion

In summary, we have demonstrated a highly selective and reproducible Cu-doped SiO_2 intermixing in various GaAs based QW heterostructures. The activation temperature required for this process is significantly lower than the typical IFVD technique. The differential blueshifts of 270 meV, 150 meV and 152 meV have been observed from the GaAs/AlGaAs DQW, InGaP/InAlGaP QW, and AlGaAs/GaAs QW laser structures, respectively. The result indicates that Cu:SiO_2 induced QW is a highly effective QWI process for GaAs-based QW structures.

References

[1] O. P. Kowalski, C. J. Hamilton, S. D. McDougall, J. H. Marsh, A. C. Bryce, R. M. De La Rue, B. Vögele, C. R. Stanley, C. C. Button and J. S. Roberts, "Universal damage induced technique for quantum well intermixing", Appl. Phys. Lett., **72**, pp. 581-583 (1998).

[2] A. C. Bryce, J. H. Marsh, D. A. Yanson, O. P. Kowalski and S. S. Kim, "Selective quantum dot intermixing for photonic devices", 5th IEEE Conference on Nanotechnology, **1**, pp. 386-389 (2005).

[3] B. S. Ooi, K. McIlvaney, M. W. Street, A. S. Helmy, S. G. Ayling, A. C. Bryce, J. H. Marsh and J. S. Roberts, "Selective quantum-well intermixing in GaAs–AlGaAs structures using impurity-free vacancy diffusion", IEEE J. Quantum Electronics, **33**, pp. 1784-1793 (1997).

[4] B. S. Ooi, A. C. Bryce, J. H. Marsh, and J. S. Roberts, "Effect of p and n doping on neutral impurity and SiO_2 dielectric cap induced quantum well intermixing in GaAs/AlGaAs structures", Semicond. Sci. Technol., **12**, pp. 121-127 (1997).

[5] N. Holonyak, Jr., "Impurity-induced layer disordering of quantum-well heterostructures: discovery and prospects", IEEE J. Sel. Top. Quantum Electron., **4**, pp. 584-594 (1998).

[6] D. G. Deppe, and N. Holonyak, Jr., "Atom diffusion and impurity-induced layer disordering in quantum well III-V semiconductor heterostructures", J. Appl. Phys., **64**, pp. R93-R113 (1988).

[7] W. D. Laidig, N. Holonyak, Jr., M. D. Camras, K. Hess, J. J. Coleman, P. K. Kapkus, and J. Bardeen, "Disordering of an AlAs-GaAs superlattice by impurity diffusion", Appl. Phys. Lett., **38**, pp.776-778 (1981).

Advanced Materials Research Vol. 31 (2008) pp 36-38
online at http://www.scientific.net
© 2008 Trans Tech Publications, Switzerland

DFB lasers with tilted waveguide for multi-wavelength generation

Lip Fah Chong[1,a], Jing Hua Teng[1,b], Ee Leong Lim[1,c], Norman Soo Seng Ang[1,d], J. R. Dong[1,e] and S. J. Chua[1,f]

Institute of Material Research Engineering, A*STAR 3 Research Link, Singapore 117602
[a]lf-chong, [b]jh-teng, [c]el-lim, [d]norman-ang, [e]jr-dong, [f]sj-chua@imre.a-star.edu.sg

Keywords: DFB laser, multi-wavelength, tilted waveguide, threshold analysis, coupled mode theory, Newton-Raphson method, index coupled DFB laser.

Abstract. In this paper, we present the theoretical investigation of index-coupled distributed feedback (DFB) laser with tilted single mode ridge waveguides. By tilting part of the ridge waveguide in various degrees, DFB laser with manifold effective grating periods can be realized. The structure is analyzed using couple mode theory in matrix form based on threshold analysis. Important parameters of DFB laser like resonant frequency and threshold gains are obtained by solving the eigen-equation. The results indicate not only that the lasing frequency is modulated by the waveguide titling angle, but also large Gain Margin (GM) can be achieved at the threshold condition which enhance the stable single mode operation in index-coupled DFB laser.

Introduction

For Dense Wavelength Division Multiplexing system, distributed feedback (DFB) semiconductor laser has become the best candidate for light source due to its stability in single mode operating and preciseness in wavelength selection. One key factor in pushing the DFB laser further into various applications is to reduce the cost in both fabrication and stock of many different wavelengths lasers. A low cost and simple way to produce multi-wavelength DFB lasers is of great interest to the address these issues. One method to make multi-wavelength DFB laser is using tilt waveguides instead of many different pitch gratings [1], which is difficult in process control and very time-consuming. It is known that index coupled DFB laser will suffer two-mode degeneracy but can be circumvent by using quarter-wave-shifted, gain coupled or DBR approaches. In this paper, we will model and simulate a dual pitch DFB laser structure that can give marginal threshold gain, which is comparable to that of quarter-wave-shifted DFB laser. To enhance the mode selectivity, we introduce a double tilted angle ridge waveguide. As shown in Fig.1, one segment of the ridge with length L1 is tiled with respect to the gratings, while the other segment L2 is kept perpendicular to gratings.

Modeling of coupled wave theory

Within the coupled mode theory of the distributed feedback wave guiding system, the governing equation is given as [2]:

$$\begin{aligned} -\frac{\partial}{\partial z}R_i(z)+(\alpha+\Delta\beta_i)R_i(z)&=iKS_i(z)*\exp(-i\phi) \\ \frac{\partial}{\partial z}S_i(z)+(\alpha+\Delta\beta_i)S_i(z)&=iKR_i(z)*\exp(i\phi) \end{aligned} \qquad \text{Eqn (1)}$$

Where $\Delta\beta_i=\beta_i-\beta_{Bragg,i}=(n_{eff}*w/c)-(n_{eff}*w_{Bragg}/c)$ and $\lambda_{Bragg}=(2\Lambda)/(\cos(\theta)n_{eff})$.

Λ is the grating period, θ the tilt angle of the ridge waveguide with respect to the normal grating vector, n_{eff} is the effective index, K the coupling coefficient, c speed of light. In each segment the electrical field is written as superposition of two counter propagating waves: $R_i(z)\exp(-iB_iz)+S_i(z)\exp(iB_iz)$. Due to the random phase of the grating at both sides of the cleaved facets, ϕ is regards as zero. Thus, the transmission coefficient can be written as

$T = |R(L)/R(0)|^2$. Next, we are going to perform *threshold analysis* of Two Segments Model based on [3]. Using the round trip gain $\rho_L \rho_R$, the resonance conditions of the laser cavity can be expressed by $\rho_L \rho_R - 1 = 0$. The threshold analysis is to the search of the eigen-modes α (threshold gain) and w (oscillating frequency).

Results and Discussion

The effect of tilt cavity upon the laser characteristic is first reported by M.A. Di Forte *et al* [4] that the feedback strength decreases when θ increases. Later, experiment conducted by W. T. Tsang *et al* [5] also reported that the K decreases as θ increases. In 1996, A. M. Sarangan *et al* [6] [7] had theoretically formulate the relationship between K and θ in a multi modes [7] and singe mode [6] ridge waveguide. Succinctly speaking, *the coupling coefficient is reduced by a factor of* $\cos(\Lambda \sin(\theta)x)$. Thus, $K(\theta = 0)$ is set arbitrary at $1/(L_1 + L_2)$ for critical coupling in our simulation and varies in the fashion according to [6]. For the simulation of threshold analysis, the parameters are set as the following: Λ=0.2395um, L1=550um, L2=50um and n_{eff}=3.23.

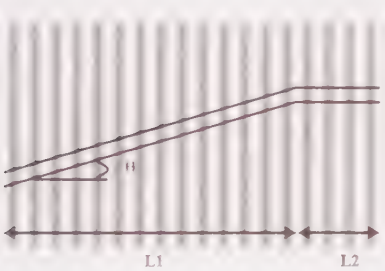

Fig.1. The proposed two section structure with L1=550um and L2=50um.

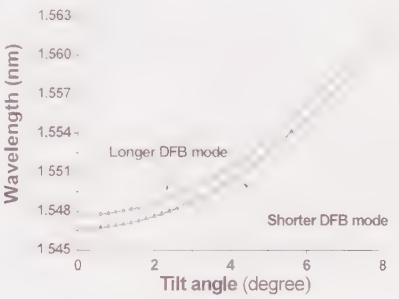

Fig. 2. The simulated lasing wavelength of the two DFB modes as a function of tilted angle.

Fig. 2 depicts the modulation of lasing wavelength by tilting the ridge at various angles. The two lines are the longitudinal modes, one at the longer wavelength and the other shorter, situated beside the forbidden gap of DFB laser. Fig. 3 is the threshold gain of these two modes vs. tilted angle. Due to the nature of degeneracy modes found in index coupled DFB laser, we observed that the tilted ridge will show preference to either of these modes at different angle and causes modes jumping. Within the range of angles $5.2^0 - 6^0$ and $7.6^0 - 8^0$, longer DFB mode has lower gain threshold, and thus it takes over shorter DFB mode as the main lasing mode. The crossing of the two lines, where the two modes share the same gain threshold, indicates degeneracy modes operation. Fig. 4 shows the transmission spectrum of the DFB laser at the threshold of the lasing mode; spontaneous emission and background noise are not consider here. The stop-band is red shifted, as the tilt angle increase from 0^0 to 8^0, and the lasing mode jumped from shorter wavelength mode to longer one at larger tilt angle. Within certain tilt angle, a very large SMSR can be achieved for the index coupled DFB laser. According to Fig. 5, the minimum achievable SMSR is 37dB at 2^0. A multi-branch DFB laser with different tilt angle had been fabricated and the measured spectra matched quite well with our simulation in the lasing wavelength the spectrum shape.

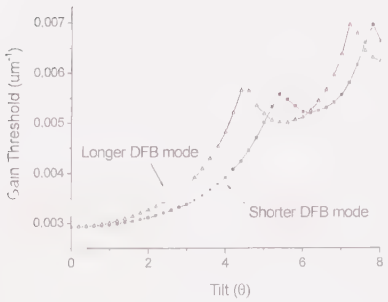

Fig. 3. The threshold gain of the two DFB modes, as a function of tilted angle.

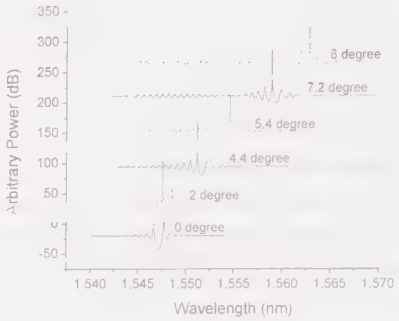

Fig. 4. The simulated transmission spectrum of dual-segment DFB laser for six different tilted angles at their respective threshold gain.

Conclusion

A simple dual pitch index-coupled DFB laser was investigated where the modulation of pitch period is accomplished by tilting the ridge. From threshold analysis, we discovered that the tilt angle shows preference to those otherwise degeneracy modes. High SMSR and thus stable single mode operation can be achieved in certain tilt angles by the introduction of gain margin between these two degeneracy modes. This novel design provides accurate wavelength shift without incurring additional cost to fabricate new grating periods and can be used to produce low cost multi-wavelength DFB arrays.

References

[1] G.P. Agrawal *et al,* IEEE J. Quantum Electron., Vol 24 (1988), p.2407.

[2] Hartmut Hillmer *et al,* J. Lightwave Technol. Vol13 (1995), p. 1905

[3] Geert Morthier and Patrick Vankwikelberge *Handbook of Distributed Feedback Laser Diodes.* (Artect House Inc. Boston.London)

[4] M.A. Di. Forte *et al,* IEEE J. Quantum Electron., Vol 14 (1978), p.560

[5] W.T.Tsang *et al,* IEEE Photon. Technol. Lett. Vol 5 (1993), p. 978

[6] A.M. Sarangan *et.al* IEEE Phtoton. Technol. Lett., Vol 8 (1996), p.1435.

[7] A.M. Sarangan *et.al* J Lightwave Technol.. Vol 14 (1996), p.1853.

Advanced Materials Research Vol. 31 (2008) pp 39-41
online at http://www.scientific.net
© 2008 Trans Tech Publications, Switzerland

Enhanced UV photodetector responsivity in porous GaN/Si(111) by metal-assisted electroless etching

L.S. Chuah[1], Z. Hassan[2], H. Abu Hassan[3]

School of Physics, University Sains Malaysia, 11800 Penang, Malaysia
[1]chuahleesiang@yahoo.com, [2]zai@usm.my, [3]haslan@usm.my

Keywords porous GaN, metal-semiconductor-metal (MSM) photodiode, RF-MBE, Si(111)

Abstract. This paper presents the structural and optical studies of porous GaN sample compared to the corresponding as grown GaN. The samples were investigated by scanning electron microscopy (SEM), high resolution x-ray diffraction (HRXRD), and photoluminescence (PL). The porous area is very uniform, with pore diameter in the range of 80-110 nm. XRD measurements showed that the (0002) diffraction plane peak width of porous samples was slightly broader than the as-grown sample. PL measurements revealed that the near band edge peak of the porous samples were red-shifted. Metal-semiconductor-metal (MSM) photodiode was fabricated on the samples. For as grown GaN sample, this detector shows a sharp cut-off wavelength at 362 nm. A maximum responsivity of 0.258 A/W was achieved at 360 nm. For the porous GaN sample, this detector shows a sharp cut-off wavelength at 364 nm. A maximum responsivity of 0.771 A/W was achieved at 363 nm.

Introduction

Ultraviolet photodetectors are important devices that can be used in various commercial and military applications. The unique physical properties of the porous layer such as, high surface area, shift of bandgap and efficient luminescence are among the special features which show promise in some future sensing applications [1]. The research in porous GaN is strongly driven by the superior physical properties such as the excellent thermal, mechanical and chemical stability, as well as the potential shift of the bandgap [2], moreover, it has been reported that porous GaN can be used as intermediate layer for the reduction of substrate induced strain [3]. In this work, porous GaN was prepared by Pt assisted electroless chemical etching.

Experimental details

The unintentionally doped n-type GaN film grown on Si(111) substrate was used in this study. The film growth has been performed in Veeco model Gen II MBE system, using standard effusion sources for evaporation of Al and Ga and nitrogen with 7N purity was channeled by RF source to generate reactive nitrogen species. The plasma was operated at typical nitrogen pressure of 1.5×10^{-5} Torr under a discharge power of 300W. In the growth chamber, Si substrate was heated at 750°C, and a few monolayers of Ga was deposited on the substrate for the purpose of removing the SiO_2 by formation of GaO_2. A RHEED reconstruction with prominent Kikuchi lines is then observed, that turns into clean Si (111) surfaces at 750 °C. To grow AlN buffer layer, substrate temperature was heated up to 850°C. Both of the Al and N shutters were opened simultaneously for 30 minutes. Subsequently, GaN epilayer was grown on top of the buffer layer for 15 minutes with substrate temperature set at 800°C.

The thickness of GaN film is about 0.06 μm with carrier concentration of 4×10^{19} cm^{-3} as determined by Hall Effect measurement. The wafer was then cleaved into few pieces (10mm x 6mm). Prior to the metallization, boiling aqua regia (3:1 HCl:HNO_3) was used to etch and clean the sample. Two narrow stripes of Pt with thickness of about 200 nm were deposited on the GaN sample by using sputtering system. . The distance between the stripes of Pt is about 4 mm. The samples were then etched in a solution of 4:1:1 HF:CH_3OH:H_2O_2 under illumination of an UV lamp with 500 W power for 60 minutes. The morphological, structural and optical properties of as grown and porous GaN samples were characterized by scanning electron microscopy (SEM), high resolution x-ray diffraction (HR-XRD), and photoluminescence (PL).

For the MSM photodiode, the structure consists of two interdigitated nickel (Ni) Schottky contacts (electrodes) with finger width of 230μm, finger spacing of 400μm, and the length of each electrode was about 3.3mm. It consists of 4 fingers at each electrode. The typical resistance of the MSM is about 10 kΩ. The spectral response was measured using a tungsten lamp, a monochromator, a chopper and a lock-in amplifier. The spectral responsivity of the UV detectors has been determined.

Results and Discussions

The morphology of the as grown and porous GaN films were characterized by plan-view scanning electron micrographs (SEM). As seen in Fig. 1, the porous area is very uniform, with pore diameter in the range of 80-110 nm. It should be noted that the porous GaN generated by electroless etching technique does not necessarily has identical morphological evolution. Diaz *et al* [4] prepared their porous GaN samples by platinum assisted electroless etching, and found that, at short etch time (< 15 min), a rich network of small pores were formed. However for longer etch times, a ridge-valley-like morphology was obtained.

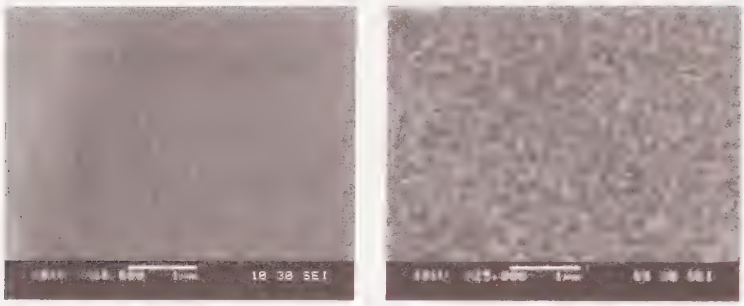

(a) (b)

Fig. 1. SEM images of the samples. (a) As grown, (b) Etched for 60 min.

In order to examine the quality of the films, ω/2θ scan of XRD rocking curve (RC) for (0002) plane was carried out. Fig. 2 shows the ω/2θ scan of the XRD RC of (0002) plane for the as grown and porous GaN/Si(111). It is interesting to note that the FWHM of porous GaN sample increases compared to the as grown sample, however, the amount of increase was small. Change of peak positions was relatively insignificant for the (0002) diffraction plane. This can be explained by the relatively smaller statistical size distribution of the pores.

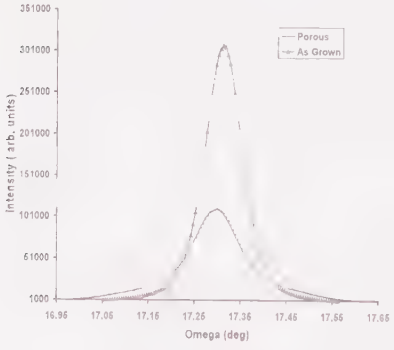

Fig. 2. RC of (0002) plane for as grown and porous GaN grown on Si(111).

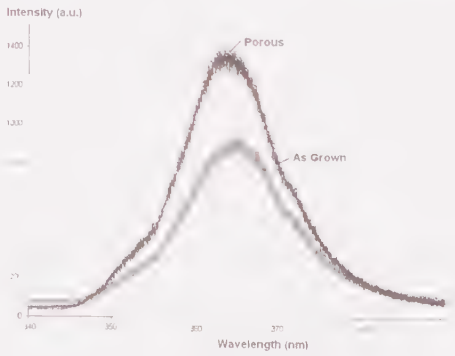

Fig. 3. PL spectra of the samples: as grown and etched under 60 min

Fig. 3 illustrates the room temperature PL spectra of as grown and porous GaN samples. The emission of the porous GaN samples were observed to be red-shifted relative to the as-grown sample. The red-shift is due to the relaxation of the compressive stress in the porous samples. The amplification of porosity-induced PL intensity could be explained by the extraction of strong PL by light scattering from the sidewalls of the GaN crystallites [5]. However, it could be also ascribed to the optical microcavity effect which is inherent to porous GaN areas characterized by strong light scattering. It has been known that optical mode density could be altered by interference due to the optical environment [6].

The spectral responsivity data for the as grown and porous GaN MSM detector are illustrated in Fig. 4. Photodetector responsivity was measured as a function of the incident light wavelength, which was from a high-pressure tungsten lamp with a 5V bias. For as grown GaN-based MSM, the detector shows a sharp cut-off wavelength at 362 nm, with a maximum responsivity of 0.258 A/W achieved at 360 nm. For porous GaN MSM detector, a sharp cut-off wavelength at 364 nm with a maximum responsivity of 0.771 A/W was achieved at 363 nm. Both of the detectors show a little decrease in responsitivity in the UV spectral region. MSM photodiode based on porous GaN shows enhanced (3x) magnitude of responsivity relative to the as grown GaN MSM photodiode. The response below the band gap obviously comes from the energy levels in the forbidden band, just like those in the photoluminescence, which mainly depend on defects and impurities in GaN films. The studies showed that porosity in GaN films could influence the structural and optical properties of the material, suggesting several advantages of porous GaN in photodetector applications.

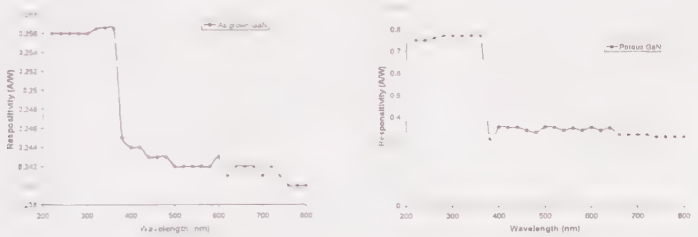

(a) (b)

Fig. 4. The responsivity as a function of wavelength for MSM detector: (a) As grown, (b) Porous GaN

Conclusions

The properties of UV photodetectors based on GaN epilayers grown on Si(111) substrates using RF-MBE were investigated. Porous GaN in this work was generated by Pt assisted electroless etching. Metal-semiconductor-metal (MSM) photodiode was fabricated on the samples. MSM photodiode based on porous GaN shows enhanced (3x) magnitude of responsivity relative to as grown GaN MSM photodiodes, suggesting advantages of porous GaN in photodetector applications.

Acknowledgments

The support from Universiti Sains Malaysia is gratefully acknowledged.

References

1. H. Sohn, S. Letant, M. J. Sailor, and W. C. Trogler, *J. Am. Chem. Soc.* **122,** 5399 (2000).
2. X. Li, Y-W Kim, P. W. Bohn and I. Adesida, Appl. Phys. Lett. **80**, (2002) 980.
3. C. K. Inoki, T.S. Kuan, C. D. Lee, A. Sagar, R. M. Feenstra, *Mater. Res. Soc. Symp. Proc.* **722**, K1.3.1 (2002).
4. D. J. Diaz, T. L. Williamson, I. Adesida, P. W. Bohn, R. J. Molnar, *J. Appl. Phys.* **94**, 7526 (2003).
5. A. P. Vajpeyi, S. Tripathy, S. J. Chua and E. A. Fitzgerald, *Physica E* **28**, 141 (2005).
6. H. Benisty, H. De Neve and C. Weisbuch, *IEEE J. Sel. Top. Quantum Electron.* **34**, 1612 (1998).

Advanced Materials Research Vol. 31 (2008) pp 42-52
online at http://www.scientific.net
© 2008 Trans Tech Publications, Switzerland

Growth, Surface morphology and optical properties of Gallium nitride nanowires

V. Suresh Kumar and J. Kumar*

Crystal Growth Centre, Anna University, Chennai – 600 025, India

* Corresponding author
Prof. J. Kumar, Director, marsjk@annauniv.edu, Tel. No. +91-44-22203569, 22352774

Keywords: Gallium Nitride (GaN), X- Ray Diffraction (XRD), Scanning Electron Microscope (SEM) and Photoluminescence

Abstract

We report on the growth mechanism, structural and optical characterstics of Gallium nitride nanowires prepared on sapphire substrates (0001) by reacting metal gallium with Gallium nitride powder and ammonia in the temperature range of 800 to 1050°C. GaN nanowires samples were characterized by using X-ray diffraction technique which shows wurtzite structure of GaN nanowires and the lattice parameters are calculated. Scanning electron microscopy images reveals that the dimension of the nanowires are around 60 – 80 nm and the length of 1 - 2 millimeters. Three Raman modes of GaN have been observed at frequencies 530, 554 and 564 cm-1. Photoluminescence spectrum reveals the band edge at 3.4 eV and gives yellow luminescence.

1. Introduction

III – V nitrides in general, and especially Gallium nitride (GaN), have been subjects of extensive research due to GaN has direct wide-bandgap energy which is ~3.4 eV and is a prime candidate for future high performance, high power optoelectronic devices because of its high melting point, good carrier mobility, and relatively high electrical breakdown field [1,2]. Catalytic growth of hexagonal GaN nanowires has opened up applications for use as UV or blue emitters, detectors, high-speed field effect transistors, and high temperature electronic devices [3]. Han et.al [4] synthesized GaN

nanorods through a carbon-nanotube-confined reaction. Subsequently, Han et.al [5] prepared GaN-carbon composite nanotubes and nanorods by arc discharge in a nitrogen atmosphere. Cheng et. al [6] formed GaN nanowires in anodic alumina membranes through a gas phase reaction of Ga_2O_3 vapour with flowing NH_3. Chen and Yeh [7] deposited GaN nanowires on a siliconwafer or a quarta plate using polycrystalline indium powder as a catalyst. Li et al. [8] produced GaN nanorods by a sublimation of GaN powder under an ammonia flow. Yashizawa et. al [9] grew self organized GaN nanocolumns on Al_2O_3 substrates by re radical source molecular beam epitaxy. Along with recent explosive research interest in nanotechnology, single crystalline GaN nanowires and nanotubes have already shown promise for realizing photonic and biological nanodevices especially as blue light emitting diodes and laser diodes. Most of the synthesis methods use Gallium metal in vapour source. We report the preparation of GaN nanowire using chemical vapour transport method and results from X-ray diffraction (XRD), scanning electron microscopy (SEM), Raman spectrum and Photoluminescence are reported.

2. Experiment

The experimental setup for the growth of GaN nanowires is decribed schematically in figure 1. The setup consist of 1 meter length quartz reactor with suitable inlet and outlet. The reactor is kept inside a double zone furnace. 5N purity of metal Gallium. GaN material and Boron trioxide (B_2O_3) are mixed in the ratio of 1:1:10 in an alumina boat and it was placed in the first zone of the reactor. Sapphire (0001) oriented substrates was initially cleaned with ferrous sulphate salt and then placed near the alumina boat in the second zone of the reactor. The furnace temperature was raised to the desired temperature in the range of 800 – 1050 °C. Nitrogen gas was allowed to flow over the Gallium surface from the start of the experiment. After reaching the desired temperature, liquid ammonia was passed through a bubbler (1hour) across the nitrogen gas flow. Nitrogen gas was used as the carrier gas to bring the ammonia molecules into the reaction zone. During the growth time ammonia molecules react with a mixture of metal gallium, GaN powder and B_2O_3. GaN vapour product are moved to the second zone and deposited on the substrate. The outgoing ammonia was passed through a bubbler

containing dilute sulfuric acid in order to neutralize the outlet gas before they were released in to the atmosphere. After the growth, the furnace is switched off and allowed to cool to room temperature. The final products of GaN nanowires are deposited on the substrate. .

3. Results and Discussions

3.1 X-ray diffraction

A typical XRD pattern of the resulting Gan nanowires is shown in the figure 2. The sharp diffraction peaks in the pattern were indexed to a hexagonal wurtzite structure. The lattice constants derived from the peak positions were a = 3.18Å and c=5.18Å, which agreed with the reported values of GaN [11]. The strong diffraction peaks relative to the background signals suggested that the resulting GaN nanowires had a high purity of the GaN woutzite phase. C.Chen et. Al [12] reported that the GaN nanowires had growth directions of [110] or [100].

3.2 Scanning Electron Microscopy

The surface morphology of the resulting material on sapphire substrates were characterized using scanning electron microscopy (SEM. Leica steroscan 440) and are shown in the figure 3(a), (b) and (c). Figure 3(a) is the SEM image of the layer deposited on sapphire substrate. It shows that the layer is composed of current nanowires and the diameters of the nanowires are about 60-80 nm. Fig 3 (b) shows the 10 KX magnification. In addition to smooth nanowires there are nanoribbons, zigzag nanorods and nanocrystal like structures on the substrates. The width and the thickness of the nanoribbons are about 10 – 40 nm. The maximum length of the nanowires is up to 200 μm. The diameter of the zigzag nanowires is about 40-80 nm. Figure 3(c) is the higher magnified SEM image of GaN nanowires. The diameter of the nanowires is around 40-80 nm.

3.3 Raman studies

The room temperature Raman spectra were measured using Ar+ laser with the incident wavelengthof 488 nm and 150 mW output power was using as the excitation source of the Raman scattering spectrometer (Model SPEX 14018). Figure 3 shows Raman spectrum of GaN nanowires. The most intensity peak at 568 cm-1 is mode of E2 symmetry of hexagonal GaN [3]. The peaks at 530 and 558 cm-1 agree with phonon vibration frequencies of A_1 (TO) and E_1 (TO) modes of the hexagonal GaN. These results agree with that of previously reported result [14] on epitaxial grown GaN on sapphire.

3.4 Photoluminescence studies

Room temperature PL spectrum of the sample was measured with using 325 nm He-Cd laser as an excitation source. Their luminescence properties were investigated using PL mechelle 900 spectrograph in the range 300 – 800 nm at room temperature using He-cd laser line of 325 nm as the excitation source. From the figure, we observed large intense broad band yellow luminescence in nanowires samples. The yellow luminescence commonly observed in GaN in a broad band peak at a phonon energy of about 2.2 eV [14,15]. This PL spectrum indicates no peak shift in comparison with the epitaxial GaN. There fore, there is a strong and broad light emission band of the crystalline GaN nanowires.

4. Conclusion

GaN nanowires were prepared by chemical vapour transport route and characterized by XRD, SEM, Raman spectrum and PL measurements. XRD measurements show that the GaN nanowires were of wurtzite structure. SEM images indicated that the dimension of the wire is ~ 60 – 80 nm. Raman spectrum indicates the phonon vibration frequencies Raman modes of Crystalline gallium nitride nanowires. PL shows the yellow luminescence property of the GaN nanowires.

Acknowledgement

Authors would like to thank Inter University Accelerator Centre (IUAC) and All India Council for Technical Education (AICTE), New Delhi for financial support.

References

[1] Nakamura. S, 1998, *Science* **281**, 956

[2] Dhara S, Datta A, Wu C T, Lan Z H, Chen K H, Chen L C, Hsu C W, Lin H M and Chen CC 2003 *Appl.Phys. Lett.* **82** 451 453

[3] Zhang J, Peng X S, Wang X F, Wang Y W, Zhang L D 2001, *Chem. Phys. Lett* **345**, 372 – 376

[4] Han W, Fan S, Li Q, Hu Y, 1997, *Science* **277**, 128

[5] Han W, Redlich P, Ernst F, Ruhle M, 2000, *Appl. Phys. Lett.* **76** 652

[6] Cheng G S, Zhang L D, Zhu Y, Fei G T, Li L, 1999 *Appl. Phys. Lett* **75** 2455

[7] Chen C, Yeh C, 2000, *Adv. Mater* **12** 738

[8] Li J Y, Chen L, Yao Z Y, Qiao Y G, Cao Y G, Lan Y C, 2000, *J. Cryst. Growth* **213** 408

[9] Yoshizawa M, Kikuchi A, Mori M, Fujita N, Kishino K, 1997, *Jpn. J. Appl. Phys.* Part II **36** L 459

[10] Vipul Srivastava, Suresh Kumar V, Puviarasu P, Thangaraju K, Thangavel R, Kumar J, 2005, *J. Cryst. Growth* **275** e2367-e2369

[11] Varadarajan E, Kumar J and Dhanasekaran R, 2004 *J. Cryst. Growth* **268** 475

[12] Chia – Chen Chen, Chun – Chia Yeh, Chun Ho Chen, Min – Yuan Yu, Hsiang Lin Lin, Jih-Jen Wu, Kuei – Hsein Peng, and Yanh – Frang. Che., 2001. J.Am. Chem. 2001, A.M Chem. Soc., 123 2791

[13] Nam C Y, Tham D.and Fischer J E, 2005 *Mater. Res. Soc. Symp. Proce.* **831**

[14] Bergman L, Bremser M, Perry W, Davis R, Dutta M, Nemanich R, 1997 *Appl. Phys. Lett.* **71** 2157

[15] V. Suresh Kumar et.al, 2006 *Nucl. Instrum. Methods* **244** 145

[16] Ridley B K, 1998, *J. Physc: Condens. Matter* **10** L 461-L 463

Figure captions

Figure 1. Experimental setup for growth and GaN nanowires

Figure 2. X – Ray diffraction spectrum of GaN nanowires

Figure 3. Scanning Electron Microscopy images of GaN nanowires.

Figure 4. Raman spectrum of GaN nanowires

Figure 5. Photoluminescence spectrum of GaN nanowires

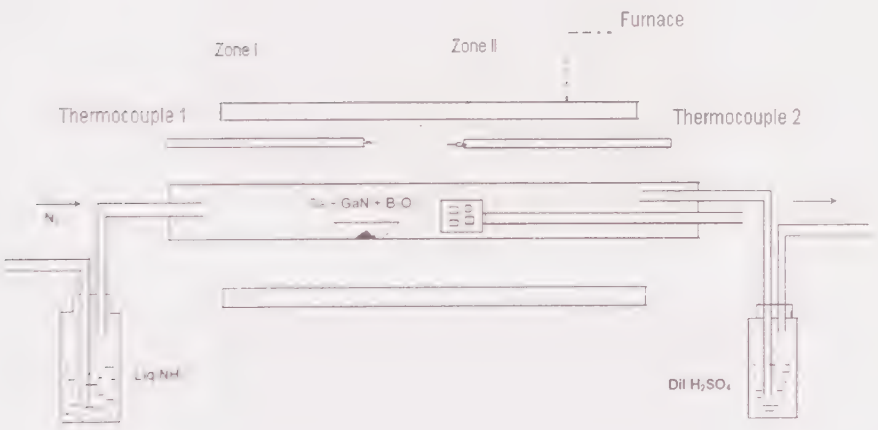

Figure 1. Experimental setup for the growth and GaN nanowires

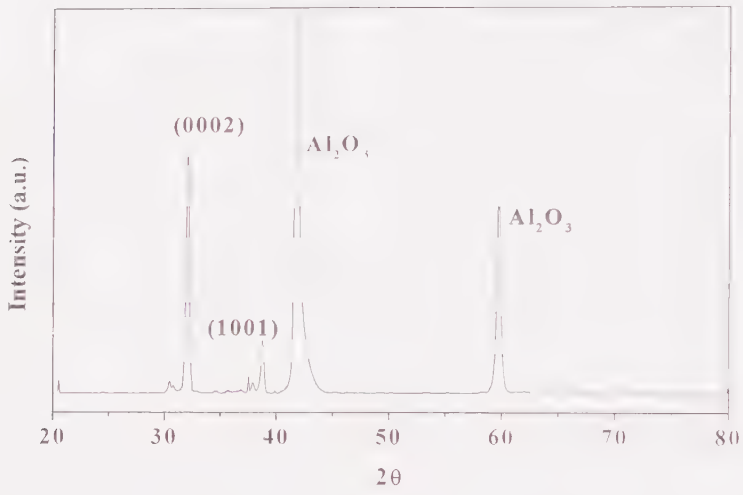

Figure 2. XRD spectrum of GaN nanowires

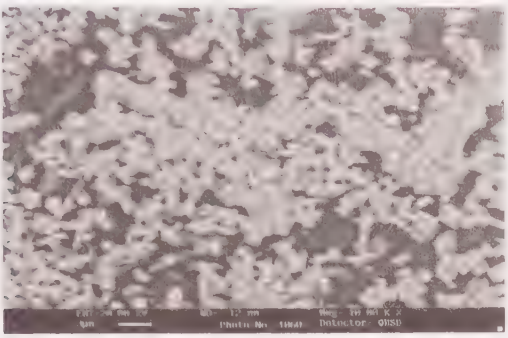

Figure 2 (a)

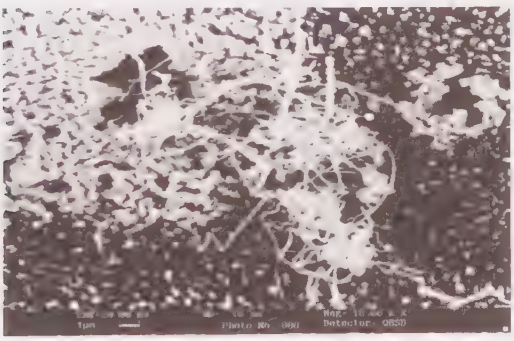

Figure (b)

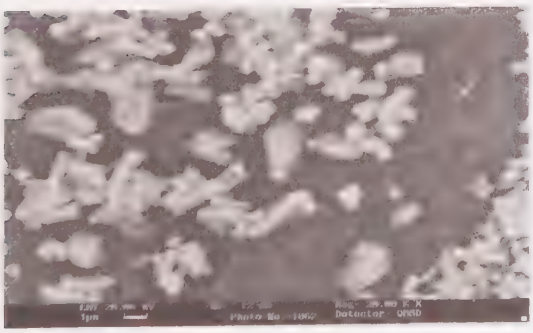

Figure (c)

Figure 2 (a),(b) and (c) SEM images of GaN nanowires

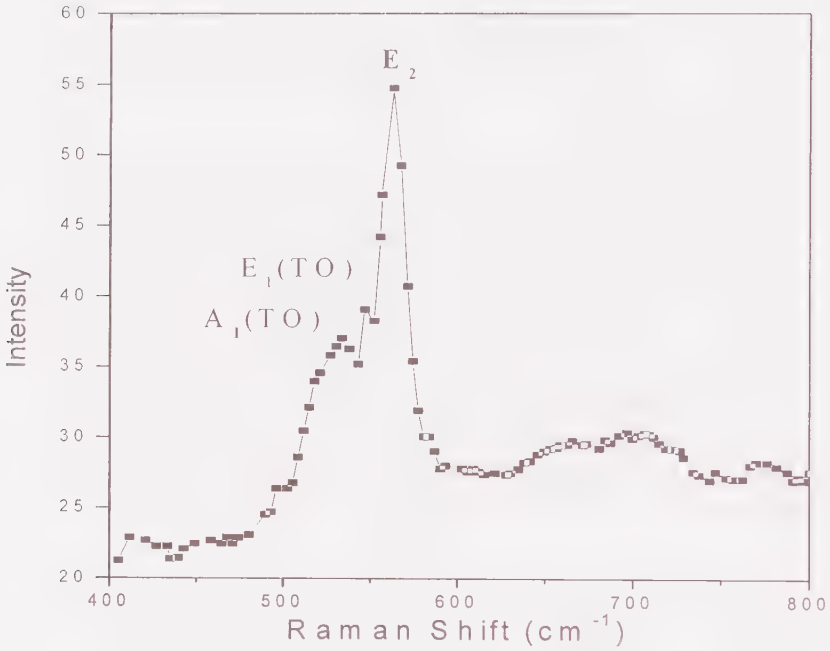

Figure 4. Raman spectrum of GaN nanowires

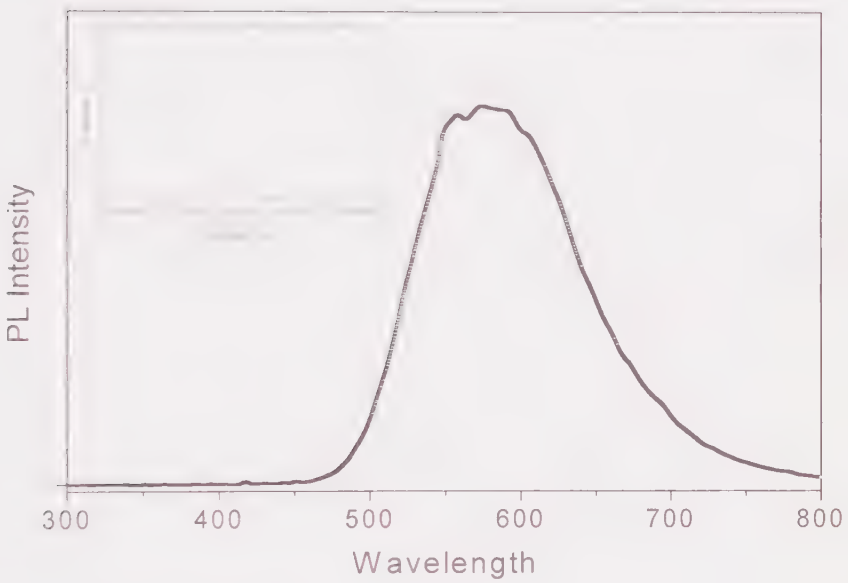

Figure 5. Photoluminescence spectrum of GaN nanowires

Advanced Materials Research Vol. 31 (2008) pp 52-55
online at http://www.scientific.net
© 2008 Trans Tech Publications, Switzerland

Optical reflection from a monolayer of embedded nano-objects covered by a thick capping layer

C.M.J. Wijers[a] and O. Voskoboynikov[b]

Department of Electronic Engineering and Institute of Electronics,
National Chiao Tung University, 1001 Ta Hsueh Rd., Hsinchu 300, Taiwan
[a]wijers@faculty.nctu.edu.tw, [b]vam@faculty.nctu.edu.tw

Keywords: optics, nano-objects, embedding

Abstract. In a hybrid discrete-continuum description the optical response of a capped monolayer of nano-objects has been determined. The monolayer emits a summation of partial plane waves obeying traditional reflection and transmission, enabling solution of the monolayer dipole strength. For thick capping layers the resulting reflection coefficients could be approximated by analytical expressions. These results have been used to investigate the feasibility of experimental detection of the optical response of nano-object monolayers.

Introduction. To examine the option to use direct gap semiconductor quantum dots and nanorings at very high frequencies requires understanding of their optical behavior. We have modeled the optical response of free floating and embedded monolayers of nano-objects in previous publications [1-3]. To turn this description into a realistic, quantitative one the capping layer, necessary to cover the monolayer, has to be included.

Theory. The system of nano-objects is shown in fig. 1. It consists of a monolayer of *InAs* quantum-dots, dielectric constant ε, arranged in a square lattice with lattice constant a_L embedded in *GaAs*, dielectric constant ε_m. This system is terminated by a *GaAs*-vacuum interface a distance h above the lattice. From outside (vacuum) an electromagnetic plane wave $\mathbf{E}(\mathbf{r},t)$ given by:

$$\mathbf{E}(\mathbf{r},t) = \mathbf{E}_0\, e^{i[\mathbf{kr}-\omega t]} \qquad (1)$$

impinges upon the capped monolayer, where ω is the angular frequency and $\mathbf{k}$ the wave vector with angle of incidence θ_i. As shown in previous publications [1-4] the electromagnetic response of a nano-object requires the dipole strength $\mathbf{p}$ as follows from:

$$\mathbf{p} = \overleftrightarrow{\alpha}\left[\mathbf{E}_L + \overleftrightarrow{\mathbf{t}}_E\,\mathbf{p}\right] \qquad (2)$$

where $\mathbf{E}_L$ is the local field, $\mathbf{t}_S$ the intracellular transfer tensor and α the bare excess polarizability [1]:

$$\overleftrightarrow{\alpha} = \varepsilon_0 V\left[\varepsilon - \varepsilon_m\right] + \frac{3}{4}\frac{e^2}{\hbar}\, r_{eh}^2\left[\hat{\mathbf{x}}\hat{\mathbf{x}}^T + \hat{\mathbf{y}}\hat{\mathbf{y}}^T\right] \times \sum_{l=0} |\langle F_{hl} \mid F_{el}\rangle_V|^2 f_{hl,el}(\omega) \qquad (3)$$

where r_{eh} is the matrix element of the spatial coordinate $\mathbf{r}$ for bulk electron and hole states. $\langle F_{hl} \mid F_{el}\rangle_V$ is the envelope overlap matrix

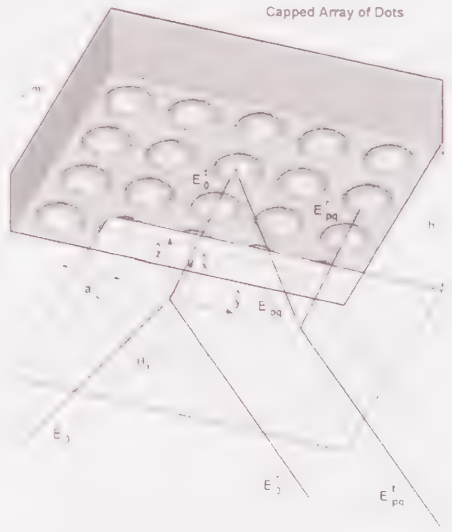

FIG.1: Layer of embedded quantum dots.

element over the volume V of the nano-object. $f_{hl,el}(\omega)$ is a complex frequency dependent function as described in [1]. For the intracellular transfer tensor $\mathbf{t}_E$ in (2) we use:

$$t_{Eu} = \frac{1}{\varepsilon_m \varepsilon_0}\left[\frac{-N_u}{V} + \frac{ik^3}{6\pi}\right] \qquad N_z = \frac{1}{1-\zeta^2}\left|1 - \frac{\zeta \cos^{-1}\zeta}{\sqrt{1-\zeta^2}}\right| \tag{4}$$

where $u = x, y, z$ and the other components N_u follow from $N_x = N_y = \frac{1}{2}(1 - N_z)$. For both expressions (3,4) the electrostatic response of the nano-object is modeled by a dielectric spheroid with principle axes a, c and $\zeta = c/a$ [4]. To apply this scheme to the case of the capped quantum dots, requires a proper expression for the local field $\mathbf{E}_L$, for which we need the electric field emitted by a lattice plane of point dipoles of dipole strength $\mathbf{p}$. Using Ewald's 3-fold integral transform [5] this field can be expressed as:

$$\mathbf{E}(\mathbf{r}) = \sum_{pq} \mathbf{E}_{pq} e^{i\mathbf{k}_{pq}\mathbf{r}} \qquad \mathbf{E}_{pq} = e^{-i\mathbf{k}_{pq}\mathbf{r}_0}\left|\frac{\mathbf{k}_{pq}\mathbf{k}_{pq}^T - \varepsilon_m k_0^2 \overleftrightarrow{\mathbf{1}}}{2i\varepsilon_m\varepsilon_0 a_L^2 \kappa_{pq}}\right|\mathbf{p} = \overleftrightarrow{\mathbf{f}}\,\mathbf{p} \tag{5}$$

The $\mathbf{k}_{pq} = \mathbf{k}_{\parallel} + \mathbf{g}_{pq} + \kappa_{pq}\hat{\mathbf{z}}$ are the wave vectors of the partial plane waves and $k_0 = \omega/c$. The site of the characteristic dipole is $\mathbf{r}_0$, the $\mathbf{g}_{pq}$ are surface reciprocal lattice vectors and $\mathbf{f}$ is the interplanar transfer tensor [5]. By combining properly this partial wave expansion and the conventional Fresnel transmission, reflection coefficients t^{MV}, r^{MV} for the medium-vacuum (MV) interface, the transmitted and reflected amplitudes $\mathbf{E}_{pq}^{t,r}$ (see Fig. 1) become:

$$\mathbf{E}_{pq}^{t} = \eta_{pq}\left[\varepsilon_m k_0^2 t_s^{MV}\hat{\mathbf{s}}\hat{\mathbf{s}}^T + \left(\frac{\kappa_{pq}^m}{\kappa_{pq}}\right)t_p^{MV}\underline{\mathbf{k}}_{pq}^{-}\underline{\mathbf{k}}_{pq}^{m\perp T}\right]\mathbf{p}$$

$$\mathbf{E}_{pq}^{r} = \eta_{pq}\left[\varepsilon_m k_0^2 r_s^{MV}\hat{\mathbf{s}}\hat{\mathbf{s}}^T + r_p^{MV}\mathbf{k}_{pq}^{m-}\underline{\mathbf{k}}_{pq}^{m-T}\right]\mathbf{p} \qquad \eta_{pq} = \frac{ie^{-i\underline{\mathbf{k}}_{pq}^{m}\mathbf{r}_0}}{2\varepsilon_m\varepsilon_0 a_L^2 \kappa_{pq}^m} \tag{6}$$

where $\hat{\mathbf{s}}$ depends on pq, s, p are the traditional polarization directions and m is the medium index. The underscore is used for the reflection operator as in [5]. The general expression from which $\mathbf{p}$ has to be derived is:

$$\mathbf{p} = \left[\overleftrightarrow{\alpha}^{-1} - \overleftrightarrow{\mathbf{f}}_B\right]^{-1} \mathrm{T}^{VM}\mathbf{E}_0 e^{i\mathbf{k}^m\mathbf{r}_0} \tag{7}$$

which for general cases can only be solved numerically. The buried intraplanar transfer tensor $\mathbf{f}_B$ accounts for all multiple reflections. For thick enough capping layers all partial waves, are rapidly decaying, apart from the $pq = 00$ contribution. Above the decay length h_D for the 10 partial wave, we can restrict the summations (6) to $pq = 00$. Decay length h_D is given by:

$$h_D = \frac{a_L}{4\pi} = 6.37\ nm \tag{8}$$

We introduce the orthogonal vectors $\mathbf{k}_m = \mathbf{k}_{00}$ and $\mathbf{k}_m^{\perp}$, having the same length k_m. In this thick layer approximation and with the yz-plane as plane of incidence (see Fig. 1), the expression for $\mathbf{f}_B$ becomes:

$$\mathbf{f}_B \approx \left(\overleftrightarrow{\mathbf{f}}' + \overleftrightarrow{\mathbf{t}}_S\right)/\varepsilon_m + e^{i\mathbf{k}_m\mathbf{r}_0}\eta_{00}\left[\varepsilon_m k_0^2 r_s^{MV}\hat{\mathbf{x}}\hat{\mathbf{x}}^T + r_p^{MV}\mathbf{k}_m^{\perp}\underline{\mathbf{k}}_m^{\perp T}\right] \tag{9}$$

The quantity $\mathbf{f}'$ is the vacuum intraplanar transfer tensor [1]. With this expression for $\mathbf{f}_B$ we can work out reflection- and transmission coefficients, as in [5], and the result becomes:

$$r_q \quad t_q^{VM} \; \frac{t_q^{MV} t_q^{VM}}{e^{-i2\kappa_m h} A_q^{-1} - r_q^{MV}} \qquad (10)$$

$$\kappa_m \left[\varepsilon_m \alpha_0 \alpha_u^{-1} - f_{Su} - t_{Su} \right] - 2\pi i a_L K_u^2$$

$$2\pi i a_L K_u^2$$

with $q = s, p$. Further $K_x = k_0 \sqrt{\varepsilon_m}$, $K_y = \kappa_m$, $K_z = k_0 \sin\theta_t$. The definitions and values for α [illegible] are as given in [1].

Numerical Results. The reflection coefficient (2) has been used to calculate the optical response of the same monolayer of quantum dots as studied in [3]. So $a_L = 80.0\ nm$ and $a = 18.45\ nm$, $c = 1.49\ nm$ are the long/short axes of the spheroidal nano-object with static relative dielectric constant $\varepsilon = 15.15$. The embedding medium ($GaAs$) has $\varepsilon_m = 13.1$. The reflectance for perpendicular incidence is shown in fig. 2. It displays the same peaks at the same energies as determined in [3] (infinite embedding). Over the whole energy range the total variation of the signal strength is 0.0001 against a background of 0.3216. This is too weak to be observed directly in a normal reflectometer.

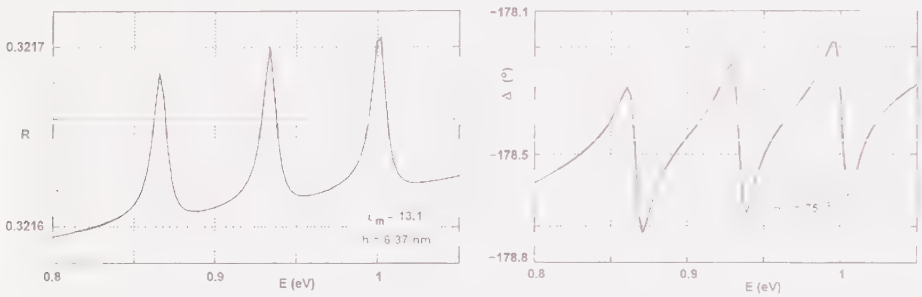

FIG.2: Reflectance for perpendicular incidence (left) and Ellipsometric angle Δ for $\theta_t = 75^\circ$ (right).

In figure 2 we show the ellipsometric angle Δ for $\theta_t = 75^\circ$, close to the Brewster angle. We see that the variation in Δ now is 0.6°, well above the detection limit of any ellipsometer, although the weak p-intensity needs special attention. Other points of attention are inhomogeneous level broadening and the deviation of the lattice from its assumed perfect shape. Since photoluminescence measurements from such systems still resolve the levels, these effects are not desctructive. In summary it should be possible to measure the linear optical characteristics of even a single monolayer of quantum dots.

Summary and Conclusions. The influence of adding a capping layer to the optical response of a monolayer of buried nano-objects (quantum dots) has been investigated theoretically. For thick capping layers the results could be simplified and an analytical expression for the reflection coefficient has been obtained. This result has been used to examine the experimental feasibility of detecting the linear optical response of a buried monolayer of quantum dots. We found that this is feasible, provided ellipsometry is used for the detection.

Acknowledgement

This work is supported by the National Science Council of the Republic of China under Contracts No. NSC-94-2811-M-009-020 and NSC-94-2112-M-009-037 and by the Ministry of Education of Taiwan under contract no. MOEATU 95W803.

References

[1] O. Voskoboynikov, C.M.J. Wijers, J.L. Liu and C.P. Lee, Phys. Rev. **B 71** 245332 (2005).

[2] O. Voskoboynikov O, C.M.J. Wijers, J.L. Liu and C.P. Lee, Eur. Phys. Lett. **70** 656 (2005).

[3] C.M.J. Wijers, J.-H. Chu, J.L. Liu and O. Voskoboynikov, Phys. Rev. **B 74** 35323 (2006).

[4] C.M.J. Wijers, J.-H. Chu and O. Voskoboynikov, Eur. Phys. J. **B 54** 225 (2006).

[5] C.M.J. Wijers and G.P.M. Poppe, Phys. Rev. **B 46** 7605 (1992).

Advanced Materials Research Vol. 31 (2008) pp 56-58
online at http://www.scientific.net
© 2008 Trans Tech Publications, Switzerland

Visible Light Emission from Ordered Nanopatterned InP Surface

S. K. Mohanta[1,a], R.K. Soni[1,b], S. Tripathy[2,c] and S.J. Chua[2,d]

[1]Physics Department, Indian Institute of Technology Delhi, New Delhi 110016, India

[2]Institute of Materials Research and Engineering, 3 Research Link, Singapore 117602

[a]m_sanjay135@yahoo.com, [b]ravisoni@physics.iitd.ac.in,

[c]tripathy-sudhiranjan@imre.a-star.edu.sg, [d]elecsj@nus.edu.sg

Keywords: Nanostructuring of semiconductor surface, photoluminescence, low-energy ion beam.

Abstract. The InP nanostructures have been fabricated by low-energy Ar^+-ion of dose 1×10^{18} cm^{-2} and energy 50 keV, at normal incidence. The InP nanodot size varies from 50 to 90 nm. Photoluminescence spectra show blue shifted visible emission band at 1.98 eV, and quenching of the band edge emission from the nanopatterned surface. The blue-shifted emission band arises due to size convoluted band-to-band emission form the surface nanodots while the defects formation in the irradiated surface leads to the quenching of band edge emission. Thermal annealing results in clustering of the patterned surface and enhancement of the band edge emission accompanied with absence of visible band. Our results show that the origin of visible emission is from the surface nanodots and not from the nanocrystallites in the implanted surface region. This is corroborated by the wavelength dependence of photoluminescence measurement by probing different depth of the disordered region.

Introduction

Large-scale ordered nanopatterned semiconductor surface induced by low-energy ion beam is useful for fabrication of template for overgrowth for multifunctional nanoscale photonic devices. The hexagonal symmetric regular nanostructures on crystalline or amorphous GaSb offers attractive potential for simple self-masking technology. Also, fabrication of self-assembled crystalline silicon nanostructures of homogeneous height, arranged in a hexagonal symmetry on Si (100) surface and high density and spatially-ordered dot structures on InP surfaces by low-energy Ar^+-ion irradiation have been demostrated [1-4]. Yuba *et al.* observed high density and spatially ordered dot structures on InP surfaces of tunable size by modulating Ar^+-ion energy, ion dose, incident angle, and sample temperature [5]. In this work, we have studied morphology and emission properties of ordered and dense InP nanodots produced by Ar^+-ion irradiation at normal incidence. The photoluminescence (PL) spectroscopy is a sensitive probe for the study of perturbation on the electronic states of the low-dimensional structures.

Experimental

The nanopatterned InP surface was fabricated by irradiating Ar^+-ion beam at normal incidence from an ion implanter on bulk n-type InP (100) sample placed in a high vacuum chamber at a pressure of 2×10^{-6} Torr. The Argon ions were accelerated at energy 50 keV with an effective current density of 25 $\mu A/cm^2$. The irradiated ion dose was 1×10^{18} cm^{-2}. Rapid thermal annealing (RTA) of the as-irradiated samples was carried out in N_2 ambient in a temperature range of 400–500°C. During RTA a proximity capped InP wafer was used. A field emission SEM (JEOL 6700FESEM) and a rapid PL mapping setup, equipped with 532 and 325 nm laser lines as excitation sources, were used for recording surface morphology and PL spectra, respectively.

Results and Discussion

Figure 1(a) shows the nanopatterned InP surface with dots size in the range of 50 nm to 90 nm. The nanopatterning of the surface is associated with surface instability between the curvature dependent sputtering and smoothing by surface diffusion induced by Ar^+-ion irradiation at normal incidence. The Bradley-Harper theory predicts that by varying sputtering parameters such as ion energy, sample temperature, and ion flux the dot size can be controlled [5]. The large density and size distribution of InP dots results from further sputtering of nanodots at high doses. The average height of the nanorods is 30 nm. The influence of RTA on morphology of the pattern surface shows clustering of the surface nanodots. The SEM images of nanopatterned InP surfaces subjected to RTA at 400 and 500 °C in N_2 ambient for 1 min. show formation of the clusters with increased dot sizes up to 200 nm at 400 °C, [Fig. 1(b)] and clustering of almost all the nanodots at 500 °C, [Fig. 1(c)]. The clustering can be caused by the dissociation of phosphorus from the surface. Also, over heating at 500°C develops cracks and damge sample surface.

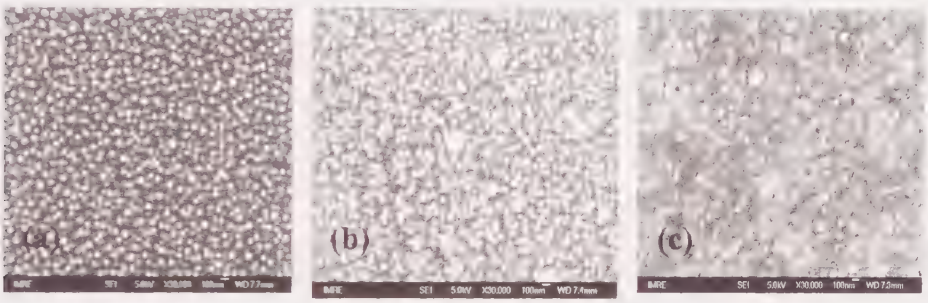

Fig. 1 SEM images of nanopatterned InP surface with an ion dose 1×10^{18} cm^{-2} and energy 50 keV (a) as-irrediated, and annealed in N_2 ambient for 1 min at temperature (b) 400 °C, and (c) 500 °C.

Figure 2 shows the room-temperature PL spectra excited at wavelength $\lambda = 532$ nm from as-irradiated and annealed nanopatterned InP surface. A strong peak at 905 nm (1.37 eV) corresponding to the band-edge emission from the bulk InP is observed. The PL spectrum from the patterned surface exhibits quenching of the band edge emission due to the deep defect levels introduced by the ion irradiation in the disordered materials leading to the enhanced contribution of the one-phonon non-radiative recombination of the photoexcited carriers. In addition, a weak and asymmetrically broadened peak appears at 625 nm (1.98 eV), similar to the case of PL observation by Facsko *et al.* [1]. The large blue shift of 0.61 eV is attributed to the quantum confinement effect in nanodots. The asymmetric broadening of the peak is associated with the size fluctuation of the surface dots. Surface recombination in the as-irradiated and uncapped InP nanodots could reduce the PL efficiency from the fabricated dots. Additionally, large density of point defect complexes can also quench the radiative emission. After annealing, the intensity of the band edge emission increases due to the removals of defects, however the blue shifted emission band disappears. The increased diffusion length of the carriers and improved optical quality of the irradiated surface after annealing resulted in the enhanced band edge luminescence, on the other hand, disappearance of the blue shifted emission with annealing can be related to the clustering of the patterned surface, as seen in our SEM images. For the annealing temperature 400 °C, the clustering of the patterned surface leads to increased dot size, up to 200 nm, and weakening of the quantum size effect [Fig. 1(b)]. At higher annealing temperature of 500 °C, clustering of almost all the dots of the nanopatterned surface occur [Fig. 1(c)]. We would like to emphasize that the radiative transitions in the surface nanodots give rise to blue shifted emission band, the contribution of nanocrystallites from the implanted surface region is either weak or absent. Charge carrier confinement induced

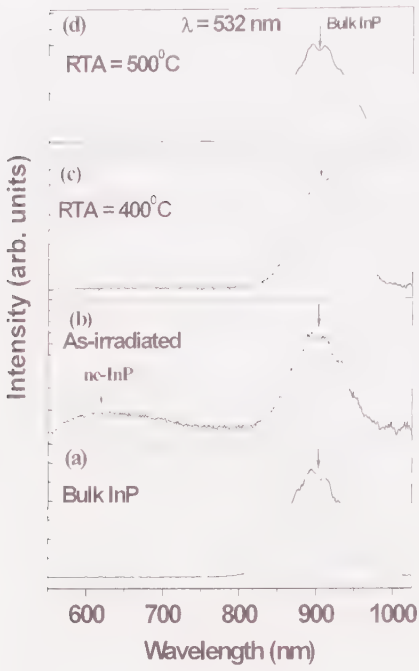

Fig. 2. Room-temperature PL spectra excited by λ = 532 nm from (a) bulk InP, (b) nanopatterned InP surface and subsequently annealed at (c) 400 °C, and (d) 500 °C.

visible emission from GaAs nanocrystals synthesized by sequential ion implantation of Ga^+ and As^- and annealing in SiO_2 matrices has been reported [6]. In our case the nonexistence of blue shifted emission from the as-irradiated and annealed samples may due to very low density or lack of formation of nanocrystallites. Using short wavelength (325 nm) for PL excitation, the spectra are mainly obtained from the near surface region with highly disorder local structure due to small probe depth. No emission is observed from the as-irradiated sample whereas annealed samples show emission in the IR region only. In our case, the appearance of the band edge emission but absence of emission in the visible region after RTA points to large cluster formation or low density of nanocrystallites in the probe volume.

Summary

Ordered InP nanodots of size 50 nm to 90 nm and height 30 nm were fabricated by Ar^--ion of dose 1×10^{18} cm^{-2} and energy 50 keV on InP surface. These dots emit asymmetric blue-shifted visible band resulting from size convoluted band-to-band emission form the surface nanodots. The thermal annealing enhances the band-edge emission from the patterned surface as a result of the improved optical quality, and the formation of clusters on the patterned surface leads to weakening of confinement and near absence of the blue-shifted visible band. We conclude that the origin of visible emission is from the surface nanodots and not from the nanocrystallites in the implanted surface region. This is corroborated by the measurement of wavelength dependence of photoluminescence, by probing different depth in the disordered region.

References

[1] S. Facsko, T. Dekorsy, C. Koerdt, C. Trappe, H. Kurz, A. Vogt, and H. L. Hartnagel, Science 285 (1999) p.1551.

[2] S. Facsko, T. Bobek, H. Kurz, T. Dekorsy, S. Kyrsta, and R. Cremer, Appl. Phys. Lett. 80 (2002) p.130.

[3] R. Gago, L. Vázquez, R. Cuerno, M. Varela, C. Ballesteros, and J. M. Albella, Appl. Phys. Lett. 78 (2001) p.3316.

[4] B. Ziberi, F. Frost, B. Rauschenbach, and Th. Höche, Appl. Phys. Lett. 87 (2005) p.033113.

[5] Y. Yuba, S. Hazama, and K. Gamo, Nucl. Instrum. Methods Phys. Res. B 206 (2003) p.648.

[6] Y. Kanemitsu, H. Tanaka, T. Kushida, K. S. Min, H. A. Atwater, J. Luminescence 87 (2000) p.432.

Advanced Materials Research Vol. 31 (2008) pp 59-61
online at http://www.scientific.net
© 2008 Trans Tech Publications, Switzerland

Dependence of the Absorption Spectra of III-V Semiconductor Quantum Dots on the Size Distribution

Subindu Kumar[1,a], Dipankar Biswas[2,b] and Tapas Das[2,c]

[1]Department of ECE, Siliguri Institute of Technology, P.O. Sukna, Siliguri 734009 (WB), India

[2]Institute of Radio Physics and Electronics, University of Calcutta, 92 Acharya Prafulla Chandra Road, Kolkata 700009, India

[a]subindukumar@hotmail.com, [b]diiibiswas@yahoo.co.in, [c]dtapas2003@yahoo.com

Keywords: Quantum Dots, Absorption Spectra.

Abstract. In recent years there have been extensive studies on III-V semiconductor quantum dots (QDs). In this paper we have formulated the absorption spectra of a realistic QD system with dot size distribution described by a Gaussian function. The dots were approximated as cubic boxes having finite potentials at the boundaries. The effects of size non uniformity on the optical absorption spectra of a realistic QD system was analyzed and the results have been compared with ideal dots having infinite potentials at the boundaries.

Introduction

The quantum dots (QDs) system is usually inhomogeneous due to the large variation of the dot size. There are reports [1,2] on the effect of a Gaussian distribution of the dot size on the optical absorption spectra. In such reports, the dots were approximated as cubic or spherical structures having infinite potential barriers at the boundaries. However realistic semiconductor QDs have finite potential barriers. In this paper we have investigated the optical absorption spectra of a QD system with non uniform size distribution described by a Gaussian function. We have approximated the QD as a cubic box with finite potential barriers. A comparative study of the ideal and realistic dots was carried out and it was found that the spectra of the realistic dots seem to be red-shifted and the line width decreases.

The Model

The energy levels (in units of $\hbar^2/mL^2$) of finite rectangular QW can be expressed as [3]

$$E(n^2) = \frac{2P^2}{(P-1)^2}\left[\left(\frac{n\pi}{2}\right)^2 - \frac{1}{3(P+1)^3}\left(\frac{n\pi}{2}\right)^4 - \frac{27P-8}{180(P+1)^6}\left(\frac{n\pi}{2}\right)^6\right] \quad (1)$$

$$n^2 = \sum n_j^2 \,,\ j = 1,2,3 \quad (2)$$

where P is the well strength parameters defined as $P = [\sqrt{(2m_0 m^* V_0/\hbar)}]L/2$, where V_0 is the height of the well (conduction/valance band) and L is the well width. m_0 and m^* are the rest mass and effective mass of the carriers (electrons/holes) respectively. The lowest state corresponds to $n^2 = 3$. For an infinite deep potential well, $P \rightarrow \infty$ and Eq. 1 reduces to the well known result

$$\lim_{P \to \infty} E(n^2) = \frac{\pi^2 \hbar^2 n^2}{2m_0 m^* L^2} \quad (3)$$

Let us now define the resonance energy of a realistic QD, having finite potential barriers, as the photon energy needed for the creation of electron-hole pair. This may be represented as

$$\hbar\omega_{real} = E_g + E_e(n^2) + E_h(n^2) \quad (4)$$

where E_g is the band gap of the semiconductor material, $E_e(n^2)$ and $E_h(n^2)$ are the confinement energies of electron and hole respectively. The resonance energy of an ideal dot having infinite potential barriers, $\hbar\omega_{ideal}$, can be expressed as

$$\hbar\omega_{ideal} = \lim_{P\to\infty} \hbar\omega_{real} = E_g + \frac{\pi^2\hbar^2}{2L^2}\left[\frac{1}{m_0 m_e^*} + \frac{1}{m_0 m_h^*}\right] n^2 = E_g + \frac{\pi^2\hbar^2 n^2}{2\mu L^2} \tag{5}$$

where $1/\mu = 1/(m_0 m_e^*) + 1/(m_0 m_h^*)$. Let us now define two dimensionless parameters: the reduced photon energies x^2_{real} and x^2_{ideal} for a realistic and ideal QD system respectively, represented as

$$x^2_{real} = \frac{\hbar\omega_{real} - E_g}{[E_e(n^2)_{L=L_0} + E_h(n^2)_{L=L_0}]/n^2} \tag{6}$$

$$\text{and } x^2_{ideal} = \frac{\hbar\omega_{ideal} - E_g}{\pi^2\hbar^2/2\mu L_0^2} \tag{7}$$

$E_e(n^2)_{L=L0}$ and $E_h(n^2)_{L=L0}$ are the values of $E_e(n^2)$ and $E_h(n^2)$ for $L = L_0$. The absorption spectra of a QD system is the superimposition of the contribution from each individual realistic dot having infinite potential barriers at the boundaries, the overall behavior is modeled by considering a Gaussian distribution of the dot size of side length L which can be represented as [1]:

$$\alpha_{ideal} = \frac{\beta_{ideal}}{2L_0^3}\sum_{(n^2)}\frac{g(n^2)}{\xi n^2}\exp\left[-\left(\frac{n}{x_{ideal}} - 1\right)^2 / 2\xi^2\right] \tag{8}$$

$$\text{where } \beta_{ideal} = \frac{(1/\sqrt{2\pi})A_{ideal}}{\pi^2\hbar^2/2\mu L_0^2} \tag{9}$$

L_0 is the average dot size of the system, D is the standard deviation, ξ (=D/L_0) is the relative standard deviation of the dot, $g(n^2)$ is the degeneracy of the energy level determined by $n^2=\sum n_j^2$. Only $\Delta n=0$ transitions are considered allowed. A_{ideal} is a constant in terms of the momentum matrix P_n [1]. Now we model the optical absorption spectra of a realistic cubic dot of finite potential barrier at the boundaries as

$$\alpha_{real} = \frac{\beta_{real}}{2L_0^3}\sum_{(n^2)}\frac{g(n^2)}{\xi n^2}\exp\left[-\left(\frac{n}{x_{real}} - 1\right)^2 / 2\xi^2\right] \tag{10}$$

$$\text{where } \beta_{real} = \frac{(1/\sqrt{2\pi})A_{real}}{[E_e(n^2)_{L=L_0} + E_h(n^2)_{L=L_0}]/n^2} \tag{11}$$

In the realm of an ideal cubic QD system, P_e, $P_h \to \infty$ and the photon frequency, $\omega = \omega_{ideal}$ such that

$$\lim_{P_e,P_h\to\infty} \beta_{real} = \frac{(1/\sqrt{2\pi})A_{ideal}}{\pi^2\hbar^2/2\mu L_0^2} = \beta_{ideal} \tag{12}$$

This agrees with the choice of our denominator of Eq. 11. Eqs. 8 and 10 represent a set of Gaussian absorption peaks with peak photon energies determined by the average dot size L_0 and represented in Eqs. 4 and 5.

Absorption Spectra of a Realistic $In_{0.7}Ga_{0.3}N/GaN$ QD System

The results of computations of the absorption spectra of $In_{0.7}Ga_{0.3}N/GaN$ QD system are shown in Figs. 1 and 2. Fig. 1 shows the plot of the lowest absorption peak ($n^2 = 3$) for $In_{0.7}Ga_{0.3}N/GaN$ QD system with different ξs. The absorption spectra for the realistic and ideal dots are denoted by solid and dotted lines respectively. The horizontal axis is the photon energy corresponding to real and ideal dots defined by Eqs. 4 and 5 respectively. The vertical axis is the relative absorption of the ideal and realistic dots defined as α_{real} / ($\beta_{real}/2L_0^3$) and α_{ideal} /

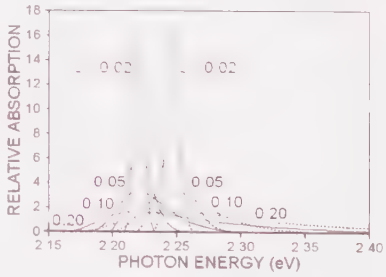

Fig. 1. Absorption spectra of the lowest transition of $In_{0.7}Ga_{0.3}N/GaN$ QD system corresponding to both real and ideal dots.

($\beta_{ideal}/2L_0^2$) according to Eqs. 8 and 10. The energy band gap of $In_XGa_{1-X}N$, E_g, was calculated from the equation [4]:

$$E_g(x) = (1-x)E_{g,GaN} + x\,E_{g,InN} - bx(1-x) \quad (14)$$

where, x is the mole fraction of indium, $E_{g,GaN}$ and $E_{g,InN}$ are the energy band gaps of GaN and InN respectively, and b is the bowing parameter. In our calculation $E_{g,GaN}$, $E_{g,InN}$, 'x', 'b' and the average dot size was assumed to be 3.4 eV, 2 eV, 0.7, 1.4 and 7.25 nm respectively. For finite potential barriers, the band offset ratio was considered to be 55 : 45 [5]. The effective masses are assumed to be $0.2m_0$ for electrons [4] and $1.56m_0$ for heavy holes [6]. The computed absorption spectra of $In_{0.7}Ga_{0.3}N$ GaN QD system is shown in Fig. 2. The solid and filled circles represent the individual absorption peaks and their superposition of the realistic dots respectively, while for ideal dots it is represented by doted and open circles. In both the cases, with ξ=0.02, all the peaks could be resolved. As ξ increases, the resolvability decreases.

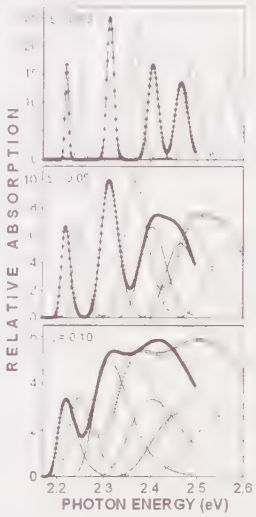

Fig. 2. Absorption spectra of the lowest four transitions of $In_{0.7}Ga_{0.3}N$/GaN QD system corresponding to both real and ideal dots.

Discussion and Conclusion

A model has been formulated to investigate the interband optical absorption of realistic QD systems having finite potentials at the boundaries. The absorption spectra of $In_{0.6}Ga_{0.4}As/Al_{0.3}Ga_{0.7}As$ QD system has been calculated. It is observed that for realistic dots there is red shift of the absorption peaks and there is a decrease in the linewidth as compared to the ideal QD system for the same size deviation. The photon energies corresponding to the Gaussian absorption peaks depend on the band gap of the semiconductor material and the confinement energies of the conduction and the valance bands. For realistic dots having finite potential barrier, the confinement energies are less as compared to ideal dots having infinite potential barriers. As a result, the absorption peaks suffer from a red shift.

The variation of the energy of the sub-bands with change in the size of the dots is much more pronounced in the case of infinite wells as compared to finite wells. Hence larger deviation in the absorption energies for a particular ξ is expected in the case of infinite wells and hence the absorption spectra become broader. Moreover in a narrow finite well less number of levels will be available for transitions which will make the spectrum narrow.

References

[1] Wei-Yu Wu, J.N. Schulman, T.Y. Hsu and U. Efron: Appl. Phys. Lett. Vol. 51 (1987), p. 710.

[2] D. L. Ferreira and J. L. A. Alves: Nanotechnology (Inst. of Phy. Pub.), Vol. 15 (2004) p. 975.

[3] David L. Aronstein and C. R. Stroud, Jr: Am. J. Phys. Vol. 68 (2000) p. 943.

[4] S. Nakamura, T. Mukai, M. Senoh, S. Nagahama and N. Iwasa: J. Appl. Phys. Vol. 74 (1993) p. 3911.

[5] D. Biswas, S. Kumar and T. Das: Thin Solid Films Vol. 515 (2007) p. 4488.

[6] Chii-Chang Chen et al: Appl. Phys. Lett. Vol. 77 (2000) p. 3758.

Advanced Materials Research Vol. 31 (2008) pp 62-64
online at http://www.scientific.net
© 2008 Trans Tech Publications, Switzerland

Conspicuous Presence of Higher Order Transitions in the Photoluminescence of $In_XGa_{1-X}N$/GaN Quantum Wells

Dipankar Biswas[1,a], Tapas Das[1,b], Sanjib Kabi[1,c] and Subindu Kumar[2,a]

[1]Institute of Radio Physics and Electronics, University of Calcutta, 92 Acharya Prafulla Chandra Road, Kolkata 700009, India

[2]Department of ECE, Siliguri Institute of Technology, P.O: Sukna, Siliguri, 734009 (WB), India

[a]diiibiswas@yahoo.co.in, [b]dtapas2003@yahoo.com, [c]sanjib_kabi@yahoo.com, [i]subindukumar@hotmail.com

Keywords: Photoluminescence, Quantum Well, Annealing.

Abstract. For successive annealing stages the photoluminescence (PL) peaks of $In_XGa_{1-X}N$/GaN quantum wells (QWs) shift initially towards red which is followed by a blue. This phenomenon contradicts the usual monotonic blueshift. We have found that the phenomena can be explained properly only if we consider recombinations from the higher sub-bands to be present in the PL of the $In_XGa_{1-X}N$/GaN QWs, which is not usual. When a strong piezoelectric field exists across a QW, as encountered in $In_XGa_{1-X}N$/GaN QWs, the probability of optical transitions from higher sub-bands of the QW become more probable. In this paper this theory has been established from experimental results.

Introduction

Recently unusual photoluminescence (PL) results on annealing of $In_XGa_{1-X}N$/GaN quantum wells (QWs) of 30 Å and 40 Å widths have been reported [1]. The QWs were subjected to thermal annealing, where, initially the PL peaks instead of shifting towards the usual blue [2], shifts towards red, and on further annealing at higher temperatures the peaks shifts towards blue.

For a proper explanation, using quantum mechanical computations and physical concepts, we emphasize on the prominence of recombination from higher sub-bands in the PLs of the $In_XGa_{1-X}N$/GaN QWs as has been already observed for AlGaN/GaN QWs [3], at nominal excitations as is necessary in PL measurements.

Experimental and Theoretical details

30 Å and 40 Å wide $In_XGa_{1-X}N$/GaN QW samples were grown on sapphire substrates by MOCVD [1], they were annealed at 800°, 850°, 900°C and PL measurements were made at each step. With progressive annealing the effective width of the QW increases along with the increase in the band gap [4]. The observed PL peak energy is the sum of the band gap energy and the energies of the sub-bands of the QW from which optical transitions take place. The nonlinear variation of the band gap E_g of $In_XGa_{1-X}N$ with In mole-fraction, x, is expressed through the equation [4]

$$E_g(x) = xE_{g,InN} + (1 - x)E_{g,GaN} - bx(1 - x) \quad (1)$$

where 'b' is the bowing parameter, $E_{g,InN}$ and $E_{g,GaN}$ represent the band gap energies of the compounds InN and GaN which are considered to be 1.95 eV and 3.4 eV respectively.

Theoretical computations were made considering 32 Å (the best fit) $In_XGa_{1-X}N$/GaN QWs where the observed phenomenon is more pronounced. The mole fraction of indium was considered to be 0.7, on the higher side from the HRTEM images [1]. The band offset ratios, effective masses of electrons and holes were considered same as in our previous report [4]. The band gap E_g of $In_XGa_{1-X}N$ has been calculated from Eq. 1. The height of the QW of $In_XGa_{1-X}N$ with GaN is sufficient to accommodate the second electron and fourth hole sub bands with parameters mentioned. General

series solution [4] was used to evaluate the electron and hole sub bands. The out diffusion of indium and the remaining indium concentrations were estimated from Fick's Law of diffusion [4]

Results and Discussions

The results obtained are shown in Figs. 1 and 2. Initially the PL peak energy is lowered and as annealing proceeds the PL peak moves to higher energies [4]. On annealing, the electron and hole levels decrease in energy as the effective well width increases. At the same time as the indium out diffuses the band gap of the well material increases. These two opposing phenomena contest and determine the final PL peak position. Initially the former is larger than the latter which produces a red shift of the PL peak. as annealing progresses and the In mole fraction drops, the latter becomes greater than the former and the PL peak undergoes a blueshift.

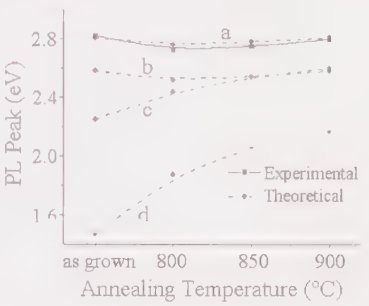

Fig. 1. Variations of the PL peak energy with annealing tempetature for two different band gaps of InN 1.95 eV and 0.7 eV. a: 32 Å, 2 – 4 transition, E_g = 1.95 eV; b: 22 Å, 2 – 4 transition, E_g = 0.7 eV; c: 32 Å, 1–1 transition, E_g = 1.95 eV; d: 22 Å, 1–1 transition, E_g = 0.7 eV.

Computations were carried out for different stages of annealing. The results depicted in Figs. 1 and 2 explain the phenomenon clearly. Since there is some uncertainty in the measurement of the well width we have presented results of 32 Å, which gives the minimum error over the four experimental data points.

We suggest the prominence of the $e_2 - h_4$ transitions in these PL spectra of the $In_XGa_{1-X}N/GaN$ QWs. In the usual PL from QWs, when the wells are irradiated with photons of high energy, the electrons may be excited to higher sub-bands. Eventually the excited electrons and holes relax to the lowest energy levels from which they recombine [5] to emit the PL spectrum corresponding to 1 – 1 transitions. When a strong piezoelectric field is present across the QWs, complex phenomena occur. Due to the strong field, the QW bends and there is a strong localization of carriers [4]. The electrons, holes and the corresponding wave functions become widely separated and their overlap is minimal. Under such conditions, transitions from higher sub-bands become more probable, particularly for the excited holes in the valence band [6,7]. It has been stressed that for strong piezoelectric fields existing across nitride QWs, the PL spectrum consists of transitions from different electron and hole levels which has been depicted by Nam *et al* [3]. The PL of a 110 Å QW of $Al_{0.5}Ga_{0.5}N/GaN$ QW is dominated by transitions from the second electron level and not the first. As analyzed and stressed by Hangleiter *et al* [6], the higher energy levels particularly in the valance band have large enough wave function overlap to make optical transitions from these levels more probable.

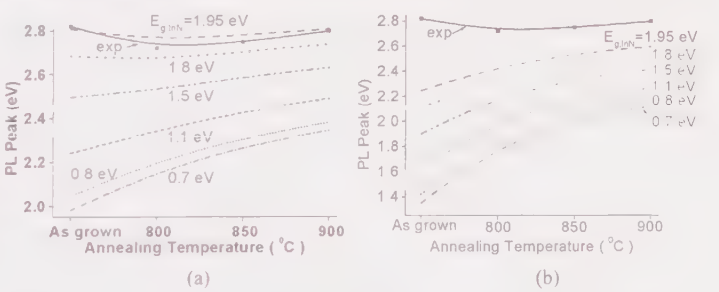

Fig. 2. Variations of the PL peak energy of 32 Å well width for (a) 2-4 transition and (b) 1-1 transition with annealing temperature for different band gaps of InN, $E_{g,InN}$. The solid curve corresponds to the experimental data.

Further to this, the $e_2 - h_4$ transitions are considered to be of prominence for the following reasons. As shown in Fig. 1, the 1 – 1 PL transitions for the 32 and 22 Å wells, 'c' and 'd' are of much lower energies than the reported experimental values and they do not show the red blue shifts (the reason for considering 22 Å wells has been reported earlier [4]). Moreover the $e_2 - h_4$ transitions with the realistic value of all the parameters match the eight experimental data points of the annealed QWs within an average error of 2% [4]. This consistency points to the $e_2 - h_4$ transitions ruling out artifacts. It may be noted that when a QW is under an electric field, the well is skewed but there is negligible change in the position of the sub-bands with respect to the bottom of the normal well [6]. As expected, the red and blue shifts are more pronounced in the 32 Å wells because in this case the sub bands fall through a larger energy as the well widens.

Some research groups claim the band gap to be 0.7 eV [8]. In Fig. 1 relevant curves of different band gaps [9,10] and transitions are shown. Fig. 2 show curves for 2-4 and 1-1 transitions respectively for various reported band gaps [11-13] of $In_xGa_{1-x}N$. It can be clearly seen that the observed unusual phenomenon can only be explained when the 2-4 transitions are considered.

Summary

To summarize, the unusual changes in the PL spectrum of annealed $In_xGa_{1-x}N/GaN$ QWs seems to be dominated by recombinations from higher sub-bands, which is rather unusual. In the typical PL from III-V QWs, when carriers are excited to higher sub-bands they eventually relax to the lowest sub-bands from which they recombine to emit the corresponding spectrum. Recombination from higher sub-bands may be attributed to the existence of a strong piezoelectric field across the QW due to which the wave functions and carriers are separated spatially and transitions from higher sub-bands seem to become more probable. Necessary computations and results have been provided to substantiate the statement that transitions from higher order sub-bands are present in the PL of $In_xGa_{1-x}N/GaN$ quantum wells.

References

[1] Yi-Yin Chung *et al*: J. Appl. Phys. Vol. 93 (2003), p. 9693.

[2] Sang-Wan Ryu *et al*: Appl. Phys. Lett. Vol. 67 (1995), p. 1417.

[3] K. B. Nam *et al*: Appl. Phys. Lett. Vol. 81 (2002), p.1809.

[4] D. Biswas, S. Kumar and T. Das: accepted for publication in Materials Letters (2007).

[5] Peter Y. Yu and Manuel Cardona: *Fundamentals of Semiconductors* (Springer-Verlag Berlin Heidelberg, 1996).

[6] A. Hangleiter *et al* : Phys. Stat. Sol.(b) Vol. 216 (1999), p. 427.

[7] Jeng-Hung Chen *et al*: Thin Solid Films Vol. 498 (2006), p. 123.

[8] Takashi Matsuoka *et al*: Appl. Phys. Lett. Vol. 81(7) (2002), p. 1246.

[9] T. V. Shubina *et al*: Phy. Rev. Lett. Vol. 92(11) (2004), p. 117407(4).

[10] Q. X. Guo *et al*: Appl. Phys. Lett. Vol. 86(23) (2005), p. 231913.

[11] J. Wu *et al*: Appl. Phys. Lett. Vol. 80 (2002), p. 3967.

[12] J. Wu *et al*: Appl. Phys. Lett. Vol. 84 (2004), p. 2805.

[13] Tokuo Yodo, Hiroaki Yona, Hironori Ando, Daiki Nosei and Yoshiyuki Harada: Appl. Phys. Lett. Vol. 80 (2002), p. 968.

Advanced Materials Research Vol. 31 (2008) pp 65-67
online at http://www.scientific.net
© 2008 Trans Tech Publications, Switzerland

The study of femto-second laser induced damage threshold on semi-insulating GaAs wafer

Li Chao-Yang[1,a], Wang Yong-Gang[2,b]

[1] Plasma physics laboratory, Beijing Institute of Graphic Communication, Beijing, China

[2] Institute of semiconductors, Chinese academy of sciences, Beijing, China

[a]zhaoyang2050@163.com. [b]chinawygxjw@163.com

Keywords: femto-second laser, ablation threshold, GaAs wafer, photon ionization

Abstract: We demonstrated an experiment of femtosecond-laser damage threshold on GaAs wafer, the damage threshold was measured from 50 to 400fs. The mechanism was discussed through injection power, pulse duration and ablation profile. The results showed that the damage threshold increased with the pulse duration, the relationship between diameter of ablation hole and laser power density was also analyzed. It was concluded that the main factor affecting the damage threshold was photon ionization and collision ionization.

1.Introduction

Recently the research on femto-second(fs) pulse laser processing is gaining more and more attention because of its ultrashort operation time and extreme-high power[1-3]. The micro machining with fs lasers have many advantages such as its low ablation threshold, ultrafast speed, less damage and non-existence of heat effect zone [4,5]. Many facts show its prominent foreground in precise nano-meter machining, bio-technology, environment protection and microelectronics etc. Although there are many fs machining studies on silicon materials, few is reported on III-V compound semiconductors like GaAs, InP etc. These materials are mainly used to fabricate diode lasers, probes and high-speed microelectric devices[6-8]. The research on these materials' fs machining holds promise for many applications in science and technology.

In this paper, we demonstrated an experiment of fs laser damage threshold using semi-insulating n-type GaAs wafer, the damage threshold after 50 pulses' processing was measured with a pulse duration of 50 fs, 200fs, 300fs and 400 fs respectively. The process mechanism was discussed through injection power, pulse duration and ablation profile. The results showed that the damage threshold by femtosecond laser increased with the pulse duration. The relationship between diameter of ablation hole and laser power density was also analyzed. It was concluded that the main factor affecting the damage threshold was photon ionization and collision ionization.

2. Experimental

A fs laser system (Spitfire 50fs-1K-HP) from Spectrum-Physics Corporation was used for this experiment. The laser system includes four parts that are pulse stretcher, regenerative amplifier, dual-way amplifier and pulse compressor respectively. When injected by the seed light that is centered at 800 nm with the pulse width 35fs, repetition frequency 82MHz, the system delivers sub 50fs, repetition frequency 1KHz, the maximum output power is 2W. The laser beam is monitored

by a He-Ne laser focused onto the machining region. Then the beam is focused with a 75mm lens. The size of light spot is measured by the knife-edge method that gives 0.3mm. For calculating the exerted power, 50 laser pulses were exposed to every ablation dot. Fig1 is the photo of ablation dots. The power augment is 0.05mW for the two adjacent dots. We suppose the damage threshold is

Fig1. The ablation dots on GaAs wafer

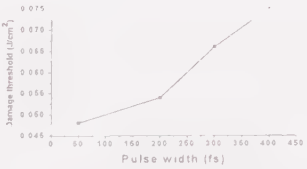

Fig2. The damage threshold with the pulse width

the critical power density while the ablation dot just appears. So the value of damage threshold is not accurate absolutely. For further investigation of ablation, the ablation holes are measured by optical and scanning electron microscopy (SEM).

3.Results and discussion

3.1 The damage threshold under different pulse width

As shown in Fig2, the damage threshold of GaAs wafer is measured under variations of laser pulse duration from 50fs to 400 fs. We can see the damage threshold increases with the argument of the pulse width and the damage threshold is found to be approximately proportional to the pulse width. This result is well accordance with the experimental formula derived from M.Lenzner's report[9]. This is because that the main factor of fs machining is multiphoton ionization. The fs laser has extremely high photon energy, the bounded electrons could transit to the free state by absorbing several photons simultaneously. Like the continuous laser, the damage of fs laser is also caused by electrons avalanche. Whereas the electrons are produced by multiphoton ionization, this is contrary to the long pulse laser in initial electrons accumulation. According to this, the damage threshold by fs laser reduces with the decrease of pulse width, and the threshold should have a certain value.

3.2 The ablation diameter with the injection power

The diameter of ablation hole is measured with SEM, as shown in Fig3. It is found that the diameter enlarges with the increase of the laser power. In the process of the machining, the energy of the free electrons heated by the laser is subsequently transferred to the GaAs lattice. This energy

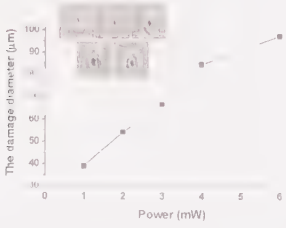

Fig3. The ablation diameter at various power, upper-left is the ablation hole

Fig4. a-the ablation profile by fs laser and b-nanosecond laser

transfer leads to the ablation of the heated zone, which is the major cause of femtosencond optical machining. The desity of seed electrons is not postulated because it no longer lies on thermal excitation of impurity states, but can be produced by multiphoton ionization. The high power can

make the electrons escaped directly from the atoms. It is a nonlinear absorption process. and the shock-like energy deposition leads to ablation, thus the threshold is independent of the melting point. With the decrease of the pulse duration, the ultrahigh peak power may induce the GaAs wafer straight evaporation by collisions between the free electrons and lattices. The ultrashort machining process and enormous energy injection reduces the ablation threshold dramatically, heat diffusion is "frozen" during the interaction. So the heat can't be diffused to the lattices nearby thus prevents the heat erosion ultimately.

3.3 The ablation profile comparison between fs and ns laser

Fig4(a) shows the image of ablation hole machined on the GaAs wafer at the power of 4mW, 150fs. From the central ablation zone on the regular morphology we can deduce that the laser beam has an excellent beam quality. The photo reveals that the fs machining produces a clean hole with no collateral damage and there does not exist thermal influence region. This is because of the ultrashort duration of the fs laser ablation. The energy mixing process is only about several picoseconds for a ultrashort pulse laser ablation, in such a short time the material in the machined region is heated directly far above the melting point to form the overheat gas. This process is so fast that the gas density increases rapidly, thus a phenomenon like phase change explosion occurs. The overheat gas is removed from the ablation hole with the laser pulses etching. Hence the fs machining could acquire a smooth, uncontaminated and more accurate effect. As a contrast, the ablation profile on GaAs wafer processed by nanosencond laser is given in Fig4(b). From the image we can see the nanosecond laser causes heating and cracking caused by thermal stresses that is very different from the fs laser ablation.

4.Conclusion

We demonstrated an experiment of femto-laser damage threshold using semi-insulating n-type GaAs wafer. The results showed the damage threshold increased with the pulse duration, comparing with the case of nanosecond laser, the threshold is dramatically small. The relationship between diameter of ablation hole and laser power density was analyzed. It was concluded that the main factor affecting the damage threshold was photon ionization and collision ionization. This study exhibited a wider application prospect in semiconductors industries. This work was supported by the scientific research common program of Beijing municipal commission (No. KM200710015002)and the youth research funds of Beijing institute of graphic communication.

References

[1] S.W. Youn, M. Takahashi, H. Goto etal.: Microelectro. Engn., Vol.83(11-12)(2006), p2482

[2] J. Krüger, S. Martin, H. Mädebach etal.: Appl. Surf. Sci., Vol.247(1-4)(2005),p406

[3] Ya Cheng, Koji Sugioka and Katsumi Midorikawa: Opt. Exp., Vol.13(18)(2005),p7225

[4] Feng, Q.; Moloney, J.V.; Newell, A.C. etal.: IEEE J. of Quan. Elect., Vol.33(2)(1997),p127

[5] Haiyi Sun , Zhizhan Xu , Tianqing Jia etal.: Chin. Opt. Lett., Vol.3(1)(2005),p60-62

[6] Wang Y-G, Li C-Y, Ma X-Y etal.: Chin. J. of Semiconductors, Vol.25(2)(2004),p148

[7] Xuemei Zheng, Ying Xu, Roman Sobolewski: Appl. Opt., Vol.42(9)(2003),p1726

[8] Zhang Q-L, Feng B-H, Zhang D-X etal.: Chin. Phys. Lett., Vol.20(10)(2003),p1741

[9] M. Lenzner, J. Krüger, S. Sartania: Phys. Rev. Lett., Vol.80(18)(1998),p4076

Advanced Materials Research Vol. 31 (2008) pp 68-70
online at http://www.scientific.net
© 2008 Trans Tech Publications, Switzerland

Temperature-Controlled Catalytic Growth and Photoluminescence Properties of ZnO Nanostructures

P. T. Huy[1,a,*], T. T. An[1,b], N. D. Chien[2,c,*], Dojin Kim[3,d]
*Hanoi Advanced School of Science and Technology (HAST)
[1]International Training Institute for Materials Science
[2]Institute of Engineering Physics
Hanoi University of Technology, 01 Dai Co Viet, Hanoi, Vietnam
[3]School of Nano Science and Technology, Chungnam National University, Korea
[a]huy@itims.edu.vn, [b]trongan@itims.edu.vn, [c]chien@itims.edu.vn, [d]dojin@cnu.ac.kr

Keywords: ZnO nanostructures, Photoluminescence, Thermal evaporation

Abstract. ZnO nanostructures with different morphologies of nanorods, nanoneedles, nanowires, and nanobelts have been synthesized by thermal evaporation of pure ZnO micropowder. Based on the appearance of the as-synthesized products observed by field emission scanning electron microscope (FE-SEM), we show that substrate temperature and catalyst are the critical factors for the formation of different morphologies of ZnO nanostructures. The photoluminescence (PL) properties of the ZnO nanostructures were investigated. The difference in PL spectra both in intensity and structure for the different ZnO nanostructures are presented. We demonstrate that under appropriate synthesis conditions, highly crystallized and defect-free ZnO nano-structures can be obtained.

Introduction

One-dimensional (1D) nanostructured materials have recently attracted significant attention because of their valuable electrical, optoelectronic, and optical properties, as well as their potential application in nanodevices and functional materials [1]. In particular, ZnO materials have received broad attention due to its wide direct bandgap of 3.37 eV at room temperature, large exciton binding energy, piezoelectric properties and excellent chemical and thermal stability. ZnO also shows a pronounced ability to build a variety of nanostructures. Different ZnO nanostructured materials such as nanowires, nanobelts, nanorods, nanorings, nanosprings, nanobridges, nanonails were grown in many laboratories. A large number of experimental methods have been employed for the manufacturing of ZnO nanostructures. These methods include chemical vapor deposition, thermal evaporation methods, chemical methods, ion beam technique, and pulsed laser deposition. In this work, we report on an effective approach for the synthesis of ZnO nanostructures based on nanoporous carbon-assisted thermal evaporation of ZnO powders. ZnO nanostructures with different morphologies of nanorods, nanoneedles, nanowires, and nanobelts were simultaneously synthesized and in bulk quantities. The structural characteristics, growth mechanism and the PL properties of the ZnO nanostructures were investigated.

Experimental

Synthesis of the ZnO nanostructures was carried out by using simple thermal evaporation of the ZnO micropowder in a horizontal tube furnace. Mixture of pure ZnO micropowders (99.99%) with sizes in the range of 60-200 μm and nano porous carbon powders in an atomic ratio of 2:1 were placed in an alumina boat and then put into the center of a quartz tube in the tube furnace. Several Si strips which were covered with a layer of Au or Pt film with thickness from 4 to 40 nm by using rf sputtering, were placed downstream in the quartz tube subsequently to act as deposition substrates for materials growth. The quartz tube was first purged with high-purity argon for 2 hours, prior to heating to eliminate oxygen in the furnace. The system was then heated to 1200 °C in a flowing Ar atmosphere. Further, the temperature of the system was raised to 1300 °C and kept at

this temperature for 30 minutes. During this second heating process, the Ar flow rate was kept in the range of 80-100 sccm. The morphology and microstructure of the ZnO nanostructures on Si wafers were examined using field emission scanning electron microscopy (FE-SEM 4800 Hitachi). PL spectra were acquired by using an excitation source with the line 325 nm (He-Cd laser) and a CCD camera (Acton, Winspec) or with a JOBIN YVON SPEX FL-3-22.

Results and discussion

From the highest temperature of 1200 °C to the lowest temperature of 800 °C, it is interesting to see that the as-grown products are distributed at five distinct regions, which can be recognized by the different color on the silicon strips as white-light-gray (zone 1), light-gray (zone 2), dark gray (zone 3), light-violet-gray (zone 4), and the dark-violet-gray (zone 5). FE-SEM study shows that depending on the temperature profile and the position on the silicon strips, ZnO nanostructures with different morphologies were formed. The morphology of the ZnO nanostructures change from nanorods (zone 1, 800-850 °C, Fig. 1a) to mixture of nanorods and nanoneedles (zone 2, 850-950 °C, Fig. 1b), nanoneedles (zone 3, 950-1000 °C, Fig. 1c), then nanowires (zone 4, 1000-1080 °C, Fig. 1d), and finally nanobelts (zone 5, 1080-1200 °C, Fig. 1e).

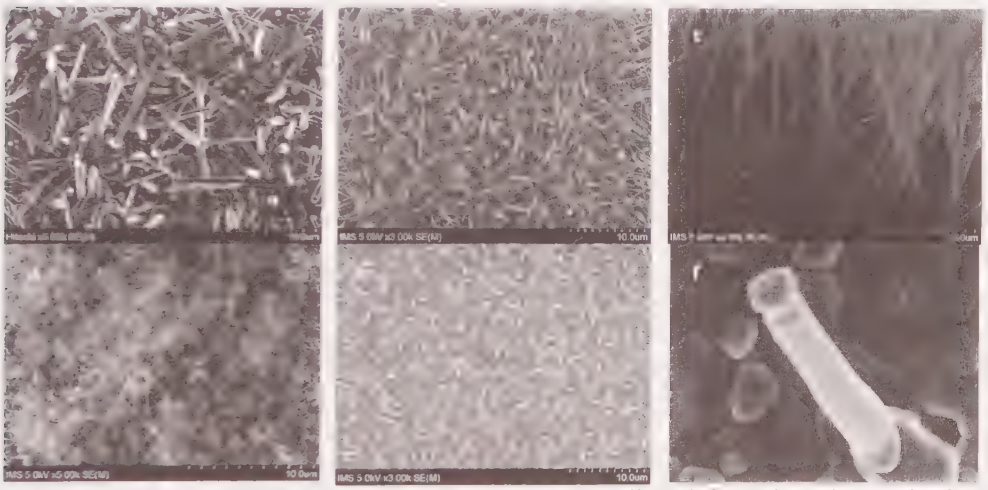

Fig. 1. FE-SEM images of different ZnO nanostructures collected from the substrate in the temperature region from 800 to 1200 °C, including: nanorods (a), mixture of nanoneedles and nanorods (b), nanoneedles (c), nanowires (d), nanobelts (e). Fig. 1f shows the solidified Au particle at the free-growing end of the nanorod.

In zone 1, the FE-SEM image Fig. 1a reveals that nanorods have diameters ranging from 100 to 800 nm and lengths up to 10 μm. With the increase of the substrate temperature to about 850-950 °C, zone 2, the FE-SEM image Fig. 1b shows that the obtained product is a mixture of nanorods and nanoneedles. As can be seen, the density of both nanorods and nanoneedles is much higher than in zone 1. With further increase of the substrate temperature to about 950-1000 °C, zone 3, the formation of nanoneedles seems to take the advantage. The product shows a change from the mixture of nanorods and nanoneedles to dominantly nanoneedles. In this zone, each obtained nanoneedle also has a longer length and smaller tip (in order of 100 nm or smaller) as shown in Fig. 1c. The major product in zone 4 (1000-1080 °C) is ZnO nanowires as shown in Fig. 2d. The nanowires have typical diameters in the range of 15-25 nm, and lengths up to tens of micrometer. In the highest temperature area, zone 5 (1080-1200 °C), the morphology of the product changes from nanowires to nanobelts. The nanobelts have widths ranging from 100 to 200 nm, and lengths up to tens of micrometer. It is noted that almost all the nanorods and nanowires were observed with a

nanoparticle at the top, see Fig. 1f. These nanoparticles are most probably the catalyst nanoparticles, which are formed from the thin Pt or Au layer coated on the silicon wafer. This observation indicates the VLS growth mechanism of the obtained ZnO nanostructures.

Fig. 2 shows room-temperature PL spectra of the nanorods (a), nanorods and nanoneedles (b), nanoneedles (c), nanowires (d), and nanobelts (e). The PL spectrum of the nanorods region shows three luminescence bands at 383 nm, 507 (very weak) and 696 nm. Whereas, the PL spectra of the nanowires and nanobelts regions are very similar and shows two emission bands with peaks at 379 nm and 507 nm. For the mixed nanoneedles, nanorods and the nanoneedles regions, a sharp, strong and dominant UV emission at 383 and 387 nm were observed, respectively for the mixed nanoneedles, nanorods, and the nanoneedles. The visible emission bands become very weak for the mixed nanoneedles, nanorods, and almost flat for the nanoneedles regions. From the literature, two emission bands appeared in the PL spectra of the ZnO nanostructures: in the UV due to the recombination of free excitons through an exciton-exciton collision process (also known as near-band-edge (NBE) emission)[2], in the visible region deep-level-emissions appeared because of oxygen vacancies [3] and zinc interstitials [4]. It is known that the NBE emission peak in the PL spectra is dependent on the crystallinity of the synthesized structures, i.e. the intensity of the UV peak is increased when the crystal quality of the grown nanostructure is improved. In our case, in zone 2, and 3, the intensity of the PL spectra of the UV emission is sharp and very strong, the visible emission is very weak or flat, the full-width-half-maximum (FWHM) of the UV peak is measured to be ~ 13 nm (120 meV), all these fact indicate that the obtained products in zone 2 and 3 are good in crystallinity with very less or even free of structural defects.

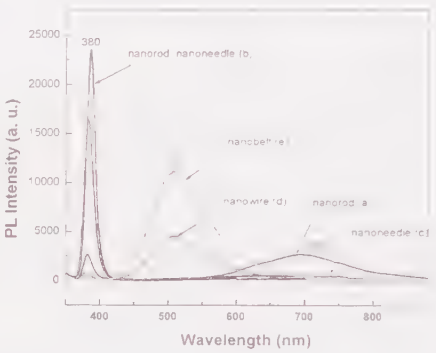

Fig. 2. Photoluminescence spectra of different ZnO nanostructures under 325 nm He-Cd laser excitation.

Conclusion

By the evaporation of the mixed ZnO and nanoporous carbon powder at 1300 °C for 30 minutes, ZnO nanostructures with different morphologies and sizes, and structures were formed. It is evident that the temperature distributions inside the tube furnace, and the catalyst play a key role in the formation of the ZnO nanostructures. Within a certain range of temperature, product with a specific morphology can be obtained. We have demonstrated that high crystallinity and defect-free ZnO nanostructures can be synthesized using our experimental set-up.

Acknowledgements

This research was supported by the National Basic Research Program Grant No. 4.050.06, and the CNU-ITIMS Local Lab 2006-2007 project.

References

[1] Z. W. Pan, Z. R. Dai, and Z. L. Wang, Science 292, 1947 (2001).
[2] Z. W. Liu, C. K. Ong, T. Tu, and Z. X. Shen, Appl. Phys. Lett. 88, 053110 (2006).
[3] K. Vamheusden, W. L. Warren, S. H. Seager, D. K. Tallant, J. A. Voigt, B. E. Gnade, J. App. Phys. 79, 7983 (1996).
[4] A. B. Djurisic, Y. H. Leung, K. H. Tam, L. Ding, W. K. Ge, H. Y. Chen, and S. Gwo, Appl. Phys. Lett. 88, 103107 (2006).

Advanced Materials Research Vol. 31 (2008) pp 71-73
online at http://www.scientific.net
© 2008 Trans Tech Publications, Switzerland

Fabrication and Optical Properties of ZnO Quantum Dots

X. H. Zhang[1,a], S. J. Chua[1,b], A. M. Yong[1,c], S. Y. Chow[1,d], H. Y. Yang[2,e], S. P. Lau[2,f], S. F. Yu[2,g] and X. W. Sun[2,h]

[1]Institute of Materials Research and Engineering, 3 Research Link, Singapore 117602, Singapore

[2]School of Electrical & Electronic Engineering, Nanyang Technological University, Nanyang Avenue, Singapore 639798

[a]xh-zhang@imre.a-star.edu.sg, [b]elecsj@nus.edu.sg, [c]anna-yong@imre.a-star.edu.sg, [d]sy-chow@imre.a-star.edu.sg, [e]hyyang@pmail.ntu.edu.sg, [f]ESPLau@ntu.edu.sg, [g]ESFYu@ntu.edu.sg, [h]EXWSun@ntu.edu.sg

Keywords: ZnO, Quantum dots, Photoluminescence

Abstract. Using a simple process of the deposition of ZnO thin films on SiO_x/Si substrates and subsequent thermal annealing, we fabricated ZnO quantum dots embedded in silicon oxide matrix. The ZnO quantum dots were characterized using transmission electron microscopy and time-integrated photoluminescence. The photoluminescence of the quantum dots show a blue-shift of 47 meV due to the quantum confinement effect.

Introduction

ZnO has attracted much attention recently because of its potential applications in optoelectronic devices operating in the ultraviolet to blue spectral region. Compared to other wide bandgap semiconductors, ZnO has an extremely large exciton binding energy of 60 meV,[1,2] which is much larger than the thermal energy at room temperature and therefore allows the survive of excitons at room temperature and above.[3] Thus the excitons play an important role in the optical properties of ZnO. Excitons in geometrically confined systems exhibit different properties as compared to three-dimensional excitons as a result of the confinement.[4-9] For example, Guo *et al.*[9] experimentally found that the third order nonlinear susceptibility of ZnO nanoparticles is ~500 times larger than that of bulk ZnO. In addition to the size-dependent spectral shifts in the absorption and emission spectra, the confinement also strongly influences the exciton radiative recombination rate. Theoretically, it has been shown that the exciton-photon coupling in ZnO quantum dots (QDs) is particularly strong and the exciton radiative recombination rate drastically varies with the dot size.[10,11] Fonoberov and Balandin[12,13] calculated the radiative lifetime of excitons in ZnO nanocrystals and predicted the size dependence of the exciton radiative lifetime. In this letter, we report the fabrication of ZnO QDs using a simple process of the deposition of ZnO thin films on SiO_x/Si substrates and subsequent thermal annealing. We show that the geometrical confinement of ZnO QDs inside the SiO_x matrix could reduce the exciton radiative lifetime. The reduction of exciton radiative lifetime is discussed in terms of exciton superradiance.

Experimental

The colloidal chemical techniques are commonly used to fabricate ZnO nanoparticles.[14,15] Other methods have also been explored to fabricate ZnO nanoparticles. Kim *et al.*[16] reported that the self-organized ZnO QDs could be grown on SiO_2/Si substrates using metalorganic chemical vapor deposition. Using a simple process of deposition of ZnO thin films on SiO_x/Si substrates and subsequent thermal annealing, we fabricated ZnO QDs embedded in silicon oxide matrix. The sample used in the present study was prepared using the following procedure. Firstly, a SiO_x layer with thickness of 200 nm was formed on n-type (001) silicon wafer by thermal annealing. Then a 100 nm thick ZnO polycrystalline film was deposited on the SiO_x layer using the filtered cathodic vacuum arc (FCVA) technique. Finally, the sample was annealed at 900°C for 10 hours in ambience.

The sample was characterized using transmission electron microscopy (TEM) and time-integrated photoluminescence (TIPL). TIPL was conducted with the excitation of 150 fs pulses centered at 325 nm from an optical parametric amplifier, which was driven by a 1 kHz Ti:sapphire regenerative amplifier. The luminescence was dispersed in a 50 cm monochromator and detected with a photomultiplier using standard lock-in amplification. The sample was secured in a close-cycle He gas cryostat for temperature-variable measurements.

Results and Discussion

Figure 1 shows the TEM images of the sample. The cross-section TEM image (Fig. 1(a)) clearly shows the existence of the ZnO QDs dispersed in the amorphous SiO_x matrix. Fig. 1(b) is the high resolution TEM image of a typical ZnO QD. It is seen that the QD has a crystalline structure with a dimension that measures 12.8 nm in length and 10.3 nm in height. From the TEM analysis, the ZnO QD has the hcp wurtzite structure with the lattice parameters a = 3.17 Å and c = 5.17 Å, which are in good agreement with the lattice parameter of ZnO bulk.[17]

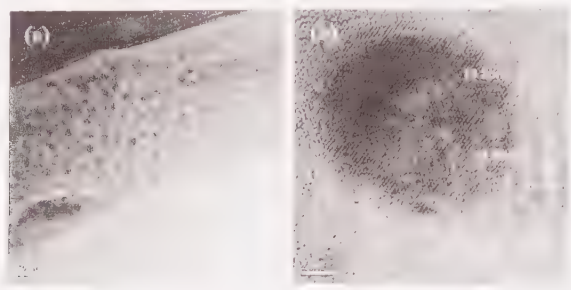

FIG. 1. TEM images of the sample. The cross-section TEM image (a) clearly shows the existence of the ZnO QDs dispersed in the amorphous SiO_x matrix. (b) The high resolution TEM image of a typical ZnO QD.

The quantum confinement effect is most directly detected as the size-dependent spectral shift in the absorption and emission spectra. Figure 2 plots the TIPL spectrum of the ZnO QDs measured at 4.3 K. The TIPL spectrum of the as-deposited ZnO film is also plotted as a comparison. For the ZnO QDs, a PL band at 3.399 eV is observed, which blueshifts by 47 meV when compared to that of the ZnO film (3.352eV). The blueshift of the PL peak caused by the quantum confinement can be described as follows,[18]

$$\Delta E = \frac{\pi^2 \hbar^2}{2R^2}\left(\frac{1}{m_e^*}+\frac{1}{m_h^*}\right) - 0.248E_{Ryd}^*, \qquad (1)$$

where $\hbar$, R, E_{Ryd}^*, are the Planck constant, the radius of QDs, and the exciton binding energy, respectively. Taking the electron and hole effective masses as $m_e^* = 0.24\ m_0$ and $m_h^* = 1.8\ m_0$,[19] and using the bulk exciton binding energy $E_{Ryd}^* = 60$ meV without considering the increase in exciton binding energy due to the weak confinement, the radius of ZnO QDs is calculated to be 5.4 nm, which is in good agreement with the TEM result. It is interesting to note that the full width at half maximum (FWHM) of the ZnO QDs (38 meV) is smaller than that of ZnO film (50 meV) and the PL spectrum of ZnO QDs has a Gaussian lineshape, suggesting the good uniformity in the size of QDs and the improvement in the crystal quality.

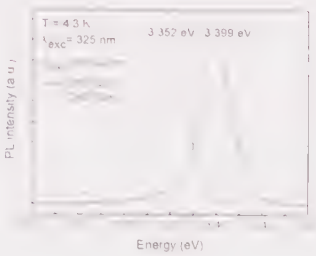

FIG. 2. The TIPL spectrum of the ZnO QDs measured at 4.3 K. The TIPL spectrum of the as-deposited ZnO is also plotted as a comparison.

Conclusion

In summary, using a simple process of the deposition of ZnO thin films on SiO_x Si substrates and subsequent thermal annealing, we have fabricated ZnO QDs embedded in silicon oxide matrix. The ZnO QDs have been characterized using TEM and TIPL. We observed a blue-shift of 47 meV in the photoluminescence of ZnO QDs due to the quantum confinement.

References

[1] W. Y. Liang and A. D. Yoffe, Phys. Rev. Lett. **20**, 59 (1968).
[2] D. C. Reynolds, D. C. Look, b. Jogai, C. W. Litton, G. Cantwell, and W. C. Harsch, Phys. Rev. B **60**, 2340 (1999).
[3] D. M. Bagnall, Y. F. Chen, Z. Zhu, T. Yao, M. Y. Shen, and T. Goto, Appl. Phys. Lett. **73**, 1038 (1998).
[4] S. Deboer and D. A. Wiersma, Chem. Phys. Lett. **165**, 45 (1990).
[5] Y. R. Kim, M. Lee, J. R. G. Thorne, R. M. Hochstrasser, and J. M. Ziegler, Chem. Phys. Lett. **145**, 75 (1988).
[6] J. Feldmann, G. Peter, E. O. Gobel, P. Dawson, K. Moore, C. Foxon, R. J. Elliot, Phys. Reb. Lett. **59**, 2337 (1987).
[7] T. Itoh, M. Furumiya, T. Ikehara, and C. Gourdon, Solid State Commun. **73**, 271 (1990).
[8] K. Misawa, H. Yao, T. Hayashi, and T. Kobayashi, J. Chem. Phys. **94**, 4131 (1991).
[9] L. Guo, S. Yang, C. Yang, P. Yu, J. Wang, W. Ge, and G. K. L. Wong, Appl. Phys. Lett. **76**, 2901 (2000).
[10] B. Gil and A. V. Kavokin, Appl. Phys. Lett. **81**, 748 (2002).
[11] V. A. Fonoberov and A. A. Balandin, Appl. Phys. Lett. **86**, 226101 (2005).
[12] V. A. Fonoberov and A. A. Balandin, Appl. Phys. Lett. **85**, 5971 (2004).
[13] V. A. Fonoberov and A. A. Balandin, Phys. Rev. B **70**, 195410 (2004).
[14] E. M. Wong and P. C. Searson, Appl. Phys. Lett. **74**, 2939 (1999).
[15] H. Zhou, H. Alves, D. M. Hofmann, W. Kriegseis, B. K. Meyer, G. Kaczmarczyk, and A. Hoffmann, Appl. Phys. Lett. **80**, 210 (2002).
[16] S.-W. Kim, S. Fujita, and S. Fujita, Appl. Phys. Lett. **81**, 5036 (2002).
[17] I. Milošević, V. Stevanović, P. Tronc, and M. Damnjanović, J. Phys.: Condens. Matter 18, 1939 (2006).
[18] Y. Kayanuma, Phys. Rev. B **38**, 9797 (1988).
[19] B. Lin, Z. Fu, and Y. Jia, Appl. Phys. Lett. **79**, 943 (2001).

Advanced Materials Research Vol. 31 (2008) pp 74-76
online at http://www.scientific.net
© 2008 Trans Tech Publications, Switzerland

Intense Photoluminescence and Photoluminescence Enhancement of Silicon Nanocrystals by Ultraviolet Irradiation

P. T. Huy[1,a,*], and P. H. Duong[2,b]
*Hanoi Advanced School of Science and Technology (HAST)
[1]International Training Institute for Materials Science (ITIMS)
Hanoi University of Technology, 01 Dai Co Viet str., Hanoi, Vietnam
[2]Institute of Materials Science, Vietnamese Academy of Science and Technology
[a]huy@itims.edu.vn, [b]duongph@ims.vast.ac.vn

Keywords: Si nanocrystals, PL Enhancement, Surface modification

Abstract. Photoluminescence (PL) from silicon nanocrystals deposited on top of silica-glass template and from silicon nanocrystals in nc_Si/SiO_2 multilayer films were studied as a function of ultraviolet (UV) laser irradiation time in vacuum. Both the films exhibit intense visible PL at room temperature under laser excitation. It was found that upon prolong irradiation time using a He-Cd laser (325 nm) the PL intensity of the films was spectacularly enhanced. The process is reversible and does not happen with excitation wavelength longer than 400 nm. Upon introducing air into the measurement chamber, a rapid decrease of the PL intensity was recorded. This observation suggests that the UV light may lead to modification of nonradiative recombination centers in the films and thus improves the emission yield of silicon nanocrystals.

Introduction

In recent years, several applications of silicon nanocrystals have been explored including light-emitting diodes, non-volatile memories, and sensitized optical amplifiers. This is the result of extensive research over the past fourteen years on porous silicon, silicon nanocrystals embedded in an SiO_2 matrix as well as on Si/SiO_2 superlattices [1]. It is generally found that well prepared and passivated Si nanocrystals exhibit photoluminescence in the wavelength range between 500 and 1100 nm. The luminescence is attributed to the recombination of quantum-confined excitons, the emission energy thus being strongly dependent on the nanocrystals size. SiO_2 is the ideal matrix for Si nanocrystals as it can passivate dangling bonds that may cause non-radiative quenching. Many different investigations have shown that silicon – silicon dioxide system is very stable to external agents when a flat interface between Si and SiO_2 is formed. In spite of this, there is still a huge puzzle to physicists concerning the UV and blue photoluminescence, which is very often observed from silicon – silicon dioxide system. The mechanism responsible for those emissions is still unclear. In this paper, we report on PL experiments done in samples in which silicon nanocrystals are deposited on nanoporous silica and on samples where several alternative thin Si and SiO_2 layers are deposited on thermally oxidized silicon wafers. We show that UV illumination in vacuum dramatically enhances the luminescence of samples annealed at high temperature.

Experimental

Two different types of samples have been prepared in our experiment. The first type of sample, namely silicon nanocrystals deposited on top of silica-glass template was prepared by using combination of sol-gel and rf sputtering methods. For this type of sample, the silica gel was first prepared by the sol-gel process using tetraethylorthosilicate $Si(OC_2H_5)_4$ (TEOS). The obtained homogeneous sol was then condensed by adding the mixed solution of H_2O, HNO_3 and C_2H_5OH. Finally, a thin film was made by the spinning method on top of thermally oxidized silicon wafer. After this spin coating step, the silicon wafer with a nanoporous silica layer was used as a substrate for deposition of the top silicon layer by rf sputtering. The thickness of the sputtered silicon layer was varied from 1 to 3 nm The second type of sample, so-called Si/SiO_2 superlattice, was fabricated by using a multitarget sputtering equipment. For this sample, firstly a 1-micron thickness SiO_2 layer was grown on a silicon wafer. Later, alternating layers of amorphous silicon and SiO_2 were deposited on the same wafer to form a superlattice. The thickness of the Si and SiO_2 layers

was 1 and 2 nm, respectively. The number of layers varied from 30 to 100 layers. Annealing was accomplished in neutral atmosphere at various temperatures. Excitation of luminescence was realized with either the 325 nm or the 442 nm line of a helium-cadmium laser. The laser beam could be focused through a microscope objective to a spot of about 12 microns diameter. Most of the experiments were done at room temperature. Experiments at room temperature were done in vacuum (10^{-3} torr), in air or in dry helium atmosphere.

Results and discussion

Fig.1 shows a typical room temperature PL spectrum of the silicon on silica-template sample which was annealed at 500 °C in air. The modulation of the spectrum is due to the interference that appears as a result of the multiple reflections of light in the cavity formed between the silicon substrate and the interface with air or vacuum. These interferences are possible because the luminescent-layer thickness is smaller than the light wavelength. In practical, the asymmetric and broad PL spectrum reveals a possibility that the spectrum is superimposed of multiple emission bands. The experimental curve in this case is well fitted by multipeak Gaussian fitting. The fitting result gives two peaks centered at around 550 and 650 nm. The band which peaks at around 650 nm has to be attributed to recombination of an electron and a hole localized on an Si=O bond on the surface of the nanocrystals [1,2]. The other band peaks at around 550 nm. We tentatively attribute this emission band to electron-hole recombination in nanocrystals [3]. Fig. 2 shows the evolution of the PL spectra of the silicon on silica sample annealed at 1100°C for 1 hour after illumination by the 325-nm line of the laser in vacuum. It is interesting to see that there is a very large enhancement of signal intensity and fringe contrast in the 2 eV region with increasing of the laser illumination time.

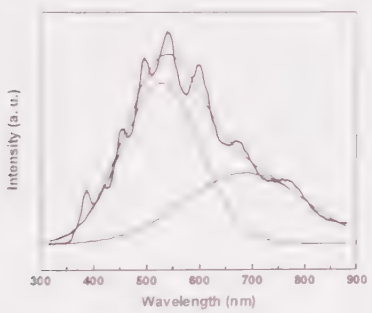

Fig. 1. PL spectra of silicon-on-silica sample under a 325 nm excitation. Two separated emission bands with peak at around 550 and 650 nm are disclosed by multipeak Gaussian fitting.

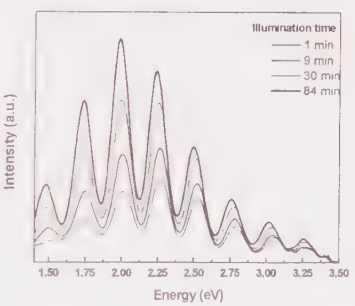

Fig. 2. Time evolution of PL spectra of a silicon-on-silica sample under continuous excitation of 325-nm He-Cd laser invacuum. The sample was annealed at 1000 °C for 1 hour.

Fig. 3 shows similar evolutions in the multilayer sample. The enhancement is larger first in the yellow then in the red and finally in the infrared region when the time of illumination increases. It can be noted that the interferences are also visible in the excitation spectrum of luminescence (not shown). Their contrast is very much enhanced after UV illumination in vacuum. Surprisingly, the enhancement of PL intensity could not be obtained with the 442 nm line of the He-Cd laser. In both cases, as soon as we introduce air into the vacuum chamber, the intensity of the PL spectrum is rapidly quenched. The final spectrum was very similar to the initial spectrum before illumination in vacuum. One should note that this enhancement and quenching effect did not happen if the sample was illuminated in helium atmosphere instead of air.

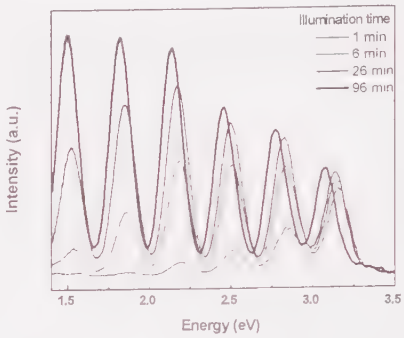

Fig. 3. Time evolution of PL spectra of a multilayer sample under continuous excitation of 325 nm laser in vacuum.

As has been discussed, the interferences appear as a result of the multiple reflections of PL in the cavity formed between the silicon substrate and the interface with air, helium or vacuum. They allow us to measure the thickness of the luminescent layer. We used the formula given in equations 14 and 15 of Ref [4] to calculate it. It turns out that this thickness is 92 nm and 150 nm in the silicon-on-silica sample and in the multilayer sample, respectively. After illumination in vacuum, the fringe contrast is very large. As stated in Ref [4], the fringe contrast can be larger than that of a transmission spectrum when the layer thickness is small, the reflection coefficient on the first interface (with air) small and on the second interface (on silicon) large. Using again the same Eqs. 14 and 15 of Ref [4], we found that, after illumination, the thickness of the luminescent layer is reduced to 45 nm. UV illumination affects only the nanocrystals, which are on the surface of the sample and exposed either to vacuum or to air. Enhancement of PL intensity is caused by illumination with light of short wavelength, which is absorbed in the nanocrystals and creates electron-hole pairs. Nevertheless, the process occurs at a depth smaller than that corresponding to the absorption coefficient of light, as shown by the fringe contrast in the interference spectrum. We conclude that a charge transfer occurs on the surface of those nanocrystals located close to the interface and in contact with the residual atmosphere. As a result, the nanocrystal surface is modified and some important non-radiative recombination processes are suppressed. The process is efficient in silicon-on-silica samples annealed at 1100°C in which nanocrystals have dangling bonds on the surface. When samples are subsequently illuminated in air, the charge transfer occurs now in the presence of oxygen and, as a result, the new modification of the surface brings the system back to the previous situation where the surface of nanocrystals presented many dangling bonds. The best candidate for the residual atmosphere in vacuum is water. It is well known that photocatalytic decomposition of water can be obtained on TiO_2 surfaces. A similar process could occur on silicon nanocrystal surfaces.

Conclusion

Under continuous excitation of 325 nm laser in vacuum, the PL intensity of the silicon nanocrystals deposited on top of silica-glass template and of silicon nanocrystals in nc_Si/SiO_2 multilayer film was spectacularly enhanced. We show that, as a result of photocatalytic decomposion of water, the dangling bonds of nanocrystals at the surface become saturated with hydrogen and the non-radiative recombination processes decrease. A second illumination in air allows the oxidation of the nanocrystal surfaces and the regeneration of the dangling bonds. The non-radiative recombination processes become important again. Photocatalytic decomposition of water is only possible because the carriers are confined in silicon nanocrystals and their energy is increased by the confinement.

Acknowledgements

This research was supported by the National Basic Research Program through Grants No. 4.050.06 and Grant No 4.084.06.

References

[1] L.T. Canham, Appl. Phys. Lett. **57**, 1046 (1990).
[2] O. Hanizumi, K. Ono, Y. Ogawa, Appl. Phys. Lett. **82** (4), 538 (2003)
[3] G. Ledoux, J. Gong, F. Huisken, O. Guillois, C. Reynaud, Appl. Phys. Lett. 80 (25), 4834 (2002).
[4] M.V. Wolkin, J. Jorne, P.M. Fauchet, G. Allan, C.Delerue, Phys. Rev. Lett. 82, , 197 (1999).

Advanced Materials Research Vol. 31 (2008) pp 77-79
online at http://www.scientific.net
© 2008 Trans Tech Publications, Switzerland

Nitrogen Interstitial Defects in GaNAs Films Grown by MOCVD

D. Sentosa[1], X-H. Tang[1,a], S. J. Chua[2], Z-Y. Yin[1]

[1] School of Electrical and Electronic Engineering, Nanyang Technological University, Nanyang Avenue, Singapore 639798

[2] Institute of Materials Research and Engineering (IMRE), 3 Research Link, Singapore 117602

[a]exhtang@ntu.edu.sg

Keywords: GaNAs; photoluminescence; thermal anneal; MOCVD

Abstract. Photoluminescence (PL) measurement shows an additional peak with stronger and broader emission at lower photon energy besides the energy band gap transition emission from GaNAs epilayer grown by MOCVD. This emission is assigned as nitrogen-nitrogen interstitial defect related emission. Effect of V/III ratio during the MOCVD growth on this defect related emission peak has been investigated. The combination of optimum V/III ratio during the MOCVD growth and post-growth rapid thermal anneal (RTA) can eliminate this defect emission peak and at the same time the GaNAs' band gap emission has been greatly improved. The PL spectra contain a single, narrow, and high intensity GaNAs' band gap transition emission after the RTA annealing. The optimum V/III ratio for growing the GaNAs films with N content < 3.5% is around 20.

Introduction

Adding a small percentage of nitrogen into III-V semiconductors can largely reduce their band gap energy. For GaAs material, one percentage of nitrogen incorporated in GaAs will introduce a reduction of 100 meV in its band gap energy [1]. However, the addition of nitrogen tends to introduce more defects into the III-V-N materials. These defects lead to a degradation of the optical quality of the III-V-N alloys due to the non-radiative (NR) centers created. Some additional peaks besides the band-to-band emission peaks were observed from these alloys. These additional peaks reside at longer photoluminescence (PL) emission wavelength and are normally with low PL intensity and often associated with nitrogen-related defect. Thermal annealing is normally employed to remove these defects. However, sometimes annealing alone cannot remove these defect-related peaks completely.

In this research, GaNAs epilayers were grown by MOCVD with nitrogen as the carrier gas. Our samples depict unusual behavior for their defect-related PL emission peak. This peak emits at longer wavelength and is more than ten times stronger than that of the band-to-band transition emission. Some samples still show a weak defect emission peak even after the thermal annealing, while the other samples surprisingly have a single, narrow, and high intensity PL emission even though the nitrogen composition of the samples is as high as 3%. The difference lies in the different V/III ratio set during MOCVD growths of these samples. Our results show that combination of the optimized V/III ratio and the thermal annealing of the as-grown sample can eliminate the defects in the GaNAs epilayers completely.

Experimental procedures

GaNAs epilayers used in this study were grown by metal organic chemical vapor deposition (MOCVD) process. Gallium, arsenide, and nitrogen precursors used for the growths were Trimethylgallium (TMGa), tertiarybutylarsine (TBAs), and dimethylhydrazine (DMHy), respectively. A 100 nm GaAs buffer layer was grown on GaAs (100) substrate at 650 °C before growing the GaNAs epilayer. Then, the substrate temperature was reduced to 550 °C for GaNAs epilayer growth. N/V ratio was varied to obtain the desired nitrogen content [2]. X-Ray diffraction (XRD) measurement at (0 0 4) Bragg reflection was employed to determine N composition of the GaNAs epilayers. The fringes in the samples' XRD rocking curve show the grown GaNAs strained epilayer is of good quality.

Samples were then undergone rapid thermal annealing from 625 °C to 775 °C with the incremental step of 50 °C for annealing duration of 60 seconds under nitrogen ambient. Samples were covered with GaAs wafers to prevent the out diffusion of As during the annealing process.
Photoluminescence (PL) measurements were carried out for the samples at 30K. In the PL measurements, a 488-nm Argon ion laser was used as the excitation source. The laser excitation power used for PL measurement was 120 mW. PL emission signal from the sample was detected by a cooled PbS detector and the detected signal was amplified through a standard lock-in amplifier before being sent to a computer for processing.

Results and Discussion

A good crystalline quality of the GaNAs epilayer grown with different nitrogen composition has been obtained. Details about the growths are provided in our other paper [3]. The interface between the buffer and epilayer is very good and abrupt from the TEM image [3]. Fig. 1 shows the typical 30-K PL of as-grown GaNAs sample. V/III ratio of this sample is 30. The nitrogen content of the sample is 1%. The intensity of the defect-related peak (DP) far exceeds the epilayer's band-to-band (BTB) transition. The DP is due to the nitrogen interstitial defect related emission. It has been explained in other paper [4].

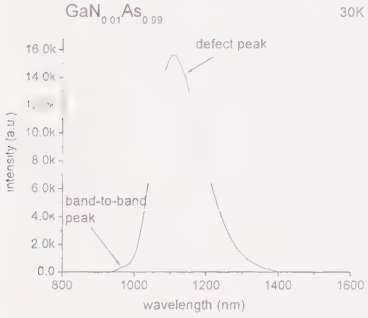

Fig. 1 30-K PL spectrum of as-grown GaNAs sample with 1% nitrogen content

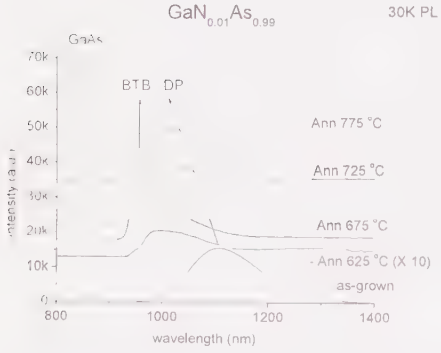

Fig. 2 30-K PL spectra of the as-grown GaNAs sample and after annealed at different temperatures. The sample is with 1% nitrogen content (Sample 1)

After thermal annealing, large reduction in DP emission intensity is observed. Figure 2 shows the changes of PL emission of GaNAs sample after annealed at different temperatures. The band-to-band (BTB) transition emission is getting stronger in intensity with increasing the annealing temperatures. The BTB PL intensity reaches saturation when the sample was annealed at 675 °C. Further increase in the annealing temperature causes the PL intensity of BTB to deteriorate and the DP to persist in the sample 1.

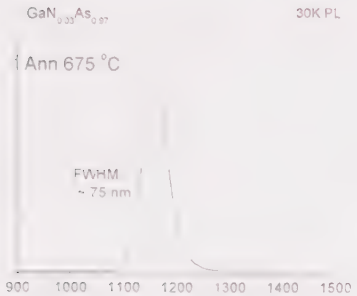

Fig. 3 30-K PL spectrum of the GaNAs sample with 3% nitrogen content (Sample 2) after thermal annealing.

Sample 2 is with higher nitrogen content, 3%, and was grown with V/III ration of 20. This sample does not have as-grown PL emission as the number of defects in the epilayer increase with its nitrogen content. After thermal annealing, the sample shows a strong single narrow PL emission peak which corresponds to the BTB transition. No DP emission is observed after thermal annealing in this sample when it was grown with lower V/III ratio. The study has been performed for different nitrogen composition with different V/III ratio samples followed by RTA of the as-grown samples. The optimized V/III ratio to obtain the defect-free PL emission after sample's annealing is found to be around 20. Higher V/III ratio during the MOCVD growths will lead to the gallium vacancy defect in the grown layers [5]. Samples grown below the optimized V/III ratio will experience arsenide vacancy defect.

Summary

The photoluminescence (PL) of GaAsN epilayers grown by MOCVD shows two distinguished peaks. The lower energy emission peak is caused by nitrogen interstitial defect. This defect peak has a strong and broad PL emission peak. Combining the optimum V/III ratio during the MOCVD growth and rapid thermal anneal of the sample after the growth completely eliminates this defect related emission peak and at the same time the GaNAs' band gap transition emission has been greatly improved. The PL spectra result in a single, narrow, and high intensity GaNAs' band gap emission after thermal annealing. This method has been carried out for samples with the nitrogen composition up to 3% and shows a promising result. The optimum V/III ratio for N content < 3.5% is around 20.

References

[1] W. G. Bi, C. W. Tu, Appl. Phys. Lett 70 (1608) 1997.

[2] X. Tang, D. Sentosa, The 13th International Conference on Metal Organic Vapor Phase Epitaxy (ICMOVPE-XIII) 2006.

[3] D. Sentosa, X. Tang, S. J. Chua, Z. Yin, E-MRS Spring Meeting 2007.

[4] D. Sentosa, X. Tang, S. J. Chua, Z. Yin, paper under submission 2007.

[5] J. Toivonen, J. Oila, K. Saarinen, T. Hakkarainen, M. Sopanen, H. Lipsanen, IEEE 2002.

Advanced Materials Research Vol. 31 (2008) pp 80-82
online at http://www.scientific.net
© 2008 Trans Tech Publications, Switzerland

Influence of Hydrogen Dilution of Silane on the Properties of nc-Si:H films grown by Layer-by-Layer deposition technique

Goh Boon Tong[1], Siti Meriam Ab. Gani[2] and Saadah Abdul Rahman[3]

Solid State Research Laboratory, Department of Physics, University of Malaya,

50603 Kuala Lumpur, MALAYSIA

[1]gohbt@um.edu.my, [2]smag@um.edu.my, [3]saadah@um.edu.my

Keywords: nc-Si:H; LBL; XRD; Raman scattering; FTIR; AFM; FESEM

Abstract. Hydrogenated nanocrystalline silicon (nc-Si:H) films produced by layer-by-layer (LBL) deposition technique were studied. The films were grown at different hydrogen to silane flow-rate ratio on crystal silicon (111) substrate. The properties of films were investigated by X-ray diffraction (XRD), micro-Raman scattering spectroscopy, Fourier transform infrared (FTIR) spectroscopy, optical transmission spectroscopy, atomic force microscopy (AFM) and field emission scanning electron microscopy (FESEM). These properties showed dependence on the hydrogen dilution of silane. Appearance of XRD peaks at diffraction angles of 28.4 ° and 56.1 ° which correspond to silicon orientation of (111) and (311) respectively, were observed in all films indicating evidence of crystallinity in the films. Raman scattering results indicated that crystallinity in the films was due to the presence of nanocrystallites embedded in an amorphous matrix. The energy gap of the films showed dependence on the hydrogen content in the films. Increase in nanocrystallite size resulted in increase in disorder at low hydrogen dilution films but films remain homogenous with increase in nanocrystallite size for the high hydrogen dilution films.

Introduction

Hydrogenated nanocrystalline silicon (nc-Si:H) thin films, with nanometer sized crystallites embedded within an amorphous matrix demonstrate superior properties for applications such as solar cells and thin film transistors (TFTs) [1]. Solar cells fabricated using nc-Si:H are more stable during light soaking while TFTs are more efficient due to enhancement of carrier mobility. The role of hydrogen is important to the properties of nc-Si:H and proposed growth model of nc-Si:H such as surface diffusion and hydrogen etching models lead to a clearer understanding of the role of hydrogen in nc-Si:H [2]. In this work, we report our investigations on the effects of hydrogen dilution of silane on the properties of nc-Si:H films prepared by layer-by-layer (LBL) deposition technique using X-ray diffraction (XRD), micro-Raman scattering spectroscopy, Fourier transform infrared (FTIR) spectroscopy, optical transmission spectroscopy, atomic force microscopy (AFM) and field emission scanning electron microscopy (FESEM).

Methodology

The nc-Si:H films were deposited on silicon (111) substrates using LBL technique in a conventional home-built radio-frequency plasma enhanced chemical vapor deposition (rf PECVD) system. During the LBL deposition, the silane (SiH_4) flow-rate was fixed at 5 sccm while the hydrogen (H_2) flow-rate was varied for each deposition process to obtained films with different H_2 to SiH_4 flow-rate ratios. The LBL technique involved alternating the growth of nc-Si:H films from the discharge of H_2 mixed with SiH_4 for 5 minutes followed by H_2 plasma treatment on the pre-grown layer for 3 minutes for a period of 64 minutes (8 cycles). The substrate temperature and pressure were maintained at 300 °C and 0.8 mbar respectively. The 13.56 MHz rf power density was fixed at 1400 mW/cm^2 throughout the deposition process for all films. The optical transmission spectra of the films were measured using a UV-VIS-NIR spectrophotometer and from these data the optical

energy gap, E_G was estimated [3]. XRD and micro-Raman spectroscopy using 514.5 nm Argon laser line were employed to investigate the crystallinity of these films. The average crystallite size, d_{XRD} of the crystallites in the films was estimated using Scherrer's formula [4]. The crystalline volume fraction, X_C was determined from the integrated intensities of Raman peaks at 520, 500 and 480 cm^{-1} which corresponds to crystalline components, grain boundaries and amorphous components respectively [5]. The hydrogen content, C_H and the ratio of integrated intensities of the Si-H_2 to Si-H absorption bands were determined from FTIR spectra [6]. Surface morphology of the film was studied using AFM and FESEM.

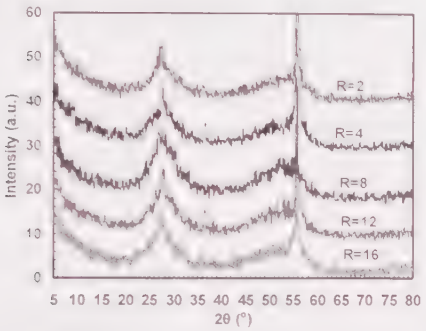

Fig. 1. XRD spectra of nc-Si:H films at different hydrogen to silane flow-rate ratio, R.

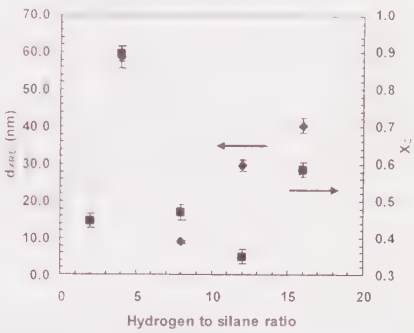

Fig. 2. Average crystallite size, d_{XRD} and crystalline volume fraction, X_C of nc-Si:H film versus hydrogen to silane flow-rate ratio, R.

Results and Discussion

Appearance of sharp diffraction peaks corresponding to Si(111) snd Si(311) at 28° and 56 ° respectively (Fig. 1) shows the presence of crystalline phase in the structure of all films deposited at different hydrogen to silane flow-rate ratio, R. Fig. 2 illustrates the variation of average crystallite size, d_{XRD} and crystalline volume fraction, X_C with R. It is observed that d_{XRD} increases to a maximum (60nm) with increase in R from 2 to 4, then it decreases to a minimum (10 nm) when R increases to 8 followed by increase in d_{XRD} with further increase in R. The trend is the same for the variation of X_C with R except that X_C decreases to a minimum at R equals to 12. High X_C films contain higher crystalline component by fraction compared to the amorphous component. The films formed with R equals to 2 and 8 have small nanocrystallites embedded sparsely within the amorphous matrix of the film. Film with high X_C of 0.9 and with large nanocrystallites of 60 nm is formed with R equals to 4. Film with R equals to 12 has low X_C with 30 nm sized nanocrystallites embedded within a highly amorphous structure. The film prepared with R equals to 16 is truly a two-phase material with reasonably sized nanocrystallites of 40 nm with X_C of 0.6. The plots of Hydrogen content, C_H and optical energy gap, E_G versus R are shown in Fig. 3. C_H decreases to a minimum when R equals to 4 and then increases up to a maximum saturation value of 10 % when R is equal to 12. E_G shows similar dependence on R as C_H but E_G continues to increase with increase in R beyond R equal to 12. The plots indicate that E_G has some dependence on C_H. Increase in R reduces C_H and E_G for films with low R (R = 2, 4), while high R (R = 8, 12 & 16) films produces a reversed dependence. Fig. 4 shows the variation of the ratio of the integrated intensities of SiH_2 to SiH absorption bands, I_{SiH_2} / I_{SiH} with R. I_{SiH_2} and I_{SiH} is proportional to the concentration of SiH_2 and SiH bonds in the film respectively. The plot of d_{XRD} with R is inserted in Fig. 4 to show the relationship between these parameters. High I_{SiH_2} / I_{SiH} roughly indicates increase in structural disorder in the film structure. Films prepared with low R become more disordered with increase in nanocrystallite size while for high R films crystallite size has very little effect on the homogeneity of the film structure. Large R films and films with small nanocrystallites are more ordered

comparatively. The AFM and SEM images of films prepared at R values of 4 and 16 confirm the results above as shown in Fig. 5. The film prepared with R equals to 4 has clusters of nanocrystallites of varied sizes (large and small) and are unevenly distributed. This explains the less ordered structure of the film. The images of the film with R equal to 16 shows a homogeneous film structure with evenly distributed nanocrystallites.

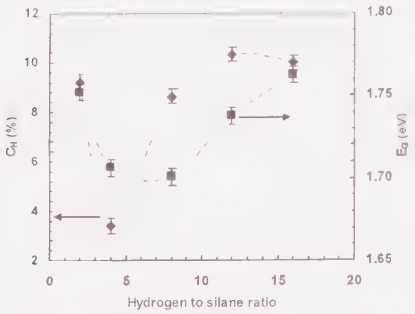

Fig. 3. C_H and E_G of nc-Si:H films versus hydrogen to silane flow-rate ratio, R.

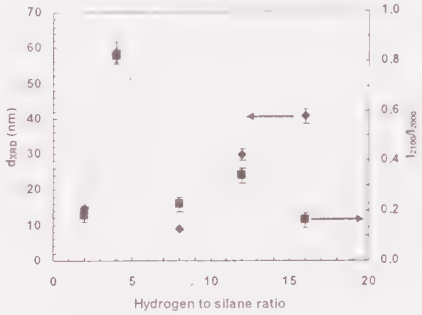

Fig. 4. Variation of d_{XRD} and I_{2100}/I_{2000} ratio with hydrogen to silane flow-rate ratio, R.

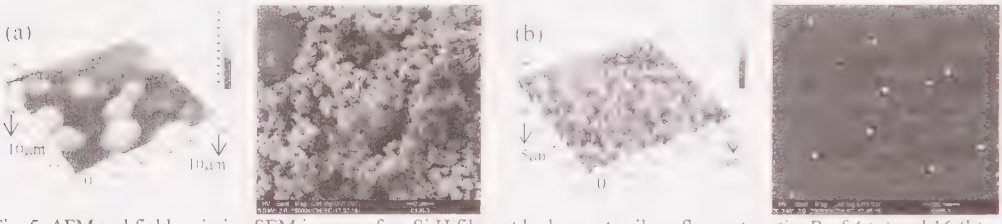

Fig. 5. AFM and field emission SEM images of nc-Si:H films at hydrogen to silane flow-rate ratio, R of 4 (a) and 16 (b).

Conclusions

Hydrogen to silane flow-rate ratio has significant influence on the H content and crystallite size in the nc-Si:H film produced using the LBL technique which directly influences the energy gap, crystalline volume fraction and the homogeneity of the film. The H plasma treatment on the pre-grown surface of the nc-Si:H layer grown by LBL technique increases crystallite size and homogeneity in low and high hydrogen to silane flow-rate ratio films respectively.

References

[1] S.F. Chen, Y.K. Fang, T.H. Lee, C.Y. Lin, S.H. Chang and T.H. Chou: Thin Solid Films Vol. 515 (2007), p. 3844.

[2] Akihisa Matsuda: J. Non-Cryst. Solids Vol. 338–340 (2004), p. 1.

[3] J. Tauc: *Amorphous and Liquid Semiconductors* (Plenum Press, New York 1974).

[4] H.P. Klung and L.E. Alexander: *X-ray Diffraction Procedures* (Wiley, New York 1974).

[5] Keda Wang, Anthony Canning, J. R. Weinberg-Wolf, E. C. T. Harley and Daxing Han: Materials Research Society Vol. 808 (2004), p. A9.53.1.

[6] A.A. Langford, M.L. Fleet, B.P. Nelson, W.A. Lanford and N. Maley: Phys. Rev. B Vol. 45 (1992), p. 13367.

Advanced Materials Research Vol. 31 (2008) pp 83-85
online at http://www.scientific.net
© 2008 Trans Tech Publications, Switzerland

Defect Mediated Photonic Behavior of ZnO Nanocrystals

Y.Y. Tay[1,a], S. Li[2], M.L. Liang[1]

[1] School of Materials Science and Engineering, Nanyang Technological University, Singapore.

[2] School of Materials Science and Engineering, NSW 2033, Australia.

[a]tayy0006@ntu.edu.sg

Fabrication of nanocrystals using chemical route with capping layers suppressed the surface defects that deteriorate its photonic properties. ZnO nanocrystals of less than 5 nm are fabricated through physical size reduction method and the mediation of defects offer interesting photonic behavior. This photonic behavior is investigated through close correlation between the crystal structure and the defects present in the material. Transmission Electron Microscopy, X-ray Diffraction as well as X-ray Photoelectron Spectroscopy have shown interesting results on this nanocrystal ZnO which would enhance our understanding on the origin of its unique photonic behavior.

Introduction

Zinc Oxide (ZnO) is an excellent wide band gap semiconductor which can be implemented in many advanced technological application. This includes catalyst, spintronics and one of the most important applications is in optoelectronic due to its remarkable luminescent property [1, 2]. This as a result enables ZnO to be used in nano-laser and random laser in recent development [3, 4].

One of the most interesting aspect of ZnO that invites tremendous interest among the scientific community is its visible emissions which are in the green (~510nm, 2.43eV), yellow (~597nm, 2.08eV) or orange (~640nm 1.94eV) emission region. Particularly, the origin of visible green emission is the most controversial. Many experimental results support the notion that oxygen plays important role in determining this emission behavior. In general, the emission behavior can be caused by different factors such as the role the dopants which modify the electronic and crystal structures of ZnO due to the introduction of different charge and atomic diameters.

The origin of the emission behavior becomes more interesting with the introduction of modifying the physical size of the material. It is known that when particles size of pure ZnO is smaller than 5nm in diameter, the effect of quantum effects appears which widen the band gap, thus the emission energy will blue shift thus changing the color of the emission [5]. Chemical route is often preferred to yield these extremely small particles due to high purities, however it can be complicated, conditions have to be stringent and usually yielding is extremely low which limits their application. In this work, we deliberately introduce defects while on the other hand reduce the size of ZnO < 5 nm which this region is known to exhibit quantum size effect. This allows us to have a better understanding on the coupling effects on the visible emission properties.

Experiment

ZnO (99.5% pure Analyticals Carlo Erba) powder was first annealed at 1200°C in ambient with ramping rate of 5°C/min and a dwelling time of 1hr. To reduce the crystal size physically in a control fashion, high energy ball milling was carried out.

The prepared ZnO materials were characterized using X-ray Diffractometer (XRD). Data were recorded using a Theta/Theta Bruker Diffractometer with a Cu Kα radiation, with a divergence slit of 2° and a 0.2mm width receiving slit. The crystal sizes of the as prepared ZnO powders were verified using JEOL 3010 HRTEM. Photoluminescence (PL) measurement was performed using Accent Rapid Photoluminescence Mapping System (RPM 2000) with a He-Cd laser source with an excitation wavelength of 325nm. XPS analysis was performed on the samples using Kratos AXIS spectrometer with a monochromatic Al Kα (1486.71 eV) X-ray radiation with a chamber pressure < 10^{-7} Pa. The instrument accuracy was found to be within ±0.3 eV.

Results and Discussion

The crystal size and its distribution is shown in Fig 1 (a) from XRD and TEM results. As

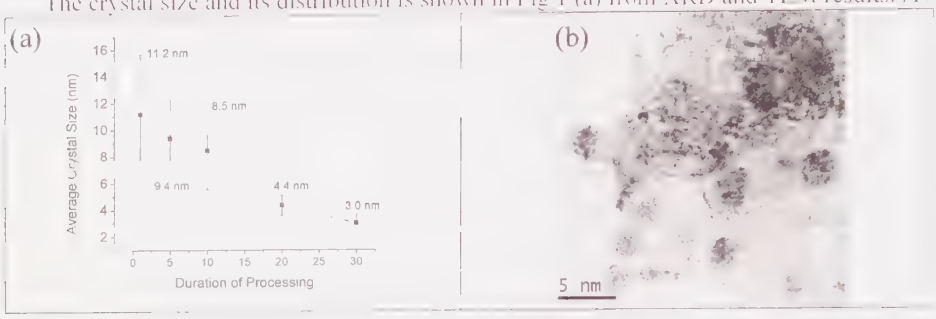

Fig 1

observed, the crystal size decreased to less than 5 nm when the duration of the processing increase by 20 hrs onwards. Fig1 (b) shows TEM images of these physically reduced ZnO with average crystal size of 3 nm.

These nanocrystals are subsequently characterized with X-ray Photoelectron Spectroscopy [Fig 2 (a)]. The initial core level binding energy of the as-received ZnO has a binding energy of 1022 eV. Notice that as the crystal size is reduced to 8.5 nm, the core level binding energy of Zn 2p 3/2 shifted to a lower binding energy to 1021.2 eV. Finally as the crystal size of 3.0 nm is obtained, the core level binding energy further reduced to 1020.9 eV. On the other hand, the emission of ZnO

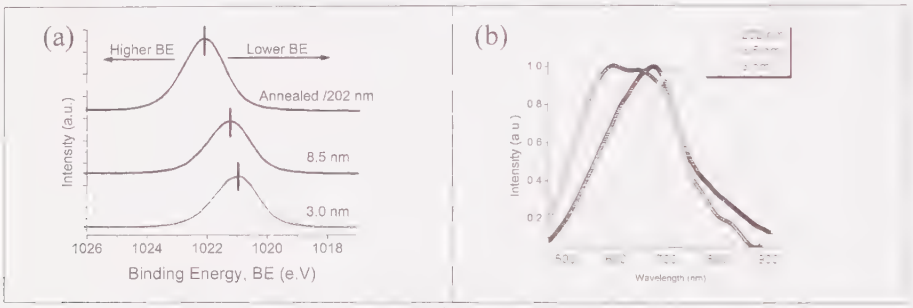

Fig 2

shows that as the crystal size is reduced 8.5 nm, there is a broadening of the orange emission region (677 nm) from the as-received ZnO to the green region (516 – 566 nm) for the physically reduced sample. Interestingly, when the crystal size is further reduced to 3.0 nm, there is a sudden shift of the emission to 701 nm. This is not expected as early mentioned of the involvement of the quantum size effect when the crystal size is less than 5.0 nm.

To explain this phenomenon, one has to understand that the special properties of the nanocrystals have a strong relationship with its surface atoms as their surface percentage increases as the size gets smaller. As the surface area increases, the nanocrystal system suffers from an increasing tension among the binding surface atoms which inevitably has high probability of creating oxygen vacancies. As a result, the green emission of the nanocrystal of 8.5 nm starts to appear which seems to be in consistence with the literature [5, 6]. This can be further verified by the result of XPS shown in Fig 3. For crystal size of 8.5 nm, the core level binding shifts towards a lower binding energy. The existence of surface oxygen vacancies reduces the electron charge transfer from the zinc ions thus increasing the shielding effect of the core which reduces the binding energy of the core level Zn 2p 3/2.

The results brought further surprises when the crystal size is reduced to 3.0 nm. To date, it is not clear why the emission red shifted instead [Fig 2 (b)]. One possible reason to explain this unqiue shifting maybe explained by Fig 2 (a). The further shifting of the core level binding might involved with the number of oxygen atoms being removed thus creating more broken bond as a result of tremendous surface distortion due to increase surface area. As a first approximation, for ZnO with an average crystal size of 8.5 nm, we can visualize that there is only a broken bond of the oxygen atom since the zinc ion is tetrahedrally bonded to four other oxygen atoms. When the average crystal size of ZnO reached 3.0 nm, the number of broken bond increase to two, thus the electron charge transfer is further reduced, thus shifting the core level binding shifted even to lower energy (1020.9 eV) [See Fig 2 (a)]. When this happens the lattice structure will be altered via arrangement of the atoms and the presence the vacancies. This will also caused a readjustment in the band structure through the interaction between atoms and the vacancies hence in this manner give rise to a red emission rather than the blue-shifting phenomenon as a result of quantum size effect [7]. The exact emission mechanism is currently investigated and will be available in the future. The excitonic UV spectra for the nanocrystal are suppressed due to the present of defects thus it is not clear if the widely known quantum confinement effect occurs.

Conclusions

In conclusion, when the size is physically reduced, oxygen vacancies are formed causing broadening of the PL emission towards the green region. However when ZnO is physically reduced to nanoscale of less than 5 nm the PL emission red shifted. Such shift could probably be attributed to the coupling of the lattice distortion and oxygen vacancies that induces changes to the electronic band structure.

Acknowledgement

The author would like to thanks Dr Chen Peng from Institute of Materials Research and Engineering (IMRE, A*Star, Singapore) and Dr Jacques Plevert for their kind assistance. Support for one of the authors (Y. Y. Tay) has been provided through a scholarship awarded by Singapore Milllennium Foundation (SMF), Singapore

References

[1] H. Nanto, T. Minami, S. Shooji and S. Tanaka: J Appl. Phys. Vol. 55 (1984), p. 1029

[2] T. Dietl, H. Ohno, F. Matsukura, J. Cibert and D. Ferrand: Science Vol. 287 (2000), p. 1019

[3] M.H., Huang, S. Mao, H. Feick, H. Yan,, Y. Wu, H. Kind, E. Weber, R. Russo and P. Yang: Science Vol 292 (2001), p. 1897

[4] H. Cao: Waves Random Media Vol. 13 (2003), p. R1-R39

[5] A.V. Dijken, E.A. Meulenkamp, D. Vanmaekelbergh and A. Meijerink: J. Phys. Chem. B Vol. 104. (2000), p. 1715

[6] X.L. Wu, G.G. Siu, C.L. Fu and H.C. Ong: Appl. Phys. Lett. Vol. 78 (2001), p. 2285

[7] M. J. Carey, T. Block, and B. A. Gurney: Appl. Phys. Lett. Vol 85 (2004), p. 4442

Advanced Materials Research Vol. 31 (2008) pp 86-88
online at http://www.scientific.net
© 2008 Trans Tech Publications, Switzerland

Surface structure dependent growth of InAs/InAlAs quantum wires on InP(100)

M.F. Casco[a], J.V. Misa[b], M. Defensor[c], A. Garcia[d], A. Salvador[e]

Condensed Matter Physics Laboratory National Institute of Physics University of the Philippines. Diliman, Quezon City, Philippines

[a]frantessa@gmail.com, [b]johnadapmisa@yahoo.com, [c]mdefensor@gmail.com, [d]alipio.garcia@gmail.com, [e]arnels@nip.upd.edu.ph

Keywords: quantum wires, surface morphology, MBE, AFM, photoluminescence, SEM, XRD

Formation of quantum wires (QWRs) or quantum dots (QDs) can be controlled by in situ surface preparation. InAs QDs and QWRs were grown on InAlAs using Riber 32P molecular beam epitaxy system. By varying the growth temperature, the surface morphology of InAlAs can be tailored. X-ray diffraction (XRD) and scanning electron microscopy (SEM) measurements were done to determine the mole fraction and surface morphology of the InAlAs layers. Atomic force microscopy (AFM) results verified the formation of quantum wires on a rough surface and quantum dots on a smooth surface. Low-temperature photoluminescence (PL) spectra revealed that the spectral positions of the wires are within of 1.0 – 1.3 μm and 1.189 μm for the quantum dots.

Introduction

InP-based InAs nanostructures are attracting attention as a good light emitter in the long-wavelength (1.3-1.5 μm) region. Normally, quantum wires are grown on ex situ prepared substrates or samples with grooved substrates [1,2]. Previous studies on quantum wire growth involves manipulation of the growth parameters such as arsenic interrupt[3], InAlAs spacer layers[2], and InAlAs buffer thickness[5]. In this work, quantum wire growth was prepared by tailoring surface morphology of the InAlAs layer. This is an in situ way of preparing the template for the growth of quantum wires.

Experimental procedures

All samples were grown using a Riber 32P MBE facility on InPacT epi-ready indium phosphide (InP) wafers oriented at (100). InAlAs layer surface morphology can be controlled either by varying the growth temperature of the InAlAs layer. InAlAs layers were grown at 510 and 530°C to investigate the effect of temperature on the resulting surface structure. The result on the effect of growth temperature on the resulting InAlAs surface was used on the study of the surface-structure-dependent formation of quantum wires and quantum dots. In this work three samples were grown. In sample A, a 0.6 μm thick InAlAs template layer was grown at 530°C. After InAlAs layer deposition, 3 stacks of InAlAs/InAs were deposited on top of the template layer. InAlAs spacer layer was grown at a substrate temperature of 510°C for 60 seconds at $5x10^{-6}$ Torr As pressure followed by 150 seconds As interrupt. InAs layer was grown with substrate temperature at 500°C for 7 seconds and As pressure at 1.0 x 10^{-5} Torr followed by a 30 second As interrupt. The growth parameters of sample A were followed by sample B except for the deposition time of InAs layer, which was increased to 13.3 seconds. This is to check for the effect of InAs layer thickness on the growth of quantum wires. On the other hand, InAlAs template of sample C was grown at 510°C and 3 stacks InAs/InAlAs with same growth parameters as sample A were deposited on top. Properties of the InAlAs surface of the three samples were investigated using XRD and SEM. InAs island formations for the three samples were observed using AFM. Low-temperature (10 K) PL was done to determine the optical properties of the quantum wires and quantum dots.

A. Preparation of the InAlAs template. The effect of growth temperature on the resulting InAlAs surfaces is shown in Figure 1(a,b). A smooth InAlAs surface was observed at 530° and a rough surface at 510°C. The computed In mole fractions of InAlAs layers based on XRD results are 0.66 for (a) and 0.64 for (b).

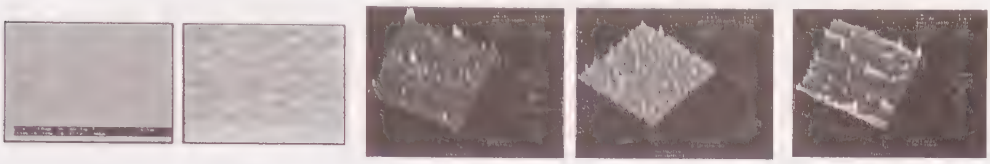

(a) (b) (c) (d) (e)

Figure 1. Shown here are SEM images of layers grown at (a) 530°C showing a smooth surface morphology and (b) 510°C showing a rough surface. AFM images of samples A (c) which has 3 ML-thick InAs and B (d) which has 6 ML-thick InAs exhibit quantum dot formations for InAlAs layers grown at 530°C. AFM image of Sample C (e) with InAlAs layer grown at 510°C shows quantum wire formations.

B. Quantum wire growth. Results obtained on the effect of growth temperature on InAlAs surface morphology were used to investigate the formation of quantum wires. AFM images of the samples are shown in Figure 1(c,d,e). The base widths of the quantum dots for Sample A grown at 3 ML-thick InAs are less than 0.2 μm and majority of them have heights less than 50 nm. Sample B grown using 6 ML-thick InAs has base widths between 0.75 – 0.2 μm and heights between 25 - 100 nm. In this size range, the InAs island structures observed in the AFM image are still considered quantum dots. Figure 1(e) shows the AFM image of Sample C. InAlAs layer of this sample was grown at 510°C and formation of quantum wires is observed. The quantum wires have base widths within 0.5 – 1.0 μm and heights within 20 – 100 nm. This wire-like shape formation is due to the memory effect of the 2D-3D growth transition wherein the structure of the 2D surface (InAlAs) is carried by the 3D structure (InAs). When the 2D-3D growth transition occurs, there is some memory of the previous 2D growth that is incorporated and this memory will in turn induce the observed anisotropy for ensuing 3D islands [6]. Thus, elongated steps of the 2D layer induce formation of wire-shaped InAs island structure. On the other hand, in the InAlAs layer with less pronounced surface anisotropy, the formation of isotropic InAs islands is predicted. This is verified by the formation of dot-shaped InAs structures on the smooth InAlAs surfaces.

C. Photoluminescence measurements. The objective of this section is to show that there is emission coming from the quantum wires seen in the AFM image. PL result at 10 K shown in Figure 2(a), exhibits peaks at 1.275, 1.175 and 1.076 μm. The absolute signal positions are attributed to the degree of confinement. PL signal broadening is closely related to the to the size distribution of the islands. Intensity of the PL signals is explained by the density of the islands. The more number of islands having the same sizes, the higher the PL intensity it exhibits. If there are buried dots in Sample C that are not seen in the AFM image, it is expected see a signal at peak b as it corresponds to the PL signal of our quantum dot sample (Figure 2(b)).

(a) (b)

Figure 2. 10K PL result for Sample C (a) showing peaks at 1.275, 1.175, and 1.076 μm while Sample A (b) emits at 1.186 μm.

Based on this PL results, it can be claimed that peak c is the emission coming from the quantum wires. Its intensity verifies the large density of wires shown in the AFM image and most importantly, it has lower energy that the quantum dot sample. The origins of peaks a and b are currently being investigated. Peak b could be due to the emission of buried quantum dots and peak a could be attributed to quasi-3D clusters [7] or a wetting layer behavior.

Summary

In this work, growth of quantum wires was realized using in situ surface preparation of InAlAs layer. AFM results verified the formation of quantum wires on a rough InAlAs surface while a smooth surface produces quantum dots. The QWR formation is attributed to the memory effect during transition from 2D to 3D growth. Low-temperature (10 K) PL measurements reveal emissions at 1.0-1.3 μm for the quantum wire sample and 1.189 μm for the quantum dot sample.

This work was supported by grants from PCASTRD/DOST and UP-OVCRD.

References

[1] J.M. Garcia, et al., J. Crystal Growth, 227-228 (2001)

[2] S.Watanabe et.al, Phys. Rev. B. 68, 193304 (2003)

[3] Brault J, et al., Journal of Applied Physics, Vol 92, No. 1, July 2006

[4] Sun ZZ, et al., Applied Physics Letters , Vol 85, No. 21, 5061-3, November 2004

[5] FA Zhao, YH Chen, XL Ye, et al., Journal of Crystal Growth, 273 (2005) 494-499

[6] Ponchet A, et al., Journal of Microelec., 26, 783, 1995

[7] Yong Zhang, et al., Phys. Rev. B. Vol. 51, No. 19 (1995)

[8] Zhang SB and Zunger A, Physical Review B, vol 53, 1343 ,1996

[9] Ogura M, Sugiyama Y, and Sugaya T, Applied Physics Letters Volume 79, Number 3, 2001, pp 371-3

[10] M. Schmidbauer, et.al., Physical Review Letters, 96, 066108, 2006

[11] Lei W, et al., Applied Physics Letters, Vol 88, 063114, 2006

Advanced Materials Research Vol. 31 (2008) pp 89-91
online at http://www.scientific.net
© 2008 Trans Tech Publications, Switzerland

Characteristics of Ge Nanocrystals Grown by RF Magnetron Sputtering

R.K. Singha, K. Das, S. Das, A. Dhar & S. K. Ray *

Department of Physics and Meteorology, I.I.T.Kharagpur 721302, India
* e-mail: physkr@phy.iitkgp.ernet.in

Abstract. We report the self-assembled growth of Ge islands of different shapes and sizes on p-Si (001) by r.f. magnetron sputtering by varying the r.f. power, growth temperature and post-deposition annealing condition. The well known Stranski-Krastanov growth mechanism due to lattice mismatch between Si & Ge leads to the formation of Ge islands, similar to a more sophisticated MBE growth, albeit at a much higher pressure in our study. Ge nanocrystals embedded in SiO_2 matrix have also been grown. Optical properties of nanocrystals exhibiting visible luminescence at room temperature are presented.

Introduction

Ge nanocrystals grown on Si (001) have been intensively studied as a model system for the formation of self-assembled quantum dots using Stranski-Krastanov growth mechanism [1]. Germanium nanocrystals or quantum dots have been grown routinely using molecular beam epitaxy [2] and chemical vapor deposition [3], with the demonstration of size quantization effects at low and room temperatures [4]. However, limited reports are available on the characteristics of Ge nanocrystals grown using plasma-assisted deposition, which allows a simple way of incorporating the nanocrystals in high band gap oxide matrices. Here we report the formation of Ge nanocrystals in SiO_2 matrix along with the self assembled growth of islands of different shapes and sizes on p-Si (001) substrates by r.f. magnetron sputtering. Microstructural and optical properties of nanocrystals as a function of growth and post-deposition annealing temperatures are presented.

Experimental

Self-assembled Ge islands were grown on Si (001) substrates by r.f. magnetron sputtering from a Ge target at different substrate temperatures (350-650°C) with r.f power varying from 30-50W. In addition, composite Ge-SiO_2 films were deposited by cosputtering from a SiGe target in oxygen atmosphere at 50W, followed by post-deposition annealing in N_2 ambient. The formation of Ge islands on Si was investigated by atomic force microscopy. The microstructure and optical properties of grown samples were characterized using high-resolution X-ray diffraction, transmission electron microscopy, Raman spectroscopy and photoluminescence spectra.

Results & Discussions

Typical representative AFM micrograph of Ge islands grown on Si (001) at a substrate temperature 650°C is shown in fig.1. The micrograph shows the growth of domed shaped Ge islands with an average diameter of 50 nm. Typically, the growth starts with a strained 2D wetting layer, but islands form after the first few monolayers. The size distribution and density of the islands extracted from the AFM micrographs for different growth temperatures using r.f power 50 W for 5 min are presented in fig.2. The density and size of islands are strongly temperature dependent, with inverse relationship to each other in order to preserve the total deposited mass, as the plasma flux rate and deposition time are same for all the samples. But at 650°C, both the density and sizes fall as compared to the islands grown at 550°C. The inset of fig.2 shows that in this case the island height increases, which in turn conserves the total deposited mass. For electronic and optoelectronic applications lateral size confinement and isolated islands distribution are essential [5]. From the study, it is clear that high temperature growth is favorable to achieve the above condition. Fig.3 shows typical Rutherford Back Scattering (RBS) spectra (simulated and experimental) of r.f magnetron deposited sample at 50W power and substrate temp. 650°C. A low value of minimum

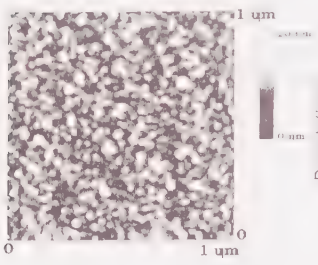

Fig.1 shows typical AFM micrograph of sample deposited at r.f power 50W for 5 min at a substrate temperature 650°C.

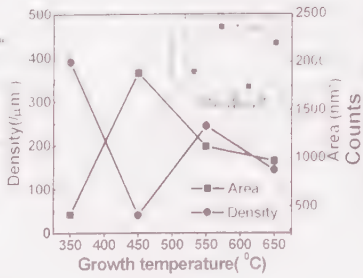

Fig. 2 shows the variation of islands density, mean area with growth temperatures. The inset shows the height variation of islands with substrate temp.

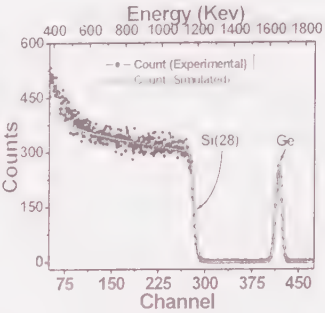

Fig. 3. Typical RBS curve of r.f magnetron deposited sample for 50W power, at 650°C for 5 min.

channeling yields of as grown Ge nanocrystal indicates good crystallinity [6]. High-resolution XRD pattern of this series of samples (not shown) revealed no dominant diffraction signals till 550°C. At 650°C, three distinct XRD peaks (111, 220, 311) of Ge are detected, which shows the growth of nanocrystalline islands in different orientations. We have also studied the effect of r.f power on the grown islands. Investigation reveals that island area and height increase at the cost of island density at low r.f power. X-ray diffraction study of Ge nanocrystals grown on Si(100) reveals that at low r.f power, the defect densities of islands are also reduced.

Figure 4 shows the plan-view TEM micrograph of Ge nanocrystals grown in SiO_2 matrices for different post-deposition annealing temperatures. The as-deposited sample does not show any well-defined nanocrystal formation. Irregular shaped small nanocrystals are present in the oxide matrix for sample annealed at 700°C, as shown in figure 4 (a). A narrow size distribution (shown in the inset) is observed for the sample with an average nanocrystal size of about 2.7 nm. A broad distribution in particle size for sample annealed at 800°C (fig.4 (b)) with average value of 13.0 nm

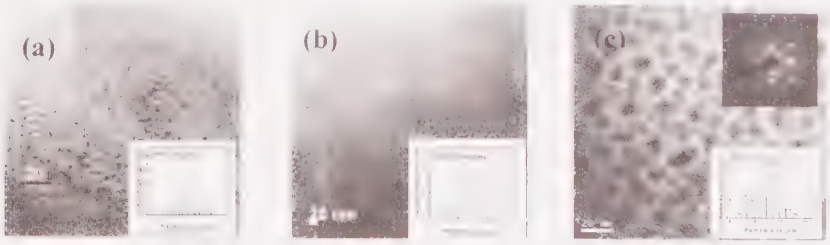

Fig. 4 TEM micrograph of the samples annealed at (a) 700°C (b) 800°C and 900°C for 60 minutes. The size distributions of the samples are given in the inset.

indicates an increase in size with annealing. Nearly spherical Ge nanocrystals are observed with uniform size distribution for 900°C annealed sample (fig. 4(c)) with size varying from 7.0 to 13.0 nm. The selected area diffraction pattern shown in the inset of figure fig.4(c) indicates the crystalline nature of Ge nanocrystals.

Figure 5 shows the Raman shift of the bulk Ge along with the samples annealed at different temperatures. A sharp peak corresponding to Ge-Ge mode in bulk sample is found to be around 302 cm^{-1}. All the nanocrystal samples show the dominant peak about 303 cm^{-1}, attributing to the Ge-Ge phonon mode. The peak position of the annealed sample is shifted to the higher wave number in comparison to the bulk Ge. The red-shift of the Raman peak position can be mainly attributed to the compressive stress experienced by Ge nanocrystals in silicon oxide matrix. The increase in line width of the Raman peaks and the presence of asymmetry in the lower wave number side is the

signature of size effect. On annealing, the size of the nanocrystals increases, which results in a decrease of the compressive stress. Thus there is no overall change in the Raman peak position on annealing.

Photoluminescence spectrum for 900°C annealed sample in fig.6 exhibits two sharp peaks at 773.1 nm (1.60 eV) and 808.3 nm (1.53 eV). The deconvoluted spectrum shown in figure 6 for the sample annealed at 900°C reveals four peaks overlapping each other. The peaks are centered around

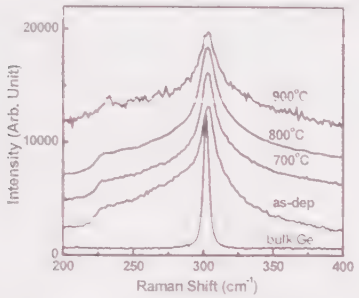

Fig. 5 Raman spectra of samples annealed at different temperatures along with the bulk Ge showing the Ge-Ge phonon modes.

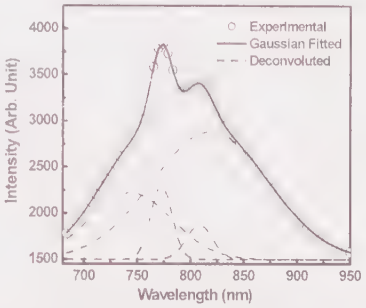

Fig. 6 PL spectrum for 900°C annealed sample. The spectrum is deconvoluted to four peaks using Gaussian fitting.

745.0 nm, 772.6 nm, 809.1 nm and 819.5 nm, which can be attributed to the size distribution of Ge nanocrystals. Using Brus' model [7], the average radius of nanocrystals is calculated to be about 4.1 nm, which is in agreement with the TEM observation.

Conclusion

We investigated the growth of self-assembled Ge islands on Si (001) substrates and in a SiO_2 matrix using RF magnetron sputtering. The shape and size evolution of islands on Si substrates with varying deposition parameters have been investigated using AFM. A lower RF power and higher growth temperature are found to be favorable for growing uniform Ge domes with good crystalline quality. TEM results show the formation of isolated spherical Ge nanocrystals in silicon dioxide matrix of size ranging from 3.0-13.0 nm. Optical characteristics of Ge nanocrystals embedded in SiO_2 have been carried out using Raman and photoluminescence spectroscopy. The emission in the visible wavelength range is attributed to quantum confinement of carriers in Ge nanocrystals.

References

[1] F. M. Ross, R. M. Tromp, and M. C. Reuter, Science Vol. 286 (1999), p. 1931.

[2] T. Merdzhanova, S. Kiravittaya, A. Rastelli, M. Stoffel, U. Denker, and O. G. Schmidt, Phys.Rev.Lett Vol. 96 (2006), p. 226103.

[3] M. Borgstrom, V. Zela and W. Seifert, Nanotechnology Vol. 14 (2003), p. 264.

[4] A.I. Yakimov, A.V. Dvurechenskii, A.I. Nikiforov, O.P. Pchelyakov, Thin Solid Films Vol. 336 (1998), p. 332.

[5] A. I. Yakimov, A. V. Dvurechenskii, A. I. Nikiforov, A. A. Bloshkin, A. V. Nenashev, and V. A. Volodin, Phys. Rev. B Vol. 73 (2006) p. 115333.

[6] M. Zhang, Z. An, C. Lin and P. K. Chu, Mat. Sc. & En. B. Vol. 114-115 (2004), p. 255.

[7] L. E. Brus, IEEE J. Quantum Electron. Vol. 22 (1986), p1909

Advanced Materials Research Vol. 31 (2008) pp 92-94
online at http://www.scientific.net
© 2008 Trans Tech Publications, Switzerland

Photoluminescence and Fractal Properties of Diverse Carbothermal Zinc Oxide Nanostructures

Eduardo R. Magdaluyo, Jr.,[1 a], Ian Harvey J. Arellano[2 b], Alvin Karlo G. Tapia[3], Roland V. Sarmago[4] and Leon M. Payawan[2]

[1]Department of Mining, Metallurgical and Materials Engineering, University of the Philippines, Diliman, Quezon City 1101 Philippines

[2]Nanostructures and Surface Chemistry Research Laboratory, Institute of Chemistry, College of Science, University of the Philippines, Diliman, Quezon City 1101 Philippines

[3]Physics Division, IMSP, University of the Philippines, Los Banos, Laguna

[4] Materials Science and Engineering Program, College of Science, University of the Philippines, Diliman, Quezon City 1101 Philippines

[a]edmagdaluyo@up.edu.ph, [b]ihjarellano@yahoo.com

Keywords: photoluminescence, fractals, nanostructure, carbothermal

Abstract. The photoluminescence of the diverse nanostructures of nonstoichiometric ZnO grown via carbothermal reduction at 900°C was investigated. Various formations of different structures like wires, rods, tubes and tetrapods resulted from the inhomogeneity of the boundary diffusion layer associated with vapor current induced in the set-up. The band gap emission of these structures was observed at around 390 nm, which corresponds to energy of 3.20 eV. The study was extended to measure changes of crystal habit of ZnO nanostructures in terms of its fractal dimension.

Introduction

Zinc oxide nanostructures (ZnO) have attracted a lot of research interests due to their remarkable applications such as UV light emitters [1], photocatalysts [2], photoelectrode [3], field-effect transistors [4], piezoelectric devices [5] and sensors [6]. Numerous studies have been focused on its synthesis, characterization and device applications. Diverse crystal habits include nanorods, nanowires, nanotubes, nanorings, nanohelices, nanosheets, nanoflower and nanotetrapods which were grown via different techniques such as physical evaporation and chemical vapor deposition [7], electrodeposition [8], hydrothermal and carbothermal route [9].

In this paper, we report the formation of diverse ZnO crystal habit via carbothermal reduction route. The as-synthesized structures exhibit unique optical properties which shed light on potential applications in the fields of nanoelectronics and nanooptics. The study was extended to investigate the fractal dimension behavior of the ZnO nanostructures. Fractal analysis describes the complexity and roughness of the spatial pattern of the diverse nanostructure formations of ZnO. This becomes a method of measuring qualities that otherwise have no clear definition on the irregularity of the observed pattern.

Materials and Methods

Diverse ZnO crystal structures were grown on silicon substrate via carbothermal route. The substrate was precleaned using standard RCA method. Three grams of finely ground zinc oxide and activated charcoal mixture were placed in a crucible and heated in an oven at 900°C for 15 minutes after which the reaction was oven-quenched. The substrate was placed on top of the crucible for the deposition of the zinc oxide. Surface morphology was investigated using SEM (Philips XL30), crystal structure was determined using XRD (Siemens Kristalloflex 760) and photoluminescence spectrum was generated at 270 nm excitation. Fractal analysis was also conducted.

Results and Discussion

The carbothermal synthesis of ZnO relies on the existence of graphite that significantly lowers the ZnO decomposition temperature due to its energy supplied during combustion [10]. The reaction mechanism observed is shown below.

$$ZnO_{(s)} + C_{(s,graphite)} \rightarrow Zn_{(g)} + CO_{(g)} \quad (1)$$
$$CO_{(g)} + \tfrac{1}{2} O_{2(g)} \rightarrow CO_{2(g)} \quad (2)$$
$$Zn_{(g)} + CO_{(g)} \rightarrow ZnO_{(s)} + C_{(s)} \quad (3)$$
$$2Zn_{(g)} + CO_{2(g)} \rightarrow 2ZnO_{(s)} + C_{(s)} \quad (4)$$

A thin epitaxial layer of nonstoichiometric ZnO was successfully grown. The nonstoichiometry of the ZnO structure is due to the sticking coefficient of oxygen at high temperatures. The diverse formation of crystal habit as shown in Figure 1 is due to the uneven exposure of silicon substrate to vapor current, which originates from the mixture of ZnO and C, causing the boundary diffusion layer to be inhomogeneous. The movement of vapor current leaves the sides of the substrate highly exposed while minimal amount reaches the central region.

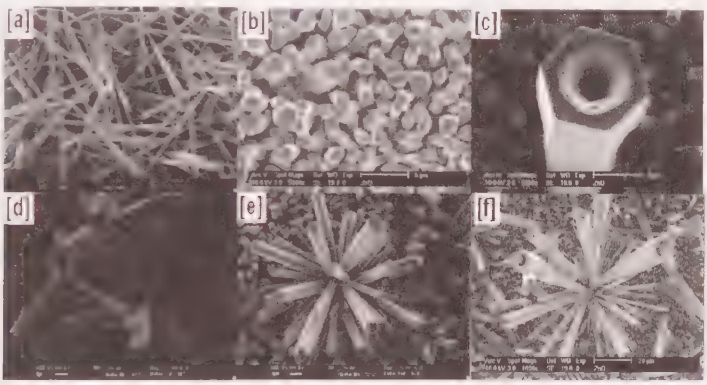

Figure 1. Diverse ZnO crystal habit [a] nanowires and sheets [b] and [e] rods [c] tube [d] tetrapods and [f] tubes sharing a common nucleation site

Nanowires grew anisotropically on the substrate's surface above the sheets. Hexagonal microrods adapted the hexagonal lattice type of ZnO. Wires and rods share the same structure but differ only in diameter, the former being smaller. These structures can extend some micrometers in length. Tubes also adapt the hexagonal structure with a hollow central region that runs throughout the structures length. Tetrapods are three-dimensional structures composed of rods that share a common center. These structures have remarkably uniform prism with six sides and faces and a hexagonal crown. The formation of flowerlike structures due to sharing of common nucleation site is thermodynamically driven. Shown in Figure 1e and 1f are rods and tubes sharing a common nucleation site. The preferential growth of ZnO structures to ZnO seed is more favorable despite the steric hindrance due to its lower surface energy relative to the silicon substrate. The difference in surface energy is due to the lattice mismatch of ZnO and Si substrate.

The wurtzite crystal structure of nonstoichiometric ZnO was confirmed by XRD analysis as shown in Figure 2. The preferential growth was directed at 002 with the lattice constants $a = 3.25$ Å and $c = 5.28$ Å. No peak was observed that corresponds to elemental Zn and C. This suggests that re-oxidation takes place as shown in the mechanism and further supported by elemental analysis. Room temperature photoluminescence (PL) was performed to examine the optical properties of these microstructures. The peak at around 388 nm and 390 nm as shown in Figure 3 correspond to the band gap emission of tetrapods and wires and rods, respectively. The presence of these UV

peaks correspond to a band gap energy of ~3.20 eV. In Figure 4 where the fractal dimension of the ZnO structures were plotted with respect to the regions they were formed, the degree of dispersion was quantified based on magnitude of the fractal dimension. High fractal value indicates wider dispersion in the substrate.

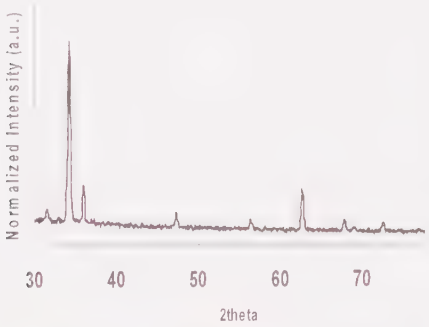

Figure 2. XRD pattern of ZnO

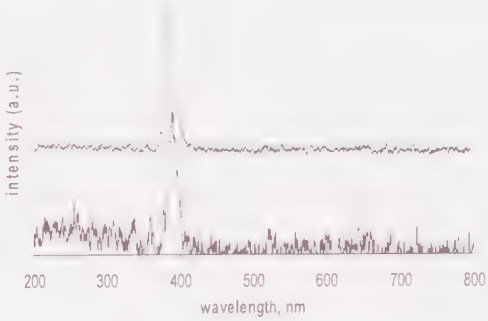

Figure 3. PL spectra showing UV band

Figure 4. Fractal dimension ZnO nanostructures with respect to the region of formation

Summary

Diverse nonstoichiometric ZnO nanostructures exhibiting good crystallinity were grown via carbothermal reduction route. The PL spectra showed a strong band gap emission corresponding to 3.20 eV with minimal emission at the visible region indicating minimal crystal defect. Fractal analysis showed that the rods are more dispersed on the substrate than the nanowires.

References

[1] S.C. Mines, S.R. Manalis and C.F. Quate: Appl. Phys. Lett. 67 (1995), p. 3918
[2] A. Umar and Y.B. Hahn: Nanotechnology 17 (2006), p. 2174
[3] N. Kumar, A. Dorfman and J. Hahm: Nanotechnology 17 (2006), p. 2875
[4] W. L. Hughes and Z.L. Wang: Appl. Phys. Lett. 82 (2003), p. 2886
[5] Dhananjay, J. Nagaraju, P.R. Choudhury and S.B. Krupanidhi: J. Phys. D:Appl. Phys. 39 (2006), p. 2664
[6] J.S. Jeong, J.Y. Lee, J.H. Cho, C.J. Lee, S.J. An, G.C. Yi and R. Gronsky: Nanotechnology 16 (2005), p. 2455
[7] M.H. Huang, Y. Wu, H. Feick, N. Tran, E. Weber and P. Yang: Adv. Mater. 13 (2001), p. 113
[8] B. Cao, W. Cai, G. Duan, Y. Li, Q. Zhao and D. Yu: Nanotechnology 16 (2005), p. 2567
[9] N. Mukherjee, P. Bhattacharyya, M. Banerjee, A. Mondal, R.T.T. Gettens, P.K. Ghosh and H. Saha: Nanotechnology 17 (2006), p. 2665
[10] E.C. Greyson, Y. Babayan and T.W. Odom: Adv. Mater. 16 (2004), p. 1348

Advanced Materials Research Vol. 31 (2008) pp 95-97
online at http://www.scientific.net
© 2008 Trans Tech Publications, Switzerland

Band structure and optical gain of 1.3 um GaAsSbN/GaAs compressively strained quantum well

B. Dong, W.J. Fan and Y.X. Dang

Nanyang Technological University, School of Electrical and Electronic Engineering, Singapore
Dong0017@ntu.edu.sg, EWJFan@ntu.edu.sg, dangyuxing@pmail.ntu.edu.sg

Keywords: Band Structure, optical gain, quantum well(QW), compressively strained

Abstract: The band structures and optical gain spectra of GaAsSbN/GaAs compressively strained quantum well (QW) were studied using 10-band k.p approach. We found that a higher Sb and N composition in the quantum well and a thicker well give longer emitting wavelength. The result also shows a suitable combination of Sb and N composition, and QW thickness can achieve 1.3 μm lasing. And, the optical gain spectra with different carrier concentrations will be obtained.

Introduction

In recent years, III–N–V semiconductor alloys have been attracting great interest due to their applications in 1.3 or 1.55 μm optical fiber communication. GaAsSbN is a potential alternative GaAs-based quaternary that can achieve 1.3μm lasers. Till now, a considerable number of studies have been carried out on III–N–V semiconductor alloys, and the results show that a small amount of nitrogen incorporated can reduce the band gap significantly[1-3]. The strong dependence of the band gap on the N content has been studied[4-6]. The advantage of GaAsSbN/GaAs arises from the fact that the band-gap energies of GaAsSbN/GaAs quantum wells (QWs) are lower than that of GaInAsN/GaAs QWs with equivalent compositions of In or Sb for a given amount value of N composition[6]. But GaAsSbN GaAs also suffer from the poor optical properties due to the N-related defects. In order to understand the band structure and optical properties of GaAsSbN/GaAs compressive-strained QW emitting at 1.3μm, 10 band *k.p* methord are used. We will focus on the band structure and the optical gain in different QW length as well as Nitrogen and Sb composition, finally find the best structure for emitting 1.3μm laser.

Method

10-band model[7] In order to take into account the influence of the band structure by nitrogen-induced level. E_N, a 10-band *k·p* model was proposed which add two more spin-degenerated states to the 8-band Hamiltonian through the follow matrix:[8,9]

$$H_c + H = \begin{bmatrix} N & 0 & V_{NC}\sqrt{y} & 0 \\ 0 & N & 0 & V_{NC}\sqrt{y} \\ V_{NC}\sqrt{y} & 0 & C & 0 \\ 0 & V_{NC}\sqrt{y} & 0 & C \end{bmatrix}, \quad (1)$$

where

$$N = E_N + \varepsilon_2(z). \quad (2)$$

We have shifted E_N by the amount of energy caused by the shear strain, $\varepsilon_2(z)$, since the origin of our calculation is at the middle of the heavy-hole and light-hole band-edge after splitting. For compressive strain, the heavy-hole band-edge is taken as the valence band maximum. We have neglected the interaction between i and the valence subbands[10], which is consistent with assumption of the band anticrossing model that the influence of E_N on valance band energy is minimal and negligible[11].

Optical Gain The optical gain spectra are calculated using[12,13]:

$$G(E) = \left[1 - \exp\left(\frac{E - \Delta F}{k_B T}\right)\right] \frac{\pi c \hbar}{n^2 E^2} R_{sp}(E),$$

$$R_{sp}(E) = \frac{ne^2 E}{\pi m_0^2 \varepsilon_0 \hbar^2 c^3} \sum_{n_c} \sum_{n_v} \iint \frac{Q^{n_c n_v}}{4\pi^2 l} f_c f_v \frac{1}{\pi} \frac{\hbar/\tau}{(E_{eh} - E)^2 + (\hbar/\tau)^2} dk_x dk_y \,, \qquad (3)$$

where $R_{sp}(E)$ is the spontaneous emission rate, $\Delta F = E_{f_c} - E_{f_v}$ is the quasi-Fermi levels separation and dependent on carrier density, E is the photon energy, e is the electron charge, ε_0 is the free-space dielectric constant, n is the refractive index, c is the speed of light, $Q^{n_c n_v}$ is the squared optical transition matrix element, E_{eh} is the transition energy, and τ is the intraband relaxation time. $\tau = 0.1$ps is used in all our calculations.

Results and discussions

The transition energy as a function of Sb composition and well width (L_w) are shown in Fig. 1 and 2, respectively. As the L_w increase, the transition energy decrease, and the transition energy decrease as the Sb composition increase. Also a bit more Nitrogen will decrease the transition energy significantly. From Figure 1, we can find the suitable well width and Sb composition for emitting of laser at 1.3μm.

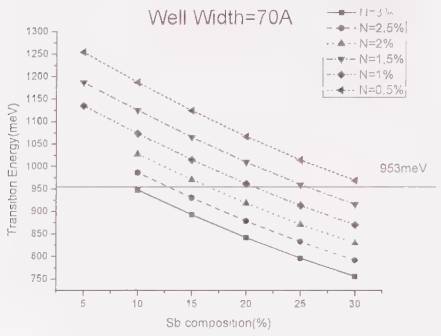

Fig.1. Transition energy of $GaAs_{1-x-y}Sb_yN_x/GaAs$ laser as a function of Sb composition and N composition at T=300K. The well width is 70 Å and barrier width is 200 Å.

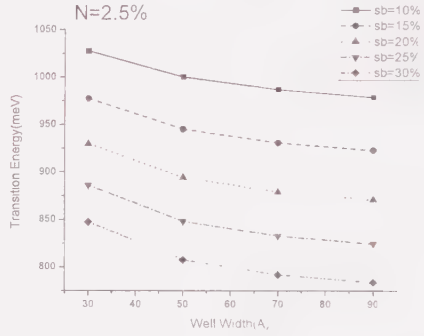

Fig.2. Transition energy of $GaAs_{1-x-y}Sb_yN_x/GaAs$ laser as a function of well width and Sb composition at T=300K. The barrier width is 200 Å and N composition is 2.5%.

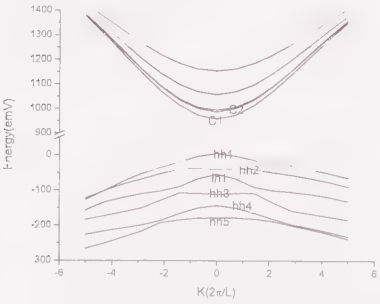

Fig.3. In-plane energy dispersion curves of $GaAs_{84.7}Sb_{12.8}N_{2.5}/GaAs$ QW sample with L_w =70Åand emitting approximately at 1.3 μm.

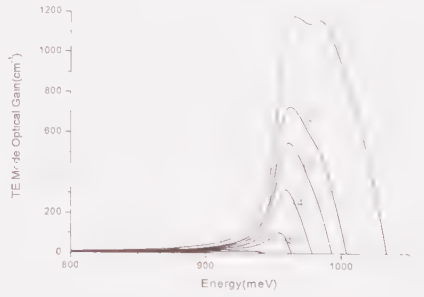

Fig.4. Optical gain spectra for TE mode at T=300 K for the $GaAs_{84.7}Sb_{12.8}N_{2.5}/GaAs$ compressively strained QW at injected carrier densities of: (1) 10 x10^{18} cm^{-3}; (2)7 x10^{18} cm^{-3}; (3)6 x10^{18} cm^{-3} (4)5 x10^{18} cm^{-3}(5)4 x$10^{18}$$cm^{-3}$

Fig.3 shows the band structure of $GaAs_{0.847}Sb_{0.128}N_{0.25}$/GaAs at well width 70Å, barrier width 200Å. The curves obtained are not parabolic especially for valence band because of the band intermixing effect. The conduction band E-k curves become flat at larger k due to N level interaction.

Fig. 4 shows the TE mode optical gain at 300K, well width 70Å, barrier width 200Å at different carrier density. This gives a gain that is larger than other composition, which can achieve a peak gain at about 1176cm^{-1}. The probability for the carriers to occupy the higher energy level is relatively smaller when the well width is small and the carrier density is small. So, the contribution to the optical gain for (2) (3) (4) and (5) is mainly from the ground-state transition between c1 and hh1. With increasing carrier density, more and more carriers occupy the higher energy levels in case (1)[14]. So, the higher transition c2–hh2 becomes an important contribution to the optical gain. C2-hh2 transition becomes even obvious when the well width increase. This is because the energy levels' separations are smaller as the well width increase. We also found that the optical gains for TE mode were enhanced while depressed for TM mode (not shown, because it is much smaller than that of TE mode) due to the compressive strain.

Conclusion

The electronic structures of compressive strained $GaAs_{1-x-y}Sb_yN_x$/GaAs QWs have been investigated using a 10x10 Hamiltonian model. The results show that as the L_w, Sb and N composition increase, the transition energy decrease. It also gives several N and Sb composition of $GaAs_{1-x-y}Sb_yN_x$ GaAs that can emit 1.3 μm laser. The Optical gain spectra for TE mode at T=300 K, well width (L_w)=70Å, barrier length 200Å for the $GaAs_{0.847}Sb_{0.128}N_{0.25}$ GaAs compressively strained QW at different injected carrier densities are obtained. It is suitable for laser emitting at 1.3 mm wavelength. The band structures and optical gain spectra obtained in this work will be useful for understanding and designing $GaAs_{1-x-y}Sb_yN_x$ GaAs QW laser diodes.

Acknowledgment

We wish to acknowledge the funding support for this project from Nanyang Technological University under the Undergraduate Research Experience on Campus (URECA) programme.

References

[1] J.N. Baillargeon, K.Y. Cheng, G. E. Hofler, P. J. Pearah, and K. C. Hsieh. Appl. Phys. Lett. **60**. 2540 (1992).

[2] W. G. Bi and C. W. Tu, J. Appl. Phys. **80**, 1934 (1996).

[3] W. Shan. W. Walukiewicz, J. W. Ager III, E. E. Haller, J. F. Geisz, D. J. Friedman, J. M. Olson, and S. R. Kurtz, J. Appl. Phys. **86**. 2349 (1999).

[4] W. G. Bi and C. W. Tu, Appl. Phys. Lett. **72**, 1161 (1998).

[5] S. Tomic *et al.*, IEEE J. Sel. Top. Quantum Electron. **9**, 1228 (2003).

[6] R. T. Senger *et al.* , Appl. Phys. Lett. **83**, 5425 (2003)

[7] S. Ridene, K. Boujdaria, H. Bouchriha, and G. Fishman, Phys. Rev. B **64**, 085329 (2001).

[8] S. Tomic, E. P. O'Reilly, R. Fehse, S. J. Sweeney, A. R. Adams, A. D. Andreev, S. A. Choulis, T. J. C. Hosea, and H. Riechert, IEEE J. Select. Topics Quantum Electron. **9**, 1228 (2003)

[9] S. A. Choulis, T. J. C. Hosea, S. Tomic, M. Kamal-Saadi, A. R. Adams, E. P. O'Reilly, B. A. Weinstein, and P. J. Klar, Phys. Rev. B **66**, 165321 (2002).

[10] E. P. O'Reilly and A. Lindsay, Phys. Stat. Sol. B **216**, 131 (1999).

[11] W. Shan, W. Walukiewicz, J. W. Ager III, E. E. Haller, J. F. Geisz, D. J. Friedman, J. M. Olson, and S. R. Kurtz, Phys. Rev. Lett. **82**, 1221 (1999).

[12] J. Minch, S. H. Park, T. Keating, and S. L. Chuang, IEEE J. Quantum Electron. **35**, 771 (1999).

[13] S. T. Ng, W. J. Fan, Y. X. Dang, S. F. Yoon, Phys Rev B **72**, 115341(2005).

[14] W.J. Fan, S.F. Yoon, M.F. Li, T.C. Chong , Physica B, **328**, 264–270 , (2003).

Advanced Materials Research Vol. 31 (2008) pp 98-100
online at http: \www scientific.net
© 2008 Trans Tech Publications, Switzerland

Fabrication of photonic crystals by holographic lithography method

Jong-Bin Yeo [a], Hyun-Yong Lee [b]

Center for Functional Nano Fine Chemicals, Faculty of Applied Chemical Engineering.,

Chonnam National University, 300 Yongbong-dong, Gwangju 500-757, Korea

[a]9911093@naver.com, [b]hyleee@chonnam.ac.kr

Keywords: photonic crystals, holographic lithography, periodic structure.

Abstract. In this study, we found out the new fabrication process condition for Photonic crystals(PCs). PCs were fabricated by holographic lithography(HL), instead of commonly used electron beam lithography(EBL). HL process enable periodic large area fabrication of PCs. Also this method can easily control the pitch of periodic patterns. We set up holographic lithography system by laser and some optical components. The source of light used laser of 442 nm wavelength. Photo-resist(PR) used DMI-150 model. The viscosity of PR is diluted with propylene glycol monomethyl ether acetate(PGMEA) which is solvent for DMI-150. This experiment is holographic lithography of rotated double exposure method for PCs pattern. The method use only one beam. Result data is shown by atomic force microscope(AFM), scanning electron microscope(SEM) and 3D contour image. At the this study, we conclude conditions which we need periodic structure for PCs. It is some factor. For example, incident angle, exposure time, rotation angle, etc. And we show incident angle calculation recipe for needed size of periodic patterns. We already manufacture PCs structure design and simulation tool. Nano structure of this paper's result is applied to designed PCs patterns.

Introduction

The photonic crystals (PCs) are artificial structures, which have a periodic dielectric structure with high index contrast[1]. The simplest example of PCs is the wings of butterfly, opal (one of jewellery), etc. We will have many potential applications from PCs, such as optical mirror, filter, amplifier, transistor, resonator, switch, laser diode (LD), wave guide, sensor, improve the efficiency of light emitting diode (LED), etc. The concept of PCs can be explained with analogy to a crystal in electronics[2]. A crystal in electronics means a periodic arrangement of atoms or molecules. PCs are periodic optical structures that are designed to affect the motion of photons in a similar way that periodicity of a semiconductor crystal affects the motion of electron. The PCs occur in nature and in various forms have been studied by science for the last 20 years. As we will see, the PCs can act as a perfect mirror for light, resonator with a frequency within a sharply defined gap, and localize light mode if there are any defects in its structure[2]. PCs mechanism is confinement or high reflection or selective transmission of light. But if we are to examine some effects in PCs structure, its size should be less than about $\lambda/4n$. Fabrication process for PCs is demanded uniformity of large area and periodic fine structure. Also PCs is difficult to fabricate. Periodic structures for PCs is usually fabricated by a standard photo lithography (SPL) or electron-beam lithography (EBL) or focused ion-beam lithography (FBIL), but SPL is spatially limited due to the diffraction of the light (typically UV) so it is difficult to reduce the periodicity to submicron size. On the other hands, EBL produces submicron patterns easily but this method is so slow and expensive. Also this method get damage in substrate. Now, we have developed a efficient method that makes the fabrication of so simple and easy. For example Dip-pen, NIL, MIMIC, atom delivery, etc. My method is based on the holographic lithography (HL). HL is simple and easy method to periodic pattern generation (i.e., photonic crystals, gratings, etc.) using holography phenomenon. Holography recodes the interference patterns between object beam and reference beam on a substrate. Using this technique with He-Cd laser and some optical component but no other special equipments, we fabricate periodic structure to reduce the size to about 2 μm ~ theoretically down to the $\lambda/2$.

Experiment

Photo-resist(PR) sample were prepared by centrifuged DMI-150 model. After spin coating deposition on the silicone wafer at 3000rpm/30sec. The PR layer were about 1100 nm in thickness. And developer was tetra-methyl ammonium hydroxide (TMAH) 2.38 %. Exposure system was organized HL system, develop system was using ultra-sonication. Our HL setup, whose schematic configuration is shown in Fig. 1, consists of three parts : light source, spatial filter, and rotational sample stage. The Light source is is a He-Cd laser emitting at 442 nm in TEM 00 mode. The ND filter is organized 30, 40, 50, 60, 80, 100 % pass filter. The spatial filter, which is composed of a pinhole and a micro objective lens, serves as a beam expander as well. In the rotation sample stage, It is organized rotation stage for incident angle and rotation holder for pattern orientation. The average intensity of both recording beams was varied between 37 to 125 mW/cm^2. And we measure diffraction efficiency (η). The readout wavelength of the pattern was done with a He-Ne laser beam (λ=632.8 nm). The set of patterns was made with a writing angle between 5° and 11°. For wavelength of 442 nm, this corresponds to periods (Λ) of 2540 nm and 1158 nm, respectively. Λ is defined as

$$\Lambda = \frac{\lambda}{2\sin\theta} \tag{1}$$

Where λ is the wavelength of incident light, θ is the incident angle at boundary. And η is defined as

$$\eta(t) = I_d(t) \cdot I_0 \tag{2}$$

Where $I_d(t)$, I_0 is the intensity of the first order diffracted beam and the zero order diffracted beam, respectively.

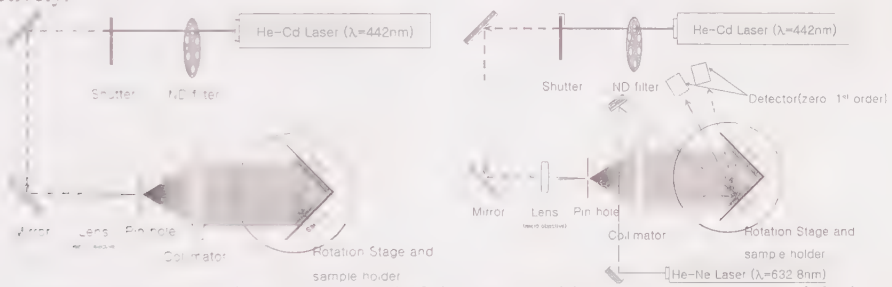

Fig. 1. Schematic diagram of the HL setup. Left is system without η measurement, right is system with η measurement.

Result and discussion

In Fig. 2, needed exposure time decrease on incident power, but maximum of diffraction efficiency is decrease. So pattern edge is blurred. Because exposure part and unexposure part has low contrast. Over exposure and high power exposure that exceeds a critical absorption quantity causes additional effects, e.g. thermal effect, against the chain breaking. And high power exposure have large tail at Gaussian beam profile.

It is shown in Fig. 3 that the kinetics of the diffraction efficiency in the samples PR. The exposure time is 20 sec (•), 45 sec (○), development time is 20 sec samples with writing angle of 5° and 11° as a function of the applied power density and exposure time. Cause to fixed developing time is mimum time of not damage for non exposure PR region. The kinetics was probed with a cw He-Ne laser at 632.8 nm. This is shown optimum condition of exposure power and time. It is 20 sec exposure time and 50 % exposure power.

In Fig. 4, (a)(b)(c) is square-lattice air-hole array pattern that was generated by applying holographic exposure twice, with a sample being rotated by 90° before the second exposure. (d)(e) is

triangle-lattice air-hole array pattern with a sample being rotated by 60° before the second exposure. And it is incident angle is (a)(b)(c) to 11°, (d)(e) to 5°.
Scanning electron microscope-image (SEM) of dot array pattern that was generated by applying holographic exposure twice, with a sample (c)(d) being rotated by 60°, (a)(b)(e) being rotated by 90° is shown in Fig. 5.

Fig. 2. The kinetics of the diffraction efficiency of amplitude reflectance gratings recorded in the PR. The power density of interfering laser beams is (●) 30 mW/cm^2, (○) 50 mW/cm^2, (▼) 60 mW/cm^2, (▽) 80 mW/cm^2, (■) 100 mW/cm^2.

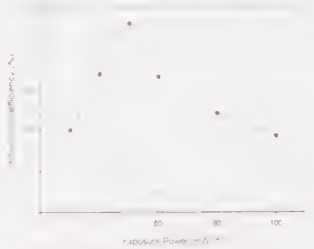

Fig. 3. The kinetics of the diffraction efficiency of relief reflectance gratings recorded in the developed PR. The power density of interfering laser beams is 30 and 100 mW/cm^2. Exposure time is 20 sec (●), 45 sec (○).

Fig. 4. AFM-image 3D profile of the surface of the 2D PCs recorded in a PR film. The image shows a surface consisting of periodic hole. (a)(b)(c) is square-lattice pattern, (d)(e) is triangle-lattice pattern.

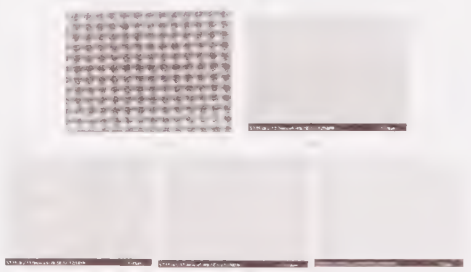

Fig. 5. SEM-image of the surface of the 2D PCs recorded on a PR film. The image shows a surface consisting of periodic dot.

Conclusion

In this article, optimum condition of pattern generation in PR DMI-150 thin film and its η have been investigated. Using a HL method based the holography phenomenon, some planar relief hole and dot 2D-PCs has been fabricated. A fabrication criterion for controlling the structure parameters of 2D-PCs, such as ratio of hole space to remained part and periods, has been already proposed[3]. This HL method appears to have potential for the fabrication of 2D-PCs. In particular, it is important that HL is easily expended to periodic pattern area exposure.
Next work, we will fabricate 2D-PCs of chalcogenide glasses for good optical properties.

References

[1] E.Yablonovitch, Phys. Rev. Lett. 58, 2029 (1987)
[2] J.D. Joannopoulos, R.D. Meade, J.N. Winn, *Photonic crystals*, p. 4 (Princeton University Press, 1995)
[3] H.Y.Lee, H.Makino, T.Yao, and A.Tanaka, Appl. Phys. Lett. 81, 4502 (2002)

Advanced Materials Research Vol. 31 (2008) pp 101-104
online at http://www.scientific.net
© 2008 Trans Tech Publications, Switzerland

Optical and Structural Properties of Multi Deposition Film Derived SiO_2-TiO_2 Systems By Sol-Gel Process

M.Z.A.Malek[a], M.T.Zainuddin[b], A. M. Abdullah[c] and A. Isnin[d]

Advanced Materials Research Centre, SIRIM Berhad, Lot 34, Jalan Hi-Tech 2/3, Kulim Hi-Tech Park,09000 Kulim, Kedah, Malaysia.

[a]zahid@sirim.my, [b]tamizi@sirim.my, [c]makarimi@sirim.my, [d]aishah_isnin@sirim.my

Keywords: SiO_2-TiO_2 systems, thick film, multi spin coating process, Si-O stretching vibrations, nanoporous.

Abstract

SiO_2-TiO_2 systems were extensively investigated in sol-gel process to fabricate passive optical planar waveguides, channel waveguides, interference filters and weather resistant optical memory discs. A high quality, crack free optical thick layer and low processing cost are key success factor for optical applications. Two formulated SiO_2-TiO_2 systems with 1% and 10% TiO_2 were deposited on 20mm x 20mm Si-wafer using multi-spin coating process was investigated on refractive index (n), build-up layer until crack appeared on film. The structure analysis of multi spin was investigated using FTIR. The value of refractive index (n) and thickness of thin films (d) were taken every deposited layer using spectroscopic reflectance and surface morphology of crack thick film by FESEM. SiO_2-TiO_2 thin film appeared peak ~950cm^{-1} associated with the Si-O stretching vibrations of Si-OH and Si-O-Ti groups by multi spin coating processes. SiO_2-TiO_2 system with 10% TiO_2 in siloxane structure was found capable on building thick layer up to 2.4 μm at 17 time cycles spins and heat treatments at 680 °C. The value of n was reduced with increasing of number of cycles and believes to form nanoporous zones between interfacial layers during hydrolysis and condensation process of each layer by multi spin coating process.

Introduction

Sol-gel derived coating SiO_2-TiO_2 system were extensively investigated use in many applications such as active or passive optical planar waveguides, channel waveguides, interference filters, weather resistant optical memory discs and bone-bonding interfaces for load-bearing implants [1]. Many researchers agreed that sol-gel methods have several advantages such as good homogeneity, ease of composition control, low processing temperature, and ability to fabricate large area coatings at low equipment cost [2]. Sol-gel processing also enables good control of composition and optical properties of the final materials. Hence, sol-gel process has been selected as a good process to control refractive index and thickness in optical thin film for optical applications [2].

One of application in optical thin film materials is to develop planar optical waveguide. There are three important points to develop materials for planar optical waveguide by sol-gel process; a) build-up thick layer [3] b) control refractive index of the materials [4] and c) allows incorporate large number of organic and inorganic additive during the glass formation [5]. Łukowiak et al. worked on silica-titania sol-gel thin film by dip coating process to form crack-free thin film at temperature 500°C [5]. Wenxiu Que ***et al.*** reported that thickness of crack free purely inorganic thin film and silica-titania thin film system can be obtained up to 0.5 μm at temperature 500°C or above [3]. Optical thick layer can be build-up in sol-gel process by multi spin coating technique and multi heat treatment process. Very little has been published so far about multi deposition

spin and multi heat treatment silica–titania waveguides [cited in Maia Seco *et al.* 2000]
Sol-gel process offers abilities to control of composition and optical properties of the final material. For example, refractive index may be controlled by the composition of the starting solutions: titanium alkoxides or other suitable precursors to tailor the refractive index to the chosen value [3]. Refractive index of materials use in core and cladding can influence properties of loss propagation in planar optical waveguide. In this paper, SiO_2-TiO_2 thin film system prepared by multi spin and multi heat treatment sol-gel process was investigated on stress fracture and refractive index to build thicker optic layer. Nevertheless, some assumption of mechanism interfaces layer in sol-gel process also reveal in this paper.

Experimental Work

2 different sol solutions of silica-titania compositions have been prepared from precursors of tetraethoxysilane(TEOS, 98% Fluka) and tetrabutoxytitanate(TTBu, 99% Across). Silica sol solution was prepared by hydrolyzed tetraethoxysilane with deionised water with presence of hydrochoric acid(HCl, 99% Aldrich) and ethanol(EtOH, 98% Fluka) as reaction catalyst and solvent respectively. Molar ratio for the reaction TEOS:EtOH:H_2O{HCl,pH 2.0} is 1:6:4. Titania sol solution was firstly chelated with acetylacetone(acac, 99% Fluka) in molar ratio TTBu:acac 1:4 then reacted with deionized water with molar ratio of TTBu:H_2O{HCl,pH 2} 1:2. Both sol solutions were mix together with composition of 1% and 10%titania to silica then the mixers were stirred for 24 hours. Mix solutions were added with different volumes of EtOH with weight ratio sol:EtOH of 1:2, 1:3 and 1:4. Mixers were aged for 18 hours before spin coating applied. Spin coating has been performed on oxidized Si wafer at 2500rpm for 30s in 10K class cleanroom.
Changes in chemical and structural properties for the coating films were measured in transmission mode using Fourier Transform Infra Red spectrometer (Nicolet Magna 150IR). Refractive index and film thickness for the coating films were measured using spectroscopic reflectance (FILMETRICS F50). Surface morphology was observed by field emission scanning electron microscope (LEOS 1512)

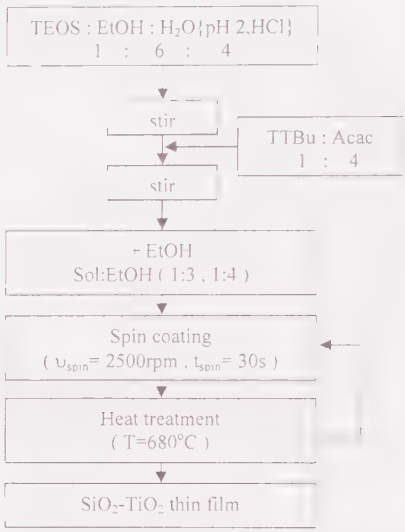

Preparation of SiO_2-TiO_2 thin film by spin coating process

Result and Discussion

Figure 1(a) and (b) shows evolution of thickness and refractive index of 99%SiO_2-1%TiO_2 and 90%SiO_2-10%TiO_2 thin films with number of deposited film and heat treatment applied. The thickness of every layer was increased occasionally in nano scale between 50-100nm for every layer deposition for both compositions shows that increment in deposited layers depend on the spin–coating technique as well as sol viscosity. On the total number of layer deposition, composition of 99%SiO_2-1%TiO_2 shows film development up 13 layers film deposited with total film thickness of 2.048μm before crack appeared on the film. On the other hand, the 90%SiO_2-10%TiO_2 composition shows capability on developing thicker total films of

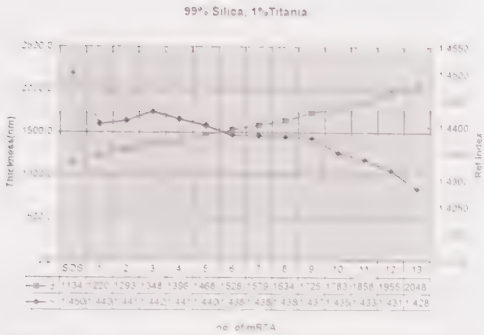

Figure 1(a): spectroscopic reflectance spectra of multi deposition of 99%SiO_2:1%TiO_2 thin film composition

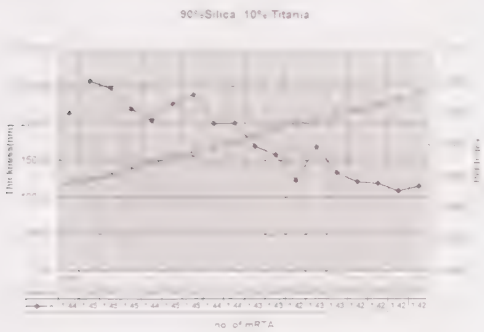

Figure 1(b):spectroscopic reflectance spectra of multi deposition of 90%SiO_2:10%TiO_2 thin film composition

2.401μm with 17 layers film deposited. With increasing number of layers deposition, the final refractive index values decrease for both compositions. Each value represents the average of 49 points on the 2.5x2.5cm^2 films. In order to understand the anomalous sintering behavior of film density as a function of number of layer deposited, structural characterization of films by using FTIR has been carried out.

Important peaks for sol-gel study of silica based materials such as siloxane(Si-O-Si) and hydroxyl(-O-H) groups were presence for both film materials. The absorption bands at 1100cm^{-1} and 3300cm^{-1} correspond to the siloxane(Si-O-Si) asymmetric stretching mode and hydroxyl (-O-H) stretching vibration mode, respectively[6]. It was observed that intensity for the peak of siloxane(Si-O-Si) groups shows that the peak already existed from the first layer deposition for both composition and still remain unchanged after multiple layers deposition applied. Observation on hydroxyl(-O-H) groups show broad peak appear for both films at the first layer deposition but the peaks becoming smaller after multiple layer deposited. The broad peak indicates that presence of high content of –OH group in the film even after the film experience heat treatment up to 680°C. High content of hydroxyl(-OH) groups in the film at this stage was believed to contribute by excess water and residual ethanol, EtOH from the ester condensation of sol gel reaction[7]. Apart from that are the silanol groups from the incomplete condensation from the previous precursors to form inorganic network. Smaller peak after multiple layer deposition indicates that vibration of –OH groups has been limited at certain wavenumber.

Figure 2(a):FTIR spectra of 99%SiO_2:1%TiO_2 thin film with single layer and multi layers deposition

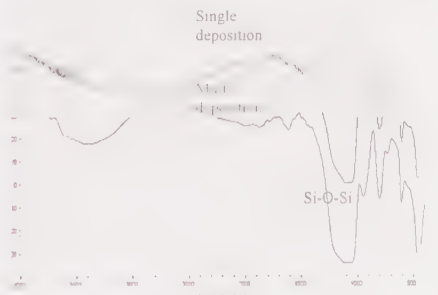

Figure 2(b):FTIR spectra of 90%SiO_2:10%TiO_2 thin film with single layer and multi layers deposition

This lead to our understanding that the –OH groups were locked as isolated in the film matrix. From this perspective, we suggested that the –OH on the film surface lead to the formation of isolated –OH interlayer after layer re-deposition. This interlayer can best explained the anomalous in multiple refractive index measurement. The –OH interlayer contributed to the formation of nano-porous phase in the film matrix which affected the speed of light on the refractive index measurement.

We believed that presence of higher content of TiO_2 in film matrix contribute to materials capabilities on development of thicker film but on the other hand multi deposition of sol gel materials introduce high -OH content on the surface which entrapped during re-spin coating and heat treatment and presence as interlayer isolated pores.

Figure 3(a) SEM micrograph of crack free $90\%SiO_2$-$10\%TiO_2$ thin film

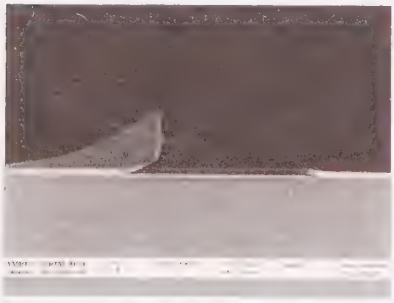

Figure 3(b) SEM micrograph shows crack originated within film materials for composition of $90\%SiO_2$-$10\%TiO_2$ thin film

Comprehensive view of the deposited layers was recorded using field emission scanning electron microscope, FESEM LEOS 1525. Figure(a) and (b) show SEM micrographs of multi deposited films of $10\%TiO_2$:$90\%SiO_2$ before and after cracking. One can observe that the cracking was originated within the film itself and this confirm our suggestion on the formation of nano-porosity in between deposited layers. We believed that this nano-porous formation in between the layers can't withstand the stress developed from film shrinkage during thermal treatment, thus promoted for film cracking.

Conclusion

Film with high titania content has the capabilities on development of thicker films. FTIR spectroscopy has shown that isolation of –OH groups occur in the films matrix with multiple layers deposition which lead to formation of nano-porous phase at interlayers.

References

[1] Xavier Orignac, H. Cristina Vasconcelos, Rui M. Almeida, Journal of Non-Crystalline Solids 217 (1997) 155-161

[2] Zhai Jiweia, Zhang Liangying, Yao Xia, S.N.B. Hodgson, Surface and Coatings Technology 138(2001)135-140

[3] Wenxiu Que*, Y. Zhou, Y.L. Lam, Y.C. Chan, C.H. Kam, Thin Solid Films 358 (2000) 16-21

[4] R. Reidfeld, Optic Materials 16 (2001) 1-7

[5] Anna Łukowiak a, Rafal Dylewicz, Sergiusz Patela, Wieslaw Stre, Krzysztof Maruszewski, article in press in Optical Materials (2005).

[6] E. Young-Joo, k.Duk-Jun, B. Byeong-Soo, "Journal of Sol-Gel Science and Technology",13,409-413(1998)

[7] J. Brinker and G.W.Scherer, "SOL-GEL SCIENCE: The Physics and Chemistry of Sol-Gel Processing" Academic Press,Inc.(1990)

Advanced Materials Research Vol. 31 (2008) pp 105-107
online at http://www.scientific.net
© 2008 Trans Tech Publications, Switzerland

Investigation of Intersubband Transition in GaAs/AlGaAs Quantum Well Infrared Photodetectors

D. S. Li , W. J. Fan[a], Y. X. Dang, B. S. Ma, D.H. Zhang, and S.F. Yoon

School of Electrical and Electronic Engineering, Nanyang Technological University, Singapore 639798, Singapore

[a] ewjfan@ntu.edu.sg

Keywords eight-band k·p model, GaAs/AlGaAs, quantum well infrared photodetectors

Abstract. We report the design, characterization and fabrication of GaAs/AlGaAs quantum well infrared photodetectors (QWIPs) to achieve intersubband transitions at expected long wavelengths. With eight-band k·p model, we calculated the E2-E1 transition energies of GaAs/$Al_{0.25}Ga_{0.75}As$ QWs with the different well widths. According to the calculation, we designed a QWIP with the estimated detection wavelength around 9 μm. The actual device structure parameters, such as well width and Al composition, were confirmed by the XRD measurements. The absorption peak at 9.46 μm and the peak responsivity at 8.7 μm are obtained, which are very close to the simulation results.

Introduction

Due to the large tunability of transition wavelength, and the mature technology of material growth and device fabrication[2], GaAs/AlGaAs quantum-well infrared photodetector (QWIP) has been extensively studied and used in the atmospheric window region of 8-14 μm for night vision system[1]. Comparing with thermal detectors[3], another distinguishing feature of QW infrared detectors is that they, as a result of the use of intersubband processes, can be implemented in chemically stable wideband-gap materials which can easily realize the uniform low-cost large-area focal-plane array applications.

QWIPs operate by photo-excitation of electrons between ground (E1) and the first excited state (E2) subbands of multi-quantum wells (MQWs) which are artificially fabricated by placing thin layers of two different, high-bandgap semiconductor materials alternately. The bandgap discontinuity of two materials creates quantized subbands in the potential wells. The structure parameters are designed so that the photo-excited carriers can escape from the potential wells and be collected as photocurrent. To adjust the detected peak wavelength in the range of 8-14 μm, the well width and the barrier composition must be changed to achieve a suitable potential profile.

QWIP design

The eight-band k·p mode combined with an envelope function approximation was utilized to calculate and analyze the subband positions in different QW structures. In this case, the strains between GaAs wells and AlGaAs barriers can be ignored, and the conduction band discontinuity was assumed as 65%. The energy subband distributions of the n-type GaAs/ $Al_{0.25}Ga_{0.75}As$ quantum wells were calculated by varying well widths. Figure.1 (a) shows the calculated energy levels as a function of the quantum well widths. In the figure, there are two bound states (E1and E2) only for well width beyond 4.5 nm, and the horizontal line indicates the $Al_{0.25}Ga_{0.75}As$ barrier height (1750 meV), and the arrows correspond to transitions of 9.2 μm and 8.4 μm for 4 nm and 5 nm well widths, respectively. When the external electrical field applied, the energy potential will tilt, and the carriers excited by the appropriate incident photons from ground states (E1) to the first excited states (E2) will be swept into the continuum state by the electrical field to form the photocurrent. Figure.1 (b) shows the calculated absorption coefficient curve peaks at 8.6 μm, for the 5 nm well width QWs. Through the analysis on simulated results, we can choose GaAs/ $Al_{0.25}Ga_{0.75}As$ QW

structure of 5 nm well and 40 nm barrier width as the investigated one, for the estimated response peak around 9 μm.

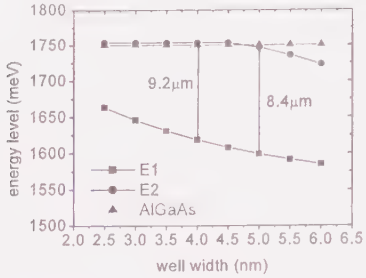

Figure. 1(a) Energy levels in $GaAs/Al_{0.25}Ga_{0.75}As$ QWs as the function of well widths

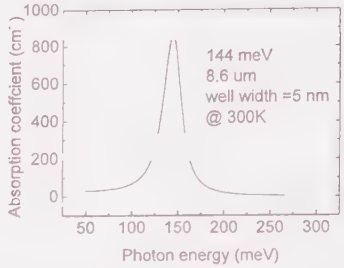

Figure.1(b) Absorption coefficient spectra of $GaAs/Al_{0.25}Ga_{0.75}As$ QWs

Fabrication , characterization and discussions

The GaAs/AlGaAs QW structure was grown by molecular beam epitaxy (MBE) on GaAs (100) semi-insulating substrate. Different from previous work, 45 periods QWs were grown to achieve high absorption[4,5] .The QWs were sandwiched by 1 μm top and 1 μm bottom Si-doped ($2x10^{18}$ cm^{-3}) GaAs contact layers. Each period consists of a 40 nm $Al_{0.25}Ga_{0.75}As$ barrier layer and a 5 nm Si-doped ($8x10^{17}$ cm^{-3}) GaAs well layer according to the above design. High-resolution x-ray diffraction (XRD) analysis was performed at the Philips HRXRD system to confirm structure parameters. Figure.2 (a) shows a good agreement between the experiment result and the simulated one of GaAs,5.1 nm/$Al_{0.25}Ga_{0.75}As$,41 nm, which comes near the designed parameters.

The intersubband absorption spectra was achieved at room temperature with a Fourier-transform infrared spectrometer using a multiple-reflection waveguide geometry fabricated by polishing two end facets at a 45° angle. Figure. 2(b) shows the absorption spectra of the above QWs, peaking around 9.46 μm at the room temperature, showing higher absorption signal-noise ratio than that of less period QWs[5].

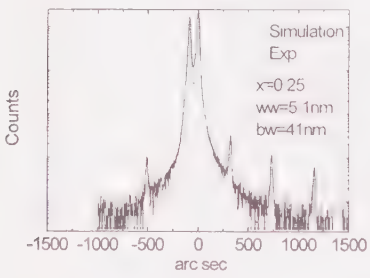

Figure.2(a) HRXRD pattern of the measured and the matched simulated pattern

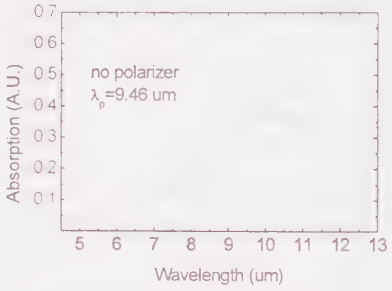

Figure.2(b) Intersurband absorption curve measured with FTIR at 300 K

To fabricate QWIP devices, the sample was subjected to pattern transferring and chemical etching process, forming the round mesas consisting of the top layer and all the QWs. The unetched doped top layer and partly etched buffer layer (1/3 thinness of this layer left after etching, beyond the mesa area) was covered by NiGeAuNiAu contact metal layers to form the electrodes for the devices. After the lift-off and annealing process, the polished 45° angle was introduced to the sample edge to allow a polarization component of the incident light along the growth direction.

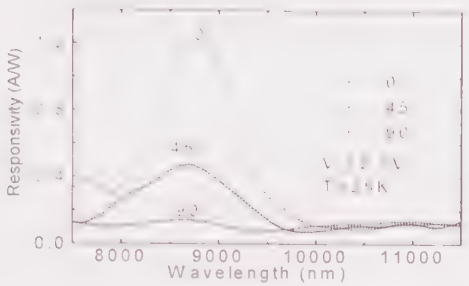

Figure.3 Photocurrent-responsivity characteristics at 25K with the polarizer of 0°, 45° and 90°

With the assembled devices under measurement, we obtained the sample's dark current and photo current spectra under various temperature and bias voltage. In the Figure 3, we observed the response curve peaking at 8.7 μm. near the calculated result, and found the peak responsitivity close to the ones of 50 periods or less QWs[6], which was shown by H.C. Liu et al[5]. When a polarizer was put in the IR light path and its degree was changed from 0° to 45°, and 90°, we found the peak at 8.7 μm gradually disappeared. In the light of selection rule [7], the disappearance of the peak under 90° polarization testifies that the response peak comes from intersubband transitions.

There is a wavelength deviation between the response peak 8.7 μm and absorption peak 9.4 μm, which maybe comes from the availability of low temperature and electrical field during response measurement. With the consideration of the parameter deviation in material growth, the possible intermixing in RTP process[9] and Stark effect[10], the theoretical predictions 8.4 μm matches well experimental response peak 8.7 μm, which testifies the validity of the eight-band model for simulation.

Conclusion

We applied the eight-band model to design the GaAs/AlGaAs QW structure for the predicted response. The samples were systemically characterized and investigated, and showed the evidence of desirable QW structures and the clear absorption peak agreeing well with the theoretical predictions. After the fabrication and response measurement, we observed the clear response peak near the calculated one.

In conclusion, this work demonstrates the validity of eight-band k·p model to determine the position of the states involved in the intersubband transitions in the QW structures and further to design QWIPs according to peak prediction.

References

[1] B. F. Levine, *J.Appl. Phys.* 74, R1 (1993).

[2] A.Krier : *Mid-infrared Semiconductor Optoelectronics*, (Springer, NewYork, 2006),p. 429.

[3] A. Rogalski. *J.Appl. Phys.*, 93, 4355 (2003).

[4] K.K.Choi : *The physics of quantum well infrared photodectors*, (World Scientific, Singapore, 1997), p. 312-313.

[5] A. G. Steele, H. C. Liu,et al., *J. Appl. Phys.* 72,1062 (1992).

[6] B. F. Levine, A. Zussman, S. D. Gunapala,, and W. S. Hobson,*J.Appl.Phys.*72, 4429 (1992).

[7] H. C. Liu, M. Buchanan, and Z. R. Wasilewski, *Applied Physics Letters* 72, 1682 (1998).

[8] Rui Q. Yang, J. M. Xu, and Mark Sweeny, *Phys. Rev. B* 50, 7474 (1994)

[9] R. K. Kupka and Y. Chen, *Applied Physics Letters.* 67,1612 (1995).

[10] Vincenzo Lordi, Homan B. *Applied Physics Letters.* 85.902 (2004).

Advanced Materials Research Vol. 31 (2008) pp 108-110
online at http://www.scientific.net
© 2008 Trans Tech Publications, Switzerland

Growth of GaN Nano-Column on Si (111) Substrate Using Au+Ga Alloy Seeding by pulsed flow method using MOCVD

Jae-Chul Song[1,a], Dong-Hun Kang[1,b], Seon-Ho Lee[1,c], Eun-Su Jang[1,d], Dong-Wook Kim[1,e], Santhakumar Kannappan[1,f] and Cheul-Ro Lee[1,g]

[1] School of Advanced Materials Engineering, Engineering College, Chonbuk National University, Chonju 664-14, Chonbuk, South Korea

[a]for-miracle@hanmail.net, [b]liebesky99@nate.com, [c]yamato-iki@hanmail.net, [d]jjston@nate.com, [e]kdw612@hanmail.net, [f]k.santhakumar@gmail.com, [g]crlee7@chonbuk.ac.kr

Keywords: GaN, MOCVD, pulse flow, nanocolumn, Au coating, Silicon substrate

Abstract. Vertical GaN nano-columns arrays were grown on Au-coated silicon (111) substrate by Au+Ga alloy seeding method and pulsed flow of Gallium and ammonia using metalorganic chemical vapor deposition (MOCVD). A gold thin film was deposited on Si using an ion coating system. The Au coated Si substrate was annealed at 800 °C under hydrogen ambient for 5 min. The pre-deposition of gallium and nitrogen was performed for 60 sec to form Au+Ga and nitrogen solid solution, which acts as the initial nucleation islands. Then Gallium and ammonia were let in pulse method. Scanning electron microscopy (SEM) image reveals a vertical growth and cylindrical in shape GaN nano-column. From the sharp PL peak intensity it is clearly seen that the dislocation density is reduced considerably and the optical quality of the nano-column is improved.

Introduction

GaN and its related alloys are generally useful to optical devices such as light emitting diodes and photodetectors in blue and ultraviolet regions because of their wide direct band gap and high electrical and thermal conductivity. Many nanotechnologies have been implemented to improve the efficiency GaN layers were studied in order to create building blocks of various sizes and shapes. GaN nano-columns are useful to improve the performance of low-dimensional high power light sources because it is anticipated that high optical gains and low lasing thresholds will be achievable when the nano-column diameter is smaller than the excition radius [1]. Recently, GaN nano-column preparation is typically based on the vapor-liquid-solid (VLS) growth mechanism and involves the use of catalysts such as Au, Ni, Fe, or In [2-4]. The catalyst creates a highly selective growth environment with growth occurring only at the catalyst location. GaN nano-columns using metallic catalyst can be integrated on silicon substrates for use as III-nitride nano-column emitters and as silicon based nano photo-detectors for data communications by photons. The major challenge faced by the GaN nano-column grown by metalorganic chemical vapor deposition (MOCVD) is that the directions of nano-columns are disordered. In order to grow GaN nano-column in unidirectional, we have adapted two step methods where Au droplets are annealed prior to nano-column growth to obtain uniform distribution and flow of the precursors into the chamber was by pulse method to obtain unidirectional growth. In this paper, we have studied the growth of GaN nano-column using pulse flow method by MOCVD technique.

Experimental procedure

GaN nano-column structures were grown on gold (Au) coated Si(111) oriented substrates by MOCVD using a horizontal quartz reactor. Prior to nano-column growth, the Si substrate surface was treated using a conventional cleaning procedure and a gold thin film was deposited using an ion sputtering system. The Au coated Si substrate surface was cleaned in acetone and isopropyl alcohol to remove any contamination on the thin film surface. The Au coated Si substrate was annealed at 800 °C under hydrogen ambient for 5 min. The group III and group V precursors were introduced

alternately in the sequence: TMGa, 1 sccm, 20 s; NH_3, 1 slm, 60 s in a pulse method for three cycles to form the seed for the nano-column growth. Further, GaN growth was began at 1040 °C for 30 min with an ambient pressure of 150 torr. The surface morphology and structural characteristic were analyzed using scanning electron microscopy (SEM) and field emission SEM (FE-SEM).

Results and discussion

Fig. 1. FE-SEM images of Au droplets for two different Au deposition thicknesses (a) 10 nm and (b) 15 nm after annealing at 800 °C for 5 min.

The first step for the growth GaN nano-column is the condensation and adhesion of Au atoms onto the surface of the Si(111) substrate to form nano sized catalytic islands.

Fig. 1 shows the SEM images of the Au/Si template after annealing at 800 °C for 5 min for the two different Au deposition thicknesses 10 nm and 15 nm. Fig. 1(a) shows a uniform Au cluster distribution on the silicon surface of size ~50 nm. Whereas, for 15 nm gold thickness, the clusters size varied from 10 nm ~60 nm unevenly distributed.

The critical feature of this mechanism is the presence of intermediates formed by the precursors and nano metallic islands, which act as catalysts between the vapor feed and solid growth at an elevated temperature and Au thin film thickness in the growth process.

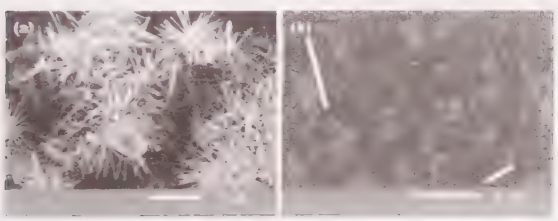

Fig. 2. SEM images of GaN nano-columns (a) without Au annealing and (b) with Au annealing.

Fig. 2(a) shows the SEM image of nano-columns without using Au annealing. The bundles of nano-columns were grown at the few regions where Au catalysts were agglomerated. GaN nano-columns could be grown all over the region using Au annealing to make droplet as shown in Fig. 2(b). However, the directions of nano-columns were disorders [5]. The direction of nano-column is very important to use for devices.

Fig. 3. FE-SEM images of vertical nano-columns using pulsed flow MOCVD.

In order to improve the unidirectional growth, pulse flow MOCVD was used to make the GaN seeds/Au droplet. By using this method, we can grow the vertical GaN nano-columns. Figure 3 shows the vertical nano-column grown by pulsed MOCVD method. During the pulsed growth mode the group III and group V precursors were introduced alternately in the sequence: TMGa, 1 sccm,

20 s; NH_3, 1 slm, 60 s. The grown GaN nano-columns were observed to be hexagonal symmetry of the sidewall facets as seen in Fig 3. High resolution FE-SEM image clearly shows the perfect hexagonal symmetry. The results suggest that a highly oriented GaN nano-column could be grown by pulse MOCVD method.

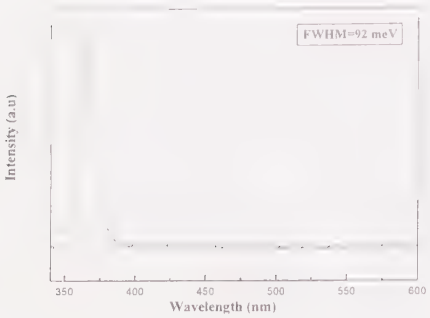

Fig. 4. PL spectra of the GaN nano-column grown on Si.

Fig. 4 shows the room temperature PL spectrum of the GaN nano-column. A strong band-edge emission is observed at 365 nm. The FWHM of the PL spectra at 365.7 nm peak was 92 meV which indicates the grown nano-columns are dislocation free with good crystalline quality. The data of PL intensity and FWHM at room temperature indicate a high optical quality of the GaN nano-column. This implies that the grown GaN nano-columns have low dislocation density with high optical emission which is useful for GaN based optoelectronic devices.

Conclusions

In summary, a novel technique was used to grow GaN nano-columns on Au-coated Si by pulse flow MOCVD method. The Au coated Si substrate was annealed prior to GaN growth to obtain nano-columns in a vertical direction. From the SEM image, GaN nano-columns grown are vertical in direction and hexagonal in shape. The uniform shape and smoothness of the nano-column clearly indicates that it could be useful for device application.

References

[1] J.R. Kim, H.M. So, J.W. Park, J.J. Kim, J. Kim, C.J. Lee and S.C. Lyu: Appl. Phys. Lett. Vol.80 (2002), p. 3548.

[2] M. Yoshizawa, A. Kikuchi, N. Fujita, K. Kushi, H. Sasamoto and K. Kishino: J.Cryst.Growth. Vol.189/190 (1998), p. 138.

[3] C.N.R. Rao, F.L. Deepak, G. Gundiah and A. Govindaraj: Progress in Solid State Chemistry Vol. 31 (2003), p. 5.

[4] F.Qian, Y. Li, S. Gradecak, D. Wang, C. J. Barrelet and C.M. Lieber: Nano Lett. Vol. 4 (2004), p. 1975.

[5] B.Y. Shim, E. Ko, J.C. Song, D.H. Kang, D.W. Kim, I.H. Lee, K.Santhakumar and C.R. Lee: Jpn. J. Appl. Phys. Vol. 46 (2007), p. 2571.

Advanced Materials Research Vol. 31 (2008) pp 111-113
online at http://www.scientific.net
© 2008 Trans Tech Publications, Switzerland

Raman study of epitaxial lateral overgrowth of GaN on patterned sapphire substrate

D.H. Kang[a], J.C. Song[b], H. Song[c], D.W. Kim[d], I.H. Lee[e],
K. Santhakumar[f] and C.R. LEE[e]

School of Advanced Materials Engineering, Engineering College, Chonbuk National University, Chonju 664-14, Chonbuk 561-756, South Korea

[a]hepesky99@nate.com, [b]for-miracle@hanmail.net, [c]honeyam@nate.com, [d]kdw612@hanmail.net, [e]ihlee@chonbuk.ac.kr, [f]k.santhakumar@gmail.com, [e]crlee7@chonbuk.ac.kr

Keywords: GaN, Patterned sapphire substrate, MOCVD, threading dislocation, lateral growth

Abstract. Structural and optical properties of gallium nitride (GaN) epilayers grown on lens shape patterned sapphire substrate (PSS) using metalorganic chemical vapor deposition (MOCVD) for various growth times were evaluated. From Raman spectra, a blue shift and reduction in the FWHM of Raman modes of GaN grown on PSS were observed when compared to GaN grown on unpatterend sapphire substrate (UPSS). From the DCXRD spectra, full width at half maximum (FWHM) value was decreased with increasing growth time. FWHM of the sample grown at 80 min was 473.5 arc sec. This indicates that there is an improvement in crystalline quality of the GaN grown on PSS as the growth time increases. From photoluminescence (PL) spectra, an increase in band edge emission intensity and a decrease in defect related yellow luminescence were observed for GaN on PSS as the growth time increased.

Introduction

III-nitride compound semiconductors like GaN and its ternary alloys have a wide and direct bandgap ranging from 0.7 eV for InN to 6.2 eV for AlN [1]. They are currently most promising materials for optoelectronic devices like light emitting diodes (LEDs) and laser diodes (LDs) operating in the red to ultraviolet wavelength region [2, 3]. These devices have been extensively used in various applications such as outdoor full-color display, back light unit in liquid crystal display and solid-state lightning and show a greater potential to replace fluorescent lamps [4]. A large lattice mismatch and thermal expansion coefficient difference between GaN and sapphire substrate lead to many defects such as threading dislocation (TD) in the epitaxial GaN film. In order to reduce the TD density, lateral overgrowth techniques such as epitaxial lateral overgrowth (ELOG) or pendeoepitaxy (PE) are introduced [5]. Recently, GaN layers grown on the patterned sapphire substrate (PSS) were successfully developed to fabricate high quality optical devices with lower TD density [6]. Improved emission efficiency is also one of the advantages of using PSS techniques. In this work, we grew high quality GaN epilayers using a lens shape PSS. The growth behaviors, structural and optical characters of GaN grown on PSS have been discussed.

Experimental process

The GaN epilayers (0002) were deposited on c-plane patterned sapphire substrate using low pressure metal organic chemical vapor deposition (MOCVD) in a horizontal quartz reactor. First, a 150 nm thick GaN buffer layer was deposited on PSS at 560 °C for 2 min to get a minimum surface roughness and dislocation density. Subsequently, GaN epilayers were deposited at 1040 °C under an ambient pressure 100 Torr. During the growth of the GaN epilayers, the flow rate of TMGa and NH_3 were 3.0 standard cubic centimeter per minute (sccm) and 1.5 standard liters per minute (slm),

respectively. Samples were prepared for various growth times from 10 to 80 min. Structural and optical characterizations were investigated by using double crystal X-ray diffraction (DCXRD), Raman spectroscopy and Photoluminescence (PL).

Results and discussions

A Schematic diagram of GaN on PSS is shown in Fig. 1. The SEM micrograph of the PSS after ICP dry etching is also given in Fig. 1. The lens height and diameter of the patterned sapphire are 1.5 and 5.8 μm, respectively. The distance between each lens is 3.7 μm.

Fig.1 Schematic diagram of GaN on PSS. The SEM micrograph shows the patterned sapphire substrate after dry etching

The structural characteristics of GaN on PSS samples with respect to growth time were analyzed by the DCXRD spectra (ω-scan) as shown in Fig. 2. The GaN (0002) peak is observed clearly at 17.3° which indicates the GaN is highly oriented along c-axis and has single crystalline character. The FWHM value of DCXRD decreased and the peak height of DCXRD increased as time increased. This indicates that the crystalline quality of the PSS GaN improves as the growth time increased with less TD density. Figure 3 shows DCXRD spectrum of GaN grown on unpatterned sapphire and patterned sapphire substrates. The FWHM of the (0002) peak is 534.41 and 473.48 arcsec, respectively. The high XRD peak intensity of the GaN epilayers using the patterned substrate with a low FWHM indicates an improved quality of the GaN when compared to the layer grown on unpatterned substrate. The narrow XRD peak of the GaN grown on PSS also suggests that a reduction of the TD density compared to the GaN grown on unpatterned substrate.

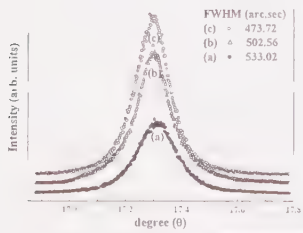

Fig. 2 DCXRD spectra of GaN on PSS for growth times (a) 10 min, (b) 40 min and (c) 80 min.

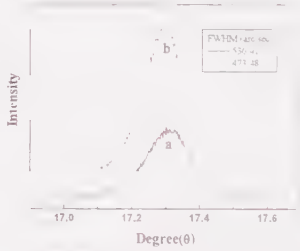

Fig. 3 DCXRD spectra of GaN (0002) grown on (a) unpatterned sapphire substrate and (b) patterned sapphire substrate.

Raman scattering provides information on vibrational states of GaN, which are sensitive to microscopic disorder. The crystalline quality can be judged from the peak shapes. Figure 4 shows Raman spectra of GaN grown on UPSS and PSS, recorded at room temperature. Lorentzian line shape was fitted to the Raman spectra and the parameters like peak position and FWHM have been obtained. Two Raman modes $E2^{(high)}$ and A1 (LO) were observed at the frequencies 570.9 and 737.7 cm^{-1}, respectively for GaN grown on PSS as seen in Fig. 4 (b). Two Raman modes $E2^{(high)}$ and A1 (LO) were observed at the frequencies 569.5 and 736.1 cm^{-1}, respectively for GaN grown on UPSS as seen in Fig. 4 (a). A blueshift is observed for E2 and A1 (LO) phonon mode from 569.59 cm^{-1} to 570.9 and 736.1 to 737.7 cm^{-1} respectively for GaN on PSS compared to GaN on UPSS. FWHM of $E2^{(high)}$ and A1 (LO) Raman mode for GaN grown on PSS are 3.93 cm^{-1} and 11.6 cm^{-1} which is relatively less compared to FWHM values of GaN grown on UPSS. The blue shift of Raman modes

peak position and reduction in FWHM clearly indicates that there is a strain relaxation during the growth in the trenchs as compared to GaN on UPSS.

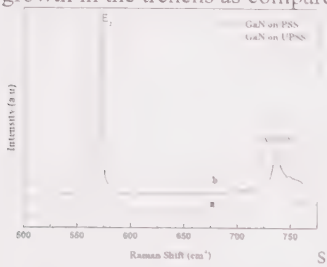

Fig. 4 Raman spectra of GaN grown on (a) unpatterned sapphire substrate and (b) patterned sapphire substrate

Fig. 5 shows the PL spectra of GaN epilayers grown on PSS at room temperature for various growth times. PL spectra of the GaN on PSS are dominated by band-edge emission at 365 nm. It is observed that the spectra exhibit significant increases in peak intensity and decreases in FWHM with the growth time. Such an enhancement in the PL intensity is due to the internal reflection on the lens surface and the decrease of the TD-induced non-radiative recombination centers. A defect related luminescence peak which observed at around 440 nm is not seen in the sample grown at 80 min. This result indicates that crystalline quality is improved and the TD density is reduced with increasing growth time.

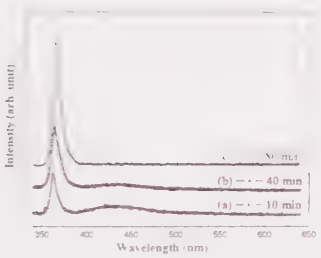

Fig. 5 PL spectra of GaN layer on PSS for growth times (a) 10 min, (b) 40 min and (c) 80 min.

Summary

In summary, GaN epilayers were grown on lens shaped patterned sapphire substrate for various growth times. DCXRD results suggest that high quality crystalline GaN is achieved with less threading dislocations. From Raman spectra, reduction in FWHM and blueshift of Raman modes of the GaN layers grown on PSS compared to GaN grown on UPSS implies enhancement in the crystalline quality. From the PL spectra, peak intensity has increased enormously. Such an enhancement in the peak intensity may be attributed to reduction in TD. Hence, by using lens shaped PSS for GaN epilayer growth after a growth time 80 min, threading dislocation density was reduced and optical properties were improved

References

[1] S.J. Pearton, F. Ren, A.P. Zhang, K.P. Lee, Mater. Sci. Eng. R 30 (2000) 55.
[2] E.F. Schubert, Light-Emitting Diodes, Cambridge University Press, New York (2003).
[3] A. Zukauskas, M.S. Shur and R. Caska, Introduction to Solid-State Lighting, Wiley, New York (2002).
[4] S. Nakamura, M. Senoh, S. Nagahama, N. Iwasa, T. Matsushita, T. Mukai, Appl. Phys. Lett. 76 (2000) 22.
[5] B. Beaumont, P. Vennegues, P. Gibart, Phys. Stat. Sol b 227 (2001) 1.
[6] K. Tadatomo, H. Okinawa, Y. Ohuchi, T. Tsunekawa, Y. Imada, M. Kato, T. Taguchi, Jpn. J. Appl. Phys. 40 (2001) L583.

Advanced Materials Research Vol. 31 (2008) pp 114-116
online at http://www.scientific.net
© 2008 Trans Tech Publications, Switzerland

Mn, Cu Doping and Optical Properties of Highly Crystalline Ultralong ZnS Nanowires

N. D. Chien[1,a], H. V. Chung[1,b], P. T. Huy[2,c], Dojin Kim[3,d] and M. Ferrari[4,e]

*Hanoi Advanced School of Science and Technology (HAST)
[1]Institute of Engineering Physics
[2]International Training Institute for Materials Science
Hanoi University of Technology, 01 Dai Co Viet, Hanoi, Vietnam
[3]School of Nano Science and Technology, Chungnam National University, Korea
[4]CNR-IFN Istituto di Fotonica e Nanotecnologie, via Sommarie 14, 38050 Povo, Trento, Italy

[a]chien@itims.edu.vn, [b]chung@itims.edu.vn, [c]huy@itims.edu.vn, [c]dojin@cnu.ac.kr,
[d]mferrari@science.unitn.it

Keywords: ZnS nanowires, Photoluminescence, Thermal evaporation

Abstract. Manganese (Mn) and copper (Cu) doping of ZnS nanowires was achieved by thermal evaporation of Mn, Cu doped ZnS nanopowders. Field emission scanning electron microscopy, and X-ray diffraction studies of the obtained ZnS nanowires demonstrate that the nanowires are single crystal structures and have diameters about 30-200 nm and lengths up to 1 millimeter. Room temperature photoluminescence (PL) measurements show a common PL peak around 520 nm for all ZnS nanowires samples, while impurity-related emission band are observed in doped ZnS nanowires. The dependence of the PL intensity on Mn doping concentration has also been investigated. It is shown that for high Mn doping concentration (10%) in the starting ZnS nanopowders, new emission bands (orange-red and red bands) are observed from the ZnS:Mn nanowires products. The origins of these new emission bands are discussed and brought up for further discussion.

Introduction

ZnS, an important semiconductor compound of the II-VI group, has a wide band gap of 3.7 eV at room temperature, and a relatively large exciton binding energy (~ 40 meV), has been extensively investigated [1]. Several ZnS nanostructures, including nanowires, nanobelts, nanoribbons, nanosaws and nanocables have been successfully synthesized using a variety of methods such as thermal evaporation, intermittent laser-ablation catalytic growth, in-situ formation in liquid templates, chemical vapor deposition, etc [2-4]. ZnS nanowires have attracted much research attention since they promise to open huge potential applications for optoelectronics and other interdisciplinary utilities such as nano LEDs, nano FETs and nano Laser [5-6]. In most of the previous studies, much effort has been paid to develop and explore methods to grow highly crystalline nanowires, and to control the size and the dimensionality of ZnS nanostructures. Much less attention has been placed on doping ZnS nanostructures with transition-metal or rare-earth elements. In this paper, we report on an effective approach for the synthesis of ZnS nanostructures doped with impurities such as Mn and Cu based on temperature-controlled catalytic growth thermal evaporation of their nanopowders. We also present individually PL spectra of pure ZnS and ZnS doped with different impurities.

Experiment

Synthesis of the ZnS nanostructures doped with impurities were carried out by using simple thermal evaporation of suitable nanopowder in a horizontal tube furnace. Home-made ZnS, ZnS:Mn, and ZnS:Cu nanopowders with average crystalline size of 2-5 nm, with Mn, Cu doping concentration of 3, and 10 at % for Mn and 0.1 at % for Cu, were placed in an alumina boat and then put into the center of a quartz tube in the tube furnace [7]. Several Si strips which were coated with a layer of Au, Pt, or Sn film with thickness from 4 to 40 nm by using rf sputtering, were placed at the

downstream end of the quartz tube subsequently to act as deposition substrates for materials growth. The quartz tube was first purged with high-purity argon for 15 minutes, prior to heating to eliminate oxygen in the furnace. The system was then heated to 950 °C at a heating rate of 10 °C per minute in a flowing Ar ambient. Further, the temperature of the system was raised to 1150 °C and kept at this temperature for 30 to 60 minutes. During this second heating process, the Ar flow rate was kept at 80 sccm. The morphology and microstructure of the ZnS nanostructures were examined by using field emission scanning electron microscopy (FE-SEM 4800 Hitachi). The structure and crystallinity were characterized and analyzed by X-ray diffraction (SIEMENS D5000). PL spectra were acquired by using an 325 nm excitation source (He-Cd laser) and a CCD camera (Acton, Winspec) or by a JOBIN YVON SPEX FL-3-22.

Results and Discussion

Fig. 1 shows FE-SEM image of the as-synthesized Cu-doped ZnS nanowires deposited on a silicon substrate coated with a 20 nm layer of gold to act as a catalyst for growth. The typical length of the nanowires varies from 100 to 300 μm, and the diameter is in the range of 30-200 nm. At one end of almost all nanowires, a solidified metal particle was observed, as shown in the inset of Fig. 1, indicating the VLS growth mechanism. The structure and crystallinity of the obtained samples were measured and analyzed by X-ray diffraction. It is shown that the nanowires have the wurtzite 2H polytype of ZnS with good crystallinity. In principle, the thermal evaporation technique is a simple process in which condensed or powder source materials are vaporized at an elevated temperature and the resultant vapor phases condense under certain conditions to form the desired products. The morphology and phase structure of products depends on not only the processing parameters but also the source materials used. In our experiment, by using Cu-doped ZnS nanopowders with the average crystalline size of only 2-5 nm, the growth process is more efficient and the obtained ZnS nanowires products under appropriate conditions can be as long as 1 mm, and homogeneously grown in an area up to 4×1 cm in dimension.

Fig. 2 shows the room-temperature PL spectrum of ZnS:Cu nanowires, excited by a 315 nm ultraviolet light. The PL spectrum is characterized by three PL bands with peak at 417, 440, and 516 nm. The UV emission at around 417 nm is often observed in ZnS nanocrystals, even in pure ZnS samples. This emission is assigned to a recombination of free charge carriers at defect sites, possibly at the surface, in ZnS nanocrystals. Until now, the origin of the blue copper emission (B-Cu) is still not clear. Possibly a center formed by the spatial association of a substitutional Cu and an interstitial Cu is involved. The peak position of this emission is also much closed to the region where defect related emissions are usually observed [8-9]. To verify the involvement of Au ions in the formation of the green emission, we have fabricated ZnS nanowires using Au, Pt or Sn as the catalysts, or even without catalyst. The PL result shows that the peak around 520 nm is a common peak. This result indicates that the presence of the Au ions may not be the cause of the green emission from ZnS nanowires as has previously been concluded. Fig. 3 displays the PL spectrum of ZnS:Mn nanowires doping with (a) 3% Mn and (b) 10% Mn. For the low Mn doping concentration sample, only a broad and asymmetric emission band is observed. The typical orange emission (due to the $^4T_1 - {}^6A_1$ transition of the Mn ions in the host) is

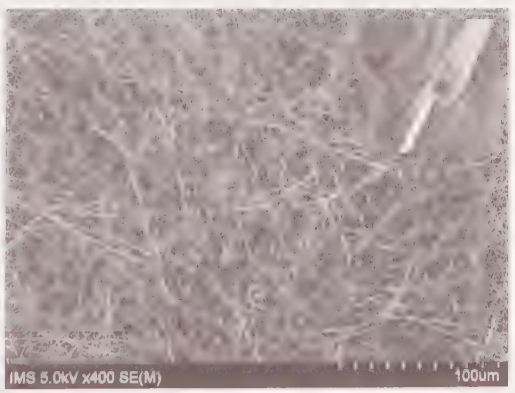

Fig. 1. FE-SEM image of the Cu-doped ZnS nanowires grown on Si wafer with Au as catalyst. The inset shows the solidified Au particle at the free-growing end of the nanowires.

not clearly visible, though a small shoulder can be seen at around 590 nm. For the sample doped with 10 at % Mn, the spectrum is composed of two emission peaks centered at 517 nm and 717 nm, a shoulder is also seen at around 647 nm. Beside the common peak at 517 nm, the additional peak at 717 nm is explained due to Mn-related impurities under the influence of ligand field [10]. This ligand field influence can be evaluated through the change in lattice constants of ZnS nanowires (a = 3.814 A^0) in comparison with the lattice constant of bulk ZnS materials (a = 3.8230 A^0).

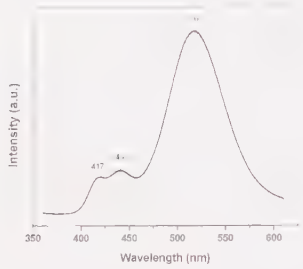

Fig. 2. Room-temperature PL spectrum of Cu-doped ZnS nanowires grown on Si wafer with Au as catalyst.

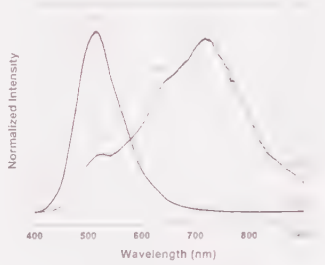

Fig. 3. PL spectra of Mn-doped ZnS nanowires (a) Mn concentration of 3 at%, (b) Mn concentration 10 at%.

Conclusion

We have presented a novel method for synthesis of doped ZnS nanostructures with different catalytic metals. The use of home-made ZnS nanopowders with average size of only 2-5 nm as the source materials for the evaporation process has resulted in the homogeneous and efficient grown of the ZnS nanowires. The PL study taken from all of our samples with various catalytic metals indicated that green emission centered at around 520 nm is a common peak, while impurity-related emission bands are observed in doped ZnS nanowires. This result indicates the important roles of dopants in controlling emission color from ZnS nanostructures.

Acknowledgements

This research was supported by the National Basic Research Program through Grant No. 4.050.06, The CNU-ITIMS Local Lab 2006-2007 project and the Third Italian-Vietnamese Executive Programme of Co-operation in S&T for 2006 – 2008.

References

[1] T. Yamamoto, S. Kishimoto, and S. Iida, Physica B 308–310, 916 (2001).
[2] R. Vacassy, S. M. Scholz, J. Dutta, H. Hofmann, C. J. G. Plummer, G. Carrot, J. Hilborn, and M. Akine, Mater. Res. Soc. Symp. Proc. 501, 369 (1998).
[3] P. Calandra, M. Goffredi, and V. Turco Liveri, Colloids Surf. A 160, 9 (1999).
[4] X. Jiang, Y. Xie, J. Lu, L. Zhu, W. Hei, Y. Qian, Adv. Mater. 13, 1213 (2001).
[5] Q. Li, C. Wang, Appl. Phys. Lett. 83, 359 (2003).
[6] F. Qian, S. Gradecjak, Y. Li, C. Y. Wen, and C. M. Lieber, Nanoletters 5 (11), 2287 (2005).
[7] B.Q. Thanh, P. V. Tuan, N. L. Hung, P. T. Huy, L. H. Ha, N. N. Long, Proceedings of the Ninth Asia Pacific Physics Conference (9th APPC), Hanoi, Vietnam, 577 (2004).
[8] Y. C. Zhu, Y. Bando, D. F. Xue, Appl. Phys. Lett 82, 1769 (2003).
[9] Y. W. Wang, L. D. Zhang, C. H. Liang, G. Z. Wang, X. S. Peng, Chem. Phys. Lett 357, 314 (2002).
[10] T. Toyama, D. Adachi, M. Fujii, Y. Nakano, H. Okamoto, J. of Non-Crystal. Solids 299–302, 1111 (2002).

Advanced Materials Research Vol. 31 (2008) pp 117-119
online at http://www.scientific.net
© 2008 Trans Tech Publications, Switzerland

In-situ Visualization of Layer Transitions during Convective Self-Assembly in a Sessile Drop

Li Gao.[1,a], Qingfeng Yan[1,2,3,b], C. C. Wong[1,2,c] Yet-Ming Chiang[2,3,d]

School of Materials Science and Engineering, Nanyang Technological University, Nanyang Avenue, Singapore 639798
[2] Singapore-MIT Alliance, N3.2-01-36, 65 Nanyang Drive, Singapore 637460
Department of Materials Science and Engineering, Massachusetts Institute of Technology, Cambridge, Massachusetts 02139, USA
[a] x050032@ntu.edu.sg [b] yanqf@ntu.edu.sg [c] wongcc@ntu.edu.sg, [d] ychiang@mit.edu

Keywords: Colloids, Self-assembly, In-situ observation.

Abstract. Convective self-assembly of colloidal spheres provides a simple method for fabricating two and three dimensional colloidal crystals. In this work, we investigated the layer transitions phenomena during colloidal self-assembly in a sessile drop by using an in-situ videoscopic set-up. The effects of surface charge, colloidal concentration, and surfactant additions were examined. The results show that the chemical environment plays an important role in colloidal self-assembly. In the case of ordered growth, different layer transition phenomena were observed when the colloidal concentration is different.

Introduction

Self-assembly of colloidal spheres is of importance from the basic research point of view and also due to their applications in various areas of science and technology, such as photonics, bio- and chemical sensors, data storage, micro-lens array, and nanopatterning.[1] However, the mechanism behind colloidal self-assembly has not been fully understood. Recent work [2] showed that the layer transition during convective self-assembly plays a very important role in structuring colloidal spheres. In this work, colloidal sphere self-assembly in a sessile drop was in-situ monitored by using a videoscope set-up. We focused on the layer transition during the formation of ordered colloidal multilayer for the cases of different chemical conditions manipulated by addition of different surfactants, colloidal spheres with different surface charges, and substrates with different charges.

Materials and method

Polystyrene Colloidal Suspension. Monodispersed polystyrene colloidal spheres with different surface charges were synthesized using emulsifier-free emulsion polymerization method with different initiators.[3] Potassium persulphate was used as the initiator to synthesize negatively surface-charged PS spheres (860 nm in size). In the case of 2, 2'-Azobis (2-methylpropionamidine) dihydrochloride (AIBA) as the initiator, positively surface-charged PS spheres (738 nm in size) was obtained. The volume fractions of the colloidal suspension used in our sessile drop experiments were ranged from 0.05% to 1%.

Surfactants. Three kinds of surfactant, i.e. nonionic surfactant Igepal CO720 (critical micelle concentration, CMC, 0.4973 $mmolL^{-1}$), anionic surfactant sodium dodecyl sulfate (SDS, CMC 8.3 $mmolL^{-1}$), and cationic surfactant dodecyltrimethylammonium bromide (DTAB, CMC 15.6 $mmolL^{-1}$) were used in our study to change the chemical environment of colloidal spheres. All the concentrations used in our study were below their CMC.

Substrates. Negatively charged glass substrates (microscope glass slides, 22 × 22 × 0.3 mm^3, Marienfeld, Germany) were prepared by rinsing with acetone, followed by ultrasonic in a mixture of concentrated sulfuric acid (96%, Ashland Chemical Inc.) and hydrogen peroxide (30%, Ashland Chemical Inc.) (H_2SO_4:H_2O_2 = 3:1, volume ratio) to obtain a hydrophilic surface. Positively charged glass substrates were prepared according to the method reported by Fulda. [4]

In-situ observation of colloidal self-assembly. In-situ visualization of colloidal self-assembly was performed by using an Olympus microscope, which was connected to a CCD camera and a computer for real-time image recording. A freshly cleaned negative or positive glass substrate was put on the microscope slide. Then, 10 μl colloidal suspensions were dropped on the glass substrate. Microscope was operated under transmission mode and focused on the edge of colloidal sessile drop to observe the layer transition during self-assembly.

Results and discussion

Charge effect on colloidal self-assembly. Convective self-assembly was in-situ monitored by dropping PS spheres with negative (860 nm spheres) and positive (738 nm spheres) surface charge onto negative or positive glass substrate. At the same time, three different surfactants (non-ionic, anionic, and cationic) were added into the colloidal suspension to investigate charge effect on the ordering of colloidal crystal growth. It was found that more ordered growth was obtained when the colloids and the substrate had the same polarity in surface charge for surfactantless and non-ionic surfactant suspensions. In the case of dissimilar polarity, the crystal growth was not ordered.

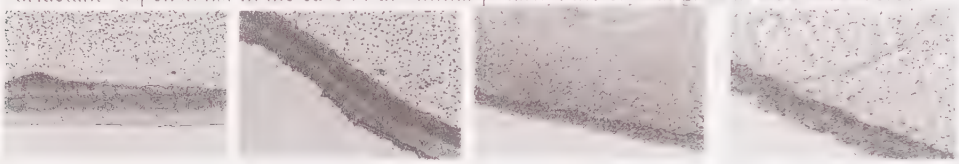

(a) (b) (c) (d)

Figure 1 Charge effects of different chemical conditions. (a) & (b) PS spheres and substrate had similar polarity in surface charge, (c) & (d) PS spheres and substrate had dissimilar polarity in surface charge.

When ionic surfactants were added, the charge effect between substrate and surfactant overwhelmed the charge effect between spheres and substrate. More ordered growth occurred when the surfactant and the substrate have similar polarity in surface charge, regardless of the surface charge state of PS spheres. If the surfactant and substrate had opposite charge, there was no obvious crystal growth.

(a) (b) (c) (d)

Figure 2 Charge effects of different chemical conditions. (a) & (b) surfactant and substrate had similar polarity in surface charge, (c) & (d) surfactant and substrate had dissimilar polarity in surface charge.

Layer transition at different colloidal concentrations. In the case of ordered growth, the layer transition from monolayer towards multilayers could be directly observed under the microscope. Initially, when the thickness of the liquid meniscus at the contact line approaches the diameter of PS sphere, capillary immersion force collects the particles into a line and grows further to form a hexagonal close-packed monolayer. The water flux from the liquid bulk phase compensates the evaporation of water at the drop periphery, which also brings particles for monolayer growth as long as the liquid film is as thick as the diameter of PS.

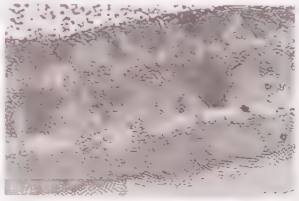

Figure 3 Layer transition in the case of a higher concentration.

However, the thickness of the liquid film near the contact line tends to increase due to the wedge shape of the meniscus, thus the subsequent arrival of particles may form bi-layer and tri-layer at the position where the thickness of the liquid film is higher than the sphere size.

At a higher concentration, the hexagonal monolayer formed first rapidly at the periphery of the drop. The late-coming colloidal spheres driven by the convective flow formed bi-layer and multilayer quickly depending on the liquid film thickness. It was found that square lattices appear during the growth transition when an n-layer crystal changes into an (n+1)-layer crystal (Fig. 3). As reported previously, such a lattice symmetry change was caused by maximizing the packing density at every location.[5,6] In other words, when the liquid film thickness was intermediate between two different layers, the maximum packing density was achieved by stacking the spheres into a square lattice rather than a hexagonal lattice.

However, at a lower colloidal concentration, it was found that the square lattice can be destabilized. As shown in Fig 4, the square lattice transition can be disrupted such that the hexagonal lattice arrangement is restored. This can be explained by the lack of particle transfer to sustain the growth of the 2nd layer. The spheres in the temporary square-lattice 2nd layer still had chance to rearrange themselves into the hexagonal-lattice 1st layer. As a result, a large area hexagonal monolayer formed (Fig. 4c). Similarly, we have observed that the transition region between bilayer and trilayer disappeared and resulted in a uniform bilayer over a large area. Therefore, it is possible to prepare large-area uniform hexagonal arrays by manipulating the colloidal concentrations together with the colloidal chemical environment.

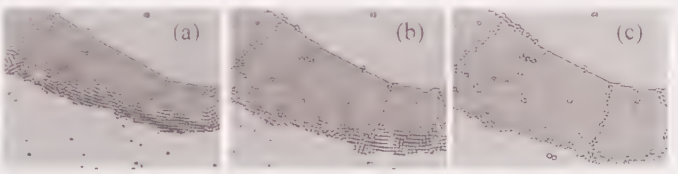

Figure 4 Layer transition in the case of a lower concentration. (a) square-lattice bi-layer appeared, (b) square-lattice bi-layer disappeared gradually, (c) only hexagonal monolayer left.

Conclusion

By in-situ observation of the colloidal self-assembly at different chemical environments and concentration, it was found that similarly charged PS and substrate in nonionic surfactant case and similarly charged surfactant and substrate in ionic surfactant case tended to give ordered growth. Under such conditions, layer transition at different colloidal concentrations was investigated. To obtain a uniform monolayer or given number of layers, one need control not only the chemical condition in the colloidal system but also the colloidal concentrations.

References

[1] Y. Xia, B. Gates, Y. Yin and Y. Lu: Adv. Mater. Vol.12 (2000), p.693.
[2] L. Meng, H. Wei, A. Nagel, B. J. Wiley, L. E. Scriven and D. J. Norris: Nano Letters Vol.6 (2006), p. 2249.
[3] S. E. Shim, Y. J. Cha, J. M. Byun and S. Choe: J. Appl. Polym. Sci. Vol. 71 (1999), p.2259.
[4] K.-U. Fulda, A. Kampes, L. Krasemann and B. Tieke: Thin Solid Films Vol. 327-329, p.752.
[5] N.D. Denkov, O.D. Velev, P. A. Kralcheveky, I. B. Ivanov, H. Yoshimura and K. Nagayama: Langmuir Vol. 8 (1992), p.3183.
[6] B. G. Prevo and O. D. Velev: Langumir Vol. 20 (2004), p.2099.

Advanced Materials Research Vol. 31 (2008) pp 120-122
online at http://www.scientific.net
© 2008 Trans Tech Publications, Switzerland

Optical and Surface Morphological Study of GaN Nanocolumn Grown on Gallium Coated Si by Molecular Beam Epitaxy

K. Santhakumar[1a], D.H. Kang[1b], J.C. Song[1c], D.W. Kim[1d], J.S. Kim[1e], M. D. Kim[2a], C.R. LEE[1f]

[1]School of Advanced Materials Engineering Engineering College Chonbuk National University. Chonju 664-14, Chonbuk 561-756, South Korea
[2]Department of Physics, Chungnam National University, 220 Gung-dong, Yuseong-gu, Daejeon, 305-764, Korea

[1a]k.santhakumar@gmail.com, [1b] for-miracle@hanmail.net, [1c]liebesky99@nate.com, [1d]kdw612@hanmail.net, [1e]kjinsoo@chonbuk.ac.kr1 [2a]mdkim@cnu.as.kr [1f]crlee7@chonbuk.ac.kr

Keywords : GaN, Nano-colum, MBE, Si substrate

Abstract. Vertically aligned GaN nanocolumn arrays were grown by molecular beam epitaxy on Gallium coated silicon substrate. The dense packing of the NCs gives them the appearance of a continuous film in surface view, but cross-sectional analysis shows them to be isolated nanostructures. The GaN nanocolumns have uniform diameters of 85 nm, lengths up to 720 nm and possess a pyramid like tip. Photoluminescence measurements of NCs show excitonic emission with a dominant, narrow peak centered at 363 nm and FWHM of 68 meV. From the Raman spectrum, peaks at 566.9 and 730 cm^{-1} are assigned to the E_2 and A_1(LO) GaN phonons modes which clearly indicates that the grown nanocolumns are highly crystalline. The grown nanocolumns are highly oriented and perpendicular to the growth surface.

Introduction

GaN-based light emitters have been successfully commercialized in spite of that the large amount of dislocations is still a big threat to the lifetime and the yield of the devices. GaN nanowires with perfect orientation will undoubtedly hold considerable technological promise for nanodevice application [1-3]. High-quality nanocolumns with low dislocation density could be potential templates for high-performance nanodevices such as light-emitting diodes, laser diodes and photodetectors. Recently, the semiconductor columnar nanostructures, i.e., nanocolumns, have aroused great attention because of their potential uses in both the mesoscopic research and the development of nanodevices. To reduce the dislocation density for higher quality, many methods have been proposed. Gallium nitride(GaN) nanocolumn grown by molecular beam epitaxy (MBE) have been demonstrated to be III-V nitride structures of high crystalline quality and low defect density even when grown on lattice mismatched substrates[4-7]. We report an approach for the growth of one-dimensional GaN nanocolumns with sharp pyramid like tips in Si substrate. A scheme is established for describing the growth process of GaN nanowire arrays using self-organization on gallium -coated Si (111) substrates. This grown nanocolumns would find wider applications in light-emitting diodes (LED), detectors, and other electronic and photonic devices.

Experimental procedure

GaN nanocolumn in this work was grown on 1.5 cm x 1.5 cm Si (111) substrate by molecular beam epitaxy (MBE). The formation of nano-sized Ga droplets on Si substrate surface was formed by evaporating Ga from effusion cell. Ga alloy droplets were found to be uniformly distributed on silicon surface. The GaN nanocolumn growth was performed under the nitrogen rich conditions. The nanocolumn morphology and size distribution were analyzed with a field emission scanning electron microscope (FESEM). Optical and structural properties of the grown GaN nanocolumn were characterized by Photoluminescence (PL) and Raman spectroscopy.

Results and discussion

Cross sectional SEM micrograph of the GaN nanocolumns grown on Si is shown in Figure. 1. It is seen that the nanocolumns are densely distributed on the Si surface forming an array pattern. Figure 2 shows FE-SEM of the GaN nanocolumns grown on Si substrate. Vertically aligned GaN nano-columns were grown uniform in diameter and length.

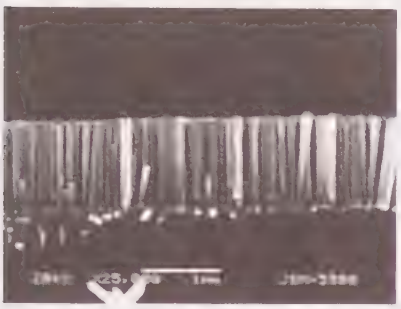

Figure. 1 shows cross sectional SEM micrograph of the GaN nanocolumns grown on Si.

The diameter and length of the nano-columns ranged from 100 to 500 nm and 1 to 6 μm, respectively. GaN nanocoulmn arrays with sharp pyramid like tips are observed on the top surface. The grown nanocolumns are of even length which would be suitable for device fabrication

Fig.2 shows FE-SEM image of GaN nano-column vertically grown on Si substrate (a) top surface and (b) cross-sectional view.

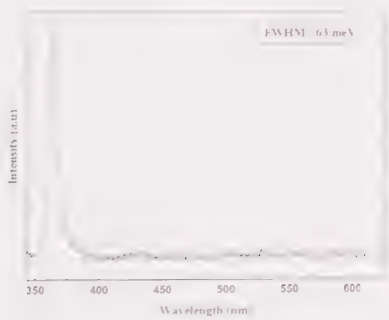

Fig. 3 Room temperature PL spectra of the GaN nano-column grown on Si

Figure 3 shows the room temperature PL spectrum of the GaN nano-column. A strong band-edge emission is observed at 363 nm. The FWHM of the PL spectra at 363 nm peak was 68 meV which

indicates the grown nano-columns are dislocation free with good crystalline quality. The narrow and sharp band emission from PL spectrum at room temperature indicates the grown nano-columns has less dislocation density with minimum defects. PL investigation indicates an improvement in the optical quality of the nano-column.

Fig. 4 Raman spectrum of GaN nanocolumn grown on Si substrate

According to group theory, $A_1(z)+2B_1+E_1(x, y)+2E_2$ optical modes are predicted at the Γ point of the Brillouin zone of hexagonal GaN [8]. The two E_2 modes are Raman active, the A_1 and E_1 modes are both Raman and infrared active, and the two B_1 modes are optically silent. Since the A_1 and E_1 modes are polar, they split into LO and transverse optical (TO) components. Figure. 4 show Raman spectrum of overgrown GaN on nano-columns by MBE method. The Raman modes measured exhibit peaks at 566.9 and 730 cm^{-1} assigned to the E_2 and $A_1(LO)$ GaN phonons, respectively [9]. From the sharp Raman modes it clearly indicates that the grown GaN nanocolumns are highly crystalline in nature with less dislocation. We have confirmed that MBE grown GaN nanocolumns are completely single crystals and epitaxially oriented on the Si (111) substrate. Our results suggest that single crystal GaN nanocolumn can be grown on Ga droplets on silicon substrate with a low dislocation density.

Conclusion

In summary, a novel technique was used to grow crystalline quality GaN nano-columns on Ga droplet coated on Si substrate using MBE system. The Ga droplet on Si substrate was annealed prior to GaN growth to obtain vertically well aligned nano-columns. The grown GaN nano-columns were vertical to the Si(111) growth plane are demonstrated and analysed with FE-SEM techniques. GaN nano-columns grown are single crystal in nature with good optical quality were confirmed by Raman spectroscopy and Pl measurements. This implies that the optical properties of GaN nano-column have high potential for GaN based optoelectronic devices.

References

[1] W. Han, S. Fan, Q. Li and Y. Hu: Science Vol.277 (1997), p. 1287.
[2] X. F. Duan and C. M. Lieber: J. Am. Chem. Soc. Vol.122 (2000), p. 188.
[3] Y. Huang, X. Duan, Y. Cui, and C. M. Lieber: Nano Lett. Vol.2 (2002), p.101.
[4] E. Calleja, M. A. Sánchez-García, F. J. Sánchez, F. Calle, F. B. Naranjo, E.Muñoz, U. Jahn, and K. Ploog: Phys. Rev. B Vol. 62 (2000), p.16826.
[5] J. Ristíc, E. Calleja, M. A. Sánchez-García, J. M. Ulloa, E. Calleja, J.Sánchez-Páramo, J. M. Calleja, U. Jahn, A. Trampert, and K. H. Ploog: Phys. Status Solidi B Vol. 234 (2002), p. 717.
[6] J. Ristíc, E. Calleja, M. A. Sánchez-García, J. M. Ulloa, J.Sánchez-Páramo, J. M. Calleja, U. Jahn, A. Trampert, and K. H. Ploog: Phys. Rev. B Vol. 68 (2003), p. 125305.
[7] K. A. Bertness, A. Roshko, N. A. Sanford, J. M. Barker, and A. V.Davydov: J. Cryst. Growth Vol. 287 (2006), p.522.
[8] W. Hayes and R. Laudon, *Scattering of Light by Crystals* (Wiley, New York, 1978).
[9] M. Kuball: Surf. Interface Anal. Vol.31 (2001), p. 987.

Advanced Materials Research Vol. 31 (2008) pp 123-125
online at http://www.scientific.net
© 2008 Trans Tech Publications, Switzerland

Nanometer-scale $In_{0.5}Ga_{0.5}As$ ring-like structure grown by droplet epitaxy

N. PANKAOW[a], S. PANYAKEOW[b] and S. RATANATHAMMAPHAN[c]

Semiconductor Device Research Laboratory, Nanotec Center of Excellence

Department of Electrical Engineering, Chulalongkorn University, Bangkok 10330, Thailand

[a]naraporn.p@student.chula.ac.th, [b]s_panyakeow@yahoo.com, [c]rsomchai@chula.ac.th

Keywords: InGaAs, GaAs, nanostructures, droplet, molecular beam epitaxy

Abstract. We have demonstrated the fabrication of InGaAs ring-like nanostructures by droplet-epitaxy technique using molecular-beam epitaxy. Dependence on the substrate temperature and the amount of indium and gallium of the nanostructural properties was investigated. It was found that increasing substrate temperature resulted in larger InGaAs ring size but with lower density and that increasing $In_{0.5}Ga_{0.5}$ amount resulted in larger InGaAs ring size but with oscillating density. Photoluminescence results confirmed the high quality of the nanocrystal.

Introduction

Ring-shape nanostructures have attracted a lot of attention due to the Aharonov-Bohm effect [1]. Particularly interesting is the magnetic properties of such quantum systems, which introduce the possibility of inducting persistent currents. Recently, the fabrication and investigation of self-assembled InAs quantum-rings have been progressing rapidly and led to a large number of theoretical and further experimental studies. Various fabrication techniques for quantum-ring have been developed and realized. Among these, Stranski-Krastanow (S-K) growth mode has become extremely attractive in the case of a lattice-mismatched system such as InAs/GaAs and InGaAs GaAs systems by capping self-assembled quantum dot [2]. On the other hand, droplet epitaxy technique can be widely applied to both the lattice-matched [3] and mismatched systems [4]. Although, the fabrication of InAs nanostructures via droplet epitaxy on GaAs substrates still has some problems such as relative low density and large size [4] due mainly to the long migration length and high segregation effect of the newly supplied adatoms, and worse optical quality. A solution to these problems is by introducing growth at low temperature and using optimum crystallization conditions [5]. Another is by using InGaAs/GaAs system [6]. However, there are only a few reports on the growth of InGaAs/GaAs nanostructures by droplet-epitaxy.

In this work, we have demonstrated the fabrication of InGaAs ring-like nanostructures by droplet epitaxy technique using molecular-beam epitaxy. The effects of substrate temperature and amount of indium and gallium on InGaAs ring-shaped nanostructures have been investigated.

Experimental procedure

The samples were grown on GaAs (100) substrates in RIBER 32P conventional solid source molecular beam epitaxy system. After removal of the native oxide by heating up the substrate to 600°C under As_4 flux until the streak reflection high-energy electron diffraction (RHEED) pattern appeared, 300 nm undoped GaAs buffer layer was grown on 580°C substrate. Then the substrate temperature was decreased to the desired temperature (120-210°C) without As_4 flux to minimize the excess As on the surface. Before $In_{0.5}Ga_{0.5}$ deposition, the background pressure in the growth chamber was reduced to less than 1×10^{-9} torr to minimize the initial interaction between InGa and arsenic during droplet forming. To investigate the effect of substrate temperature while $In_{0.5}Ga_{0.5}$ deposition and $In_{0.5}Ga_{0.5}$ thickness, two sample series were fabricated. For the first series, an

$In_{0.5}Ga_{0.5}$ amount of 3 ML was deposited with a different substrate temperature of 120, 150, 180, and 210°C, respectively. For the second series, a different amount of $In_{0.5}Ga_{0.5}$, 2, 3, 4, and 5 ML, was deposited. Finally, the $In_{0.5}Ga_{0.5}$ droplets were exposed to As_4 flux with the beam equivalent pressure of 6×10^{-6} torr at 180°C for 5 minutes to crystallize the droplets to form $In_{0.5}Ga_{0.5}As$ nanostructures. After the growth was finished, all the samples were characterized for their surface morphology by atomic force microscope (AFM). For the photoluminescence (PL) measurement, another sample was grown repeatedly under the condition of 3 ML InGa droplets and 210°C substrate, with additional 100-nm-thick GaAs cap layer by migration-enhanced epitaxy [7] at 300°C and annealed at 400°C under As_4 flux for a few minutes.

Results and discussion

Fig. 1(a) shows the AFM images of the samples prepared by varying substrate temperature with 3 ML InGa droplets. The size and density of InGaAs ring-shaped nanostructures depends on substrate temperature as shown in fig. 1(b) and fig. 1(c), respectively. The size is increasing but the density of InGaAs rings is decreasing while increasing the substrate temperature. The outer diameter of the ring is varying between 122-162 nm and the density of the rings is varying between 1.6×10^{8}-8.6×10^{8}/cm^2. Fig. 2(a) shows the AFM images of the samples prepared by varying the amount of $In_{0.5}Ga_{0.5}$ between 2-5 ML under constant substrate temperature of 150°C. From fig. 2(b), the size of InGaAs ring-shaped nanostructures is increasing while increasing the amount of $In_{0.5}Ga_{0.5}$ deposited. The outer diameter of InGaAs rings is between 127-141 nm. However, the density of InGaAs rings is *oscillating* while increasing $In_{0.5}Ga_{0.5}$ amount, as shown in fig. 2(c). While the amount of $In_{0.5}Ga_{0.5}$ is increased from 2 to 3 ML, the density of the rings is increasing. The density however decreases when increasing the $In_{0.5}Ga_{0.5}$ amount is further increased between 3-4 ML and turn to increase again when the $In_{0.5}Ga_{0.5}$ amount increase from 4 to 5 ML. The

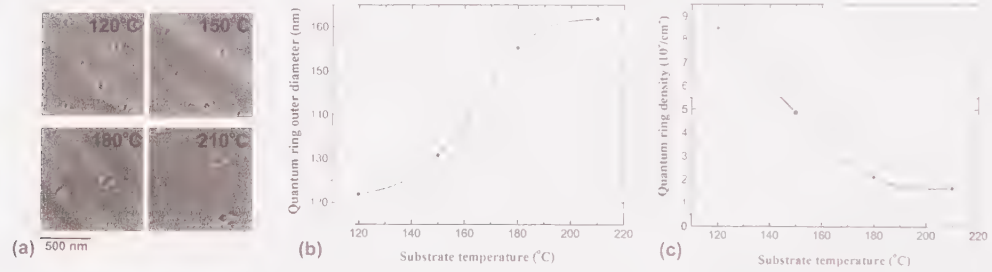

Fig. 1 (a) AFM images of $In_{0.5}Ga_{0.5}As$ nanostructures on GaAs at different substrate temperature. (b) and (c) the dependence on substrate temperature of ring-shaped nanostructure outer diameter density, respectively. The coverage of $In_{0.5}Ga_{0.5}$ droplet was 3 ML.

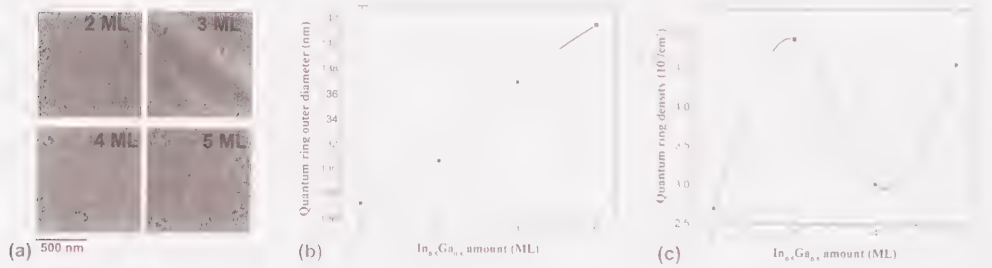

Fig. 2 (a) AFM images of InGaAs nanostructures on GaAs after $In_{0.5}Ga_{0.5}$ deposition at 150°C with different amount of $In_{0.5}Ga_{0.5}$. (b) and (c), the dependence on $In_{0.5}Ga_{0.5}$ amount of ring-shaped nanostructure outer diameter and density, respectively.

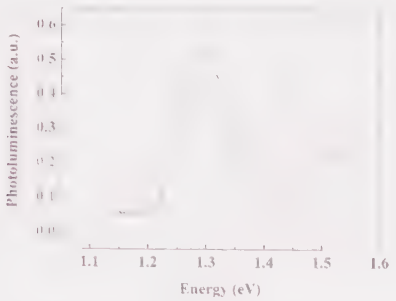

Fig. 3 PL spectra of the $In_{0.5}Ga_{0.5}As$ ring-shaped nanostructures measured at 77 K.

oscillation of density while increasing $In_{0.5}Ga_{0.5}$ amount are due to the wetting nature of GaAs surface, the interfacial energy of the deposit at $In_{0.5}Ga_{0.5}$ droplets and GaAs interface, and temperature. One explanation is that $In_{0.5}Ga_{0.5}$ droplets act like electrochemical drills" etching away the substrate to form nanoholes [7]. Further studies on this observation are under progress. Fig. 4 shows the PL spectra at 77 K of the InGaAs ring-shaped nanostructures grown by droplet epitaxy at 210°C with 3 ML InGa droplets. The PL peak is 1.3 eV with respective FWHM of 0.1 eV. The PL spectral line around 1.5 eV is attributed to GaAs.

Conclusions

We have demonstrated the fabrication of InGaAs ring-like nanostructures by droplet epitaxy technique using molecular beam epitaxy. The growth process is initiated by depositing indium and gallium to form the droplets and exposing As_4 flux to crystallize the droplets into InGaAs. The effects of substrate temperature and amount of indium and gallium on the forming of InGaAs ring-shaped nanostructures were investigated. The ring-like nanostructure exhibits PL emission, indicating high crystal qualities.

Acknowledgements

This work is supported by the Thailand Research Fund (TRF), National Nanotechnology Center (Nanotec), and Chulalongkorn University. We also wish to thank Mr. Boonchuay SUPMONCHAI for his fruitful discussion, Mr. Supachok THAINOI, Mr. Pornchai CHANGMAUNG, Mr. Poonyaseri BOONPENG, and Ms. Wipakorn JEWASUWAN for their technical assistance.

References

[1] Y. Aharonov, D. Bohm, Phys. Rev., vol. 115 (1959), pp.485.
[2] Axel Lorke, R. Johannes Luyken, Jorge M. Garcia, and Pierre M. Petoff, Jpn. J. Appl., Part 1, vol. 40 (2001), pp. 857.
[3] T. Mano, N. Koguchi, J. Crystal Growth, vol. 278 (2005), pp.108.
[4] J.-M. Lee, D.H. Kim, H. Hong, J.-C. Woo, and S.-J Park, J. Cryst. Growth, vol. 212 (2000), pp.67.
[5] Jong Su Kim and Nobuyuki Koguchi, Appl. Phys. Lett., vol. 85 (2004), pp.5893.
[6] Y. Horikoshi, M. Kawashima, and H. Yamaguchi, Jpn. J. Appl. Phys., vol. 27 (1988), pp.169.
[7] T. Mano, K. Watanabe, S. Tsukamoto, H. Fujioka, M. Oshima, N. Koguchi, J.Cryst. Growth., 209 (2000), pp.504.
[8] Zh. M. Wang, B. L. Liang, K. A. Sablon, and G. J. Salamon, Appl. Phys. Lett., vol. 90 (2007), pp.113120.

Advanced Materials Research Vol. 31 (2008) pp 126-128
online at http://www.scientific.net
© 2008 Trans Tech Publications, Switzerland

The Gas Sensitvity Character of WO_3 Nanosized Material

HUANG Shi-zhen[1,a], LIN Wei[1,b] , CHEN Wen-zhe[1,c]

[1]Department of Electronic science Applied Physics, Fuzhou University,Fuzhou 350002,China

[a]email: hs501@fzu.edu.cn

[b]email: mqks@fzu.edu.cn

[c]email: cwz@fzu.edu.cn

Key words: Nanosized material; WO_3; NO_2

Abstract

By thermal decomposition, WO_3 nanosized material was prepared as sensitive material and doped SiO_2 nanosized material has been prepared using Sol-Gel process. NO_2 gas-sensing elements have been manufactured with prepared material. The element is sensitive to NO_2 with fairly good selectivity. Micro-structure of the material was analyzed by SEM, and the sensing mechanism was discussed.

1. Introduction

NO_2 is a kind of toxic brown gas with irritative smelling. Exhausts of industrial production and vehicles contain NO_2, and monitoring on NO_2 emission had been an environmental issue concerned by relative departments. Because of its smaller particle, huge BET, dramatical surface effect, volume effect and quantum effect, nanosized material shows good gas-sensing characters. WO_3 is a material developed in recent years. In this experiment, NO_2 gas-sensing element was prepared using a special method by doping SiO_2 with WO_3 .This element was of high sensitivity and selectivity to NO_2.

2. Experimentals

2.1 Preparation of WO_3 sensing material

(1) To dissolve some ammonium tungstate in deionized water, add certain proportion of $Si(OC_2H_5)_4$ Hydrolyzed solution , aging for 15 days, , the solution became intermixture of ammonium tungstate white precipitation and $Si(OC_2H_5)_4$ colloidal sols. White powder was obtained when the mixtures were dried. By heating the white powder in muffle furnace in different temperatures for different sessions of time, yellow powders were obtained. That is tungsten oxide nanosized material doped with certain proportion of silicon dioxide. [1,2].

$$(NH_4)_2WO_4 \xrightarrow{600C^\circ} WO_3 + 2NH_3 + H_2O \qquad Si(OC_2H_5)_4 + 2H_2O \rightarrow SiO_2 + 4C_2H_5OH$$

(2) To decompose tungsten oxide by heating tungstate decomposite directly.

(3) Tungsten oxide powder(AR) purchased in markets.

2.2 Fabrication of the element

WO_3 of different mixture ratios were grinded for 2h , added some deionized water to grind them into slurry and then fabricate spheroid element with heater winding by specific method and then sintered the element in muffle furnace in different temperatures for different sessions of time after drying.

3. Results and discussion

3.1 Material phase analysis

Prepare WO_3 powder by thermal decomposition method and prepare SiO_2 Powder using Sol-Gel method, their grain size are both smaller than 100nm. While the grain size of tungsten oxide powder

(AR) purchased in markets is bigger. The pure WO_3 and SiO_2 powder mixtures were analyzed by XRD ,the average grain size of tungsten oxide is 58 nm. WO_3 and SiO_2 spectral peaks were found in XRD spectrum , so the material proved to be tungsten oxide doped with silicon dioxide.

3.2 Affection of silicon dioxide on micro-structure of the material

Adopt pure WO_3 powder without adding silicon dioxide; the element was poor in mechanical performance, and hard to be sintered to be an element. Doped with silicon dioxide, the mechanical performance of the element was enhanced. At the same time, it results in richness of pores in the material. Figure 1(a) and figure 1(b) are SEM pictures of microstructure of materials doped with SiO_2 and pure WO_3 respectively. Compared with that of pure WO_3(as figure1(b)),SiO_2 Doped WO_3 (as figure1(a)): The surface of the material is porous in structure, adsorption area of surface is larger, and these will dramatically enhance the sensitivity of the material. But if the amount of SiO_2 doped was over 15wt%, the porosity of the material will decrease.

Fig.1(a) : SEM image of WO_3 doped SiO_2

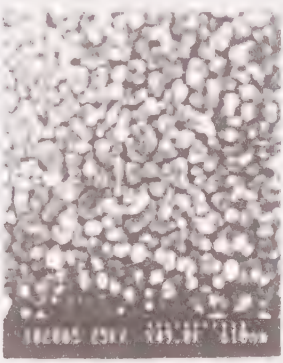

Fig.1(b) : SEM image of pure WO_3

3.3 Sensing performance of the material

3.3.1 Relationship between sinter temperature and sensing performance of the element

The initial output voltage of the element increases with the rising of sinter temperature, while the sensitivity to NO_2 decreases. In the sinter temperature of 500-600℃ , surface activity of grains of the sensing material is strong and BET of the material is large, result in high sensitivity to NO_2 of the material. If sinter temperature is higher than 800℃ , surface of the material inactivates, grain aggregates and grows, porosity of the material decreases, result in decrease in sensitivity. 。

3.3.2 Sensitivity and selectivity of the elements

Table 1 shows the sensitivity of the element to 10×10^{-6} NO_2 and 1000×10^{-6} NH_3, H_2, CO and C_4H_{10}. We can see it is proved to be an element of excellent sensitivity and selectivity to NO_2 in proper conditions.

Table 1 : sensitivities to different gases of the element

The gas	NO_2	H_2	C_4H_{10}	NH_3	CO
concentration	10×10^{-6}	1000×10^{-6}	1000×10^{-6}	1000×10^{-6}	1000×10^{-6}
sensitivity	1000	5.1	3.3	2.1	1.2

3.3.3 Affection of operating temperature on sensitivity and response-recovery of the element

Constrain to certain range, the lower of the operating temperature, the higher the sensitivity and selectivity to NO_2 is, the longer the response-recovery time of the element are. Figure 3 shows curve of response-recovery of the element in 10×10^{-6} NO_2 in operating temperature of 150°C. Its response time is about 10s, and recovery time is about 45s.

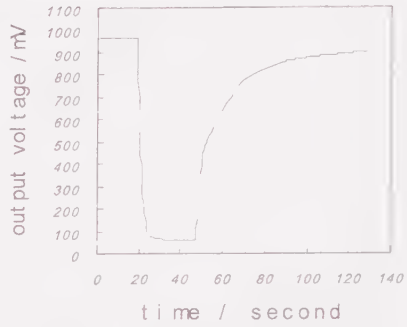

Figure 2 : Curve of response-recovery of the element

3.4 Mechanism analysis

WO_3 is a kind of surface conductance dominated n type semiconductor material , which can absorb oxygen on its surface and become adsorbed oxygen ions with negative charges[3].So the electron concentration of the bulk decreases ,making the conductance decreased. NO_2 is a kind of oxidative gas , when WO_3 touches with it , NO_2 is adsorbed and follow reactions happens:

$$NO_2 + e^- \rightarrow (NO_2)^-_{ads}$$

$$NO_2 + O^-_{2ads} + 2e^- \rightarrow (NO_2)^-_{ads} + 2O^-_{ads}$$

It lead to further decrease of the conductance of the sensing material. According to the fact that the sensitivity to lower concentration of NO_2 of the element is hundreds of times higher than the sensitivity to higher concentration of disturbing gases, it means another mechanism may work in the process, that is, adsorbed NO^-_{2ads} may catalyze the adsorbed oxygen ions. Reactions are as follows :

$$(NO^-_2)_{ads} + O^-_{2ads} \rightarrow 2O^-_{ads} + NO_2$$

$$NO_2 + e \rightarrow (NO^-_2)_{ads}$$

Series of reactions result in adsorption of quantities of free electrons on the surface of the material, and dramatically decrease of major carrier, leading to decrease of conductance of the material. When the element is operated in lower temperature, free electrons in WO_3 can react with NO_2 more easier , therefore, the conductance of the material decreases. So the sensitivity of the element is higher when it is operated in lower temperature.

On the other hand , this surface conductance dominated sensing material has excellent sensitivity and selectivity to NO_2 thanks to porous nano-structure of WO_3 - SiO_2.

4. Conclusions:

Prepare WO_3 nanosized material by thermal decomposition, doping with nanosized SiO_2 fabricated by Sol-Gel method to form the porous structural compound material. On mechanism, adsorbed $(NO^-_2)_{ads}$ catalyze O^-_{2ads} . The element made from this material shows excellent sensitivity and selectivity to NO_2, and its response–recovery is good enough to be an ideal element of NO_2 sensing.

References

[1] Xiu sheng Wang, Liang ying Zhang, Xi Yao: Functional Material, Vol.29 (1998), p.276-277
[2] Jun Bao, Guo xing Xiong, Jin hua Gu: Film Science and Technology, Vol.18(1998), p.42-44
[3] Yu Hua-liang, Huang Shi-zhen, Lin Wei, Chen: Chinese Journal of Sensor and actuators, Vol.18 (2005), p.325-328

Advanced Materials Research Vol. 31 (2008) pp 129-131
online at http://www.scientific.net
© 2008 Trans Tech Publications, Switzerland

Effect of oxygen flow rate and temperature on the structure of DC sputtered nanocyrtsalline copper oxide films

M. J. Chiang[*a], C. W. Wu[b] and H. E. Cheng[c]

Department of Electro-Optical Engineering, Southern Taiwan University, Tainan 710, Taiwan

[a]mjchiang@mail.stut.edu.tw, [b]m95r0212@webmail.stut.edu.tw, [c]sean@mail.stut.edu.tw

Keywords: copper oxide, nanocrystalline, structure

Abstract. Copper oxide, a direct band gap semiconductor with band gap about 1.21-1.51 eV, has been regarded as a promising material for photovoltaic. Nanocrystalline copper oxide films have been synthesized on Si by dc sputtering method. The effects of oxygen flow rate and deposition temperature on the microstructure of nanocrystalline copper oxide films were investigated. X-ray diffraction analysis shows that a broaden peak of Cu_2O (111) at 36.72^0 was observed at the deposition condition of DC power 150 W, pressure $2*10^{-2}$ Torr, substrate temperature 100 °C, Ar flow rate 15 sccm and O_2 flow rate 1sccm. With increasing the oxygen flow rate to 3 and 5 sccm, CuO (-111) could be observed at 36.58^0. The increase of oxygen flow rate resulted in the film formation from Cu_2O to CuO. SEM pictures show that copper oxide films exhibit nanosize grains. X-ray diffraction patterns of CuO films deposited at 50~200 °C show that only (-111) plane is obtained. The SEM pictures show that the grain size increases with the deposition increases.

Introduction

The development of p-type semiconductor is one of the key technologies for p-n junction based devices, such as diodes, transistors and light-emitting diodes [1]. Copper oxide coating is known to show p-type conductivity and as a consequence, it is attracting increasing attention. CuO is a p-type semiconductor with a band gap of 1.21-1.51 eV and a monoclinic structure [2-3]. It has unique features such as low cost, non-toxicity, the abundant availability of copper, a theoretical solar cell efficiency of 18% and relatively formation of the oxide layer. Copper oxide composite systems are also attractive due to their super-conduction properties. In this study, the effects of oxygen flow rate and deposition temperature on the structure evolution and surface morphology of copper oxide was investigated.

Experimental details

Copper oxide was deposited by means of dc reactive magnetron sputtering on p-Si(100) substrate at a substrate of 100 °C using a Cu target (99.99% purity) and Ar sputtering gas. The substrate was cleaned with acetone and deionized water prior deposition. Oxygen was introduced into the chamber during the deposition near the substrate to form copper oxide or cuprous oxide. The flow rate of oxygen used as reactive gas was changed from 1~5 sccm to see its effect on the film phase and microstructure. The film thickness was kept typically at 0.5~0.6 μm as determined by α-step. Table1 shows the deposition

Table1 Deposition parameters of copper oxide films

Deposition parameters	
Ar flow rate (sccm)	15
O_2 flow rate (sccm)	1~5
dc power (W)	150
Pressure (torr)	$2*10^{-3}$
Temperature (°C)	50~200
Deposition time (min)	15~25

parameters used in this study. Field emission scanning electron microscope (FESEM, Philip XL-40FEG) was used to observe the film surface morphology. The crystal structure properties were studied by X-ray diffraction (XRD) in the θ-2θ mode using Cu-Kα radiation.

Results and discussion

The X-ray diffraction patterns of the films formed at various oxygen flow rate are shown in Fig.1. The films were polycrystalline in nature with monoclinic and cubic structures. The film deposited at oxygen flow rate 1sccm showed a peak at 2θ=36.72° corresponding to the (111) plane of Cu_2O. As the oxygen flow rate increased to 3 sccm, the film exhibited a peak centered at 35.58° corresponding to the (-111) plane of CuO was obtained. It is observed that the peak intensity increased with the oxygen flow rate increased to 3sccm thereafter it decreased at higher oxygen flow rate.

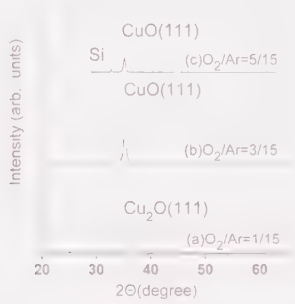

Fig.1 X-ray diffraction patterns of copper oxide with different oxygen flow rate. (a)1sccm, (b)3sccm, (c)5sccm

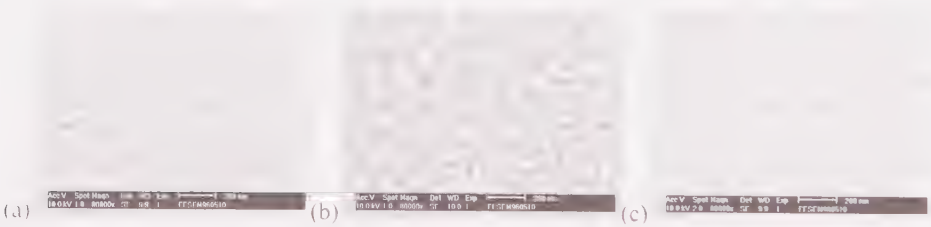

Fig.2 Surface morphologies of copper oxide deposited at different oxygen flow rate. (a)1sccm, (b)3sccm, (c)5sccm

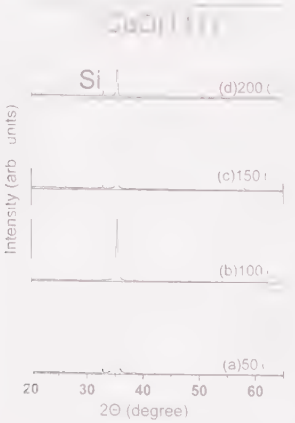

Fig.3 X-ray diffraction patterns of copper oxide films deposited at different substrate temperature. (a)50°C, (b)100°C, (c)150°C, (d)200°C.

The surface morphology and grain size of the films deposited at various oxygen flow rate were shown in Fig.2(a)~2(c). Nanosize grains ranging from 30 to 70 nm were obtained with changing the oxygen flow rate. According to the X-ray diffraction pattern in Fig.1(b), the film deposited at oxygen flow rate 3 sccm has the highest peak intensity and smallest width at half maximum. It means the film obtained at 3 sccm should have better crystallinity. Fig.3 shows the X-ray diffraction patterns of CuO films deposited at different substrate temperature. It is observed that CuO (-111) could be formed from 50 to 200 °C with power 150 W, pressure $2.5*10^{-2}$ Torr and O_2/Ar flow ratio at 3/15. The SEM pictures in Fig.4 show that the CuO films grain size increase with the deposition temperature increasing.

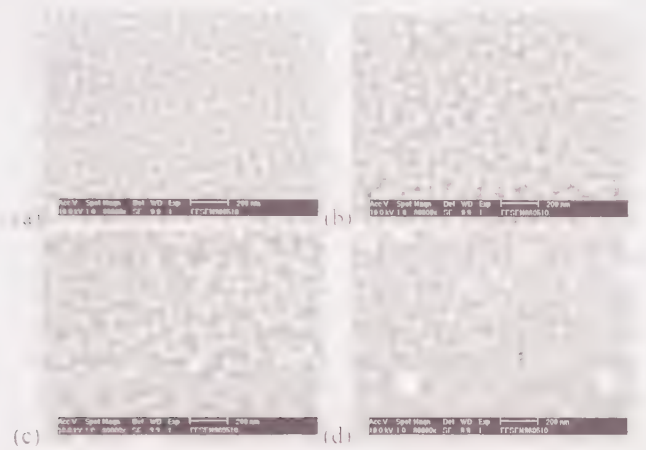

Fig.4 Surface morphologies of copper oxide deposited at different substrate temperature. (a)50°C, (b)100°C, (c)150°C, (d)200°C.

Conclusions

The nanocrystalline copper oxide films with grain size 30-50 nm were deposited by dc reactive magnetron sputtering method on silicon substrate. The influences of oxygen flow rate and deposition temperature on copper oxide structure have been observed and analyzed. X-ray diffraction analysis shows that a broaden peak of Cu_2O (111) at 36.72^0 was observed at the deposition condition of DC power 150 W, pressure $2*10^{-2}$ Torr, substrate temperature 100 °C, Ar flow rate 15 sccm and O_2 flow rate 1sccm. With increasing the oxygen flow rate to 3 and 5 sccm, CuO (-111) could be observed at 36.58^0. SEM pictures show that copper oxide films exhibit nanosize grains. X-ray diffraction patterns of CuO films deposited at 50~200 °C show that only (-111) plane is obtained. The SEM pictures show that the grain size increases with the deposition temperature increasing.

Acknowledgement

The authors would like to thank the National Science Council of Taiwan for the financial support under the project "NSC95-2221-E-218-077".

References

[1] E.M. Alkoy and P.J. Kelly: Vacuum Vol. 79 (2005), p221.

[2] B. Balamurugan and B.R. Metha: Thin Solid Films Vol. 396 (2001), p90

[3] F. Marabelli, G.B. Parraviciny and F.S. Drioli: Phys. Rev. B Vol. 52 (1995), p1433.

Advanced Materials Research Vol. 31 (2008) pp 132-134
online at http://www.scientific.net
© 2008 Trans Tech Publications, Switzerland

In–mole-fraction and thickness of ultra-thin InGaAs insertion layers effects on the structural and optical properties of InAs quantum dots

P. BOONPENG [a], S. PANYAKEOW [b], and S. RATANATHAMMAPHAN [c]

Semiconductor Device Research Laboratory, Nanotec Center of Excellence
Department of electrical Engineering, Chulalongkorn University, Bangkok 10300, Thailand
[a]poonyaseri@hotmail.com, [b]s_panyakeow@yahoo.com, [c]rsomchai@chula.ac.th

Keyword: InGaAs insertion layers, InAs quantum dots, molecular-beam epitaxy system, GaAs

Abstract. InAs quantum dots (QDs) have been grown by solid-source molecular beam epitaxy on different $In_xGa_{1-x}As$ ($0 \le x \le 0.3$) to investigate the effect of In-mole-fraction and thickness of InGaAs insertion layer (IL) on the structural and optical properties of the QDs. The density of QDs directly grown on GaAs is 1×10^{10} cm^{-2}, and increase to $1.4\text{-}1.8\times10^{10}$ cm^{-2} on InGaAs layers which depend on the In-mole-fraction and thickness of InGaAs layers. The effects of In-mole-fraction and thickness of InGaAs insertion layer on optical properties of the QDs are studied by photoluminescence (PL). The FWHM of PL spectrum corresponds to the size distribution of the QDs.

Introduction

Self-assembled InAs/GaAs quantum dots (QDs) have been studied extensively over the last decade due to its possibility for various applications such as single-electron transistors and QDs lasers [1]. One important issue in QD structure is gain saturation because of the finite number of states in QD structures. In order to overcome this limitation, it is necessary to increase the dot density without optical property degradation. A common method to increase the dot density is to grow multi-stacks of QDs. However, the number of repeatedly grown QDs layers is limited by plastic relaxation of the stress [2]. Therefore, it is attractive to increase the dot density in one stack. Many researchers have used different matrices layer instead of a GaAs matrix to achieve high-density dots [3].

In this work, we compare the structural and optical properties of InAs QDs on 1-4 ML $In_xGa_{1-x}As$ ($0 \le x \le 0.3$) insertion layer with that on a GaAs surface. The atomic force microscope (AFM) and photoluminescence (PL) are used in this study.

Experimental Procedure

Samples studied here were grown on GaAs (100) substrates in a solid source molecular beam epitaxy system (Riber 32P). The growth process was monitored by a 15 KV reflection high-energy electron diffraction (RHEED) system. After removal of native oxide by heating the substrate at 600°C under As_4 beam. A 300 nm GaAs buffer layer was grown at 600°C and followed by an InGaAs layers grown at 500°C. The In-mole-fraction of InGaAs layers were 0.1, 0.2 and 0.3 and the thickness of InGaAs layers were 1, 2, 3, and 4 monolayer (ML). Then, 1.9 ML InAs QDs were grown at 500°C with a constant growth rate of 0.05 ML/s. Finally, a GaAs capping layer with a thickness of 100 nm was grown at 500°C. We also prepared the samples without capping layer for the observation of surface morphology by AFM. For PL tests, these samples were grown repeatedly with an additional 100 nm cap layer. An 488 nm line Ar-ion laser was used an excitation source, and the data were obtained by InGaAs PIN photodetector. We also grew InAs directly on GaAs substrates as reference samples for AFM and PL measurements.

Results and discussion

AFM results of QDs grown without and with a 1-4 ML $In_xGa_{1-x}As$ ($0 \le x \le 0.3$) IL are shown in Fig. 1(a). The dot densities are approximately 1.02×10^{10}-1.78×10^{10} cm^{-2} with increasing

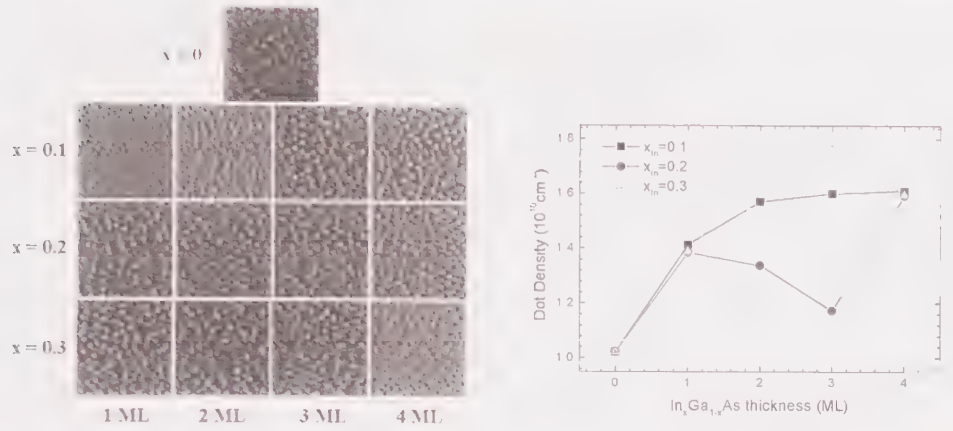

(a) (b)

Fig. 1 (a) AFM images of InAs QDs grown on 1-4 ML $In_xGa_{1-x}As$ ($0 \le x \le 0.3$) IL. (b) Dot Density of InAs QDs as a function of the In composition and thickness of the InGaAs IL.

indium composition and thickness of InGaAs IL. The increase in the dot densities is assumed that, as the indium composition increase, pre-existing indium atoms play a role of nucleation sites and an origin of the shortened diffusion length [4]. Fig. 1 (b) shows the relation of dot density of InAs QDs as a function of the In composition and thickness of the InGaAs IL. The highest density of 1.78×10^{10} cm^{-2} of InAs QDs is obtained for 3 ML $In_{0.3}Ga_{0.7}As$ IL.

Fig. 2 clearly shows the differences in the 77 K PL spectra under varied In-mole fraction and thickness of InGaAs layer. By increasing the indium composition and thickness of the IL, the PL line width and wavelength are broadened and blue-shifted. We attribute the broadening and blue-shifting to the dispersion of the size distribution of InAs QD. In the case of the 1-4 ML $In_{0.3}Ga_{0.7}As$ IL, the dot size is smaller than all of the cases (20% and 10% indium) due to the blue-shifted PL spectra. It is assumed that the blue-shift results from the reduction in dot size caused by the segregation of indium atoms on the InGaAs matrix materials when increasing an indium composition [5]. Fig. 3 shows the relation FWHM of InAs QDs as a function of the In composition and thickness of the InGaAs IL. We obtain the narrowest line width of 49 meV of InAs QDs from a 3 ML $In_{0.1}Ga_{0.9}As$ IL.

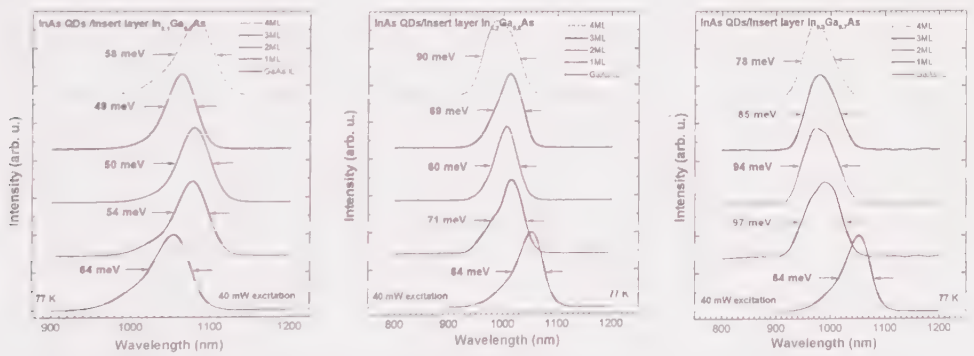

(a) x = 0.1 (b) x =0.2 (c) x = 0.3

Fig. 2 Comparison of PL spectra of InAs QDs grown on 1-4 ML $In_xGa_{1-x}As$ ($0 \le x \le 0.3$) IL at 77 K with an excitation intensity of 40 mW.

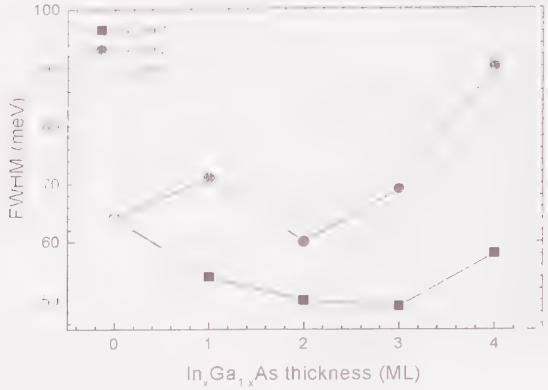

Fig. 3 FWHM of InAs QDs as a function of the In composition and thickness of the InGaAs IL.

Conclusions

We have systematically investigated the effect of a 1-4 ML $In_xGa_{1-x}As$ ($0 \le x \le 0.3$) IL on the optical and structural properties of InAs QDs. The line width of PL spectra of InAs QDs with IL can be improved by changing the In composition and thickness of the IL. The line width was narrowed to 49 meV at 77 K and the highest density of InAs QDs was 1.78×10^{10} cm^{-2}.

Acknowledgements

This work is supported by Thailand Research Fund (TRF), National Nanotechnology Center (Nanotec), Ministry of Education through the commission of higher education (CHE), Center of Excellence for Power Technology (CEPT) and Chulalongkorn University.The authors also would like to thank Mr. Boonchuay Supmonchai for his fruitful discussion, Mr Supachok Thainoi, Mr. Pornchai Changmaung, and Ms. Wipakorn jevasuwan for their technical assistance.

References

[1] K. Mukai, O. Nobuyuki, S. Mitsuru, and S. Yamzaki, Jpn. J. Appl. Phys., Part 2 vol. 33 (1994), p. L1710.

[2] J.He, B. Xu, Z.G. Wang, S.C. Qu, F.Q. Liu, T.W. Zhu, X.L. Ye, F.A. Zhao, Z.Q. Meng, J. Cryst. Growth vol. 240 (2002), p. 395.

[3] G. Park, O. B. Shchekin, D . L. Huffaker, and D. G. Deppe, IEEE photonics Technol. Lett. vol. 13 (2000), p. 230.

[4] A.R. Kovsh, A.E. Zhukov, A.Y. Egorov, V.M. Ustinov, Y.M. Shrenyakov, M.V. Maksimov, A.F. Tsatsulnikov, B.V. Volocik, A.V. Lunev, N.N Ledentsov, P.S. Kopev, Z.I. Alferov, Semiconductor vol. 32 (1998), p. 997.

[5] V.M. Ustinov, N.A. Maleev, A.E. Zhukov, A.R. Kovsh, A.Yu. Egorov, A.V. Lunev, B.V. Volovik, I.L. Krestnikov, Yu.G. Musikhin, N.A. Bert, P.S. Kop'ev, Z.h.I. Alferov, N.N. Ledentsov, D. Bimberg, Appl. Phys. Lett. vol. 74 (1999), p. 2815.

Advanced Materials Research Vol. 31 (2008) pp 135-137
online at http://www.scientific.net
© 2008 Trans Tech Publications, Switzerland

Investigation of Electrical Properties in Chalcogenide Thin Film according to Wave Length

H. Choi[a], H. K. Kim, Y. W. Koo, K. H. Nam, S. M. Koo, W. J. Cho, H. B. Chung[b]

431-1, B-Ma Bldg. 4F, Kwangwoon University, 447-1, Wolgye-Dong, Nowon-Gu, Seoul, Korea 139-70a

[a]heoragi79@hotmail.com, [b]hbchung@kw.ac.kr,

Keywords: chalcogenide, amorphous, resistance change, PMC(Programmable Metallization Cell), photo-doping, non volatile

Abstract. Programmable metallization cell (PMC) memory is based on the electrochemical control of nanoscale quantities of metal in thin films of solid electrolyte. We investigate the nature of thin films formed by the photo-dissolution of Ag into Ge-Se-Te glasses for use in programmable metallization cell devices. Glassy alloys of a-$Ge_{25}Se_{75-x}Te_x$(x = 0, 25) are prepared by well known melt-quenching technique. Thin films of a-$Ge_{25}Se_{75-x}Te_x$(x = 0, 25) glassy alloys are evaporated by vacuum evaporation technique at ~10^{-6} torr on glass substrate at room temperature. Optical properties in this study concerns photo-diffusion of Ag on Ag-doped Ge-Se-Te electrolytes. With these promising properties, the composition a-$Ge_{25}Se_{75-x}Te_x$(x = 0, 25) is recommended as a potential candidate for PMC-RAM.

Introduction

Amorphous Ge-Se thin films attract attention because of ease of preparation, ultra-fine pattern ability and wide glass-forming range, which can make various structures easily fabricated by different types of preparation [1]. Amorphous chalcogenide thin films have attracted much attention as a new advanced and replaceable technology material because of their interesting electrical, optical and thermal properties including resistance and reflectance change.[2-3] We have been studied the development of new composition of the improvement of hologram grating diffraction efficiency for 3D real-time optical information mass-memory storage medium on amorphous chalcogenide thin films.[4] Analyzing the basic mechanism, we investigated the resistance of Ag doped chalcogenide thin film varied by applied voltage bias direction from about 1MΩ to several tens Ω. As well as the opposite direction voltage bias applied, the resistance value return to higher value. As the result of these resistance change effect, it was found that these effect were agree with Programmable Metallization Cell-RAM (PMC-RAM). It has been demonstrated that Programmable Metallization Cell (PMC) memory shows great promise as a future low energy non-volatile solid state memory. The technology utilizes the electrochemical formation and removal of metallic pathways in thin films of solid electrolyte. In this paper, we investigate the nature of thin films formed by the photo-doping of Ag into chalcogenide materials for use in programmable metallization cell devices. Optical properties in this study concerns photo-diffusion of Ag on Ag-doped Ge-Se-Te electrolytes. These devices rely on metal ion transport in the film so produced to create electrically programmable resistance states. The results imply that a Ag-rich phase separates due to the reaction of Ag with free atoms from the chalcogenide materials.

Experiment

The a-$Ge_{25}Se_{75-x}Te_x$(x = 0, 25) bulk glasses were prepared by a conventional melt quenching technique. a-$Ge_{25}Se_{75-x}Te_x$(x = 0, 25) thin films were prepared by thermal evaporation of the bulk at a deposition rate of about 2 Å/s on SiO_2/Ni(100nm)/p-type Si(1 0 0) kept in vacuum ~$2x10^{-6}$ Torr. No intentional control of the substrate temperature was made. The final deposited film thickness was in order of 60nm. Following this, a silver 30nm thick was deposited without breaking vacuum. As the

shown Fig. 1, the Ag was then dissolved into the base glass by photodissolution at room temperature using exposure to Ar laser(433nm) and He-Ne laser(632.8nm) broadband source with an energy density at the wafer surface of 1 J/cm^2. Following dissolution, an additional 100 nm of Ag was added to ensure a continuous oxidizable source for electrodeposition and this also acted as the top electrode. Electrical characteristics of the test devices were obtained by connecting the electrodes, via tungsten probes held in micromanipulators in a vibration and electromagnetic interference-isolated probe station, to a semiconductor parameter analyzer (SPA - Agilent 4155B).

Results and Discussion

Fig. 2 describes a resistance-voltage plot of Ag-doped $Ge_{25}Se_{50}Te_{25}$ electrolyte that is exposed by He-Ne laser. An initial resistance value was $10^9\Omega$ at fabricated device. Until initial 4.5V, it was changed near initial resistance value while at 4.52V around shown sharply changed resistance of 85kΩ in the same time of voltage applies. The low resistance state was maintained until 5V. Repeatedly, the device switches at -4.58V from an on-state resistance above 85kΩ to an off-state resistance, $10^9\Omega$. Fig. 3 shows a representative resistance-voltage plot of Ag-doped $Ge_{25}Se_{75}$ electrolyte that is exposed by He-Ne laser. The applied voltage sweep was 0V to +5.0 V to -5.0 V and the current limit is 50 μA. The device switches at 3.89V from an off-state resistance, R_{off}, above $10^7\Omega$ to an on-state resistance, R_{on} = 4.5kΩ, more than three orders of magnitude lower for this programming current. The device transition to a high resistance state occur at -3.83V. Continuing the negative sweep, the off resistance remains above $10^7\Omega$ as the voltage is swept out to -5.0V. In this case, because of VAPs's doping by electrical combine of defect-pair of chalcogenide thin film which is diffused by photo-dissolution of Ag ion in the chalcogendie, the electro-resistance is sharply decrease and maintain low resistance state by the irradiation of induced light. We used an electrical energy to induce Ag ion to diffuse beside optical energy. As a result, it maintained low resistance state(a bond of Ag^+ ion - VAPs) at forward bias and high resistance state(Ag^+ density change by the destruction of bond) at reverse bias. We induced Ag doping phenomenon by electrical energy at amorphous chalcogenide thin film. Fig. 4 shows a resistance-voltage plot of Ag-doped $Ge_{25}Se_{50}Te_{25}$ electrolyte that is exposed by Ar laser. An initial resistance value was $10^9\Omega$ at fabricated device. It was changed near initial resistance value while at 3.26V around shown sharply changed resistance of 85kΩ in the same time of voltage applies. Conversely, the device switches at -3.31V from an on-state resistance above 85kΩ to an off-state resistance, $10^9\Omega$. Fig. 5 gives an example of resistance-voltage plot of Cu-doped $Ge_{25}Se_{75}$ electrolyte that is exposed by Ar laser. For forward bias experiment, it decreased resistance about $10^4\Omega$ at 2.53V. When it was applied reverse bias, it could explore a change of resistance about $10^7\Omega$ at -2.51V in same device. In this experiment, we confirmed that photo-doping by Ar laser shows lower switching voltages compared to exposed devices by He Ne laser. This result showed that during the process for Ag-doped a-$Ge_{25}Se_{75-x}Te_x$(x = 0, 25) devices photo-doped by He-Ne laser, not enough Ag ions got into a-$Ge_{25}Se_{75-x}Te_x$(x = 0, 25) We can confirm this with the early resistance of the device and the ratio of the resistance ON state. As a result of the experiment of photo-doping by lasers with varied wave lengths, it is considered that it is relatively more effective for the device to be photo-doped by laser with low wave length with the same energy.

Summary

We have investigated the metal photo-doping effect and electrical characterization in the system of Ag(30nm)/ a-$Ge_{25}Se_{75-x}Te_x$ (60nm) using the Ar laser and He-Ne laser. As a result, the technology stores data in a Ag based chalcogenide thin film. These devices have excellent switching characteristics application for programmable metallization cell. During the process of photo-doping the device by Ar laser with the shortest wave length, the lowest on-off switching voltage was obtained. Especially, $Ge_{25}Se_{75}$ devices shows lower switching voltage compared to $Ge_{25}Se_{50}Te_{25}$. Through this experiment, we confirmed that the dissolution of Ag entering chalcogenide thin film differs according

to the wave length of laser, and that the closer to UV the wave length gets, the more effective photo-doping is.

Acknowledgements

This research was supported by the MIC (Ministry of Information and Communication), Korea, under the ITRC (Information Technology Research Center)support program supervised by the IITA (Institute of Information Technology Assessment) (IITA-2006-C1090-0603-0018).

References

[1] H.Y. Lee, H.B. Chung: J. Vac. Sci. Technol. Vol. B15 (1997), p.818-822.

[2] H.B.Chung and C.Y.Park: J.of KIEE. Vol.29 (1979), p.111.

[3] H.Y.Lee, S.H.Park, J.Y.Chun and H.B.Chung: J. Appl. Phys. Vol. 83 (1998), p.5381.

[4] J.I.Park, J.T.Lee, C.H.Yeo, Y.J.Lee, J.B.Kim and H.B.Chung: Jpn. J. Appl. Phys. Vol.42 (2003), p5090.

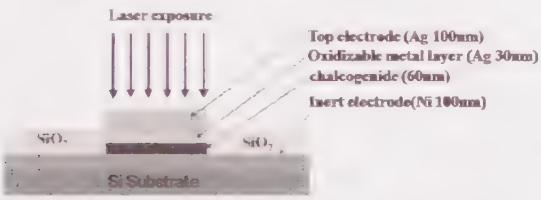

Fig. 1 Schematics of photo-doping process and fabricated devices

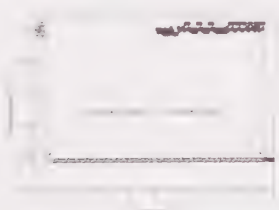

Fig. 2. A resistance-voltage plot of Ag-doped $Ge_{25}Se_{50}Te_{25}$ electrolyte that is exposed by He-Ne laser.

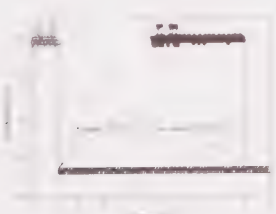

Fig. 3. A resistance-voltage plot of Ag-doped $Ge_{25}Se_{75}$ electrolyte that is exposed by He-Ne laser.

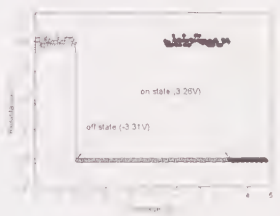

Fig. 4. A resistance-voltage plot of Ag-doped $Ge_{25}Se_{50}Te_{25}$ electrolyte that is exposed by Ar laser.

Fig. 5. A resistance-voltage plot of Cu-doped $Ge_{25}Se_{75}$ electrolyte that is exposed by Ar laser.

Advanced Materials Research Vol. 31 (2008) pp 138-140
online at http://www.scientific.net
© 2008 Trans Tech Publications, Switzerland

Luminescence Properties of ZnS:Er Quantum Dots With NIR Excitation

Xiaosong Zhang[1, 2], Xiaoyi Dong[1], Guiyun Kai[1], Dongqing Dong[2], Yanfang Zhang[2] and Zhi Wang[1]

[1] Key Laboratory of Opto-electronic Information and Technology, Institute of Modern Optics, Nankai University, Tianjin 300071, China

[2] Tianjin Key Laboratory for Photoelectric Materials and Devices, Tianjin University of technology, Tianjin 300191, China

email: zhangxiaosong@tjut.edu.cn

Keywords: ZnS:Er quantum dots, Infrared excitated, photoluminescence, aqueous medium,

Abstract. ZnS:Er quantum dots were prepared in the aqueous medium from readily available precursors. The construction, morphology and luminescence properties of the ZnS:Er quantum dots were evaluated by XRD,TEM and photoluminescence spectra. Furthermore, the 1590 nm emission of the ZnS:Er quantum dots excited by a 785.0 nm NIR laser were discussed.

Introduction

Semiconductor quantum dots (QDs) are nanometer-sized crystals in the size range of 1-10 nm diameter with unique chemical and physical properties, especially photophysical properties [1-3]. QDs become good candidates for applications in light-emitting diodes (LEDs), laser, luminescent bio-probes and bio imaging *in vivo* and photoelectrochemical cells [4-7]. Moreover, infrared-emitting quantum dots, excited by the near infrared light source, accomplish the requirement and can be used for the deep-tissue imaging. In addition, lasers emitting in the infrared region have attracted considerable interest due to its using for eye-safe laser application in optical communication, medicine and laser radar. Specially, Er doped quantum dots have been fabricated for infrared applications because of unique properties [8], in which ZnS as a great host media for dopant have been intensively studied for infrared applications due to lower phonon energies (which reduce the extent of electron-phonon interaction and improve the laser performance) and non-toxic [9]. However, Little investigation of infrared-emitting quantum dots excited by the near infrared light source has been investigated. In this research, we present free-standing ZnS:Er quantum dots from readily available precursors. And luminescent properties of ZnS:Er quantum dots with the varying initial concentration of Er^{3+} excited by the near infrared excitation were studied.

Experimental procedure

All steps of the synthesis were carried out at room temperature and all chemicals used were AR grade. A aqueous solution of $Zn(CH_3COO)_2 \cdot 2H_2O$ was added to $Na(PO_3)_n$ with vigorous stirring at room temperature. Then $Er(CH_3COO)_3 \cdot nH_2O$ was added in small portions to this solution. The mixture was sonicated to ensure complete dissolution. Next, Na_2S was added at a low flow rate, and a suspension was formed at this stage. The reaction temperature was maintained at ambient temperature for 2 h under constant stirring. The ZnS:Er quantum dots were isolated by centrifugation, washed twice. Three kinds of ZnS:Er quantum dots were prepared in this way by varying the initial amount of Er^{3+} salt used during the fabrication. Powder X-ray diffraction (XRD) spectra were collected on a Rigaku D/MAX 2500 X-ray diffractometer with the Kαline of Cu as a radiation source. Size and morphology of ZnS:Er quantum dots were measured using a FEI Tacnai G2 F20 field emission transmission electron microscope. Photoluminescence (PL) spectra of ZnS:Er quantum dots were performed on an ACCENT rpm2000 Apace Scan Fluorescence Spectrum excited by the 785.0 nm near infrared (NIR) laser at room temperature.

Results and Discussion

X-ray Diffraction. The construction of ZnS:Er quantum dots was characterized by XRD. XRD patterns of three kinds of quantum dots samples containing (b) 4%, (c) 10% and (d) 20% (in molar ratio) of Er^{3+} ions are shown in Fig. 1 respectively. It can be seen that all samples exhibit one phase. And this phase has the equilibrium structure of zinc blende crystal, which is displayed as an underlying pattern [vertical lines in Fig. 1 (a)]. The diffraction peaks of ZnS:Er QDs are broadened prominently, which is characteristic of nanoparticles. Yet, no peak corresponding to erbium compounds is observed, demonstrating that Er^{3+} ions are dispersed in ZnS matrix.

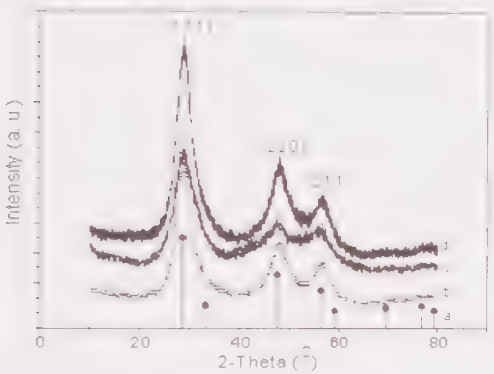

Figure 1. XRD patterns of ZnS:Er quantum dots: (a) bulk ZnS blende peak position; (b) QD doped with 4% Er^{3+} ions; (c) QD doped with 10% Er^{3+} ions; and (d) QD doped with 20% Er^{3+} ions.

Figure 2. HRTEM of 4% Er^{3+}-doped ZnS:Er quantum dots at room temperature in bright field.

Transmission Electron Microscopy. High-resolution transmission electron microscopy (HRTEM) allows the imaging of individual crystallites and the development of a description of the size and the shape of particles in a sample. The HRTEM image of 4% Er^{3+}-doped ZnS:Er quantum dots at room temperature is shown in Fig. 2. The shape of particles is approximately spherical, and diameters are 4nm for ZnS:Er quantum dots. By comparing the result of XRD and HRTEM, the quantum dots size calculated from XRD pattern is in accord with the result from HRTEM image.

Photoluminescence. One of important factors in selecting the host material for infrared emission is the phonon energy of the lattice vibrations. ZnS as a great host media for dopant is of great interest due to lower phonon energies and non-toxic [9]. The room temperature photoluminescence spectra of ZnS:Er quantum dots samples containing (a) 4%, (b) 10% and (c) 20% (in molar ratio) of Er^{3+} ions pumped by the 785.0 nm laser are shown in Fig. 3. These three spectra all have broad emission between 1550 nm and 1610 nm centered at 1590 nm, which can be attributed to the $^4I_{13/2} \rightarrow {}^4I_{15/2}$ transition. The intensity of the 1590 nm emission significantly increases with the increase of the Er concentration, while the peak position does not shift. And the concentration quenching is not shown in this study. The characteristics of the 1.5 μm emission are almost identical to the emission observed for Er^{3+} ions in some nanoparticales corresponding to $^4I_{13/2} \rightarrow {}^4I_{15/2}$ transition. In ZnS:Er quantum dots, Er^{3+} ions occupy Zn^{2+} lattice sites in the ZnS host lattice. ZnS:Er quantum dots had a wider fluorescence spectrum in 1590nm region. It is because that the symmetry of ZnS:Er quantum dots descend remarkably, additionally lower symmetry of the Er^{3+} ions neighborhood structure causes the Γ_8 states of $^4I_{15/2}$ and $^4I_{13/2}$ to split further into two Kramer doublet states, therefore more transitions occur and lead to the broad emission in photoluminescence spectra.

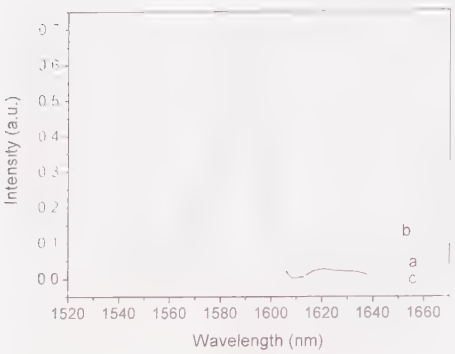

Figure 3 Photoluminescence spectra of ZnS:Er quantum dots pumped by the 785.0 nm laser with the dopant concentration: (a) doped with 4% Er^{3+} ions; (b) doped with 10% Er^{3+} ions; (c) doped with 20% Er^{3+} ions.

Summary

ZnS:Er quantum dots prepared in the aqueous medium from readily available precursors were investigated in this study. The construction, morphology and luminescence property of ZnS:Er quantum dots was characterized by XRD, HRTEM and PL. The shape of the particles is approximately spherical, and the diameters are approximate 4nm for ZnS:Er quantum dots. The laser wavelength at 785.0 nm was utilized as the excitation source. ZnS:Er quantum dots had a wider fluorescence spectrum in 1590nm region through the $^4I_{13/2} \rightarrow {}^4I_{15/2}$ transition. With the increase of the Er concentration, the intensity of the emission significantly increases. Hopefully, ZnS:Er quantum dots, as the reference optical material, can be applied into infrared bio-probes and bio-imaging, sensor, and optical communication device.

Acknowledgements

The authors are grateful to the Tianjin Natural Science Foundation (Grant No. 07JCYBJC06400), the National Key Basic Research and Development Program of China (Grant No. 2003CB314906) and the National Natural Science Foundation of China (Grant No. 10674074).

References

[1] DaeGwi Kim, Tetsuya Kuwabara, and Masaaki Nakayama: Journal of Luminescence, Vol. 119-120 (2006), p. 214

[2] W.Q. Peng, S.C. Qu, G.W. Cong, X.Q. Zhang and Z.G. Wang: Thin Solid Films, Vol. 499 (2006), p. 104

[3] Xiaosong Zhang,Xiaoyi Dong, Yange Liu, Guiyun Kai, Zhi Wang, Lan Li, Xu Han and Yan Li: Journal of Optoelectronics·Laser, Vol. 17 addition (2006), p. 76

[4] Michael J. Bowers II, James R. McBride, and Sandra J. Rosenthal: Journal of American chemical society, Vol. 127 (2005), p. 15378

[5] Roger F Uren: Nature Biotechnology, Vol. 22 (2004), p. 38

[6] Wen Jiang, Eli Papa, Hans Fischer, Sawitri Mardyani and Warren C.W. Chan: TRENDS in Biotechnology, Vol.22 (2004), p. 607

[7] Yan Xiao and Peter E. Barker: Nucleic Acids Research, Vol. 32 (2004), p. e28

[8] Thomas Schmidt, Gerd Muller, Lubomir Spanhel, Klaus Kerkel and Alfred Forchel: Chemistry of Materials Vol 10 (1998), p.65

[9] S. C. Qu, W. H. Zhou, F. Q. Liu: Applied physics letters, Vol. 80 (2002), p. 3605

Advanced Materials Research Vol. 31 (2008) pp 141-149
online at http://www.scientific.net
© 2008 Trans Tech Publications, Switzerland

The Synthesis and Crystallography of Some Novel ZnO Nano- and Micro-Crystals and Structures

Zongmu LI, Faqiang XU, Wenhua ZHANG

National Synchrotron Radiation Laboratory, University of Science and Technology of China, Hefei, Anhui 230029, PR China

A variety of novel hierarchical ZnO structures, such as intergrowth crystals, nanorings encircled nanoprisms, microtowers etc., have been synthesized by evaporation of zinc powder at 420 ~ 450 °C. The growth mechanisms of these interesting ZnO crystals were discussed, respectively. The ZnO microstructures with various morphologies may have potential applications in catalyst carrier, chemical sensors and optoelectronic microdevices.

Introduction

As a wide-band semiconductor, ZnO has been intensively studied in recent years to exploit the unique properties of this special compound, meanwhile a variety of micro- and nanometer ZnO crystals with oriented structures, such as nanowires,[1] tetrapods,[2] nanobelts,[3] hierarchical nanostructures,[4] nanoplates,[5] nanorings and nanobows,[6] nanotubes[7] etc., have been prepared. Since the microstructures of these ZnO crystallites have been proved to play crucial roles in the determination of their properties, the ability to control the shapes or specific morphologies of ZnO crystals, including the crystal size, orientation and aspect ratio, is becoming one of the challenging issues in extending their applications.

In the typical chemical vapor transport (CVT) or chemical vapor deposition (CVD) method, the temperature up to 900°C or even higher were usually used to synthesize ZnO crystallites.[9,10] In vapor-liquid-solid (VLS) process, the catalysts were adopted which inevitably have an impact on the properties of the ZnO nanowires and other nanostructures.[11,12] Therefore, to synthesize ZnO single or complex structures with controlled crystalline morphology, orientation and surface architecture under catalyst-free and mild conditions is still a significant challenge. Here we used a low-temperature and catalyst-free method to synthesize ZnO crystallites, several novel microstructures have been obtained, which may help us to understand the growth mechanisms of diversiform shapes of ZnO crystals.

Experimental Section

A p-type silicon wafer was used as the substrate to prepare the intergrowth ZnO crystals. It was cleaned with acetone and deionized water subsequently. The zinc powder (99.999%) was arranged in a self-made quartz boat and the clean Si wafer was placed above zinc powders. The distance between the Si wafer and the zinc powder ranged from 2 mm to 5 mm. After the Zn powder boat was placed in a quartz tube located in a horizontal tube furnace, the quartz chamber was filled with flowing argon gas (120 sccm) for 30 min and was heated to 420 ~ 450 °C at a rate of 20 °C/min. When the system reached the desired working temperature, the process of synthesizing ZnO microstructures was maintained for 120 min. After the growth, the furnace was cooled to room temperature slowly. A field emission scanning electron microscopy (FESEM, JSM-6700F) equipped a field emission gun was used for the high-resolution FESEM measurement. The crystal structure and the phase measurements were analyzed by powder X-ray diffraction (XRD). The X-ray diffraction data were collected on a D/max-rA diffractometer with Cu Kα as the excitation source. The room temperature PL spectra were performed on LABRAM-HR (JY) equipped with a He-Cd laser (325nm).

Results and Discussion

By collecting the products from different positions in the quartz tube and adjusting the ambience within the system, a series of novel ZnO hierarchical structures from micro- to nanometer scale, including intergrowth of micrometer ZnO crystals, nanorings and nano-, microprisms and microtowers were obtained by heating the zinc powder to 420 ~ 450 °C.

1. Intergrowth of micrometer ZnO crystals

Figure 1 shows the FESEM images of the 3D microstructures formed by the intergrowth of ZnO crystallites on a Si wafer at 450°C. Figure 1a is a low-magnification image showing the initial stage of the intergrowth process. It can be seen from Figure 1b that porous, complex, three-dimensional networks have been built by oriented ZnO chains. As seen from another high-magnification picture (Figure 1c), the chains are about several tens of micrometers long and each chain consists of several polyhedrons and the magnitude of the polyhedron is about 1~3 μm. Figure 1d is a cross-shaped ZnO nanostructure. Although this kind of structure is usually found in minerals, such as staurolite, the

penetration twin is rarely observed in artificial crystals. Closer examination of these nanostructures reveals that the chains seem to be assembled by well-faceted crystalline units along an axis, which indicates that each chain may have formed an individual bulk crystal, not aggregates of several polyhedrons.

How the complex ZnO microstructure formed is an interesting issue, especially when taking into the fact that they formed at relative mild temperature and pressure. In nature, the intergrowth of minerals was a familiar phenomenon but rarely observed in vapor-phase synthesis. The intergrowth of minerals like calcite came into being under very high pressure and temperature and experienced long geological ages. Understanding the growth nature of such materials is not a trivial task because they formed via a very complex and long process and it's difficult to reproduce the growth environments in the synthesis. Therefore, the formation mechanism of the synthetic intergrowth structures is worth of discussion. Recently Penn and Banfield presented a new mechanism called "oriented attachment (OA)" when they observed that anatase titanium and iron oxide particles could coalesce to give bigger crystals under hydrothermal conditions[13]. According to the OA mechanism, well-defined ZnO nanorods have been grown from individual nanoparticles and the synthesis of three-dimensional structures has been suggested [14]. According to the characters of our products, the growth of ZnO microchains could be attributed to the imperfect OA mechanism in the vapor phase. When the zinc powder was heated to 400 ~ 450 °C, a high zinc vapor pressure can be produced because of the low evaporation temperature of zinc metal. In an atmosphere containing trace of oxygen, the evaporated 'floating' zinc can be easily oxidized to produce lots of ZnO crystallites. As a result, a ZnO-rich zone would be formed between the materials boat and the substrate at equilibrium. The ZnO crystallites will be transferred near the substrate surface by the gas flow. At the initial stage, it is inevitable for the ZnO microcrystals to collide constantly with the Si surface to form a monolayer of ZnO crystallites as shown in Figure 3a. The absorbed ZnO crystallites possess different shapes with different orientation facets exposed. Afterwards, the arriving crystallites continued to aggregate and subsequent deposition occurred on the microsteps of the ZnO polyhedrons. The occurrence of highly anisotropic growth may be inherent in the wurtzite III-V system, which offers an opportunity for forming the one-dimensional nano- or microstructures in a wide range of process conditions.[15] The synthesis of intergrowth ZnO suggests that other complex three-dimensional architecture may be targeted by this approach.

To understand the crystal structure and optical properties of the ZnO microstructures, X-ray diffraction (XRD) and photoluminescence (PL) spectra were measured. The XRD pattern in Figure 2 reveals the overall crystal structure and phase quality of the products. The diffraction peaks can be indexed to hexagonal-structured ZnO, well the strong intensities relative to the background indicate the high purity of the resulting products. The PL spectra of the hierarchical nanostructure ZnO at room temperature were obtained using an excitation of 325nm He-Cd laser. From Figure 3, an intense PL peak centered at ~382 nm and a weak green light emission at ~520 nm were observed, corresponding to the near bandgap edge emission and the deep-level or trap-state emission, respectively[16].

2. Nanorings and nano-, microprisms

ZnO nanorings prepared by Wang[17] et al are very peculiar structures, which are formed by self-coiling of nanobelts due to long-range electrostatic interaction. But the diameters of the rings smaller than 0.8 μm have not reported because they are energetically unfavorable. In our systemically synthesized ZnO nanostructures, a bunch of ZnO rings with diameters as small as 100 nm on zinc oxide nanorods were detected over the surface of the residual powders after the thermal evaporation of zinc powder at 425 °C. The FESEM images in Figure 4a-d show the details of the nanorings bunched on a nanorod. Figure 4b clearly shows that the nanorings are not circular but hexagonal, which enclose the six side faces of the nanorod. This also indicates that the nanorods are hexagonal prisms rather than cylinders. By careful observation, the nanorings are not parallel each other and the distance between the rings are range from 0.2-2 μm. The inner diameter of the ZnO ring is about 100 - 200 nm as same as the diameter of the nanoprism. The image in Figure 4d is an extreme case when the hexagonal prisms are too thick. It can be seen that when the diameter of ZnO prism is bigger than 1 μm, no orbicular nanorings are formed. As a result, many ZnO stripes adhering to the hexagonal prism were detected as if the stripes were too short to enclose the ZnO prisms.

According to the Kong's calculation,[18] the diameter of a free-standing zinc oxide nanoring has a threshold, that is to say, the nanoring structure is energetically unfavorable once the diameter of the nanoring is smaller than the threshold. While in our case, the nanorings are not free-standing but

enclose the side faces of the prisms, such kind binding mode may be favorable for minimizing the surface energy. So the diameters of the nanorings may not be limited by the calculation model, nanorings with much smaller diameters could be formed.

The PL properties of the nanorings and the prisms were also shown in Figure 3. It is clear that similar PL properties with an intensive UV peak at 380 nm and a weaker green band around 510 nm were observed compared with the PL spectrum of the intergrowth ZnO though they have great differences in morphologies. The room temperature PL spectrum shows excellent optical quality of the nanorings and prisms, and therefore, these ZnO nanostructures could be used as building blocks of optical nanoscale devices.

3. Microtowers

When the zinc powder was vaporized in air flow, another interesting hierarchical structure, namely, tower like ZnO columns were produced in the remains. As the corresponding FESEM images show in Figure 5, the as-observed ZnO microtowers were uniform both in size and morphology. These columns are about several tens of micrometers in length, 3 μm in diameter. As can be seen from Figure 5a, most of the products have irregular polyhedrons on the end, while a few of them have terrace tips. The FESEM image shown in Figure 5b reveals that the side surfaces of the typical tower-like column are well-faceted and very clean. The most striking feature is that the columns have clear terraces surfaces, as shown in Figure 5b-d. Figure 5d shows an amplified top-view image of a single column, which indicates the tops of some nanorods are very flat, and the cross section of the column has an irregular polygon structure.

The tower-like structures reported in this study are similar to the ZnO fibers with periodic junctions,[19] the differences lie on two modifications in our experiment, low synthesizing temperature and catalysts free. Since no catalyst was used, the growth of such ZnO structure is suggested to be governed by the VS process [20] in which the morphologies are primarily controlled by temperature and the supersaturation extent [21]. The variation of the microtower dimensions also indicates that the growth is a kinetic-driven process. The oxygen partial pressure may play an important role in determining the different morphologies of ZnO structures.[22]

Conclusion

In summary, several kinds of novel nano/microstructures of ZnO have been synthesized by using a low-temperature, catalyst-free method. The crystallites exhibit excellent crystallographic quality judging from the narrow UV emissions excited by a 325nm He-Cd laser at room temperature and are suggested to form through an OA process in gas phase. It's believed that these new ZnO structures could be of new particular technological applications in optic and electronic minidevices. Moreover, this work offers a simple and catalyst-free route to explore the new structures of ZnO or other functional materials.

References

[1] Huang, M. H.; Mao, S.; Feick, H.; Yan, H.; Wu, Y.; Kind, H. weber, E.; Russo, R.; Yang, P. *Science*, **2001**, *292*, 1897.

[2] Yan, H. Q; He, R. R; Pham, J.; Yang, P. D. *Adv. Mater*. **2003**, *15*, 402.

[3] Pan, Z. W.; Dai, Z. R.; Wang, Z. L. *Science*, **2001**, *291*, 1947.

[4] Lao, J.; Wen, J.; Ren, Z. *Nano letter*. **2002**, *2*, 1287.

[5] Tian, Z.; Voigt, J. A.; Liu, J.; Mckenzie, B.; Mcdermott, M. J.; Rodriguez, M. A.; Konishi, H.; Xu, H. *Nat. Mater*. **2003**, *2*, 821.

[6] Kong, X.; Ding, Y. Yang, R.; Wang, Z. L. *Science*, **2004**, *303*, 1348.

[7] Hughes, W. L.; Wang, Z. L. *J. Am.Chem. Soc.* **2004**, *126*, 6703.

[8] Xing, Y. J.; Xi, Z. H.; Xue, Z. Q.; Zhang, X. D.; Song, J. H.; Wang, R. M.; Xu, J.; Song, Y.; Zhang, S. L.; Yu, D. P. *Appl. Phys. Lett.* **2003**, *83*, 1689.

[9] Huang, M. H.; Wu, Y.; Feick, H.; Tran, N.; Weber, E.; Yang, P. *Adv. Mater*. **2001**, *13*, 113.

[10] Wang, G. Z.; Ma, N. G.; Deng, C.J.; Yu, P.; To, C.; Y. Hung, N. C.; Aravind, M.; Ng, Dickon H. L. *Mater. Lett*. **2004**, *58*, 2195.

[11] Gu, G.; Burghard, M.; Kim, G. T.; Düsberg, G. S.; Chiu, P. W.; Krstic, V.; Roth, S.; Han, W. Q. *J. Appl. Phys*., **2001**, *90*, 5747.

[12] Nguyen, P.; Ng, H. T.; Meyyappan, M. *Adv. Mater*. **2005**, *17*, 1777.

[13] (a) Penn, R. L.; Banfield, J. F. *Science*, **1998**, *281*, 969. (b) Banfield, J. F.; Welch, S. A.; Zhang, H.; Ebert, T. T.; Penn, R. L. *Science*, **2000**, *289*, 751.

[14] Pacholski, C.; Kornowski, A.; Weller, H. *Angew. Chem. Int. Ed.* **2002**, *41*, 1188.

[15] Wang, Z. L. *Nanowire and Nanobelets-Materials, Properties, and Devices*; Tinghua University Press: Beijing, 2004, Vol I.

[16] Huang, M. H.; Wu, Y.; Fieck, H.; Tran, N.; Weber, E.; Yang, P. D. *ADV. Mater.* **2001**, *13*, 113

[17] Kong, X. Y.; Ding, Y.; Yang, R. S.; Wang, Z. L. *Science*, **2004**, *303*, 1348.

[18] Kong, X. Y.; Wang, Z. L. *Nano. Lett.* **2003**, *3*, 1625.

[19] Huang, L. S.; Wright, S.; Yang, S. G.; Shen, D. Z.; Gu, B. X.; Du, Y. W. *J. Phys. Chem. B.* **2004**, *108*, 19901.

[20] Levitt, A. P.; Ed.; Whisker Technlology; Wiley-interscience: New York, 1970.

[21] Wang, Z. L. *Annu. Rev. Phys. Chem.* **2004**, *55*, 159.

[22] Hao, Y. F.; Meng, G. W.; Ye, C. H.; Zhang, X. R.; Zhang, L. D. *J. Phys. Chem. B.* **2004**, *109*, 12704

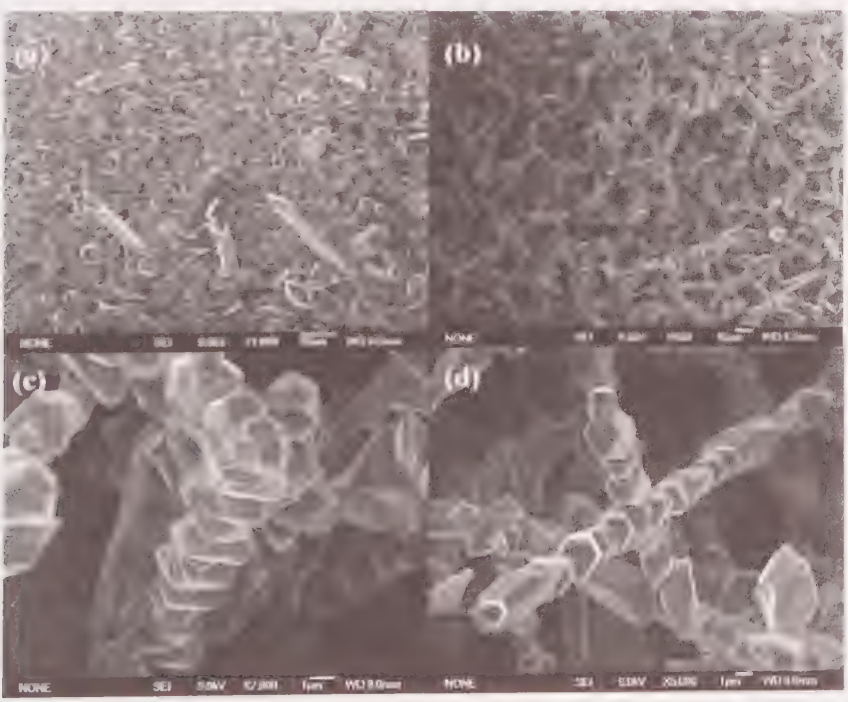

Figure 1. SEM images of oriented ZnO microstructures: a) A low-magnification image showing the uniformity of the microstructure, b) High-magnification of the columns of ZnO, c) A cross-shaped ZnO column composed of small hexagonal microrods and polyhedrons

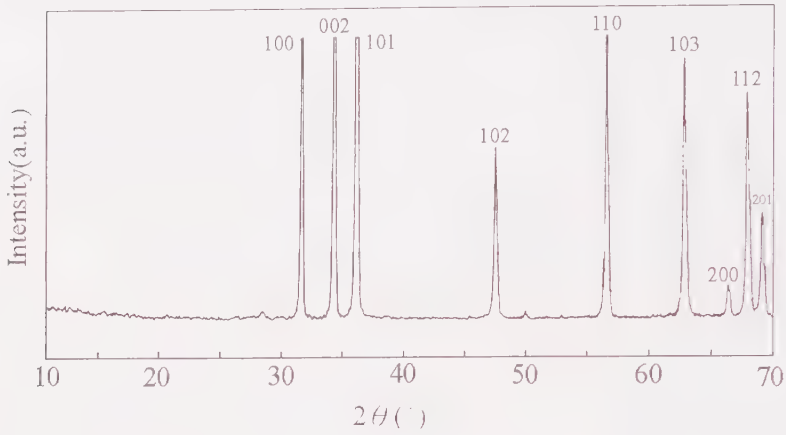

Figure 2. XRD pattern of the 3D structure formed by the intergrowth ZnO cryatallites.

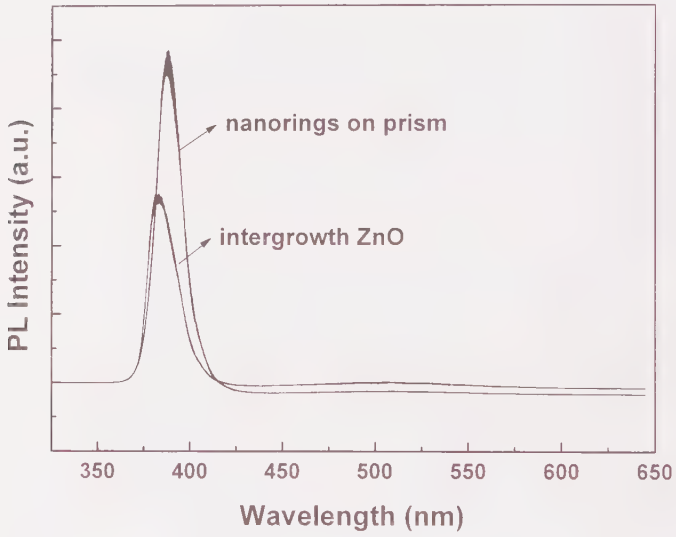

Figure 3. Room temperature PL spectra of ZnO products.

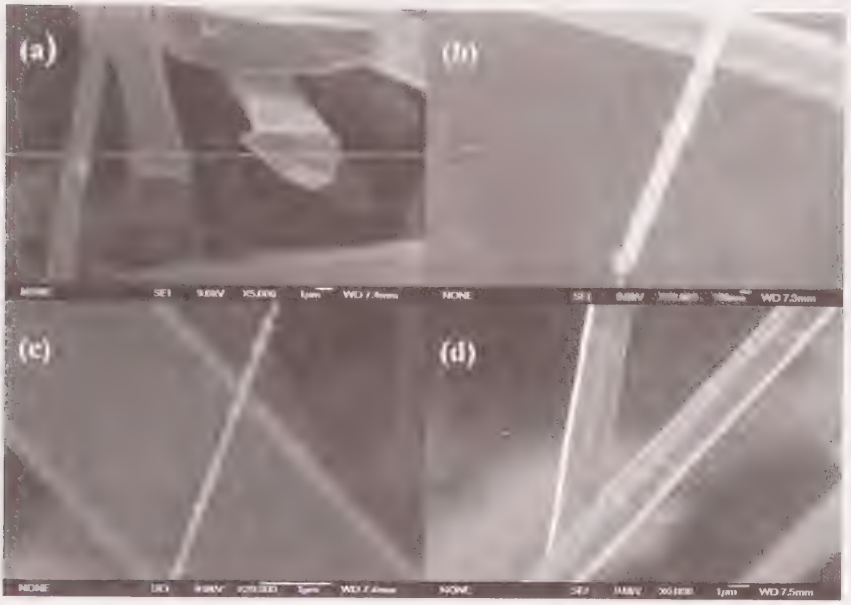

Figure 4. FESEM images of nanorings on nanoprisms.

Figure 5. FESEM images of the microtower-like ZnO.

Advanced Materials Research Vol. 31 (2008) pp 150-152
online at http://www.scientific.net
© 2008 Trans Tech Publications, Switzerland

Degradation of Photoluminescence in CdTe Nanoparticles Due to Cl_2 Contamination

Hannah C. Gardner, Birju Patel, Cristina Bertoni, Diego E. Gallardo, Steve Dunn

Nanotechnology Centre, Cranfield University, Cranfield, Bedfordshire, MK430AL, UK
s.c.dunn@cranfield.ac.uk

Keywords: CdTe, Nanoparticles, Quantum Dots, Chlorine, Photoluminescence.

Abstract. Nanostructured CdTe is proving a popular material for a variety of modern applications. Here, we report photoluminescent deterioration of CdTe due to Cl_2 contamination. Cl_2 gas was bubbled through a 2ml suspension of thioglycolic acid capped CdTe nanoparticles whilst photoluminescence was monitored. With the addition of only 0.02ml of Cl_2 a loss of luminescence intensity was observed. Addition of 0.4ml of Cl_2 resulted in a 70% loss of luminescence intensity, a 21nm shift in wavelength, and a large narrowing of the full-width-at-half-maximum. Cl_2 attacks the Cd-S bond in the thiol capping layer of the nanoparticle, disrupting the passivation of the nanocrystal, and allowing the formation of non-radiative trap states. Smaller nanocrystals with a larger surface area to volume ratio are more heavily affected as is shown in the selective reduction of intensity from the smaller particles resulting in a narrower full-width-at-half-maximum and an apparent photoluminescence shift. A decrease in overall intensity is seen due to the lower number of emitting particles.

Introduction

Semiconductor CdTe is proving a popular material for an abundance of applications. Nanoparticles of CdTe have been used as bioprobes [1], incorporated into light emitting devices [2,3] and even used as temperature sensitive gels [4]. Thin films of CdTe can be active components in solar cells [5] and nanowires of CdTe show potential in nanoelectronics [6]. Thus a study into factors affecting the properties of CdTe will have relevance over a wide range of nanosciences.

The broad wavelength transparency of MgF_2 makes it an ideal material for many optical applications. However, previous (unpublished) work in our group incorporating MgF_2 into light emitting devices showed fluorine to have a detrimental effect on electroluminescence from CdTe. To further investigate this effect, analogous experiments with Cl_2 gas have been conducted.

Several researchers have looked at the effects of annealing CdTe in a Cl_2 containing atmosphere and have reported both enhancement [7,8] and deterioration [8] of luminescence. Potter et al [8] suggest the deterioration of electroluminescence is due to over exposure to either S or Cl_2. The aim of this study is to look at the effects on luminescence of post-preparative Cl_2 treatment on CdTe nanoparticles.

Experimental

All CdTe nanoparticles used in this report were obtained from Dr. N. Gaponik at TU Dresden and were stored in the dark at 3-5°C prior to use. The nanoparticles were synthesized in aqueous solution and were coated with a capping layer of thioglycolic acid (TGA); the stability of the suspensions is high, they can be stored for months without degradation [9].

Photoluminescence spectra were recorded using a Varian Cary Eclipse Spectrophotometer with an excitation beam of 365nm. Atomic force microscope (AFM) images were taken using a Digital Instruments Dimension 3000 in tapping mode. Cl_2 gas was produced by the gradual addition of HCl to $KMnO_4$ and used immediately.

Results and Discussion

Cl_2 gas was bubbled through a 2ml suspension of TGA capped CdTe nanoparticles and photoluminescence spectra were recorded. Fig. 1 shows the changes in wavelength and intensity of the photoluminescence spectral maximum as the amount of Cl_2 added is increased. The wavelength of the peak maximum changes from 626 nm in the reference sample to 647 nm after 0.4 ml of Cl_2 has been added. Over the same period the intensity of the luminescence drops to ~30% of its original value. The deviation from a linear trend is assumed to be due to inaccuracy in measuring the volume of Cl_2 added.

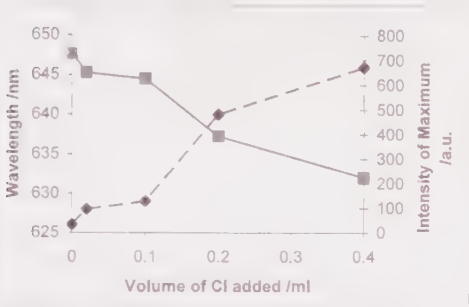

Figure 1 Wavelength (dotted line) and intensity (solid line) changes in the spectral peak maximum of a CdTe nanoparticle suspension as the amount of Cl_2 added is increased

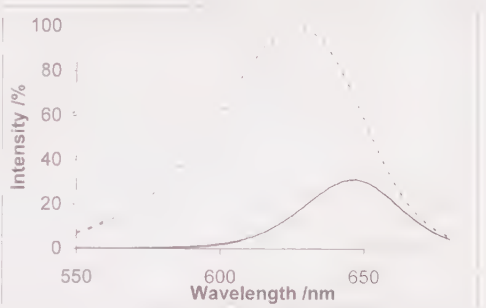

Figure 2 Photoluminescence spectra of a CdTe nanoparticle suspension before (dotted line) and after (solid line) Cl_2 addition.

Fig. 2 shows the photoluminescence spectra before and after 0.4ml of Cl_2 has been bubbled through the suspension. The full-width-at-half-maximum (FWHM) decreases from 62nm in the reference sample to 45nm after Cl_2 treatment, showing that the size dispersion of nanoparticles has been greatly confined. The Cl_2 contaminated spectra shows a selective loss of luminescence intensity from the smaller, higher energy, nanoparticles resulting in both a shift of the peak maximum and an overall loss of intensity.

As Cl_2 is bubbled through the suspension the gas attacks the TGA capping layer of the nanoparticles. TGA is bonded to the nanoparticle through a sulfur-cadmium bond. Cl_2 reacts in a ligand displacement reaction removing the thiol and creating a cadmium-chlorine bond. Displacement of the passivation layer allows the formation of surface trap states [10]. Surface traps provide lower energy non-radiative pathways for the recombination of electron-hole excitons. Once these traps are accessible a loss of luminescence occurs. Smaller particles are affected first and more severely as they have a larger surface area to volume ratio thus more of their active area is exposed to the Cl_2.

A disruption to the TGA passivation layer allows nanoparticles to agglomerate as the charged capping layer, that acts to repel other nanocrystals, has been removed. Fig. 3, shows AFM images of the CdTe suspension before and after Cl_2 contamination. The Rmax and Rms (Rq) of the untreated suspension are 18.95nm and 1.634nm respectively whereas the Cl_2 treated sample has Rmax 59.04nm and Rms (Rq) 5.179nm. The particles in the Cl_2 treated (right-hand) image appear to have grown significantly in size. This increase in perceived size is caused by agglomeration of the particles in suspension. Agglomeration contributes to the loss of luminescence intensity: as a nanoparticle becomes part of a cluster energy is transferred between the individual nanoparticles, and quantum confinement is reduced or lost, reducing the nanoparticle's ability to produce visible radiation [11].

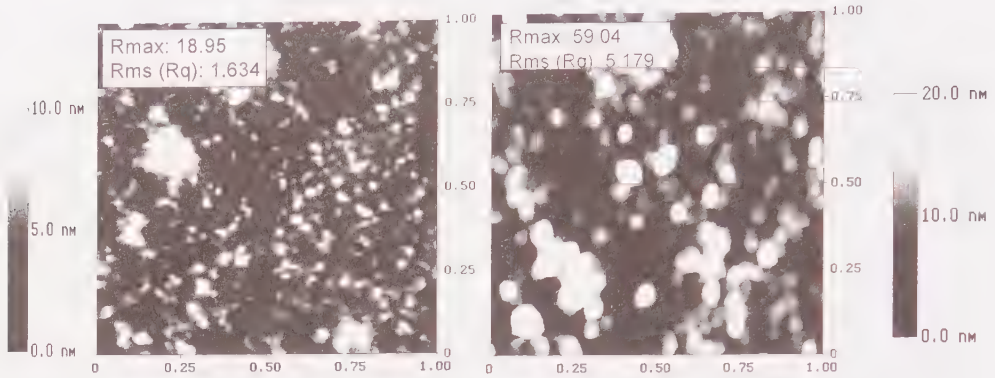

Figure 3 AFM images of a CdTe suspension before (left) and after (right) Cl_2 contamination. Suspensions have been deposited onto glass substrates to allow imaging.

Summary

Cl_2 gas bubbled through a suspension of CdTe nanoparticles was found to change the wavelength and intensity of emission and cause agglomeration. By attacking the thiol capping passivation layer of the nanoparticle Cl_2 allows surface trap states to form. Once formed these trap states provide lower energy and non-radiative pathways for the recombination of excitons. This decreases the number of luminescent nanoparticles. Smaller nanoparticles are affected more strongly as they have a higher surface to volume ratio.

Acknowledgements

We thank the EPSRC for funding HCG with a DTA Grant and Dr N. Gaponik of TU Dresden for production of the CdTe nanoparticles.

References

[1] Y.G. Zheng, S.J. Gao and J.Y. Ying: Adv Mater. Vol 19, (2007) p. 376.

[2] D.E. Gallardo, C. Bertoni, S. Dunn, N. Gaponik and A. Eychmüller: Adv Mater in press (2007)

[3] C. Bertoni, D.E. Gallardo, S. Dunn, N. Gaponik and A. Eychmüller: Appl Phys Lett Vol 90 (2007) 034107.

[4] J. Li, X. Hong, Y. Liu, D. Li, Y. Wang, J. Li, Y. Bai and T. Li: Adv Mater Vol 17 (2005) p. 163.

[5] J. Britt and C. Ferekides: Appl Phys Lett Vol 62 (1993) p. 2851

[6] Z. Tang, N.A. Kotov and M. Giersig: Science Vol 297 (2002) p. 237

[7] M.A. Hernández-Fenollosa, D.P. Halliday, K. Durose, M.D. Campo and J. Beber: Thin Solid Films Vol 431-432 (2003) p. 176

[8] M.D.G. Potter, D.P. Halliday, M. Cousins and K. Durose: Thin Solid Films Vol 361-362 (2000) p. 248

[9] N. Gaponik, D.V. Talapin, A.L. Rogach, K. Hoppe, E.V. Shevchenko, A. Kornowski, A. Eychmüeller and H. Weller: J. Phys. Chem. B Vol 106 (2002) p. 7177.

[10] J.E. Bowen Katari, V.L. Colvin and A.P. Alivisatos: J. Phys. Chem. Vol 98 (1994) p. 4109.

[11] H. C. Gardner, D.E. Gallardo, S. Dunn, A. Eychmüller and N. Gaponik: J Nanosci. Nanotech. In press (2007).

Advanced Materials Research Vol. 31 (2008) pp 153-15
online at http://www.scientific.net
© 2008 Trans Tech Publications, Switzerland

Preparation and characterization of Zn-Se bilayer structure

M. Singh* J.S. Arora, Kamlendra Awasthi, R. Nathawat & Y.K.Vijay

Department of Physics, University of Rajasthan, Jaipur-302004 INDIA

*e-mail:mangej_singh@yahoo.com

Key words: Nanostructure, Bilayer, Semiconductor, RBS, XRD

Abstract. The Zn-Se bilayer structure prepared using thermal evaporation method at pressure 10^{-5} Torr. These films annealed in the vacuum for two hours on different constant temperatures. The optical band gap was found to be varying with annealing temperature due to removal of defects and increase in grain size. It was also observed by the X-ray diffraction pattern the grain size of the film increase with annealing temperature. The lattice constant of hexagonal structure of these films is found to be a =b=4.42Å and c=5.68Å. The dominant peaks to be at 23.2°,28° and 43.9° having values (100), (002) and (111) respectively. The Rutherford back scattering data of these films confirmed the mixing of elements with time.

Introduction

Zinc –selenide can be both a n and p-type semiconductor with a direct band gap(2.7 eV) at room temperature. It is suitable material for red, blue and green light emitting diodes, photochemical cells [1, 2]. ZnSe films was found to be direct transition semiconductor having the absolute maxima of its conduction and valence band at k=0 on the basis of absorption [3] and emission spectra [4].

Since last decade, there has been increased interest in ZnSe because this is a promising candidate for polymer nanocomposite semiconducting devices [5]. The ZnSe is used as cap and buffer layer in hybrid structure of magneto optical devices [6]. The rapid thermal annealing studies carried out by Singh et al [7] and suggested that variation of optical band gap within the range of ZnSe material, which may be due to compositional variation at interface of bilayer and increasing grain size of film with annealing time and R.B.S confirm the mixing of bilayer [7]. However, the self –compensation effect [3] and the residual impurity effect [8] still makes it difficult to control the p or n-type condition and the carrier concentration in these materials. The longer time of annealing in nanostructure thin film is necessary to suppress the creation of native defects and to obtain abrupt impurity profiles between bilayer structures. There has been no report on Zn-Se bilayer strucucture prepared by annealing and characterization of these films.

The ZnSe films were prepared on glass substrate by evaporation of Zn and Se from individual sources and a bilayer structure was fabricated. The novel character of this paper is to prepared nanostructure thin film bilayer structure to understand the inter diffusion reaction kinematics.

In this paper, we are presenting the method of preparation of bilayer structure and characterization by optical transmission spectra, Rutherford back scattering data and x-ray diffraction technique.

Experimental

The samples were prepared by thermal evaporation method using vacuum coating unit at a pressure of 10^{-5} torr, Zinc foils(99.99%) and pure selenium (99.99%) from the BDH chemical, Poole UK are placed into two different boats in the vacuum chamber. The glass substrate cleaned by plasma sputtering technique was placed in the substrate holder above the boats caring materials. A film of Zinc and selenium having thickness 30nm and 30nm, respectively deposited to get bilayer structure. the thickness of film measured by Quartz crystal thickness monitor and isothermal annealed in vacuum for two hours at different temperature to get bilayer structure. The XRD data were taken in range 15 -60° by using the XRD (model D8 Advance) is acquired from Bruker AXS German and

available in material science division, Inter University Accelerator Centre, New Delhi. The instrument employs CuKα1 radiation from a sealed tube generator. The Cu source generates the X-ray beam at wavelength of 0.154nm. The RBS data have been recorded at the institute of physics,Bhubunesware (India) pelletron with alpha beam (He^{2+}) of 3.05MeV. The back scattered alpha was recorded at angle (160°) using a surface barrier detector. The transmission spectra of vacuum annealed ZnSe thin films is taken at room temperature in the wavelength range of 340-700nm with the help of Hitachi spectro-photometer model 330.

Results and Discussion

XRD of bilayer structure

Fig. 1 shows the XRD pattern of ZnSe bilayer structure having thickness 60nm. These films annealed in vacuum at temperature 335K and 435K for interdiffusing the films to prepare semiconductor. The Fig 1 shows XRD pattern for Zn-Se films annealed at 335K for two hours in vacuum. This film shows different peaks among them the dominant peaks to be at 23.2°,28° and 43.9° having hkl values (100), (002) and (111) respectively. These peaks satisfied hexagonal structure of films is with lattice constant a =b=4.42Å and c=5.68Å. The XRD pattern of as deposited thin film found to be amorphous reported in our earlier paper [7]. However peaks found in XRD is due to annealing effects that reduced the defects and increase the grain size of film.

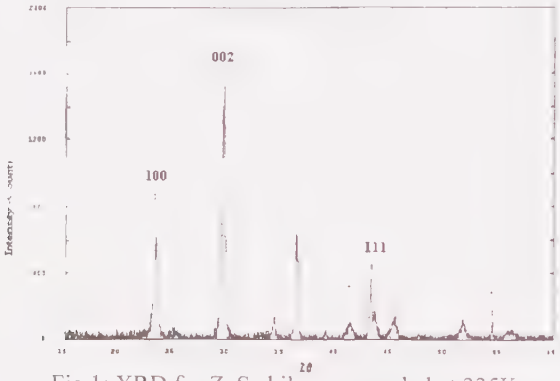

Fig.1: XRD for ZnSe bilayer annealed at 335K

Optical band gap

Fig. 2 shows the transmission spectra of ZnSe nano bilayer structure. This figure suggests that transmission is increases with annealing temperature. It may be due to crystallization occurs by annealing in thin films. The optical band gap of these films calculated by using Tauce relation [9]

$$\alpha h\nu = A\,(E_g - h\nu)^{1/2}$$

Where E_g is the optical band gap; A an constant, and α absorption coefficient.

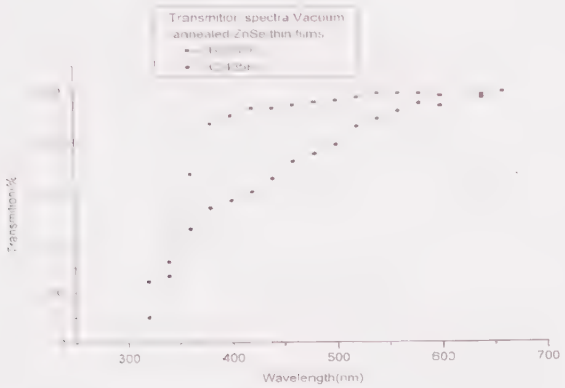

Fig.2 Transmission spectra of ZnSe bilayer structure

Fig.3 (a) & 3(b) shows the graph between $(\alpha h\nu)^2$ versus energy(eV) of photon on ZnSe thin films assuming it to be the direct band gap material. The intercept of straight line to energy axis used to find the optical band gap. The band gap of thin film samples of Zinc selenides varies from 3.12 to 3.02eV with annealing temperature. The observed value is higher than reported value it may be due to tailoring of the optical band gap in nanostructures thin films. It is also observed that the value of optical energy band gap decreases with increase in an annealing temperature.

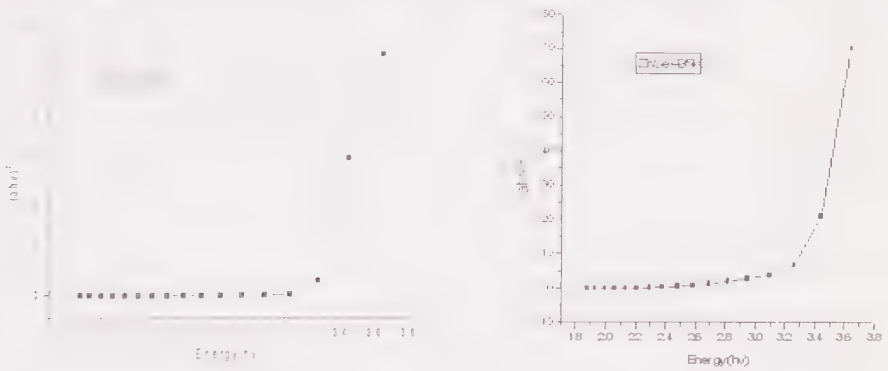

Fig.3 Optical band gap of ZnSe bilayer annealed (a) at 335K (b) at 435K

The active role of grain boundary and defects migration on annealing would be expected to occur in crystallization [10]. The increase in optical transmittance was related to the increase in grain size of the films with increasing the substrate temperature [11]. In our case, Increase in grain size that was confirmed by our XRD measurements. In order to account for this higher band gap than reported values in literature due to tailoring of optical band gap by nanostructure thin films.

Rutherford back scattering spectrometry

The RBS is single rapid, sensitive and nondestructive depth profiling technique and is most suitable for quantitative analysis to explain intermixing of bilayer. We have observed in Fig.4 that the count versus channel graph in which the peaks of ZnSe pristine is found to be separate but with annealing they found to be merge each other and diminished in lower side that confirm the mixing of material and preparation of semi conducting films.

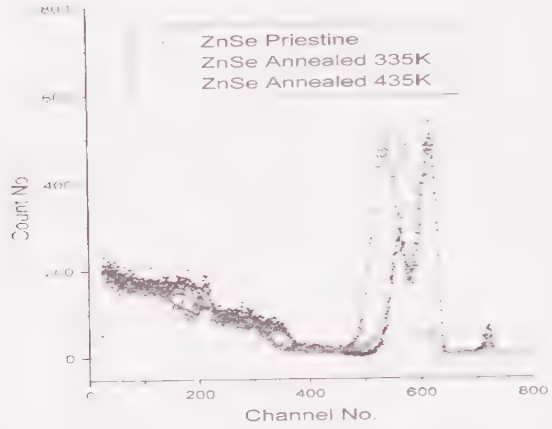

Fig.4: RBS spectra of ZnSe bilayer structure

The dominant peaks after annealing at 335 ° for two hours found to be shifted towards left hand side and also found to be broaden that is confirm the mixing of element each other. That result also satisfied our earlier RBS studies in case of rapid thermal annealing [7] but in this nanostructure bilayer structure shows the shifting in left side as well as broadens. But it was also observed that at higher broaden effect eliminated and peak found to shift in mid side of separated peaks. In as deposited films the peak of Zn found to be at channel number 580 and for Se at channel number 610 as our earlier studies [7] but after annealing peaks is found to shifted with annealing temperature. It was also observed that peak to valley ratio is the annealed sample has decreased, indicating substantial interdifussion. These observations well agree with Holloway and Sinclair [12] in case of Ti-Si thin films. The broaden of peaks in case of Au/Si bilayer structure observed by authors [13] with ion influence.

Conclusion

1. The bilayer structure useful to prepare semiconductor.
2. Vacuum annealing nanostructure thin film tailored optical band gap of material.
3. The prepared structure found to be hexagonal with lattice constant a=b=4.42 and c=5.68.
4. The Rutherfourd back scattering data of these films confirmed the mixing of elements with annealing temperature.

Acknowledgements

Authors are thankful to U.G.C for minor research grant to provide for this work. The thanks are due for Mr.P.K.Kulahari IUAC for XRD and Dr.B.shekhar for Bubhanesawer for RBS.

References

[1] S.Ignatowicz,A.kobendza, Semiconducting thin films of $A^{II}B^{IV}$ compounds,John wilely&sons,New York,PWN polish Scientific publishers,Warsaw 1990.

[2] H.E Ruda, in H.E.Ruda (ed) widegap II-VI compounds for Opto-Electronic applications,chapman and Hall ,UK 1992.

[3] E.Loh,R.Newman, J.Phys.Chem solids 21(1961)324

[4] R.E.Halsted,M.aven, Bull.Am.Phys.Soc.6(1961)312

[5] D.kaushik, M.Sharma,A.B.Sharma and R.K.Pandey Proceeding of DAE solid state physics symposium (2006)293.

[6] M.sakuma,K.Hyoini,I.Souma,A.Murayama and Y.oka Phys.state sol(b) 241no.3(2004)664.

[7] M.Singh and Y.K.Vijay Applied surface science 239(2004)79

[8] W.Stutius,J.Electron Mater.10(1981)95

[9] J.Tauce, in J.Tauce(Ed.) Amorphous and liquid semiconductors ,Plenum press,New York 1974 p159

[10] R.N.Bhargava, In R.bhargava(Ed.) Propertiies of wide bandgap II-VI semiconductors, INSPEC,IEE,London ,UK 1997.

[11] H.Kim,J.S.Horwitz,A.pique,C.MGilmore,D.B.Chrisey, Appl.Phys.A69(1999)5447

[12] K.Hollowy,R.Sinclair. j.Appl.Phy 61(4) (1987)

[13] R.khalfaoui and S.Tobbeche Vacuum 78(2005)341

Advanced Materials Research Vol. 31 (2008) pp 158-160
online at http://www.scientific.net
© 2008 Trans Tech Publications, Switzerland

The formation of InP ring-shape nanostructures on $In_{0.49}Ga_{0.51}P$ grown by droplet epitaxy

W. JEWASUWAN[a], S. PANYAKEOW[b], and S. RATANATHAMMAPHAN[c]

Department of Electrical Engineering Chulalongkorn University, Bangkok 10330, Thailand
[a]wipakornj@yahoo.com, [b]s_panyakeow@yahoo.com, [c]rsomchai@chula.ac.th

Keyword: nanostructure, molecular-beam epitaxy, droplet-epitaxy, InP, GaAs

Abstract. We report on the fabrication of self-assembled InP ring-shape nanostructures on $In_{0.49}Ga_{0.51}P$ by droplet molecular-beam epitaxy. The dependency of InP ring-shape nanostructural properties on substrate temperature and indium deposition rate is investigated by ex situ atomic force microscope (AFM). The nano-craters are formed when indium deposition at 120°C while the ring shape quantum-dot molecules are formed when indium deposition at 150°C or higher. The size, density and pattern of InP ring-shape nanostructures strongly depend on substrate temperature and indium deposition rate during indium deposition.

Introduction

Recently, fabrication methods for semiconductor nanostructures such as quantum dot and quantum ring have been widely reported [1,2]. These structures have significant potential for quantum information [3], quantum computing [4], and magneto-optic device applications [5]. Several groups have realized semiconductor nanostructures in lattice-mismatched systems, using the Stranski-Kratanow (SK) growth mode [6,7]. Some groups have reported about droplet epitaxy technique which can be applied in not only lattice-matched systems but also lattice-mismatched systems by incorporation of group V into group III element droplets deposited on a III-V compound semiconductor substrate [8,9]. In this paper we present about the fabrication of InP ring-shape nanostructures by solid source molecular-beam epitaxy technique. Atomic force microscopy (AFM) images reveal how InP ring-shape nanostructures are formed with the change of substrate temperature and indium deposition rate.

Experimental procedure

All samples were fabricated in a RIBER 32P conventional solid-source molecular-beam epitaxy system. A GaP decomposition cell was used as a P_2 source for InP and InGaP. A typical sample consisted of a 300 nm-thick GaAs buffer layer grown at 600°C on GaAs (100) substrate, followed by a 200 nm-thick $In_{0.49}Ga_{0.51}P$ grown at 470°C and indium droplets were formed under the desired conditions by varying the substrate temperature and indium deposition rate. Then, the indium droplets were exposed for 5 minutes under P_2 beam at 200°C. After the growth was finished all samples were examined using AFM. In this work, two series of samples were fabricated : (a) to investigate the substrate temperature dependence, a constant In thickness of 3.2 monolayer (ML) was deposited with a deposition rate of 0.75 ML/s without P_2, the substrate temperature were set to 120, 150, 180 and 210°C respectively ; (b) to investigate the indium deposition rate, an indium amount of (approximately) 3.2 ML was deposited at 250°C with different indium deposition rates of 0.25, 0.4, 0.75, 1 and 1.6 ML/s, respectively

Results and discussion

(a) Effect of substrate temperature

The AFM images in Fig.1 show the dependency of surface morphology on the substrate temperature at a constant 0.75 ML/s indium deposition rate. The indium thickness was fixed at 3.2 ML. Fig. 1 (a) is an AFM image of nanometer-scale craters formed at 120°C. The outer diameter of the crater is approximately 84 nm while the inner diameter is approximately 24 nm, the average height is 1.3 nm and the density is 7.4×10^8 cm^{-2}. It also shows a contrast to ring-shape quantum-dot

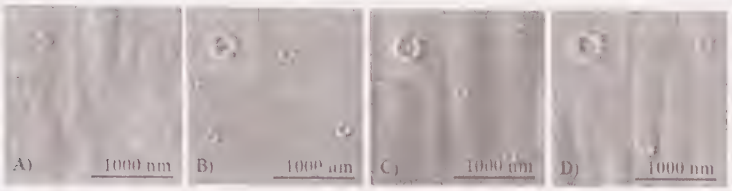

Fig. 1 AFM images of InP nanostrcutures after indium deposition at 250°C with a constant indium deposition rate of 0.75 ML/s and crystallization at 200°C under 4×10^{-6} torr P_2 flux for 5 minutes with substrate temperature of (a) 120°C, (b) 150°C, (c) 180°C and (d) 210°C, respectively

Table 1 Summarized results of InP ring-shape nanostructure samples at various substrate temperature with a constant indium deposition rate of 0.75 ML/s.

Substrate Temperature (°C)	Morphology	Density (cm^{-2})	Average outer diameter (nm)	Average inner diameter (nm)	Height (nm)	Number of dot/ring
120	Crater	7.4×10^{8}	84.1	23.5	1.3	-
150	Ring-shape quantum-dot molecule	1.1×10^{8}	174.0	79.5	1.5	6-10
180	Ring-shape quantum-dot molecule	9.5×10^{7}	167.8	84.9	1.9	9-13
210	Ring-shape quantum-dot molecule	8.4×10^{7}	176.3	91.8	3.5	5-10

molecule formed in Fig. 1 (b)-(d). Fig.1 (b)-(d) show a similar dependent of ring-shape quantum-dot molecules which have been formed at 150, 180, and 210°C, respectively. The density of ring-shape quantum-dot molecules is varying between 8.4×10^{7}-1.1×10^{8} cm^{-2}. Increasing the substrate temperature causes a drastic change in density, size, and the number of dots in a molecule. The average diameter and height of quantum-dot in a molecule also depend on the substrate temperature. Statistics of the average ring diameter, height, and number of dots in a molecule are summarized in the table 1.

(b) Effect of indium deposition rate

Fig. 2 shows the dependency of surface morphology on the indium deposition rate at substrate temperature of 250°C. The indium thickness was fixed at approximately 3.2 ML. In all samples, ring-shape quantum-dot molecules have been formed. The density of ring-shape quantum-dot molecules is varying between 2.3×10^{7}-1.4×10^{8} cm^{-2}. Increasing the indium deposition rate causes a drastic change in density, size, and the number of dots in a molecule. Statistics of the average ring diameter, height, and number of dots in a molecule are summarized in table 2.

The InP ring-shape nanostructures are made by the formation and spread of indium droplets. These droplets were deposited on $In_{0.49}Ga_{0.51}P$ surface. The formation of ring-shape quantum-dot molecules depends on the indium deposition rate, spreading behavior of indium on $In_{0.49}Ga_{0.51}P$

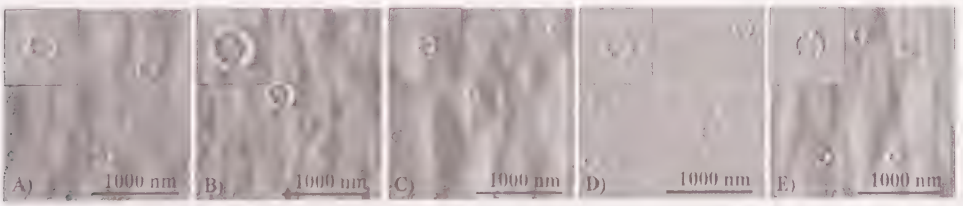

Figure 2 AFM images of InP nanostructures after indium deposition at 250 °C and crystallization at 200°C under 4×10^{-6} torr P_2 flux for 5 minutes with indium deposition rate of (a) 0.24 ML/s (b) 0.4 ML/s, (c) 0.75 ML/s, (d) 1 ML/s and (e) 1.6 ML/s, respectively. The coverage of indium droplet was approximately 3.2 ML.

Table 2 Summarized results of InP ring-shape quantum-dot molecule samples at various indium deposition rate with a constant indium thickness of 3.2 ML by approximately.

Deposition rate (ML/s)	Morphology	Density (cm^{-2})	Average outer diameter (nm)	Average inner diameter (nm)	Height (nm)	Number of dot/ring
0.25	Ring-shape quantum-dot molecule	4.2×10^{7}	210	137	3.4	6-13
0.4	Ring-shape quantum-dot molecule	2.3×10^{7}	314	158	4.3	9-13
0.75	Ring-shape quantum-dot molecule	1.4×10^{8}	157	81	2.5	4-9
1	Ring-shape quantum-dot molecule	6×10^{7}	144	31	3.3	9-13
1.6	Ring-shape quantum-dot molecule	1.6×10^{7}	186	107	4.3	8-14

surface, and the substrate temperature. The deviations are due to the wetting nature of $In_{0.49}Ga_{0.51}P$ surface, the interracial energy of the deposit at Indium droplets and $In_{0.49}Ga_{0.51}P$ interface, and temperature. Further studies on this observation are under progress.

Conclusions

In conclusion, we have presented a simple method of preparing ring-shape InP nanostructures on $In_{0.49}Ga_{0.51}P$ by solid-source molecular-beam epitaxy using droplet epitaxy technique. The effects of substrate temperature and indium deposition rate on the surface morphology, density, and size of self-assembled InP nanostructures were investigated. The surface morphology depends strongly on the substrate temperature. The crater is formed at 120 °C while the ring-shape quantum-dot molecule is formed when the substrate temperature is increased to 150 °C or more. The density, height, and average number of dot per molecule are found to be dependent on the substrate temperature and the indium deposition rate.

Acknowledgements

This work is supported by Thailand Research Fund (TRF), National Nanotechnology Center (Nanotec), Ministry of Education through The commission of Higher Education (CHE), Center of Excellence for Power Technology (CEPT) and Chulalongkorn University. The authors also would like to thank Mr. Boonchuay Supmonchai for his fruitful discussion, Mr Supachok Thainoi, Mr. Pornchai Changmaung, and Mr. Poonyasiri Boonpeng for their technical assistance.

References

[1] B.C. Lee, O.Voskoboynikov, C.P. Lee: Physica E Vol. 27 (2004), p. 87.
[2] G. Sek, J. Misiewicz, K. Ryczko, M. Kubisa, F. Heinrichsdorff, O. Stier and D. Bimberg: Solid State Communications Vol. 110, Issue 12(1999), p. 657.
[3] W. Wieczorek, T. Warming, M. Geller, D. Bimberg, G.E. Cirlin, A.E. Zhukov and V.M. Ustinov: Applied Physics Letter Vol. 88 (2006), p. 182107.
[4] V. danos, E. D'Hondt, E. Kashefi and P. Panangaden: Electronic Notes in Theoretical Computer Science Vol.170 (2007), p. 73.
[5] A. Hogele, M. Kroner, S. Seidl, K. Karrai, M. Atature, J. Dreiser, A. Imamoglu, R.J. Warburton, A.Badolato, B.D. Gerardot and P.M. Petroff: Applied Physics Letter Vol. 86 (2005), p. 221905.
[6] T.V. Lippen, R. Notzel, G.J. Hamhuis and J.H.Wolter: Journal of Applied Physics Vol. 97 (2005), p. 044301.
[7] A. Kurtenbach, C.Ulrich, N.Y. Jin-Phillipp, F. Noll, K. Eberl: Journal of Electronic Materials Vol. 25, No. 3 (1996), p. 395.
[8] K. Watanabe, N. Koguchi and Y.Gotoh: Japanese Journal of Applied Physics Vol. 39 (2000), p. L79.
[9] T. Mano, N.Koguchi: Journal of Crystal Growth Vol. 278 (2005), p.108.

Advanced Materials Research Vol. 31 (2008) pp 161-163
online at http://www.scientific.net
© 2008 Trans Tech Publications, Switzerland

Development of Low Size Dispersion, High Volume Fraction and Strong Quantum confined CdS_xSe_{1-x} Quantum Dots Embedded in Borosilicate Glass Matrix and Study of their Optical Properties

A. Verma[1,a], P. K. Bhatnagar[1,b], P. C. Mathur[1,b], S. Nagpal[2,c], P. K. Pandey[1,d] and J. Kumar[1,e]

[1] Department of Electronic Science, University of Delhi South Campus, Benito Juarez Road, New Delhi-110021, INDIA.

[2] Department of Physics and Electronics, Rajdhani College, University of Delhi, Raja Garden, New Delhi-110015, INDIA.

[a] abhiverma10@gmail.com, [b] promod48@rediffmail.com, [c] snagpal@rajdhani.du.ac.in, [d] pandeypraveen@hotmail.com, [e] jitender_does@yahoo.co.in

Keywords: II-VI Quantum Dots, Borosilicate Glass Matrix, Size Dispersion, Shallow Trap Centers.

Abstract. Quantum Dots (QDs) of CdS_xSe_{1-x} embedded in borosilicate glass matrix (BGM) have been grown using colored glass filter (RG695). Double-Step (DS) annealing method was adopted in which nucleation is achieved at a lower temperature (475°C) without any crystallization. To obtain crystallization on these nucleation centers, the annealing temperature is raised to 575°C at which the nucleation rate is negligible. QDs of various average radii and volume fractions are grown by varying the annealing duration from 3 to 11hrs. QDs corresponding to higher annealing duration are found to have low size dispersion (SD) and high volume fraction but weak quantum confinement, while, the QDs corresponding to lower annealing durations have high quantum confinement due to their much lower radii as compare to Bohr exciton radius, their SD is high and volume fraction low. For nonlinear optical applications the SD must be low and volume fraction should be high. Attempt has been made to optimize the two parameters. Further it has been concluded that there is no contribution of the band edge recombination to the PL and the origin of the PL is due to shallow traps existing in the volume of the QDs. Studies of absorption and PL have also been made on the samples aged for 18, 24 and 36 months. It is found that the effect of aging is to increase the absorption coefficient, reduce the shallow trap centers and reduce the SD.

Introduction

Quantum dots of group II-VI compound semiconductors embedded in BGM have drawn considerable attention. Wide band gap semiconductor QDs doped glasses have been investigated intensively during last two decades because of their enhanced nonlinear optical properties, ultra fast response time, photoluminescence properties in the visible region and potential for developing new optoelectronic devices such as optically bistable elements, optical switches, transistors, modulators, laser diodes, optical harmonic generators, and optical memories [1-7].

For device applications the size and SD of QDs must be controlled by proper choice of temperature and duration of annealing. DS annealing procedure to grow CdS_xSe_{1-x} QDs has been adopted to achieve low SD, stronger quantum confinement and high volume fraction [8].

Experimental Details

Colored glass filter, RG695 containing CdS_xSe_{1-x} ($x = 0.08$) [9] procured from Schott, Germany, was first bleached at a temperature of 975°C for about 3hrs, and then cut into small pieces of about 5mm x 5mm using a diamond wheel cutter. QDs were grown on these samples using DS annealing method [10]. The samples were prepared and characterized using UV-VIS Spectrophotometer (Shimadzu UV-160) and Photoluminescence (PL) Spectrophotometer (Ar^+ ion CW laser at 488nm with 5mW power for 5-minute exposure time).

Results & Discussion

Nucleation, crystallization and coalescence stages of diffusion-controlled growth process in II-VI QDs embedded in BGM are characterized by their different activation energy, i.e., $E_{nuc} < E_{cry} < E_{coal}$. Therefore, during nucleation the development of small nuclei can be obtained at comparatively low annealing temperature than that of crystallization stage, where high annealing temperature and low annealing duration give rise to a rapid increase in size of QDs. The variations of optical absorption coefficient with energy for CdS_xSe_{1-x} QDs grown using DS annealing techniques are shown in Fig. 1 (D3 to D9 represent DS annealing duration from 3 to 9hrs). The difference between the 1st exciton peak of QD samples and the bulk bandgap of $CdS_{0.08}Se_{0.92}$ (ΔE) increases sharply with the decrease in average radii of QDs or annealing duration, as shown in Fig. 2. This is due to the fact that the QD radii are much smaller than their exciton Bohr radius. The sharp red shift in 1st exciton peak (Fig. 2) and decrease in the absorption coefficient intensity (Fig. 1) for D9 sample is attributed to coalescence [2] because the surface tension starts playing its role and diffusive mass transfer from smaller particles to larger ones starts dominating the growth dynamics.

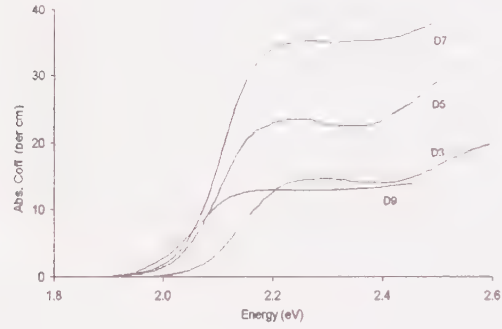

Fig. 1 Optical absorption spectra of CdS_xSe_{1-x} QD samples.

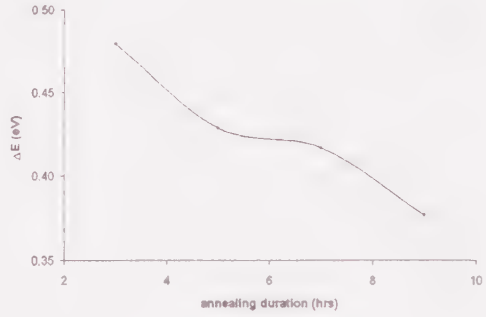

Fig. 2 Shift in 1st exciton peak with the annealing duration. (At 575°C)

The red shift in 1st exciton peak is found to be 110meV, the average radii of QDs varies from 2.85 to 3.2nm and the SD decreases from 11.9 to 10.3% as annealing duration increased from 3 to 9hrs. These values were calculated by comparing the experimental absorption curves with the curves generated using Effective Medium Approximation (EMA) theoretical model [7,8,11-13]. The effects of aging at room temperature have also been studied. The aging occurs due to the fact that the CdSSe glass solution again attains a supersaturated condition at low temperature. Therefore, the diffusion of semiconductor particles continue to take place even at room temperature that bring change in various parameters, which are important in opto-electronic device design calculations. Therefore, it is very important to study growth dynamics at room temperature. For a typical case, it was found that after 24 months of aging, the average radii increased from 3.05 to 3.12nm with the increase in number of QDs by 190% and the SD decreased from 10.8% to 9.9%, as shown in Fig. 3. After that no significant change was found in these parameters for the next 12 months. This shows that the system attains almost a stable nature after 24 months of aging as far as absorption parameters are concerned.

The photoluminescence (PL) measurements show a Stokes shift between the broad PL and optical absorption peak of 309meV, indicating that PL is due to radiative recombination centers provided by the shallow traps, which are created at the semiconductor-glass matrix interface, with the overlapping of quasi-free recombination band [14]. The PL intensity decreases not only with the increase in annealing duration but also found to decrease with the passage of time due to aging, though at a slower rate. Fig. 4 shows that in 36 months the concentration of the shallow-trap centers decreases substantially.

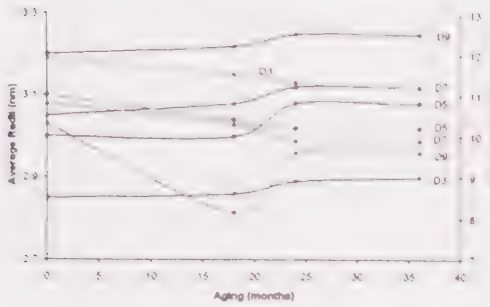

Fig. 3 Effect of Aging on average radii (dark lines) and size dispersion (light lines) of CdS_xSe_{1-x} QDs.

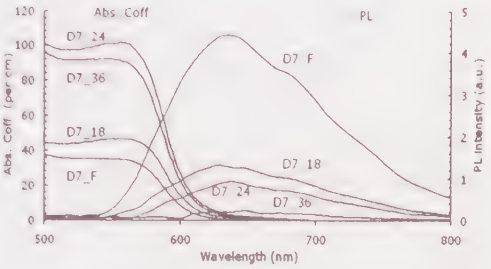

Fig. 4 Comparison of PL Spectra of Aged Samples along with their respective Optical Spectrum.

Conclusion

CdS_xSe_{1-x} QDs with strong quantum confinement, reduced SD and higher volume fraction were obtained using DS annealing method with optimized annealing temperature and duration. Any attempt to further reduce the SD will decrease the quantum confinement. Therefore, a trade off has to be made between the SD and the quantum confinement to get maximum advantage of nonlinear properties for the optoelectronic devices. Aging of 24 months, make the device more stable and traps are completely eliminated in 36 months duration.

Acknowledgment

Authors are thankful to Department of Science and Technology (DST), Govt. of India, India for financial support. Authors also wish to thank to Dr. S. N. Sharma from National Physical Laboratory (NPL), New Delhi, India, for providing facility of PL measurements.

References

1. S. Santhi, F. Trojanek, Physica, E 27 (2005), 38.
2. S.V. Gaponenko, *Optical Properties of Semi. Nanocrystals*, Cambridge University Press (1998).
3. P. Nemec and P. Maly, J. App. Phy. 87 (2000), 3342.
4. M. Bayer, O. Stern, P. Hawrylak, S. Fafard and A. Forchel, Nature 405 (2000), 923.
5. E. Hanamura, Phys. Rev. B 37 (1987), 1273.
6. J. Yumoto, S. Fukushima, and K. Kubodera, Optics Lett. 12 (10), (1987), 832.
7. P.K.Pandey, K.Sharma, S.Nagpal, P.K.Bhatnagar and P.C.Mathur, PSS (b) 240 (2003), 134.
8. K. Sharma, P.K. Pandey, S. Nagpal, P.K. Bhatnagar and P.C. Mathur, Phys. Scr. 73 (2006), 125.
9. G.P. Banfi, V. Degiorgio and B. Speit, J. Appl. Phys. 74 (1993), 6925.
10. A.Verma, S.Nagpal, P.K.Pandey, P.K.Bhatnagar and P.C.Mathur, J. Nano. Res. (2006), in press.
11. M.H.Yukselici, P.D. Persans and T.M. Hayes, Phys. Rev. B. 52 (1995), 11763.
12. L. Banyai and S.W. Koch, *Semi. Quant. Dots*, World Scientific Publishing Co. Pte. Ltd. (1993).
13. B.G.Potter, J.H. Simmons, P. Kumar and C.J. Stanton, J. Appl. Phys. 75 (1994), 8039.
14. F. Henneberger, Optics of Semiconductor Nanostructures (Akadenic Verlag), (1993).

Advanced Materials Research Vol. 31 (2008) pp 164-166
online at http://www.scientific.net
© 2008 Trans Tech Publications, Switzerland

Tuning Of Energy Band Gaps In Ternary Semiconductors

Rita John

Department of Physics, Mother Teresa women's University, Kodaikanal, India.
john_abraham@sify.com

Keywords: Ternary pnictides, dirct and pseudodirect compounds, metallisation, bulk modulus.

Abstract. The first principle investigations on electronic structure of ABC_2 (A = Cd; B = Si, Ge, Sn; C = P, As) pnictides using the Tight Binding Linear Muffin Tin Orbital (TB-LMTO) method within the Atomic Sphere Approximation (ASA) is reported. Variation of Eg with pressure reveals the direct and pseudodirect natures of these compounds. $CdSiP_2$ shows a pseudo direct and $CdGeP_2$, $CdSnP_2$, $CdSiAs_2$, $CdGeAs_2$ and $CdSnAs_2$ show direct band gap natures. Semiconductor to metal transition at high pressures is observed. Metallisation volumes $(V/Vo)_m$ and pressures (P_m), bulk modulus (B_o) and its pressure derivative (B_o^1) are reported. Correlation connecting Bo and the unit cell volume (Vo) is established.

Introduction

The II-IV-V_2 pnictide semiconductors are analogs of the III-V semiconductors with diverse optical, electrical and structural properties [1]. The influence of structural parameters on the energy gaps and the band gap anomalies of ABC_2 (A = Cd; B = Si, Ge, Sn; C = P, As) compounds are discussed in our earlier paper [2]. In the present paper we report the results of the first principles investigations on the direct and pseudodirect natures of these compounds, variation of band gaps with the application of pressures, calculated values of bulk modulus (B_o) and its pressure derivative (B_o^1) and a correlation between Bo and unit cell volume (V_o). The unit cell of these compounds are in general compressed along the tetragonal axis. This is described by $\eta = 2\text{-}c/a > 0$; a and c being the lattice constants. The anions are displaced from their tetrahedral positions described by $u = 4x\text{-}1$, x being the abscissa of the anion in units of a. More details can be found in [3].

Method of Calculation

The electronic structure calculations where performed using semi - relativistic self-consistent TBLMTO method within ASA [4]. The von Barth - Hedin exchange correlation scheme has been used to compute the exchange correlation potential [5]. The calculations were performed for 1088 irreducible k points. Self-consistency in the eigen-values was achieved to an accuracy of 10^{-5} Ryd. The lattice parameters and the structural parameters are obtained by systematically minimizing the parameters around the experimental values. We used the total energy approach to calculate the equilibrium volume. Our computed equilibrium structural parameters a,c and u are given in Table 1.

Results and Discussion

Direct and Pseudodirect Compounds. The band structures of these compounds at ambient pressure have the similar generic nature and are similar to the one we have reported for Zn based pnictides in [3] and Cd based pnictides in [2]. The details of band structure are deliberately avoided to explain other concepts. Shay and Wernick have defined the direct and pseudodirect ABC_2 compounds. If the II-IV-V_2 ternary is direct and its corresponding III-V binary analog is an indirect band gap semiconductor, then the ternary is said to be pseudodirect semiconductor [1]. They have predicted $CdSiP_2$ to be the pseudodirect. The present band structure calculation on these ternary pnictides and their binary analogs at ambient pressure confirms their prediction. At equilibrium volume the band gap of the $CdSiP_2$ is pseudodirect at $\Gamma_{4v} \rightarrow \Gamma_{3v}$, which corresponds to an indirect band gap from Γ to X of its isoelectronic binary GaP, Fig.1. The compounds $CdGeP_2$ $CdSnP_2$, $CdSiAs_2$, $CdGeAs_2$, $CdSnAs_2$ are direct with similar direct band gap natures in their corresponding binaries.

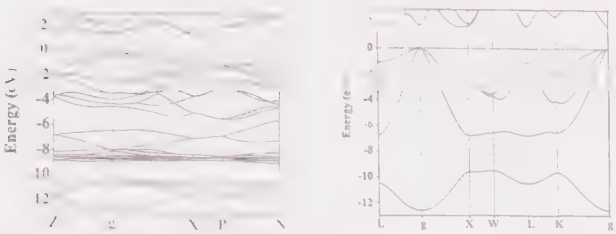

Fig.1 Band structures of $CdSiP_2$ and GaP at V/Vo=1

A. Jayaraman et al have reported an increase in energy gap (E_g) with the hydrostatic pressure [6]. Shay and Wernick have reported two types of behaviour of these compounds – an increase in E_g with pressure is exhibited by the direct and decrease in E_g by the pseudo direct compounds [1]. In the present work, volume with respect to its unit cell volume (V/Vo) is reduced to apply theoretical pressure on these compounds. $CdSiP_2$ shows a gradual fall in E_g at Γ on application of pressure confirming its pseudodirect band gap nature with a positive value for dE_g/d (V/Vo). $CdGeP_2$, $CdSnP_2$, $CdSiAs_2$, $CdGeAs_2$ and $CdSnAs_2$ show a rise in E_g at Γ revealing the direct band gap nature. However in the present study we find that on application of pressure further E_g at Γ falls gradually. As a consequence, the direct band gap changes to pseudodirect at high pressure, leading to a change of all interband transitions existing in these materials in agreement with Chiker et al [7] for $CdXP_2$ (X=Si, Ge, Sn) compounds.

Metallisation at High Pressure. The band structure calculations are performed for all compounds in the compressed volume range by varying V/Vo in steps of 0.005 assuming the chalcopyrite structure. This closer mesh is chosen to ensure the accuracy of the metallisation volumes. All these compounds undergo metallisation under pressure via indirect band gap closure between Γ and X. The band structure of $CdSiP_2$ after metallisation is shown in Fig. 2. The metallisation volumes with respect to V_0 i.e. $(V/V_0)_m$ and the corresponding metallisation pressures (P_m), calculated using the Vinet's equation of state are shown in Table 1 [8]. It should be noted that the value of $(V/V_0)_m$ decreases when the B atom is replaced with smaller atom (Sn to Ge then to Si) while it increases when Cd is replaced by Zn, which can be seen from our earlier work on six Zn pnictides [3].

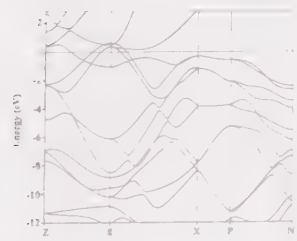

Fig.2 Band structure of $CdSiP_2$ after metallisation

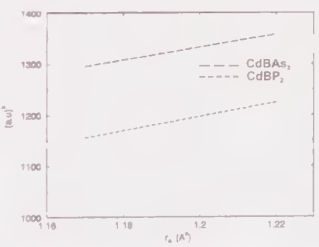

Fig.3 Radii of B atom vs. V_0 Vegard's law

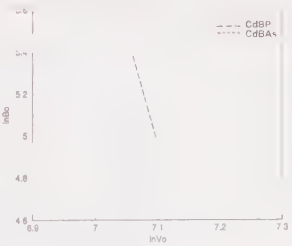

Fig.4 Correlation between B_0 and V_0

As Si becomes a metal and then a superconductor under the application of pressure and so is the case with some of the III-V binaries, one can expect superconductivity in all these pnictides at higher pressures. It should also be noted that $CdSnAs_2$ has already been reported to be a superconductor on application of pressure [9].

Bulk modulus and Cell Volume. A systematic variation in the cell volume with the atomic radius is observed when Si is replaced by Ge and Sn atoms in accordance with Vegard's law [10], Fig.3. The bulk modulus (B_o) and its pressure derivative (B_o^1) are calculated from the pressure-volume relation by fitting the calculated total energies in Vinet's [8] equation of state. A linear relationship similar to that of Newmann [11] for I-III-VI_2 chalcopyrites was obtained in the case of II-IV-V_2 pnictides also as shown in Fig. 4. B_0 decreases with the increase in size of B atom in any ABC_2 (A = Cd; B = Si, Ge, Sn; C = P, As) pnictide revealing the increase of hardness with the decrease in size of B atom which is actually the reason for decreasing trend of $(V/V_0)_m$ as one goes form Sn to Ge then to Si in any ternary pnictides.

Table 1. The equilibrium structural parameters a,c,u [2] used for the calculation, bulk modulus (B_o), its pressure derivative (Bo'), metallisation volume, $(V/V_0)_m$ and pressure, P_m.

Compound	a (A°)	c (A°)	u	Bo (Mbar)	Bo'	$(V/V_0)_m$	P_m (Mbar)
$CdSiP_2$	5.665	10.724	0.270	2.35	6.82	0.485	15.89
$CdGeP_2$	5.742	11.060	0.266	1.27	7.16	0.510	7.698
$CdSnP_2$	5.923	11.563	0.235	1.31	7.16	0.535	6.391
$CdSiAs_2$	5.832	11.345	0.268	2.35	6.92	0.465	19.599
$CdGeAs_2$	5.923	11.567	0.266	1.27	7.09	0.505	7.863
$CdSnAs_2$	6.123	12.015	0.235	1.18	7.89	0.550	6.182

Conclusion

The electronic band structure calculations are performed for ABC_2 (A = Cd; B = Si, Ge, Sn; C = P, As) ternary compounds using TBLMTO method within ASA. The direct and pseudo direct natures of band gaps are investigated. $CdSiP_2$ is pseudo direct and $CdGeP_2$, $CdSnP_2$, $CdSiAs_2$, $CdGeAs_2$ and $CdSnAs_2$ are direct band gap semiconductors. Metallisation occurs at high pressures in all these compounds. B_0 decreases with the increase in size of B atom in any ABC_2 (A = Cd; B = Si, Ge, Sn; C = P, As) pnictide revealing the fact that the hardness increases with the decrease in size of B atom. A linear relation between ln Bo and lnVo is also established. The present study on behaviour of ternary pnictide on pressure, dependence of their hardness on its structural parameters will give an idea of tuning the band gaps to suit a particular application.

References

[1] J.L. Shay and J.H. Wernick : *Ternary Chalcopyrite semiconductors: Growth, Electronic Properties and applications*, (Pergamon, Oxford, 1974).

[2] Rita John, Solid State Phenomena, 124-126, (2007), p.57

[3] R. Asokamani and R.Rita, Phys. Stat. Sol. (b), 226, (2001), p. 375

[4] O.K. Andersen and O. Jepsen, Phys. Rev. Lett, 53, (1984), p.2571

[5] U.Von Barth and L. Hedin, J.Phys. C, 5, (1972), p.1629

[6] A. Jayaraman, V. Narayanamurti and R.G. Maines, Phys. Rev., B, 14, (1976), p.3516

[7] F. Chiker, B. Abbar, A.Tadjer, S. Bresson, B. Khelifa, and C. Mathieu, Physica B 349, (2004), p.181

[8] P. Vinet, J.Phys. C, 1, (1989), p.1941.

[9] H. Katzman, T. Donohue, W.F. Libby, H.L. Luo and J.G. Huber, J. Phys. Chem., 30, (1969), p.1609

[10] R.Asokamani : *Solid State Physics* (Anamaya, India, 2006), 35.

[11] H.Neumann, Phys. Stat. Sol. (A), 96, (1986), p.201

Advanced Materials Research Vol. 31 (2008) pp 167-169
online at http://www.scientific.net
© 2008 Trans Tech Publications, Switzerland

Luminescence Properties of ZnS:Mn Quantum Dots

Xiaosong Zhang[1,2], Lan Li[1], Dongqing Dong[1], Zhi Wang[2], and Xiaoyi Dong[2]

[1]Tianjin Key Laboratory for Photoelectric Materials and Devices Tianjin University of technology Tianjin 300191, China

[2]Key Laboratory of Opto-electronic Information and Technology Institute of Modern Optics Nankai University, Tianjin 300071, China

email: zhangxiaosong@tjut.edu.cn

Keywords: ZnS:Mn quantum dots, aqueous medium, photoluminescence, picosecond laser

Abstract. ZnS:Mn quantum dots were prepared in the aqueous medium from readily available precursors. The construction, morphology and luminescence properties of the ZnS:Mn quantum dots were evaluated by XRD, TEM and photoluminescence spectra. The blue and orange emission of the ZnS:Mn quantum dots excited by a 532nm picosecond laser were discussed.

Introduction

Semiconductor quantum dots (QDs) have been extensively studied in recent years [1-3], owing to their novel chemical and physical properties, especially photophysical properties. They are good candidates for applications in light-emitting Diodes (LEDs) [4], photoelectrochemical cells [5], luminescent bio-probes and bio imaging *in vivo* [6-8] and laser [9]. Mn-doped ZnS semiconductor quantum dots, as one kind of the typical semiconductor materials possessing the unique properties of quantum dots, have been intensively studied. Traditionally, zinc sulfide has been studied both in bulk and thin film form for a long time. It has been used all along for its wide and direct band gap by doping it with various elements. In 1994, Bhargava and Gallagher [10] reported the first realization of a ZnS semiconductor nanocrystal doped with Mn isoelectronic impurities. From then on, many researchers are trying to synthesize the Mn-doped ZnS quantum dots and the considerable attention has been paid to optical properties of ZnS:Mn quantum dots [1,2,11]. However, previous experimental observation and theoretical investigation of ZnS:Mn quantum dots principally focused on the fabrication method and luminescent mechanism excited by the ultraviolet excitation source. Little information of the luminescent properties of ZnS:Mn quantum dots excited by the excitation source in the visible region, which has advantages for applications in the biological fluorescence label and imaging, has been investigated. In addition, finding the efficient method to fabricate high quality quantum dots is farther research. In this research, we present free-standing ZnS:Mn quantum dots and good disperse ZnS:Mn in the aqueous medium from readily available precursors. And the luminescent properties of ZnS:Mn quantum dots with varying initial concentration of Mn^{2+} excited by the excitation source in the visible region were studied.

Experimental procedure

A aqueous solution of $Zn(CH_3COO)_2 \cdot 2H_2O$ was added to $Na(PO_3)_n$ with vigorous stirring at room temperature. Then $Mn(CH_3COO)_2 \cdot nH_2O$ was added in small portions to this solution. The mixture was sonicated to ensure complete dissolution. Next, Na_2S was added at a low flow rate, and a white suspension was formed at this stage. The reaction temperature was maintained at ambient temperature for 2 h under constant stirring. The ZnS:Mn quantum dots were isolated by centrifugation, washed twice. ZnS:Mn over-coated surfactant quantum dots dispersed in dilute water and place in quartz cuvette. Three kinds of ZnS:Mn quantum dots were prepared in this way by varying the initial amount of Mn^{2+} salt used during the fabrication. Powder X-ray diffraction (XRD) spectra were collected on a Rigaku D/MAX 2500 X-ray diffractometer with the K α line of Cu as a radiation source. Size and morphology of ZnS:Mn quantum dots were measured using a FEI Tecnai G2 F20 field emission transmission electron microscope. Photoluminescence (PL)

measurements of ZnS:Mn nanocrystals were measured using a laser and a spectrofluorometer. The emission spectrum was also measured using an OCEAN OPTICS HR2000 fiber spectrofluorometer. The laser light source was the second harmonic generation of a Nd:YAG laser operating at 532nm wavelength, 35 picosecond pulse width, 10 Hz repetition rate.

Results and Discussion

X-ray Diffraction. The construction of ZnS:Mn quantum dots was characterized by XRD. Figure1 shows the XRD patterns of three kinds of quantum dots samples containing (b) 5%, (c) 10% and (d) 20% (in molar ratio) of Mn^{2+} ions respectively. It can be seen that all samples exhibit one phase. This phase has the equilibrium structure of zinc blende crystal, which is displayed as an underlying pattern [vertical lines in Fig. 1 (a)]. The diffraction peaks are broadened prominently, which is characteristic of nanoparticles. No peak corresponding to manganese compounds is observed, demonstrating that Mn^{2+} ions are dispersed in ZnS matrix.

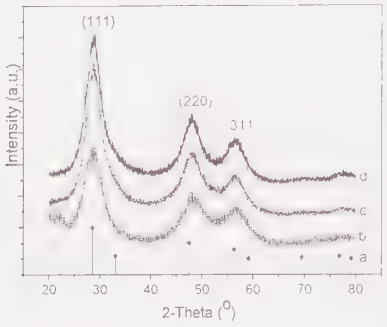

Figure 1. XRD patterns of ZnS:Mn quantum dots: (a) bulk ZnS blende peak position; (b) QD doped with 5% Mn^{2+} ions; (c) QD doped with 10% Mn^{2+} ions; and (d) QD doped with 20% Mn^{2+} ions.

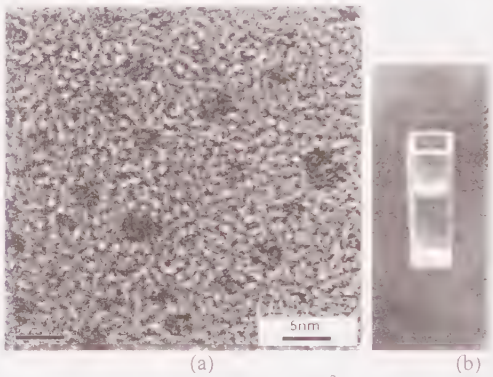

(a) (b)

Figure 2. (a) HRTEM of 10% Mn^{2+}-doped ZnS:Mn quantum dots at room temperature in bright field. (b) Photograph of ZnS:Mn quantum dots dilute water solution.

Transmission Electron Microscopy. Figure 2 (a) shows the HRTEM image of 10% Mn^{2+}-doped ZnS:Mn quantum dots at room temperature. The shape of the particles is approximately spherical, and the diameters are 4nm for ZnS:Mn quantum dots. By comparing the result of XRD and HRTEM, the quantum dot size calculated from XRD pattern is in accord with the result from HRTEM image. At the same time, Fig. 2 (b) shows a sample of ZnS:Mn over-coated surfactant quantum dots dispersed in dilute water and place in quartz cuvette.

Photoluminescence. The room temperature PL spectra were recorded for the samples with different Mn^{2+} concentration under the 532nm picosecond laser pulsed excitation. In Fig.3, the maximum peak at 532nm is from the scattering light of the excitation source. The linear UV-visible absorption spectrum of ZnS:Mn quantum dots was investigated [11]. The absorption band of ZnS:Mn quantum dots is mainly in the UV region and the absorption edge occurs around 350nm, which indicates that ZnS:Mn quantum dots have no linear absorption at 532nm. Thus, the emission of ZnS:Mn quantum dots excited by 532nm laser pulses can be attributed to two-photon excition. The emission band ranging from 390nm to 450nm can be assigned to the recombination of free charge carriers at defect sites in the ZnS nanocrystals. With the increase of the doping level, the intensity of blue emission increases while the peak position does not shift. The orange emission around 595 nm can be attributed to the intraion transition of the Mn^{2+} impurity. The characteristics of the orange Mn^{2+} emission are almost identical to the emission observed for Mn^{2+} in bulk ZnS. Mn^{2+} ions occupy Zn^{2+} lattice sites in the ZnS host lattice. In the PL process, an electron is excited from the ZnS valence band across the band gap. The photoexcited electron subsequently decays by a nonradiative

recombination process to $^4T_1$ level in Mn^{2+} ions, then decays radiatively to the $^6A_1$ level. The intensity of orange emission significantly increases with the increase of the Mn concentration while the peak position does not shift. The concentration quenching is not shown in this study.

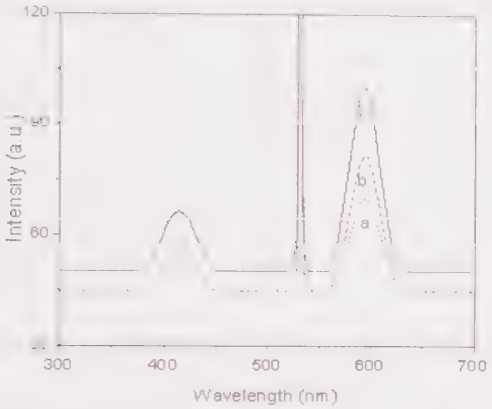

Figure 3 Photoluminescence spectra of ZnS:Mn quantum dots pumped by 532nm laser with different dopant concentration: (a) doped with 5% Mn^{2+} ions; (b) doped with 10% Mn^{2+} ions; (c) doped with 20% Mn^{2+} ions.

Summary

ZnS:Mn quantum dots prepared in the aqueous medium from readily available precursors were investigated in this study. The construction, morphology and luminescence property of ZnS:Mn quantum dots was characterized by XRD, HRTEM and PL. The shape of the particles is approximately spherical, and the diameters are approximate 4nm for ZnS:Mn quantum dots. The blue emission around 425nm and orange emission around 595 nm can be attributed to the intraion transition recombination of free charge carriers at defect sites in the ZnS nanocrystals.and of the Mn^{2+} impurity respectively. With the increase of the Mn concentration, the intensity of blue and orange emission significantly increases.

Acknowledgements

The authors are grateful to the Tianjin Natural Science Foundation (Grant No. 07JCYBJC06400), the National Key Basic Research and Development Program of China (Grant No. 2003CB314906) and the National Natural Science Foundation of China (Grant No. 10674074).

References

[1] Lixin Cao, and Shihua Huang: Journal of Luminescence, Vol. 114 (1992), p. 293

[2] W.Q. Peng, S.C. Qu, G.W. Cong, X.Q. Zhang and Z.G. Wang: Thin Solid Films, Vol. 499 (2006), p. 104

[3] DaeGwi Kim, Tetsuya Kuwabara, and Masaaki Nakayama: Journal of Luminescence, Vol. 119-120 (2006), p. 214

[4] Michael J. Bowers II, James R. McBride, and Sandra J. Rosenthal: Journal of American chemical society, Vol. 127 (2005), p. 15378

[5] D.V. Talapina, S.K. Poznyakb, and N.P. Gaponika: Physica E, Vol.14 (2002), p. 237

[6] Roger F Uren: Nature Biotechnology, Vol. 22 (2004), p. 38

[7] Wen Jiang, Eli Papa, Hans Fischer, Sawitri Mardyani and Warren C.W. Chan: TRENDS in Biotechnology, Vol.22 (2004), p. 607

[8] Yan Xiao and Peter E. Barker: Nucleic Acids Research, Vol. 32 (2004), p. e28

[9] H. Eisler, V.C. Sundar and M.G. Bawendib: Applied physics letters, Vol. 80 (2002), p. 4614

[10] Bhargava R N and Gallagher D.: Phys. Rev. Lett., Vol. 72 (1994), p. 416

[11] Zheng Jiajin, Zhang Gulan, Guo Yangxue, Wang Xiaoyan, Chen Wenju, Zhang Xiaosong, and Hua Yulin: Chin. Phys. Lett. Vol. 23 (2006) p. 3097

Advanced Materials Research Vol. 31 (2008) pp 170-172
online at http://www.scientific.net
© 2008 Trans Tech Publications, Switzerland

Surface and Structure of Porous Silicon Layers

Jingmei LU [1, a], Xuan CHENG [2, b]

[1] Department of Chemistry, Xiamen University, Fujian 361005, P. R. China
[2] Department of Materials Science and Engineering, State Key Laboratory for Physical Chemistry of Solid Surfaces, Xiamen University, Fujian 361005, P. R. China

[a] ljmei2006@xmu.edu.cn, [b] xcheng@xmu.edu.cn

Keywords: Porous Silicon, Electrochemical Impedance Spectroscopy (EIS), In-situ Characterization

Abstract. The porous silicon (PS) layers were fabricated on n(100) and n(111) silicon by applying the constant and repeated currents in different HF solutions. The electrochemical impedance spectroscopy (EIS) was used to in-situ characterize the Si/electrolyte interface before and after the PS formations. The surface and structure of PS layers were examined in terms of electrochemical/surface parameters.

Introduction

Preparations of porous silicon (PS) layers can be readily controlled by different current or voltage signals [1-3]. Scanning electron microscopy (SEM) can visually observe surface morphologies of PS layers; however, the information about PS formation is limited. Electrochemical impedance spectroscopy (EIS) has been demonstrated to be a quick and sensitive method to study Si dissolution and electropolishing in HF solutions [1, 4]. An equivalent circuit is usually proposed to represent the Si/electrolyte interface and parameters are fitted with experimental data to interpret electrochemical and surface properties. In this investigation, the PS layers were prepared on the n(100) and n(111) Si in different HF-containing solutions. The surface and structure of PS layers were studied by SEM and in-situ EIS techniques. The electrochemical kinetic and interfacial parameters were evaluated.

Experimental

The n(100) Si (2~4 Ω·cm) and n(111) Si (<0.02 Ω·cm) were purchased from the Shanghai silicon material factory in China. The EIS measurements were done using PGSTAT 30 AutoLab electrochemical working station (Switzerland). The applied ac amplitude was ±10mV. A conventional three-electrode cell was used with the Si, Pt foil and saturated calomel electrode (SCE) as the working, counter and reference electrodes, respectively. The i~V curves with a scan rate of 0.5 $mV \cdot s^{-1}$ and in-situ EIS spectra were recorded under a daylight before and after the current applications. The surface morphologies of PS layers were obtained using a LEO 1530 field emission scanning electron microscope (Oxford, Germany) without coating. More detailed test information is provided in Table 1.

Results and Discussion

Figure 1 presents typical i~V curves and surface morphologies of n(100) and n(111) Si in different HF solutions. The characteristic three regions of PS formation, transition and

electropolishing were observed as evident in Fig. 1(a)-(b). It was also seen in Fig. 1(a) that the current densities of n(100) were slightly larger by the addition of the ethanol in HF solutions. Figure 1(b) shows that the current densities of n(111) were higher than those of n(100) in HF and C_2H_5OH solutions. The faster reaction rate resulted from n(111) might be attributed to its higher doping concentrations.

Table 1. The details of the experimental condition

	i-V Curves		PS Layers		
	n(100) Si	n(111) Si	n(100) Si		n(111) Si
	0~6V (vs. OCP)		0.5mA 30min	0.5mA/2s→0mA/2s →-0.5mA/2s 300 cycles	1mA/2s→0mA/2s →-0.5mA/2s 150 cycles
2% HF	2% HF: C_2H_5OH=1:1 (volume ratio)	2%HF: C_2H_5OH=1:1 (volume ratio)	2%HF: C_2H_5OH=1:1 (volume ratio)	2%HF: C_2H_5OH=1:1 (volume ratio)	2%HF:H_2O:HCl:C_2H_5OH =50:20:150:280 (mass ratio)
Fig.1(a)	Fig.1(a)(b)(c)	Fig.1(b)(d)	Fig.2(a)(d)	Fig.2(b)(e)	Fig.2(c)(f)

As evident in Fig. 1(c) and (d), the silicon surface after the anodic polarization (Fig. 1(b)) became rough and a sponge-like structure of PS layers were observed on both n(100) and n(111). Fairly uniformly distributed pores with occasionally a very large square pore were formed at the n(100) surface (Fig. 1(c)), while less rough but uniformly distributed pores and possible electropolishing surface were coexisted at the n(111) surface when tested at the same conditions (Fig. 1(d)). The smooth surface layer formed at the top of PS layers in Fig. 1(d) might be related to silicon oxides since visible current oscillations occurred with n(111) as evident in Fig. 1(b).

It was revealed that the PS layers with different microstructure could be formed when applying constant I/E signals or with variable I/E patterns [3]. To in-situ characterize the PS formation, two different variations of current patterns (see Table 1) were tested, and then compared with the continuous current application. The results are given in Fig. 2. In all cases, similar sponge-like structure of PS layers was observed for both n(100) and n(111) with more interconnected and finer textures as seen in Fig. 2(b). In the equivalent circuit shown in Fig. 2(e), R_0 represents the resistances of the solution and silicon, (R_1Q_1) are caused by the non-ohmic contact between the silicon and the non-rust steel sheet, and (R_2Q_2) are related to the charge

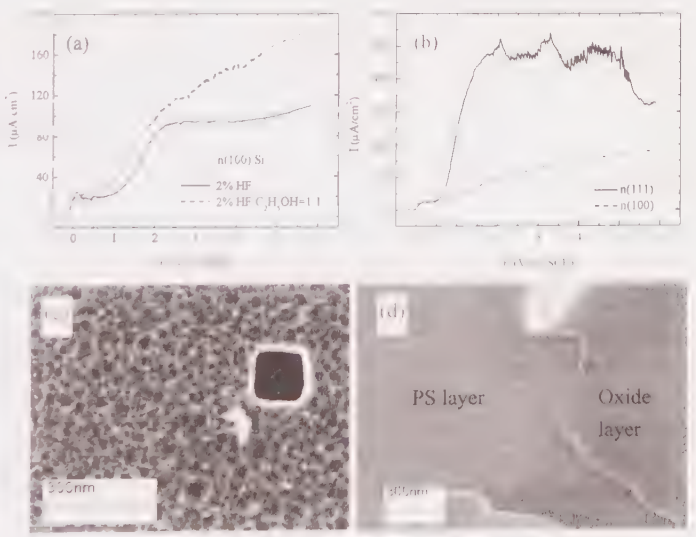

Fig. 1 Typical i-V curves and SEM images for n(100) and n(111)

transfer resistance and the double layer charging capacitance at the silicon/solution interface. The interfacial electrochemical reaction rate is inversely proportional to R_2 values, while the interfacial surface roughness is directly linked to Q_2 values. Thus, the different R_2 and Q_2 values given in Fig. 2(d) to Fig. 2(f) imply that the Si/HF interfacial characteristics before and after the PS formation varied substantially. After the formation of PS layers (the open-circle symbols in Figs. 2(d)-(e)), the n(100) surface with the constant current applications was rougher than that with the repeated current applications as indicated by larger Q_2 and smaller R_2 values. The reaction products might be continuously removed by applying the repeated currents and the exposure of the fresh surface might result in faster but more uniform reaction rate at the pore tip. It was postulated that the PS growth might be accelerated in depth not at surface. For n (111), the surface morphologies (Fig. 2(c)) appeared very similar to those of n(100) shown in Figs. 2(a)-(b), however, the surface was rougher (Q_2 values in Fig. 2(f) is larger than that in Fig. 2(e)) than n(100) with the repeated current applications in different solutions. The reaction rate of n(111) (indicated by the smaller R_2 values) was also faster than that of n(100) because of its highly doped nature. The EIS analysis seems to be very sensitive to the PS layers formed and can be used for a rapid in-situ surface analysis.

Summary

The EIS analysis was powerful to in-situ study Si/HF interfaces. The different current applications and electrolytes resulted in variations in PS layers.

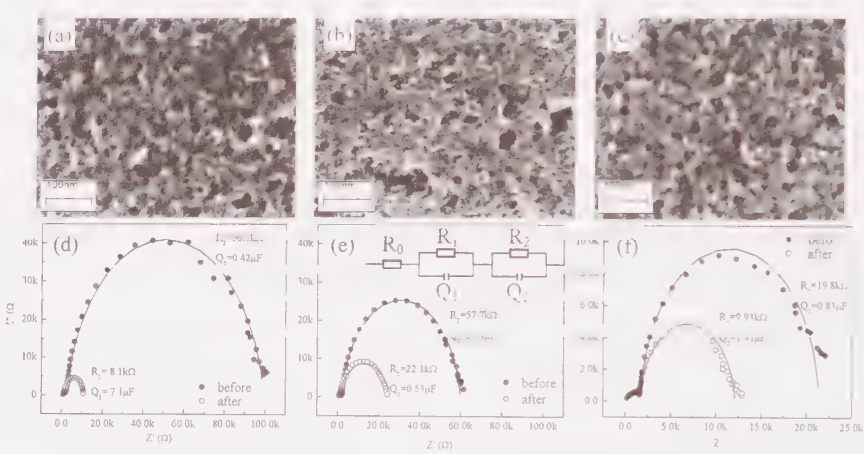

Fig. 2. SEM images after various current applications and Nyquist plots of n(100) and n(111) before and after various current applications in different HF solutions. Detail experimental information is given in Table 1.

References

1. Searson, P.C. and X.G. Zhang, *The Anodic Dissolution of Silicon in HF Solutions.* Journal of The Electrochemical Society, 1990. **137**(8): p. 2539-2546.
2. Zangooie, S., R. Jansson, and H. Arwin, *Microstructural control of porous silicon by electrochemical etching in mixed HCl/HF solutions.* Applied Surface Science, 1998. **136**(1-2): p. 123-130.
3. Xuan Cheng , Z.-D.F., Guang-Feng Luo, *Effect of potential steps on porous silicon formation.* Electrochimica Acta, 2003. **48**: p. 497-501.
4. P. A. Forsh, M.N.M.V.Y.T.P.K.K., *Impedance spectroscopy of in-plane anisotropic porous silicon films.* physica status solidi (c), 2007. **4**(6): p. 1981-1985.

Advanced Materials Research Vol. 31 (2008) pp 173-175
online at http://www.scientific.net
© 2008 Trans Tech Publications, Switzerland

Broadband emission in InAs/InGaAlAs quantum-dash-in-well laser

Boon S. Ooi[1,a], Hery S. Djie[1], Amr.S. Helmy[2], James C.M. Hwang[1]
Center for Optical Technologies and Electrical and Computer Engineering Department,
Lehigh University, Bethlehem, PA 18015, USA.
[2]Department of Electrical and Computer Engineering, University of Toronto,
Ontario, Canada M5S 3G4
[a]Corresponding author: bsooi@lehigh.edu

Keywords: Quantum dash, Quantum dot, Broadband emission, Semiconductor Laser.

Abstract. We report on the development of wide gain InAs/InGaAlAs/InP quantum-dash structure for broadband diode laser and amplifier. Characterizations of this material system have been performed using spectroscopy and microscopy techniques. Gain-guided broad area laser fabricated using this material system exhibits lasing wavelength coverage of up to 76 nm at ~1.64 μm center wavelength from simultaneous multiple confined states lasing at room temperature.

Introduction

Ultra-broad and continuous spectrum generation is an interesting physical phenomenon and an attractive technology for many applications. The development of a viable technology to generate continuous lasing spectrum crossing multiple communication bands in near-infrared will bring significant advances and impact to optical fiber communications, imaging, metrology, spectroscopy and sensing. To date most ultra-broadband sources are generated using nonlinear-optical transformations of ultra-short laser pulses and photonic crystal fiber based approaches. Although Gmach, *et al* demonstrated broadband stimulated emission at mid-IR using the quantum cascade approach, this method of generating broadband semiconductor laser is complex and the laser exhibits extremely low quantum efficiency at room temperature (RT) [1].

In this paper, we report on the development of a new class of diode laser that produces ultra-broad stimulated emission that inherits from the interband transition operation of quasi-zero-dimensional quantum confined heterostructure at near-IR region. Our novel device fabricated in InAs/InGaAlAs quantum-dash-in-well structure exhibits RT lasing wavelength coverage of up to 76 nm at ~1.64 μm from simultaneous multiple confined states lasing. This compact, cost effective and high efficiency broadband diode laser will unfold many new ideas across inter-disciplinary fields in photonics.

Experiments

The self-organized InAs/InAlGaAs QDash device structure was grown by molecular beam epitaxy (MBE) on (100)-oriented S-doped InP substrate. The laser structure is a *p-i-n* configuration with the active region consists of four sheets of InAs dashes, each embedded within a 7.6 nm thick compressively-strained $In_{0.64}Ga_{0.16}Al_{0.2}As$ QW and a 30 nm thick tensile-strained $In_{0.50}Ga_{0.32}Al_{0.18}As$ barrier [1]. The surface morphology and device cross-section of InAs QDashes were investigated using an atomic force microscopy (AFM) and the cross sectional transmission electron microscopy (TEM) prepared along [110] and [1$\bar{1}$0] orientations, respectively. TEM images were taken under the (002) dark field projection that is much more sensitive to chemical

composition than to strain, the contrast observed should be dominated by group-III atomic composition contrast. State-filling photoluminescence measurement was performed at cryogenic temperature using a 532 nm diode pumped solid state laser as an excitation source. The optical pumping density is varied by adjusting the circular neutral density filter. Broad area lasers with 50 μm wide oxide stripes were fabricated using the standard semiconductor laser fabrication process. The laser optical cavity is aligned along [110] orientation and is perpendicular to the dash direction to maximize the optical gain. The QDash laser was tested under pulsed operation of 10 μs pulse width and 1 % duty cycle. The optical spectra were acquired using optical spectrum analyzer with wavelength resolution of 0.05 nm.

Results and discussion

Fig. 1(a)-(b) show the plane-view AFM from the uncapped QDash grown on sample surface, and the [110] and [$1\bar{1}0$] cross-sectional TEM images from the laser structure taken under the (002) dark field projection. The QDash nanostructure consists of three-dimensional finite wire preferentially aligned along the [$1\bar{1}0$] direction composed of dot-like and dash-like islands, that are formed from the coalescence of two or more dot-like islands. QDash assembly has an average height of 3.2 nm, an average width of 18 nm, and the base or length varied from 20 to 75 nm. The island density is high with area coverage of greater than 70%. Considering the large dispersion in shape, size and composition, the inhomogeneous dash ensemble causes the energy spreading in the confining potentials and a broadening in the optical gain, which is useful for the wideband optical devices such as superluminescent diodes (SLED) [2] and semiconductor optical amplifier (SOA) [3].

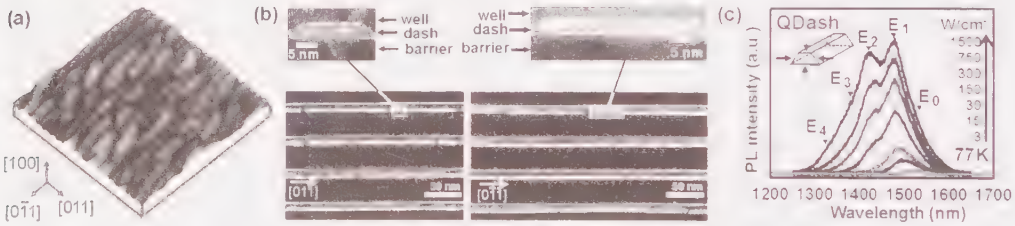

Fig.1. (a) The plane-view AFM image of surface QDash structures (area of 0.5x0.5 μm^2: height contrast of 8 nm); (b) The cross-sectional TEM images of buried QDash laser structures under (002) dark-field taken from different crystal orientations. (c) Optical power dependent PL spectra at 77 K taken from InAs QDashes within InAlGaAs matrix revealing the systematic filling of quantized states. The confined energy subbands are indicated with the arrow.

State-filling PL spectroscopy was performed by varying optical pumping density of laser excitation. As noted from Fig. 1(c), the QDash material exhibits quantized states (E_0 to E_4) with small energy separation, i.e. energy spacing between E_0 and E_1, ΔE, of 30 meV. At highest excitation density (1500 W/cm^2), a large number of minima in QDash spectra are populated, resulting a broad emission line. These properties corroborate the quasi-continuous interband transition characteristics in QDash assembly over a wide wavelength range.

As-cleaved broad area lasers with 50 μm wide oxide stripes were fabricated from the QDash laser using the standard laser fabrication process. Fig. 2(a) depicts the electroluminescence (EL) spectrum of QDash showing fine structures from different confined energy subbands that are well correlated to different lasing peaks with varying cavity length. Up to three distinct laser emissions

(1.65, 1.62, and 1.59 μm) from E_0, E_1 and E_2 energy transitions were obtained at $1.1\times J_{th}$ from lasers with cavities L of 1000, 300, and 150 μm, respectively. The distinct lasing wavelength peak is attributed to the finite modal gain for each quantized state in QDash assembly. Fig. 2(b) shows the light-current (L-I) characteristics of the QDash laser (L = 600 μm). The corresponding threshold current density and slope efficiency are 2.6 kA/cm^2 and 0.165 W/A. Up to 400 mW total output power has been measured at $J = 4.5\times J_{th}$ at 20°C from the device. From the dependence of J_{th} on temperature, the temperature characteristic T_0 of 43.6 K in the range of 10 to 70°C has been obtained. At injection below 1.5 $\times J_{th}$, there is only ground state lasing E_0 with the wavelength coverage of up to 10 nm [Fig. 2(c)]. The broad E_0 lasing spectrum suggests the collective lasing from QDashes with different geometries. Above 1.5 $\times J_{th}$, the dual-state lasing occurs. The simultaneous lasing from both E_0 and $E_1$is attributed to the relatively slow carrier relaxation rate and population saturation in the ground state in low-dimensional quantum heterostructures [4]. The transition from mono-state to bi-state lasing is marked with a slight kink in the L-I characteristics. The bi-state lasing spectrum is progressively broadened with increasing carrier injection up to a wavelength coverage of 54 nm at $J = 4.5\times J_{th}$. The corresponding side-mode suppression ratio of lasing spectra is over 25 dB and a ripple measured from the wavelength peak fluctuation within 10 nm span is less than 3 dB.

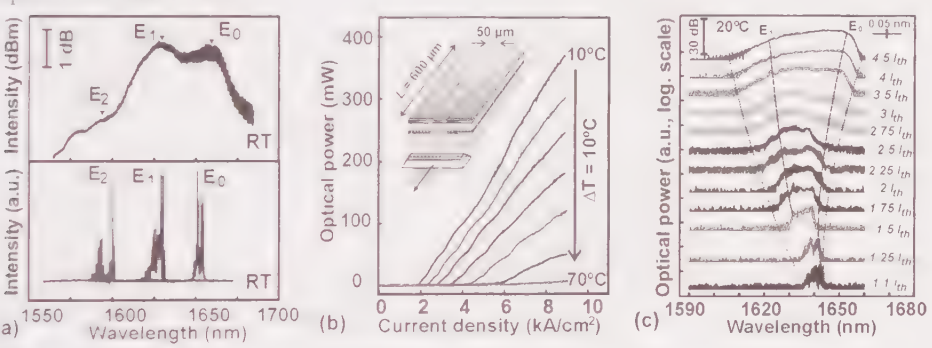

Fig. 2. (a) The spontaneous emission spectrum of QDash laser (L = 300 μm) at $0.8\times J_{th}$ (top) and the lasing spectra at $1.1\times J_{th}$ from QDash laser with varying cavity length. (b) The L-I characteristics of ultrabroadband QDash laser (L = 600 μm) with the cavity orientated perpendicular to the dash direction (inset). (c) The lasing spectra from QDash laser with varying injection current. The lines are as the guide to the eyes indicating the confined state lasing lines, E_0 and E_1 (dashed lines) and the wavelength coverage of laser emission (dotted lines).

Summary

The unprecedented broadband laser emission at RT up to 76 nm wavelength coverage has been demonstrated in the inhomogeneous InAs/InAlGaAs QDash structure. The results suggest that the quasi-one-dimensional QDash material can be utilized as a gain media for the generation of novel broadband semiconductor laser source and amplifier.

Reference:

[1] C. Gmachl et al, Nature Vol. 415 (2002), p.883.

[2] H.S. Djie et al., IEEE Photon. Technol. Lett. Vol. 18 (2006),p.1747.

[3] A. Somers et al., Appl. Phys. Lett. Vol.89 (2006), p. 061107.

[4] A. Markus et al., Appl. Phys. Lett. Vol. 82 (2003), p.1818.

Advanced Materials Research Vol. 31 (2008) pp 176-178
online at http://www.scientific.net
© 2008 Trans Tech Publications, Switzerland

Improved Carbon Counter electrodes for Dye Sensitized Solar Cells

H. S. Lee[1, a], H. Y. Lee[1, b], S. Y. Ahn[2, c], K. H. Kim[3, d], J. Y. Kwon[1, e]

[1]Department of Electrical Eng., Myongji University, Yongin, 449-728, Korea

[2]Sebang Hi-Tech CO., LTD R&D Center 45-1, Changwon, 641-120, Korea

[3]Department of Chemistry, Myongji University, Yongin, 449-728, Korea

[a]hslee611@hanmail.net, [b]hylee@mju ac kr, [c]ahn-nb@hanmail net, [d]kkh422@hanmail net, [e]illbul@hanmail.net

Keywords: carbon counter electrodes, DSSCs, TiO_2, chemical sintering

Abstract. We fabricated improved carbon counter electrodes to improve conversion efficiency of dye sensitized solar cells (DSSCs). Unlike conventional carbon counter electrodes, we added small quantity of TiO_2 nano powder and used chemical sintering methodology developed by Park's group to make surface morphology of the electrodes to change. Through these methods, we could observe change of surface morphology of carbon electrodes and influences on short circuit current density (J_{SC}) and conversion efficiency.

Introduction

Dye sensitized solar cells (DSSCs) have been investigated actively due to its merits in economic, scientific and technical aspects since their conversion efficiency was recorded more than 10 % [1-3]. Several groups tried to substitute Pt electrodes used commonly as counter electrodes for carbon electrodes because Pt materials was very expensive [1,2,4]. However, the carbon electrodes were not only resulted in lower conversion efficiency but also needed higher temperature, more than 450 [°C], than Pt electrodes [2]. K. Imoto et al. were made carbon electrodes used organic binders in low temperature (150 [°C]). Though conversion efficiency of the cell used carbon electrodes was low, they found that surface morphology of the carbon electrodes play an important role in conversion efficiency of cells [5]. In this paper, to make surface morphology to be changed, we applied TiO_2 nano powder [2] and chemical methodology developed by park et al. [6] to carbon counter electrodes. Fabricated electrodes were investigated its surface morphology, and then we measured the conversion efficiency of the cells that had the modified carbon electrodes.

Experimental procedure

Fabrication processes and measurement. Preparation of TiO_2 electrodes used commercialized TiO_2 powder, P25 (Degussa), was referred to previous experiments [4,7]. Carbon paste was composed of activated carbon (BET surface area: 36 [m^2/g]), carbon black, distilled water, CMC (Carboxy methyl cellulose) as binders and ethanol. Among these chemicals, CMC content was fixed on 6 wt%. The paste was stirred for 6 h. Stirred paste was deposited on 1 cm^2 area of ITO glass and was dried at 150°C for 1 h (Carbon-a) [2,5,7]. Other three pastes were prepared in the same way. First thing was added 6 wt% TiO_2 nano powder (Carbon-b), Second thing was added 10 wt% ammonia and 10 wt% acetic acid according to chemical sintering methodology (Carbon-c) and the last one was added the three chemical in carbon paste (Carbon-d). Prepared TiO_2 electrodes were immersed in 0.03M N719 dye (Solaronix) solution at room temperature for 24 h in the dark. The electrodes were rinsed with absolute alcohol and were attached to carbon electrodes. Liquid electrolytes which consist of 0.5 M LiI, 0.05 M I_2, 0.5M 4-TertButyl Pyridine and 3-Methoxy Propionitrile were injected between them [7]. Surface morphology of electrodes was measured by AFM (atomic force microscope) and FE-SEM (field emission scanning electron microscope). Conversion efficiency of the cells was measured using I-V curve tracer and solar simulator under AM 1.5 (100mW/cm^2).

Results and Discussion

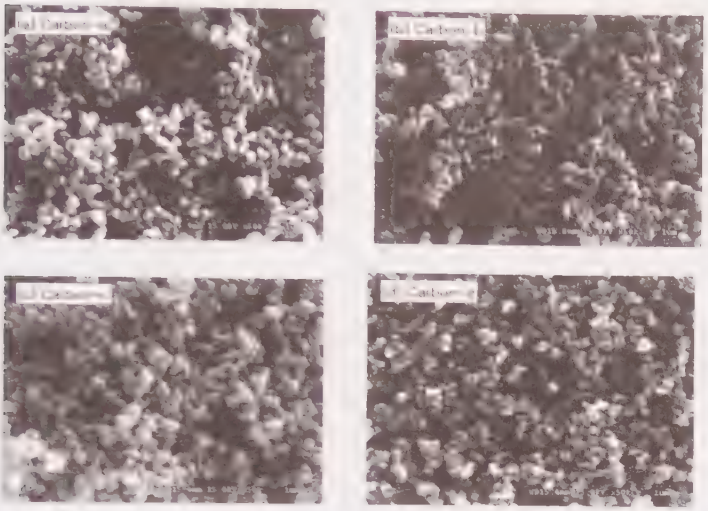

Fig. 1 Surface morphology of the carbon electrodes

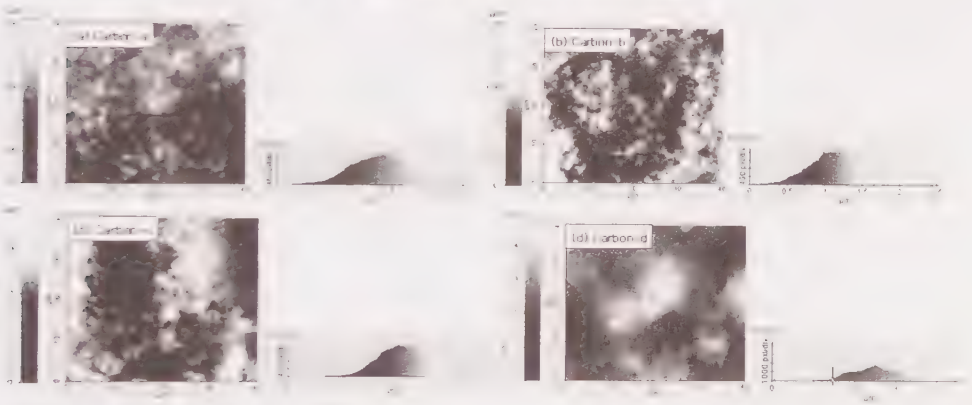

Fig. 2 Surface analysis by AFM

Fig. 1 (a) and Fig. 2 (a) show surface morphology and histogram of conventional carbon electrodes used binders. Fig.1 (b) and Fig. 2 (b) show effects of adding TiO_2 nano powder. Their surface is more compact than Carbon-a because pores of the carbon electrodes were well filled with TiO_2 nano powder. The reason for this phenomenon is that TiO_2 nano particles (21 [nm]) smaller than activated carbon particles (several [μm]) and carbon black particles (several tens [nm]) [5]. From its histogram, we could see narrowed distribution of histogram as proof of compacted surface. Carbon-c shown Fig. 1 (c) and Fig. 2 (c) have rougher surface than Carbon-a (RMS

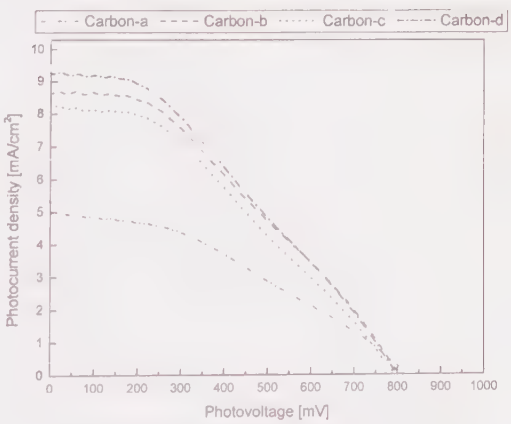

Table 1 Changed efficiency of cells

roughness 392.286 => 689.165) through process of dispersion and flocculation that was occurred by ammonia and acetic acid added in its paste. We could observe histogram of Fig. 2 (c) as proof of roughed surface. Carbon-d of Fig. 1 (d) and Fig. 2 (d) shows more uniform pore and more wide distribution of histogram than other electrodes. In addition, the electrode have rougher surface than Carbon-a (392.286 => 460.593) though it is less rough than Carbon-c. This is because the three materials added have influence on surface morphology of carbon electrodes. We found that carbon electrodes with uniform and rough surface morphology could be made appropriate combination of TiO_2 nano powder, ammonia and acetic acid.

Fig. 3 and table 1 show characteristic curves and values of the cells. Although most values were slightly decreased, J_{SC} largely increased. Especially, J_{SC} of Carbon-d doubled nearly in comparison with that of the Carbon-a. These variations are thought to be the results of enhancement of interconnection between carbon particles by TiO_2 nano powder and formation of rougher surface which can increase chemical activity between carbon materials and electrolytes by chemical sintering methodology. That is to say, TiO_2 nano powders play a role in an inter-connector between carbon particles to enhance electron paths inner carbon electrodes and chemical sintering methodology make roughness of carbon electrodes to increase, which help chemical activity to occur well. Therefore, Carbon-d which has these two advantages, namely have more uniform surface and rougher morphology, act as a better carbon counter electrode.

	Jsc [mA/ cm^2]	V_{OC} [mV]	FF	Π[%]
Carbon-a	4.987	821.6	0.362	1.485
Carbon-b	8.641	801.9	0.359	2.488
Carbon-c	8.230	791.6	0.357	2.325
Carbon-d	9.308	797.2	0.349	2.589

Table 2 Changed efficiency of cells (active area : 1 [cm^2])

Conclusion

We could fabricate DSSCs used carbon materials to counter electrodes. By applying the TiO_2 nano powders and the chemical sintering methodology to carbon electrodes, we could make carbon electrodes with rougher and more uniform surface and know the fact that changed surface have an effect on J_{SC}. As a result, these changes helped efficiency of DSSCs to be increased.

References

[1] B. O'Regan, M. Gratzel, Nature 353 (1991) 737

[2] A. Kay, M. Gratzel: Sol. Energy Mater. Sol. Cells, Vol. 44 (1996), p. 99

[3] M. Gratzel: Prog. Photovlt. Res. Appl., Vol. 8 (2000), p. 171

[4] K. Imoto, K. Takahashi, T. Yamaguchi, T. Komura, J. I. Nakamura, K. Murata: Sol. Energy Mater. Sol. Cells, Vol. 79 (2003), p. 459

[5] Y. Saito, S. Kambe, T. Kitamura, Y. Wada, S. Yanagida: Sol. Energy Mater. Sol. Cells, Vol. 83 (2004), p. 1

[6] N. G. Park, K. M. Kim, M. G. Kang, K. S. Ryu, S. H. Chang, Y. J. Shin: Adv. Mater., Vol. 17 (2005), p. 2349

[7] H. S. Lee, S. J. Kim, J. Y. Kwon, J. C. Park, H. Y. Lee: J. of KIEEME, Vol. 20 (2007), p.337

Advanced Materials Research Vol. 31 (2008) pp 179-181
online at http://www.scientific.net
© 2008 Trans Tech Publications, Switzerland

Development of Fabrication Process and Electrostatic Microactuator for a Mechanically Tunable 2-D Photonic Crystal

B. Paul Chaudhuri[a], B. Thubthimthong[b] and F. A. Chollet[c]

School of Mechanical and Aerospace Engineering, Nanyang Technological University, Singapore
[a]paul0007@ntu.edu.sg, [b]born0002@ntu.edu.sg, [c]mfachollet@ntu.edu.sg

Keywords: Photonic Crystal, Comb-drive Microactuator

Abstract. In this present work we have taken the first step to implement theory into practice. We have conceived of a novel MEMS fabrication process to create a two-dimensional (2-D) photonic crystal made of a flexible polymer, such as SU-8. This SU-8 polymer is embedded with an array of cylindrical silicon pillars and this whole photonic crystal can be compressed by a comb-drive microactuator. The comb-drive microactuator was designed to produce a force in order to compress
the photonic crystal by 3%, and, hence, it can tune the photonic band gap. We fabricated 2-D photonic crystals of size 795 x 270 μm^2, 500 x 80 μm^2, 400 x 40 μm^2 and 772 x 225 μm^2. By applying DRIE technique, we have successfully fabricated the 2-D photonic crystal as well as the comb-drive microactuator using one contiguous process. Our process which has proved to be feasible can also be scaled down to the nanometer scale.

Introduction

Photonic crystals (PCs) have been the subject of intense research over the last two decades. Various types of photonic crystals have been fabricated using a host of techniques. Most of the ones that were produced earlier on had an invariable band gap. However, in recent years a variety of methods have been explored to achieve tunability of the PC band gap. Till date, the maximum tunability achieved in the most popular type of PCs using liquid crystals has been around 15%. Thus, there exists a large gap which can still be tuned, given the optimal means. A mechanical mean using MEMS was proposed and validated recently, though just theoretically [1],[2].

Microactuator Design

The microactuator was designed according to the required force to compress the PC by its width. The dimensions of the proposed photonic crystal were 20-μm-wide, 4.5-μm-high and 100-μm-long. During compression, 3% reduction in length was expected. To obtain the required compressive force, we used a 2-D finite-element model to estimate Young modulus of the PC. The model was comprised of SU-8 matrix and Si pillars whose diameters were 300 nm and the lattice constant was 600 nm forming triangular lattice. Due to computing limitation, our PC model dimensions were 3 μm in width and 6 μm in length. This corresponds to 50 Si pillars in total. The displacement-compressive load relationship was obtained and plotted. The slope of the plot which identified the effective Young modulus of the PC was found to be 5.5 GPa. The maximum von Mises stress was found to be well below compressive yield strength of both Si and SU-8. After obtaining the effective Young modulus of the PC, we calculated the required compressive force which became 0.0075 N. Since 3% reduction in length was required, the displacement of the microactuator was 3 μm. Therefore, we designed 3 folded flexures to restrict the motion of the microactuator rotor and to support it. The electrostatic fingers were designed to be 3 μm in width and 30 μm in length. The gap between the fingers was 3 μm and there were 2171 fingers in total. The microactuator would operate at actuating voltage around 124 V. After the design, we verified by finite-element analysis that the microactuator structure would not fail from its maximum yield strength during operation. We also predicted the operating resonant frequency of the microactuator would be around 2.5 kHz using the formula given by Legtenberg [3].

Fabrication Process

Fig. 1 shows the fabrication process steps. The fabrication started from a standard <100> silicon wafer. AZ-9260 positive photoresist was used through out the fabrication process. This photoresist can be dissolved in acetone much quicker than SU-8. Therefore, our use of SU-8 as a material of the device was possible. Isolating trenches were first created via deep reactive iron etching (DRIE). The trench width was designed to be 3 μm, and because of this we showed that our following technique could be employed to fill up such trenches whose width was more than 2 μm, the limitation of growing silicon dioxide. The technique of filling up the trenches (Fig. 1(b) - Fig. 1(d)) is also repeatable, thus, the trench width is not a critical restriction. To do this, the trenches were partially filled by thermal oxidation first. After the first thermal oxidation, low-pressure chemical vapor deposition (LPCVD) of polysilicon was performed to further fill up the trenches. When the trenches were filled, repetition of the process was stopped. Although conductive polysilicon was used, this did not cause short circuit, because the total thickness of non-conductive silicon dioxide from first silicon dioxide layer was as much as 4 μm (2 μm from each side of the trenches). Once the isolating trenches were fully filled, polysilicon wet-etching using KOH and silicon dioxide wet-etching using HF were performed in order to remove the two types of layers on the wafer surface. The top parts of the isolating trenches were also removed but only as much as the thickness of the layers on the wafer surface. Afterwards nanopattern for the Si pillars was created by e-beam lithography, however, at this stage we tried out the feasibility of the process by creating Si micropillars using DRIE instead (Fig. 1 (e)). To create the photonic crystal matrix, SU-8 was spin-coated, photopatterned for only the PC areas, and cured. Chemical mechanical polishing (CMP) was employed to level the SU-8 down to the same level as the Si pillars'. Another step of DRIE was carried out in order to create the comb-drive microactuator structure. Afterwards, another wafer was bonded to the first wafer using SU-8 and the whole device was released by back-side etching.

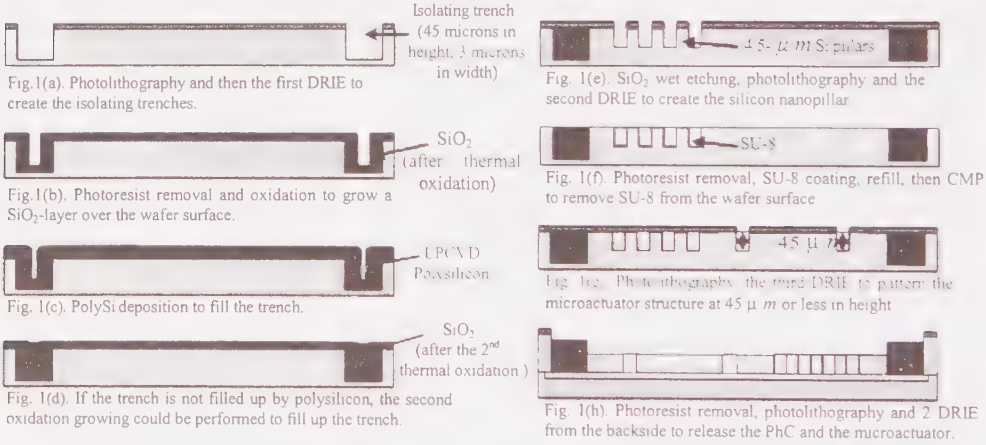
Isolating trench (45 microns in height, 3 microns in width)
Fig.1(a). Photolithography and then the first DRIE to create the isolating trenches.
SiO_2 (after thermal oxidation)
Fig.1(b). Photoresist removal and oxidation to grow a SiO_2-layer over the wafer surface.
LPCVD Polysilicon
Fig. 1(c). PolySi deposition to fill the trench.
SiO_2 (after the 2nd thermal oxidation)
Fig. 1(d). If the trench is not filled up by polysilicon, the second oxidation growing could be performed to fill up the trench.
45- μm Si pillars
Fig. 1(e). SiO_2 wet etching, photolithography and the second DRIE to create the silicon nanopillar
SU-8
Fig. 1(f). Photoresist removal, SU-8 coating, refill, then CMP to remove SU-8 from the wafer surface
45 μm
Fig. 1(g). Photolithography, the third DRIE to pattern the microactuator structure at 45 μm or less in height
Fig. 1(h). Photoresist removal, photolithography and 2 DRIE from the backside to release the PhC and the microactuator.

Fig. 1. Fabrication steps for the mechanically tunable 2-D photonic crystal.

Fabrication Results

So far we have verified that the fabrication steps are feasible. We separately fabricated the isolation trenches. Since our trenches were not fully filled after the second oxidation, another polysilicon LPCVD was carried out so as to further fill the trenches. The trenches were 45 μm in depth and became almost 4 μm in width. Since the function of the trenches is not only to isolate the comb-drive microactuator from substrate but also to support the microactuator structure, the trenches were designed such that they were long and meandering (Fig. 2). Fig. 2 displays a filled trench with openings at its corners. When the trench corners could not be sealed by the polysilicon due to wider

trench width, HF could flow down the trenches and could remove the oxide layers inside the trench. However, other part of the trenches which were filled up would still support the microactuator structure. Thin layers observed at the middle of a trench in Fig. 3 are the polysilicon which was not

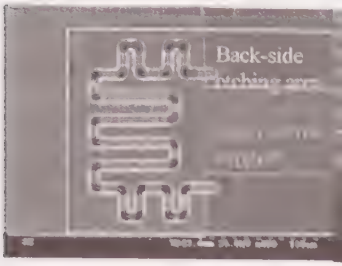

Fig. 2. Isolating trench for a stator comb support.

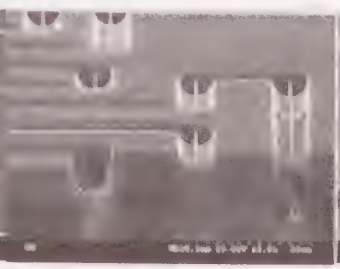

Fig. 3. A cross-sectional view of an isolating trench.

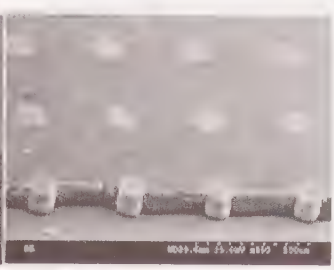

Fig. 4. A Si pillar array embedded in SU-8.

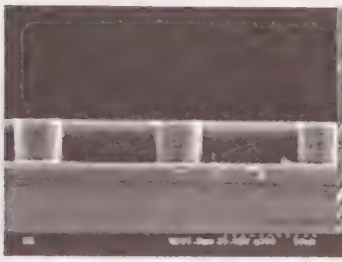

Fig. 5. Cross-sectional view of the PC prototype after CMP.

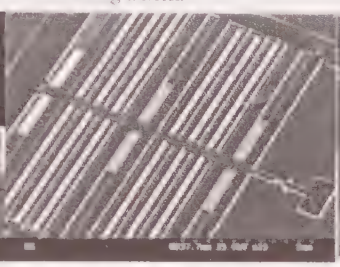

Fig. 6. An overview picture of the comb-drive microactuator.

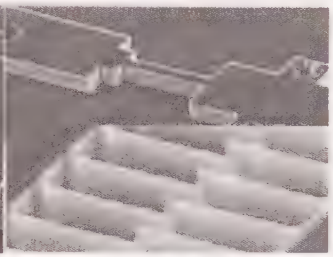

Fig. 7. Operating area of the PC.
Fig. 8. The interdigitated fingers.

etched by HF. This is as expected because we want to use polysilicon to seal the trenches in case there were keyholes below due to non-uniformity of the trench side surfaces. The next fabrication step was for the photonic crystal. We tried out the feasibility of this process by creating the Si pillars at micrometer scale. Fig. 4 shows the Si pillars embedded in SU-8 matrix after CMP. It can be seen from Fig. 5 that the silicon pillars and SU-8 matrix were at the same level, and the SU-8 had filled up the cavity between the pillars. PDMS which has much lesser stiffness, if used, could yield a much higher deformation at the same actuation voltage. But the problem, we found, with PDMS was that the entire PDMS layer was stripped off from the wafer surface during the CMP due to its soft nature. Lastly the microactuator structure was fabricated by another DRIE. Fig. 6 gives an overview picture of the comb-drive microactuator. The dimensions of the microactuator were around 4 mm by 6 mm. The middle long structure in Fig. 7 represents where the tunable PC will be fabricated. Fig. 8 displays the interdigitated fingers of the stator and the rotor.

Conclusions

We designed a comb-drive microactuator for a tunable 2-D photonic crystal. The microactuator was characterized by means of finite-element analysis. We developed the fabrication process for the mechanically tunable 2-D PC, albeit at micrometer scale. In our future work, we will scale down the PC fabrication to nanometer scale so that the actual device can be realized and tested in the end. In parallel, we will theoretically explore the optical properties of the photonic crystal in order to compare it with our future test results

References

[1] M. Tinker et al., in: Photonic Materials, Devices and Applications, edited by Gonçal Badenes et al., volume 5840 of Proceedings of SPIE, p. 147-p. 154, SPIE, Bellingham, WA (2005).

[2] W. Park and C. J. Summers, *Appl. Phys. Lett.* 85, 4845 (2004)

[3] Legtenberg R., Groeneveld A.W. and Elwenspoek M., *Journal of Micromechanics and Microengineering*, Vol. 6, pp 320-329 (1996).

Advanced Materials Research Vol. 31 (2008) pp 182-184
online at http://www.scientific.net
© 2008 Trans Tech Publications, Switzerland

Nano-scale bandgap engineering using nitrogen implantation: quantum-well, quantum-dash and quantum-dot nanostructures

Y.-H. Ding[1, a], V. Hongpinyo[1], H. S. Djie[1], B. S. Ooi[1, b]

Center for Optical Technologies and Electrical and Computer Engineering Department,
Lehigh University, Bethlehem, PA 18015, USA.

[a]yud205@lehigh.edu, [b]bsooi@lehigh.edu

Keywords: Quantum well, Quantum dash, Quantum wire, Quantum dot, intermixing, disordering.

Abstract. Nano-scale spatial wavelength engineering of quantum nanostructures using nitrogen ion-implantation induced intermixing has been developed for tuning the bandgap of quantum-well, quantum-dash-in-well, and quantum-dot nanostructures. High performance bandgap-tuned quantum-well and quantum-dash lasers fabricated using this technique has been demonstrated.

Introduction

The spatially selective bandgap engineering using postgrowth layer intermixing has been successfully applied for the high-density photonic integrated circuits due to its simplicity and effectiveness. Neutral ion-implantation induced intermixing (IID) using phosphorous implantation technique has been favored due to its compatibility with the semiconductor manufacturing, its controllability and reproducibility without introducing significant free carrier absorption[1,2]. Recently, we have developed the nitrogen-based IID (N-IID) process to alter spatially the material bandgap through the enhancement of group-III interdiffusion [3-5]. The light damage introduced by N ions can prevent the generation of loop clusters that usually produces extended defects with the implantation of large atomic size elements.

Following the advance development of the low-dimensional heterostructures grown on InP substrate, there has been an increasing interest to apply the intermixing process that offer the combined advantages of postgrowth bandgap engineering covering wavelength emission from 1.1 to 1.6 μm and the attractive characteristics of delta-like density of states [4]. Here, we further extend the N-IID process capability to induce the group-III and/or group-V intermixing in quantum-well (QW), quantum-dash-in-well (DWELL), and quantum-dots (QD) nanostructures. N-IID is shown to universally enhance both group-III and group-V sublattice intermixing. Up to 320 nm wavelength shift has been achieved at relatively low processing temperatures (650 °C). With the optimized process conditions, high quality bandgap tuned QW and DWELL lasers with reduced threshold current density has been fabricated and tested.

Experiments

Three different quantum structures on InP substrate are used in our experiments: (i) InGaAs/InGaAsP strain-balanced QWs; (ii) InAs/InAlGaAs DWELL; and (iii) InAs/InP QD that enables the evaluation of intermixing efficiency of group-III and –V, group-III only, and group-V only, respectively. These samples were implanted at a dose of 5×10^{12} cm^{-2} and energy of 1500 KeV. Up to 1000 nm thick SiO_2 layer was used as an implant mask for non-device structure to allocate the peak damage near or at the active region. This mask layer was removed to prevent impurity-free induced vacancy disordering (IFVD) effect [5] prior to annealing in a rapid thermal processor. The

annealing duration is fixed at 2 min and the temperature is selected high enough to promote the efficient intermixing for implanted sample without introducing unwanted intermixing effect on the control (non-implanted) sample. Subsequently, broad area lasers are fabricated from QW and DWELL laser structures from as-grown, control, and intermixed samples and tested at room temperature under pulsed operation (10 μs pulse width; 1% duty cycle).

Results and discussion

Fig. 1 depicts photoluminescence (PL) spectra at 77 K from QW, DWELL, and QD at annealing temperatures of 750°C, 700°C, and 650°C, respectively. The control sample only exhibits a small bandgap shift (<10 nm) with respect to the as-grown. In contrast, all intermixed samples show significant bandgap blue-shifts of 68 nm, 160 nm, and 320 nm with respect to the control sample for QW, DWELL, and QD, respectively from group-III and/or –V intermixing. Dual-peak of PL spectra from intermixed QWs is attributed to the different interdiffusion rates of our strained-balanced asymmetric QW structures consisting two set of multiple wells. The degree of intermixing increases progressively as the nanostructure dimension reduces from 1D QW to 3D QD structures hence surface to volume ratio of nanostructure becomes larger [7].

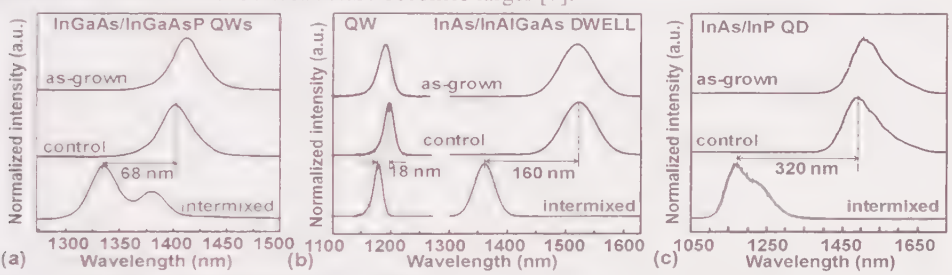

FIG1. The 77 K PL spectra from as-grown, control, and intermixed (a) InGaAs/InGaAsP QWs laser, (b) InAlGaAs QWs and InAs InAlGaAs DWELL partial structure, and (c) InAs/InP QDs partial structure. The InAlGaAs QW structure has an identical active region to the DWELL structure, except for the absence of the InAs QDs. For partial structures [(b) and (c)], 1000 nm SiO_2 layer was used as a mask to project the majority damage around the active region.

We investigate the effect of defect position in InGaAs/InGaAsP QW laser by masking the sample during implantation with variable SiO_2 layer thickness. Fig. 2 depicts the PL spectra under low excitation power from intermixed InGaAs/InGaAsP QW laser to excite mostly the upper QWs layer. At 500 nm SiO_2 mask, the intermixing degree is the largest as the majority of defect is estimated just above the upper QW layers. As the defect are placed further away from the active region, the intermixing efficiency decreases. In all cases, the enhanced intermixing is observed due to the long-range defect migration created by N implantation. No significant broadening in PL linewidth is observed indicating that the optical quality is not degraded after intermixing. A set of bandgap tuned lasers are fabricated and tested from these samples. The lasing spectrum is acquired at 1.1x J_{th}, therefore the lasing wavelength is associated with the upper QWs set emission. The as-grown laser exhibits threshold current density J_{th} of 2.03 kA/cm^2 while intermixed lasers lase at significantly lower threshold level. The threshold current gradually decreases as the implant mask is thicker suggesting that the indirect N-IID is preferable to induce intermixing while preserving the intermixed material quality [4]. The lasing peak of bandgap tuned laser agrees well with the PL data of intermixed QW samples.

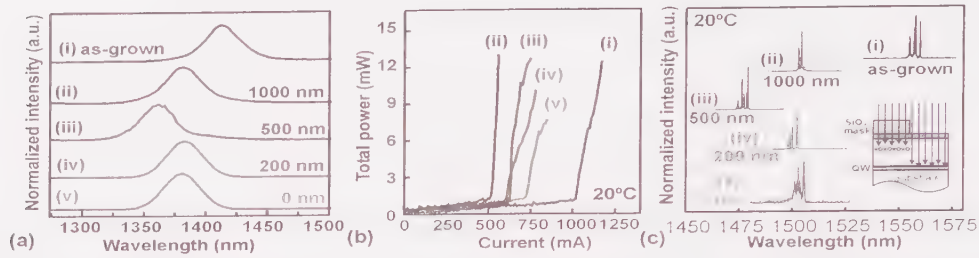

Fig.. 2. (a) The intermixed PL spectra from InGaAs/InGaAsP QW laser structure that are implanted with 0 nm to 1000 nm thick SiO_2 implant mask. Up to 200 nm SiO_2 causes the most defects at the QWs active region (direct implantation) and thicker implant mask causes the defect profile peak further away from active region (indirect implantation). The corresponding light-current characteristics (b) and the lasing spectra taken under the injection level of $1.1xJ_{th}$ at room temperature. The inset shows the implant mask that modulates the N implant depth in QW laser structure.

Fig. 3 summarizes the laser characteristics and emission for DWELL laser after indirect NIID by masking DWELL sample with 200 nm SiO_2 during implantation. The as-grown and control lasers shows J_{th} of 1.80 and 1.28 kA/cm^2, while intermixed laser begins to lase at 1.16 kA/cm^2. Similar to InGaAs/InGaAsP QWs, the reduction of J_{th} in DWELL is also notable for the intermixed device [6]. The amount of blue-shifts in laser wavelength peak is consistent with the blue-shift obtained from PL data earlier.

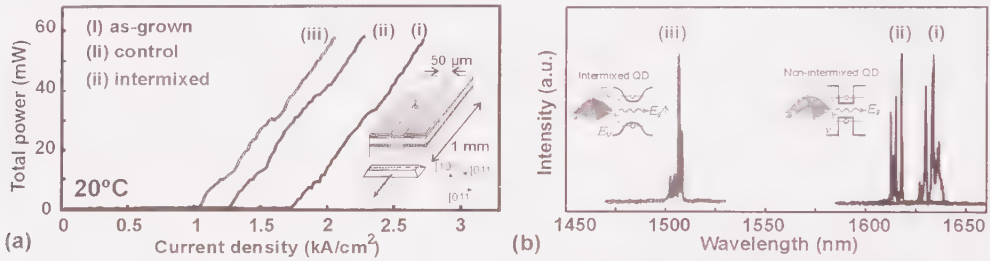

Fig. 3. (a) LI characteristics and (b) laser spectra from (i) as grown, (ii) control and (iii) intermixed InAs InAlGaAs DWELL lasers. The intermixing was performed with N-implantation onto 200 nm thick SiO_2 layer. The inset gives the laser cavity alignment, which is perpendicular to the dash direction to maximize the gain.

Summary

Postgrowth bandgap engineering using N-IID has been performed to promote universal intermixing on various quantum heterostructures with up to 320 nm blue-shift in PL wavelength peak for QD material. Band gap tuned QW and DWELL lasers were fabricated with significant J_{th} reduction and up to 127 nm wavelength blueshift. Our result indicates that N-IID enables the realization of high-performance photonic integrated devices in a simple and cost-effective way.

Reference:

[1] H.S, Lim et al.: IEEE Photonics Technol. Lett. Vol. 14 (2002), p 594

[2] V. Aimez et al.: IEEE J. Sel. Top. Quantum Electronics, Vol. 8 (2002), p870.

[3] H. S. Djie, B. S. Ooi and V. Aimez: Appl. Phys. Lett. Vol. 87 (2005), p. 261102.

[4] H. S. Djie, Y. Wang, D. Negro and B. S. Ooi: Appl. Phys. Lett. Vol. 90 (2007), p. 031101.

[5] Y. Wang, H. S. Djie, and B. S. Ooi: Appl.Phys. Lett. Vol. 88 (2006), p. 111110.

[6] H. S. Djie et al.: IEEE Photonics Technol. Lett. Vol. 18 (2006), p. 2329.

[7] O. Gunawan, H. S. Djie and B. S. Ooi: Phys. Rev. B Vol. 71 (2005), p. 205319.

Advanced Materials Research Vol. 31 (2008) pp 185-188
online at http://www scientific.net
© 2008 Trans Tech Publications, Switzerland

Higher Crystalline Volume Yields from Excimer Laser Crystallization of Amorphous Silicon with an Asymmetrical Peak Pulse Profile

A.A.D.T. Adikaari[a], N.K. Mudugamuwa[b] and S.R. P. Silva[c],

Nano-Electronics Centre, Advanced Technology Institute, University of Surrey,

Guildford GU2 7XH, U.K.

[a]d.adikaari@surrey.ac.uk, [b]n.k.mudugamuwa@surrey.ac.uk, [c]s.silva@surrey.ac.uk

Keywords: excimer laser, crystallized silicon, asymmetric pulse.

Abstract. Excimer lasers have been utilized for the crystallization of hydrogenated amorphous silicon for electronic applications. These lasers typically operate in the ultraviolet and hence photons are absorbed by the silicon thin films within a few nanometres of the surface, melting and solidifying the silicon on a nanosecond timescale, often without affecting the underlying substrate. This technique enables the use of inexpensive substrates, such as glass, which are highly preferable for low cost, large-area electronic devices. The depth of crystallization becomes important for applications such as photovoltaics, which depends on a number of factors; with laser beam shape one of the most significant. A Gaussian beam profile has been reported to be best suited for controlled evolution of hydrogen during crystallization with minimum surface damage. Previous reports show the typical energy densities of crystallization, comparing the crystalline volume and surface roughness of the resultant films for different film thicknesses. We report significant reductions of laser energy densities for crystallization by modifying the Gaussian pulse profile, while retaining the controlled evolution of hydrogen from hydrogenated amorphous silicon films. An asymmetrical, shorter pulse profile retains the desirable gradual leading edge of the Gaussian pulse for controlled evaporation of hydrogen, while increasing the peak energy. The resultant films show increased surface roughness along with higher crystalline volumes, which may be beneficial for photovoltaics.

Introduction

Excimer lasers have been utilized for crystallization of hydrogenated amorphous silicon (a-Si:H) for thin-film transistor applications and photovoltaics [1,2,3]. Typically lasing in the ultraviolet, excimer lasers energy is highly coupled to a-Si:H due to the high absorption coefficients at these wavelengths. Photons are absorbed by the thin a-Si:H film within a few nanometres of the surface, with melting and solidifying occurring on a nanosecond timescale. The quick, shallow process often leaves the underlying substrate unaffected, enabling the use of low melting point substrates. Glass is such a substrate, which is very attractive for large area electronics due to its low cost.

Most of the research in laser crystallization has been directed towards thin film transistor applications, and therefore the film thickness investigated has been around 100 nm. The research has been focused on to realising large grained polycrystalline silicon, with minimum surface roughness occurring upon crystallization. [4] A number of beam shapes has been utilized for crystallization, starting with a "top-hat" profile, as shown in Fig. 1(a). However, explosive evaporation of hydrogen from a-Si:H during crystallization resulted in increased surface roughness.[5] Therefore, a Gaussian profile [Fig. 1(b)] was reported as the best shape to systematically evaporate hydrogen in a multiple pulse crystallization regime, with a scanning laser pulse. We have further modified the beam into an asymmetrical shape, [Fig. 1(c)] which yields higher crystalline volumes compared with the conventional semi-Gaussian pulse profile, at a given laser energy density. [6]

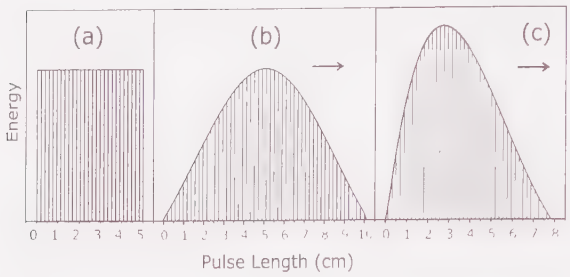

Fig. 1: Comparison of excimer laser pulse profiles used for crystallization. Top-hat (a), semi-Gaussian (b), and asymmetric (c) profiles. The shaded area represents the energy of the pulse, equal for all three cases. Arrows show scan direction.

Experimental

Chemical vapour deposited 300 nm thick *a*-Si:H on SiN (100 nm)/glass substrates was used for the experiments. The films contain 10% atomic hydrogen, as specified by the deposition facility. A KrF Lambda Physik excimer laser (LPX 210i), operating at 248 nm with a 25 ns full width at half maximum pulse duration, was used for crystallization. The laser pulse incident on the silicon film was imaged using a set of image capture apparatus involving a camera. For this work, a 4×8 mm^2 laser pulse with constant energy along the short axis and an asymmetric peak profile along the long axis (Fig. 1c) was used. The pulse profile was arrived at mathematically, by curve fitting to the normalized image intensity profile. The same procedure was followed to model the Gaussian pulse profile used in Ref. 2, which is of similar width but 10 mm long. Since the short axis energy profile is constant for both pulse shapes, the areas under the fitted curves of the long axis profile were equated and the corresponding normalized peak energy for the asymmetric pulse was calculated.

The *a*-Si:H films on glass were crystallized in vacuum, at a base pressure of 5×10^{-4} mbar, by scanning along the laser pulse with steeper trailing edge. The scanning speed for the experiment was 2.5 mm/s, with pulse repetition rate maintained at 50 Hz. A series of incremental energy densities of up to 200 $mJcm^{-2}$ per pulse was used for crystallization, with 25 $mJcm^{-2}$ increments. Experimental details are as similar to that used for crystallization of *a*-Si:H with the Gaussian pulse profile in Ref. 2, for comparison purposes, apart from the laser pulse profile and maximum energy density used. The resultant films were investigated with Raman spectroscopy with a Renishaw 2000 operating with a 782 nm laser. The Raman spectra were used to calculate the crystalline volume fractions, as reported in Ref. 2. The rms roughness of each film was calculated from atomic force microscopic data, obtained using a Digital Instruments Dimension 3100 scanning probe microscope.

Results & Discussion

Fig. 2 show the crystalline volume fractions of 300 nm thick excimer laser crystallized silicon films, calculated from Raman spectra. With the Gaussian profile, the films show crystalline volumes at energies above 50 $mJcm^{-2}$. However, with the asymmetric pulse, crystalline volume is evident at

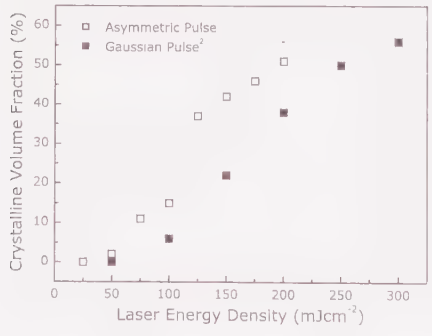

Fig. 2: Crystalline volume fractions of 300 nm excimer laser crystallized silicon calculated from Raman spectra. Solid symbols show the crystalline volume fractions of thin films crystallized with the Gaussian pulse, reproduced from Ref. 2. The open symbols represent values for laser crystallized silicon with the asymmetric pulse.

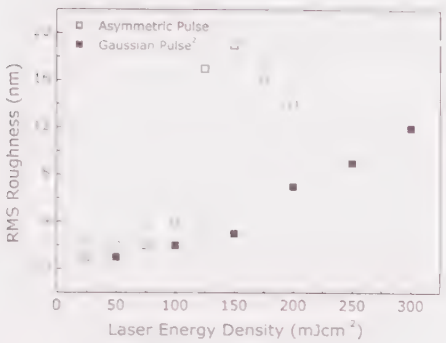

Fig. 3: rms roughness of 300 nm thick excimer laser crystallized silicon obtained from atomic force microscopy over a 25 μm^2 area. Solid symbols show the roughness of thin films crystallized with the Gaussian laser pulse, reproduced from Ref. 2. The open symbols represent values for laser crystallized silicon with the asymmetric laser pulse.

energy densities as low as 50 $mJcm^{-2}$. A clear trend of higher crystalline volumes is observed at lower energy densities, as compared to, with the Gaussian pulse. The higher crystalline volume is proposed to be due to the higher peak energy of the asymmetric pulse. For a given energy density, the energy delivered close to the peak is higher for the asymmetrical pulse, which results in increased melt depths, yielding higher crystalline volumes.

Fig. 3 shows rms roughness of 300 nm thick excimer laser crystallized silicon obtained from atomic force microscopy over a 25 μm^2 area. The roughness has clearly increased for the films crystallized with the asymmetrical pulse. With Gaussian pulse, the roughness increases gradually with the increase of crystallization laser energy. However, with asymmetric pulse, the roughness indicates a "step" behaviour, where it's below 4 nm up to 100 $mJcm^{-2}$ and ~16 nm for energies from 100 to 200 $mJcm^{-2}$. The increased roughness is suggested to be caused by the higher peak energy intensity of the asymmetric pulse. The roughness can be controlled to an extent by changing the peak energy of the pulse, giving improved design freedom for applications such as solar cells as a light trapping mechanism as well as surface area increasing methodology. Similar crystallization behaviour is expected for films with different film thickness and a complete analysis of 300 nm and 500 nm thick films are given elsewhere.[6]

Summary

A conventionally used Gaussian beam profile is modified for laser crystallization of amorphous silicon. An asymmetrical, shorter pulse profile retains the desirable gradual leading edge of the Gaussian pulse for controlled evolution of hydrogen, while increasing the peak energy. The resultant films show increased surface roughness along with higher crystalline volumes at a lower energy density as compared to crystallization with a Gaussian pulse. The surface roughness of the films crystallized with the asymmetric pulse has increased compared to film crystallized with the Gaussian pulse. The increased surface roughness can be used as a light trapping surface for solar cells. The roughness can be controlled so that the surface area of the film is increased as desired for photovoltaic applications.

Acknowledgments

The authors thank J.M. Shannon and Phillips Research Laboratories, Redhill, Surrey, UK, for the supply of *a*-Si:H samples. This work is supported by the Portfolio Partnership Award from EPSRC.

References

[1] S. D. Brotherton, Semicond. Sci. Technol. **10**, (1995) p 721

[2] A. A. D. T. Adikaari and S. R. P. Silva, J. Appl. Phys. **97**, (2005) 114305

[3] H. Azuma, A. Takeuchi, T. Ito, H. Fukushima, T. Motohiro, and M. Yamaguchi, Sol. Energy Mater. Sol. Cells **74**, (2002), p 289

[4] J. S. Im, H. J. Kim, and M. O. Thompson, Appl. Phys. Lett. **63**, (1993), 1969

[5] D. J. McCulloch and S. D. Brotherton, Appl. Phys. Lett. **66**, 2060 (1995)

[6] A. A. D. T. Adikaari N. K. Mudugamuwa and S. R. P. Silva, Appl. Phys. Lett. **90**, (2007) 171912

Advanced Materials Research Vol. 31 (2008) pp 189-191
online at http://www.scientific.net
© 2008 Trans Tech Publications, Switzerland

Distributed feedback laser using buried dielectric grating

J. H. Teng[1,a], L. F. Chong[1,b], J. R. Dong[1,c], S. J. Chua[1,d], Norman S. S. Ang[1,e], Y. J. Wang[1,f], and Ee Leong Lim[1,g]

Institute of Material Research Engineering, 3 Research Link, Singapore 117602
[a]jh-teng, [b]lf-chong, [c]jr-dong, [d]sj-chua, [e]norman-ang, [g]el-lim@imre.a-star.edu.sg
[f]wangyanjun@mbetech.com.sg

Keywords Distributed feedback lasers, grating, dielectric grating, complex-coupled DFB, epitaxial lateral overgrowth (ELO), semiconductor laser

Abstract. In this paper, we report a DFB laser diode with a buried SiO_2 grating. Epitaxy lateral overgrowth by metalorganic chemical vapour deposition (MOCVD) is conducted to grow the p-type InP cladding layers in the nano-patterned dielectric grating template. The large refractive index difference between SiO_2 and InP results an index coupling coefficient κ of about 250 cm^{-1}. The fabricated DFB laser showed a side mode suppression ratio larger than 45 dB measured. The technology developed can also be used for other applications that require high efficiency grating structure.

Introduction

The conventional distributed feedback (DFB) lasers typically have low efficiency gratings constructed from two different semiconductor materials with a small refractive index difference, e.g. InP and InGaAsP for ~1.55 μm wavelength device. A relatively long grating structure is thus required to provide the required reflectivity. The stop band could also be much narrower than the gain bandwidth, which leads to unstable single mode operation or low side mode suppression ratio. DFB lasers with grating formed by semiconductor and air had been reported [1]-[3]. But they require either very deep reactive ion etching or wafer fusions, which are complex and difficult in process control. It has been proposed to use the low refractive index AlOx to form the gratings [4]. The high contrast in refractive index will greatly enhance the grating coupling coefficient and improve the device performance for low noise ratio and threshold gain, high resistance to external feedback and stable single mode operation. On the other hand, the introduction of gain coupling to form a complex coupled DFB laser, even with a small amount of gain coupling, can solve the longitudinal mode degeneracy and enhance the device's dynamic performance [5], [6]. In this letter, we demonstrate a DFB laser using a SiO_2/InP grating structure embedded inside the top InP waveguide layer. The large refractive index contrast between the SiO_2 and the InP provides a large index coupling coefficient, while the insulating nature of the dielectric material offers the gain modulation in the quantum wells through the current blocking effect.

Device structure and fabrication

The structure was grown by low pressure MOCVD on a S-doped InP. The laser active region consists of four 1% compressively strained $In_{0.76}Ga_{0.24}As_{0.85}P_{0.15}$ quantum wells with thickness of 5 nm and lattice matched $In_{0.76}Ga_{0.24}As_{0.52}P_{0.48}$ barriers with thickness of 10 nm. It is sandwiched by 70 nm think $In_{0.76}Ga_{0.24}As_{0.52}P_{0.48}$ inner confinement layers and 80 nm thick $In_{0.82}Ga_{0.18}As_{0.39}P_{0.61}$ outer confinement layers. Another 10 nm InP space layer was added on top of the upper confinement layer. The sample was then coated with a 50 nm thick SiO_2 film by plasma enhanced chemical vapor deposition and patterned using laser holographic method and reactive ion etching to form a SiO_2 grating with a period of around 240 nm. Epitaxial lateral overgrowth (ELO) technique by MOCVD was used to grow the top p-InP layer into the SiO_2 grating template. Fig. 1 shows the schematic diagram of the cross section of the DFB laser with buried SiO_2 grating (a), the refractive index pattern of grating (b) and the gain pattern in the active region (c). The insulating nature of the dielectric material will block the current flow through the SiO_2 part, as shown by arrows in Fig. 1. This will cause a carrier concentration modulation in the underneath quantum wells, which in turn

will induce a gain modulation as shown in Fig. 1 (c). Even though the gain coupling is much weaker than the index coupling, it still gives the benefit of higher single mode yield offered by gain coupling. The dielectric grating has better current blocking function than the n-p-n junction type grating, especially at large current injection and elevated junction temperature.

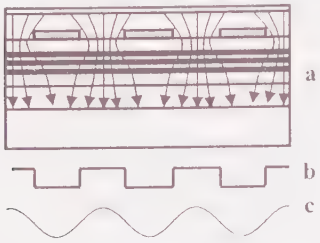

Fig. 1. Schematic diagram of (a) the cross section (b) the refractive index (c) gain pattern

Fig. 2. TEM picture of the ELO grown InP in the SiO_2 template

Figure 2 shows the TEM picture of the ELO InP in the SiO_2 grating template. As can be seen from the Fig. 2, the coalescence boundary is void free and a small air gap was formed above SiO_2 strip, which is whiter in the TEM picture than the SiO_2 part. A 4 μm wide and ~1.2 μm deep ridge waveguide laser was processed, cleaved and tested without any facet coating.

Results and Discussion

The grating coupling coefficient κ is proportional to $\int \Delta[n^2(x,z)] \quad E^2(x)dx$ where x is the vertical direction of the laser layer structure, $E(x)$ is the electric field distribution and Δn is the refractive index difference between the two materials that form the grating. Fig. 3 is the simulation of coupling coefficient versus different materials that form the grating. By choosing appropriate materials, the coupling coefficient for a certain grating depth and waveguide structure can be much higher than the conventional semiconductor grating formed by InP and InGaAsP. The buried SiO_2 grating used in current laser structure can produce a coupling coefficient of about 250 cm^{-1}. The stronger coupling, besides of reducing threshold gain and enhancing stability of single mode operation, etc. also provides more flexibility in device design. The required laser cavity length to produce a 90% reflectivity could be four times shorter by using SiO_2 grating than using conventional InP/InGaAsP grating. Fig. 4 is the high resolution lasing spectrum measured at room temperature at injection current of 1.5 I_{th} Lasing wavelength is around 1599.97 nm. The side mode suppression ratio (SMSR) is more than 45 dB and 3dB spectrum width is about 0.25 Å. The threshold current for a 500 μm cavity is about 46 mA, smaller than that of 60 mA from Fabry-Perot laser diode using the same quantum wells and the same waveguide structure. The cleaved DFB laser diodes can easily get stable single mode operation and are insensitive to any probable feedback from the fiber-end during spectrum measurement. This is the merit of both strong index coupling and partial gain coupling.

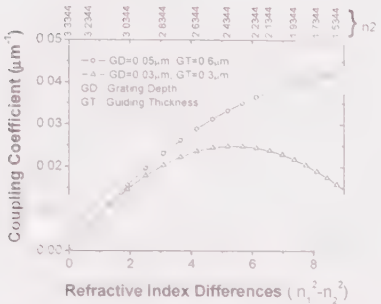

Fig. 3. Coupling coefficient for choice of different grating materials

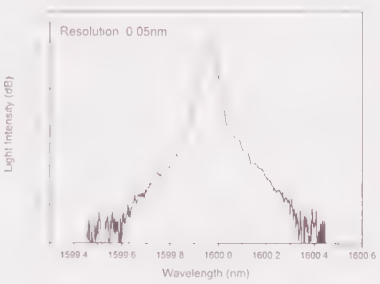

Fig. 4.TEM picture of the ELO grown InP in the SiO2 template

Conclusion

A new type of DFB laser with dielectric grating was demonstrated. The SiO_2 grating is buried by using the epitaxial lateral overgrowth method. It can provide a strong index coupling as well as some gain coupling. Without any specific facet coating, the device can get a stable single mode output with a SMSR higher than 45dB. The dielectric grating structure can also be used for other device applications that require high efficient wavelength selective gratings.

References

[1] Satoshi Oku, Tetuyoshi Ishii, Ryuzo Iga, and Takuo Hirono, IEEE J. Sel. Top. Quantum Electron., Vol. 5 (1999), p.682.

[2] M. Imada, S. Noda, H. Kobayashi, and G. Sasaki, IEEE J. Quantum Electron., Vol. 35 (1999), p.1277.

[3] H.Abe, S.G. Ayling, J.H. Marsh, R.M. De La Rue and J.S. Roberts, IEEE Photon. Tech. Lett., Vol 7, (1995) p. 452.

[4] P. C. Ku, Jacob A. Hernandez, and C. J. Chang-Hasnain, IEEE Photon. Technol. Lett., Vol. 15 (2003), p.75.

[5] Chih-Wei Hu et al. IEEE Photon. Technol. Lett. Vol. 18 (2006), p. 1551.

[6] S. W. Park, C. K. Moon, J. C. Han, and J. I. Song, IEEE Photon. Technol. Lett., Vol. 16 (2004), p. 1426.

Advanced Materials Research Vol. 31 (2008) pp 192-195
online at http://www.scientific.net
© 2008 Trans Tech Publications, Switzerland

ELECTRICAL PROPERTIES AND UV RESPONSE OF SINGLE ZnO NANOROD

Le Hong Quang[1a], Chua Soo Jin [1,b]

[1]Institute of Material Research and Engineering,3 Research Link Singapore 117602

[a]lehq@imre.a-star.edu.sg, [b]elecsj@nus.edu.sg

Keywords: Nanostructure, II-VI compound.

Abstract. Single ZnO nanorods with diameters of 100nm were directly grown on GaN surface by using low-temperature hydrothermal synthesis. Individual nanorods were removed from the substrate and placed between the Au contact pads and the current voltage measurement was proceeded to characterize the electrical properties of the ZnO nanorods. By using thermionic field emission model of Padovani and Stratton , the resistivity, carrier concentration, electron mobility can be extracted with the values of 0.14 Ωcm, $9.2x10^{16}/cm^3$,$33.82cm^2V^{-1}s^{-1}$, respectively. The single ZnO nanorods also showed high sensitivity to the UV light (325nm). Under the UV illumination, the UV induced current increase nearly 10 times than the dark current. In addition, the nanorods also exhibited a slow UV response due to the effects of the oxygen ions on the surface of the nanorods.

ZnO is an attracting material with large direct band gap (E_g = 3.35eV) , having great applications in gas sensing , surface acoustic devices, varistor and transparent thin film transistor . Recently, ZnO nanostructures have been attracted much attention for observation of quantum effects. Besides, these nanostructures also have potential applications in nanoscale optoelectronic devices. The large surface area of the nanorods also makes them attractive for gas and chemical sensing. There have been extensive efforts on ZnO nanowires, nanorods synthesis but much less on the transport properties and manipulate the current in the nanostructures. In addition, there has been a little done on retrieving the parameter of semiconducting nanostructures from the I-V characteristics.

For the last four decades it has been well-known that the photoresponse of n type ZnO films shows a slow decay process in conduction controlled by surface effects. Photoconduction in the ZnO films is primarily governed by desorption and adsorption of oxygens. In spite of such vigorous research on these types, photocurrent and its mechanism have not been currently understood well.

Here, ZnO nanorods were synthesized and placed on the top of two Au electrodes. The current voltage (I-V) characteristics of the nanorods were investigated. Furthermore, from the I-V characteristics, the resistivity, electron concentration and mobility of the nanorod are extracted by using thermionic field emission model of Padovani and Stratton. The photoresponse and photoconduction mechanism of the nanorods under the UV illumination was also discussed.

Figure 1: The ZnO nanorod bridge two Au electrodes

The preparation of ZnO the nanorods has been described as follows: Zinc acetate was first dissolved in deionized water at room temperature. Then, ammonia hydroxide was added to create an alkaline environment (pH ~ 10). The resulting suspension was transferred into a Teflon-lined stainless steel autoclave. Next, the GaN sample, was dipped into the solution and suspended in the autoclave by a tantalum wire. The resultant nanorods were obtained with typical length 1.5-2 μm and diameter in the range of 80-120 nm after 4 hours at 100 °C .

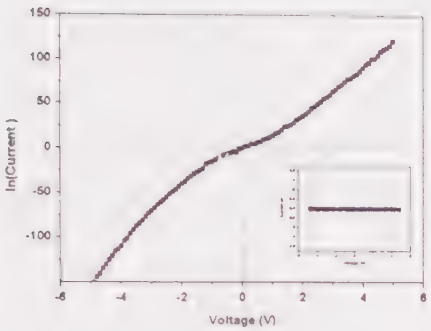

Next, the lithography and e-beam evaporation was used to pattern the Au electrodes on sapphire. The resulted Au electrodes had few mm lengths and 100 μm in diameter. The separation of these metal contacts was 1.5 μm. After releasing the ZnO nanorods from the GaN , the ZnO nanorods was transferred to the Au electrodes. Those rods which were well-connected to the Au electrodes would be chosen for further I-V characterization (Figure 1).

The current voltage measurement of single ZnO nanorod connecting between 2 Au electrodes was proceeded. The result current –voltage (I-V) curve of our device in the dark was given in Fig 2. The current increased with the bias as the voltage was scanned from -5 to 5V. From the inset in figure 2, I-V characteristic of the Au electrodes without ZnO was also measured with very small current (in the order of pA). It clearly showed that the Au electrodes are well-isolated and the observed nearly-linear I-V characteristic is actually from the Au-ZnO metal semiconductor contact.

In order to extract electrical parameters from the ZnO nanorod, let's consider the metal (Au)-Semiconductor (ZnO) –metal (Au) structure (figure 3). Although the barrier height between Au and ZnO is small (0.75), we still can consider it as a Schottky contact. For general nanostructure (nanorod, nanowires) based MSM structure, the conventional thermionic emission theory fail in analyzing the electrical transport behavior due to small signal of these nano-electronic devices which is comparable to the tunneling current from metal to semiconducting nanorod (few tens of nA). Therefore, in low dimensional system, the tunneling current is not negligible and become the dominating mechanism under reverse bias. As a result, the nanorod based metal-semiconductor-metal structure is usually modeled using the thermionic field emission model of Padovani and Stratton [1].

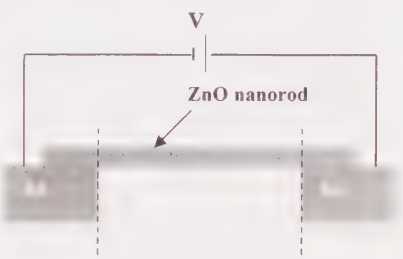

Figure 3: Schematic view of Metal (Au)-Semiconductor (ZnO)-Metal (Au) structure

For the reverse bias voltage V and an intermediate temperature, the tunneling current is mainly the thermionic field emission current and the current density through schottky barrier is given by

$$J_1(V,\varphi_b)=-J_s(V,\varphi_b)\exp V(q/kt-1/E_o) \qquad (1)$$

Where J_s is a slowly varying function of applied bias given by

$$J_s=[(A^*T(\pi qE_{00})^{1/2})/k]^*\{q(V-\zeta)+q\varphi_b/(\cosh^2(qE_{00}/kT)\}^{1/2}\exp(-\varphi_b/E_0)$$

Where $A^*=4\pi m^*qk^2/h^3$ is the Richardson constant of the semiconductor,

ζ is the distance from the Fermi energy to the bottom of the conduction band (0.1 eV for ZnO),

φ_b is the schottky barrier height, k is the Boltzmann constant ,

q is the magnitude of the electronic

The current through the forward biased Schottky barrier may be modeled by the classic thermionic emission equation $J_2(V,\varphi_b)=AT^2\exp(-q\varphi_b/kT)\exp(qV/kT-1)$

The total current I was given by $\ln I=\ln(SJ)=\ln S+V(q/kT-1/E_0)+\ln J_s$

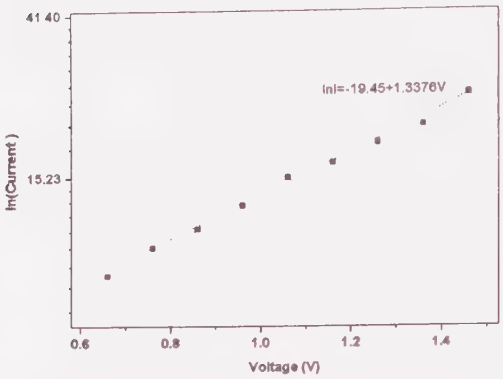

Figure 4: The logarithmic plot of current I as a function of voltage V under weak forward bias

where J current density through the schottky barrier ; S is the contact area associated with this barrier

E_0 :parameter depending on the carriers' density

J_s : a slowly varying function of applied bias

This logarithmic plot of the current I as a function of the bias V give approximately a straight line of slope $q/kT\text{-}1/E_0$ (Figure 4). Electron concentration n can be then obtained via E_0. The electron mobility can be calculated using the relation $\mu=1/(nq\rho)$ With ρ being the resistivity of the nanorod

The resistance can be calculated by differentiating the I-V curve in the large bias regime $R=dV_2/dI \approx dV/dI$

The resistivity of the ZnO nanorod is given by $\rho = R.\ A/L$

With R is the resistance of the nanorod,

A is cross-sectional area and L is the length of nanorod (diameter 100 nm and length 2 μm)

The electron mobility of the nanorod can be calculated $\mu =1/(nq\rho)$

Where: $n= N_d$ is the electron concentration, P is the resistivity of the nanorod

In summary, from the I-V characteristic of single ZnO nanorod, some parameters of the semiconducting nanorod can be calculated and compared with ZnO film in table 1.

	ZnO nanorod	ZnO film [2]
Resistivity (Ωcm)	0.1413	NA
Carrier concentration (cm^{-3})	$9.25.10^6$	$1.2.10^{17}$
Electron mobility ($cm^2V^{-1}s^{-1}$)	33.82	130

***Table 1:** A compilation of resistivity, electron mobility, carrier concentration obtained in ZnO nanorod calculated by using thermionic model and reported values for ZnO film.*

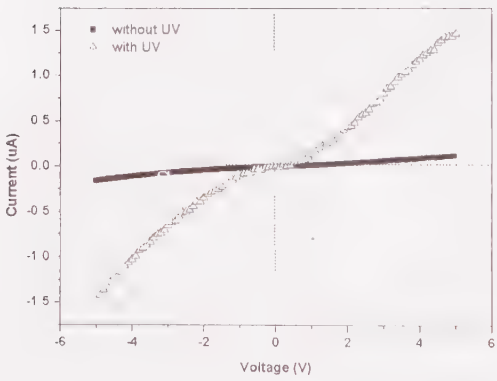

***Figure 5:** The I-V curve of single ZnO rods in the dark and under ultraviolet illumination*

The effect of UV light on the electrical properties of ZnO nanorods was also studied. The UV light had a wavelength of 255nm with the power density of $5.76\mu m/cm^2$. Figure 5 showed the I-V curves in the dark and under UV illumination for comparison. Under UV illumination, the conductance increased from 0.7 to 6μS, approximately 10 times larger than the dark current at a same given voltage (at 5V).

Figure 6 showed the UV response of the ZnO nanorod under the UV illumination. The current through individual ZnO nanorods jump under UV illumination and slowly decrease after turning off the UV light. The jump of the current was attributed to the enhanced carrier density in the nanorods and the reduced depletion width. This behavior could be explained by simply considering electron hole generation from the bulk and the effect of oxygen ions on the surface of the ZnO nanorods

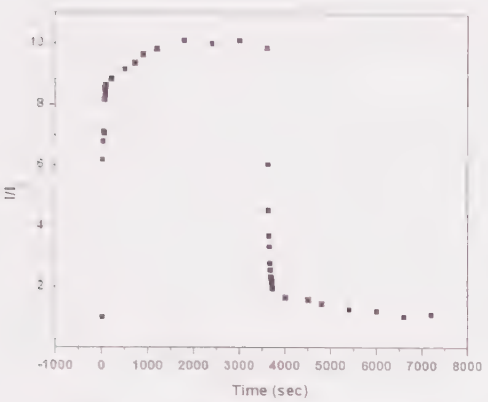

Figure 6 : Response of the current through individual ZnO rods to UV illumination

It has been unambiguously established that oxygen chemisorptions plays a profound role in enhancing photosensitivity of bulk of thin film ZnO [3,4]. The photoresponse of ZnO is believed to consist of two parts: a solid state process where an electron and hole are created ($h\nu \rightarrow h^+ + e^-$) and a two step process involving oxygen species adsorbed on the surface. In the dark, oxygen molecules adsorb on the oxide surface as negatively charged ion by capturing free electrons of the n type oxide semiconductor

$$O_2 (g) + e^- \rightarrow O_2^- (ad)$$

Thereby, these negatively charge ions will create a depletion layer with low conductivity near the nanowire surface. Upon exposure to UV light, when the photons are incident, photogenerated holes migrate to the surface and discharge the negatively charged adsorbed oxygen ions through the surface electron hole recombination

$$h^+ + O_2^- (ad) \rightarrow O_2 (g)$$

Meantime, photo-generated electrons destruct the depletion layer. Electrons produced at the same time increase the conductivity of the nanorod. As a result, the conductivity of the nanowire increases significantly. The oxygen ions capture the photoexcited holes, which liberates the oxygen species and leads to both an enhanced carrier density in the nanorods and narrower depletion width. This will lead to the jump of the current. After turning off the UV light, the electron hole recombination resulted in a decrease in current. In addition, the oxygen molecules just adsorbed on the ZnO nanowires surface capture the free electron in nanowires. This process greatly reduced the current. The observed slow decrease rate of the UV response was not only controlled by the oxygen concentration in the ambient but also affected by the recovery of the modified surface chemistry [5]. The photoresponse of our ZnO nanorods was slower than that of single nanowires in other report [6]. This may be due to the contacts between the ZnO nanorods and Au electrodes.

Electronic transport through individual ZnO nanorods and their UV response were studied. The almost linear and symmetry I-V characteristic was observed. By treating the transport in the nanorod as in a metal-semiconductor-metal structure and basing on thermionic field emission model of Padovani and Stratton, the resistance, carrier concentration and mobility of ZnO nanorod was extracted. Finally, our study also revealed that ZnO nanorods were sensitive to UV illumination. The UV illumination resulted in a jump of the current by increasing the net carrier density and decreasing the depletion width. This finding implies a potential application of individual ZnO nanorod to room temperature optical switch.

Acknowledgement: The authors would like to thanks Dr Teng Jing Hua , Dr Soh Chew Beng (IMRE-A-Star-Singapore) for their helps in this project.

References

[1] F.A.Padovani and R.Tratton, Solid State Electron 9 1966 695
[2] H.Kato,M.Sano,K.Miyamoto,T.Yao, Jpn. J.Appl.Phys Part I 42 2003 2241 .
[3] Y.Takahashi et all, Jpn J.Appl. Phys. 33 1994 6611,
[4] L.Liu et all J.Electr. Mat. 29 2000 69
[5] M.S.Arnold, Ph.Avouris,Z.W.Pan, J.Phys Chem B 107 2003 659
[6] Q.H.Li,Q.Wan,Y.G.Wang,Appl. Phys. Lett 86 2005 263101

Advanced Materials Research Vol. 31 (2008) pp 196-198
online at http://www.scientific.net
© 2008 Trans Tech Publications, Switzerland

Population dynamics of excitons in silicon nanocrystals structures under strong optical excitation

Olga A. Shalygina[1,a], Denis M. Zhigunov[1], Dmitrii A. Palenov[1], Victor Yu. Timoshenko[1], Pavel K. Kashkarov[1], M. Zacharias[2,b], Paul M. Koenraad[3,c]

[1]M.V. Lomonosov Moscow State University, Physics Department, 119992 Moscow, Russia

[2]Albert-Ludwigs-University Freiburg, Georges -Kohler-Allee, 79110 Freiburg, Germany

[3] Eindhoven University of Technology, Den Dolech 2, 513, 5600 MB Eindhoven, The Netherlands

[a] olga@vega.phys.msu.ru, [b] zacharias@imtek.uni-freiburg.de , [c] P.M.Koenraad@tue.nl

Keywords: photoluminescence, silicon nanocrystals, erbium ions, energy transfer

Abstract. We report on the experimental and theoretical studies of population/depopulation dynamics of excitons in the structures with Si nanocrystals in SiO_2 matrix (nc-Si/SiO_2) under strong optical excitation. The experimental results are explained using a phenomenological model based on rate equations for coupled system of energy donors (excitons) and energy acceptors (erbium ions). Exciton luminescence is found to exhibit superlinear dependence for Er-doped samples. At the same time the Er-related luminescence at 1.5 μm shows a saturation of the intensity and shortening of the lifetime, which are attributed to the population inversion of the Er ions states. The obtained results demonstrate that nc-Si/SiO_2:Er systems can be used for applications in Si-based optical amplifiers and lasers, compatible with planar Si-technology.

Introduction

Being the basic material of the semiconductor electronics crystalline silicon (c-Si) has indirect band gap and hence the efficiency of interband radiative recombination in c-Si is relatively low. Investigations of the novice Si-based materials with high light emission efficiency at optical or electrical pumping are therefore of current importance. In this way great attention is attracted to the study of low-dimensional structures such as silicon nanocrystals ensembles (nc-Si). If the size of nc-Si is about several nanometers the probability of interband radiative recombination rises significantly due to increase of uncertainty of the quasi-momentum of charge carriers. By varying of nanocrystals size it is possible to control band gap and therefore the position of photoluminescence spectrum of excitons confined in nc-Si [1].

The possibility of silicon nanocrystals to transfer their energy to different acceptors is well known, which may be used for sensitizing of the photoluminescence of rare-earth ions [2]. The most promising as an energy acceptor rare-earth ion is Er^{3+} due to its emission at 1.5 μm produced by $^4I_{13/2} \rightarrow {}^4I_{15/2}$ transitions in internal 4f-shell which corresponds to the absorption minimum of optical fibers [3]. The investigation of optical properties of nc-Si/SiO_2 structures under intensive optical excitation is important for their possible applications in Si-based optical amplifiers and lasers.

Experimental details

Structures of nc-SiO/SiO_2 were prepared by thermal crystallization of amorphous SiO/SiO_2 superlattices at 1100 °C [4]. The mean size of nc-Si, d, was varied from 1.5 to 4.5 nm by changing the SiO layer thickness, d_{SiO}, from 2 to 6 nm, $d_{SiO2} = 4$ nm [5]. Inset in Fig. 1 shows a transmission electron microscopy (TEM) cross-sectional image of a nc-Si/SiO_2 structure. Dense arrays of nearly spherical Si nanocrystals (black fields) embedded in the SiO_2 matrix are well distinguished. The total thickness of nc-Si/SiO_2 multilayer of the samples was about 100-300 nm, depending on d_{SiO}. Selected samples were implanted by Er ions at 300 keV with dose of $2 \cdot 10^{15}$ cm^{-2} (average Er

concentration $N_{Er} \sim 10^{20}$ cm^{-3}). After implantation the samples were annealed at 900°C in order to heal out the implantation induced defects.

Photoluminescence (PL) was excited by using a N_2-laser (photon energy $E_{ex} = 3.7$ eV, pulse duration $\tau_p = 10$ ns, repetition rate 100 Hz) or a He-Cd laser ($E_{ex} = 2.8$ eV). The PL signal was dispersed by a 50 cm monochromator and was detected by InGaAs photodiodes (spectral range 0.7 - 2.2 eV) or CCD array (spectral range 1.1 - 2.2 eV). PL spectra were corrected for spectral response of the measurement system. Transients of the Er-related PL under pulsed laser excitation were detected by an InGaAs photodiode with time response ~0.2 ms.

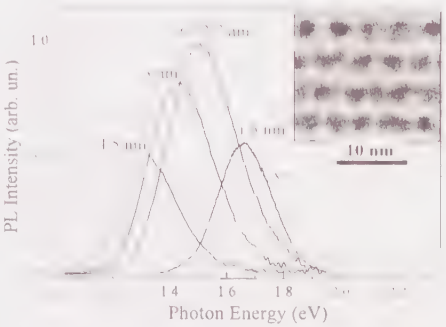

Fig. 1. PL spectra of undoped nc-Si/SiO_2 structures with different d ($E_{ex} = 3.7$ eV, T = 300 K). Inset: TEM image of a sample with $d = 3$ nm.

Results and discussion

Fig. 1 shows room temperature PL spectra of nc-Si SiO_2 structures. The PL band maximum shifts from 1.3 to 1.7 eV while d decreases from 4.5 to 1.5 nm. The intrinsic PL of nc-Si is commonly explained by the radiative recombination of excitons confined in nc-Si, while the size dependent spectral shift is attributed to the quantum confinement effect [6]. A considerable width of the PL band can be explained by nc-Si size distribution as well as by phonon-assistant electron-hole recombination [6]. The external quantum yield of the exciton PL was found to reach ~1% for the samples with $d = 3 - 4$ nm at room temperature [5].

A strong quenching of the exciton PL and an appearance of the Er^{3+} emission at 0.8 eV were observed for the investigated nc-Si/SiO_2 structures after doping with Er [5]. It should be noted, that at the same excitation conditions the Er^{3+} PL intensity of the reference sample of a-SiO_2:Er was about 3 orders of magnitude weaker [5]. The efficient Er^{3+} PL of the nc-Si SiO_2 structures is explained by the excitation of Er^{3+} ions due to the energy transfer from nc-Si [5].

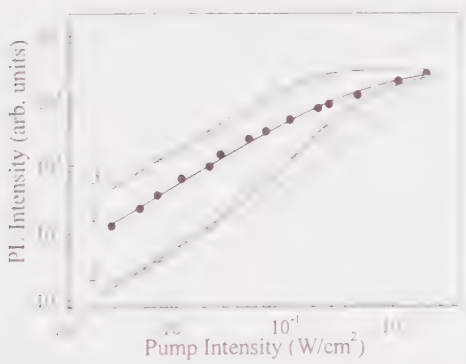

Fig. 2. Calculated (lines) and experimental (dots) dependences of PL intensities of nc-Si/SiO_2:Er structures ($N_D = 10^{19}$ cm^{-3}) on pump intensities: exciton PL in undoped sample ($N_A = 0$) (*1*), exciton (*2*) and Er^{3+} ions (*3*) PL in Er-doped sample ($N_A = 10^{19}$ cm^{-3}). Other model parameters: $\sigma = 0.7 \cdot 10^{-15}$ cm^2, $\tau_D = 1.1$ ms, $\tau_A = 3$ ms, $E_{ex} = 2.8$ eV, $\gamma = 1.1 \cdot 10^{-15}$ cm^{3}s^{-1}. T = 10 K. Dashed line shows linear dependence.

The dependences of PL intensities of undoped and Er-doped samples on excitation intensity were different. Fig. 2 shows these data for the samples at low temperature. One can see that dependence of the exciton PL intensity of undoped sample (solid circles) is sublinear at pump intensities $I_{ex} > 0.1$ W/cm^2. This fact can be explained by increasing the non-radiative Auger-recombination in nc-Si. However, the corresponding dependence for the Er-doped sample (open circles) does not saturate but becomes even superlinear at $I_{ex} > 0.02$ W/cm^2. This fact implies a suppression of the non-radiative recombination rate for the excitons in nc-Si. At the same pump the intensity of the Er^{3+} PL at 0.8 eV (triangles) exhibits a tendency to the saturation, which indicates that a larger part of the optically active ions is excited.

The experimental results are explained by considering a phenomenological model based on rate equations for coupled system of energy donors (excitons) and energy acceptors (erbium ions).

$$\frac{dN_{D1}}{dt} = N_{D0} \cdot \sigma \cdot \phi - \frac{N_{D1}}{\tau_D} - \gamma \cdot N_{D1} \cdot N_{A0},$$

$$\frac{dN_{A1}}{dt} = \gamma \cdot N_{D1} \cdot N_{A0} - \frac{N_{A1}}{\tau_A}.$$

(1)

N_{D0} and N_{D1} –concentrations of nc-Si, containing 0 and 1 exciton ($N_{D0} + N_{D1} = \text{const}$); N_{A0}, N_{A1} – Er^{3+} ions concentrations in the ground and excited states ($N_{A0} + N_{A1} = \text{const}$); τ_D – effective exciton lifetime; τ_A –lifetime of ions Er^{3+}; σ – nc-Si optical absorption cross section; ϕ – pump photon flux; γ – energy transfer coefficient.

One can see a good agreement between theoretical and experimental dependences for the exciton luminescence is observed (fig. 2, curves *1* and *2*). In particular, the superlinear dependence of exciton luminescence on pump intensity is not due to stimulated transition in silicon nanocrystals ensembles but well described by the suppression of the energy transfer process from the excitons to the energy acceptors (in our case Er^{3+} ions) due to the population inversion of their levels. Difference between the calculated and measured curves for Er-doped structures (curve *3*) is caused by simplicity of the model, which neglects the distribution of Er ion - Si nanocrystals distance (dispersion of γ) as well as the multilevel structure of Er ions.

Summary

Theoretical simulations and experimental studies carried out for nc-Si/SiO_2:Er structures have shown that the nonlinear behavior of dependence of exciton PL on pump level may be explained by suppression of energy transfer to Er ions (or/and some centers) due to the population inversion of their levels. The obtained results demonstrate that nc-Si/SiO_2:Er systems can be used as basis for active medium in desired Si-based optical amplifiers and lasers.

Acknowledgments

The work was partially supported by INTAS (grant No. 05-104-7656), Russian Foundation for Basic Research (grants Nos. 05-02-16735, 06-02-16987, 06-02-90879, 06-02-08023) and Ministry of Education and Science of the Russian Federation.

References

[1] Sh. Takeoka, M. Fujii, Sh. Hayashi. Phys. Rev. B. Vol. 62 (2000), p. 16820-25.

[2] G. Franzo, V. Vinciguerra, F. Priolo. Appl. Phys. A. Vol. 69 (1999), p. 3-12.

[3] M. Fujii, M. Yoshida, Y. Kanzava, S. Hayashi, K. Yamamoto. Appl. Phys. Lett. Vol. 71 (1997), p. 1198.

[4] M. Zacharias, J. Heitmann, R. Shcholz, U. Kahler, M.Schmidt, J. Bläsing. Appl. Phys. Lett. Vol.80 (2002), p. 661.

[5] V. Yu. Timoshenko, M. G. Lisachenko, O. A. Shalygina, B. V. Kamenev, D. M. Zhigunov, S. A. Teterukov, P. K. Kashkarov, J. Heitmann, M. Zacharias. J. Appl. Phys. Vol. 96 (2004), p. 2254.

[6] D. Kovalev, H. Heckler, G. Polisski, F. Koch. Phys. Stat. Sol. (b). Vol. 215 (1999), p. 871.

Advanced Materials Research Vol. 31 (2008) pp 199-201
online at http://www.scientific.net
© 2008 Trans Tech Publications, Switzerland

Investigation of Morphology and Photoluminescence of Hydrothermally-Grown ZnO Nanorods Grown On Substrates Pre-coated with ZnO Nanoparticles

C. B. Tay[1, a] and S. J. Chua[2,b]

Department of Electrical and Computer Engineering, National University of Singapore
21 Lower Kent Ridge Road, Singapore 119077

[2]Institute of Materials Research and Engineering, 3 Research Link, Singapore 117602

[a]taycb@nus.edu.sg, [b]elecsj@nus.edu.sg

Keywords: Zinc oxide, nanorods, solubility of zinc, hydrothermal growth, photoluminescence.

Abstract. We show that the rod-like morphology of hydrothermally-grown ZnO nanorods can be obtained on any substrate, pre-coated with ZnO nanoparticles, when pH<7.3 or pH>10.1. When pH>10.1, three types of morphology, from uniform nanorods to large clustered rods, can be distinguished based on the solubility of zinc. In line with classical thermodynamics, the density of nanorods increases when the solubility of zinc decreases. We also report that the orange defect peak photoluminescence can be reduced, while the UV peak increased by decreasing the pH of the growth solution.

Introduction

Hydrothermal growth of ZnO nanorods provides a simple, large-scale, low temperature route (60-100°C) compared to other well-established methods such as vapor phase transport or MOCVD. A wide range of growth precursors, typically consisting of a zinc salt, a base and occasionally a surfactant, have been reported. Despite these advantages, its wide-spread application has been limited by a lack of understanding of the factors controlling the growth mechanism and concerns on the quality of the grown ZnO. Here we report the growth and photoluminescence dependence on the pH and solubility of the solution consisting of zinc acetate dehydrate and aqueous ammonia.

Experiment

A clean substrate is spin-coated several times with ZnO nanoparticles. The ZnO nanoparticles were prepared by stirring a solution containing 0.2M KOH and 0.1M $Zn(CH_3COO)_2.2H_2O$, hereon denoted as ZnAc, in methanol at 60°C for 2 hours. Growth of ZnO nanorods was carried out in a bottle with an autoclavable screw cap. The growth solution was prepared by adding a certain amount of ZnAc followed by aqueous ammonia (NH_3) (30% w/w) into DI water in room temperature. The amount of ZnAc and NH_3 were systematically varied. The substrate is suspended, facing downwards, away from the bottom of the bottle. The bottle is sealed and placed into a convection oven set at 97°C for 3 hours. After the growth, the substrate was removed from the bottle, rinsed thoroughly with DI water and allowed to dry in air at room temperature.

Results and Discussion

When the concentration of ZnAc is kept constant at 0.02M and the concentration of ammonia is varied, it is found that rod-like morphology is obtained when the solution pH<7.4 or pH>10.1. For values in-between, poor coverage and flower-like morphology is observed. These are shown by the SEM images in Fig. 1. From classical thermodynamics, the free energy change for nucleation is the sum of the free energy change for the formation of the nucleus surface and phase transformation, which can be written as [1]

$$\Delta G = 4\pi r^2 \gamma + \frac{4}{3}\pi r^3 \Delta G_V \tag{1}$$

where γ is the interfacial energy and ΔG_v is the change of Gibbs free energy per unit volume of the solid phase. The critical nucleus radius r^* and the critical energy for nucleation to occur, ΔG^*, can be obtained by setting $d\Delta G/dr = 0$ giving:

$$\Delta G^* = \frac{16\pi V}{3k^2T^2} \cdot \frac{\gamma}{(\ln c/c_o)^2} \tag{2}$$

where V is the atomic volume, k is the Boltzmann constant, T is the growth temperature, c is the solute concentration and c_o is the solubility of zinc in the solution. It is known that γ decreases as the pH moves away from the point of zero charge (PZC) of zinc oxide [2], which has been reported to be between 8.7 and 9.7 [3,4]. When the pH < 7.4 or pH > 10.1, γ and ΔG^* have reduced to a very small value such that nucleation occurs readily, leading to a uniform coverage of rods.

When γ has reduced to a minimum value, c_o begins to play a more important role in determining the value of ΔG^*. This can be seen from Fig. 2, where growth is carried out in the pH range of about 10 ~ 11. In Region 1, as the ZnAc concentration, c, is increased, c_o decreases while the density of nanorods increases. From equation (2), this implies that c_o term is the dominant term leading to an overall decrease in ΔG^*. Three types of morphology can be distinguished based on c_o. In region I where c_o<0.88mmol/l, we obtained uniform coverage of nanorods while in region III where c_o>1.56mmol/l, large clustered rods are obtained. In region II where 0.88< c_o< 1.56 mmol/l, a transition region where both nanorods and large clustered rods exist. To confirm the dependence on c_o, a sample is grown in a solution of 0.006M ZnAc and 0.38M ammonia. As expected a mixed morphology was obtained as shown in the inset of Fig. 2. These trends are independent of substrate because of the coating of ZnO nanoparticles prior to growth.

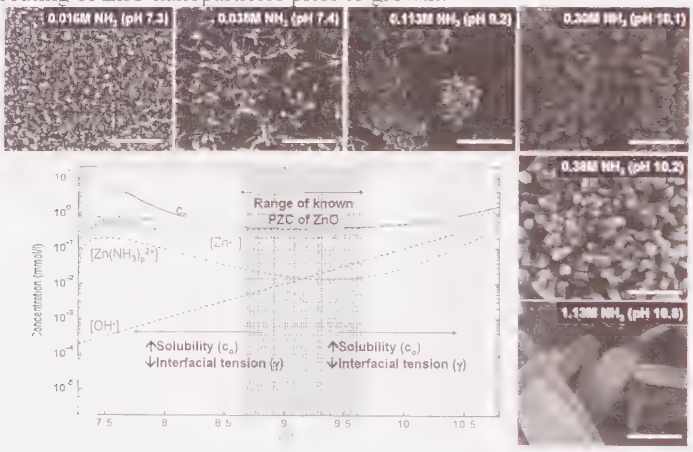

Fig. 1. Plot of various species concentrations against pH. The green areas show regions where rod-like morphologies can be obtained while red region show the known range of PZC of ZnO. The SEM images show the ZnO morphologies for various solution pH while ZnAc is kept at 0.02M. All the scale bars are 1 μm.

Room-temperature Photoluminescence (PL) Spectra

The room-temperature PL spectra of various samples grown in different solution pH are shown in Fig. 3. The UV is enhanced while the orange defect peak (580nm) is reduced as the growth solution pH is reduced. The orange defect peak, which is typical of hydrothermally-grown ZnO nanorods, can be removed during growth by growing in the region where pH < 7.3, eliminating the need for high temperature post-annealing process (typically >500°C). The reduction of orange defect peak at low

pH may be due to the Zn^{2+} rich solution, where lattice rearrangement can proceed at a fast rate, and thus reduce the defect density

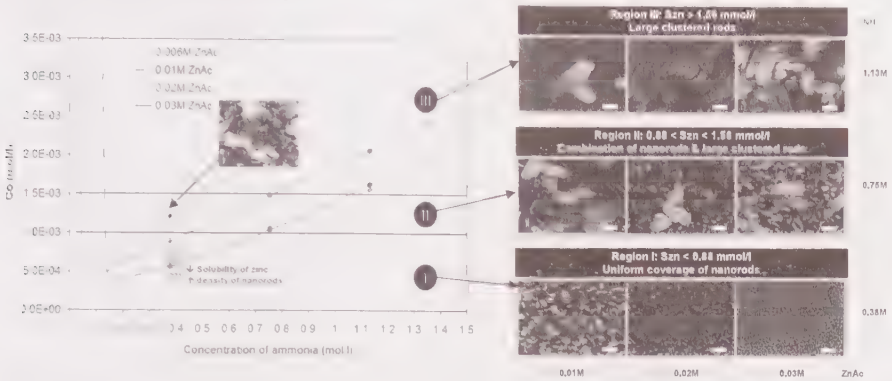

Fig. 2. Plot of c_o against amount of ammonia. Three distinct morphologies indicated by regions I, II and III. can be predicted based on solubility. SEM images show the top view of the ZnO nanorods grown at different precursor concentrations. All the scale bars are 1μm.

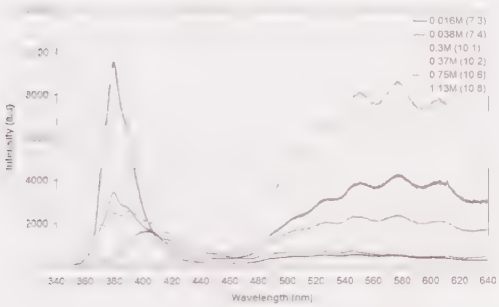

Fig. 3. PL spectra of samples grown in different solution pH. Orange PL peak can be reduced by reducing the pH of growth solution.

Summary

We have shown that rod-like morphology of ZnO can be obtained by ensuring the solution pH<7.3 or pH>10.1. When pH >10.1, three types of morphology can be distinguished based on the solubility of zinc. Large clustered rods are obtained when the c_o>1.56 mmol/l while uniform nanorods are obtained when c_o<0.88 mmol/l. A combination of nanorods and large clusters of rods are obtained for values in between. We have also shown that the density of nanorods increases with a decrease in solubility of zinc. By decreasing the pH of the growth solution below 7.3, the orange defect peak can be reduced while the UV peak enhanced.

References

[1] A. S. Myerson and R. Ginde in: *Handbook of Industrial Crystalization,* edited by A. S. Myerson, chapter, 2, Butterworth-Heinemann, Boston (1993).

[2] L. Vayssieres: Int. J. Nanotechnology, Vol. 2 No. 5 (2005), p.441

[3] J. P. Brunelle: Pure & Appl. Chem., Vol. 50 (1978), p. 1211

[4] D. Andeen, J. H. Kin, F. F. Lange, G. K. L. Goh and S. Tripathy: Adv. Func. Mater., Vol. 16, (2006), p.799

Advanced Materials Research Vol. 31 (2008) pp 202-205
online at http://www.scientific.net
© 2008 Trans Tech Publications, Switzerland

Dicing Laminated Wafer for QFN 3D Stacked Die Packaging

S. Abdullah[1(b)], Z. Endut[1(a)], I. Ahmad[1(c)], A. Jalar[1] and S. M. Yusof[2(d)]

[1]Faculty of Engineering, Universiti Kebangsaan Malaysia, 43600, Selangor, Malaysia.
[2]AIC Semiconductor Sdn. Bhd. Lot 26 & 27, Jalan Hi-Tech 4, Kulim Hi-Tech Industrial Park, Phase 1, 09000, Kulim, Kedah, Malaysia

[(a)] rg253c@yahoo.com, [(b)] shahrum1@gmail.com, [(c)] haji_ibrahim@yahoo.com, [(d)] suhaila_yusof@aicsemicon.com

Keywords: Dicing, die attach film, blade, surface analysis

Abstract. Nowadays, die attach film (DAF) gaining popularity in microelectronic packaging as integral part in facilitating the growth of wafer level packaging and stacked die packaging. DAF applied to the backside of wafers prior to saw have many advantages, such as the elimination of the epoxy dispensed process step and the reduction of epoxy related failure mode. However, the dicing process for DAF wafer usually associated with sidewall chipping, DAF whiskering and crack that will affect reliability of Quad Flat Non-Leaded (QFN) stacked die. Blade properties and characteristics are the crucial factor in analyzing the DAF dicing results. In this paper, we evaluate the blade characteristics before and after DAF wafer dicing process for our stacked die packaging. The qualitative measure by means of the Scanning Electron Microscope (SEM) and Energy Dispersive X-Ray (EDX) analysis were performed in order to understand the lamination and dulling effect on blade surface. The obtained results showed that sawing polymeric material such as wafer laminated with DAF induces lamination of polymeric material onto the blade surface and reduce blade cutting edge. As a result, reduce the quality of DAF dicing process.

Introduction

Wafer dicing is mechanical process used in the microelectronics industry for die separation. Using nickel matrix as a binder to hold diamond particles, the dicing blade will shear the material away by applying stress levels that break the internal crystallographic bonds. Hence, the die will be separated. With the continued reduction in package thickness and integrated function with more flash and memory silicon chip were combined together, the thinner die needed in order to achieve stacked die configuration [1]. However, moderate stresses could result in detrimental fracture in the die due to its brittle nature [2]. To overcome this failure, die attach film (DAF) was introduced to replace epoxy as adhesive materials. DAF materials have many advantages; eliminates excessive bleed out and controlled bond line thickness [3]. The trade off in using DAF is the challenge at DAF wafer dicing. Sawing DAF wafer is à complicated process due to composition and hardness of bi-material structure. The silicon die is known to be brittle in property, where else DAF tape is made up from vicious liquid polymeric materials with silica or alumina filler is added to change the DAF properties. Various reports showed that the DAF wafer dicing will results in die cracking, DAF whiskering and chipping. Lateral cracks as shown in Fig.1(a) is usually reported in many literatures on DAF wafer dicing [4]. Lateral cracks are found to be initiated from the bottom side of the die and resulted from the stress concentration on edges of the die during the dicing process. In some cases, the crack may extend from one corner to the other corner of the die and give significant reliability issues. On the non-laminated wafer, however, there is no presence of lateral cracks. Therefore, it is believed that the additional layer of DAF material plays a role in lateral crack formation.

Experimental Procedures

In order to understand a role of DAF materials on lateral cracks, blade for DAF wafer singulation process that produced lateral cracks is used in this study. Both blades before and after DAF wafer sawing is used and examined using JEOL Field Emission-Scanning Electron Microscope (FE-SEM) and Oxford Elemental Dispersive Energy (EDX). FE-SEM is used to analyze blade surface and EDX is used for elemental mapping. Sample was coated with gold to prevent electron charging.

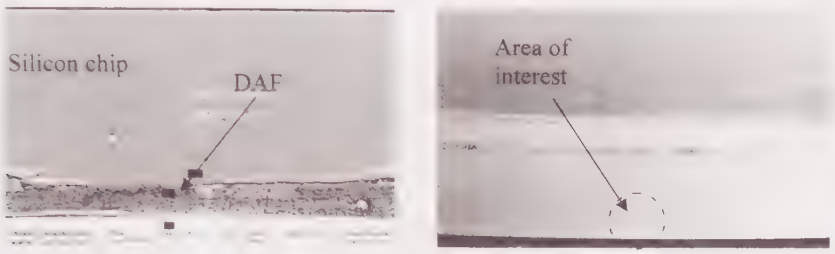

(a) (b)

Figure 1(a) Lateral crack on DAF laminated wafer (b) Blade surface

Results

Blade used and area of interest as shown in Fig 1(b). Before DAF wafer dicing, the blade shows the diamond particles in nickel binder as shown in Fig. 2 and the EDX mapping shows the diamond particles represent by carbon element distributed randomly in nickel matrix. During dicing, self sharpening mechanism occurred where new diamond grits are continuously being exposed from the binder as new cutting tool. The size of diamond or diamond grit is important as it control the load and edge quality of the saw kerf. Larger diamond particles also will gives better quality and lesser lateral cracks [4].

However, during DAF wafer dicing, DAF materials will remain on the blade as shown in Fig 3. DAF materials clogs the cutting blade which blocks the free space between the blade diamond that is used to remove the cutting debris. This can be seen in EDX mapping of carbon element that showed the reduced diamond particles in the blade surface compare to unused blade result. This causes the blade to dull and reduce the exposure of new diamonds grits towards the blade surface. A clogged blade equivalent to a blunt blade a causes the debris to push against the work pieces material, creating added stress and high blade loads that resulted in greater chipping and lateral cracks [5].

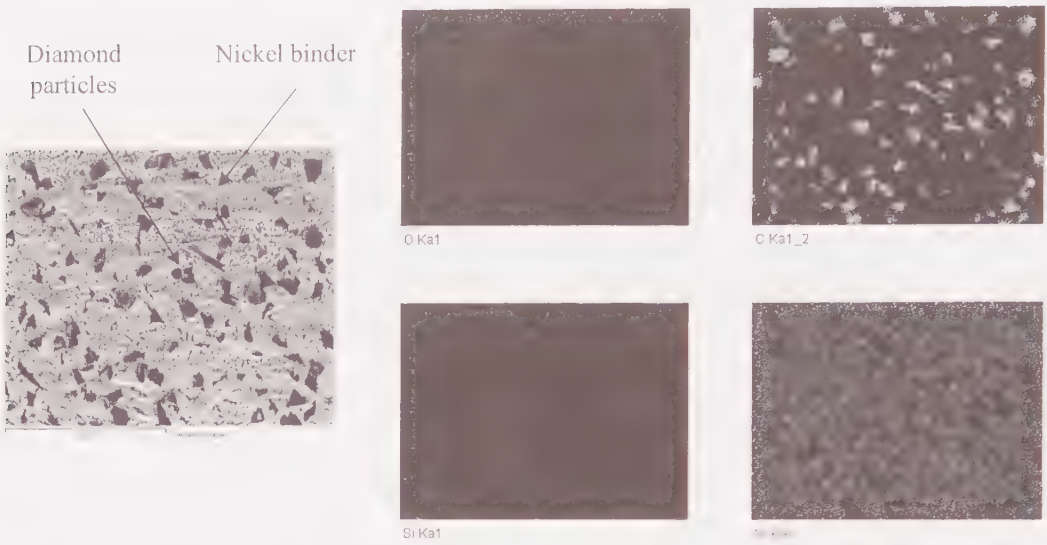

Figure 2 Elemental mapping of unused blade using EDX

Figure 3 Elemental mapping of used blade using EDX

Summary

In this paper, we evaluated blade used for DAF wafer dicing to understand effect of blade characteristics on lateral cracks issue. The results show that the DAF material has clogged the cutting blade surface resulting the blade to behave like blunt blade. This explained the silicon chip lateral crack occurred during DAF wafer dicing.

References

[1] W.H. Young, Y. Akito, and G. Richard, " Advances in 3D packaging – Trends and technologies for multichip die and package stack," in Proc. VLSI Packaging Workshop of Japan, (2002), pp. 32-38

[2] S.F. Popelar, "An investigation into the fracture of silicon die used in flip chip applications," (1998)

[3] Y.M. Cheung and A.C. M. Chong, "New proposed adhesive tape application mechanisme for stacking die applications," in Proc. Electronics Packaging Technology, (2003), pp. 309-315

[4] S.W Wang & M.C. Yo, "4 mil DAF die thickness sawing capability study," International Electronic Manufacturing Technology, (2006) pp. 207

[5] H.H. Jiun, I. Ahmad, A. Jalar & G. Omar, "Effect of laminated wafer toward dicing process and alternative double pass sawing method to reduce chipping," In IEEE Trans. On Electronic Packaging Manufacturing, (2006) pp. 17

Advanced Materials Research Vol. 31 (2008) pp 206-208
online at http://www.scientific.net
© 2008 Trans Tech Publications, Switzerland

DFB Waveguide All-Optical Switching Devices Employing Pump-Induced Refractive Index Change in GaInAsP

Tetsuya Mizumoto[1,a], Yoichi Akano[1,b], Kazuhiko Tamura[1,c], and Masaki Yoshimura[1,d]

[1]Dept. of Electrical and Electronics Engineering, Tokyo Institute of Technology

2-12-1 Ookayama, Meguro-ku, Tokyo 152-8552, Japan

[a] tmizumot@pe.titech.ac.jp, [b] y_akano@wave.pe.titech.ac.jp, [c] tamura@wave.pe.titech.ac.jp,

[d] m_yoshimura@wave.pe.titech.ac.jp

Keywords: all-optical switching, pump-induced refractive index change, distributed feedback waveguide

Abstract. A pump-induced refractive index change was measured in a passive GaInAsP waveguide together with its temporal response. Also, the temporal response of distributed feedback (DFB) waveguide transmittance modulated by the pump-induced index change was experimentally investigated for an application to all-optical switching devices.

Introduction

All-optical switching has attracted much attention for ultra-fast optical signal processing. Possible application of all-optical switching technology includes a photonic network, which requires fast optical signal processing, such as label-payload separation, label recognition, label rewriting, optical signal storage. Bit-wise operation of switching device is needed in some of these applications. For a fast switching operation, it is essential to use the physical phenomena that exhibit fast response. Also, a device structure should be designed so as not to restrict fast switching operations.

We have demonstrated all-optical switching functions in the distributed feedback (DFB) waveguide that includes the intensity-dependent refractive index change of GaInAsP guiding layer [1]-[4]. To explore the usability of this device for the ultra-fast optical switching, we investigated the temporal response of the index change induced by a pump pulse as well as the speed limitation associated with a device structure.

In this article, we describe the experimental results of pump-induced refractive index change in GaInAsP focused on its temporal response and its sensitivity to the pump intensity. We also describe the temporal response of transmittance in the GaInAsP DFB waveguide.

Pump-Induced Refractive Index Change

The pump-induced refractive index change of GaInAsP was measured by using the loop mirror interferometer that had a temporal resolution of sub-ps [5]. The measurement setup is shown in Fig.1. The output of wavelength-tunable fiber pulse laser is used as a pump source. Using a bandwidth limited O/E converter, a part of pump pulse is O/E converted to generate a broad electrical signal that is used to modulate a CW probe light. This enables one to synchronize a probe light with a pump pulse. The imbalance between two probe components traveling contra-directionally in a fiber loop is output from the transmitted port of interferometer. The pump and probe wavelength are in a range between 1530nm and 1570nm throughout the measurement.

The sample waveguide consists of a 450nm-thick bulk GaInAsP core layer lattice-matched to a (100) InP substrate. The bandgap wavelengths λ_g of GaInAsP are 1200nm, 1300nm, and 1410nm.

Single mode rib waveguides are formed by etching a 300-nm thick InP cladding layer with a CH_4/H_2 reactive iron etching technique. The width and height of rib are 2.5-3μm and 250nm, respectively.

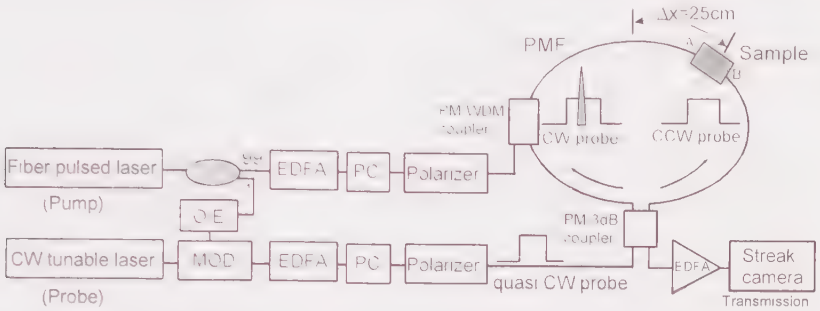

Fig. 1 Setup for the measurement of pump-induced index change.

A typical response of transmitted output is shown in Fig. 2(a). The transmitted probe is modulated by a pump pulse. This trace includes modulation due to absorption as well as a phase change induced by the pump pulse in the GaInAsP waveguide. We measure the absorption contribution separately (Fig. 2(b)), and subtract it from the measured response of fiber loop transmittance to obtain the phase change, i.e., the index change alone (Fig. 2(c)). It is observed in Fig. 2(c) that a temporal response of index change follows the input pump pulse of 4ps FWHM. Such a fast response of index change is considered mainly due to an optical Stark effect. When the peak intensity of the pump pulse is increased, a slow component of index change appears with a recovery time of several hundred pico-second. This is attributable to the real carrier excitation through two-photon absorption in GaInAsP. The critical power above which the slow component becomes prominent is approximately $20MW/cm^2$ for GaInAsP with λ_g=1410nm.

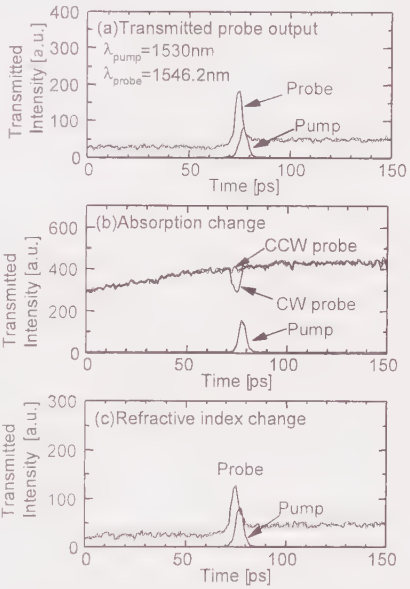

Fig.2 Measured temporal response of pump-induced transmittance change in a fiber loop (upper trace), absorption change (middle trace) and index change (lower trace).

The measured amplitude of index change was $-0.5x10^{-12}$, $-1x10^{-12}$ and $-4x10^{-12}cm^2/W$ for GaInAsP with λ_g=1200, 1300 and 1410nm, respectively. Note that the negative sign of coefficient was determined by other experiments done in a DFB waveguide. These values agree well with theoretical predictions based on a two-band model [6].

Temporal Response of Probe Transmittance in DFB Waveguide

We measured the temporal response of transmittance induced by the index change of a GaInAsP DFB waveguide [7]. The pump pulse of 1530nm was butt-coupled into the DFB waveguide together with the probe light whose wavelength 1539.4nm was set at the shorter wavelength edge of Bragg reflector's stop band. Due to a negative index change induced by a pump pulse, the Bragg wavelength shifts to a shorter wavelength side. This brings about a decrease in the probe transmittance. The

response is affected by the temporal index change induced by a pump pulse together with the inherent bandwidth limitation associated with a periodic structure.

It was observed that the transmittance of probe light is modulated by a pump pulse of 4ps width. The modulated waveform of probe light shown in Fig. 3 exhibited an instantaneous response in a front edge and a slightly slow tail in a recovery process. Although the slight broadening of probe response is observed, it can be said that the DFB-based optical switching device operates with a ps-order pump pulse. Also, the response shown in Fig. 3 can be used for an inverting gate function for optical signals.

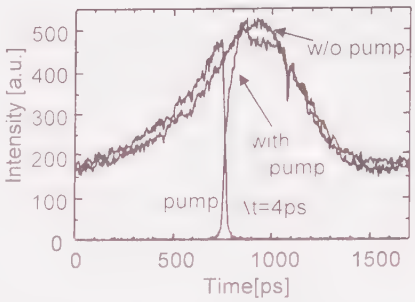

Fig.3 The measured temporal response of probe light modulated in a DFB waveguide by a pump pulse.

All-Optical Functional Device Based on DFB Switch

An optical Flip-Flop function can be achieved by controlling all-optically the DFB-based bistable switch. To reset the high state of DFB-bistable device, one can use an inverting gate function of DFB-based switch, where the probe wavelength is on the shorter wavelength edge of stop band. A preliminary performance was obtained in a fabricated chip integrated with bistable and inverting gate functions together with set and reset signal input ports.

Summary

From the temporal response measurement of pump-induced index change, we conclude that the GaInAsP does exhibit a fast index change that follows a ps-order pump pulse with peak pump intensity below 20MW/cm^2. This is usable in constructing all-optical switching devices that can handle >100Gbps optical signals in a bit-wise manner. Also, the bandwidth limitation due to a periodic structure in a DFB waveguide seems not to be a serious problem for processing 100Gbps signals. Detailed study is now under way on the switching dynamics in a periodic waveguide experimentally as well as theoretically.

References

[1] K.Nakatsuhara, T.Mizumoto, R.Munakata, Y. Kigure, and Y.Naito: *IEEE Photonics Technology Letters*, Vol.10 (1998), pp.78-80

[2] K.Nakatsuhara, T.Mizumoto, E.Takahashi, S. Hossain, Y.Saka, B.-J.Ma, and Y.Nakano: *Applied Optics*, Vol.38 (1999), pp.3911-3916

[3] K.Nakatsuhara, T.Mizumoto, S.Hossain, S.-H. Jeong, Y.Tsukishima, B.-J.Ma, and Y.Nakano: *IEEE J. Selected Topics QE*, Vol.6 (2000) , pp.143-149

[4] S.-H.Jeong, H.-C.Kim, T.Mizumoto, J. Wiedmann, S.Arai, M.Takenaka, and Y.Nakano: *IEEE J. Quantum Electronics,* Vol.38 (2002), pp.706-715

[5] J.-K.Seo and T.Mizumoto: *Jpn. J. Applied Physics*, Vol.45 (2006), pp.2612-2617

[6] M. S.-Bahae, D.C.Hutchings, D.J.Haga, and E.W. V.Stryland: *IEEE J. Quantum Electronics*, Vol.27 (1991), pp.1296-1309

[7] T. Mizumoto, J.-K. Seo, and N. Tanaka: *2005 IEEE LEOS Annual Meeting (LEOS 2005)*, Sydney (2005), ML-6, pp.131-132

Advanced Materials Research Vol. 31 (2008) pp 209-211
online at http://www.scientific.net
© 2008 Trans Tech Publications, Switzerland

Study of thermal-anneal-induced rearrangement of N-bonding configurations in GaInNAs/GaAs quantum well

V. Dixit[1, a], H. F. Liu[2, b] and N. Xiang[1, c]

[1]Centre for optoelectronics, Department of Electrical & computer engineering,
National University of Singapore, Singapore 117576

[2]Institute of Materials Research and Engineering, 3 Research Link, Singapore 117602

[a] vdixit@nus.edu.sg [b] liuhf@imre.a-star.edu.sg , [c] elexn@nus.edu.sg

Keywords: Short Range Order, quantum well, GaInNAs, photoluminescence, blueshift.

Abstract. Blueshifts of photoluminescence (PL) peak wavelength from GaInNAs/GaAs quantum well (QW) at various annealing temperatures have been studied. Our results indicate that as-grown GaInNAs GaAs QW sample has N-Ga_3In_1 phase, which changes to a mixture of N-Ga_3In_1 and N-Ga_2In_2 after annealing. The activation energy characterized for short range order is 2.38 eV, which is smaller than that for the diffusion process (3.196 eV). This indicates that the short range order is the dominant mechanism for PL blueshift at relatively low annealing temperature and for short time annealing.

Introduction

GaInNAs dilute nitride quantum wells (QWs) grown on GaAs substrate have been widely investigated for their promising applications in the telecom wavelengths region. To improve the solubility of nitrogen in GaInAs and to avoid phase separation of GaInNAs into GaInAs and GaN, molecular beam epitaxy (MBE) growth of GaInNAs material is carried out at low temperature (< 480 ^{O}C) [1]. This low temperature growth leads to a high defect density in the crystal and poor photoluminescence (PL) properties. Postgrowth annealing improves the PL efficiency of the GaInNAs / GaAs QWs, but also produces an undesirable blueshift. Blueshift has been attributed to In/Ga interdiffusion across the QW interface and reorganization of nitrogen-bonding configuration, N-In_mGa_{4-m} ($0 \le m \le 4$), in short range order (SRO) clusters [2,3]. Klar *et al.* attributed the blueshift to the rearrangement of N-bonding configuration into five discrete sets of bandgap (corresponding to N-In_0Ga_4, N-In_1Ga_3, N-In_2Ga_2, N-In_3Ga_1, and N-In_4Ga_0) which have different transition energies [4]. Similar conclusions were reported by Tournie *et al.* where post-annealing PL measurements from GaInAs and GaAsN did not show any blueshift but from GaInNAs it showed a blueshift of 67 meV. In his experiments, X-ray diffraction measurements and transmission electron microscopy did not show any compositional change in GaInNAs indicating the reorganization of N-bonding configuration [5]. Our earlier report suggests that SRO is a dominant mechanism for short time annealing and Ga/In interdiffusion is a dominant mechanism for long time annealing [6]. In this article, we present a theoretical analysis on the PL blueshift in GaInNAs / GaAs single QW, based on our experimental data. SRO N-bonding has been analyzed in detail.

Experiment

The QW structure analyzed in this study was an 8-nm $Ga_{0.628}In_{0.372}N_{0.015}As_{0.985}$/GaAs single QW grown on GaAs (100) substrate by solid-source MBE. Nitrogen was produced by a radio-frequency (RF) plasma source. The QW was sandwiched between the 500-nm GaAs buffer and 100-nm GaAs cap layers. The growth temperature of the QW was 460 °C. The GaAs buffer and cap layers were grown at 580 °C. After the growth, the as-grown wafer was cut into small pieces and the small pieces of samples were repeatedly annealed in a nitrogen atmosphere of a rapid thermal annealing (RTA) chamber at temperatures of T_{ann} = 680, 700, 750, and 800 °C for different time

durations. There were no extra dielectric-capping layer on top of the samples, but a GaAs wafer covered the samples during the annealing. After the annealing, the PL spectra were measured at room temperature. Detailed experimental procedure was described in Ref. [6].

Analysis and Discussions

Incorporation of nitrogen into GaInAs forms a nitrogen-localized state, E_N. The interaction of GaInAs extended conduction band with nitrogen related localized state results in unusually low bandgap of GaInNAs alloy [4,7]. We calculate the electron-to-heavy-hole transition energy, $E_{e1\text{-}Hh1}$, by solving the Schrödinger equation for conduction-band and heavy-hole band under effective mass envelop function scheme [8] for five different N-bonding configurations, $N\text{-}In_mGa_{4-m}$ ($0 \le m \le 4$) in GaInNAs/GaAs QW, which is listed in Table 1.

Table 1: The the calculated, $E_{e1\text{-}Hh1}$ corresponding to $N\text{-}In_mGa_{4-m}$ configurations

N-bonding configuration	Transition energy, $E_{e1\text{-}Hh1}$ (eV)
$N\text{-}In_4Ga_0$	0.9247
$N\text{-}In_3Ga_1$	0.9553
$N\text{-}In_2Ga_2$	0.9811
$N\text{-}In_1Ga_3$	1.0023
$N\text{-}In_0Ga_4$	1.0194

Table 2: The best fitting values of ΔE_{SRO} and τ for different annealing temperatures

Annealing Temperature (°C)	ΔE_{SRO} (eV)	
	M (eV)	τ (seconds)
680	17.5	91.648
700	20.1	59.615
750	16.02	12.616
800	13.36	3.804

The measured PL peak energy from as-grown sample is 0.9535 eV which is close to the calculated $E_{e1\text{-}Hh1}$ for $N\text{-}Ga_3In_1$ phase, 0.9553 eV. This indicates that our as-grown sample has $N\text{-}Ga_3In_1$ configuration, in agreement with the reports from Hugues et al [9]. MBE growth of GaInNAs is carried out under non-equilibrium conditions where bonding energy favors the atomic arrangement with Ga-N bonds instead of In-N bonds [10]. Thus we assume the SRO configuration of GaInNAs QW before the GaAs cap layer growth was $N\text{-}Ga_4In_0$. GaAs cap layer grown on GaInNAs QW had an inherent self-annealing effect, due to higher growth temperature for GaAs compared to QW [11]. The blueshift due to self-annealing is 29.3 meV, obtained by comparing the PL peak energy from as-grown sample and the calculated $E_{e1\text{-}Hh1}$ for $N\text{-}Ga_4In_0$ phase.

During the annealing process local strain effect dominates [12], where reports show the coexistence of interdiffusion along with N-bonding configuration rearrangement [6, 9]. Solving the diffusion equation, the Fick's second law of diffusion, derives interdiffusion induced change in concentration profile. The In concentration profile is characterized by diffusion length $L_D=\sqrt{D_0 \exp(-E_a/kT_{ann})t_{ann}}$, where D_0 is diffusion constant, E_a is the activation energy for diffusion, T_{ann} is the annealing temperature and t_{ann} is the annealing time. Concentration profile was used to determine strain profile and potential profile for various subbands (conduction, heavy-hole and light-hole bands) to calculate $E_{e1\text{-}Hh1}$ transition energies for various diffusion lengths.

We use genetic algorithm (GA) to fit the PL peak energy variation as a function of annealing time. The experimental PL data were taken from Ref. [6] with the un-capped samples (see Ref. [6] fig. 6). GA based approach have shown excellent accuracy in determining diffusion parameters without a need for Arrhenius plot [13]. An exponential function is introduced to profile the rearrangement rate of nitrogen-bonding configuration, $\Delta E_{SRO}=\Delta E_0*(1-\exp(-t_{ann}/\tau))$ where ΔE_{SRO} is the blueshift due to SRO as function of annealing time, ΔE_0 is cumulative SRO blueshift and τ is the annealing temperature dependent time constant which controls the reorganization rate of nitrogen-bonding configuration. Four parameters, {Ea, D_0, ΔE_0, and τ}, have been selected for the optimization. The mean square error has been minimized for fitting the measured PL blueshift with the calculated blueshifts due to SRO and interdiffusion, summed over all experimental data at different annealing times, $e=\sum_{T_{ann}}\sum_{t_{ann}}\left[E_{PL}-\Delta E_{SRO}-F\_diff\right]^2$, where, E_{PL} is measured PL blueshift and

E_{diff} is PL blueshift due to interdiffusion, determined from calculated $E_{e1\text{-}Hh1}$ for corresponding diffusion length. The best-fit parameters obtained for the short-range order are listed in Table 2.

The average blueshift caused by SRO for post-growth annealing in our experimental temperature rage is about 17 meV, which is smaller than the calculated change in $E_{e1\text{-}Hh1}$, 26 meV, for the N-bonding configuration to change from N-Ga_3In_1 to N-Ga_2In_2 phase. The smaller ΔE_{SRO} implies that annealing at 680-800 °C results in an N-environment with the coexistence of N-Ga_3In_1 and N-Ga_2In_2. This is in close agreement with results by Kudraweic *et al* (see Fig 3 (b) in Ref. [14])

The activation energy for interdiffusion obtained by the GA method is E_a= 3.196 eV. This value is close to the E_a = 3.25 eV obtained from the simple linear fitting model of interdiffusion for the same experimental data [6]. The advantage of using the GA method is that all the annealing temperatures are considered together in the GA based fitting that introduces self-consistency in parameters determined. The activation energy estimated from Arrhenius plot of $1/\tau$ versus $1/kT$ (data in Table 2) for the SRO rearrangement is 2.37 eV, which is less compared to the activation energy for interdiffusion, 3.196 eV. This supports the conclusion that the SRO mechanism is dominant at relatively low annealing temperature and at the early stage of the annealing process.

Conclusion

We have studied the thermal annealing induced PL blueshift from GaInNAs/ GaAs QW. The PL peak energy as a function of annealing time duration in the temperature range of 680 – 800 °C have been analyzed using a genetic algorithm based fitting. Our calculations suggest the N-Ga_3In_1 bonding configuration in the as-grown QW sample. Post-growth thermal annealing changes the configuration to a mixture of N-Ga_3In_1 and N-Ga_2In_2. The activation energy characterized for SRO rearrangement of the N-bonding configurations, 2.38 eV, is smaller than that of the diffusion process. This result implies that SRO should be the dominant mechanism for PL blueshift at lower annealing temperatures and short duration annealing.

References

[1] P. R. Chalker, T. J. Bullough, M. Gass, S. Thomas, and T. B. Joyce: J. Phys.: Condens. Matter **16**, S3161 (2004)
[2] E. tournie, M.-A. Pinault, and A. Guzman: Appl. Phys. Lett. **80**, 4148 (2002)
[3] Z. Pan, L. H. Li, W. Zhang, Y. W. Lin, R. H. Wu, and W. Ge: Appl. Phys. Lett. **77**, 1280 (2000)
[4] P.J. Klar, H. Gruning, S. Schafer, K. Volz, W. Stolz, and W. Heimbrodt: Physical Review B, Vol **64**, 121203 (R) (2001)
[5] J.-M. Chauveau, A. Trampert, and K. H. Ploog: Appl. Phys. Lett. **84**, 2503 (2004)
[6] H. F. Liu, V. Dixit, and N. Xiang: J. Appl. Phys. **99**, 013503 (2006)
[7] J. –Y. Duboz, J.A. Gupta, Z. R. Wasilewski, J. Ramsey, R. L. Williams, G. C. Aers, B. J. Riel, and G. I. Sproule: Phys. rev. B **66**, 085313 (2002)
[8]K. J. Moore, G. Duggan, P. Dawson, and C.T. Foxon: Phys. Rev B **38**, 5535 (1988).
[9] M. Hugues, B. Damilano, J.-M. Chauveau, J.-Y. Duboz, and J. Massies: Phys. rev B **75**, 045313 (2007)
[10] T. matsuoka, T. Sasaki, and A. Katsui: Optoelectron. devices Technol. **5**, 53 (1990)
[11] M. Pessa, C. S. Peng, T. Jouhti, E.-M. Pavelescu, W. Li, S. Karirinne, H. F. Liu, and O. Okhotnikov: IEE Proc.: Optoelectron. **150**, 12 (2003)
[12] Sarah Kurtz, J. Webb, L. Gedvilas, D. Friedman, J. Geisz, J. Olson, R. King, D. Joslin, and N. Karam: Appl. Phys. Lett. **87**, 748 (2001)
[13] O. M. Khreis, and I. S. Al-Kofahi: Semiconductor Science and Tech. **20**, 320 (2005)
[14] R. Kudrawiecz, G. Sek, J. Misiewicz, L. H. Li, and J. C. Harmand: Solid State Commun. **129**, 353 (2004)

Advanced Materials Research Vol. 31 (2008) pp 212-214
online at http://www.scientific.net
© 2008 Trans Tech Publications, Switzerland

Nano size Lanthanum Doped Semiconductors: Synthesis, Characterization and Their Photocatalytic Activity

S. Anandan[1,a], Y. Ikuma[2,b*], T. Kudoh[3,c] Y. Ogita[4,d] and V.Murugesan[5,e]

[1,2] Department of Applied Chemistry, [3,4] Department of Electrical & Electronics Engineering, Kanagwa Institute of Technology, 1030 Shimoogino, Atsugi, Kanagawa 243-0292, JAPAN
[5] Department of Chemistry, Anna University, Chennai 600 025, INDIA

[a]sanandan@chem.kanagawa-it.ac.jp, [b*]ikuma@chem.kanagawa-it.ac.jp, [c]tsugu@ele.kanagawa-it.ac.jp, [d]ogita@ele.kanagawa-it.ac.jp, [e]v_murugu@hotmail.com

Keywords: La-doped TiO_2/ZnO, monocrotophos; degradation; relative photonic efficiency

Abstract. In the present study, La-doped TiO_2 and ZnO nano particles were synthesized and extensively characterized by various sophisticated techniques such as XRD, nitrogen adsorption, UV-Vis, AFM and XPS. Rough and highly porous surface of La-doped photocatalysts was observed by AFM, which is critical for enhancing the photocatalytic activity. Degradation and mineralization studies of monocrotophos (MCP) revealed that 1 wt% La-doped TiO_2/ZnO exhibits high activity compared to that of pure TiO_2/ZnO.

Introduction

TiO_2 and ZnO are well-known semiconductors with strong photocatalytic activity and have a great potential for applications such as environmental purification, decomposition of organic pollutants and production of hydrogen gas. However, the applications of TiO_2 and ZnO are yet limited by the fast recombination of electron-hole pairs and their wide band gap, which corresponds to the UV region [1]. Several attempts have been made to improve the efficiency of photocatalyst such as supporting, coupling and doping the material with adsorbents, semiconductors and metals respectively. However, transition metal doped TiO_2/ZnO suffers from a thermal instability or an increase in the carrier recombination centers [2]. Alternatively, rare earth-doped metal oxides are potentially attractive materials for various optical and electronic applications because such materials exhibit unique physical (thermal stability) and chemical properties [3]. Synthesis of lanthanum doped TiO_2/ZnO using thin films is the only method of producing La-doped TiO_2/ZnO reported so far. However, this method has some disadvantages for industrial applications due to high cost of the process and tedious synthetic procedures. So it will be very interesting and challenging to develop metal doped semiconductors with cost effectiveness and by simple methods. In the present study, we report on the synthesis and characterization of La-doped TiO_2/ZnO and their photocatalytic activity for the degradation of MCP in aqueous suspension.

Experimental

La-doped TiO_2 was prepared by sol-gel method using titanium tetra isopropoxide and lanthanum nitrate hexahydrate (La $(NO_3)_3.6\ H_2O$) as titanium and lanthanum sources, respectively while for La-doped ZnO, zinc nitrate hexahydrate and lanthanum nitrate hexahydrate were used as the source for Zn and La respectively. The crystallinity of pure and La-doped semiconductors (TiO_2/ZnO) was analyzed by X-ray powder diffraction using PANalytical X-ray diffractometer. Surface morphology of pure and La-doped semiconductors (TiO_2/ZnO) was investigated by atomic force microscope (Digital Instruments, 3100). The presence of elements and chemical states of the catalysts were examined by ESCALAB 200 X-ray photoelectron spectrophotometer (XPS) (VG Scientific) with monochromatic Mg Kα excitation source. The cylindrical photochemical reactor setup was used for the degradation of MCP and degradation and mineralization of MCP was monitored by HPLC (Shimadzu, Model: SPD-10A VP) and a TOC analyzer (Shimadzu, Model: 5000A) equipped with a single injection auto sampler (ASI-5000).

Results and Discussion

X-ray diffraction pattern

The powder X-ray diffraction patterns of TiO_2, 1 wt% La-doped TiO_2, 1 wt% La-doped ZnO and ZnO are shown in Fig. 1a, b, c& d respectively. The distinctive TiO_2 peaks appears in Fig.1a at 25.43°, 37.92°, 48.09°, 54.58° and 62.81° corresponding to the anatase (101), (103), (200), (211) and (204) crystal planes (JCPDS-21-1272) respectively. The XRD patterns of La-doped TiO_2 (Fig.1b) show the same pattern as that of pure TiO_2. No extra peak was found for La^{3+} ions which is due to the presence of small amount of La^{3+} ions in La-doped TiO_2 (Fig.1b). Hence this observation precludes the formation of any separate phase due to La^{3+} ions. Similarly, the XRD pattern of La-doped ZnO (Fig.1c) catalyst is almost similar to that of ZnO (Fig.1d), suggesting that there is no change in the crystal structure upon La loading. The crystallite size of pure TiO_2, ZnO, 1 wt% La-doped TiO_2 and 1wt% La-doped ZnO was calculated using Scherrer equation and are found to be 53.11 nm, 40.0 nm, 19.87 nm and 21.24 nm. The decrease in particle size of La-doped semiconductors is mainly attributed to the presence of La-O-Ti or La-O-Zn on the surface of the doped samples, which hinders the growth of crystal grains [4].

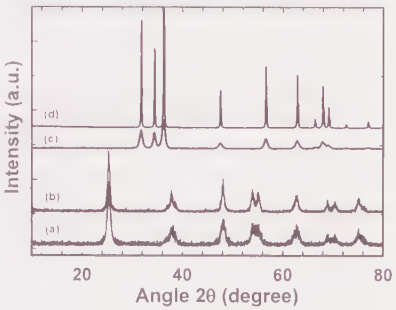

Figure 1: XRD patterns of pure and La-doped semiconductors

Nitrogen adsorption measurements

The Brunauer-Emmett-Teller (BET) specific surface area of TiO_2, 0.5,1 and 2.0 wt% La-doped TiO_2 is 118.5m^2/g, 110.2 m^2/g, 98.36m^2/g and 65.4m^2/g respectively while ZnO and 1 wt% La-doped ZnO exhibited 53.11 m^2/g and 39.56 m^2/g respectively. The pore diameters of TiO_2, 0.5,1 and 2.0 wt% La-doped TiO_2 are are 2.718 nm, 2.94 nm, 4.267 nm and 6.5 nm respectively whereas ZnO and 1 wt% La-doped ZnO showed 1.131 nm and 2.378 nm respectively. Decrease in surface area and increase in pore diameter of La-doped TiO_2 is mainly due to La-doping on TiO_2 nano particles. Large surface area and pore diameters of La-doped semiconductors allows an easy diffusion of the pollutant molecules in and around the semiconductor, thus enhancing the adsorption of pollutant molecules and it`s intermediate on the surface of the catalysts.

X-ray photoelectron spectroscopic analysis

The XPS survey spectrum of La-doped TiO_2 is shown in Fig. 2. The presence of La^{3+}, Ti-2p and O 1s are clearly seen in the Fig.2 and the binding energies for Ti $2p_{3/2}$, O 1s and La 3d are 459.0, 531 and 841 eV respectively. To investigate the La^{3+} in La-doped TiO_2, we measured the La 3d core levels, as shown in inset of Fig.2. La 3d spectrum appears broad and this is due to La^{3+} in the lattice of La_2O_3 and La^{3+} sites that make interaction with oxidic sites of TiO_2. Similarly, the survey spectrum of La-doped ZnO and core level spectra of La 3d confirmed the presence of La^{3+} (840.2), Zn-LMM (265 eV) and O 1s (530.8 eV) in La-doped ZnO.

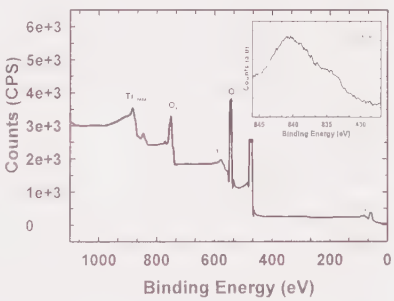

Figure 2: XPS spectra La-doped TiO_2

UV-Visible (UV-Vis) and atomic force microscope (AFM) analysis

The UV-Visible absorption spectra of La-doped semiconductors showed that the absorption band shifts towards shorter wavelength by about 14 nm upon La loading. This could be mainly attributed to the quantum size effect as well as the strong interaction between the surface oxides of Ti or Zn and La. Jing et al [5] reported that as particle size decreases, the optical absorption threshold shifts to the blue, which can be attributed to the quantum size effect. They observed the band shift of 10-15 nm for the crystal size of ZnO between 12-25 nm. Similarly in our studies we observed the band shift of 14 nm for the crystal size between 19-21 nm. The average surface roughness value derived from AFM analysis for pure and 1 wt% La-doped TiO_2 was 0.304 nm and 0.576 nm respectively. The introduction of La^{3+} in the lattice of TiO_2 can control the grain growth and enhance the surface roughness of TiO_2 catalysts. The high rough and porous surface of La-

doped TiO_2 is beneficial for enhanced photocatalytic activity for the degradation of organic pollutants present in aqueous solution [6].

Photocatalytic degradation and mineralization of MCP

In order to evaluate the photocatalytic activity of TiO_2/ZnO and La-doped TiO_2/ZnO (1 wt%) a series of experiments were carried out for MCP degradation in aqueous suspension with the light of wavelengths 254 and 365 nm. The photocatalytic degradation of MCP follows pseudo-first order kinetics and the apparent first order rate constants (k) and $t_{1/2}$ values of pure semiconductors and La-doped semiconductors are summarized in Table 1. La-doped TiO_2/ZnO (1 wt%) showed higher rate of degradation than pure TiO_2/ZnO for the light of wavelength of 254 nm. Decrease in the rate constant (9 x 10^{-2} min^{-1}) at higher loading (2 wt%) is mainly ascribed to the mismatch between the thickness of charge layer and the depth of the light penetration for separating photo-induced electron-hole pairs which enhances the recombination of photo-generated electron–hole pairs. _In order to study the complete mineralization of MCP for TiO_2/ZnO and La-doped TiO_2/ZnO (1 wt%), the plot of total organic carbon value of MCP with time is illustrated in Fig.3. La-doped TiO_2/ZnO (1 wt%) exhibited TOC removal of 100 % and 90% whereas pure TiO_2/ZnO showed 40% and 35% TOC removal respectively within 3 h under the same experimental conditions. Small grain size, high surface roughness value and suppression of electron-hole recombinations were the main reasons for the enhanced photocatalytic activity of La-doped semiconductors. It is interesting to note that the photocatalytic activity of La-doped TiO_2 is higher than that of La-doped ZnO due to the high specific surface area and roughness value of the former than the later. The enhanced photocatalytic activity of La-doped semiconductors was further supported by relative photonic efficiency values as shown in Table 1.

Table 1: Summary of kinetic results and relative photonic efficiency of catalysts

Catalyst	k [x 10^{-2} min^{-1}]	$t_{1/2}$ [min]	Relative photonic efficiency
TiO_2	6.0	11.6	1.36 ± .01
La- TiO_2	14.0	5.0	2.33± 0.01
ZnO	5.3	13.2	1.03± 0.01
La-ZnO	10.1	6.9	1.57± 0.01

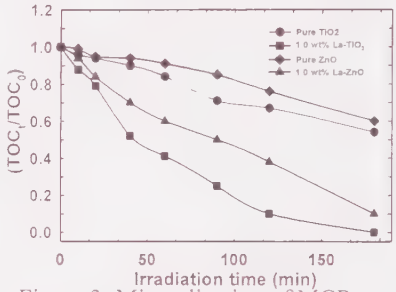

Figure 3: Mineralization of MCP over pure and La-doped semiconductors

Conclusion

La-doped TiO_2/ZnO catalysts were successfully synthesized and characterized by various sophisticated techniques. La-doped semiconductors could efficiently decompose monocrotophos in aqueous solution under UV light. La-doped TiO_2/ZnO was found to be very active and their rate constant was 2.33 and 1.90 times higher than that of corresponding pure TiO_2/ZnO catalysts. Small particle size, high surface area, high surface roughness and porous surface are the reason for the high photocatalytic activity of La-doped TiO_2/ZnO than that of pure TiO_2/ZnO for the removal of MCP.

Acknowledgement

The authors acknowledge the Ministry of Education, Culture, Sports, Science and Technology (MEXT) for the funding through "High-Tech Research Center" a project for private universities, 2004-2008.

References

1. Z. Zou, J. Ye, K. Sayama and H. Arakawa: Nature vol. 414 (2002), p. 625
2. W. Choi, A. Termin and M.R. Hoffmann: J.Phys.Chem. vol. 98 (1994), p. 13669
3. S. Tamil Selvan, T. Hayakawa and M. Nogami: J. Phys. Chem. B vol.103 (1999), p. 7064
4. J. Lin, J.C. Yu, D. Lo and S.K. Lam: J. Catal. Vol. 183 (1999), p. 368.
5. L. Jing, Z. Xu, X. Sun, J. Shang and W. Cai: Appl. Surf. Sci. vol.180 (2001), p.308
6. M.O. Abou-Helal and W.T. Seeber: Appl. Surf. Sci. vol. 195 (2002), p. 53

Advanced Materials Research Vol. 31 (2008) pp 215-217
online at http://www.scientific.net
© 2008 Trans Tech Publications, Switzerland

Structural Investigation of Cubic-phase InN on GaAs (001) Grown by MBE Under In- and N-rich Growth Conditions

S. Kuntharin[1], S. Sanorpim[1, a], T. Nakamura[2], R. Katayama[2] and K. Onabe[2, b]

[1]Department of Physics, Faculty of Science, Chulalongkorn University, Bangkok 10330, Thailand
[2]Department of Advance Material Science, The University of Tokyo, Kashiwanoha, Kashiwa 277-8561, Japan
[a]Sakuntam.S@chula.ac.th, [b]onabe@k.u-tokyo.ac.jp

Keywords: c-InN, In-rich growth condition, high resolution x-ray diffraction, Raman scattering

Abstracts. We have investigated effect of the In- and N-rich growth conditions on the structural modification of cubic-phase InN (*c*-InN) films grown on GaAs (001) substrates by rf-plasma-assisted molecular beam epitaxy (RF-MBE). High resolution x-ray diffraction (HRXRD) and Raman scattering measurements were performed to examine the hexagonal phase generation in the *c*-InN grown films. It is evident that higher crystal quality *c*-InN films with higher cubic phase purity (~82%) were achieved under the In-rich growth condition. On the other hand, for the N-rich growth condition, the *c*-InN films exhibited higher incorporation of hexagonal phase, which is generated in the cubic phase through the incidental stacking faults on the *c*-InN (111) planes. Our results demonstrate that the In-rich growth condition plays a critical role in the growth of high quality *c*-InN films with higher cubic phase purity.

Introduction

Indium nitride (InN) is a very attractive material for future optoelectronic devices due to its outstanding of material properties such as smallest electron effective mass and smallest direct bandgap among III-nitride semiconductors [1]. In fact, InN crystallizes usually in either a thermodynamically stable wurtzite structure with a hexagonal symmetry or a metastable zinc-blende structure with a cubic symmetry [2, 3]. Less work has been done with cubic phase InN (*c*-InN) than with hexagonal phase InN (*h*-InN). However, some physical properties of *c*-InN are more suitable for device applications. It has been demonstrated that *c*-InN grown on GaAs substrate can be used to fabricate light-emitting diodes (LEDs) with an upright structure and can be incorporated in the mature GaAs device technology more easily than *h*-InN. Further, zinc-blende structure, which has the cubic symmetry, is expected to have a higher mobility due to its lower phonon scattering such the higher crystallographic symmetry [4]. However, high quality *c*-InN films with high cubic-phase purity are usually prepared under certain special growth conditions due to the metastable nature of *c*-InN.

In this paper, we report effect of the growth conditions, namely In- and N-rich growth conditions, on the structural modification of the *c*-InN films grown on GaAs (001) substrates by the rf-plasma-assisted molecular beam epitaxy (RF-MBE).

Experiment

The *c*-InN films for this study were grown at the University of Tokyo by RF-MBE in a system described elsewhere [5]. A standard MBE source provides the In flux. A rf-plasma source was used to produce active N flux. The growth temperature was varied in the range of 450-500 °C. While the In flux and the rf power were kept constant at 1.5×10^{-4} Pa and 300 W, respectively. To change the V/III ratio, the supplied N_2 flow rate was varied in the range of 1.5 – 2.5 sccm. According to these growth conditions, it is found that the In- and N-rich growth conditions can be controlled by the growth temperature and the supplied N_2 flow rate as well as the V/III ratio. The *c*-InN films were characterized by high resolution x-ray diffraction (HRXRD), scanning electron microscopy (SEM), atomic force microscopy (AFM), optical microscopy and Raman scattering.

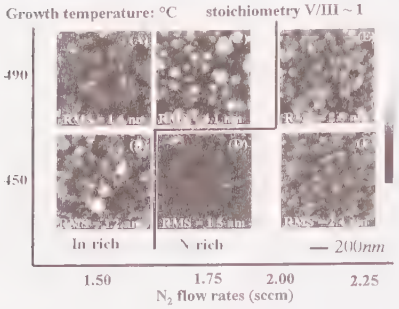

Fig. 1 AFM images of the *c*-InN films grown at different growth temperatures and supplied N_2 flow rates.

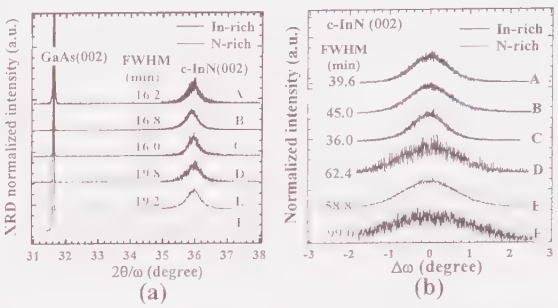

Fig. 2 (a) (002) 2θ/ω HRXRD profiles and (b) ω-rocking curves of the corresponding *c*-InN films.

Results and discussion

The key issue to identify the growth conditions is the In droplets [5], which are seen on the surface for lower supplied N_2 flow rates and higher growth temperatures. An appearance of the In droplets indicate an insufficient V/III ratio, resulting in the In-rich growth condition. On the other hand, the In-droplet-free surface reflects that the growing surface is under the N-rich growth condition. Details of the film morphology are given elsewhere [5]. Here, we evaluated an impact of the In- and N-rich growth conditions on the size of the grains in our films. Figure 1 shows AFM plan-view images of the films grown at different growth temperatures and supplied N_2 flow rates. The condition for the surface-stoichiometry is designated by the bolded line. In the particular example of Fig. 1, it is clearly seen that the In- and N-rich growth conditions strongly effect on the size of the grains. For the In-rich growth condition, the surface RMS roughness of the films increases with decreasing growth temperature. In contrast, for the N-rich growth condition, the surface RMS roughness of the films increases with increasing growth temperature. The results suggest that, unlike the N-rich growth condition [5], the formation of grains in the *c*-InN films grown under In-rich growth condition is caused by limited surface diffusion processes due to the insufficient V/III ratio.

The (002) HRXRD 2θ/ω and (002) ω-rocking curves are shown in Figs. 2(a) and 2(b), respectively. Full width at half maximum (FWHM) of the *c*-InN (002) reflections obtained from 2θ/ω and ω-rocking curves for all the films grown under the In-rich condition (bolded line) are narrower than that for the films grown under the N-rich condition (thinned line). The narrowest FWHM of ω-scan is around 36 min for the film grown at 490°C with supplied N_2 flow rate of 1.50 sccm. These results indicate that the *c*-InN films with higher crystal quality can be archived under the In-rich condition.

Finally, we evaluated the possible impact of the In- and N-rich growth conditions on the hexagonal phase generation in the *c*-InN films. Figure 3 shows X-ray reciprocal space mappings with the incident azimuth axis of the X-ray beam along the <1-10> direction of the InN films grown under In-(sample A, Fig. 3(a)) and N-rich (sample E, Fig. 3(b)) growth conditions. It is seen that the GaAs (002) and *c*-InN (002) diffractions were observed at ω = 18° and the *h*-InN (10-11) diffractions were observed at ω = 18 ± 7°. This indicates that the hexagonal phase incorporated in the cubic phase through the incidental stacking faults on the *c*-InN (111) planes as known for *c*-GaN grown on GaAs [6]. Further, amount of the incorporated hexagonal phase was determined from the ratio of the integrated X-ray diffraction intensities of the cubic (002) and hexagonal (10-11) diffractions measured by the ω-scan [7]. It is found that the cubic phase purity as high as more than 82% was obtained for the *c*-InN film grown under the In-rich growth condition with growth temperature of 490°C and supplied N_2 flow rate of 1.50 sccm. On the other hand, the hexagonal phase structure becomes dominated in the *c*-InN films grown under the N-rich growth condition. We also find that, as shown in Fig. 4, Raman spectra of the *c*-InN films grown under the N-rich

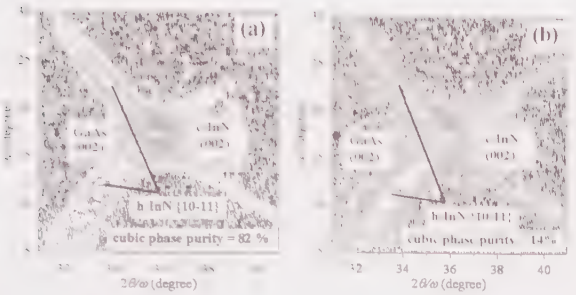

Fig. 3 X-ray reciprocal space mappings of the InN films grown at 490 °C with the N_2 flow rates of (a) 1.5 sccm (sample A) and (b) 2.25 sccm (sample E).

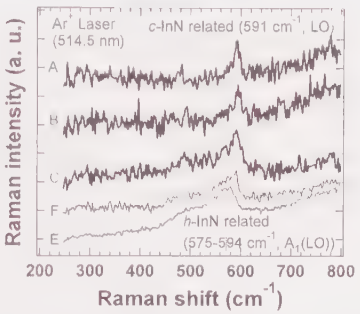

Fig. 4 Raman spectra of the c-InN films grown at different growth temperatures and N flow rates.

growth condition (samples E and F) include hexagonal A_1 longitudinal optical (LO)-phonon mode at 591 cm^{-1} [8] as well as the cubic longitudinal optical (LO)-phonon mode at 594 cm^{-1} [8, 9]. The broadening of Raman spectra is attributed to disorder-activated Raman scattering, relating to phonon density of state of *c*-InN crystal [9]. On the other hand, no *h*-InN related Raman features were observed from the *c*-InN films grown under the In-rich growth condition (samples A, B and C). The difference in the Raman spectra is in connection with the different amount of incorporated hexagonal phase in the *c*-InN films, which agrees well with the results of HRXRD.

Summary: The effects of the In- and N-rich growth conditions on the structural modification of *c*-InN films grown on GaAs (001) substrates by RF-MBE were investigated. Higher crystal quality *c*-InN films can be achieved under the In-rich growth conditions with the narrower FWHM of ω-scan of 36 min and higher cubic phase purity of 82%. Our results demonstrate that the surface-stoichiometry plays a critical role in the growth of single structural-phase *c*-InN with higher crystalline quality.

Acknowledgements: This work was supported in part by Thailand Research Found (Contact Number MRG5080141) and Graduate School, Chulalongkorn University.

References

[1] A. G. Bhuiyan, A. Hashimoto and A. Yamamoto: J. Appl. Phys. Vol. 94 (2003), p. 2779

[2] S. V. Ivanov, T. V. Shubina, V. N. Jmerik, V. A. Vekshin, P. S. Kop'ev and B. Monemar, J. Crystal Growth Vol. 269 (2004), p. 1

[3] D.J. As, D. Schikora and K. Lischka: phys. stat. sol. (c) Vol. 6 (2003), p. 1607

[4] O. Brandt, H. Yang, H. Kostial, K.H. Ploog : Appl. Phys. Lett. Vol. 69 (1996), p. 2707

[5] T. Nakamura, K. Iida, R. Katayama and K. Onabe: phys. stat. sol. (b) Vol. 235 (2003), p. 1451

[6] S. Sanorpim, E. Takuma, R. Katayama, K. Onabe, H. Ichinose and Y. Shiraki: phys. stat. sol. (b) Vol. 234 (2002), p. 840

[7] H. Tsuchiya, K. Sunaba, S. Yonemura, T. Suemasu, and H. Seki: Jpn. J. Appl. Phys. Vol. 36 (1997), p. L1

[8] Y. Iwahashi, H. Yaguchi, A. Nishimoto, M. Orihara, Y. Hijikata and S. Yoshida: phys. stat. sol. (c) Vol. 3 (2006), p. 1515

[9] H. W. Leite Alves, J. L. A. Alves, L. M. R. Scolfaro, J. R. Lite: Mater. Sci. Eng. Vol. B93, p. 90

Advanced Materials Research Vol. 31 (2008) pp 218-220
online at http://www.scientific.net
© 2008 Trans Tech Publications, Switzerland

MOVPE growth window for high-Nitrogen GaAsN alloy films for long wavelength emission

S. Sanorpim[1, a], F. Nakajima[2], R. Katayama[2] and K. Onabe[2, b]

[1] Department of Physics, Faculty of Science, Chulalongkorn University, Phayathai Rd., Pathumwan, Bangkok 10330, Thailand

[2] Department of Advanced Materials Science, The University of Tokyo, 5-1-5 Kashiwanoha, Kashiwa, Chiba, 277-8561, Japan

[a]Sakuntam.S@chula.ac.th, [b]onabe@k.u-tokyo.ac.jp

Keywords: III-V-Nitrides, GaAsN, MOVPE.

Abstract. The high quality GaAsN epitaxial films with the typical thickness of 150-200 nm and the N contents up to 5.5% were grown by MOVPE. The maximum N content of 2.75% at the growth temperature of 550 °C was enhanced to 5.1% at 500 °C and 5.5% at 450 °C. The lower growth temperature may efficiently suppress desorption of N atoms from the growing surface. The narrow high-resolution X-ray diffraction peaks and the clear Pendellösung fringes indicate that the GaAsN films with high uniformity and fairly flat interface were obtained. The 6K-photoluminescence (PL) peak energy of the GaAsN films was varied from 1.38 eV to 1.01 eV with increasing N content up to 2.75%, but no near-band-edge emission was observed in the higher-N-content films, indicating the increase of nonradiative recombination centers caused by the N-related lattice imperfections. Besides, after post growth thermal annealing at 650 °C for 2 min, PL spectrum shows that the near-band-edge emission as low as 0.97 eV (1.3 μm) have been achieved with the film of 5.1% N.

Introduction

There is considerable interest in mixed, narrow band gap, III-V-nitride alloys such as GaAsN and related quaternary InGaAsN [1-4]. The large difference in electronegativities and lattice constants between GaAs and GaN results in a huge optical bowing coefficient and significant bandgap decrease for even small N contents (N < 0.05%) [1-3, 4]. This makes GaAsN and related quaternary InGaAsN alloy materials interesting for optoelectronic applications in the infrared wavelength range (λ = 1.3 and 1.55 μm) [1]. Moreover, it is a challenge to incorporate the possibly high N contents in the GaAsN alloys beyond the limit of extreme immiscibility which is the characteristic of the III-V-N alloys. In this paper, we report the metalorganic vapor phase epitaxy (MOVPE) growth of higher N-content GaAsN alloy layers on the GaAs (001) substrates using tertiarybutylarsine (TBAs) and dimethylhydrazine (DMHy) as As and N precursors. We have carefully studied the growth parameters and the N incorporation. With optimum growth conditions, the highly strained GaAsN layers with N contents up to 5.5% were successfully grown on the GaAs substrates. Photoluminescence (PL) was studied in the view of effects of N incorporation on the optical property of the GaAsN bulk layers.

Experiment

GaAsN samples were grown by low-pressure (60 Torr) MOVPE using trimethylgallium (TMGa), DMHy and TBAs as the source materials of Ga, N and As, respectively. All GaAsN layers were grown on GaAs (001) substrates at temperature ranging from 475 to 550 °C. The [TBAs]/[TMGa] ratio was optimized to be 15. The flow rate of DMHy was varied in the range of 0 to 5000 μmol/min. N content (x) in the $GaAs_{1-x}N_x$ layers was determined from the combination of symmetrical (004) high-resolution X-ray diffraction (HRXRD) and reciprocal lattice mapping of asymmetrical (115) reflection [5]. Optical properties of the GaAsN films were characterized using PL measurements. The 325 nm line of a Cd-He laser (excitation power of 1.0 W/cm2) was employed as an excitation source.

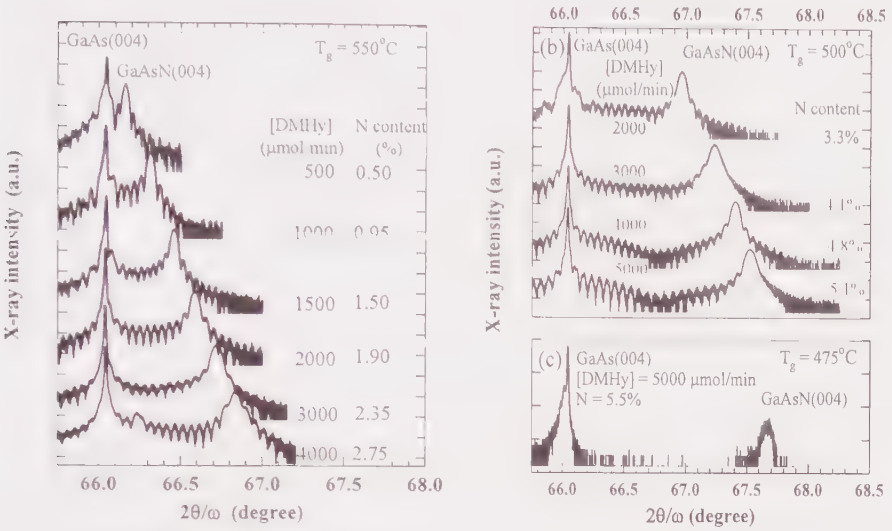

Fig. 1. (a) (004) HRXRD profiles of GaAsN alloy layers grown with increasing DMHy molar flow rate. The N content was estimated from the (115) X-ray reciprocal space mapping. (004) HRXRD profiles of the GaAsN alloy layers with different DMHy molar flow rates grown at lower growth temperatures of (b) 500 and (c) 475°C.

Results and discussion

All GaAsN samples in this study were examined by HRXRD in order to determine the N content and verify the structural quality. Figure 1 shows (004) HRXRD profiles of a set of the GaAsN samples grown at 550 °C with different DMHy molar flow rates. As shown in the figure, compared with GaAs, the peak shift to the higher diffraction angles was clearly observed with increasing DMHy flow rate from 0 to 4000 μmol/min ($0 < N \leq 2.75\%$), indicating the decrease of lattice constant with the N incorporation. The narrow diffraction peaks and the clear Pendellosung fringes indicate that GaAsN layers with high crystal quality were coherently grown on the GaAs substrate, which was confirmed by X-ray reciprocal space mapping measurements (not shown). Note that for higher DMHy molar flow rates (> 4,000 μmol/min), the diffraction peak corresponding to GaAsN tends to degrade the crystalline quality. Furthermore, Pendellosung fringes are hardly observed from the GaAsN layers grown with the DMHy molar flow rates higher than 4000 μmol/min.

Figures 1(b) and 1(c) show a set of (004) HRXRD profiles obtained from the GaAsN layers grown at lower growth temperatures of 500 °C and 475 °C, respectively. It is found that the maximum N content of 2.75% at the growth temperature of 550 °C (Fig. 1(a)) was enhanced to 5.1% and 5.5% at 500 °C and 475 °C, respectively. The lower growth temperature may efficiently suppress the decomposition of N atoms from the growing surface. It is clearly seen that such high N-containing GaAsN layers are coherently strained and are of good epitaxial quality. These results are the evidence of high crystal quality films with higher N contents up to 5.5%, obtained by the enhanced incorporation of N at lower growth temperatures in spite of a large miscibility gap. It is noticeable that since the difficulty of the growing GaAsN bulk film with higher N contents ($3.0\% < N < 5.5\%$), such a well-defined X-ray diffraction peaks and the Pendellösung fringes are commonly difficult to be observed.

Figure 2 illustrates the 6 K-PL spectra of the GaAsN layers with various N contents ($0.5\% \leq N \leq 5.1\%$). The peak energy of PL spectrum was varied from 1.38 eV to 0.96 eV with increasing N content

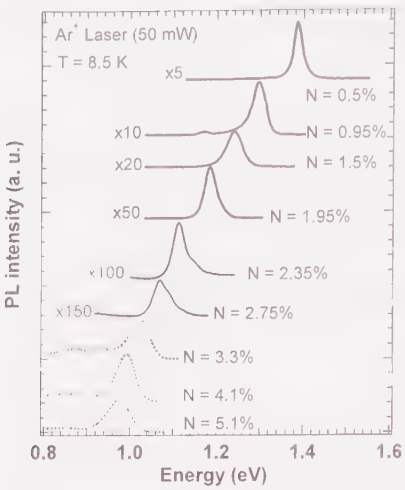

Fig. 4 6 K photoluminescence spectra of GaAsN layers as a function of N content ($0.5\% \leq N \leq 5.1\%$). Dotted lines indicate the PL spectra of GaAsN-related near-band-edge emission after post growth thermal annealing at 650°C for 2 min .

up to 5.1%. It is clearly seen that, the spectrum shows a red-shift with increasing N content, but PL intensity decreased with increasing N content. It should be noted that luminescence signal cannot be detected from the higher N-containing GaAsN samples ($N > 3\%$). To improve the PL intensity, the GaAsN layers were post-growth thermal annealed at 650°C for 2 min, as indicated by the dotted lines. This is due to the highly non-radiative recombination centers in such high N-containing samples [6]. Additionally, a near band gap emission was observed, which was associated with localized states at low temperature.

Summary

The MOVPE growth conditions of high N-content GaAsN bulk films and their structural and optical properties were investigated. The dependence of N incorporation on the DMHy molar flow rate and the growth temperature was examined. Under optimized growth conditions, the high quality GaAsN films with high N contents up to 5.5% were obtained by the absorption of DMHy at lower growth temperatures. The 6 K-PL spectra demonstrated the emission down to ~0.97 eV due to the N incorporation. The present results demonstrated that the growth temperature and the DMHy molar flow rate are, therefore, key parameters in the growth of dilute-nitride-arsenide alloy semiconductors to achieve the higher N-containing films for long wavelength emission.

Acknowledgement

This work was supported by the Thailand research fund (Contact Number MRG488001).

References

[1] M. Kondow, K. Uomi, A. Niwa, T. Kitatani, S. Watahiki, and Y. Yazawa: Jpn. J. Appl. Phys. Vol. 35 (1996), p. 1273

[2] M. Weyer, M. Sato, and H. Ando: Jpn. J. Appl. Phys. Vol. 31 (1992), p. L853.

[3] S. Sato and S. Satoh: J. Cryst. Growth 192 (1998), p. 381.

[4] S. R. Kurtz, A. A. Allerman, E. D. Jones, J. M. Gee, J. J. Banas and B. E. Hammons, Appl. Phys. Lett., Vol. 74(5) (1999), p. 729

[5] K. Uesugi, N. Morooka, and I. Suemune: Appl. Phys. Lett., Vol. 74 No. 9 (1999), p. 1254

[6] I. A. Buyanova, W. M. Chen, and B. Monemar: MRS Internet J. Nitride Semicond. Res. Vol. 6 (2001), p. 2

Advanced Materials Research Vol. 31 (2008) pp 221-223
online at http://www.scientific.net
© 2008 Trans Tech Publications, Switzerland

A Comparison of the Structural Quality of High-In Content InGaAsN Films Grown on InGaAs Pseudosubstrate and on GaAs Substrate

S. Sanorpim[1, a], P. Kongjaeng[1], R. Katayama[2] and K. Onabe[2]

[1]Department of Physics, Faculty of Science, Chulalongkorn University, Phayatai Rd., Pathumwan, Bangkok 10330, Thailand

[2]Department of Advanced Materials Science, The University of Tokyo, 5-1-5 Kashiwanoha, Kashiwa 277-8561, Japan

[a]Sakuntam.S@chula.ac.th

Keywords: InGaAsN, pseudosubstrate, structural property, MOVPE

Abstract. The use of an InGaAs buffer layer was applied to the growth of thick $In_xGa_{1-x}As_{1-y}N_y$ layers with higher In contents ($x > 30\%$). In order to obtain the lattice-matched InGaAsN layer having the bandgap of 1.0 eV, the $In_{0.2}Ga_{0.8}As$ was chosen. In this work, the $In_{0.3}Ga_{0.7}As_{0.98}N_{0.02}$ layers were successfully grown on closely lattice-matched $In_{0.2}Ga_{0.8}As$ buffer layers (InGaAsN/InGaAs). Structural quality of such layers is discussed in comparison with those of the $In_{0.3}Ga_{0.7}As_{0.98}N_{0.02}$ layers grown directly on the GaAs substrate (InGaAsN/GaAs). Based on the results of transmission electron microscopy, the misfit dislocations (MDs), which are located near the InGaAsN/GaAs heteroepitaxial interface, are visible by their strain contrast. On the other hand, no generation of the MDs is evidenced in the InGaAsN layer grown on the $In_{0.2}Ga_{0.8}As$ pseudosubstrate. Our results demonstrate that a reduction of misfit strain though the use of the pseudosubstrate made possible the growth of high In-content InGaAsN layers with higher crystal quality to extend the wavelength of InGaAsN material.

Introduction

The $In_xGa_{1-x}As_{1-x}N_x$ alloys are one of the most promising materials for the applications of long wavelength laser diodes (LDs) operating in the 1.3 - 1.55 μm region. Almost the InGaAsN based heterostructures, which are grown on the GaAs under the lattice-matching condition, have been established [1, 2]. This also makes the $In_xGa_{1-x}As_{1-y}N_y$ alloy system interesting for multijunction (MJ) solar cells [3, 4]. In order to decrease the bandgap, it is required to increase the N or In concentrations still further. However, due to a large miscibility gap, random alloys in the high N concentration regime tend to phase separate resulting in a degradation of both the structural and optical properties. To suppress the phase separation and obtain better crystal quality of InGaAsN in the 1.3 μm range, it is indispensable to increase the In content and reduce the N content in the InGaAsN layer. This results in high compressive strain of over 1.5% in the layer. Therefore, the crystal quality and reliability of

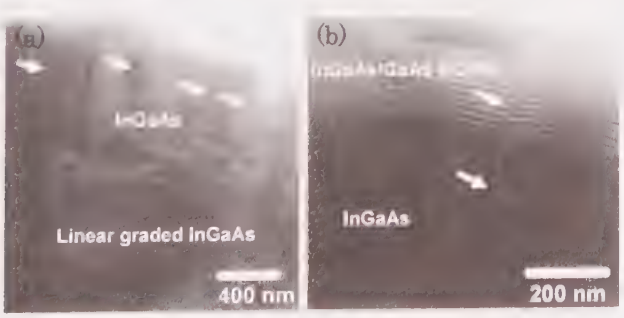

Fig. 1 The cross sectional <110> TEM images of (a) $In_{0.2}Ga_{0.8}As$ on a linearly-graded InGaAs buffer layer and (b) $In_{0.2}Ga_{0.8}As$ on a strained InGaAs/GaAs multi-quantum wells.

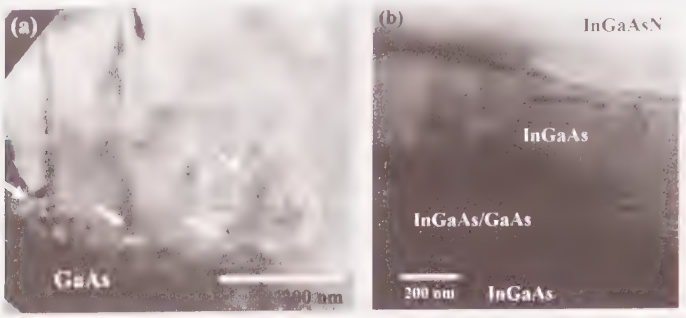

Fig. 2 Cross-sectional <110> TEM images of $In_{0.3}Ga_{0.7}As_{0.98}N_{0.02}$ alloy films on (a) GaAs and (b) $In_{0.2}Ga_{0.8}As$ substrates. The arrows represent the positions of TDs.

the thick InGaAsN layer may be degrade when the total thickness of the layers is beyond the critical thickness. In order to reduce the excessive strain on the heterointerface, the introduction of a strain relaxed InGaAs buffer layer is purposed [6].

In this work, the strain relaxed $In_{0.2}Ga_{0.8}As$ buffer layer was used as a substrate for the growth of thick $In_xGa_{1-x}As_{1-y}N_y$ layers with higher In contents ($x > 0.3$). Typically, the $In_xGa_{1-x}As_{1-y}N_y$ ($x \sim 0.30$ and $y \sim 0.02$) layers were grown on the closely lattice-matched $In_{0.2}Ga_{0.8}As$ pseudosubstrate (InGaAsN/InGaAs). For a comparison, another $In_xGa_{1-x}As_{1-y}N_y$ ($x \sim 0.30$ and $y \sim 0.02$) layer was grown on the highly strained GaAs substrate (InGaAsN/GaAs). The aim of this work is to compare the crystal quality of InGaAsN/InGaAs and InGaAsN/GaAs, which was investigated by transmission electron microscopy (TEM) and high resolution X-ray diffraction (HRXRD).

Experiment

The pesudo-lattice-matched InGaAs substrates (pseudosubstrate) were prepared by metalorganic vapor phase epitaxy (MOVPE); the detailed sample structure is described elsewhere [6]. After a 1.5 μm-thick linearly-graded $In_xGa_{1-x}As$ buffer layer with the final In content of ~20% was deposited, a 900 nm-thick constant $In_{0.2}Ga_{0.8}As$ layer was grown. The gradation is approximated to be 0.8%In/65 nm. This InGaAs composition is chosen so that the InGaAsN layer having the bandgap of 1.0 eV is lattice-matched. Then, strained multi-quantum wells (MQWs), which consisted of 10 periods with equal layer thicknesses of $In_{0.2}Ga_{0.8}As$ and GaAs, was grown on the top of the constant $In_{0.2}Ga_{0.8}As$ layer. Finally, a 500 nm-thick constant $In_{0.2}Ga_{0.8}As$ layer was grown as a pseudosubstrate layer.

To compare the structural quality, $In_xGa_{1-x}As_{1-y}N_y$ layers with In and N contents of $x \sim 0.3$ and $y \sim 0.02$ were grown on both the GaAs and $In_{0.2}Ga_{0.8}As$ substrates by MOVPE at 550°C using 1,1 dimethylhydrazine (DMHy) as a N precursor. The In and N contents were determined by high resolution X-ray reciprocal mapping measurement, in which the strain in the layer was taken into account. By TEM analysis, we observed defects near the interface and in the layer.

Results and discussion

Figure 1(a) shows a cross-sectional TEM image of $In_{0.2}Ga_{0.8}As$ buffer later on a linear-graded InGaAs layer (LG-InGaAs). It is clear that there is a large number of misfit dislocations (MDs) confined at the LG-InGaAs region, which is due to strain relaxation. Note that there are not only misfit dislocations at the graded region, but also defects in the constant $In_{0.2}Ga_{0.8}As$ region. Figure 1(b) shows the cross-sectional TEM image of $In_{0.2}Ga_{0.8}As$ on the strained $In_{0.2}Ga_{0.8}As$/GaAs MQWs. It is found that the MDs are located near $In_{0.2}Ga_{0.8}As$/GaAs heteroepitaxial interface. The most of threading dislocations are spread throughout the quantum well region indicated by arrows. As an expectation, only a few of them thread up in the $In_{0.2}Ga_{0.8}As$ top layer. There is an evidence for some filtering of

TDs by the quantum wells due to their bending at the heteroepitaxial interfaces. According the facts of the above structural results, it is clear that high-quality strain-relaxed InGaAs buffer layer could be achieved by a combination of the LG and multi-quantum wells.

Figures 2(a) and 2(b) show the cross sectional TEM images of $In_{0.3}Ga_{0.7}As_{0.98}N_{0.02}$ on GaAs and $In_{0.3}Ga_{0.7}As_{0.98}N_{0.02}$ on $In_{0.2}Ga_{0.8}As$ substrates, respectively. For $In_{0.3}Ga_{0.7}As_{0.98}N_{0.02}$ on $In_{0.2}Ga_{0.8}As$, no generation of MDs at the interface was observed. It is known that the $In_{0.3}Ga_{0.7}As_{0.98}N_{0.02}$ layer is grown coherently due to the small lattice-mismatch with the $In_{0.2}Ga_{0.8}As$ substrate (~ 0.3%). Meanwhile, for the $In_{0.3}Ga_{0.7}As_{0.98}N_{0.02}$ on GaAs shown in Fig. 2(b), there are not only misfit dislocations at the interface due to the larger lattice-mismatch (>0.55%), but also defects in the InGaAsN layer.

Reduction in the misfit strain though the use of pseudosubstrates made possible the growth of the higher In-content (x ~ 0.3) InGaAsN layer with high structural quality necessary for the development of the MJ solar cells. Our results also demonstrate that the pseudo-substrate is effective for the reduction of not only the dislocation density but also the non-uniform distribution of In and N which are not detected as the PL measurement (not shown). It is known that these In- and N-rich microscopic regions may act as quantum dots in varied sizes, leading to a long wavelength PL spectrum with broad emission peak [7, 8].

Summary

We demonstrate that a combination of the use of LG and MQWs is a promising method to achieve high-quality strain-relaxed InGaAs buffer layers as a substrate for the large lattice-mismatched InGaAsN layers with high In-content. We investigated the effectiveness of the InGaAs substrate in improving structural quality of a lattice-mismatched high In-content $In_{0.3}Ga_{0.7}As_{0.98}N_{0.02}$ on GaAs. Transmission electron microscopy confirmed that dislocations in InGaAsN on GaAs were effectively reduced with the addition of the InGaAs pseudosubstrate. We conclude that the use of InGaAs substrate is a promising route to obtain thick InGaAsN films with a narrow bandgap and high structural quality to widen the potential use.

Acknowledgements: This work was supported in part by Thailand Research Found (Contact Number MRG5080141) and Graduate School, Chulalongkorn University.

References

[1] M. Kondow, T. Kitatani, S. Nakatsuka, M. C. Larson, K. Nakahara, Y. Yazawa and M. Okai: IEEE, J. Select. Topics Quantum Electron, Vol. 3 (1997), p. 719

[2] M. Weyer, M. Sato and H. Ando: Jpn. J. Appl. Phys. Vol. 31 (1992), p. L853

[3] M. Kondow, T. Kitatani, K. Nakahara and T. Tanaka: Jpn. J. Appl. Phys. Vol. 38 (1999), p. L1355

[4] S. R. Kurtz, A. A. Allerman, E. D. Jones, J. M. Gee, J. J. Banas and B. E. Hammons: Appl. Phys. Lett. Vol. 74(5) (1999), p. 729

[5] I. A. Buyanova, W. M. Chen, and B. Monemar: MRS Internet J. Nitride Semicond. Res. Vol. 6 (2001), p. 2

[6] P. Kongjaeng, S. Sanorpim, T. Yamamoto, W. Ono, F. Nakajima, R. Katayama and K. Onabe: J. of Crystal Growth Vol. 298 (2007), p. 111

[7] F. Nakajima, S. Sanorpim, T. Yamamoto, T. Takuma, R. Katayama, H. Ichinose, K. Onabe and Y. Shiraki: phys. stat. sol. (c) Vol. 0, No. 7 (2003), p. 2778

[8] H. P. Xin, K. L. Kavanagh, Z. Q. Zhu, and C. W. Tu: J. Vac. Sci. Technol. Vol. B 17 (1999), p. 1649

Advanced Materials Research Vol. 31 (2008) pp 224-226
online at http://www.scientific.net
© 2008 Trans Tech Publications, Switzerland

Optical Transitions in InGaPN/GaP Single Quantum Wells on GaP(100) Substrates by MOVPE

S. Sanorpim[1, a], D. Kaewket[1], S. Tungasmita[1], R. Katayama[2] and K. Onabe[2]

[1]Department of Physics, Faculty of Science, Chulalongkorn University, Phayatai Rd., Pathumwan, Bangkok 10330, Thailand

[2]Department of Advanced Materials Science, The University of Tokyo, 5-1-5 Kashiwanoha, Kashiwa 277-8561, Japan

[a]Sakuntam.S@chula.ac.th

Keywords: III-(III)-V-N, InGaPN, PL, PLE, quantum confinement effect, MOVPE

Abstract. Optical transitions in the $In_{0.050}Ga_{0.950}P_{0.975}N_{0.025}$/GaP lattice-matched single quantum wells (SQWs) with different well widths (L_Z = 1.6 - 6.4 nm) have been investigated by low-temperature photoluminescence (PL) and PL-excitation (PLE). PL spectra showed the strong visible emission from the samples which attracted to a variety of optoelectronic device applications such as light emitting and laser diodes. Comparing to the bulk film, the PL peak position and the fundamental absorption edge of PLE spectra exhibit blue-shift, which is corresponded to the quantum confinement effect by the well. Comparison between the absorption edge of PLE spectra and the finite square well calculation demonstrate that the effective bandgap energy of the InGaPN/GaP system is might be originated mainly from the N-related localized states.

Introduction

The InGaPN material has attracted considerable interest for the high-brightness light-emitting and laser applications such as automotive lighting, optical media reader/writer, billboard, media display panel and traffic lights, etc. Due to the huge bandgap bowing, the incorporation of N drastically reduces the bandgap energy with the majority of the reduction resulting from the lowering of conduction band, as in the case of InGaAsN [1]. The same effect is also expected for the InGaPN material. Furthermore, InGaPN is a material that can be lattice-matched to GaP, with a narrower bandgap than GaP [2]. These introduce the InGaPN/GaP structure as an alternative heterostructure with a large barrier height for an electron confinement in the InGaPN/GaP quantum structures, and exhibit higher characteristic temperature for laser application. However, less work has been done with the InGaPN/GaP quantum structures [1, 3]. Previously, we reported on the successful growth of the

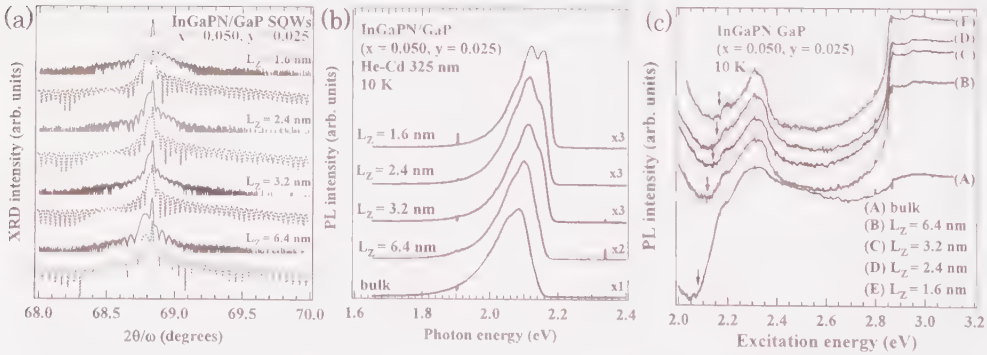

Fig. 1 (a) HRXRD profiles, low-temperature (10 K) (b) PL and (c) PLE spectra for the InGaPN/GaP SQWs (x = 0.050, y = 0.025) with different well-widths L_Z = 1.6 – 6.4 nm as well as the bulk layer. The arrows in (c) indicate the absorption edge of the PLE spectra.

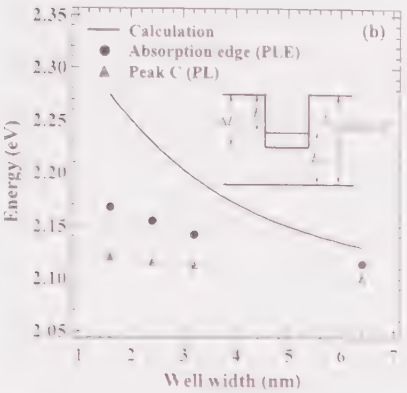

Fig. 2 Dependence of the transition energy and the well-width for the theoretical calculation and the absorption edge, as well as the PL peak position. The inset shows the band alignment of the InGaPN/GaP SQW structure.

lattice-matched $In_xGa_{1-x}P_{1-y}N_y$/GaP bulk layer with the N content as high as $y = 0.071$ [4, 5].

In this work, based on such growth conditions, the $In_{0.050}Ga_{0.950}P_{0.975}N_{0.025}$/GaP lattice-matched single quantum wells (SQWs) with various well-widths were grown and investigated by low-temperature photoluminescence (PL) and PL-excitation (PLE) measurements and high-resolution X-ray diffraction (HRXRD). We also evaluated the confinement effect and the optical transitions in the $In_xGa_{1-x}P_{1-y}N_y$/GaP lattice-matched SQWs using the finite-depth single-square well model.

Experiment

All the $In_xGa_{1-x}P_{1-y}N_y$/GaP lattice-matched SQWs and the $In_xGa_{1-x}P_{1-y}N_y$ bulk layers used in this study were grown on GaP (001) substrates by MOVPE, using trimethylgallium (TMGa), trimethylindium (TMIn), PH_3 and 1,1-dimethyhydrazine (DMHy) as the Ga, In, P and N precursors, respectively. After the growth of the around 0.3 μm-thick GaP buffer layer at 710°C, a thin InGaPN well layer and a GaP cap layer were respectively grown at 635°C. The well-width and composition of the $In_xGa_{1-x}P_{1-y}N_y$ well layers, which were confirmed by HRXRD measurements via the dynamical-theory simulation software, were controlled to be L_Z = 1.6 - 6.4 nm and $x = 0.050$ and $y = 0.025$, respectively. The $In_{0.050}Ga_{0.950}P_{0.975}N_{0.025}$ layer without the GaP cap layer was also prepared for a comparative study.

The optical experiments at low temperature (10 K) were carried out using PL and PLE spectroscopes. PL measurement was performed using the 325 nm-line of He-Cd laser (1.0 W/cm^2) as the excitation source. PLE measurement was done using monochromatic light dispersed with a 0.27 m monochromator from a 500 W Xenon lamp.

Results and Discussion

(004) HRXRD 2θ/ω profiles of the $In_{0.050}Ga_{0.950}P_{0.975}N_{0.025}$/GaP SQWs with various well-widths (L_Z = 1.6 - 6.4 nm) are shown as in Fig. 1(a). The dynamical-theory simulation results are also displayed in Fig. 1(a) as the dotted curves. Good agreement between the simulated and experimental data demonstrates that the $In_{0.050}Ga_{0.950}P_{0.975}N_{0.025}$/GaP lattice-matched SQWs with excellent crystal quality and fairly flat interfaces have been successfully grown on the GaP substrate.

Figure 1(b) shows 10 K-PL spectra for the corresponding lattice-matched SQWs together with the bulk layer. Emission from the lattice-matched SQWs with narrower well-widths is shifted to higher energies. The PL spectra also show an evidence of the strong light emission in the visible (λ = 560 – 680 nm) region. Comparing to the bulk layer, the PL peak position and the fundamental absorption edge of PLE spectra (see Fig. 1(c)) exhibit a blue-shift, which is consistent with the quantum confinement by the well. Moreover, it is found that an extra peak appears at higher-energy side of the main peak when the well-width is about L_Z = 3.2 nm or narrower. Nevertheless, this feature grows up and shifts toward the higher energies with a decreasing of well-width. Since, for the N concentration close to y = 0.02, the average distance between the N atoms is about 1.3 nm [10], which is comparable to the width of the narrowest well (L_Z = 1.6 nm). Thus, the N concentration in the $In_{0.050}Ga_{0.95}P_{0.975}N_{0.025}$ well near the interfaces with the GaP barrier is expected as somewhat lower than $y = 0.025$. As a result, the splitting of this PL sub-peak might be caused by the recombination of localized excitons due to the well-width fluctuations, which are induced by random distribution of the N atoms within the well.

To examine the optical transitions, the finite-depth single-square well model without the effects of hydrostatic strain was used to interpret the PL and PLE results obtained from the lattice-matched InGaPN/GaP SQWs. The PLE absorption edge of the bulk layer (2.08 eV) is used as the effective bandgap of the InGaPN well to calculate the conduction-band offset (ΔE_C) at 10K. The barrier potential is determined by energy level of the indirect bandgap of GaP (2.35 eV at 10 K). In addition, it is known that adding small amount of N decreases the bandgap, which mainly affects the conduction band (CB) states leading to a small valence-band offsets (ΔE_V) [6]. Thus, the value of ΔE_V can be approximated to be zero, in our case. Consequently, the value of ΔE_C is estimated to be about 270 meV at 10 K.

Figure 2 shows the PL peak position and PLE absorption edge as a function of well-width together with the calculated optical transition energies using the finite-depth single-square well model. The PLE absorption edge has the same trend with the calculated optical transition energies, confirming the quantum confinement effect by the well. However, with a reduction of well-width, the PLE absorption edges exhibit lower increasing of the energy than the calculated optical transition energies. This difference might be due to the difference in an exciton effective mass for each SQW sample. It is known that in the dilute III-V-N alloy system, the electron effective mass is significantly increased with incorporation of N. However, in this work, we have calculated the optical transition energies using the same value of the exiton effective mass for the well and barrier regions. Particularly note that, it is also include the behavior mass effect to explain the well-width dependence of the transition optical energies. On the other hand, the PL peak positions are much lower in the energy than the PLE absorption edges and the calculated value of optical transition energies. This evidence implies that such PL emission might be originated from the localized states, which are attributable to the N-related band edge fluctuation in the well.

Summary: We investigated the optical transitions in the $In_{0.050}Ga_{0.950}P_{0.975}N_{0.025}$/GaP lattice-matched SQWs with various well widths (L_Z = 1.6 - 6.4 nm). 10 K-PL and PLE results for the lattice-matched SQWs with varied well-widths have been revealed to confirm the quantum confinement by the well. Comparing with the bulk layer, the PL peak position and the fundamental absorption edge of PLE exhibit blue-shift for SQWs with narrower well-widths and lower In and N concentrations. These blue-shifts were interpreted using the finite-depth single-square well mode which believed to be predominantly determined by the quantum confinement effect to the well.

Acknowledgements: This work was supported in part by Thailand Research Found (Contact Number MRG5080141).

References

[1] M. Kondow, K. Uomi, A. Niwa, T. Kitatani, S. Watahiki and Y. Yazawa: Jpn. J. Appl. Phys., vol. 35 (1996), p. 1273.

[2] K. Onabe, T. Kimura, N. Nakadan, J. Wu, Y. Ito, S. Yoshida, J. Kikawa and Y. Shiraki: presented at *ICCG-13/ICVGE-11* (2001), Kyoto.

[3] V. A. Odnoblyudov and C. W. Tu: Appl. Phys. Lett., vol. 89 (2006), p. 111922.

[4] S. Sanorpim, F. Nakajima, R. Katayama, N. Nakadan, T. Kimura, K. Onabe and Y. Shiraki: Physica status solidi (c), vol. 7 (2003), p. 2773.

[5] S. Sanorpim, F. Nakajima, R. Katayama, N. Nakadan, T. Kimura and K. Onabe: J. Cryst. Growth, vol. 275 (2005), p. 1017.

Advanced Materials Research Vol. 31 (2008) pp 227-229
online at http://www.scientific.net
© 2008 Trans Tech Publications, Switzerland

Annihilation of threading dislocations in regrown GaN on electrochemically etched nanoporous GaN template with optimization of buffer layer growth

C. B. Soh[1#], H. Hartono[2], S. Y. Chow [1], S. J. Chua[1,2,3*]

[1] Institute of Materials Research and Engineering, 3 Research Link, Singapore 117602.
[2] Singapore-MIT Alliance, National University of Singapore, 4 Engineering Drive 3, Singapore 117576.
[3]Department of Electrical and Computer Engineering, National University of Singapore, 2 Engineering Drive 3, Singapore 117576.
[#] Electronic mail: cb-soh@imre.a-star.edu.sg
[*] Electronic mail: elecsj@nus.edu.sg

Abstract. Nanoporous GaN template has been fabricated by electrochemical etching to give hexagonal pits with nano-scale pores of size 20-50 nm in the underlying grains. Electrochemical etching at The effect of GaN buffer layer grown at various temperatures from 650°C to 1015°C on these as-fabricated nano-pores templates are investigated by transmission electron microscopy. The buffer layer grown at the optimized temperature of 850°C partially fill up the pores and voids with annihilation of threading dislocations, serving as an excellent template for high-quality GaN growth. This phenomenon is, however not observed for the samples grown with other temperature buffer layers. The PL spectrum for the regrowth GaN on nanoporous GaN template also shows an enhancement of PL intensity for GaN peak compared to as-grown GaN template, which is indicative of its higher crystal quality. This makes it as a suitable template for subsequent device fabrication.

Introduction

Group III-Nitride has been emerged as essential material for growth of LEDs in the blue and the green spectra region whereas Arsenide is used for emission in the higher wavelength, namely, red. However, the lattice-mismatched and the difference in thermal expansion coefficient between GaN and the sapphire generate a high density of dislocations as well as residual strain.[2] The interest in generating porous GaN arises from report that it can acts as a sink for threading dislocations and accommodate the strain.[3] In this work, we have report on the study of UV-assisted electrochemical etching of GaN followed by regrowth to generate a high quality of GaN material.

Experimental Details

The GaN is grown by Emcore MOCVD system. First a LT-GaN buffer is grown at 530°C, before the temperature is raised to 1020°C to grow a 1.8 um thick Si-doped GaN epilayer. The porous GaN was fabricated using UV-assisted electrochemical etching in 2M of NaOH solution for an hour using Pt rod as the cathode. Fig 1 a shows the SEM image of as-grown Si-doped GaN sample and Fig 1b gives the surface morphology when etching has been carried out for a duration of 0.5 hrs with applied current of 20mA. The etching first takes place at the center of the grain structures of monocrystalline GaN, leading to the formation of hexagonal etched pits with a size of 200-300 nm.[4] As the etch duration increases to an hour, etching then takes place in the underlying grains, creating smaller pores of size 25-60 nm as illustrated in Fig 1c. The effect of varying current density applied for the etching process is also studied. With increase in the current applied from 5.0mA cm^2, 10mA/cm^2 to 20mA/cm^2, as shown in Fig 1d, 1c and 1e respectively, the density of the smaller pores in the underlying grain increases and the hexagonal etched pits are also more defined.

However, when the current density is further increases to 30mA/cm^2, the smaller pores enlarged and merged to form a bigger pore of size greater than 50 nm. The size of the pores is less uniform as compared to etching at I= 20mA/cm^2. Dislocations define the grain boundaries of porous GaN and remain unetched since they are likely to be charged.[5] However at higher applied current, some of the grain boundaries start to physically broken off. This accounts for the irregular hexagonal etched pits at 30mA/cm^2. Hence optimized etching takes place with a drive current of ~20 mA/cm^2.

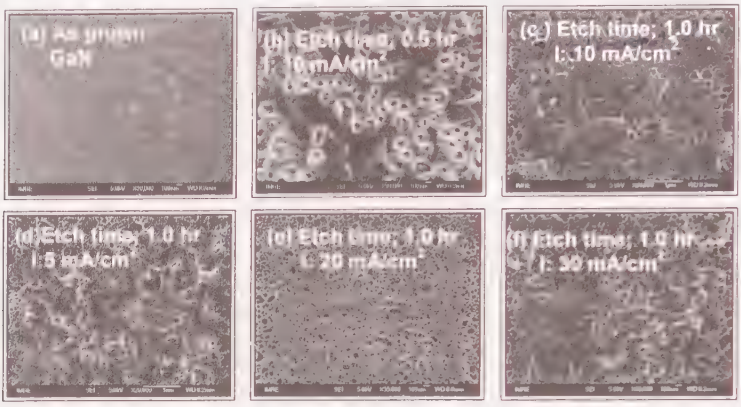
(a) As grown GaN
(b) Etch time; 0.5 hr I: 10 mA/cm^2
(c) Etch time; 1.0 hr I: 10 mA/cm^2
(d) Etch time; 1.0 hr I: 5 mA/cm^2
(e) Etch time; 1.0 hr I: 20 mA/cm^2
(f) Etch time; 1.0 hr I: 30 mA/cm^2

Fig 1a Surface morphology of (a) as-grown GaN and etched GaN with applied current and duration (b) I= 10 mA/cm^2, 0.5 hrs (c) I= 10 mA/cm^2, 1.0 hrs (d) I= 5.0 mA/cm^2, 1.0 hrs (e) I= 20 mA/cm^2, 1.0 hrs and (f) I= 30 mA/cm^2, 1.0 hrs.

The sample is then cleaned in DI water using ultrasonic bath for 5 mins before it is loaded back into the MOCVD chamber for re-growth. An 100 nm thick undoped GaN buffer layer was grown at 750^{0}C, 850^{0}C and 1015^{0}C before grown of the high temperature (HT) GaN layer. Since the NH_3, trimethylIndium (TMI), trimethylgallium (TMG) gas flow was kept fixed; growth temperature of buffer layer is the determining factor in the quality of the subsequent GaN layer.

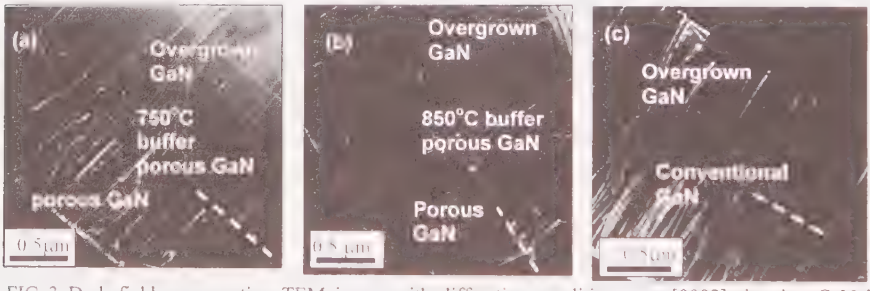

FIG 3 Dark field cross-section TEM image with diffraction condition, g = [0002] showing GaN layer subsequently grown on the porous GaN template with different temperature buffer layers. The dotted line indicates the interface of porous GaN region and the subsequently grown GaN layer. (a) There is no TDs reduction in the re-grown GaN sample when the buffer layer is grown at the temperature of 650°C and 750°C. (b) The TDs in regrown GaN were significantly reduced with annihilation of the TDs at the interface of the 850°C buffer layer with porous GaN template. (c) Overgrown of GaN on GaN template shows no reduction in threading dislocation density.

Figure 3 a, b and c shows the dark field cross-section TEM image for the overgrown GaN on porous GaN template with buffer layer grown at 750°C and 850°C and without the buffer layer respectively. In general, threading dislocations which includes the screw, edge and mixed dislocations, with Burgers vectors $\mathbf{b} = [0001]$, $\mathbf{b} = 1/3[11\bar{2}0]$ and $\mathbf{b} = 1/3[1\bar{1}\bar{2}3]$ respectively, have

been observed in epitaxially grown GaN.[6] With diffraction condition, g = [0002], only screw and mixed dislocations are visible. For the sample with a 750°C-GaN buffer layer, with diffraction condition, g = [0002], there is not much reduction in the TDs density in the thick GaN layers as dislocations propagate beyond the buffer to overgrown GaN layer. However, it is clear that overgrown GaN on 850°C buffer layer has lesser TDs. Some of these dislocations undergo bending back to the underlying porous GaN layer while others branched together to give a single propagating dislocation. A growth temperature of 850°C is the optimized buffer layer growth condition for dislocation reduction in subsequent overgrown GaN on nanoporous GaN template. Most of the TDs were annihilated in the porous GaN region or at the interface with the thin buffer GaN layer. For overgrown GaN on GaN template, a high threading dislocation density is still observed with minimal reduction in dislocation density as illustrated in Fig 3c. Figure 4 shows the a three times enhancement in the PL intensity for regrowth GaN on porous GaN with an insertion of GaN buffer grown at 850°C as compared to regrowth GaN on GaN template. The regrowth on porous GaN has a FWHM of 4.45 nm, much narrower than the 5.34 nm for that on as-grown GaN.

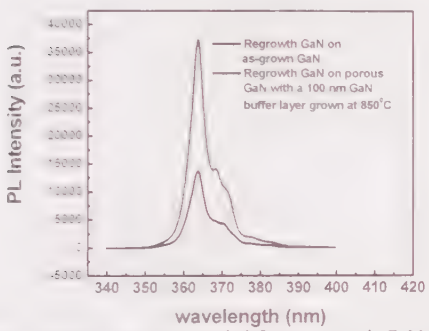
Regrowth GaN on as-grown GaN
Regrowth GaN on porous GaN with a 100 nm GaN buffer layer grown at 850°C
PL Intensity (a.u.)
wavelength (nm)
340 350 360 370 380 390 400 410 420

Fig 4. MicroPL spectra recorded from regrowth GaN on GaN and porous GaN template with a GaN buffer layer of 850°C

In summary, UV-assisted electrochemical etching in NaOH solution with a current density of 20 mA/cm^2 enables us to obtain well defined nanopores of size 20 to 60nm. There is a substantial reduction in threading dislocation for regrowth GaN with buffer of 850°C. The PL result shows an enhancement in intensity with an reduction in the FWHM value. This will serve as a good GaN template for LEDs.

References

1. S. Nakamura, M. Senoh, S. Magahama, N. Iwasa, T. Yamada, T. Matsushita, H. Kiooku, Y. Sugimoto, Jpn. J. Appl. Phys. L74 .1998 (1996)
2. S. Nakamura, M. Senoh, N. Iwasa, T. Yamada,T. Matsushita, Appl. Phys. Lett. **73**, 832 (1998).
3. A. P. Vajpeyi, S. J. Chua, S. Tripathy, E. A. Fitzgerald, W. Liu, P. Chen, L. S. Wang, Electrochemical and Sol. Stat. Lett. **8**, (4), G85-88 (2005).
4. H. Hartono, C. B. Soh, S. Y. Chow, S. J. Chua, Appl. Phys. Lett. **90**, 171917 (2007).
5. C. B. Soh, S. J. Chua, H. F. Lim, D.Z. Chi, S. Tripathy, W. Liu, J. Appl. Phys. **96**, 1341 (2004)
6. S. K. Mathis, A. E. Romanov, L. F. Chen, G. E. Beltz, W. Pompe, J. S. Speck, J. Cryst. Growth **231**, 371 (2001).

Advanced Materials Research Vol. 31 (2008) pp 230-235
online at http://www.scientific.net
© 2008 Trans Tech Publications, Switzerland

Optical Nanowires for Microwave Applications

D.Decoster[1,a], M.Carette[1,b], M.Lesecq[1,c], D.Lauvernier[1,d], M. Zegaoui[1,e], D.Bernard[1,f], J.-P. Vilcot[1,g], J. Chazelas[1,2,h]

[1]IEMN, Cité Scientifique, Avenue Poincaré, BP 60069, 59652 Villeneuve d'Ascq Cedex France

[2]Thales Airborne Systems, 1 Bd Jean Moulin, 78852 Elancourt, France

[a]didier.decoster@iemn.univ-lille1.fr, [b]michele.carette@ed.univ-lille1.fr,
[c]marie.lesecq@ed.univ-lille1.fr, [e]malek.zegaoui@iemn.univ-lille1.fr,
[f]dorothee.bernard@iemn.univ-lille1.fr, [g]jean-pierre.vilcot@iemn.univ-lille1.fr
[h]jean.chazelas@iemn.univ-lille1.fr, [h]jean.chazelas@fr.thalesgroup.com

Keywords: nanophotonics, microwave photonics, nanometric waveguides

Abstract. In this paper, we propose to take advantage of specific properties of nanophotonics to achieve microwave functions which are difficult to get with more conventional ways. With this goal, we developed new technologies to fabricate III-V nanowaveguides. Two ways were explored: the first one by deep etching of conventional epitaxies and the second one by embedding nanowires in polymer. We show in this paper some results on first devices mainly based on nanowires embedded in polymer.

Introduction

There are a lot of activities in nanophotonics showing their attractive new properties. At the same time, some microwave functions are difficult to achieve with conventional techniques. The goal of our research is to explore what could bring nanophotonics for microwave applications. For example, it is difficult to obtain wide bandwidth true time microwave delay, which is a basic brick for optically supply array antennas; this microwave function could, may be, use the generation of slow waves at the band edge of a photonic crystal [1]. Another example is the sampling of microwave signal, which is, up to now, impossible to get with large dynamic in the high frequency domain; we could expect that all-optical switching based on non-linear effects in ultra-small volume of material could help us to answer this need [2].

Due to the fact that we want to develop devices which fulfill industrial requirements, able to be easily transferred into industry with efficient electro-optic materials, our approach is mainly based on III-V nanowires.

We explored two ways. The first one is based on the fabrication of nanowaveguides by deep etching of conventional InP epitaxies. The main advantage is the possibility to deposit electrodes to obtain active devices, but leaky modes can increase the propagation losses, and also some sensitivity to polarization can occur. Several devices were fabricated and characterized [3, 4] showing propagation loss around 2 dB/mm and a few dB in 5µm radius 90° microbends. All-optical functions were also demonstrated [5]. The second way is based on III-V nanowires embedded in polymer with a high index contrast, as in SOI based devices. In principle no leaky modes propagate into the substrate, and we can benefit for a symmetrical structure to have no sensitivity to polarization, but we expect to have difficulties to deposit electrodes; it means that only all-optical functions can be implemented. In the following sections, we will precise our studies on devices based on III-V nanowires embedded in polymer, starting with the technological process.

III-V nanowires in polymer : technological process

Our waveguides, drawn Fig. 1, are made of GaAs or InP nanowires buried in a low index polymer matrix. We choose BCB as polymer matrix due to its good technological and optical properties, matching our needs.

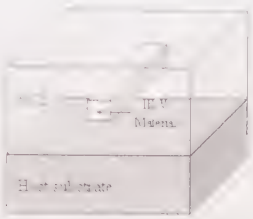

Figure 1: Structure of III-V/BCB nanowire

The fabrication process, summarized Fig. 2, is based on four main steps which are successively the epitaxy, the waveguide core patterning by Electron Beam Lithography (EBL), its etching by Reactive Ion Etching (RIE) and the BCB wafer bonding.

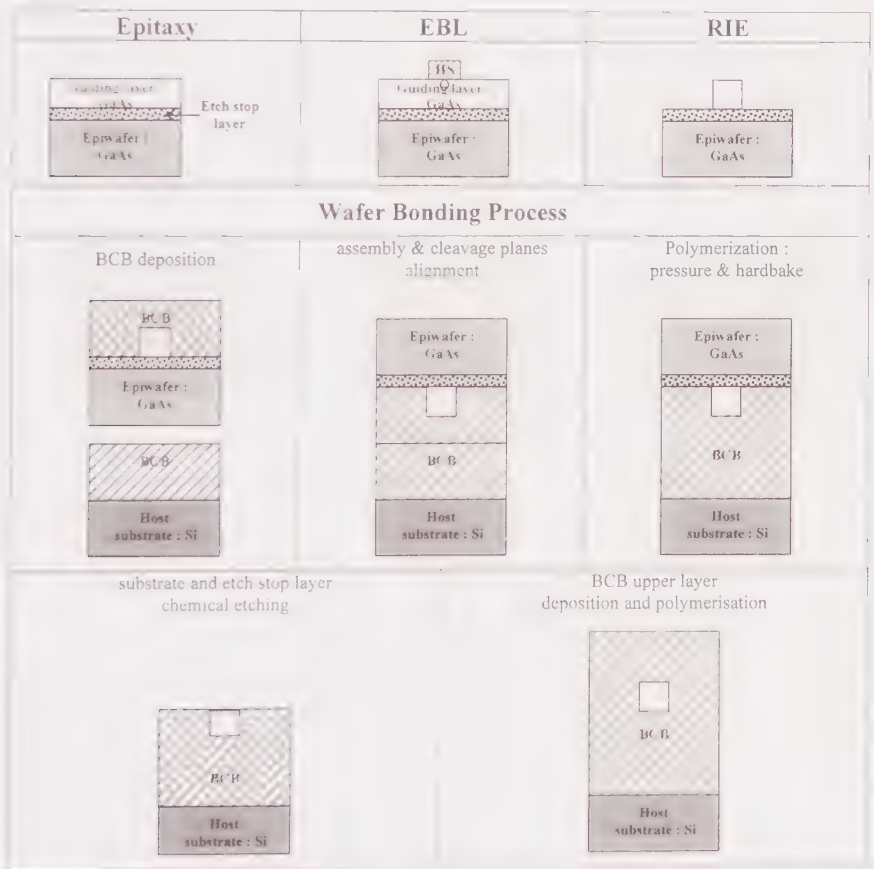

Figure 2: main steps of the technological process

The epitaxial structure is grown by Molecular Beam Epitaxy (MBE). It consists of an etch stop layer (GaInP or GaInAs) under the core layer in GaAs or InP (300 nm thick).

Patterns are defined on a negative electronic resist by EBL because they are as small as 300 nm, and even smaller. We use HydrogenSilsesQuioxane (HSQ) as the resist mask since it has shown a really good definition and a very small linewidth fluctuations. Moreover HSQ can act directly as a hard mask for the GaAs or InP RIE. In fact, by means of an oxidation thanks to an O_2 plasma treatment, we can transform the HSQ in a structure close to the silica one, enhancing so its etching resistance.
We used KOH-based solution as developer and we obtain well defined HSQ patterns (Fig. 3) with a vertical edge roughness estimated at 0.92 nm.

100 nm wide line | 1 µm radius bend | Bragg grating

Figure 3: examples of HSQ resist pattern

These patterns are afterwards etched into the guiding layer by RIE to complete the nanowire definition. We use a $SiCl_4$/Ar (CH_4/H_2/Ar) chemistry to etch the GaAs (InP) guiding layer down to the etch stop layer.
This step is critical as sidewall roughness arises mainly during the etching. Now, it is the main source of propagation loss in strongly confined and extremely small waveguides [6].
At the end of this steps the HSQ resist mask is removed using HF, and we have our nanowires (Fig. 4) above the etch stop layer and epitaxial substrate.

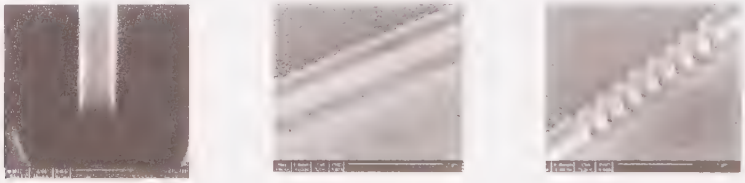

cross section of a 100 nm wide nanowire | 300 nm wide nanowire | Bragg grating

Figure 4: GaAs nanowires after HSQ resist mask removal

It has now to be inserted in the polymer matrix by a wafer bonding technology. This step is the key point of our process since it will form both the bottom confinement layer and the binding layer between the core and the host substrate.
The used technology, detailed in [7], has 3 main parts. First, a layer of BCB is spun onto each substrate, the pattern one and the host one, with a thickness of 2 µm. This will not only allow the BCB to fill every gap and to completely cover the 300 nm-thick patterns on the epiwafer, but also easies the next steps. After a hotplate softbake, aiming at avoiding bubbles entrapment in the BCB coating, the host substrate is flipped onto the patterned wafer taking care to align the cleavage planes. This is performed on a hotplate at 130°C since the BCB is well softened at this temperature, allowing us to move one substrate above the over without damaging the nanowires. At this time, the BCB is not yet polymerized so the final step of the bonding process is to perform the polymerization, at 250°C during one hour and under inert atmosphere, to avoid any change in the BCB optical index. But to obtain a good bonding and a good BCB layer distribution, we apply before this hardbake, a pressure of 1bar during 1h at 130°C.

To end the process, it remains us to remove the epiwafer and the etch stop layer, using $H_2SO_4/H_2O_2/H_2O$ and HCl chemical solutions, and to spun the upper BCB layer.
This process leads to a good bonding with BCB filling every gap of our patterns (Fig. 5). The thermal stability of this structure is ensured up to the BCB glass transition temperature (T_g), estimated close to 350°C.

Bragg grating in BCB after substrate removal

cross section of a GaAs/BCB waveguides

Figure 5: GaAs nanowires in BCB matrix

Properties of the devices

Nanowires can have a square cross-section of 300 x 300 nm² to ensure a singlemode propagation almost insensitive to the polarisation state. The strong confinement of light into the III-V core allows sharp bend with low loss (0.60 dB/turn and 0.80 dB/turn for respectively TE and TM mode using a radius of 5 µm) and prevents a light escape into the substrate. Propagation losses are moderate (5 dB mm for GaAs/BCB waveguides at λ=1.55µm).

When the nanowire width decreases, the optical mode extends strongly outside the core into the BCB and the effective index goes down to the BCB one (Fig. 6). These properties are used to make a reverse taper shape spot size converter to enhance the fibre/waveguide coupling. Its width varies from 80 nm (at the fibre input facet) to the waveguide width (300 nm) on a length of 90 µm. The coupling improvement is measured to about 9 dB.

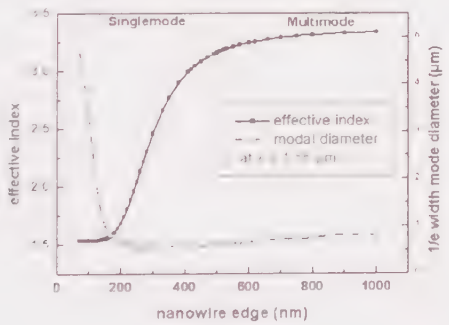

Figure 6 : effective index and optical mode diameter versus square nanowire width.

The nanovolumes of our waveguides lead us to study their behaviour under high power to explore limitation due to non-linear effects.
Characterizations were carried out with a 1.55 µm laser amplified by an EDFA (Erbium doped fibre amplifier). We present here (Fig.7) the results for 100 x 300 nm² and 300 x 300 nm² nanowires having a length of 1 mm and 1.4 mm respectively.

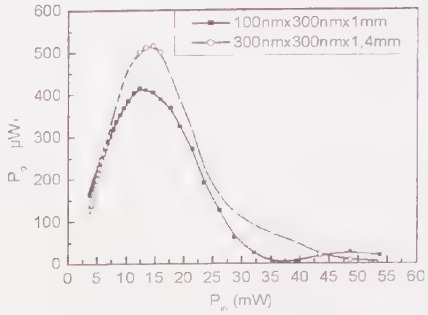

Figure 7: Output power versus injected power at λ=1.55 μm

For an injected power lower than 10 mW, both structures show a linear behaviour. For a greater input power, the output power decreases strongly, indicating some non-linear effects.

Towards ultra-fast all-optical switching.

Pump-probe optical transmission experiments carried out on heavily Be doped InGaAs material have shown a ultra short recombination time (t_r < 400 fs) [8]. Hereby we propose two structures using this material in order to elaborate ultra-fast all optical switches based on the absorption saturation principle. A thin layer of InGaAs is put inside (Fig. 8) or above (Fig. 9) a 300 x 300 nm² InP nanowire allowing a high light confinement. With a pump signal, we saturate the absorption states to turn the switch on. As the volume of the absorbing material is small, we expect the saturation with a relatively low energy optical pulse (lower than 1 pJ).

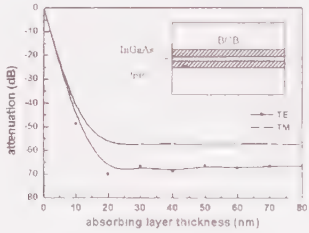

Figure 8: light absorption versus absorbing layer thickness for a 400 μm long nanowire
Insert: cross-section of the device along the propagation axis

These two structures were studied by Beam Propagation Method in 3 dimensions, in order to evaluate the attenuation level obtained compared to a waveguide without absorbing material.
For the first structure, a very thin absorbing layer is inserted inside the nanowire. In this case, the whole waveguide is used as switch and leads to a good absorption for TE and TM polarisations (Fig. 8: 20 nm leads to more than 50 dB of attenuation). The fabrication of this structure requires no additional technological steps to the nanowire process.

The second structure consists in an absorbing zone defined on the nanowire and whose length and position can be chosen. Even if it is necessary to add new technological steps to the nanowire process, it becomes possible to integrate the component into a photonic integrated circuit and to design switches networks. However, the level of attenuation reached with this structure is lower (at maximum 50 dB of attenuation in TE mode) than the first one. Moreover, as the structure is not symmetric, the absorption is polarisation dependent (Fig. 9).

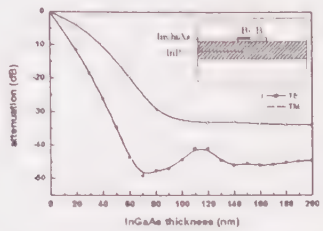

Figure 9. light absorption versus InGaAs thickness for a 100 µm long absorbing zone
Insert : cross-section of the device along the propagation axis

Conclusion

We demonstrated here the possibility to fabricate very compact photonic integrated circuits. The propagation loss in the corresponding waveguides is not too significant due to the allowed compactness. The coupling loss to the optical fiber can also be optimized as low as a few dB per facet, which is promising to get packaged devices.
Calculation made on such devices with ultra-small volume (300 nm x 50 nm x 500 µm) convince us that non-linear effects will appear at low pump optical power and that high dynamic ON/OFF ratios could be reached. First experimental results seem to confirm this assumption. Further works are in progress to demonstrate this concept and to apply it for the sampling of microwave signals.

References

[1] M. Povinelli, Steven Johnson, and J. Joannopoulos : Optics Express Vol. 13 (2005), p. 7145

[2] T. Liang, L. Nunes, T. Sakamoto, K. Sasagawa, T. Kawanishi, M. Tsuchiya, G. Priem, D. Van Thourhout, P. Dumon, R. Baets, and H. Tsang : Optics Express, Vol. 13 (2005), p. 7298

[3] S. Dupont, A. Beaurain, P. Miska, M. Zegaoui, J.-P. Vilcot, H.W. Li, M. Constant, D.Decoster and J. Chazelas : Electronics Letters, Vol 40 (2004), p. 865

[4] P. Miska, M. Beaugeois, C. Lethien, A. Beaurain, H.-W. Li, J.-P. Vilcot, D. Decoster, J. Chazelas, M. Bouazaoui, L. Dobrzynski, A. Akjouj, B. Djafari-Rouhani and J.-O. Vasseur : Microwave and Optical Technology Letters , Vol. 45 (2005), p.315

[5] M. Beaugeois, M. Lesecq, B. Pinchemel, S. Maricot, M. Bouazaoui, J.P. Vilcot : Optics Letters, Vol.32 (2007), p. 35

[6] K.K.Lee, D.R.Lim, HSIN-CHIAO L., A.Agarwal, J.Foresi and L.C.Kimerling : Applied Physics Letters, Vol. 7 (2000), p1617

[7] D. Lauvernier, M. Carette, J.-P. Vilcot, D. Bernard and D. Decoster, ECS Transaction, Vol.3 (2006), p 305

[8] D. Vignaud, J. F. Lampin, E. Lefebvre, M. Zaknoune and F. Mollot : Applied Physics Letters, Vol. 80 (2002), p. 4151

Advanced Materials Research Vol. 31 (2008) pp 236-241
online at http://www.scientific.net
© 2008 Trans Tech Publications, Switzerland

Quantum information processing in photonic crystals

Mahi R. Singh

Department of Physics and Astronomy, University of Western Ontario, London, Canada N6A 3K7

Abstract: We have studied the quantum information processing phenomenon in photonic crystals doped with four-level nanoparticles. This phenomenon occurs due to the switching mechanism in the system. We consider that one of the transition energies of nanoparticles is coupled near resonantly with a photonic band gap edge. The dipole-dipole interaction between the nanoparticles has also been included. It is found that the system switches between the transparent and nontransparent states due to the dipole-dipole interaction and the band edge coupling. This is an interesting finding and can be used to produce logical photon switches in the quantum information processing.

Introduction

There is a considerable interest in studying quantum quantum switching and information processing in gases by using control laser fields [1]. The mechanism for the quantum switching was achieved in gases by nonlinear coupling between atoms and control laser fields. One of the properties studied in atomic gases is electromagnetically induced transparency (EIT) which produces a switching mechanism. The EIT effect has also been studied by the author [2] and others in photonic crystals doped with impurities in the presence of laser beams [2, 3]. Many interesting phenomena have been predicted in these materials due to the presence of the energy gap [2-7]. For example, Petrosyan and Kurzki [2] have found the photon-photon correaltion and entnaglement in photonic crystals doped with four-level atoms. The present author has found an anomalous EIT in photonic band gap materials which are doped with an ensemble of four-level nanoparticles [3]. We have also studied the enhancement of the refractive index, the coherent photon trapping and Stark effects in these materials [4]. In the above works the dipole-dipole interaction (DDI) between particles has been neglected.

The aim of the present work is calculate the absorption coefficient for photonic crystals doped with four-level nanoparticles whose one of the transitions is coupled near resonantly with a photonic band gap edge. This coupling will be called the band edge coupling (BEC) in the rest of the paper. It is also considered that the nanoparticles are interacting with each other by the dipole-dipole interaction. The time dependent Schrödinger equation method of reference [2] has been used to calculate the absorption coefficient. Recently the DDI has been studied in these materials by the author to study the quantum coherence and interference phenomena [6]. Numerical simulations have been performed for an isotropic photonic crystal. We have found that the system switches between the transparent and nontransparent states due to the DDI and BEC. This is an interesting finding and can be used to produce logical photon switches for quantum information processing.

Absorption Coefficient

In PBG materials the dielectric constant varies periodically in space. These materials can be constructed in one, two and three dimensions. Recently John's group [7] has calculated the energy spectrum of an isotropic three dimensional PBG material. This material is made of dielectric spheres. The spacing between the spheres is taken as b and radius is taken as a. They have obatined following dispersion relation

$$\cos(kL) = \left[(1+n)^2/4n\right]\cos\left((2na+b)\omega_k/c\right) - \left[(1-n)^2/4n\right]\cos\left((2na-b)\omega_k/c\right) \qquad (1)$$

Here ω_k is the frequency of photon inside the PBG crystal and k is the wave vector of the photon. The speed of light is c and n is the refractive index of the dielectric spheres. This equation gives energy gap at $k = k_0 = \pi / L$ where L is the lattice constant. In the effective mass approximation (EMA) the energy ε_k given in Eq. (1) can be expanded near $k = k_0$ using the Taylor series as

$$\omega_k = (\omega_k)_{k=k_0} + \left(\frac{\partial \omega_k}{\partial k}\right)_{k=k_0} (k-k_0) + \frac{1}{2}\left(\frac{\partial^2 \omega_k}{\partial^2 k}\right)_{k=k_0} (k-k_0)^2$$

$$\left(\frac{\partial \omega_k}{\partial k}\right)_{k=k_0} = 0 \qquad \left(\frac{\partial^2 \omega_k}{\partial^2 k}\right)_{k=k_0} = -\frac{cL^2}{a(1+n)^2 \sin\left(\frac{4na\omega_c}{c}\right)}$$

Here $\omega_c = (\omega_k)_{k=k_0}$ is the lowest frequency of the upper band. The dispersion relation in the EMA is written as

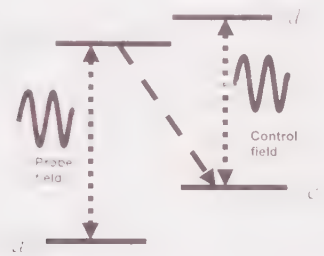

Fig. 1. Figure shows a schematic diagram of a four-level nanoparticle.

$$\omega_k = \omega_c + C(k-k_0)^2, \quad C = -2ac/\sin(4na\omega_k / c) \tag{2}$$

We have taken and b=2na. Using the above equation the density of states (DOS) $\rho(\omega_k)$ has been calculated as

$$\rho(\omega_k) = \frac{Vk_0^2}{(2\pi)^3}\frac{dk}{d\omega_k} = \frac{Vk_0^2}{2(2\pi)^3\sqrt{C}}\frac{\Theta(\omega_k - \omega_c)}{\sqrt{\omega_k - \omega_c}} \tag{3}$$

Here $\Theta(\omega_k - \omega_c)$ is the step function. It was introduced to take care of the band gap which lies below $\omega_k < \omega_c$. Note that the DOS has a singularity at $\omega_k = \omega_c$.

We have used only the four levels of the nanoparticles in calculating the susceptibility. The energy levels of the nanoparticles are denoted by $|a\rangle, |b\rangle$, $|c\rangle$ and $|d\rangle$. A monochromatic probe laser of frequency ω_μ and Rabi frequency Ω_μ is applied to the system. This field couples level $|a\rangle$ and $|b\rangle$. A control filed of Rabi frequency Ω_ν and frequency ω_ν couples levels $|c\rangle$ and $|d\rangle$. The level $|a\rangle$ decays to the level $|d\rangle$ due to the BEC. This atomic level configuration has also been considered in reference [2]. We have also considered that the nanoparticles are interacting with each other via DDI. The model Hamiltonian for the system is written as $H = H_0 + H_{AP} + H_{AR} + H_{dd}$

$$H_0 = \hbar\omega_{ab}(\sigma_{ab}^z + 1/2) + \hbar\omega_{bc}(\sigma_{ac}^z + 1/2) + \hbar\omega_{cd}(\sigma_{cd}^z + 1/2) + \sum_k \hbar\omega_k \left(p_k^+ p_k\right) \tag{4}$$

$$H_{AF} = -\hbar\Omega_\mu [\sigma_{ab} e^{-i(\omega_\mu - \omega_{ab})t} + \sigma_{ab}^- e^{i(\omega_\mu - \omega_{ab})t}] - \hbar\Omega_\nu [\sigma_{bc}^+ e^{-i(\omega_\nu - \omega_{cd})t} + \sigma_{bc}^- e^{i(\omega_\nu - \omega_{cd})t}]$$

$$H_{AR} = -\sum_k \hbar g_k [p_k \sigma_{bc}^+ e^{-i(\omega_k - \omega_{bc})t} + p_k^+ (\varepsilon_k)\sigma_{bc}^- e^{i(\omega_k - \omega_{bc})t}],\ g_k = \left(\omega_{bc}\mu_{bc}/\hbar\right)\sqrt{\left(\hbar/2\varepsilon_0\omega_k V\right)}\vec{e}_k.\vec{u}$$

$$H_{dd} = -\hbar\Lambda_{ab}\left(\rho_{ab}\sigma_{ab}^+ + \rho_{ba}\sigma_{ab}^-\right),\ \ \Lambda_{ab} = 2N\mu_{ab}^2/3\varepsilon_0\hbar$$

Here ω_{ab}, ω_{bc} and ω_{cd} are the transitions frequencies for the transitions $|a\rangle \leftrightarrow |b\rangle$, $|b\rangle \leftrightarrow |c\rangle$, $|c\rangle \leftrightarrow |d\rangle$, respectively. The operators $\sigma_{ij}^z, \sigma_{ij}^\pm$ are Pauli's operators [3]. The operators p_k and p_k^+ denote the annihilation and creation operators of photon, respectively. Here g_k is the BEC constant [7]. The quantities $\vec{e}_k$ and $\vec{u}$ are the unit vectors of dipole moment and the polarization, respectively and are taken in the same direction. V is the volume of the sample and ε_0 is the Coulomb constant. N is the density of nanoparticles. $\rho_{ab} = C_a C_b^*$ and $\rho_{ba} = C_a^* C_b$ where C_a and C_b are the probability amplitudes for levels $|a\rangle$ and $|b\rangle$, respectively. H_0 is the Hamiltonian of photons and nanoparticles. H_{AF} is the interaction Hamiltonian between nanoparticles and the laser fields [8]. H_{AF} is the BEC term and H_{dd} is the DDI term [6].

We now calculate the absorption coefficient for the transition $|a\rangle \rightarrow |b\rangle$ due to the probe laser field. The absorption coefficient is related to the imaginary part of the susceptibility (i.e. $\chi = \mu_{ab}\rho_{ab}/\varepsilon_0 E_\mu$ [1]). The density matrix ρ_{ab} appearing in the susceptibility from the Schrödinger equations method as

$$-i\hbar\frac{d|\Psi(t)\rangle}{dt} = \left(H_0 + H_{AF} + H_{AR} + H_{dd}\right)|\Psi(t)\rangle \tag{5}$$

We consider the follwing solutions

$$|\Psi(t)\rangle = C_a(t)|a,1_\mu,0_k,1_\nu\rangle + C_b(t)|b,0_\mu,0_k,1_\nu\rangle + \sum_k C_{c,k}|c,1_k,0_\mu,1_\nu\rangle + \sum C_{d,k}|d,1_k,0_\mu,0_\nu\rangle \tag{6}$$

The wave function has been taken from the reference [2]. We found the following Schrödinger equations

$$\frac{dC_a}{dt} = i\Omega_\mu^* C_b + i\left(\Lambda_{ab}\rho_{ba}\right)C_a$$

$$\frac{dC_b}{dt} = d_b C_b + i\Omega_\mu C_a + i\left(\Lambda_{ab}\rho_{ab}\right)C_a + i\int d\omega_k \rho(\omega_k) g_k C_{c,k}$$

$$\frac{dC_{c,k}}{dt} = d_c C_{c,k} + ig_k^* C_b + i\Omega_\nu^* C_{d,k}$$

$$\frac{dC_{d,k}}{dt} = d_d C_{d,k} + i\Omega_\nu C_{c,k}$$

$$d_b = i\delta_\mu - \gamma_b,\ d_c = i\left(\delta_a - \delta_k\right) - \gamma_c,\ d_c = i\left(\delta_\mu - \delta_k + \delta_\nu\right) -$$

$$\delta_\mu = \omega_\mu - \omega_{ba},\ \delta_k = \omega_k - \omega_{bc},\ \delta_\nu = \omega_\nu - \omega_{dc}.$$

Here γ_b, γ_c and γ_d are the decay rates for levels $|b\rangle$, $|c\rangle$ and $|d\rangle$, respectively. Following the method of reference [2] and after the rigorous mathematical manipulation we get the following the expression of the susceptibility χ as

$$\chi = \chi_0 \left| \frac{\gamma_b \sqrt{\kappa}}{\left(\quad \sqrt{\kappa} - \beta \right) - \quad \sqrt{\kappa}} \right| \tag{7}$$

$$\kappa = i\gamma_{cd} + \left(\delta_\mu - \delta_c - \xi_c \right) \quad \beta = \frac{\mu_R^2 \omega_R^2}{\hbar \varepsilon_0 \pi c^3} \quad \gamma_{cd} = \gamma_c + \frac{|\Omega_c|^2 \gamma_d}{\delta_c^2} \quad \xi_\nu = \frac{|\Omega_c|^2}{\delta_c} \quad \delta_c = \omega_\nu - \varepsilon_c / \hbar$$

Here χ_0 is the normalization constant. The variables ξ_ν, β and Λ_{ab} are called the control field, BEC and DDI parameters, respectively.

Numerical Simulations

In this section we have considered an isotropic photonic crystal. The parameters appearing in the absorption coefficient are taken from the reference [2]. All the frequencies in this section are measured with respect to γ_b. We have taken the band edge at δ_ν=1. The absorption coefficient ($\mathrm{Im}(\chi)$ has been plotted in Fig. 2 and Fig 3 without the DDI. In Fig. 2a the effect of the control field has been neglected (i.e. ξ_ν=0) and decay rate is taken as γ_c=0.001. Note that in Fig. 2a when β is zero there is one peak at δ_μ=0. As the value of β increases the peak splits into two peaks. This type of splitting is also called the Autler-Townes splitting [2]. The spectrum has a minimum which corresponds to zero absorption (i.e. transparent state). This splitting is because the transition $|a\rangle \rightarrow |b\rangle$ lies very close to the band edge where BEC effect is very strong due to the singularity in the density of states (see Eq. (3)).

In Fig. 2b the effect of the decay rate of level $|c\rangle$ γ_c is plotted in the presence of the strong BEC effect (i.e. β=1). When the decay rate is very small (i.e. γ_c=0.001), the spectrum has two peaks. However, it is interesting to note that as the decay rate increases the two split peaks merge into one. This shows that the Autler-Townes splitting depends on the decay rate of the level $|c\rangle$.

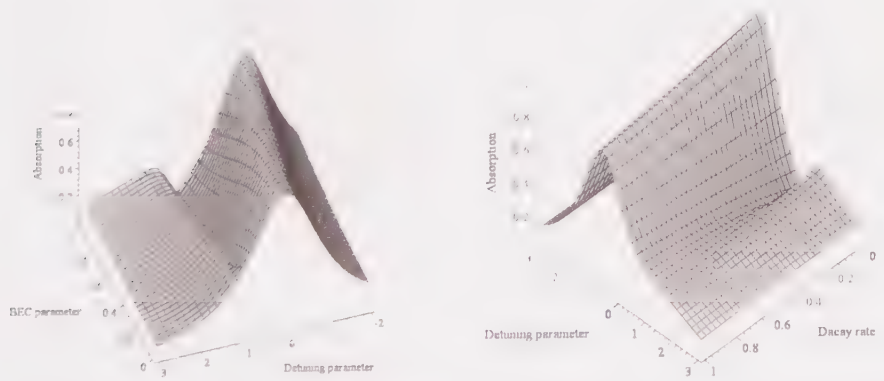

Fig. 2. (a) The absorption (in arbitrary unit) is plotted a function of β_e and δ_μ (left figure). Here γ_c=0.001. (b) The absorption (in arbitrary unit) is plotted a function of γ_c and δ_μ (right figure). Here β=1.

In figure 3 the absorption is plotted as a function of control field parameter ξ_ν. Note that as the strength control field increases the minimum moves to left. This means that the location of the transparent state changes as the intensity of the control field changes. In other words, the system can be switched between the transparent and nontransparent states by tuning the control field. This effect can be used to make switching devices from PBG crystals.

The effect of the DDI is plotted in Fig 4 (i.e. Λ_{ab}=3). It is interesting to note that the right peak moves toward the band edge where the left peak moves away from the band edge (see fig. 4a). The band edge lies at δ_μ=1. However, the position of the minimum is not affected by the DDI. The left peak lies within the band gap and is called the photon-atom bound state [2]. Therefore, the location of the photon-atom state can be controlled by the DDI. This is a very interesting result.

In figure 4b the absorption spectrum is plotted as a function of DDI parameter. As the intensity of the DDI parameter increases the absorption becomes zero (transparent state). Therefore, the system can also be switched between the transparent and nontransparent states due to the DDI.

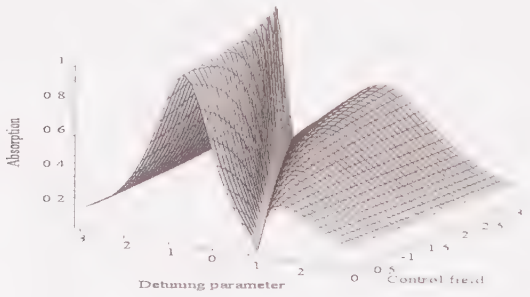

Fig. 3. The absorption (in arbitrary unit) is plotted functions of β and δ_μ (left figure).

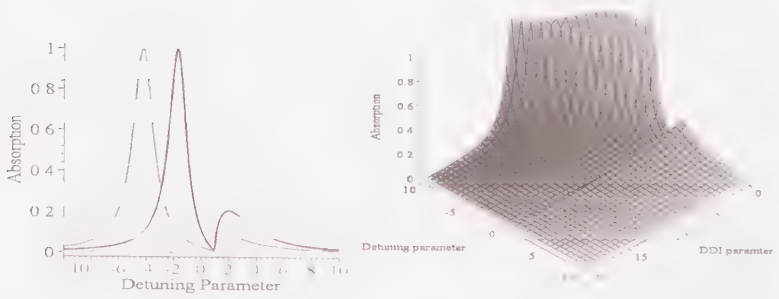

Fig. 4. (a) The absorption (in arbitrary unit) is plotted as functions of δ_μ (left figure). Here Λ_{ab}=3, γ_{cd}=0.001, β=2. (b) The absorption (in arbitrary unit) is plotted functions of Λ_{at} and δ_μ (right figure). Here γ_{cd}=0.001 and β=2.

References

[1] M. O. Scully and M.S. Zubairy, Quantum Optics (Cambridge University Press, Cambridge, 1997).

[2] D. Petrosyan and G. Kurizki, Phys. Rev. A 64, 23810 (2001).

[3] Mahi R. Singh, Phys. Rev. A70, 33813 (2004).

[4] S. John, Phys. Rev. Lett., 58, 2486 (1987); E. Yablonovitch, Phys. Rev. Lett. 58 2059 (1987).;

[5] V. I. Rupasov and Mahi R Singh, Phys. Rev. Lett. 77, 338 (1996); Mahi R. Singh, Phys. Rev. 69, 23807 (2004) Mahi R. Singh and I. Haque, J. Phys C19, 156229 (2007).

[6] Mahi R. Singh, Phys. Lett. A 363, 177 (2007); J. Phys. B 39, 5153 (2006); J. Phys. B 40, 675 (2007); J. Modern Optics 52, 1857 (2007); Phys. Rev. A 75, 43809 (2007).

[7] M. Florescu and S. John, Phys. A69, 053810 (2004), S. Jogn and J. Wang, Phys. Rev. B 43, 12772 (1991).

Advanced Materials Research Vol. 31 (2008) pp 242-245
online at http://www.scientific.net
© 2008 Trans Tech Publications, Switzerland

Phase Transition in Photonic Crystals Doped with Nanoparticles

Mahi R. Singh

Department of Physics and Astronomy, University of Western Ontario, London, Canada N6A 3K7

Abstract: We have study the phenomenon on of phase transition in photonic band gap (PBG) materials doped with four-level nanoparticles in the presence of the dipole-dipole interaction. Numerical simulations for the real susceptibility have been performed for an isotropic PBG material. It is found that the real susceptibility has a singularity for a certain value of the nanostructure concentration. This is a signature of the phase transition in the system.

Introduction

Recently, the interesting effects have been predicted in photonic band gap (PBG) materials due to quantum coherence and interference [1]. For example, we have studied electromagnetically induced transparency in PBG materials doped with an ensemble of four-level nano-particles. It is found that the electromagnetically induced transparency effect disappears when one of the resonance frequencies lies close to the band edge. We have also investigated the ac Stark effect and presence of solitons in these materials. In these papers [1], the authors have considered that the density of doped nanoparticles is small so that the dipole-dipole interaction (DDI) between particles can be neglected.

The aim of this paper is study the phase transition due to the effect of the dipole-dipole interaction PBG materials doped with four-level nanoparticles. The dipole-dipole interaction has been studied in these materials by the author to study the electromagnetically induced transparency, two-photon absorption, dark states etc [2]. The PBG materials have an energy gasp [3, 4] which plays an important role in finding new physical phenomena in these materials [1-4].

A schematic diagram of the four-level atom is shown in Fig. 1. A probe laser field is applied to the system and it induces a dipole moment in each particle. The nanoparticles are interacting with each other via induced dipole-dipole interaction. An expression of the real susceptibility has been obtained when the probe laser field is in resonant with one of transition energies of the atoms. To derive the real susceptibility the master equation method of reference [5] has been used. Numerical simulations have been performed for an isotropic PBG material. It is found that the real susceptibility has a singularity for a critical value of the dipole-dipole interaction parameter. This is a signature of the phase transition in the system.

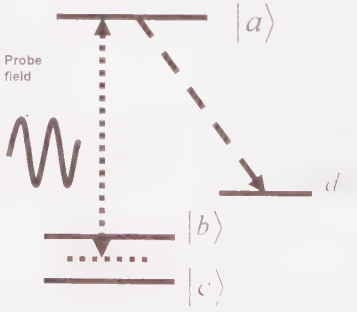

Fig. 1. Figure shows a schematic diagram of a four-level nanoparticle. The four levels are denoted by $|a\rangle$, $|b\rangle$, $|c\rangle$ and $|d\rangle$. A probe laser couples levels $|a\rangle$ to levels $|b\rangle$ and $|c\rangle$. Level $|a\rangle$ decays to level $|e\rangle$ due to the interaction between the nanoparticles and the PBG crystal.

Phase Transition

We consider an isotropic photonic crystal which is made from dielectric spheres. This crystal has an energy gap between energies ε_v and ε_c where ε_c and ε_v are the minimum and maximum energies of the upper and lower bands, respectively. The lower band is called the valence band whereas the upper band is called the conduction band. This nomenclature has been taken from the semiconductor physics.

We have used only the four levels of the nanoparticles in calculating the susceptibility. The energy levels are denoted by $|a\rangle$, $|b\rangle$, $|c\rangle$ and $|d\rangle$. The nanoparticles are prepared as a linear combination of levels $|b\rangle$ and $|c\rangle$ where both states have the same amplitudes.

A monochromatic probe laser of frequency ω_p is applied to the system (see Fig. 1). It couples level $|a\rangle$ to levels $|b\rangle$ and $|c\rangle$. We consider in this paper that level $|a\rangle$ decays to the level $|d\rangle$ due to the interaction between the nanoparticles and the photonic crystals. The line width due to the interaction between the nanoparticles and photonic crystals has been calculated in references [5].

We have also considered that the nanoparticles are interacting with each other via the dipole-dipole interaction. The expression of the real sociability has been derived when the probe field is resonant with the transition $|a\rangle \leftrightarrow |c\rangle$. This gives $\varepsilon_p = \varepsilon_{ac}$. Following the method of reference [5] we get the following expression of the real susceptibility χ as follows

$$\chi = \left(\frac{2\mu^2 N_0}{\hbar \varepsilon_0 \gamma} \right) \left[\frac{X}{1 - C_\lambda X} \right] \tag{1}$$

where the variable X is obtained as

$$X = \frac{\gamma^2 \left(\gamma Z_{ae}^2 + \gamma_c\right) \left\{ \delta_{ab} A - B \left[\delta_{ab} - \left(\gamma Z_{ae}^2 + \gamma_b\right) \right] \right\} - \gamma^2 B}{2\sqrt{2} \left(\gamma Z_{ae}^2 + \gamma_c\right) \left[\delta_{ab}^2 + \left(\gamma Z_{ae}^2 + \gamma_b\right)^2 \right]}$$

$$A = \frac{\rho_{aa}^0}{\gamma_a Z_{ae}^2} - \frac{\rho_{bb}^0}{\gamma_b};$$

$$B = \frac{\left|\rho_{bc}^0\right|}{\sqrt{\left(\omega_{bc}^2 + \left(\gamma_c + \gamma_b\right)^2\right)}};$$

$$C_\lambda = \left(\frac{2\mu^2 N_0 \lambda}{3\varepsilon_0 \hbar \gamma} \right)$$

$$\gamma = \left| \frac{(2n\pi)(1+n)}{4n} \right| \left| \frac{\sqrt{\left[16n^2 (1+n)^2 - (\cos[(4na)\omega_{ac}] - (1-n)^2 (1+n)^2\right]}}{\left[(1+n)^2 (4na)/4nc\right] \sin\left[(4na)\omega_{ac}/c\right]} \right|^{-1/2}$$

Where γ_b and γ_c are the decay linewidths of levels $|b\rangle$ and $|c\rangle$, respectively. ω_{bc} is the transition frequency for levels $|b\rangle$ and $|c\rangle$. N_0 is the density of nanoparticles and μ is the atomic dipole. Here δ_{ab} is called detuning parameter and is defined as $\delta_{ab} = \omega_p - \omega_a$. γ is atomic decay frequency of an atom in the free space. C_λ is called the DDI parameter. Z_{ae}^2 is the square of the formfactor

which is responsible of the decay linewidth of level $|a\rangle$. The formfactor has the information about the coupling of nanoparticles with the PBG crystal.

The above expression has been derived when the imaginary susceptibility is zero. In fact in reference [4] it has been shown that the absorption coefficient is zero for this type of atomic configuration. This is known as electromagnetically induced transparency. This phenomenon occurs due to coherence and interference of two photon emission from the excited state to two lower states.

Numerical Simulations

For the present calculations, we have considered that the isotropic crystal is made up of spheres with refractive index n, radius a and the lattice constant L. The crystal parameters are taken as $n = 1.2$ and $(a/L) = 0.21$. These parameters give $\varepsilon_v = 1.72$ eV and $\varepsilon_c = 1.88$ eV. All the energies in the numerical simulations of the susceptibility are measured with respect to the decay rate energy γ of an atom in the free space. The parameters appearing in the susceptibility expressions are taken as $\rho_{aa} = 0.01$, $\rho_{bb} = \rho_{cc} = 0.495$, $|\rho_{cb}| = 0.495$, $\varepsilon_{bc} = \gamma_b$ and $\gamma_a = \gamma_b = \gamma_c = 2\gamma$.

The absolute value of the real susceptibility is plotted as a function of the DDI parameter in Fig. 2. We have considered that the decay resonance energy lies away from the band edge i.e. $\varepsilon_{ae} = 0.3\varepsilon_v$. Note that the real susceptibility has a singularity at a certain value of the DDI parameter. It can see from eqn. (1) that the denominator can become zero for a certain value of C_3.

It is known in the solid state physics that when the system has a phase transition, the susceptibility has a singularity [6]. It means that the singularity in the susceptibility corresponds to a phase transition in the system. It implies that a phase transition in the present system can be observed just by varying the density of the nano-particles and keeping the resonance energy constant.

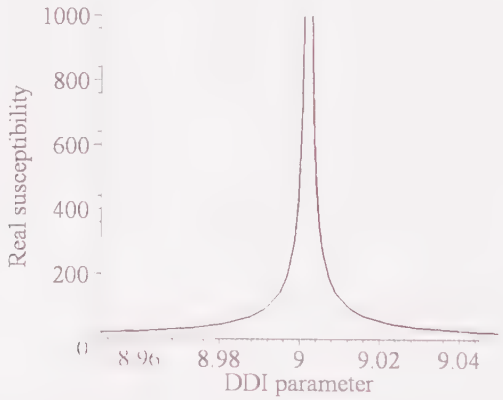

Fig. 2. The figure shows the plot of the absolute value of real susceptibility (in arbitrary unit) versus the DDI parameter.

References

[1] V. I. Rupasov and Mahi R Singh, Phys. Rev. Lett. 77, 338 (1996); Phys. Lett. A 222, 258 (1996); Mahi R. Singh, Phys. Rev. A 70; 033813 (2004); Mahi R. Singh and I. Haque, J. Phys C19, 156229 (2007).

[2] Mahi R. Singh, Physics Lett. A 363, 177 (2007); J. Phys. B 39, 5153 (2006); J. Phys. B 40, 675 (2007); J. Modern Optics 52, 1857 (2007).

[3] S. John, Phys. Rev. Lett., 58, 2486 (1987); E. Yablonovitch, Phys. Rev. Lett. 58 2059 (1987).;

[4] J. D. Joannopoulos, R. D. Meade, and J. N. Winn, *Photonic Crystals* (Princeton University Press, New Jersey, 1995) ;J.-M. Lourtioz, H. Benisty, V. Berger, J.-M. Gerard, D. Maystre, A. Tchelnokov, and P.-N. Favennec, *Photonic Crystals: Towards Nanoscale Photonic Devices* (Springer, Berlin, 2005).

[5] Mahi R. Singh, Phys. Rev. A 75, (8pp) (2007); Phys. Rev. A 70, 33813 (2004).

[6] C. Kittel, Introduction to Solid State Physics, (John Wiley & Sons Inc., New York, 1986).

Advanced Materials Research Vol. 31 (2008) pp 246-248
online at http://www.scientific.net
© 2008 Trans Tech Publications, Switzerland

InGaAsP/InP Electroabsorption Modulator with Single-Sided Large Optical Cavity by Low-Pressure MOCVD

H.Yang[1 a], M.K.Chin[1 b],Desmond C.S. Lim[2 c],S.Y.Lee[1 d],C.W. Lee[1 e] ,H.L.Zhu[3 f]

[1] School of EEE, Nanyang technological University (NTU), Singapore 639798
[2].DSO National Laborataries, 20, Science Park Road, Singapre 118230.
[3] National Key Lab of Optoelectronics, Institute of Semiconductors, CAS, Beijing, China 100083

[a]yanghua@ntu.edu.sg; [b]EMKChin@ntu.edu.sg; [c]drlcs@dso.org.sg;
[d]sylee@pmail.ntu.edu.sg; [e]Cheewei_lee@pmail.ntu.edu.sg; [f] zhuhl@red.semi.ac.cn

Keywords: Electroabsorption Modulator, Large Optical Cavity, MOCVD, Optical Profile, Coupling Efficiency, Saturation Power

Abstract. An InGaAsP/InP Electroabsorption Modulator (EAM) with single-sided large optical cavity (LOC) was studied and fabricated by low-pressure Metal Organic Chemical Vapor Deposition (MOCVD). Results show that the optical profile of EAM is greatly improved by the LOC structure, which is expected to increase the coupling efficiency and the optical saturation power.

Introduction

EAMs are widely used in optical communication system thanks to their small size, low driving voltage, high bandwidth and easy integration with other semiconductor optical components [1, 2]. However, there are still some drawbacks limiting its use- large coupling loss and low saturation power. Most EAMs' symmetric p-i-n three layers waveguide structure produces elliptical optical profiles because of the difference in optical confinement between vertical and horizontal directions: the horizontal spot size is much larger than the vertical one, thus it mismatches with the circular mode of fiber and results in low coupling efficiency and high coupling cost. On the other hand, the multi-quantum well EAMs have relatively lower optical handling abilities because of their electric field screening effect caused by pile-up of the photo-generated carries, especially the holes in the wells. Both low coupling efficiency and saturation power will limit the RF gain of EAMs, a vital component in EAMs' application in analog optical links. Integrating spot size converters on both ends of EAMs to obtain the fiber-matched optical spot has been demonstrated by many reports [3, 4], and seems effective in increasing the coupling efficiency. However, complex device structure and fabrication processes lead to yield reduction and high cost. In this paper, we demonstrate a simple structure that can improve the optical profile of EAM and increase its coupling efficiency. This structure adopts very thick InGaAsP lower confined waveguide layer to form a large optical cavity (LOC) , which is also potentially helpful in improving the saturation power.

Design and Fabrication

Figure1 shows the schematic structure of our EAM's cross section. The active region is strained InGaAsP/InGaAsP multi-quantum well structure with a total thickness of 252 nm and bandgap wavelength of 1500 nm, the 1.1Q and 1.2Q stands for quaternary InGaAsP material with the photoluminescence (PL) wavelength of 1.1 μm and 1.2 μm respectively, and the ridge of the waveguide is 3 μm wide and 200 μm long.

Beam Propagation Method (BPM) was used to study the optical profile of EAM with different lower waveguide thickness. Figure 2 is the simulated near-field spots of EAMs in which, (a) is the result of traditional symmetric waveguide EAM with both upper and lower waveguide thickness of 100 nm, whereas in (b),(c) and (d), the upper waveguides are 50 nm thick, and the lower waveguide layers are 0.6 μm,1.0 μm and 1.5 μm, respectively. Fig. 2(a) shows that the optical profile of

symmetric waveguide structural EAM is elliptical- the diameter in the horizontal direction is much larger than that of the vertical one. As the thickness of the lower waveguide increases, the optical profile spreads downward, so that the vertical spot diameter gets larger and the spot becomes more rounded. When the thickness is 1.5 μm, a better fiber-matched mode is obtained. On the other hand, if the lower waveguide layer is too thick, then its epitaxial growth may cause large strains and defects in the material, which will subsequently degrade the quality of material.

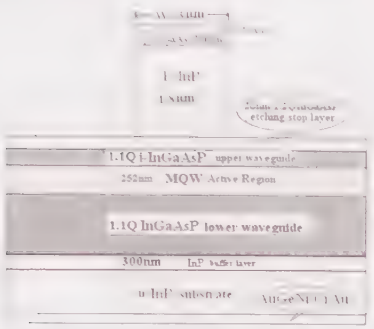

Fig.1 Cross Section of EAM structure

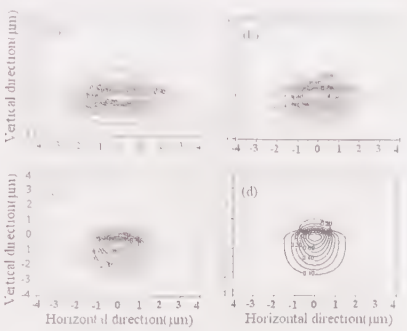

Fig.2 Contour map of Optical profile of EAMs with different lower waveguide thicknesses

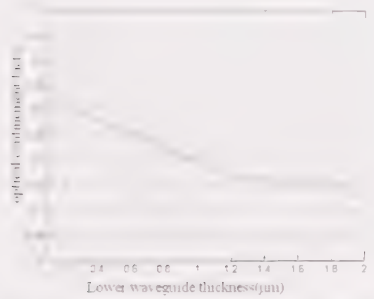

Fig.3 Optical confinement factor of EAM with different lower waveguide thicknesses

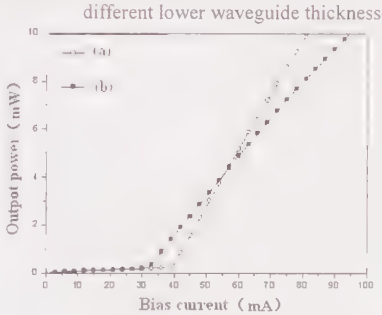

Fig.4 P-I curve of EAMs with thin (a) and 1.5 μm thick lower waveguide layer (b)

Fig.3 shows the calculated confinement factor of EAMs with different lower waveguide thickness. As expected, the confinement factor decreases with increasing the thickness of lower waveguide layer. A small optical confinement is desirable for high saturation power operation of EAM.

In fabrication, the greatest challenge lies in the growth of high-quality thick lower waveguide InGaAsP material. Low- pressure MOCVD system AIXTRON-200 with a horizontal reactor was used to grow the material shown in Fig.1 on S-doped InP (100) oriented substrate. The reactive precursors used are trimethylindium (TMIn), triethyl- garium (TEGa), arsine (AsH3) and phosphine (PH3). The growth pressure and temperature are 22 mbar and 655 °C, respectively. Through strict control of the growth conditions and adjusting the parameters, high quality material was obtained. In addition, material without LOC was grown for comparison. PL spectrum and XRD measurements show that the quality of the material with 1.5 μm thick lower waveguide layer is nearly the same as the one without LOC.

Fabrication processes are very simple, similar to that of the traditional EAM with semiconductor etching and metal evaporation methods.

Results and Discussion

The fabricated shallow ridged EAM has the same structure as the Fabry-Perot laser diode, thus it can lase under a forward current bias, and the emission can be used to observe its optical profile. Fig.4 shows the Power vs. current curve (P-I) of the EAMs functioning as F-P laser diodes and

Fig.5 and Fig.6 are measured near-field spots and far-field angles under the forward bias condition. From the measurement results, both EAMs (with and without LOC) can lase and have a high output power. This is a further proof that the grown material has good quality. The measured near-field spot with LOC is more circular than that of the traditional EAM. In Fig.6, the far-field angles of the two types of EAMs do not differ much in the horizontal direction, but the vertical angles of the EAM with LOC is reduced to 35° compared to 52° for the EAM without LOC. In the experiment, the coupling of the EAM with LOC to fiber is easier and the coupling efficiency is higher compared to that of the traditional EAM. These are the benefits of better fiber mode matched optical profile of EAM with LOC.

Fig.5 Images of near-field profile for EAM (a) without and (b) with LOC consisting of 1.5 μm thick lower waveguide layer.

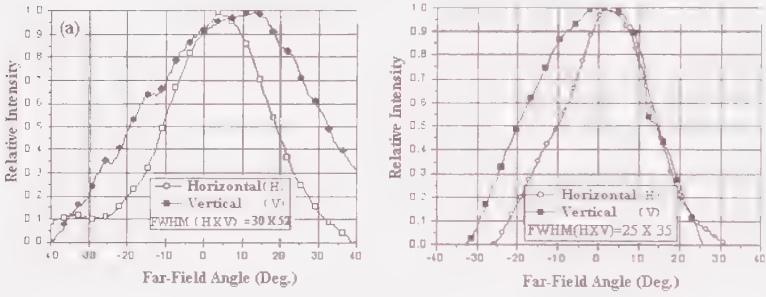

Fig.6 Far-field angles of EAMs without LOC (a) and with LOC (b)

Conclusion

In conclusion, InGaAsP/InP EAMs with single-sided LOC were successfully fabricated using Low-Pressure MOCVD. The simulated and experimental results have shown that with the introduction of LOC structure in the traditional symmetric p-i-n waveguide EAM, the optical profile is more symmetric and rounded, giving a smaller optical confinement factor and a higher coupling efficiency between the EAM and a conventional fiber.

References

[1] Z.X.Bian, J.Christofferson, A.Shakouri: Appl. Phys. Lett. Vol.83(2003), p.3605

[2] Q. Zhao, J.Q.Pan, J.Zhang, G.T.Zhou, J.Wu, F.Zhou, B.J.Wang, L.F.Wang, W.Wang: Acta Phys. Sin.Vol.55 (2006), p.1259

[3] M.Wada, M.Kohtoku, K.Kawano, S.Kondo, Y.Tohmori, Y.Kondo, K.Kishi, Y.Sakai, I.Kotaka, Y.Noguchi, Y.Itaya: Electron. Lett Vol.31(1995),p. 1252

[4] L.P. Hou, H.L.Zhu, F.Zhou, J.Bian, W.Wang: Semicond.Sci.Technol. (2006) Vol.20, p. 912

Advanced Materials Research Vol. 31 (2008) pp 249-253
online at http://www.scientific.net
© 2008 Trans Tech Publications, Switzerland

Demonstration of the formation of porous silicon films with superior properties formed on polished (100) Si with screen-printed back contacts

Priyanka Singh[1], Shailesh N Sharma[1*], G. Bhagavannarayana[2], M. Husain[3] and M. Lal[1]

[1]Electronic Materials Division, National Physical Laboratory, Dr. K.S. Krishnan Marg, New Delhi-110 012, India.

[2] Materials Characterization Division National Physical Laboratory Dr K.S. Krishnan Marg, New Delhi-110 012, India.

[3] Department of Physics, Jamia Millia Islamia, New Delhi, India.

[*]email: shailesh@mail.nplindia.ernet.in

Keywords: porous silicon, back contacts, screen-printing & thermal evaporation.

Abstract. Porous silicon (PS) layers were formed by anodization on polished substrates of (1 0 0) Si at different current densities for a fixed anodization time of 30 mins. using different screen-printed/evaporated back contacts (Ag, Al) respectively. The PS films has been characterized by high resolution X-ray diffraction (HRXRD), photoluminescence (PL), Scanning Electron Microscopy (SEM) and Fourier Transform Infrared (FTIR) techniques respectively. Porosity and thickness of PS layers were estimated by gravimetric analysis. The properties of PS formed using screen-printed Ag & Al as the back contacts **(SP-(Ag/Al))** was found to be superior as compared to the corresponding films with evaporated back contacts **(EV-(Ag/Al)).** The PS formed with screen-printed Ag & Al-back contacts shows better crystalline perfection, higher stability, higher PL efficiency and negligible PL decay compared to that formed with evaporated Ag & Al- as the back contact for the same current density and time of anodization.

Introduction

Screen-printed (SP) metallization is the most widely used contact formation technique for commercial Si-solar cells [1]. Although photolithography, metal evaporation or sputtering are the most well-established metallization techniques for solar cell fabrication [2]. However, these technologies are time consuming and expensive. Screen-printed contact technology is a more rapid metallization process and cost-effective as compared to sputtering and evaporation methods [1]. The utility of PS as an anti-refection coating in solar cells is well-known but it is imperative to prepare PS with less defect density in order to improve the solar cell efficiency [2]. In this work, by means of high resolution XRD, PL and FTIR studies, the superiority of PS films formed with Ag /Al as the screen-printed back contacts **(SP-(Ag/Al))** have been demonstrated as compared to the corresponding ones with evaporated back contacts **(EV-(Ag/Al))** for its possible application in photovoltaics.

Experimental

Boron doped p type Si polished wafers of (100) orientation, 1 Ω- cm resistivity and 285 μm thickness with either **(SP-(Ag/Al))** or **(EV-(Ag/Al))** back contacts were used for preparing PS. PS was formed by the standard anodization process in a mixture of HF and C_2H_5OH (1:1 by volume) using Si as the anode and Pt as the counter electrode in an acid resistant container. The anodization was carried out at (I_d) ~20 to 60 mA cm^{-2} for a fixed anodization time of 30 mins. The details of the contact formation & characterization techniques can be found elsewhere [3].

Results and Discussion

The porosity and thickness of **SP-(Ag/Al)** & **EV-(Ag/Al)** PS films varied from 40-52% and 100-200 nm respectively. Typical PL curves for **SP-(Ag/Al)** & **EV-(Ag/Al)** PS films formed at $I_d \sim 20$ mA cm^{-2} are shown in Fig. 1. As evident from Fig.1, the absolute PL intensities ($\lambda_{PL\ Peak} \sim 680$-690 nm) of **SP-(Ag/Al)** PS films are quite high. However, for corresponding **EV-(Ag/Al)** films, a weak PL spectra ($\lambda_{PL\ Peak} \sim 740$ nm) was obtained (Fig. 1). This difference in PL spectra for the same $I_d \sim 20$ mA cm^{-2} could be apparently due to the fact that the silicon skeletons not being narrow enough for quantum confinement for **EV-(Ag/Al)** PS films. The stability of these PS films with different back contacts were evaluated by monitoring the decay of the PL peak intensity as a function of laser-exposure time. **For PS film formed with Ag as the screen-printed back contact (SP-Ag).** less PL decay was observed however, for **PS film formed with Ag as the evaporated back contact (EV-Ag)**, a significant PL decay was observed as shown in the inset of Fig. 1. This is a good indication of the stability of the surface bond configurations for PS films with screen-printed back contacts.

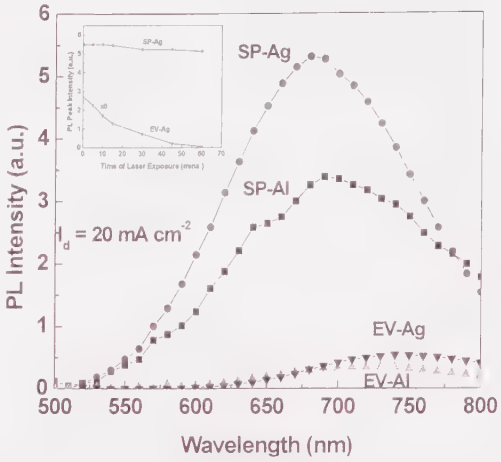

Fig. 1 Photoluminescence (PL) spectra of the **(SP-(Ag/Al)) and (EV-(Ag/Al))** *PS samples at $I_d = 20$ mA cm^{-2}.*

Fig. 2 shows the FTIR spectra of **SP-Ag** and **EV-Ag** PS films. The Ag-SP PS films exhibits mainly Si-H related features at ~ 2100 cm^{-1}(stretching mode), 907 cm^{-1}(bending mode) & 660 cm^{-1} (wagging mode) and Si-O mode at ~ 1045 cm^{-1} while **EV-Ag** films exhibits relatively less intense Si-H features but prominent Si-O mode ~ 1132 cm^{-1}. Here, shift of Si-O related mode from 1042 cm^{-1} to 1132 cm^{-1} indicates an increase in the oxidation state (x) of the SiO_x species [3]. Thus, the effect of oxidation is felt more on **EV-Ag** PS films as compared to corresponding **SP-Ag** films. Similar results were also observed for **SP-Al** and **EV-Al** PS films as well. The inset of Fig. 2 shows the SEM images depicting the surface morphology of **SP-Ag** (right-inset) & **EV-Ag** (left-inset) PS films for $I_d \sim 20$ mA cm^{-2}. **Here, a plain featureless surface morphology similar to that of polished Si substrate is observed for EV-Ag film indicating little or no PS formation while for SP-Ag films, a distinct formation of PS indicating microstructural variations as observed by changes in SEM contrast is revealed.**

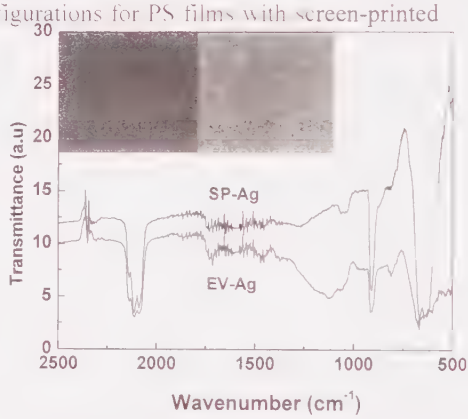

Fig. 2 FTIR spectra of ***EV-Ag*** *&* ***SP-Ag*** *PS films for $I_d \sim 20$ mA cm^{-2}. The left and right insets show their corresponding morphologies as depicted by SEM.*

Fig. 3 shows capacitance-voltage (C-V) curves measured between +2 and -2 V at room temperature in the dark at 1 KHz for **EV-Ag** and **SP-Ag** PS films. The C-V curves are similar to those of a typical MIS (metal-insulator-semiconductor) capacitor with a p-type substrate. From fig. 3, the C-V curve corresponding to **SP-Ag** PS forms a proper hysteresis loop while **EV-Ag**

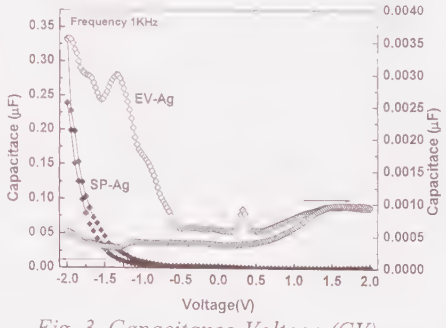

Fig. 3 Capacitance-Voltage (CV) characteristics for ***EV-Ag and SP-Ag*** *PS films prepared at $I_d = 20$ mA cm^{-2}.*

PS film shows oscillatory and noisy features and exhibits low values of capacitance ($\mu F\ cm^{-2}$) showing the presence of defects/interface states [4].

Fig. 4(a-c) shows the diffraction curves recorded in symmetrical Bragg geometry for (400) diffracting planes for polished Si substrate before anodization, **EV-Al** and **SP-Al** PS films ($I_d \sim 20$ mA cm^{-2}) respectively. Here, a sharp DC (Fig 4(a)) with full width at half maximum (FWHM) ~ 8 arc s shows good quality Si substrate as this value is quite close to that expected from the plane wave dynamical theory of X-ray diffraction for a perfect crystal [5]. For **EV-Al** PS film, the DC shows only a single peak having the FWHM value of 11 arc s (Fig. 4(b)). It is well known that due to pores on the surface of Si crystal, the tensile stress develops due to expansion of the crystalline lattice surrounded by pores and dangling bonds and lead to a slight increase in the lattice constant of the PS film [4]. Due to change in lattice constant of PS film, another peak is expected at a lower diffraction angle with respective to the substrate peak. However, the observed single peak shows that either the PS film has low thickness (~ few nm as also observed from gravimetric results) due to which diffracted X-ray intensity could not be measured or the quality of the film is inferior. Similar features were observed for **EV-Ag** PS films as well. However, for **SP-Al** PS film, the DC (Fig. 4(c)) shows a well resolved satellite peak at an angular distance of ~160 arc sec due to the porous film formed on the Si substrate. The inset in the Fig. 4(c) shows its amplified view. As confirmed from our earlier studies [3], the peak at lower angle with respect to the substrate peak position indicates that the perpendicular lattice constant of the PS film is more than that of the substrate. The strain ($\Delta a/a$) normal to the interface due to this lattice mismatch can be obtained from Bragg equation in its differential form given by,

$$\Delta a/a = -\cot\theta_B \Delta\theta \qquad (1)$$

where, $\Delta\theta$ is the angular separation between film and substrate peaks and θ_B being the Bragg diffraction angle. The film peak at negative side shows that the film has a tensile stress due to pores around Si crystalline strands. For **EV-Al** PS film, (Fig. 4(b)) the strain obtained from Eqn. (1) is $(28.7\pm1) \times 10^{-4}$. Thus from above, the DC's shows that PS films formed using screen-printed contacts were superior in quality as compared to thermal evaporated ones. Fig. 5(a-c) shows DC of **SP-Ag** PS films corresponding to $I_d \sim 10$, 20 & 30 mA cm^{-2} respectively. For low $I_d \sim 10$ mA cm^{-2}, the DC (Fig. 5(a)) shows a satellite peak due to PS film at an angular distance of 138 arc s. Though the height of the film peak is much smaller than that of the substrate peak, the peak position could be measured with an uncertainty of ± 2 arc s with an overall uncertainty of ± 5 arc s in the value of angular distance between film and substrate peaks. The value of strain ($\Delta a/a$) thus obtained from the Eqn. (1) is $(24.7\pm1) \times 10^{-4}$. Similarly, for PS at $I_d = 20$ mA cm^{-2}, the DC (Fig. 5(b)) shows a well resolved film peak with higher peak intensity as compared to fig. 5(a)) indicating increase in PS

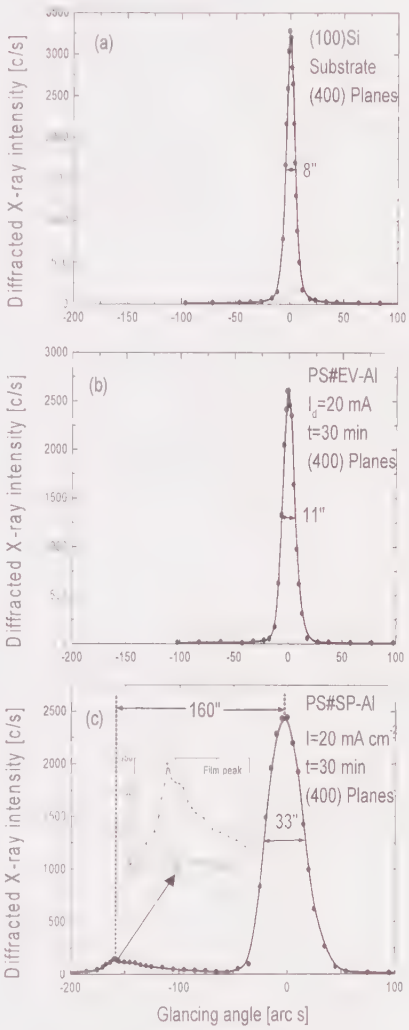

*Fig. 4: Diffraction curves recorded for (400) diffracting planes using MoKα_1 radiation: (a) Blank Si wafer and (b) & (c) **EV-Al and SP-Al** PS films respectively.*

thickness with increase in I_d from 10 mA cm^{-2} to 20 mA cm^{-2} respectively. This is expected as the pore-depth increases with increase in I_d. However, the peak seperation also increases from 138 to 160 arc s with corresponding increase in tensile stress from its initial value of 24.7 to 28.7 x 10^{-4}. This may be attributed to the possibly a small increment of pore size in addition to increase in the pore depth. The increase in PL intensity & its blue-shift with increase in I_d from 10 to 20 mA cm^{-2} is also a testimonial to this. From fig. 4(c) & 5(b), the peak separation is almost the same (~ 160 arc s) even though the back contacts are different (Ag instead of Al). In contrast to the DCs of curves (a) and (b) of Fig. 5, curve (c) does not show any noticeable film peak as I_d increases further to 30 mA cm^{-2}. The disappearance of film peak at I_d ~ 30 mA cm^{-2} (Fig. 4, (c)) indicates that at this I_d, the bonds between Si atoms of film and substrate no longer exists and the film peels off from the substrate as was also observed visually. Similar behavior is also observed for **SP-Al** PS films for I_d> 20 mA cm^{-2}.

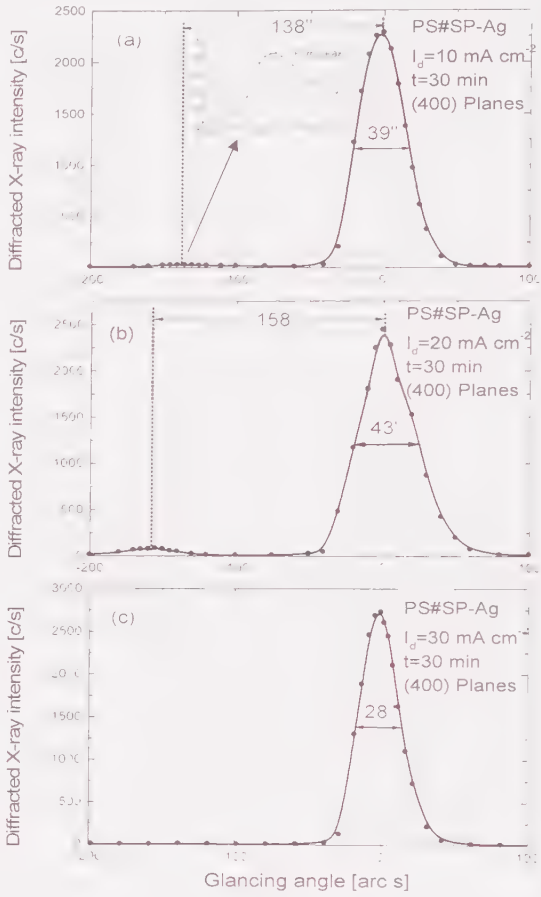

Fig. 5: Diffraction curves recorded for (400) diffracting planes using MoKα_1 radiation for ***SP-Ag*** *PS films at different I_d: (a) 10, (b) 20 and (c) 30 mA cm^{-2}.*

Conclusion

High-resolution XRD, PL, SEM, FTIR & capacitance-Voltage studies showed that the **(SP-(Ag/Al))** PS films formed on polished Si (100) substrates under the same conditions of anodization are superior as compared to **(EV-(Ag/Al))** PS films respectively. PS layers with different back-contacts and their interfaces have been characterized by recording diffraction curves and measuring lattice mismatch/strain and the radius of curvature due to induced biaxial stress caused by the lattice expansion of PS film due to pores. **SP-(Ag/Al)** PS films exhibits better crystalline perfection, higher stability, higher film thickness, H-passivated surfaces and low defect density as compared to **EV-(Ag/Al)** PS films. The results conclusively demonstrates the viability of screen -printing contact technology for the possible application of PS films in Si-solar cells.

Acknowledgements

We thank Director NPL for providing the facilities for the successful completion of this work. Thanks to Dr. Ritu Srivastava (NPL) for CV measurements. Priyanka acknowledges MNES for providing NRE fellowship.

References

[1] T. Sun, J. Miao, R. Lin, Y. Fu, Sol. Energy Mater. Sol. Cells 85 (2005) 73.

[2] G. Cankaya, N. Ucar and A. Turut, Int. J. Electronics, 87 (10) (2000) 1171.

[3] G. Bhagavannarayana, Shailesh N. Sharma, R.K. Sharma And S.T. Lakshmikumar, Materials Chemistry and Physics, 97 (2-3), (2006) 442.

[4] Priyanka, Shailesh N Sharma, S. Salam, M. Husain and M. Lal, Sol. Energy Mats.& Solar Cells, 91 (15-16) (2007) 1510.

[5] G. Bhagavannarayana and P. Zaumseil, J. Appl. Phys. 82, (1997) 1172.

Author Index

A

Abdullah, A.M. 101
Abdullah, S. 202
Abdul Rahman, S. 80
Ab. Gani, S.M. 80
Abu Hassan, H. 39
Adikaari, A.A.D.T. 185
Ahmad, I. 202
Ahn, S.Y. 176
Akano, Y. 206
An, T.T. 68
Anandan, S. 212
Anderson, J. 33
Ang, N.S.S. 30, 36, 189
Arellano, I.H.J. 92
Arora, J.S. 153
Awasthi, K. 153

B

Bais, G. 23
Barvestani, J. 7
Begum, N. 23
Bernard, D. 230
Bertoni, C. 150
Bhagavannarayana, G. 249
Bhatnagar, P.K. 161
Bhatti, A.S. 23
Biswas, D. 59, 62
Boonpeng, P. 132

C

Carette, M. 230
Casco, M.F. 86
Chaudhuri, B.P. 179
Chazelas, J. 230
Chen, W.Z. 126
Cheng, H.E. 129
Cheng, L. 11
Cheng, X. 170
Chiang, M.J. 129
Chiang, Y.M. 117
Chien, N.D. 68, 114
Chin, M.K. 17
Chin, M.K. 246
Cho, W.J. 135
Choi, H. 135
Chollet, F.A. 179
Chong, L.F. 30, 36, 189
Chow, S.Y. 71, 227
Chua, S.J. 30, 36, 56, 71, 77, 189, 192, 199, 227
Chuah, L.S. 39
Chung, H.B. 135
Chung, H.V. 114

D

Dang, Y.X. 95, 105
Das, K. 89
Das, S. 89
Das, T. 59, 62
Decoster, D. 230
Defensor, M. 86
Dhar, A. 89
Ding, Y.H. 33, 182
Dixit, V. 209
Djie, H.S. 33, 173, 182
Dong, B. 95
Dong, D.Q. 138, 167
Dong, J.R. 30, 36, 189
Dong, X.Y. 138, 167
Du, A.Y. 17
Du, R.R. 33
Dunn, S. 150
Duong, P.H. 74

E

Endut, Z. 202

F

Fan, W.J. 95, 105
Ferrari, M. 114
Franciosi, A. 23

G

Gallardo, D.E. 150
Ganjoo, A. 33
Gao, L. 117
Gao, Y. 14
Garcia, A. 86
Gardner, H.C. 150
Guo, Y.P. 20

H

Hartono, H. 227
Hassan, Z. 39

Helmy, A.S. 173
Hongpinyo, V. 33, 182
Hu, X. 11, 14
Huang, C.M. 20
Huang, D.X. 27
Huang, S.Z. 126
Husain, M. 249
Huy, P.T. 68, 74, 114
Hwang, J.C.M. 173

I
Ikuma, Y. 212
Isnin, A. 101

J
Jabeen, F. 23
Jain, H. 33
Jalar, A. 202
Jang, E.S. 108
Jewasuwan, W. 158
Jia, C.Y. 11
Jiang, W.J. 14
John, R. 164

K
Kabi, S. 62
Kaewket, D. 224
Kai, G.Y. 138
Kalafi, M. 7
Kang, D.H. 108, 111, 120
Kashkarov, P.K. 196
Katayama, R. 215, 218, 221, 224
Kim, D.J. 68, 114
Kim, D.W. 108, 111, 120
Kim, H.K. 135
Kim, J.S. 120
Kim, K.H. 176
Kim, M.D. 120
Koenraad, P.M. 196
Kongjaeng, P. 221
Koo, S.M. 135
Koo, Y.W. 135
Kudoh, T. 212
Kumar, J. 42
Kumar, J. 161
Kumar, S. 59, 62
Kuntharin, S. 215
Kwok, H.L. 4
Kwon, J.Y. 176

L
Lal, M. 249
Lau, S.P. 71
Lauvernier, D. 230
Le, H.Q. 192
Lee, C.R. 108, 111, 120
Lee, C.W. 246
Lee, H.S. 176
Lee, H.Y. 176
Lee, H.Y. 98
Lee, I.H. 111
Lee, S.H. 108
Lee, S.Y. 246
Lesecq, M. 230
Li, C.Y. 65
Li, D.S. 105
Li, L. 167
Li, S. 83
Li, Z.M. 141
Liang, M.L. 83
Lim, D.C.S. 246
Lim, E.L. 30, 36, 189
Lin, W. 126
Liu, H.F. 209
Liu, H.R. 27
Liu, Y.P. 20
Lu, J.M. 170

M
Ma, B.S. 105
Magdaluyo, E.R. 92
Malek, M.Z.A. 101
Martelli, F. 23
Mathur, P.C. 161
Misa, J.V. 86
Mizumoto, T. 206
Mohanta, S.K. 56
Mudugamuwa, N.K. 185
Murugesan, V. 212

N
Nagpal, S. 161
Nakajima, F. 218
Nakamura, T. 215
Nam, K.H. 135
Nathawat, R. 153

O
Ogita, Y. 212

Onabe, K. 215, 218, 221, 224
Ooi, B.S. 33, 173, 182

P
Palenov, D.A. 196
Pandey, P.K. 161
Pankaow, N. 123
Panyakeow, S. 123, 132, 158
Patel, B. 150
Payawan, L.M. 92
Piccin, M. 23
Prevenslik, T. 1

Q
Que, W.X. 11, 14

R
Ratanathammaphan, S. 123, 132, 158
Ray, S.K. 89
Ren, X.M. 14
Rubini, S. 23

S
Salvador, A. 86
Samargo, R.V. 92
Sanorpim, S. 215, 218, 221, 224
Santhakumar, K. 108, 111, 120
Sentosa, D. 17, 77
Shalygina, O.A. 196
Sharma, S.N. 249
Silva, S.R.P. 185
Singh, M. 153
Singh, M.R. 236, 242
Singh, P. 249
Singha, R.K. 89
Soh, C.B. 227
Soltani Vala, A. 7
Song, H. 111
Song, J.C. 108, 111, 120
Soni, R.K. 56
Sun, M. 11
Sun, X.W. 71
Sun, Z. 11
Suresh Kumar, V. 42

T
Tamura, K. 206
Tang, X.H. 17, 77
Tapia, A.K.G. 92
Tay, C.B. 199
Tay, Y.Y. 83
Teng, J.H. 17
Teng, J.H. 30, 36, 189
Thubthimthong, B. 179
Timoshenko, V.Y. 196
Tong, G.B. 80
Tong, W.J. 27
Tripathy, S. 56
Tungasmita, S. 224

V
Verma, A. 161
Vijay, Y.K. 153
Vilcot, J.P. 230
Voskoboynikov, O. 52

W
Wang, L.L. 11
Wang, Y.G. 65
Wang, Y.J. 189
Wang, Y.Y. 20
Wang, Z. 138, 167
Wijers, C.M.J. 52
Wong, C.C. 117
Wu, C.W. 129
Wu, M. 27

X
Xiang, N. 209
Xu, F.Q. 141

Y
Yan, Q.F. 117
Yan, Z.J. 20
Yang, H. 246
Yang, H.Y. 71
Yeo, J.B. 98
Yin, Z.Y. 17, 77
Yong, A.M. 71
Yoon, S.F. 105
Yoshimura, M. 206
Yu, S.F. 71
Yusof, S.M. 202

Z
Zacharias, M. 196
Zainuddin, M.T. 101
Zegaoui, M. 230
Zhang, D.H. 105
Zhang, J.X. 17

Zhang, W. 14
Zhang, W.H. 141
Zhang, X.H. 71
Zhang, X.S. 138, 167
Zhang, Y.F. 138
Zhigunov, D.M. 196
Zhu, H.L. 246

Keyword Index

A
Ablation Threshold 65
Absorption Spectra 59
All-Optical Switching 206
Amorphous 135
Annealing 62
Aqueous Medium 138, 167
Asymmetric Pulse 185
Atomic Force Microscopy (AFM) 80, 86
Au Coating 108
Azobenzene 11

B
Back Contacts 249
Band Structure 95
Bilayer 153
Blade 202
Blueshift 209
Borosilicate Glass Matrix 161
Broadband Emission 173
Bulk Modulus 164

C
c-InN 215
Carbon Counter Electrodes 176
Carbothermal 92
CdTe 150
Chalcogenide 135
Chemical Sintering 176
Chlorine 150
Colloids 117
Comb-Drive Microactuator 179
Complex Coupled DFB 189
Compressively Strained 95
Conductivity Measurements 4
Copper Oxide 129
Coupled Mode Theory 36
Coupling Efficiency 27, 246
Crystal Quality 17
Crystalllized Silicon 185

D
Degradation 212
DFB Laser 36
Dicing 202
Die Attach Film 202
Dielectric Grating 189
Direct Compound 164
Disordering 182
Distributed Feedback Lasers 189
Distributed Feedback Waveguide 206
Droplet 123
Droplet Epitaxy 158
DSSCs 176

E
Eight-Band k p Model 105
Electroabsorption Modulator 246
Electrochemical Impedance Spectroscopy (EIS) 170
Embedding 52
Energy Transfer 196
Epitaxial Lateral Overgrowth 189
Erbium Ions 196
Excimer Laser 185

F
Femtosecond Laser 65
Field Emission Scanning Electron Microscopy (FE-SEM) 80
Fractal 92
FTIR 80

G
GaAs 123, 132, 158
GaAs Wafer 65
GaAs AlGaAs 105
GaAsN 218
GaInNAs 209
Galium Nitride (GaN) 42, 108, 111, 120
GaNAs 77
Grating 189
Growth Mode 17

H
Hall Measurements 4
High Resolution X-Ray Diffraction 215
Holographic Lithography 98
Hopping 4
Hydrogenated Nanocrystalline Silicon (nc-Si:H) 80
Hydrothermal Growth 199

I
II-VI Compounds 192
II-VI Quantum Dots 161

III-(III)-V-N 224
III-V Nitrides 218
Impurity Diffusion 33
Impurity Free Vacancy Induced Disordering 33
In-Rich Growth Condition 215
In Situ Characterization 170
In Situ Observation 117
InAs Quantum Dot 132
Index Coupled DFB Laser 36
Infrared Excitated 138
InGaAs 123
InGaAs Insertion Layers 132
InGaAsN 221
InGaPN 224
InP 158
Intermixing 182

L

La-Doped TiO_2/ZnO 212
Large Optical Cavity 246
Lateral Growth 111
LBL 80
Left Handed Material 7
Lift-Off 30
Low-Energy Ion Beam 56

M

MBE 86, 120
Mean Free Distance 4
Metal Contact 30
Metal-Semiconductor-Metal (MSM) Photodiode 39
Metallisation 164
Microwave Photonics 230
MOCVD 77, 108, 246
MOCVD Threading Dislocation 111
Molecular Beam Epitaxy 123, 158
Molecular-Beam Epitaxy System 132
Monocrotophos 212
Morphology 17
MOVPE 17, 218, 221, 224
Multi Spin Coating Process 101
Multi-Wavelength 36

N

Nano-Objects 52
Nanocolumn 108, 120
Nanocrystalline 129
Nanometric Waveguides 230
Nanoparticle 150
Nanophotonics 30, 230
Nanoporous 101
Nanorods 199
Nanosized Materials 126
Nanostructures 92, 123, 153, 158, 192
Nanostructuring of Semiconductor Surface 56
Nanowires 23
Newton-Raphson Method 36
No_2 126
Non Volatile 135

O

Optical Gain 95
Optical Profile 246
Optical Switch 11
Optics 52
Organic-Inorganic Hybrid 11, 14

P

Passivation 30
Pattern 14
Patterned Sapphire Substrate 111
Periodic Structure 98
Phonon Modes 23
Photo-Doping 135
Photoluminescence 42, 56, 62, 68, 71, 77, 86, 92, 114, 138, 150, 167, 196, 199, 209
Photon Ionization 65
Photonic Applications 14
Photonic Band Gap 20
Photonic Crystal 7, 20, 98, 179
Photonic Crystal Waveguide 27
Photonic Integrated Circuits 33
Picosecond Laser 167
PI 224
PL Enhancement 74
PLE 224
Porous GaN 39
Porous Silicon 170, 249
Programmable Metallization Cell (PMC) 135
Pseudodirect Compound 164
Pseudosubstrate 221
Pulse Flow 108
Pump-Induced Refractive Index Change 206

Q
QED 1
Quantum Confinement Effect 224
Quantum Dash 173, 182
Quantum Dots 1, 17, 59, 71, 150, 173, 182
Quantum Well 33, 62, 95, 182, 209
Quantum Well Infrared Photodetectors 105
Quantum Well Intermixing 33
Quantum Wire 86, 182

R
Raman Scattering 23, 80, 215
RBS 153
Relative Photonic Efficiency 212
Resistance Changes 135
RF-MBE 39
Ridge Waveguide 30

S
Saturation Power 246
Scanning Electron Microscope (SEM) 42
Scanning Electron Microscopy (SEM) 86
Screen Printing 249
Self Assembly 117
Semiconductor 153
Semiconductor Laser 30, 173, 189
Shallow Trap Centers 161
Short Range Order 209
Si Nanocrystal 74
Si-O Stretching Vibrations 101
Si Substrate 120
Si(111) 39
Silicon Nanocrystals 196
Silicon Substrates 108
SiO_2-TiO_2 Systems 101
Size Dispersion 161
Sol-Gel Technique 11, 14
Solubility of Zinc 199
Structural Property 221
Structure 129
Surface Analysis 202
Surface Modification 74
Surface Morphology 86
Surface States 7

T
Tapered Waveguide 27
Ternary Pnictides 164
Thermal Annealing 77
Thermal Evaporation 68, 114, 249
Thick Film 101
Thin Film 11, 14
Threshold Analysis 36
Tilted Waveguide 36
TiO_2 176
Trap States 4

V
Vertical Deposition Method 20

W
WO_3 126

X
X-Ray Diffraction (XRD) 42, 80, 86, 153

Z
Zinc Oxide 199
ZnO 71
ZnO Nanostructures 68
ZnS Nanowires 114
ZnS:Er Quantum Dots 138
ZnS:Mn Quantum Dots 167

ISBN 0-87849-471-5, ISBN-13 978-0-87849-471-2
Advanced Materials Research Vol. 31
Electronically available at http://www.scientific.net